Proceedings in Marine Science 8

Estuarine and Coastal Fine Sediments Dynamics

INTERCOH 2003

J.P.-Y. Maa, L.P. Sanford and D.H. Schoellhamer (Editors)

Preface

The twenty-seven papers in this monograph are selected from the manuscripts submitted to the International Conference on Cohesive Sediment Transport (INTERCOH 2003) held at the Virginia Institute of Marine Science (VIMS), College of William and Mary, Gloucester Point, Virginia, USA, during October 1-4, 2003. The papers presented in this monograph represent topics ranging from basic research (*e.g.*, flocculation, erosion, deposition, consolidation) to practical applications (*e.g.*, simulation of turbidity maxima in estuaries, transport of cohesive sediment during dredging). All of the manuscripts received at least two external peer reviews, and many were revised prior to final acceptance. Because the obvious titles had already been used by the six monographs from previous INTERCOH meetings, it became necessary to add the conference name and year to the title for this monograph. Therefore, the title "Estuarine and Coastal Fine Sediment Dynamics - INTERCOH 2003" was selected.

Only ten days before the conference, Hurricane Isabel swept through North Carolina and Virginia. Wind and storm surge caused significant damage in Virginia and resulted in a week-long power outage at VIMS. The last hurricane to pass through this region with such destructive force occurred nearly 70 years ago. Perhaps serving as an appropriate reminder for the conference, Isabel also deposited a lot of cohesive sediment on the VIMS campus. Despite these extraordinary circumstances, and thanks in large part to the tremendous effort of the VIMS staff, the conference proceeded as scheduled with about 100 participants from all over the world.

Financial support from HydroQual Inc., HoHai University, Korea Ocean Research and Development Institute, National Cheng-Kong University, the U.S. Geological Survey, and the Virginia Institute of Marine Science made this conference possible. The time and resources contributed by each participant were equally critical to make INTERCOH 2003 a great experience in exchanging new knowledge and exploring new approaches for understanding cohesive sediment dynamics. Finally, we would like to extend our thanks to J.-I. Kwon, H.-K. Ha, J.-Y. Kim, B. Marshall and C. Hornsby for helping with the logistics of the conference, and to Susan Stein for her editing assistance.

Additional information about INTERCOH conferences and proceedings volumes, past and future, may be viewed at www.intercoh.com.

Jerome P.-Y. Maa
Virginia Institute of Marine Science
College of William and Mary

Lawrence P. Sanford
Horn Point Laboratory
University of Maryland Center for Environmental Science

David H. Schoellhamer
U.S. Geological Survey

Estuarine and Coastal Fine Sediments Dynamics
J.P.-Y. Maa, L.P. Sanford and D.H. Schoellhamer (editors)

Preliminary findings of a study of the upper reaches of the Tamar Estuary, UK, throughout a complete tidal cycle: Part I: Linking hydrodynamic and sediment cycles

Bass, S.J.[a], A.J. Manning[a,b] and K.R. Dyer[a]

[a] School of Earth, Ocean and Environmental Sciences, University of Plymouth, Devon, PL4 8AA, UK.
[b] HR Wallingford, Howbery Park, Wallingford, OX10 8BA, UK.

KEY WORDS
Turbidity maximum, stratification, floc size, settling velocity, concentrated benthic suspension, Tamar Estuary

Preliminary results are presented from an experiment in the turbidity maximum region of the Tamar Estuary, UK, to acquire detailed particle information of the suspension in relation to the main physical and biochemical driving processes throughout several complete tidal cycles. Results presented here focus on the relationship between the evolving suspension characteristics and physical mechanisms through one tidal cycle. The experiment took place over 5 days during April 2003. *In-situ* floc properties (including floc settling velocity, size, shape and effective density) were measured using the video-based INSSEV system. Profiles of full water column velocity, salinity, temperature and suspension concentrations were supplemented with detailed near bed measurements of turbulence and sediment concentrations. Measurements were made during several days approaching spring tides and the results exhibit a strong contrast in flood and ebb hydrodynamics which is reflected in the observed vertical distribution of sediment and particle characteristics. The flood tides were short and well-mixed with high values of turbulent shear stress causing rapid erosion and resuspension at the onset of the turbidity maximum. Suspension concentrations were relatively evenly distributed vertically reaching concentrations of 1.1 kg/m^3 at the INSSEV height of 0.5 m. In contrast ebb tides exhibited tidal straining and development of a concentrated benthic suspension layer with a lutocline in the

region of the INSSEV height. Concentrations at this height reached 1.4 kg/m^3 while the INSSEV sampling height was just below the lutocline. Particles within the turbidity maximum on the ebb tide were typically much larger than the flood, with up to 30% greater than 400 μm just inside the lutocline. Turbulent shear stress measurements during the ebb exhibited a significant reduction in the region of the lutocline due to sediment stratification.

1. INTRODUCTION

Predicting the mass transport and deposition of cohesive sediments is highly desirable in estuarine and coastal environments where fine particles play an important role in issues relating to, for example, pollution, benthic ecology, water clarity and sedimentation. From the stand-point of estuarine environmental management, measuring and predicting when during a tidal cycle mud is suspended or deposited is crucial. For instance, the phase of suspension concentration is vital in determining residual flux magnitudes and directions, benthic ecology will depend on when fine particles are deposited, or knowing times of suspended load transport may be necessary before discharging waste. This paper addresses in particular the phase relationship between estuarine cohesive suspension characteristics and hydrodynamics over a tidal cycle.

The behaviour of fine sediments is complicated in particular by their cohesive nature and tendency to form aggregates or flocs which are both larger and less dense than the individual constituent particles. As a consequence there are delays or lags in the response of the sediment properties to velocity, shear stress and turbulence. In an oscillating tidal current, phase differences may occur as a result of slow and variable settling velocities, advection of non-local sediment, varying bed yield strengths and the time taken for resuspended sediment to be mixed upwards through the water column. In relation to the tidal cycle the phase differences of settling velocity, floc density and concentration become important in controlling net transport magnitudes and directions (Bass *et al.,* 2002; 2003). This paper presents preliminary results of quantitative floc size and settling velocity, and concentration measurements with an emphasis on the evolving behaviour through the full tidal cycle. In particular the cycle in hydrodynamics and suspension characteristics are related to the evolution of floc settling velocity, size and density.

Observations of fine sediment suspensions suggest that, except in highly energetic conditions, most of the sediment mass occurs in flocs (Kranck and Milligan, 1992). The flocculation of particles is a function of the mechanisms which bring the particles into

contact (*e.g.* differential settling or turbulence) and the mechanisms that make them stick together (*e.g.* salinity or organic matter content) (van Leussen, 1988). Sediment concentration may also play a role in increasing flocculation. In addition to increasing particle collisions, turbulent shear may also act to break up aggregates (McCave, 1985) and various observations have demonstrated the role of shear stress in limiting the maximum floc size in both shelf (Berhane *et al.*, 1997; Hill *et al.*, 2001) and estuarine environments (Dyer *et al.*, 2002a, Manning, 2001).

The processes of aggregation and disaggregation are still not well enough understood to describe fully theoretically and at the moment predictions tend to rely on empirical generalisations. Until recently, lack of reliable floc measurements limited studies of the complex interactions between the factors affecting flocculation (shear, salinity, organic content and concentration) and floc characteristics. Laboratory experiments do not reliably represent field situations because of the difficulty of reproducing the chemical, physical and biological processes involved and *in-situ* measurements have historically been unreliable because of floc disruption when sampling (van Leussen, 1988). The recent advent of *in-situ* video techniques has allowed reliable, simultaneous measurements of floc size and settling velocity from which floc density may be estimated. Particle characteristics presented here were made using the low-intrusive INSSEV instrument (Fennessey *et al.*, 1994b) to measure *in-situ* floc settling velocity and size. These results are compared with near-bed measurements of vertical sediment concentration distribution, turbulence and currents throughout a complete tidal cycle. Detailed analysis of floc spectra is reported in the Part II companion to this paper (Manning *et al.*, in press). Such comprehensive data sets are still relatively sparse and will benefit cohesive sediment studies in general.

2. METHODS

Field data were acquired during a 5- day experiment from April 13th to 17th in the Tamar estuary in south-western England. The Tamar estuary is classified as a drowned-river valley, experiencing semi-diurnal tidal ranges of 4.7 m and 2.2 m at spring and neap tides respectively. Sediment in the estuary is predominantly composed of cohesive silts and clay admixtures supplied by river input. The experiment was in the turbidity maximum region near the Calstock boatyard (Fig. 1) which has been used for earlier experiments and its characteristics are well-documented (Uncles and Stephens, 1993). The channel width at the deployment site was 75 m. Throughout the experiment the tide ranged in height from about 0.5 m to 4.5 m with peak currents speeds of ~1 m/s. Data presented here represent results 3 days in advance of peak spring tides.

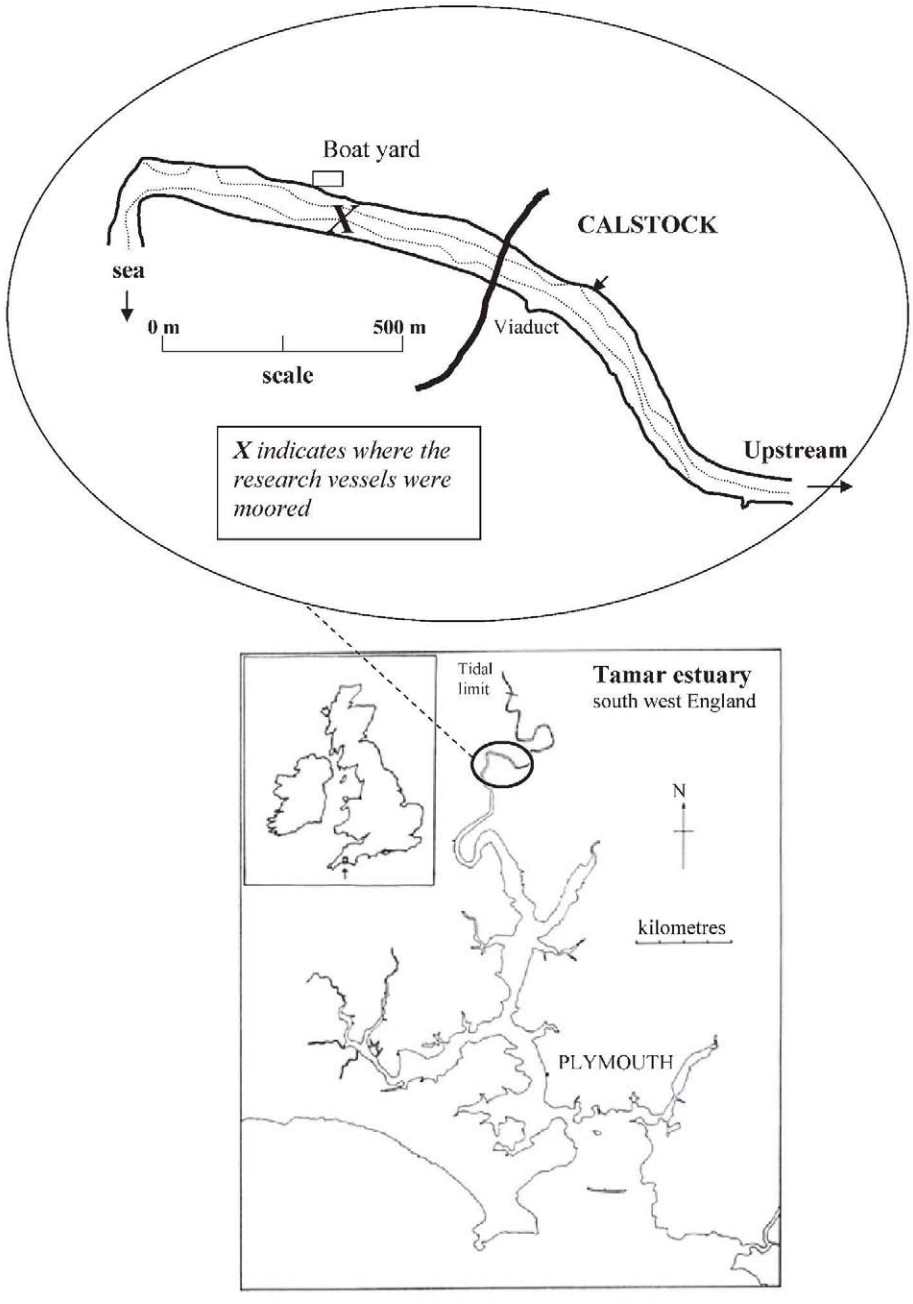

Fig. 1. Location diagram of the Tamar estuary showing the Calstock sampling station.

Instruments were mounted on a frame that was lowered to the bed from the moon pool of an anchored pontoon RP AMAP-1. The frame was positioned so that the instruments were facing the dominant alongstream flow. Results presented here were obtained from the instruments described below. High resolution near-bed mass concentrations were obtained using a vertical array of six Optical Backscatter Sensors (OBSs) from the POST system (Christie *et al.*, 1997) mounted on the frame from 0.05 to 0.98 m above bed. Calibration of the OBS took place on site using *in-situ* suspension samples. The POST system also included 4 2D electromagnetic current meters (EMCMs) arranged in pairs at 0.5 and 0.75 m to measure 3D components of flow. Two 3D Nortek acoustic doppler velocimeters (ADVs) mounted alongside OBSs at about 0.1 and 0.5 m provided detail of the turbulence and vertical distribution of current velocities in the lower boundary layer. Turbulent shear stress at the ADV heights were estimated using the turbulent kinetic energy approach (*e.g.*, Kim *et al.*, 2000).

Vertical profiles of salinity, temperature and suspension concentrations were obtained every 15 minutes using a Seabird Systems SBE 19-03 CTD together with a Downing OBS. Corresponding velocity profiles through the water column were obtained using a Valeport 108 mk III impeller current meter.

The INSSEV video system was used to measure floc settling velocity, size and floc populations. These quantities are measured manually after the deployments from the video monitor using initial image calibrations to convert to actual dimensions. Further details of floc data processing are given in Manning *et al.* (in press). During the experiment measurements were taken approximately every 15 minutes. Pumped water samples were obtained from 0.1 and 0.5 m above bed every half hour. Filtered samples were used to verify OBS and INSSEV estimates of suspended mass concentration and to estimate the percentage of organic matter content by loss-on-ignition tests.

3. RESULTS

3.1 Salinity and current velocity profiles

Depth profiles of current velocity and salinity over a tidal cycle on April 15th, 3 days before peak spring tides, are presented in Fig. 2, measurements starting half-way through the ebb tide. The shape of the tidal curve is asymmetric with a short flood (~5 hours) and long ebb (~7 hours) reflecting the decrease in depth as the wave moves up the estuary. Tidal height ranged from 0.5 to 4.5 m. The same measurements taken on adjacent days, April 14 and 16th, show a similar pattern in current and salinity measurements to those presented here.

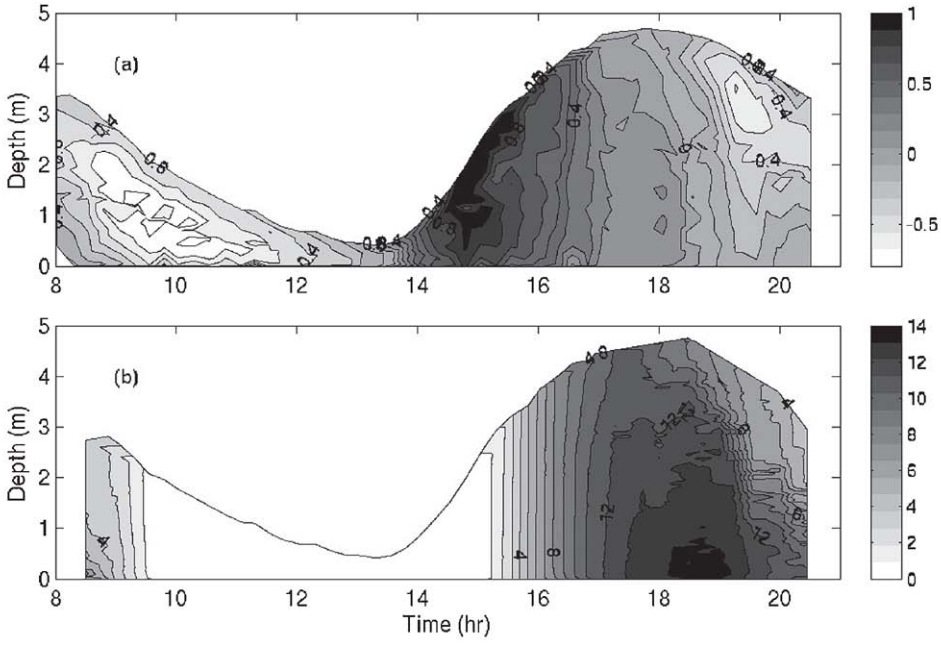

Fig. 2. Contour plot of (a) current velocities (m/s) and (b) salinity (psu) on April 15th.

The flood tide started at 13:30 h, coinciding with low water, and reaching current speeds of 1 m/s at the water surface. High water occurred at 18:00 h, 20 minutes after the start of the ebb tide at the water surface. The start of the ebb at the bed lagged the ebb at the surface by an hour. Depth profiles of salinity (Fig. 2b) show the water column as well mixed throughout the flood with salt water appearing at all depths at ~14:45 h. Peak salinities of about 14 psu were reached near the bed around high water.

Evidence of tidal straining on the ebb tide is apparent in the current and salinity profiles from 18:00 h on. The ebb started at the surface at 17:40 h, reaching the bed about an hour later and producing stratification in salinity. At 19:30 h, tidal-straining induced shear appears to have produced turbulent mixing towards the bed creating a minor peak in the ebb current speed near the bed with corresponding reduction in salinity at all depths below the halocline. The same pattern was repeated on adjacent days.

3.2 Turbidity maximum dynamics

Suspended sediment concentration profiles through the tidal cycle are presented in Fig. 3. Note that concentrations near the bed that appear inverted are an artefact of saturation of the optical sensor at concentrations above several kg/m^3 leading to an underestimate of concentration. While absolute magnitudes are suspect the results are useful for showing the general evolution of the vertical sediment distribution through a tidal cycle. Comparison with single height estimates of near-bed concentrations from both pumped samples and OBS mounted on the rig (Fig. 4a) show qualitatively similar results of relative concentration variations.

On the ebb tide the increase in suspended sediment concentrations at 9:00 h associated with the passage of the turbidity maximum occurred about half an hour before the disappearance of salt water. High concentrations of mud persisted for 3 hours so that the turbidity maximum occurred mostly within fresh water and just inside the tip of the salt intrusion.

On the flood tide sediment concentrations rose rapidly with current speed at 14:30 h leading the arrival of the salt intrusion at 14:45 h. The sediment started to settle as soon as current speeds slackened at about 15:15 h. With the appearance of salt water most of the sediment fell out of suspension fairly rapidly however elevated concentrations persisted for about 2 hours so that the turbidity maximum appeared mostly within the tip of the salt wedge. A minor peak in sediment concentration observed near the bed just after 16:00 h on the flood tide (seen in both Figs. 3 and 4a) was not apparently related to any increase in near-bed current shear suggesting advection of a concentrated near-bed muddy suspension layer.

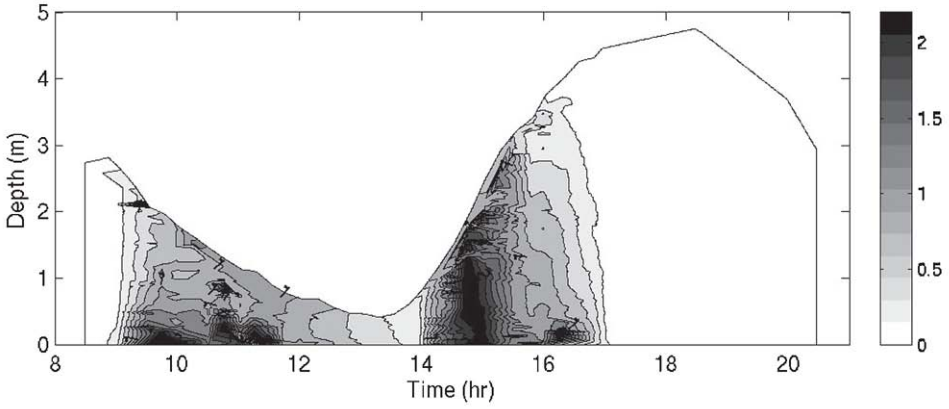

Fig. 3. Contour plot of suspended solids concentration (kg/m^3).

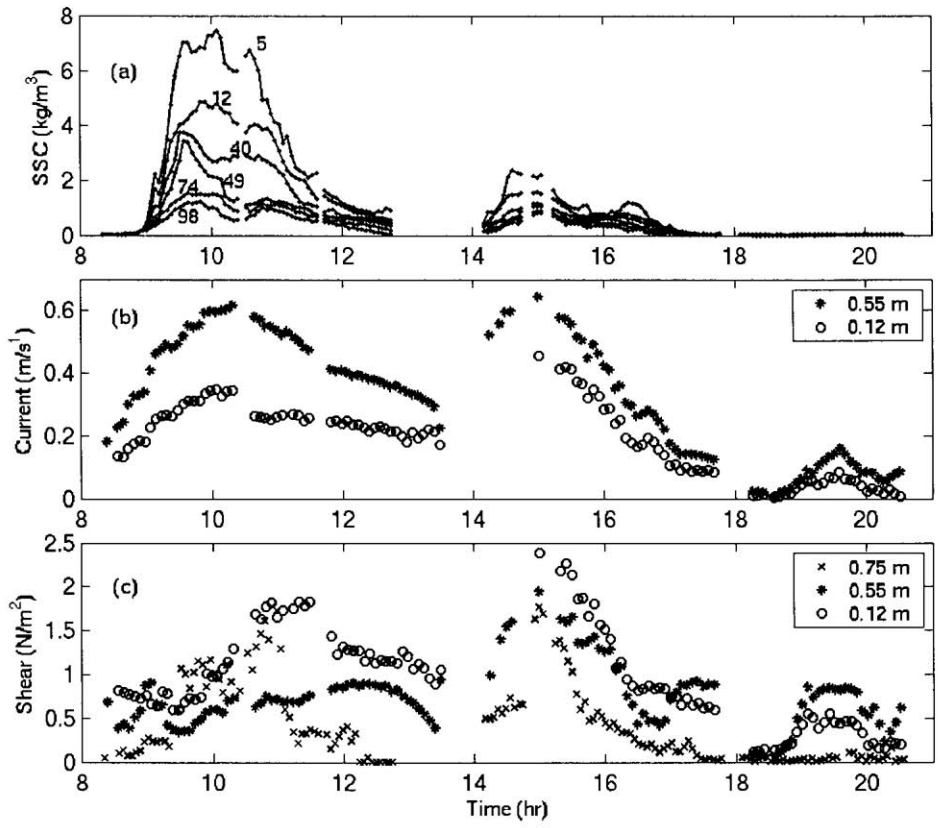

Fig. 4. (a) Optical backscatter estimates of suspension sediment concentration (SSC) from 0.05 to 0.98 m above bed (heights of the OBS are labelled in centimetres). (b) ADV measurements of current speeds at 0.1 and 0.55 m tide above bed. (c) Turbulent shear stress estimates at 0.75, 0.55 and 0.12 m above bed.

Corresponding current speeds from two ADVs at 0.12 and 0.55 m above bed are displayed in Fig. 4b. Gaps in the data appear at slack water (~14:00 and 18:00 h) when the instrument frame was turned to face into the along-stream flow. The latter half of the ebb in the morning exhibits a broad peak in current speed between 10:00 and 10:30 h reaching ~0.59 m/s at 0.55 m and ~0.32 m/s at 0.12 m above bed. On the flood tide the flow accelerated quickly reaching ~0.6 m/s at 0.55 m and ~0.44 m/s at 0.12 m

above bed within 1.5 hours of the start of the flood. The peak current speeds at 0.55 m were of similar value on both ebb and flood while peak current speeds at 0.12 m were about 0.1 m/s higher on the flood indicating greater bed shear stress. The start of the ebb tide in the evening in Fig. 4b shows a minor peak in currents speeds at about 19:30 h, also apparent in the Valeport velocity profiles in Fig. 2a discussed earlier, appears to be the result of mixing toward the bed induced by tidal straining.

Comparing current speeds with OBS estimates of concentration at 0.1 m, concentrations on the ebb tide increased and decreased in phase with current speeds. On the flood tide concentrations increased with current speeds reaching a peak concentration in phase with peak current speeds and exhibiting a settling lag.

The OBS estimates of sediment concentration from 0.05 to 0.98 m above the bed give more detail of the vertical distribution of sediment near the bed. The striking contrast in flood and ebb suspension conditions in the bottom 1 m is the higher concentrations below 0.5 m and large vertical gradient apparent on the ebb tide. Ebb tide concentrations at 0.05 m approached 8 kg/m^3 with a change in concentration of 6.5 kg/m^3 over 0.93 m (the distance between bottom and top OBS) suggesting the development of a Concentrated Benthic Suspension (CBS) layer during the ebb flow. In contrast flood tide concentrations reached 2.5 kg/m^3 with a 2 kg/m^3 difference over 0.93 m.

On the ebb tide the largest vertical gradient in sediment concentration occurred between the OBS at 0.05 and 0.12 m – about 3 kg/m^3 over 0.07 m equivalent to 40 kg/m^4 – which persisted for most of the duration of the turbidity maximum (Fig. 5). The gradient between the sensors located at 0.49 and 0.74 m (~8 kg/m^4) apparent at the beginning of the turbidity maximum reduced dramatically by an order of magnitude to less than 1 kg/m^4 while at the same time the vertical gradient between 0.4 and 0.49 m rose from ~8 kg/m^4 to 20 kg/m^4. These variations in gradients shown in Fig. 5 suggest development of a lutocline within the first half hour of the passage of the turbidity maximum initially somewhere between 0.49 and 0.74 m which then fell to a height between 0.4 and 0.49 m at about 10:15 h and persisted while concentrations in the turbidity maximum remained high. In contrast, the flood suspensions remained better mixed and vertical concentration gradients reached about 10 kg/m^4 between 0.12 and 0.05 m.

Turbulent kinetic energy (TKE) estimates of shear stress from the 2 ADVs located at 0.12 and 0.55 m above bed and the EMCMs at 0.75 m are shown in Fig. 4c. On the ebb tide in the morning turbulent shear stress was initially suppressed due to damping by high near-bed concentrations resulting in a lag with respect to ebb tidal current speeds. Throughout the passage of the turbidity maximum turbulence in the region of the lutocline at 0.55 m appears to be suppressed relative to turbulence closer to the bed

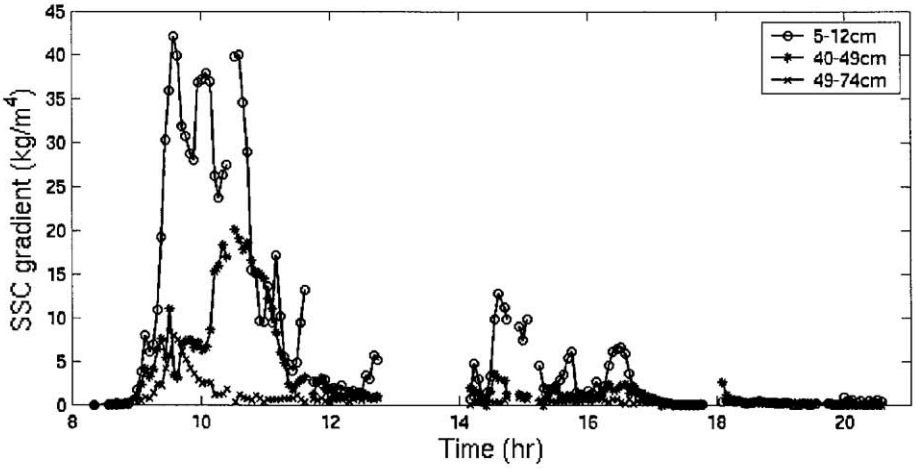

Fig. 5. Vertical gradients in suspended sediment concentration (SSC) between OBS at 0.05 and 0.12 m (circles), 0.4 and 0.49 m (stars), and 0.49 and 0.74 m (crosses).

at 0.12 m and further away (0.75 m) from the bed due to stratification by suspended sediment. Relative to the turbulent shear stress at 0.12 m and 0.75 m drag reduction at 0.55 m is particularly apparent during the high concentration gradients on the ebb tide when the upper ADV lay just above the lutocline from about 10:15 h. A reversal in ADV turbulent shear stress estimates occurred at about 17:00 h where the stress at 0.55 m was greater than that at 0.12 m associated with deceleration of the flood tide at the surface leading deceleration at the bed. A second reversal from 19:00-20:00 h coincided with turbulent mixing generated by shear from tidal straining at the start of the ebb tide in the evening. These results are consistent with previous measurements at this site showing drag reduction associated primarily with large vertical gradients in suspended sediment concentration (Dyer *et al.*, 2002a)

3.3 Particle characteristics

Mean particle size, settling velocity and effective density through the tidal cycle as measured using the INSSEV instrument are presented in Fig. 6. Details of particle spectra are discussed in Manning *et al.* (in press). Settling velocities and particle sizes were highest on the ebb tide reaching peaks simultaneously of about 3.8 mm/s and 250 μm respectively. These peaks in size and settling velocity coincided with peak sediment concentrations at the INSSEV height and correspond to the period when the INSSEV

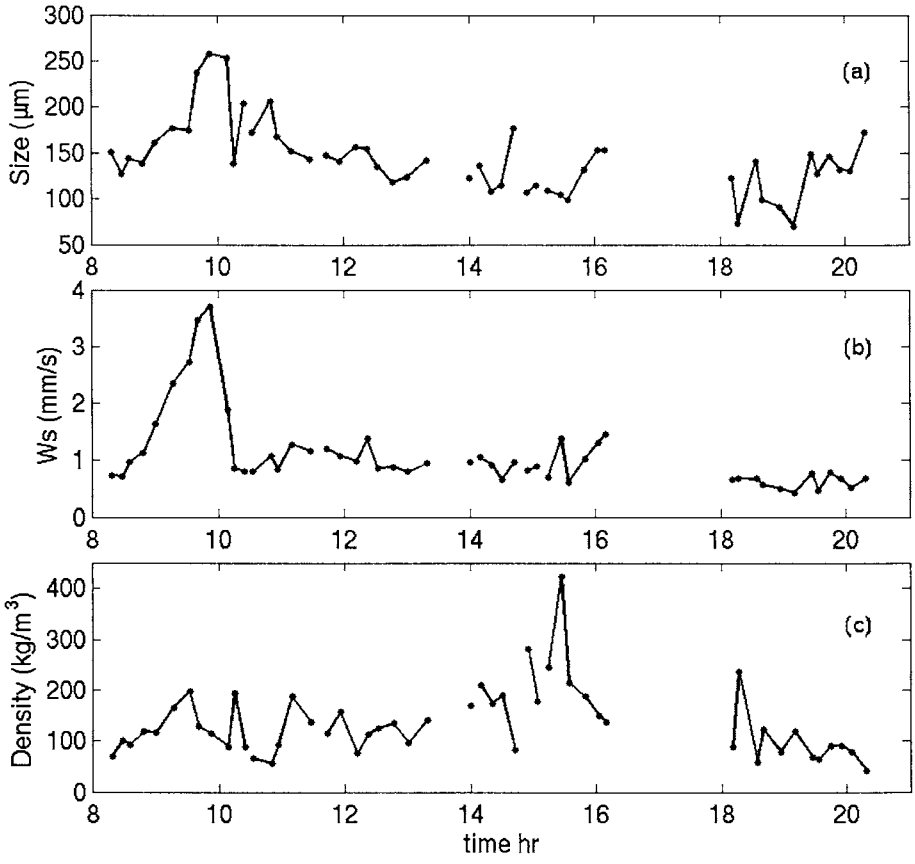

Fig. 6. Particle mean values of (a) equivalent spherical diameter, (b) settling velocity, w_s, and (c) effective density measured from the INSSEV samples.

sampling height was below the lutocline from about 9:30 to 10:15 h, thus maximum mean settling velocity and particle size are associated with particles within the CBS layer.

At the start of sampling around 8:00 h mean particle size was about 150 μm rising rapidly to the maximum value of 250 μm with increasing concentrations. After 10:15 h concentrations at the INSSEV height diminished while concentration gradients increased so that the samples were within the region of increased turbulence damping due to sediment stratification. Mean particle size also decreased rapidly from 250 to values around 200 μm and then followed a decreasing trend throughout the remainder

of the ebb tide and into the flood. The smallest mean particle size of 75 μm occurred just after high water after which an increasing trend is observed up to about 150 μm at the end of the sampling period mid-way through the evening ebb tide.

Mean settling velocity followed a pattern similar to mean particle size. Values started about 0.8 mm/s at 8:00 h and after reaching a maximum just before 10:00 h, settling velocity dropped sharply to values close to 1 mm/s through the remainder of the ebb and flood tide. A slight decrease to values around 0.8 mm/s is apparent from high water and the start of the ebb tide.

Smaller mean particle size through peak concentrations on the flood tide are possibly a result of breakdown of larger macroflocs upon resuspension with high current shear. Previous measurements at this location have shown that turbulent shear is the most effective mechanism controlling both floc formation and break-up (Dyer *et al.*, 2002b). Macroflocs, as referred to here adopt the definition of Manning (2001) as greater than 160 μm. Associated mean effective density (Fig. 6c) show increased values during the flood tide resuspension with the highest value occurring when particles had started to settle suggesting a hierarchy of settling with larger macroflocs settling out quickly as the current slackened and a higher proportion of smaller denser particles remaining in suspension. Outside of the turbidity maximum at the beginning of the ebb, the increasing trend in mean particle size with low effective densities and settling velocities reflects an increase in organic content measured from water samples.

4. CONCLUSIONS

The preliminary results presented here give a comprehensive picture of the evolution of particle characteristics and the dominant physical controls through a full tidal cycle. Within the turbidity maximum significant differences are apparent in suspension characteristics on the flood and ebb tides which are associated with the contrast in the near-bed hydrodynamics. On the flood tide rapid current acceleration and resuspension of sediment occurred at the onset of the turbidity maximum followed by advection. The flood tide suspension was characterised by sediment well-mixed vertically and a larger percentage of smaller, denser microfloc particles. During the passage of the turbidity maximum on the ebb tide a CBS layer developed causing significant turbulent shear reduction and sediment stratification. Particle populations within the CBS layer had characteristically larger mean particle sizes. Peak mean particle size coincided with peak mean settling velocity and peak sediment concentration at the sampling height. Particle populations during low concentrations outside of the turbidity maximum had typically low settling velocities and effective

densities with particle size spectra that appeared to be controlled by the relative increase in organic content. Further analysis will relate the evolution of mass settling fluxes and sediment transport to the varying particle populations. The results demonstrate the wide variability in near bed dynamics and range of particle size, settling velocity and density in the sediment population at one location at one height above bed. Such data provide valuable information for future model development and validation.

ACKNOWLEDGEMENTS

The authors are grateful for the assistance of the following people during the Tamar experiments: Peter Ganderton for his technical support; Ulrick Lumborg (University of Copenhagen) who coordinated the water sampling operation; Ben William for his continued help throughout the study and during the preparation of the RP-AMAP1; David Doxaran for coordinating the gravimetric analysis and the crew of the RV *Tamaris*. The experiment was funded by the Natural Environmental Research Council under contract No. NER/M/S/2002/00108.

REFERENCES

Bass, S.J., J.N. Aldridge, I.N. McCave and C.E. Vincent. 2002. Phase relationships between fine sediment suspensions and tidal currents in coastal seas. *Journal of Geophysical Research*, 107 (C10), 3146-3160.

Bass, S.J., I.N. McCave, J.M. Rees and C.E. Vincent. 2003. Estimating fine sediment fluxes in coastal seas: validity of point measurements. In: *Coastal Sediments '03* (CD-ROM), East Meets West Productions, Corpus Christi, Texas, USA.

Berhane, I., R.W. Sternberg, G.C. Kineke, T.G. Milligan and K. Krank. 1997. The variability of suspended aggregates on the Amazon Continental Shelf. *Continental Shelf Research*, 17(3), 267-285.

Christie, M.C., C.P. Quartley and K.R. Dyer. 1997. The development of the POST system for *in-situ* intertidal measurements. *The 7th International Conference On Electrical Engineering in Oceanography*, Publication No. 439, 39-45.

Dyer, K.R., A.J. Bale, M.C. Christie, N. Feates, S. Jones and A. J. Manning. 2002a. The turbidity maximum in a mesotidal estuary, the Tamar Estuary, UK: I. Dynamics of suspended sediment. In: *Fine Sediment Dynamics in the Marine Environment.* Winterwerp, J.C. and C. Kranenburg (eds.), Elsevier, Amsterdam, 203-218.

Dyer, K.R., A.J. Bale, M.C. Christie, N. Feates, S. Jones and A.J. Manning. 2002b. The turbidity maximum in a mesotidal estuary, the Tamar Estuary, UK: II. The floc properties. In: *Fine Sediment Dynamics in the Marine Environment.* Winterwerp, J.C. and C. Kranenburg (eds.), Elsevier, Amsterdam, 219-232.

Fennessey, M.J., K.R. Dyer and D.A. Huntley. 1994a. Size and settling velocity distributions of flocs in the Tamar Estuary during a tidal cycle. *Netherlands Journal of Aquatic Ecology*, 28, 275-282.

Fennessey, M.J., K.R. Dyer and D.A. Huntley. 1994b. INSSEV: an instrument to measure the size and settling velocity of flocs *in-situ*. *Marine Geology*, 117, 107-117.

Hill, P.S., G. Voulgaris and J.H. Trowbridge. 2001. Controls on floc size in a continental shelf bottom boundary layer. *Journal of Geophysical Research*, 106(C5), 9533-9542.

Kim, S.-C., C.T. Friedrichs, J.P.-Y. Maa and L.D. Wright. 2000. Estimating bottom stress in tidal boundary layer from acoustic doppler velocimeter data. *Journal of Hydraulic Engineering*, 126(6), 399-406.

Kranck, K. and T.G. Milligan. 1992. Characteristics of suspended particles at an 11-hour anchor station in San Francisco Bay, California. *Journal of Geophysical Research*, 97, 11373-11382.

Manning, A.J. 2001. A Study of the Effect of Turbulence on the Properties of Flocculated Mud. Ph.D. thesis, University of Plymouth.

Manning, A.J., S.J. Bass and K.R. Dyer. (In press). Preliminary findings of a study of the upper reaches of the Tamar Estuary, UK, throughout a complete tidal cycle: Part II. *In-situ* floc spectra observations. In: *Estuarine and Coastal Fine Sediment Dynamics – INTERCOH 200.* Maa, J.P.-Y., L.P. Sanford and D.H. Schoelhammer (eds.), Elsevier, Amsterdam (this volume).

McCave, I.N., 1985. Mechanics of deposition of fine-grained sediments from nepheloid layers. *Geo-Marine Letters*, 4, 243-245.

Uncles, R.J. and J.A. Stephens. 1993. Nature of the turbidity maximum in the Tamar Estuary, UK. In: *Estuarine Coastal Shelf Science*, 36, 413-431.

van Leussen, W. 1988. Aggregation of particles, settling velocity of mud flocs: a review. In: *Physical Processes of Estuaries.* Dronkers, J. and W. van Leussen (eds.), Springer, Berlin, 347-403.

Estuarine and Coastal Fine Sediments Dynamics
J.P.-Y. Maa, L.P. Sanford and D.H. Schoellhamer (editors)

Preliminary findings of a study of the upper reaches of the Tamar Estuary, UK, throughout a complete tidal cycle: Part II: *In-situ* floc spectra observations

Manning, A.J. [a, b], S.J. Bass [a] and K.R. Dyer [a]

[a] University of Plymouth, School of Earth, Ocean and Environmental Sciences, Coastal Processes Research Group, Portland Square Building, Plymouth, Devon, PL4 8AA, UK
[b] HR Wallingford Ltd., Howbery Park, Wallingford, Oxfordshire, OX10 8BA, UK

KEY WORDS
Flocculation, turbulent shear, floc size, settling velocity, effective density, INSSEV instrument, suspended particulate matter, Tamar estuary, turbidity maximum, mass settling flux

A series of field experiments funded by the Natural Environmental Research Council were conducted in the upper reaches of the Tamar estuary (UK), which placed the measurements within the tidal trajectory of the turbidity maximum. The aim of the study was to examine how the distribution of floc characteristics evolved with respect to changes in the turbulent shear stress, suspended concentration and biological constituents, throughout a complete tidal cycle. The main objective of the experiment was to measure simultaneous floc properties (which included: floc size, shape, settling velocity, effective density, porosity and floc dry mass) using the optical INSSEV instrument and associated hydrodynamic components, *in-situ*, throughout a complete tidal cycle. This paper reports the preliminary findings of the measurements made on the 15th April 2003, during a spring tide. During the ebb a concentrated benthic suspension layer formed in close proximity to the bed producing a peak concentration of 4.2 g/l and a maximum shear stress of about 1.5 N/m^2. The more dynamic flood produced a shear stress which exceeded the peak ebb stress by 0.15 N/m^2. This in turn meant that the suspended matter was more evenly mixed throughout the entire water column on the

flood. Local salinity values ranged from 14 at high water, down to completely fresh at low water. A total of 24 INSSEV floc samples were collected on the ebb flow and a further 34 floc populations were obtained on the flood. A combination of a shear stress of 0.38 N/m^2 and a concentration of 4.2 g/l, produced the optimum flocculation conditions which was signified by a bi-modal floc distribution. The microflocs represented 25% of the population, but only 9% of the dry floc mass. These microflocs were generally dense, slow settling aggregates, with typical effective density values of 80-1550 kg/m^3 and settling velocities ranging from 0.03-1.1 mm/s. The macroflocs, which constituted the second mode, contained 91% of the floc mass, one third of which were flocs over 400 μm in spherical-equivalent diameter. These macroflocs had individual settling velocities ranging between 2.2 to 7 mm/s. This translated into the macrofloc fraction constituting 98% of the total mass settling flux.

1. INTRODUCTION

The behaviour and depositional characteristics of estuarine fine-grained sediments is complicated by their cohesive nature and potential to flocculate. Turbulent shear has been identified from both recent field studies by Dyer *et al.* (2002), and laboratory experiments conducted by Manning and Dyer (1999), as the most effective aggregational mechanism in controlling both floc growth and break-up. However, the process of mud flocculation is still not understood well enough to be fully described theoretically. This is primarily due to a lack of reliable *in-situ* measurements, which are required to quantify and parameterise the different aspects of flocculation. Field settling tubes such as the "Owen tube" (Owen, 1976) are highly disruptive to the very fragile floc structures. *In-situ* photography and laser particle sizers, although less intrusive, only provide a measure of floc size with no indication of floc density or settling rate. The recent advent of low intrusive *in-situ* video based instrumentation has provided a reliable tool whereby, the simultaneous measurements of floc size and settling velocity can be made from within a turbulent estuarine water column. However, due to the low number of reliable *in-situ* video floc samplers in existence, comprehensive data sets from such instruments are still a rarity.

This paper describes the preliminary results from measurements of floc spectra which were acquired on the 15th April 2003 in the Tamar estuary (UK) during a series of Natural Environmental Research Council (NERC) funded experiments. The aim of this field study was to build on earlier experiments which were conducted at this location on a sub-tidal cycle time scale, in particular the results of the main EC MAST III

COSINUS project experiment (Berlamont, 2002; Winterwerp *et al.*, 2002) and the earlier studies of Fennessy *et al.* (1994a), by examining how the distribution of floc characteristics evolve with respect to changes in the turbulent shear stress, suspended matter concentration and biological constituents, during a tidal cycle. The main objective of the experiment was to measure simultaneous floc properties and hydrodynamic components, *in-situ*, throughout a complete tidal cycle. The floc characteristics of particular interest included: floc size, shape, settling velocity, effective density, porosity and floc dry mass. The overall scope of the data, concepts of the experiment and how mean floc properties varied in response to the estuarine hydrodynamics throughout a tidal cycle, are presented in the companion Part I paper in this volume (Bass *et al.*). Whereas this paper reports and compares quantitatively, examples of detailed flocculation spectral characteristic at selected points in the tidal cycle. Also, examples of floc images, together with their respective floc properties, will be used to qualitatively illustrate specific floc types from which a floc population is composed.

2. METHOD

2.1 Experimental site

The sampling was conducted in a straight channel section in the upper reaches of the mesotidal Tamar estuary (south-west England), near Calstock Boat Yard (Fig. 1). This placed the measurements within the tidal trajectory of the turbidity maximum. The mean tidal range varies between 3.2 m at neaps through to about 4.7 m at spring tides. The estuary width at the sampling site was about 75 m, and the low water depth was approximately 0.6 m. The Tamar is topographically dendritic in shape and has numerous meanders, with wide mud flats exposed at low water. The estuary is classified as a flood dominant, partially-mixed ria (Dyer, 1997). From source to estuary mouth it is approximately 75 km in length. However, the tidal influence only extends 31 km inland. It was expected that considerable erosion and settling would occur throughout a tidal cycle, and that processes would be dominated more by vertical fluxes driven by the bed boundary conditions, rather than internal shear.

2.2 Data acquisition

Through depth profiles of salinity, temperature and suspended solids concentration were taken at least every 15 minutes using a Seabird Systems Seacat SBE 19-03 CTD together with a Downing optical backscatter gauge (OBS). Corresponding variations in

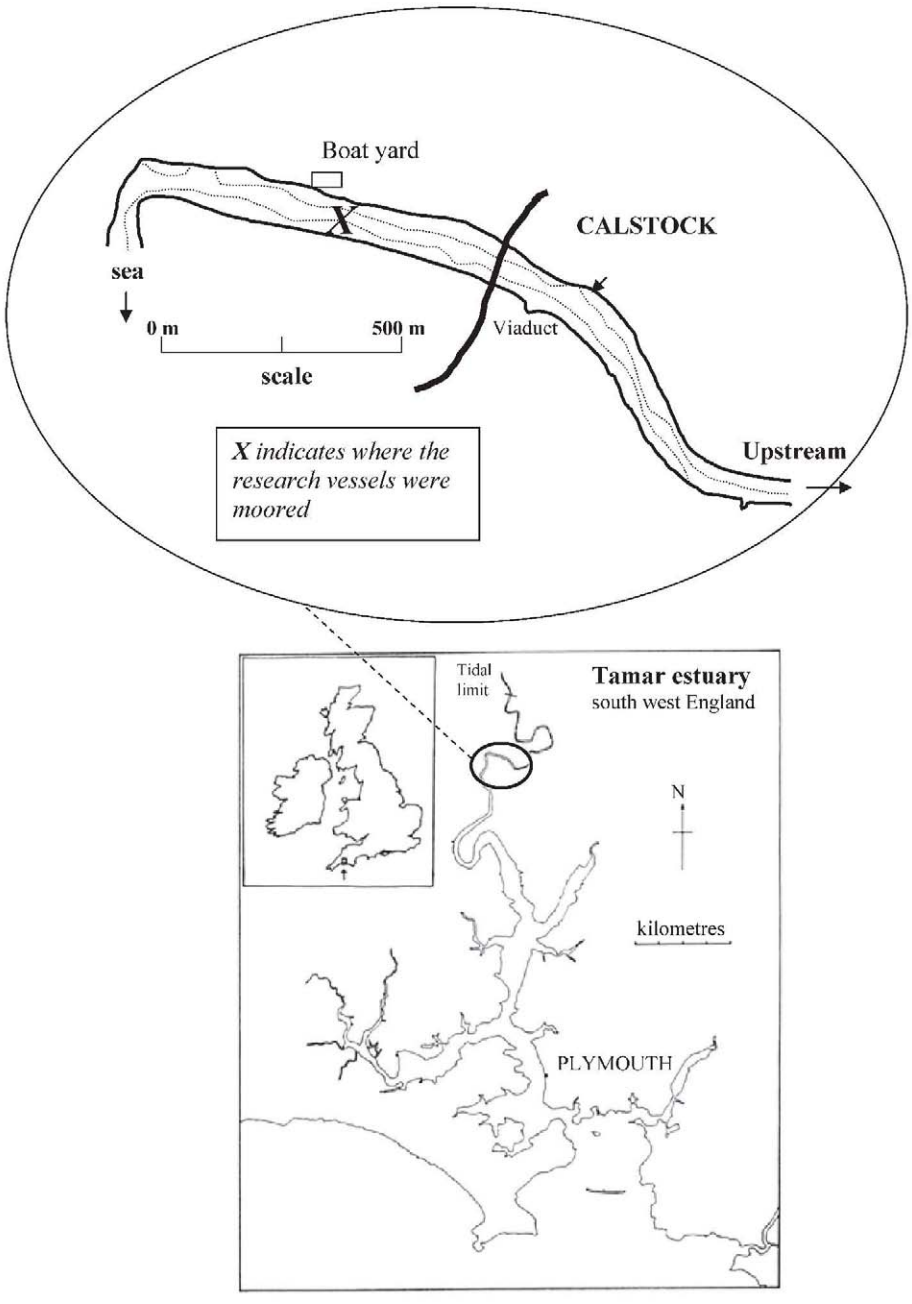

Fig. 1. Location diagram of the Tamar estuary showing the Calstock sampling station.

the mean flow velocity through the water column were provided by a Valeport 108 mk III impeller current meter. Water samples for suspended solids calibration were extracted by a Peristaltic pump at heights of 10 cm and 50 cm above the estuary bed. All filtration was conducted on site. Estimates of the amount of organic content present in the suspended matter were deduced from loss-on-ignition tests.

Typically 80% of the turbulent energy generated by the flowing estuarine water occurs within the bottom 10-15% of the water column (van Leussen, 1994). Detailed measurements of the near-bed hydrodynamical structure were gathered at an acquisition rate of 18 Hz (and low pass filtered at 5 Hz) using the POST – Profile Of Sediment Transport - system (Christie *et al.*, 1997). The system consisted of four 2 cm diameter discus shaped electro-magnetic flow meters (EMCMs), and five OBSs, two of which were mounted close to the EM sensors. The EM sensors were arranged in pairs to measure the streamwise u, cross-channel v, and vertical w components of the flow, at both 0.5 m and 0.75 m above the bed. Changes in water depths were monitored using a Druck 2 bar absolute pressure transducer.

Flocs, although stable in flowing turbulent water, easily break apart when sampled in response to additional shear created during acquisition (Eisma *et al.*, 1997). Therefore, the primary floc data was acquired at a nominal height of 0.5 m above the estuary bed, using the INSSEV – IN-Situ Settling Velocity - instrument (Fennessy *et al.*, 1994b). The sampling apparatus comprises two interconnected chambers which allow flocs to be sampled directly from within a turbulent water column, whilst creating minimal disruption to the observed flocs. A high resolution monochromatic Pasecon tube miniature underwater video camera located in an aperture in the lower settling chamber wall viewed the settling flocs. The floc images were recorded by an analogue S-VHS video recorder which produces a practical lower resolution limit of 20 μm.

The POST sensors were mounted on a vertical pole, which was positioned adjacent to the INSSEV sampling unit, on a heavy bed frame. Figure 2 illustrates the complete instrumentation bed frame configuration awaiting deployment. The instrumentation bed frame was deployed through the moon-pool of a four-point anchored pontoon, the *RP AMAP-1*, from a mid-channel position. All surface electronics were housed in the laboratory of the *RV Tamaris*, a Rotork Sea Truck, which was tied along side the pontoon. To prevent vortex shedding occurring at the open ends of the INSSEV stilling chamber, the rig was aligned to within $\pm 5^{\circ}$ with the dominant streamwise flow. This was achieved through the use of control ropes attached to the outside of the frame to control orientation during lowering and a digital 2-axis tilt sensor which provided a direct readout of rig positioning on the bed. The rig sat on the bed for the entire duration, sampling data from within an Eulerian reference frame, with the exception of

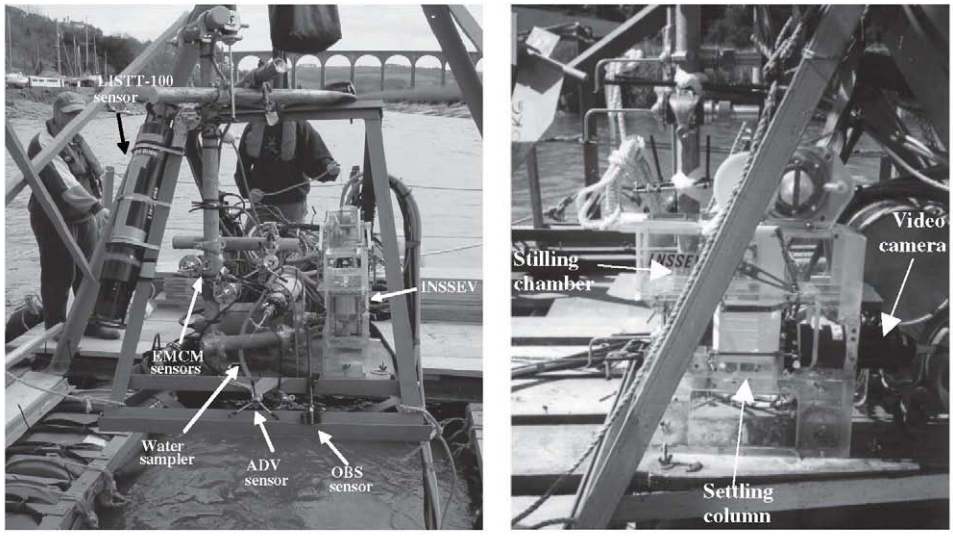

(a) (b)

Fig. 2. INSSEV, EMCM, ADV and OBS sensors mounted on the estuarine bed frame – (a) front view and (b) side view.

recovery to replace the INSSEV settling column water with a solution of different salinity, or to re-align the rig as the tidal direction changed.

2.3 Floc data analysis

Floc settling velocities and aggregate dimensions were obtained directly from the video recordings (post-processed manually) and translated into the real size dimensions by applying a video image calibration factor (Manning and Fennessy, 1997). Dimensions were measured both along the axis in the direction of settling (D_Y), and the axis normal to it (D_X), from which a height:width ratio could be determined.

To aid in the interpretation of the INSSEV floc size data, the two orthogonal floc dimensions were then converted into a spherical-equivalent floc diameter, D, by equation 1.

$$D = (Dx \cdot Dy)^{0.5} \quad (1)$$

Each floc population was also divided into twelve size bands, to aid in the interpretation of floc property distributions across each spectrum.

The direct analysis of floc density, for example by settling extracted flocs in sucrose solutions, is not possible, because even if the very fragile aggregates survive the sampling process, the floc porewater may be replaced by the sucrose solution. However, the INSSEV measurement technique means that the individual floc size and rate of fall are measured simultaneously. Therefore, if a floc is settling within the viscous Reynolds region (*i.e.,* when the particle Reynolds number, R_e, < 0.5), the effective density (ρ_e) for each floc could be obtained by applying a Stokes' Law relationship:

$$\rho_e = (\rho_f - \rho_w) = \frac{Ws\ 18\mu}{D^2\ g} \tag{2}$$

where μ the dynamic molecular viscosity of water and g is gravity. The effective density, also referred to as density contrast, is the floc bulk density (ρ_f) less the ambient water density (ρ_w). The water density was calculated from measured salinity and water temperature data using the International Equation of State of Sea Water, 1980 (Millero and Poisson, 1981). For instances where the R_e exceeded 0.5, the Oseen modification (Schlichting, 1968), as advocated by ten Brinke (1994), was applied to Eq. 2 in order to compensate for the increased inertia created during settling.

Stokes' Law assumes the settling particles are small spheres, but observations have shown that flocs are often by no means spherical. However both Alldredge and Gotschalk (1988) and Gibbs (1985) found from direct measurements, that organic composite aggregates whose shape varied from spherical, such as long comets with height:width ratios of to 1.6:1, had settling rates very similar to those of nearly spherical particles. Therefore, the implementation of a spherical equivalent diameter in Eq. 2 is valid.

The entire floc spectrum of each INSSEV sample was measured. A series of algorithms derived by Fennessy *et al.* (1997), were then applied to the INSSEV floc size, settling velocity and effective density data, and used to calculate individual values of floc porosity and floc dry mass. It was assumed that the flocs originated from a constant sample volume of water within the decelerator chamber, it was then possible to transform the INSSEV derived floc mass into a Suspended Particulate Matter (SPM) concentration spectral distribution. The INSSEV reference sample volume was 400 mm^3 of fluid and is prescribed by: the nominal video image width (4 mm), a optical 1 mm depth of field, and the height of the INSSEV stilling chamber (100 mm).

2.4 Hydrodynamic data analysis

The EM flow sensors produced a continuous record of velocity time-series files, each file covering 4096 values, about 3 minutes and 47 seconds in duration. Reynolds classic statistical decomposition of unsteady flow was applied to each data file and used to separate the turbulent fluctuating components from the burst-mean value. The deviations from the mean taken over each file record duration define the turbulent velocity components.

As all three orthogonal components of the flow were measured, turbulent shear stresses were calculated using the *turbulent kinetic energy* method. This approach is much less sensitive to slight sensor misalignment, than both the Reynolds stress and logarithmic profile techniques (Heathershaw, 1979). Values of turbulent kinetic energy, E (Stapleton and Huntley, 1995), were calculated for each file by:

$$E = 0.5\ \rho_w \left(\overline{u'^2} + \overline{v'^2} + \overline{w'^2}\right) \tag{3}$$

where ρ_w is the ambient water density, and $\overline{u'^2}$, $\overline{v'^2}$ and $\overline{w'^2}$ are the three turbulent variance components. Assuming the turbulent energy production equals the energy dissipation (Nakagawa and Nezu, 1975), the turbulent shear stress (τ) can be regarded as being proportional to the turbulent kinetic energy (Soulsby, 1983), and was calculated by Eq. 4.

$$\tau = 0.19 \cdot E \tag{4}$$

3. RESULTS

3.1 Main variables

The tidal sampling run conducted on the 15th April 2003 commenced at 08:10 British Standard Time (BST), which was 2 hours after predicted local high water on an ebb flow. The 4 m deep water column was partly stratified with a surface salinity of 4.7, gradually increasing to 12 in the proximity of the estuary bed (Fig. 3A). By 09:45 the water column was fresh throughout for the latter stages of the ebb. The asymmetric distortion in the tidal curve, primarily due to the estuary topography and the effects of tidal straining, were seen to have prolonged the ebb beyond the predicted time of low water at 12:16 by a further 1 hour and 15 minutes.

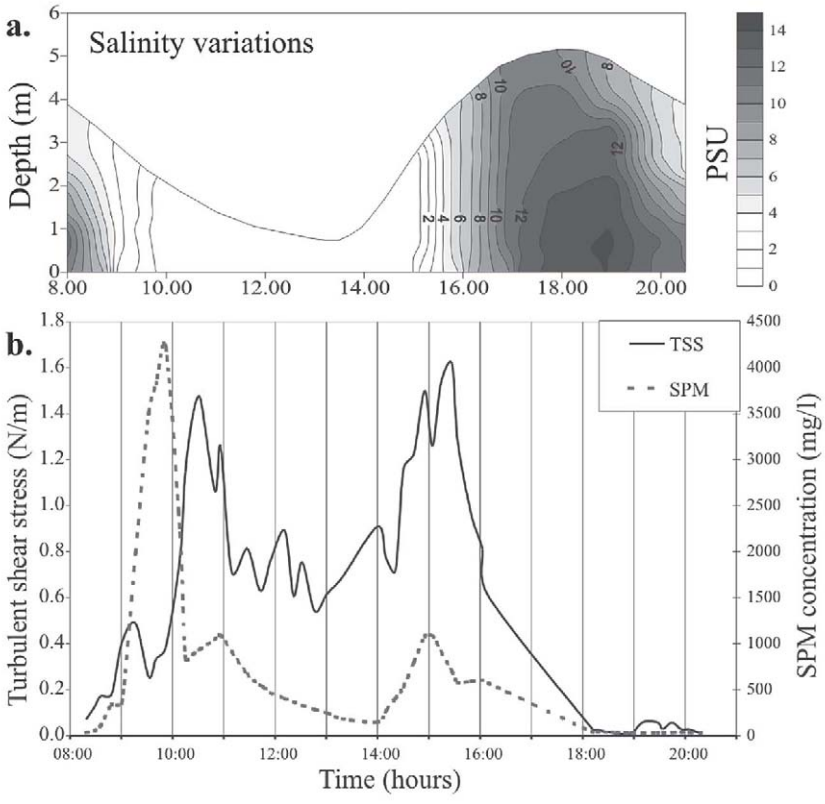

Fig. 3. Time series of variations in: (a) full depth salinity, (b) turbulent shear stress and suspended particulate matter concentration (both at 0.5 m above the bed) for the spring tide on the 15th April 2003.

The experimental deployments experienced high spring tidal conditions, and the macro-tidal range produced a highly dynamic water column. The near-surface current attained an ebb velocity of about 0.8 m/s by 10:30 and this coincided with a peak turbulent shear stress of ~1.5 N/m^2 which developed at the nominal INSSEV sampling height of 0.5 m above the estuary bed (Fig. 3). SPM concentration rose in response to the accelerating flow and reached a maximum concentration of 4.2 g/l (at the INSSEV height) by 09:52. Further inspection of the complete OBS array showed that a Concentrated Benthic Suspension (CBS) layer had developed by this time. The INSSEV sampling apparatus was completely immersed within the CBS for the periods between

9:20-10:10 and 10:40-11:00, where the lutocline rose to a height of 55-70 cm above the estuary bed. The suspended concentration rapidly decreased in the region above the lutocline. The formation of the CBS layer had the net effect of creating turbulence damping within the layer, and accounted for the observed reduction in turbulent shear within the CBS. Drag reduction was also instigated at the lutocline. The dynamics of CBS layers have been examined from both field observations and laboratory simulations, by Dyer *et al.* (2004) and Mory *et al.* (2002), respectively.

The salt intrusion arrived at the sampling location on the flood as a well-mixed vertical wall at 15:45 with a salinity of 2. By 19:00 hr the near bed salinity had increased to 14, reducing in the upper one metre, to a salinity of 3. The flood water advancement in the upper estuary had the appearance of a constant thickness saline layer pushing under a wedge of fresher water. A maximum surface flow velocity was achieved just over one hour into the flood, and this was nearly double the peak velocity observed during the ebb. The maximum turbulent shear stress on the flood (0.5 m above the estuary bed) exceeded the peak ebb shear stress by 0.15 N/m^2. Initial observations suggested that the amount of particulate matter in suspension was severely restricted on the flood, with a near bed concentration of only 1.1 g/l recorded at 15:00. However, depth profiles of concentration revealed that the flood-dominant tide had mixed the suspended matter more evenly throughout the entire water column.

A more detailed study of the phase relationships which develop between the hydrodynamic activity and the entrained solids are reported in Bass *et al.* (this volume).

3.2 Floc properties

A total of 24 INSSEV floc samples were collected on the ebb flow prior to local Low Water (LW) at 13:15. Figure 4 shows the floc characteristics for sample 15-04. The population comprised 309 individual flocs, 300 of which were under 220 μm in diameter. The remaining nine flocs were all 340 μm in size and had a settling velocity of 2.3 mm/s. Sample 15-04 was collected at 08:49 (LW- 4:26), just prior to the turbidity maximum reaching the Calstock station, which accounted for a low concentration of 340 mg/l. Of the total mass concentration, 84% was evenly distributed throughout the 80-120 μm Size Band Three (SB 3), and 160-240 μm (SBs 5 and 6) flocs (Fig. 4c). Manning (2001) defines macroflocs as those flocs with spherical-equivalent diameters which exceed 160 μm. When comparing the settling velocities, the macrofloc fraction fell at an average rate of 1.85 mm/s, whereas the smaller sized flocs (*i.e.*, the microflocs) were settling at a velocity three times slower. At this point in the ebb, the salinity at the INSSEV sampling height was only 3.5, and this indicated that the majority of the retreating salt wedge had passed through the upper estuary. The low turbulent condi-

tions (shear stress = 0.18 N/m^2) had permitted the more organic-rich (organic content = 19%) cohesive particles in suspension to flocculate, and this was reflected in the flocs throughout SBs 3-7, possessing high porosities (91-97.5%), and effective densities generally under 100 kg/m^3.

By 09:30, the turbidity maximum was ebbing seaward through the Calstock location. Prior to this, the shear stress at the INSSEV height was steadily rising in response to the faster flowing ebb current. Sample 15-09 (Fig. 5) was obtained at 09:52 (LW-3:23) from within the CBS layer which had formed close to the bed during the advection of the main body of the turbidity maximum. The SPM concentration was 4.2 g/l at 0.5 m above the bed, and the turbulent energy damping associated with this high suspended concentration level suppressed the turbulent shear to only 0.38 N/m^2. A very distinctive change had occurred within the floc population. The earlier fairly even floc size distribution, had been replaced by a distinctly bi-modal population, both modes demonstrating very different floc characteristics. The first mode was composed of microflocs up to 129 μm in diameter. This was 246 individual flocs which represented a quarter of the total population. The remaining 75% of the floc population were large macroflocs ranging from 171-607 μm in diameter and these aggregates had individual settling velocities ranging between 2.2 to 7 mm/s. In comparison to sample 15-04, the maximum floc size had now doubled.

A further 34 floc populations were obtained using the INSSEV instrument on the flood. The stronger flood current velocities meant the returning turbidity maximum was more homogeneously mixed throughout the water column, which in turn produced a peak SPM concentration (at 0.5 m) of about 1 g/l at 14:55 (LW+1:40). The corresponding shear stress was 1.5 N/m^2 and the distribution of floc mass for Sample 15-31 (Fig. 6) was positively skewed, with the primary mode occurring at SB 6 (200-240 μm). The maximum floc size had risen to 263 μm, an increase of 50 μm from those measured 55 minutes earlier in the flood, although the macroflocs were less than half the diameter of those observed within turbidity maximum on the ebb. Settling velocities spanned from 0.06-2.9 mm/s.

At local high water slack (18:34), the SPM had fallen below 40 mg/l and the turbulent shear stress was only 0.01 N/m^2. At this point in the tide, the INSSEV instrument only captured 55 individual flocs to form sample 15-49 (Fig. 7). Floc sizes for 54 of the aggregates ranged between 47-223 μm. The one exception was a solitary floc with a spherical-equivalent diameter of 444 μm and it was settling at a velocity of 4 mm/s.

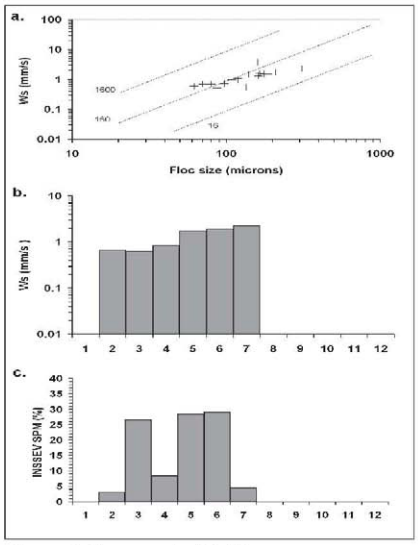

Figure 4. Floc sample 15-04

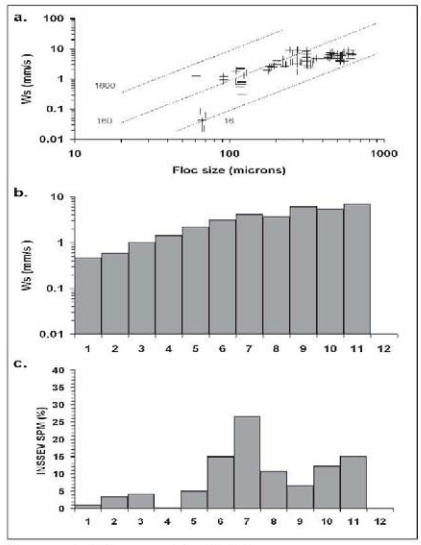

Figure 5. Floc sample 15-09

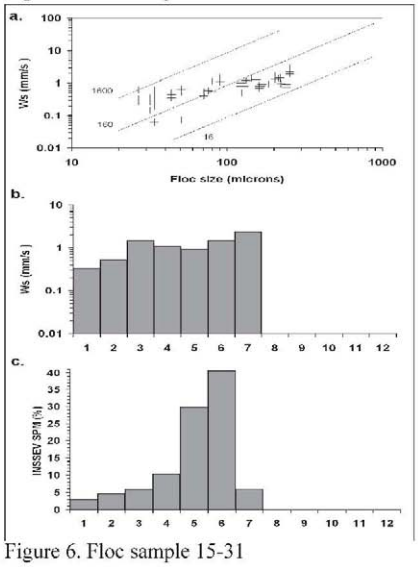

Figure 6. Floc sample 15-31

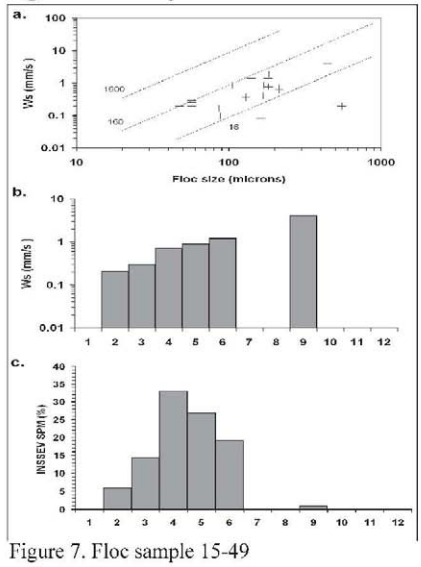

Figure 7. Floc sample 15-49

Size Band	1	2	3	4	5	6	7	8	9	10	11	12
Floc size (μm)	< 40	40 -80	80 -120	120 -160	160 -200	200 -240	240 -320	320 -400	400 -480	480 -560	560 -640	> 640

Figs 4-7. (a) illustrates the relationships between floc size and settling velocities of individual flocs, with diagonal full lines showing the effective density (kg/m^3); (b) shows the size band distribution of settling velocity; and (c) shows the size band distribution of SPM concentration.

4. DISCUSSION AND CONCLUSIONS

Manning (2004a) has identified a turbulent shear stress region of 0.32-0.42 N/m^2 which tends to provide the optimum level of constructive inter-particulate collisions which most effectively stimulates the production of fast settling macroflocs. On many occasions these turbulent conditions can produce dual modes in the size-settling velocity distributions of specific floc populations (Manning, 2004b). Whereby a separate clustering of macroflocs and microflocs develop, and these are separated by only a minor number of transitional aggregates. This was the case for floc sample 15-09 (Fig. 5), where the stress and concentration were 0.38 N/m^2 and 4.2 g/l, respectively. Although a quarter of the population were microflocs, in terms of dry floc mass, the microfloc fraction only constituted 9% of the total content. These microflocs were generally dense slow settling aggregates, with typical effective density values of 80-1550 kg/m^3 (corresponding microfloc median ρ_f = 277 kg/m^3) and settling velocities ranging from 0.03-1.1 mm/s (corresponding microfloc median Ws = 0.6 mm/s). This cluster of small slow settling flocs microflocs represents a portion of the population which had not been incorporated into higher order flocs. These microflocs could be either: awaiting aggregation, the result of break-up, or a fraction that would not aggregate.

The macroflocs, which constituted the second mode, contained the remaining 91% of the floc mass, one third of which constituted flocs over 400 μm in diameter. These macroflocs had individual settling velocities ranging between 2.2 to 7 mm/s, with a median Ws = 3.1 mm/s. This translates into the macrofloc fraction constituting 98% of the total mass settling flux, which equalled 18 $g/m^2/s$. One can hypothesise that the particles in suspension have flocculated into their most efficient spectral distribution, *i.e.,* in terms of the number of fast settling macroflocs produced. The combined influence of concentration and turbulent shear on the control of the macrofloc properties agrees with hypotheses offered by both Puls *et al.*, (1988), and Kranck and Milligan (1992).

Previous studies at the Calstock site by Manning and Dyer (2002a) have shown that the suspended sediments comprising the turbidity maximum during spring tide conditions, typically processed total carbohydrate concentrations which were 5-7 times greater than within the suspended matter located outside the main body of the turbidity maximum. The high abundance of these natural adhesives, in particular extra-cellular polymeric substances, could also partly account for the high proportion of the suspended matter remaining as fast settling macroflocs within the turbidity maximum due to increased collision efficiency.

There was a particularly wide range in floc effective density throughout the sample 15-31 population (Fig. 6a). There were flocs of the same size, which had a wide range of settling velocities and effective densities. It was also evident that aggregates with the same settling velocity, could display distinctly different densities and sizes. This can be partly explained in terms of the composition of the matter in suspension. The resultant floc property spectrum are then a response to the high level of turbulent activity producing high intensity inter-particle collisions. At this point in the tidal cycle, water sampling revealed a sudden rise in the organic content (up to 40%) in the mid to upper section of the water column. This was primarily large amounts of vegetation trapped in the residual circulation of the estuary, and this matter headed the flood advance of the turbidity maximum. One could speculate that the lower density of the macrofloc fraction of sample 15-31 (all under 70 kg/m^3) could be attributed to their primarily organic composition. These macroflocs were 90% porous. In contrast, the predominantly mineral based microflocs were 7-40% porous and had effective densities ranging from 200-1550 kg/m^3.

The data obtained from INSSEV is both quantitative and qualitative. The qualitative is a description of the form of the flocs and how they change in both time and space. In contrast to other floc sampling devices, INSSEV utilises an optical miniature underwater video camera to obtain the floc data from the settling column, and in turn this provides high quality visual information on the flocs directly under examination (Manning and Dyer, 2002b).

During periods of the tidal cycle when observations were made outside the turbidity maximum, the particulate matter remaining in suspension tended to be over 25% organic, and hence the flocs had a different structure, *e.g.*, a number of the macroflocs were slower settling (Ws ~1.8-2.3 mm/s) and very low effective density (ρ_e < 45 kg/m^3) flocs. These flocs had an organically linked microfloc chain preceding a trailing upper small macrofloc core. In their entirety these aggregates resemble a "seahorse" (Fig. 8).

Within the turbidity maximum, the fastest settling flocs were mainly, cluster-types which were ragged in appearance (Fig. 9a) displaying Dx and Dy of 460 μm and 600 μm, respectively. These macroflocs fell at a rates of 6-10 mm/s. However, the other macrofloc captured in the same frame (Fig. 9b) shows that the joining of two aggregates only 270 μm in diameter, produced a floc with similar settling characteristics to those of the single large cluster macrofloc (Fig. 9a).

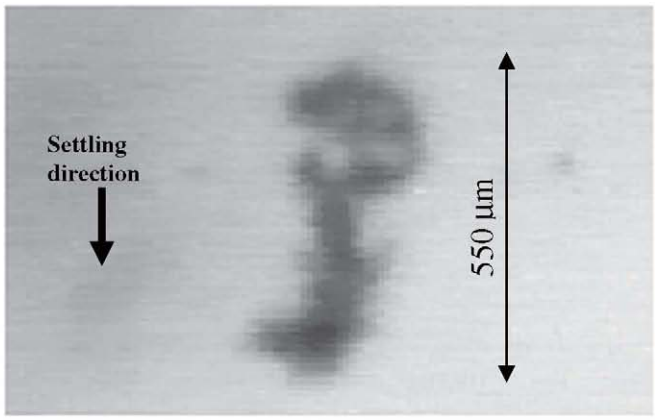

ig. 8. A small, slow ettling stringer type floc vhich resembles a sea- orse.

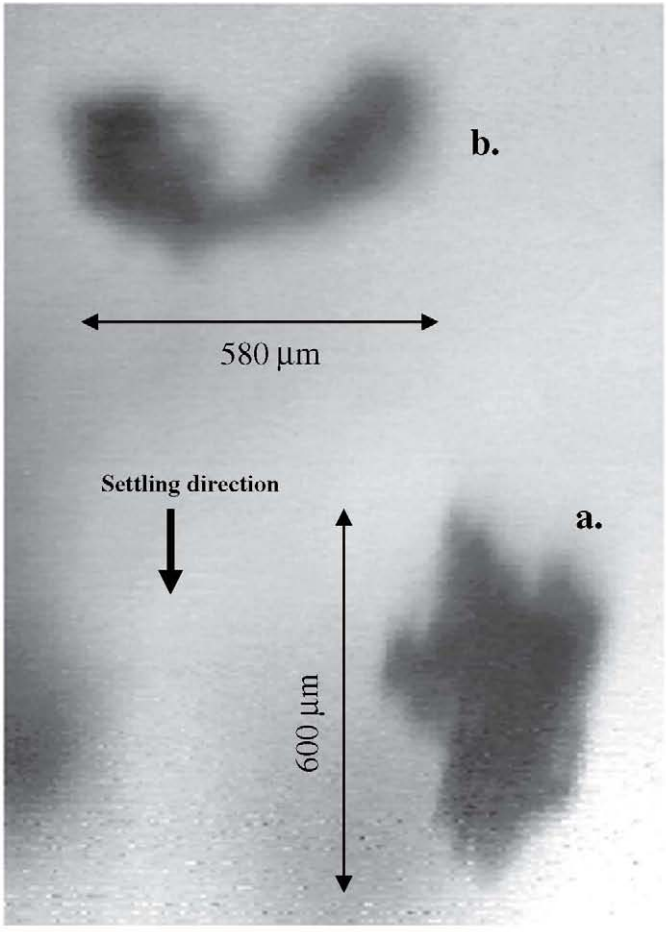

Fig. 9. (a) A ragged cluster-type macrofloc and (b) a simple stringer composed of two macroflocs possibly bonded by sticky organic fibres.

In summary, the preliminary findings from this study have shown that the distribution of both cohesive particulate mass and how fast it settles, changes rapidly throughout a tidal cycle. A knowledge of these depositional flux spectra are a prime requirement for accurate estuarine sediment transport modelling (*e.g.,* Petersen *et al.*, 2002), and these trends can only be observed by low intrusive instruments such as INSSEV, which can estimate floc effective density (through simultaneous size and settling velocity observations) of each individual floc from a respective population. Without this type of measurement, it is not possible to apportion the SPM concentration with any confidence between the microfloc and macrofloc groups. It is not possible to accurately assess either settling velocity or effective density variations within a floc population, by the use of underwater photography or laser-based particle sizers such as a LISST type instrument (Agrawal and Pottsmith, 2000), particularly within the important zones of highly concentrated mud suspensions (> 2-4 g/l).

ACKNOWLEDGEMENTS

The authors would like to thank the following persons who assisted during the Tamar estuary experiments: Peter Ganderton for his technical support; Ulrik Lumborg (University of Copenhagen) who coordinated the water sampling operation; Ben Williams for his continued help throughout the study and during the preparing of the RP-AMAP1; David Doxaran for coordinating the gravimetric analysis, and the crew of the RV Tamaris. The Tamar estuary experimental programme was funded by the NERC under contract No.NER/M/S/2002/00108. The preparation of this paper was partially funded by HR Wallingford Ltd. (UK), and the DEFRA / EA Joint Flood and Coastal Defence Research & Development Programme in Fluvial, Estuarine and Coastal Processes: Estuary Process Research (EstProc) project (under contract No. FD1905/CSA5966).

REFERENCES

Agrawal, Y.C. and H.C. Pottsmith. 2000. Instruments for particle size and settling velocity observations in sediment transport. *Marine Geology*, 168 (1-4), 89-114.

Alldredge, A.L. and C. Gotschalk. 1988. *In-situ* settling behaviour of marine snow. *Limnology and Oceanography*, 33, 339-351.

Bass, S.J., A.J. Manning and K.R. Dyer. This volume. Preliminary findings from a study of the upper reaches of the Tamar Estuary, UK, throughout a complete tidal cycle: Part I. Linking sediment and hydrodynamic cycles. In: *Estuarine and Coastal Fine Sediment Dynamics – INTERCOH 2003*. Maa, J.P.-Y., L.P. Sanford and D.H. Schoellhamer (eds.), Elsevier, Amsterdam, this volume.

Berlamont, J.E. 2002. Prediction of cohesive sediment transport and bed dynamics in estuaries and coastal zones with integrated numerical simulation models. In: *Fine Sediment Dynamics in the Marine Environment.* Winterwerp, J.C. and C. Kranenburg (eds.), Elsevier, Amsterdam, 1-4.

Christie, M.C., C.P. Quartley and K.R. Dyer. 1997. The development of the POST system for *in-situ* intertidal measurements. *The 7th International Conference On Electrical Engineering In Oceanography*, (London, England). Publication No. 439, 39-45.

Dyer, K.R., 1997. *Estuaries: A physical introduction.* 2nd Edition, Wiley & Sons Ltd., Chichester, 195 pp.

Dyer, K.R., A.J. Bale, M.C. Christie, N. Feates, S. Jones and A.J. Manning. 2002. The turbidity maximum in a mesotidal estuary, the Tamar Estuary, UK. Part II: The floc properties. In: *Fine Sediment Dynamics in the Marine Environment.* Winterwerp, J.C. and C. Kranenburg (eds.), Elsevier, Amsterdam, 219-232.

Dyer, K.R., M.C. Christie and A.J. Manning. 2004. The effects of suspended sediment on turbulence within an estuarine turbidity maximum. *Estuarine, Coastal and Shelf Science*, 59, 237-248.

Eisma, D., K.R. Dyer and W. van Leussen. 1997. The *in-situ* determination of the settling velocities of suspended fine-grained sediment – a review. In: *Cohesive Sediments: 4th Nearshore and Estuarine Cohesive Sediment Transport Conference.* Burt, N., R. Parker and J. Watts (eds.), John Wiley & Son, Chichester, 17-44.

Fennessy, M.J., K.R. Dyer and D.A. Huntley. 1994a. Size and settling velocity distributions of flocs in the Tamar Estuary during a tidal cycle. *Netherlands Journal of Aquatic Ecology*, 28, 275-282.

Fennessy, M.J., K.R. Dyer and D.A. Huntley. 1994b. INSSEV: an instrument to measure the size and settling velocity of flocs *in-situ*. *Marine Geology*, 117, 107-117.

Fennessy, M.J., K.R. Dyer, D.A. Huntley and A.J. Bale. 1997. Estimation of settling flux spectra in estuaries using INSSEV. In: *Cohesive Sediments: 4th Nearshore and Estuarine Cohesive Sediment Transport Conference.* Burt, N., R. Parker and J. Watts (eds.), John Wiley & Son, Chichester, 87-104.

Gibbs, R.J. 1985. Estuarine flocs: their size settling velocity and density. *Journal of Geophysical Research*, 90 (C2), 3249-3251.

Heathershaw, A.D. 1979. The turbulent structure of the bottom boundary layer in a tidal current. *Geophysical Journal of the Royal Astronomical Society*, 58, 395-430.

Kranck, K. and T.G. Milligan. 1992. Characteristics of suspended particles at an 11-hour anchor station in San Francisco Bay, California. *Journal of Geophysical Research*, 97 (C7), 11373-11382.

Manning, A.J. 2001. *A study of the effects of turbulence on the properties of flocculated mud.* Ph.D. Thesis. Institute of Marine Studies, University of Plymouth, 282 pp.

Manning, A.J. 2004a. The observed effects of turbulence on estuarine flocculation. In: *Sediment Transport in European Estuaries.* Ciavola, P., M. B. Collins and C. Corbau (eds.), *Journal of Coastal Research, Special Issue,* SI 41, 90-104.

Manning, A.J. 2004b. Observations of the properties of flocculated cohesive sediment in three western European estuaries. In: *Sediment Transport in European Estuaries*, Ciavola, P., M. B. Collins and C. Corbau (eds.), *Journal of Coastal Research, Special Issue,* SI 41, 70-81.

Manning, A.J. and K.R. Dyer. 1999. A laboratory examination of floc characteristics with regard to turbulent shearing. *Marine Geology*, 160, 147-170.

Manning, A.J. and K.R. Dyer. 2002a. A comparison of floc properties observed during neap and spring tidal conditions. In: *Fine Sediment Dynamics in the Marine Environment.* Winterwerp, J.C. and C. Kranenburg (eds.), Elsevier, Amsterdam, 233-250.

Manning, A.J. and K.R. Dyer. 2002b. The use of optics for the *in-situ* determination of flocculated mud characteristics. *Journal of Optics A: Pure and Applied Optics, Institute of Physics Publishing*, 4, S71-S81.

Manning, A.J. and M.J. Fennessy. 1997. *INSSEV (In Situ Settling Velocity instrument) - 1.3: Operator Manual.* Internal Report for Institute of Marine Studies, University of Plymouth, 25 pp.

Millero, F.J. and A. Poisson. 1981. International one-atmosphere equation of state seawater. *Deep-sea Research*, 28 (A), 625-629.

Mory, M., N. Gratiot, A.J. Manning and H. Michallet. 2002. CBS layers in a diffusive turbulence grid oscillation experiment. In: *Fine Sediment Dynamics in the Marine Environment.* Winterwerp, J.C. and C. Kranenburg (eds.), Elsevier, Amsterdam, 139-154.

Nakagawa, H. and I. Nezu. 1975. Turbulence in open channel flow over smooth and rough beds. *Proceedings of the Japan Society of Civil Engineering*, 241, 155-168.

Owen, M.W. 1976. *Determination of the settling velocities of cohesive muds.* Wallingford, England: HR Wallingford, Report No. IT 161, 8 pp.

Petersen, O., H.J. Vested, A.J. Manning, M.C. Christie and K.R. Dyer. 2002. Numerical modelling of mud transport processes in the Tamar Estuary. In: *Fine Sediment Dynamics in the Marine Environment.* Winterwerp, J.C. and C. Kranenburg (eds.), Elsevier, Amsterdam, 643-654.

Puls, W., H. Kuehl and K. Heymann. 1988. Settling velocity of mud flocs: results of field measurements in the Elbe and the Weser Estuary. In: *Physical Processes in Estuaries.* Dronkers, J. and W. van Leussen (eds.), Springer-Verlag, Berlin, 404-424.

Schlichting, H. 1968. *Boundary-layer theory.* McGraw-Hill, New York, 747p.

Soulsby, R.L. 1983. The bottom boundary layer of shelf seas. In: *Physical Oceanography of Coastal and Shelf Seas.* Johns, B. (ed.), Elsevier, New York, 189-266.

Stapleton, K.R. and D.A. Huntley. 1995. Sea bed stress determinations using the inertial dissipation method and the turbulent kinetic energy method. *Earth Surface Processes and Landforms*, 20, 807-815.

ten Brinke, W.B.M. 1994. Settling velocities of mud aggregates in the Oosterschelde Tidal basin (The Netherlands), determined by a submersible video system. *Estuarine, Coastal and Shelf Science*, 39, 549-564.

van Leussen, W. 1994. Estuarine macroflocs and their role in fine-grained sediment transport. Ph.D. Thesis, University of Utrecht, The Netherlands, 488pp.

Winterwerp, J.C., A.J. Bale, M.C. Christie, K.R. Dyer, S. Jones, D.G. Lintern, A.J. Manning and W. Roberts. 2002. Flocculation and settling velocity of fine sediment. In: *Fine Sediment Dynamics in the Marine Environment.* Winterwerp, J.C. and C. Kranenburg (eds.), Elsevier, Amsterdam, 25-40.

Estuarine and Coastal Fine Sediments Dynamics
J.P.-Y. Maa, L.P. Sanford and D.H. Schoellhamer (editors)

Aggregation and breakage rates in the flocculation of estuarine cohesive sediments

Neumann, L. E. and T. Howes

Division of Environmental Engineering, School of Engineering, The University of Queensland, St Lucia Qld 4072 Australia

KEY WORDS
Flocculation, collision efficiency, breakage rate, population balance.

A Couette device was used to flocculate estuarine sediments from the Brisbane River, Australia. The evolution of flocculation was monitored on-line using the Lasentec Focused Beam Reflectance Method (FBRM), a particle sizer based on laser reflectance. The flocculation experiments were performed under different shears and salinities to evaluate the influence of those parameters on the flocculation and breakage rates.

The experimental data was used with a population balance model to evaluate the collision efficiency and the breakage rates. The population balance considered fluid shear as the only aggregation mechanism and splitting and erosion as the breakage mechanisms. The collision efficiency and breakage rates for both mechanisms were obtained by solving the population balance model for different experimental conditions.

The collision efficiency was found to decrease as the shear rates increase, while the breakage rates increase with the shear. The collision efficiency ranged between 0.2 – 0.7 with a shear variation of 8.5 – 28.35 s^{-1}. The breakage rate coefficient ranged from 1.1 – 2.7 $cm^{-1}s^{-1}$ in the splitting mechanism and 0.0016 - 0.0072 $cm^{-1}s^{-1}$ in the erosion mechanism.

The experiments using different salinities demonstrated that the collision efficiency increases slightly with salinity. The breakage coefficients are independent of the salinity suggesting that the shear strength does not depend on the salinity.

1. INTRODUCTION

The cohesive sediments found in estuaries are usually in the form of flocs formed under varied conditions. The transport of these sediments depends on their size and settling velocity, which are linked to the Floc Size Distribution (FSD). The changes in the size distribution depend on the rates of flocculation, breakage and deposition of the system. These factors are dependent on the local shear stress, salinity, organic content and other biological factors. While the qualitative influence of these parameters, such as an increase of shear reducing the mean size of the flocs, is known, there are no quantitative measurements of the influence of those parameters on flocculation and breakage rates.

Population balances have been used to study flocculation in several systems, such as polystyrene suspension (Spicer and Pratsinis, 1996) and activated sludge (Biggs and Lant, 2002). They also have been applied to the modelling of aggregation and settling in stormwater ponds (Krishnappan and Marsalek, 2002) and also proposed to model the behaviour of cohesive sediments (Lick and Lick, 1988). In the polystyrene and activated sludge systems, experimental data was used to solve the inverse problem of the population balance. This allowed for the calculation of experimental parameters such as collision efficiencies and breakage rates and to quantify the influence of parameters such as shear on the flocculation.

This paper presents a Population Balance Model (PBM) used with experimental data to quantify the influence of shear and salinity on the flocculation of cohesive sediments. The sediments were flocculated in a Couette device and the evolution of the FSD was tracked using a laser reflection device. The model presented here can be used with the data to extract the collision efficiencies and breakage rate under different conditions. These parameters allow the use of the PBM to predict the flocculation of cohesive sediments.

2. EXPERIMENTAL SET UP

The experimental apparatus used in the flocculation experiments is shown in Fig. 1. The apparatus consists of a FBRM particle sizer, a Couette device, a sampling cell and a motor/controller.

A Couette device consists of two concentric cylinders with a constant gap between them. One or both of the cylinders can be rotated, producing several flow types. When the outer cylinder is rotated, the flow is either laminar or turbulent and the transition

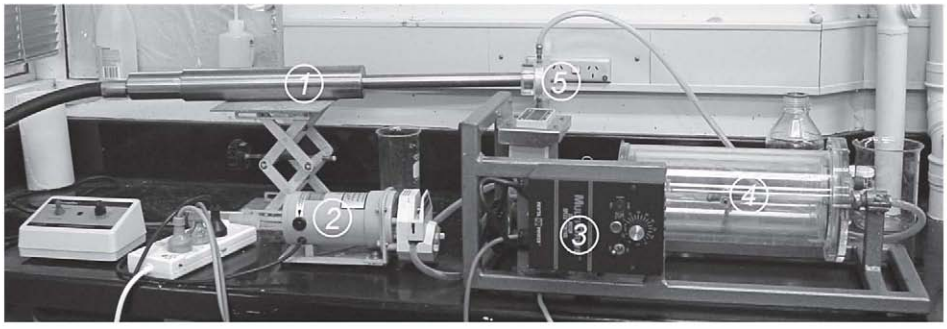

Fig. 1. Schematic view of experimental set-up. (1. FBRM; 2. Peristaltic pump; 3. Motor/Tachometer; 4. Couette device; 5. Sampling cell).

speed depends on the fluid properties and the apparatus geometry. If the inner or both cylinders are rotated several different flows can be produced (Andereck *et al.*, 1986). In a narrow gap Couette with laminar flow there is small variation of the shear stress throughout the gap between the two cylinders.

In this study, the inner cylinder was fixed, while the outer one rotates, because in this case the transition from laminar to turbulent flow happens at a higher transitional angular velocity ω_T than when the inner cylinder rotates. The transition velocity is given as (Kaufmann, 1963)

$$\omega_T = r_o \frac{\mathrm{Re}_c \mu}{(r_o - r_i)\rho} = \frac{1900.\mu}{r_o(r_o - r_i)\rho} \tag{1}$$

where Re_c is the critical Reynolds number and r_o and r_i are the outer and inner cylinder radius.

The outer cylinder had an internal radius of 65 mm and the inner one had an external radius of 60 mm, resulting in a gap of 5 mm and the theoretical maximum velocity is 5.85 s^{-1} (55.86 rpm). However experiments with dye injection shown that the flow remained laminar with velocities up to 6.80 s^{-1} (65 rpm).

The length of the outer cylinder was 300 mm and both cylinders were made of acrylic tubing. The length to gap ratio should be as high as possible to minimize the impact of end effects, which can cause secondary flows in both ends of the device (Ives and Bhole, 1975). The sampling points were located in the middle of the stationary cylinder, diametrically opposed to each other. This ensured that the sampling points were located in an area remote from the end effects.

The particles were pumped through the sampling cell using a peristaltic pump placed downstream to minimise the effects of floc breakage with a flow rate of 1.21 cm^3/s (Re_{tube} = 192.6, $diameter_{tube}$ = 8 mm) being used. This flow was high enough to avoid the large flocs being deposited inside the tube and small enough to minimise floc breakage inside the tube, before the pump.

The floc size was evaluated using a Focused Beam Reflectance Method (FBRM, Lasentec Inc., Redmond) model M500, with software version 6, build 12. Its measuring principle consists of a focused laser beam, rotating at 75 rad/s while describing a circle of 8.4 mm in diameter. When the focal point intercepts a particle, the probe measures the back scattered light. The product of the velocity of the beam and the duration of the pulse produces a chord length. A more detailed description of the instrument can be found elsewhere (Law *et al.*, 1997; Ruf *et al.*, 2000).

The FBRM then produces a Chord Length Distribution (CLD), instead of a particle size distribution such as in laser diffraction instruments. Although these two different distributions are related, they don't have a straightforward relationship. The FBRM can be used in very high particle concentrations and it does not make any *a priori* assumptions about the particles' sizes, while laser diffraction does assume that the particles are hard spheres. As the flocs have a structure far from spherical and are porous, the laser diffraction results are somewhat biased, as its FSD represents the population of solid spheres that would produce the measured diffraction pattern. The diffraction pattern produced on the measurement of the flocs is affected by the edges of particles as well as the possibility of multiple scattering. The particle shape can affect laser diffraction results, when the particles are not spherical in shape (Gabas *et al.*, 1994; Heffels *et al.*, 1996; Naito *et al.*, 1998). CLD does not make any assumption regarding the particle shape while laser diffraction will show the flocs as having an "equivalent diameter."

The FBRM has an option that allows the user to change the interpretation of the back reflected signal, choosing between a "Fine" (F) or "Coarse" (C) electronics. When a non smooth surface such as a floc is scanned, the reflected signal may be discontinued at edges or rough points in the particle surface. The F electronics might interpret the discontinuity as two different particles, while the C electronics would see them as one. The C electronics however tend to overlook the fines, so here the F electronics was used in all experiments.

The manufacturer recommends that the focal point position should be kept at a position .02 mm inside the instrument window. Moving the focal point inside the suspension has the effect of increasing the number of counts and this procedure is applied in many studies (Monnier *et al.*, 1996; Law *et al.*, 1997). However, care must be taken as the focal position affects the response of the FBRM and should be kept at a constant

position if measurements are to be compared. Here the focal position was placed outside the window, 0.48 mm into the suspension, to avoid the interference of particles sticking to the window and then being counted with every rotation of the focal point.

The flocculation experiments for different shear rates were performed using water samples collected 30 cm below the water surface at a location 33 km from the Brisbane River mouth, one hour before the end of flood tide on a spring cycle on 10/Nov/2003. The volumetric concentration of the samples was 0.0095% and they were stored in individual sample bottles. The sample was introduced in the Couette device mounted vertically until all the air was eliminated. The Couette was then placed in the horizontal position and rotated at constant speed until a steady state in the flocs mean chord length was achieved. The evolution of the mean was measured over 1 min intervals using the F electronics and no weights. The mean velocity gradients use in the experiment are on the range of 17 – 56 s^{-1}(a_{max} = 8.5 – 28 s^{-1}, see Appendix A for parameter definitions). The current velocities on the Brisbane River can reach up to 2 m/s, which would result in mean velocity gradient G in the excess of 50 s^{-1} (van Leussen 1994).

The same procedure was adopted for the experiments with different salinity, however these samples were prepared by centrifugation and addition of freshwater or seawater. Four samples were then prepared, one with 500 ml of seawater added, one with 500 ml of distilled water, one with 900 ml of seawater and a sample with no addition of water. All the samples had the same solids concentration. This procedure was adopted to avoid the mixture of particles of the mouth of the river, which can be from seawater nature, with the particles from the middle of the estuary, as they tend to have different properties as demonstrated to the Alde River by Hunter and Liss (1982). The difference in properties for the sediments in the mouth and the middle estuary of the Brisbane River is also supported by a study on its sediments (Howes, 2002). It demonstrated that the sediments in the mouth of the river have a higher mean size and a higher organic content than the sediments found in the middle section of the estuary.

3. MODEL

The more common approach when using population balance equations in flocculation studies is to discretize the otherwise continuous particle size domain into size class intervals. The most common approach is use a geometric progression with the upper limit of a size interval being twice the limit of the lower limit. In other words, the size classes have a geometric progression of size two. The particles are assumed to be distributed evenly in each size interval. One of the problems with this approach is a

tendency of over predict the number density in the larger size intervals (which correspond to the large particles in the population). This problem can be minimized by using a size ratio smaller than two, making the grid finer. A downsize of this approach is that a larger number of equations are then required to describe the same particle population domain, thus increasing the computational load to solve the population balance.

An alternative approach was presented by Kumar and Ramkrishna (1996), where the grid does not have any *a priori* defined grid geometry. Their method can conserve as many moments as required, and the approach used here conserves mass and numbers. A schematic grid in this method is presented in Fig. 2. Here particles in a size range from volume v_i to v_{i+1} are assumed to be concentrated in a single point x_i, located in the middle of the interval, called a pivot point.

When two particles collide and flocculate, all the particles' properties are properly conserved if the newly formed particle has a volume that matches a representative size. If the new particle does not match a representative size, the particle properties will not be automatically conserved. The approach that follows assigns a new particle that does not match a representative size to its two adjoining sizes to conserve two properties (numbers and mass). If a particle of volume v is formed between two sizes x_i and x_{i+1}, it can be represented using two fractions $a(v,x_i)$ and $b(v,x_{i+1})$. In a collision of two particles with volumes j and k, the following equations must be satisfied in order to conserve volume and numbers:

$$a(v,x_i)+b(v,x_{i+1})=1 \tag{2}$$

$$a(v,x_i)v_i+b(v,x_{i+1})v_{i+1}=v_j+v_k \tag{3}$$

This approach can be used to derive a general equation for the flocculation of particles. The term on the left hand side represents the variation of the number of particles with time. The first term on the right hand side of Eq. 4 represents the birth of particles in the *ith* interval from collisions of particles of sizes smaller or equal to the *ith* interval. The second term represents the death of particles due to aggregation with particles from all classes.

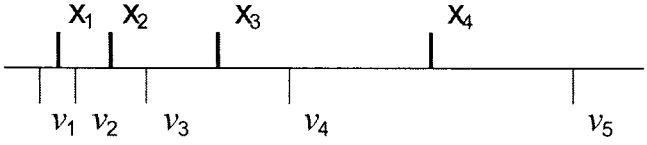

Fig. 2. General grid with representative points

$$\frac{dN_i(t)}{dt} = \sum_{\substack{j,k \\ x_{i-1} \le (x_j + x_k) \le x_{i+1}}}^{j \ge k} \left(1 - \frac{1}{2}\delta_{j,k}\right) \eta \beta(j,k) N_j(t) N_k(t) - N_i(t) \sum_{k=1}^{M} \beta(i,k) N_k(t) \tag{4}$$

and

$$\eta = \frac{x_{i+1} - v}{x_{i+1} - x_i}, x_i \le v \le x_{i+1} \tag{5}$$

or

$$\eta = \frac{v - x_{i-1}}{x_i - x_{i-1}}, x_{i-1} \le v \le x \tag{6}$$

where N_i is the number of particles in size class i, M is the number of size classes, t is the time, β is the collision frequency function and δ is the Kronecker delta function, where

$$\delta_{mn} = \begin{cases} 0 & \text{if } m \neq n \\ 1 & \text{if } m = n \end{cases} \tag{7}$$

A general breakage equation can be described as

$$\frac{dN_i(t)}{dt} = \sum_{k=i}^{M} n_{i,k} \Gamma_k N_k(t) - \Gamma_i N_i(t) \tag{8}$$

and

$$n_{i,k} = \int_{x_i}^{x_{i+1}} \frac{x_{i+1} - v}{x_{i+1} - x_i} B(v, x_k) dv + \int_{x_{i-1}}^{x_i} \frac{v - x_{i-1}}{x_i - x_{i-1}} B(v, x_k) dv \tag{9}$$

where Γ_i is the breakage frequency and $B(v, x_k)$ is the number of particles formed in the interval v to v + dv due to the breakage of a particle x_k.

These equations can be combined to represent simultaneous aggregation and breakage:

$$\frac{dN_i(t)}{dt} = \sum_{\substack{j,k \\ x_{i-1} \le (x_j + x_k) \le x_{i+1}}}^{j \ge k} \left(1 - \frac{1}{2}\delta_{j,k}\right) \alpha\eta\beta(j,k) N_j(t) N_k(t) - N_i(t) \sum_{k=1}^{M} \alpha\beta(i,k) N_k(t) + \sum_{k=i}^{M} n_{i,k} \Gamma_k N_k(t) - \Gamma_i N_i(t) \tag{10}$$

There is no definition *a priori* of the form of the aggregation and/or breakage functions in the derivation of these equations, so it can be applied with most of the functions. There is not also a definition of the grid format, which can be adapted to suit the problem in question, allowing for a more computationally efficient formulation.

Flocculation by Brownian motion and differential settling were assumed to be negligible in this case. The only mechanism used in the model for aggregation was fluid shear, given by:

$$\beta_{SH}(j,k) = a_{\max}\left(v_j^{1/3} + v_k^{1/3}\right)^3 \tag{11}$$

where a_{max} is the maximum strain rate for laminar Couette flow following Kramer and Clark (1997):

$$a_{\max} = \frac{2\omega_T r_0^2 r_i^2}{\left(r_0^2 - r_i^2\right)^2} \ln\left(\frac{r_0}{r_i}\right) \tag{12}$$

The formulas above are different from the common approach of Camp and Stein (1943), which has been demonstrated to underestimate the shear rate in a Couette device (Kramer and Clark, 1997).

This aggregation model assumes that particles are solid spheres; collisions are only binary; the volume of a floc is the sum of the volume of the two parent particles; and short-range forces and hydrodynamics effects are not directly considered (Han and Lawler, 1992). These assumptions are oversimplifications as the particles have porous structures of varied shapes.

When two or more particles collide to form a floc, usually the resultant floc has a higher volume than the sum of the volume of the original particles due to its increased porosity.

When the particles are approaching each other, three aspects should be taken in account. At a small distance, van der Walls forces increase the chances of particle collision as they attract each other. On the other hand, presence of charged particle surfaces

creates a diffuse layer of oppositely charged ions in the fluid surrounding the particles. When two particles with the same charge approach, electric fields due to the ion layers tend to repulse the particles.

The hydrodynamics of the fluid must also be considered. As the particles approach each other, the fluid between them must move out of the way and therefore affect the floc trajectories.

As a result of the model assumptions, it tends to over predict the rate of collisions. The model corrects this distortion using an experimental parameter, the collision efficiency α. It represents the probability of cohesion of two particles after they collide.

The models for breakage are not as well developed as the models for aggregation, being empirical in most cases. Two different models are assumed in the model, splitting and erosion (Fig. 3).

In the splitting mechanism, binary breakage is assumed with an equal probability of producing a child particle of any size. Obviously the other particle has a size such as that mass is conserved. Particles smaller than 4 μm are assumed to be primary particles and all particles larger than this size can be broken by splitting. The breakage function is

$$B_s(v, v_k) = \frac{2}{v_k} \tag{13}$$

The breakage frequency is assumed to depend on the particle size

$$\Gamma_{kb} = A_b . v_k^{1/3} \tag{14}$$

where A_b is the splitting rate.

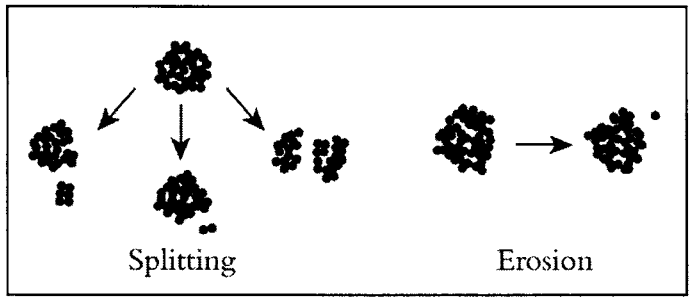

Fig. 3. Schematic representation of breakage mechanisms, splitting (left) and erosion (right)

The erosion mechanism is shown in the right side of Fig. 3, and it is assumed that a small particle is detached from the surface. As a result, a small and a large fragment are produced. This mechanism is described as (Schuetz and Piesche, 2002)

$$B_e(v,v_k)=\left(\frac{1}{v/v_k+\gamma}+\frac{1}{1-v/v_k+\gamma}-\frac{2}{\gamma+0.5}\right)\frac{I}{v} \tag{15}$$

where $\gamma = 0.01$ and

$$I=2\left(\ln\left(\frac{1+\gamma}{\gamma}\right)-\frac{1}{\gamma+0.5}\right)^{-1} \tag{16}$$

$$\Gamma_{ke} = A_e\, v_k^{1/3} \tag{17}$$

The data from the flocculation experiments is used to solve the inverse problem of the population balance. The model requires as initial conditions the number fraction on each size class. The experimental data provided by the FBRM is presented as numbers per channel. As the model uses fewer intervals than the data, the number on each interval is evaluated by interpolation using a cubic Hermite polynomial and the number density in each interval.

With the initial conditions and an initial guess for the collision efficiency and the breakage rates, the population balance is solved. An error function is calculated using a least squares method to compare the experimental and modelled data. The common approach in flocculation studies is to use the mean size as the property to be tracked (Spicer and Pratsinis, 1996; Biggs and Lant, 2002). As different particle size distributions can have the same mean size, this approach can lead to a good agreement on the mean size. However there may be a poor prediction of the final distribution, with under or over prediction of the population in certain size classes.

To avoid this problem, the approach here uses not only the mean size but also the particle density, avoiding a large difference on the final distributions between the model and the experimental data. The population in tails of the distribution are used as part of the error function due to their importance in estuaries. Most of the volume of sediments is concentrated in the large sizes, affecting the sediment transport, while the smaller sizes on the other hand usually do not settle and are responsible for the turbidity of the system.

The objective function used took the form

$$Min\,J(\alpha, A_b, A_e) = w_1 \sum_{t=0}^{t=final} \left(d_{50\exp} - d_{50model}\right)^2 + w_2 \sum_{t=0}^{t=final} \left(f_{N\exp} - f_{Nmodel}\right)^2 \qquad (18)$$

where w_1 (= 0.1 μm^{-1}) and w_2 (= 2000 μm) are weights, d_{50} is the number mean size and f_N is the number density.

The model was solved with 18 size classes from 1 – 500 μm and a geometric grid with a volume class ratio ≈ 2.82 using MATLAB and the simplex algorithm (Nelder and Mead, 1965). The third moment of the distribution remained constant in all cases indicating that mass was conserved.

4. RESULTS AND DISCUSSION

The simulated lines follow closely the experimental data in all cases (Fig. 4), with a tendency for a small under prediction at the start of the experiment, and an over predic-

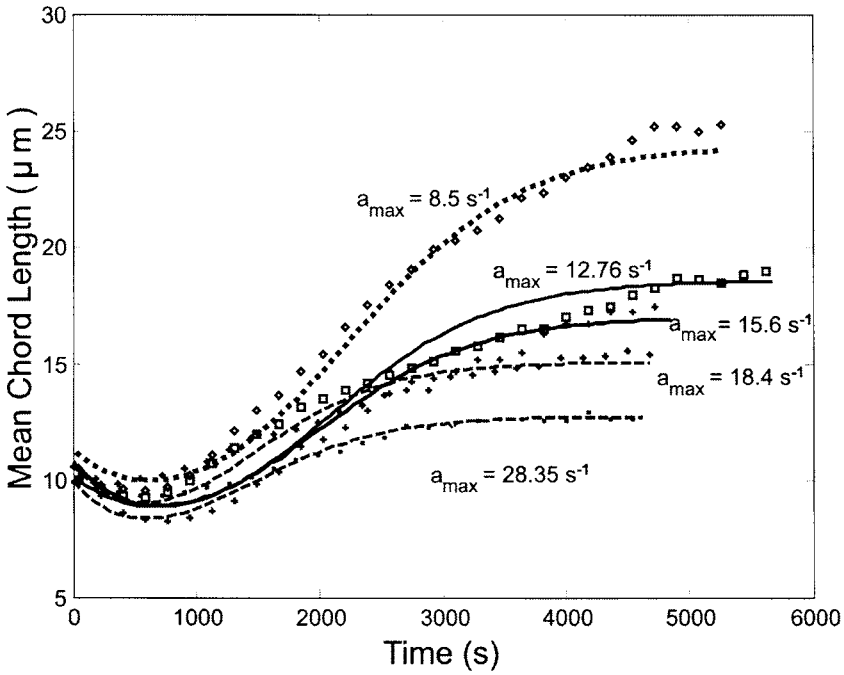

Fig. 4. Experimental (points) and simulated (lines) mean chord length for different shear rates.

tion at the end. This behaviour is also seen in models for wastewater sludge (Biggs and Lant, 2000) and inorganic flocs (Spicer and Pratsinis, 1996), probably because the physics of the problem are not completely described in the model. In all the experiments, the mean size of the sediments initially decreases before starting to increase. This is explained by the way the mean size is calculated. It has been demonstrated that under certain conditions the number mean size can decrease with aggregation or increase with breakage. This is just a quirk of the averaging procedure in the evaluation of the mean (Neumann *et al.*, 2004).

The parameters used to construct the lines in Fig. 4 were obtained by solving the inverse problem and its values are shown in Table 1.

An experimental measurement of the collision efficiencies of estuarine sediments was done by Edwaltz *et al.* (1974), using a simple equation for monodisperse system as developed by Smoluchowski. The values for different mineral fraction in the Pamlico estuary ranged from 0.05-0.022. The equation used did not take into account different sizes or the existence of breakage. van Leussen (1994) predicted values in the order of 0.01–0.1, with the values indicating the two extremes of low and high cohesiveness. To the range of velocities used in these experiments, the collision efficiencies are between 0.2 – 0.7. In comparison to other systems, the cohesiveness found here is smaller than the one assumed by Spicer and Pratsinis (Spicer and Pratsinis, 1996). They assumed an efficiency of 1 (meaning that all collisions are successful) when flocculating polystyrene particles with aluminium sulphate as a flocculant. The only parameter changing with shear was the breakage rate.

The other values found in the literature come from activated sludge, in a study by Biggs and Lant (2000). The collision efficiency varied from 2.1×10^{-4} to 5.1×10^{-4}. These values are much smaller than it would be expected, as activated sludge flocculates easily, with flocs reaching more than 2 mm. The values obtained in this case were small probably due to an error in the estimate of the initial numbers used to solve the popula-

Table 1. Couette velocities, strain rates, collision efficiencies and breakage rates.

Speed (rpm)	a_{max} (s^{-1})	α	A_b (cm/s)	A_c ($cm^{-1}s^{-1}$)
30	8.50	0.6169	1.1001	0.0016
45	12.76	0.4049 ± 0.005	1.5422 ± 0.005	0.0026 ± 0.0001
55	15.60	0.3353	1.6065	0.0042
65	18.40	0.3354	2.1819	0.0063
100	28.35	0.2081	2.6814	0.0072

tion balance. As the number variation depends on the square of the concentration, and error of 2 orders of magnitude in the initial numbers would reduce the values of the collision efficiency by 4 orders of magnitude.

The relationship between the maximum strain rate a_{max} and the collision efficiency is presented in Fig. 5. The collision efficiency decreases exponentially with the strain rate.

The comparison of the values for the breakage rate with other literature values is not possible, as these values depend on the breakage function assumed in the model. The breakage coefficients are described using a power law as proposed by Pandya and Spielman (1982) where

$$A = A'G^{y} \tag{19}$$

Two power laws relationships were obtained, one for the erosion mechanism and one for the breakage mechanism:

$$A_e = A_e^{'} a_{\max}^{ye} = 0.0085 a_{\max}^{1.36}, \quad \textit{for erosion breakage} \tag{20}$$

$$A_b = A_b^{'} a_{\max}^{yb} = 0.2249 a_{\max}^{0.75}, \quad \textit{for splitting breakage} \tag{21}$$

Figure 6 shows that the splitting mechanism has a higher frequency in comparison to the erosion mechanism. On the other hand, the erosion mechanism increases with the

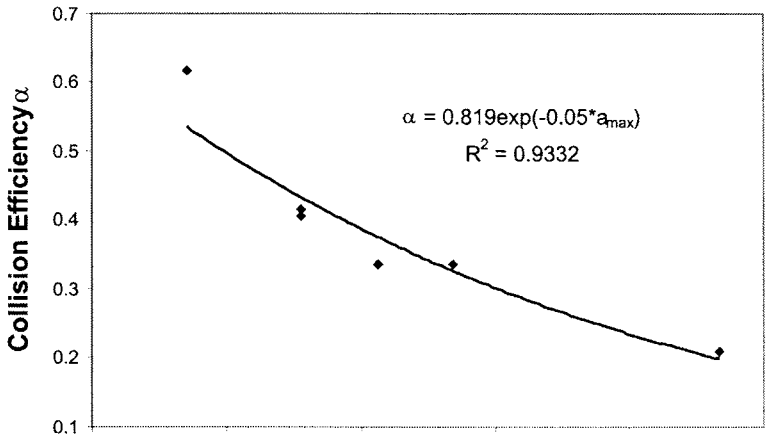

Fig. 5. Collision efficiency as a function of the strain rate a_{max} (solid line is the best fit equation).

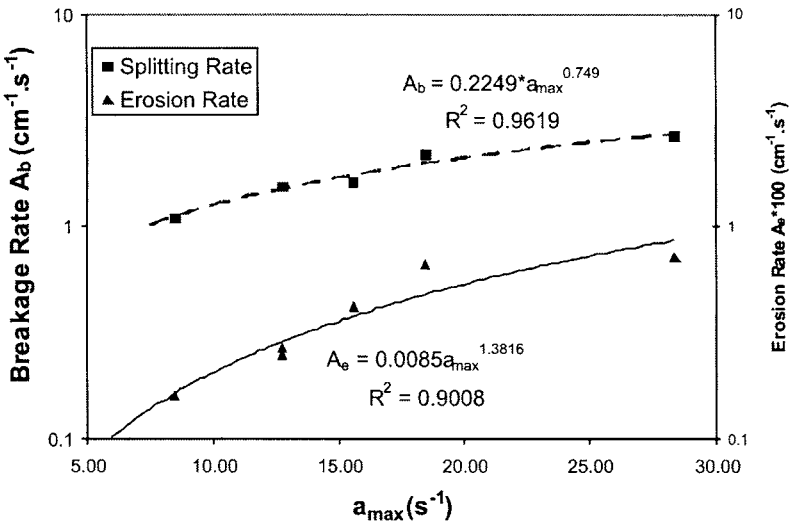

Fig. 6. Breakage and erosion rates as a function of strain rate a_{max} (lines are best fit curves).

strain rate more rapidly than the splitting mechanism. This indicates that the erosion mechanism can be more important as the maximum strain rate increases.

The decrease of mean size of the distribution can now be explained using the experimental results. First, as the shear increases, the probability of collisions increase, however as the collision efficiency decreases, fewer collisions are successful in binding the particles. Second, the breakage rates increase with the increase in shear. The net result of these effects is the decrease in the mean size.

The results for the experiments with different salinities (Fig. 7) indicate that the effects are not significant. The salinity of the samples was measured using conductivity measurements transformed to practical salinity using the Practical Salinity Scale 1978 (Eaton *et al.*, 1998).

The behaviour of the curves with under and over prediction of the mean is similar to the case with different shears. The values for the collision efficiency and the breakage rates are shown in Table 2.

In the first stages of research about the flocculation of estuaries, salinity was regarded as being a major factor influencing the aggregation of sediments as the formation of the turbidity maximum in estuaries usually occurs in areas towards the end of salinity intrusion. However later studies demonstrated that the formation of a turbidity maxi-

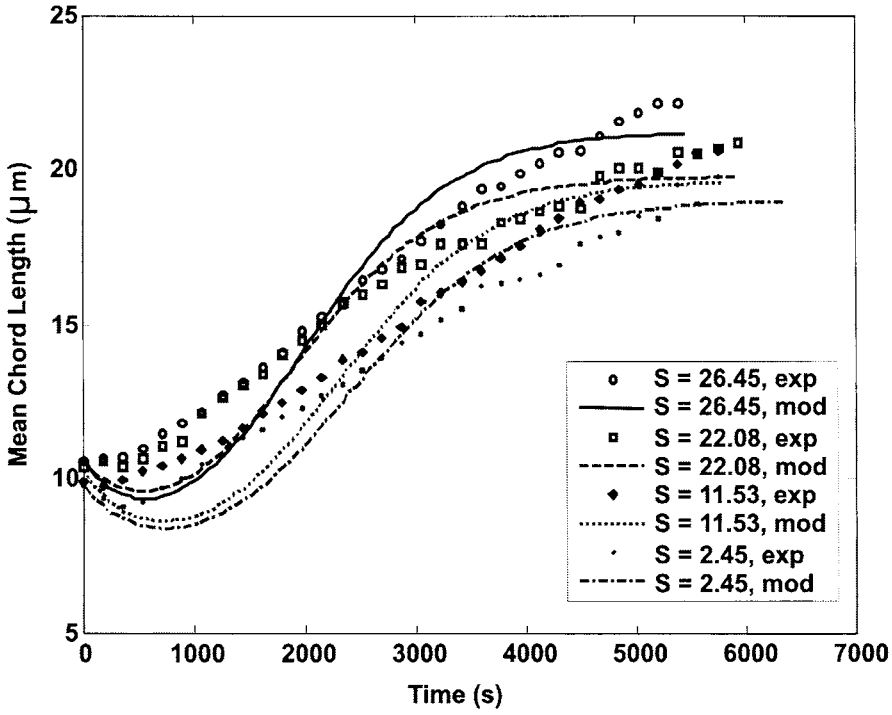

Fig. 7. Experimental (points) and simulated (line) mean chord length for different salinities (a_{max} = 12.76 s^{-1}).

mum depends primarily on the hydrodynamic conditions and the influence of the salt water on them, but not on flocculation. A study by Whitehouse, cited in Postma (1967) found that some sediments need as little as 2 ppt of salt to completely flocculate, but for Montmorillinite complete flocculation occurs only at a salt concentration of 18 ppt. On the other hand, Eisma *et al.* (1980) indicated that salt flocculation is a limited process only important for particles with small diameter.

Table 2: Practical salinity, collision efficiencies and breakage rates.

Practical Salinity	α	A_b ($cm^{-1}s^{-1}$)	A_e ($cm^{-1}s^{-1}$)
2.45	0.4419	1.1839	0.0033
11.53	0.4635	1.2935	0.0026
22.08	0. 5097	1.2852	0.0025
26.43	0. 5153	1.2078	0.0041

The slight increase in collision efficiency with salinity (Fig. 8) represents a much smaller (about 16.6%) influence when compared to the effects of shear (almost 200 %). In this case, the flocculation seems to be dominated by the velocity field in the Couette. In cases where there is not a velocity field (*i.e.*, turbulence) to drive the collisions and differential settling and Brownian motion are the dominant mechanisms, salinity might be important.

This increase in the collision efficiency is probably due to the changes in the double layer. As the concentration of salt increases, the double layer thickness decreases and the repulsive force between the particles also decrease, facilitating the aggregation of particles.

While the increase in salinity seems to increase the likelihood for a collision, it does not affect the breakage rates, by either the splitting or erosion mechanisms. The different ion concentrations do not play a role in holding the primary particles together.

5. CONCLUSIONS

This paper demonstrates the use of population balances to measure the cohesiveness of estuarine sediments in the form of collision efficiencies as well as breakage rates. The flocculation experiments were conducted using a Couette device and a FBRM particle sizer. The experiments showed the influence of different shear rates and salinities on the flocculation of the sediments.

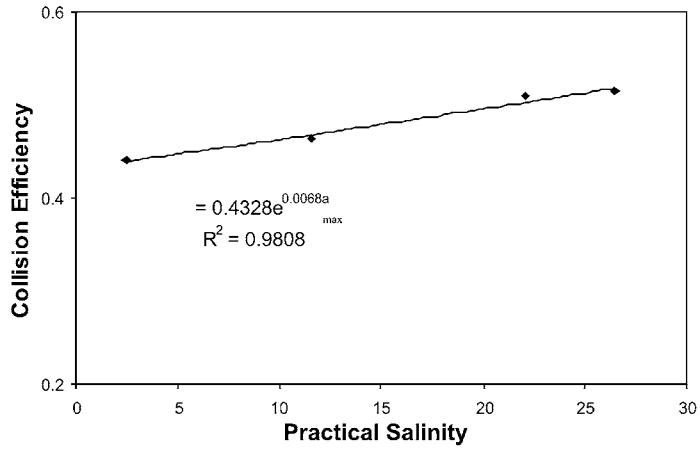

Fig. 8. Collision efficiency as a function of salinity (solid line is best fit curve).

The paper demonstrates that the mean size of the distribution is inversely proportional to the shear. This is caused by two factors. As the shear increases, the collision efficiencies decrease and the breakage rates increase. The net result of these effects is the decrease in the mean size.

For the range of salinities in this study, the increase in salinity had a minor effect on the flocculation of sediments in comparison to the influence of shear rates. An increase in salinity does increase the flocculation rates probably due to alterations on the electrical double layer. It was found that different salinities have no influence on the breakage rates.

The population balance model used here have an aggregation kernel dependent on shear and the size of both colliding particles, as well as two breakage mechanisms, splitting and erosion. While the breakage mechanisms cannot be compared to other studies, the collision efficiencies are in the expected order of magnitude. This technique can be applied for different sediments to quantify the influence of different parameters such as shear, salinity, organic content and composition on the flocculation of cohesive sediments.

ACKNOWLEDGMENTS

The main author has been supported by the Australian Government's Cooperative Research Centre (CRC) program, through a scholarship from the CRC for Coastal Zone, Estuary & Waterway Management.

REFERENCES

Andereck, C.D., S.S. Liu and H.L. Swinney. 1986. Flow regimes in a circular Couette system with independently rotating cylinders. *Journal of Fluid Mechanics*, 164, 155-183.

Biggs, C.A. and P.A. Lant. 2000. Activated sludge flocculation: On-line determination of floc size and the effect of shear. *Water Research*, (34) 9, 2542-2550.

Biggs, C.A. and P.A. Lant. 2002. Modelling activated sludge flocculation using population balances. *Powder Technology*, (124) 3, 201-211.

Camp, T.R. and P.C. Stein. 1943. Velocity gradients and internal work in fluid motion. *Journal of the Boston Society of Civil Engineers*, (30) 4, 219-237.

Eaton, A.D., L.S. Clesceri, A.E. Greenberg and M.A.H. Franson (Eds.). 1998. *Standard Methods for the Examination of Water and Wastewater.* American Public Health Association, Washinton DC, 1220 p.

Edwalz, J., J. Upchurch and C. O'Melia. 1974. Coagulation is estuaries. *Environmental Science and Technology*, (8) 1, 58-63.

Eisma, D., J. Kalf and M. Veenhuis. 1980. The formation of small particles and aggregates in the Rhine Estuary. *Netherlands Journal of Sea Research*, (14) 2, 172-191.

Gabas, N., N. Hiquily and C. Laguerie. 1994. Response of laser diffraction particle sizer to anisometric particles. *Particle & Particle Systems Characterization*, (11) 2, 121-126.

Han, M. and D.F. Lawler. 1992. The (relative) insignificance of G in flocculation. *Journal of American Water Works Association*, (84) 10, 79-91.

Heffels, C.M.G., P.J.T. Verheijen, D. Heitzmann and B. Scarlett. 1996. Correction of the effect of particle shape on the size distribution measured with a laser diffraction instrument. *Particle & Particle Systems Characterization*, (13)5, 271-279.

Howes, T. 2002. *Riverine Turbidity Processes: Final Report.* CRC for Coastal Zone, Estuary & Waterway Management, Brisbane, 73 p.

Hunter, K.A. and P.S. Liss. 1982. Organic matter and the surface charge of suspended particles in estuarine waters. *Limnology and Oceanography*, (27) 2, 322-335.

Ives, K.J. and A.G. Bhole. 1975. Study of flow through Couette flocculators- I. Design for uniform and tapered flocculation. *Water Research*, 9, 1085-1092.

Kaufmann, W. 1963. *Fluid Mechanics,* McGraw-Hill, New York, 452 p.

Kramer, A.T. and M.M. Clark. 1997. Influence of strain rate on coagulation kinetics. *Journal of Environmental Engineering*, (123) 5, 444-452.

Krishnappan, B.G. and J. Marsalek. 2002. Modeling of flocculation and transport of cohesive sediment from an on-stream stormwater detention pond. *Water Research*, (36) 15, 3849-3859.

Kumar, S. and D. Ramkrishna. 1996. On the solution of population balance equations by discretization .1. A fixed pivot technique. *Chemical Engineering Science*, (51) 8, 1311-1332.

Law, D.J., A.J. Bale and S.E. Jones. 1997. Adaptation of focused beam reflectance measurement to *in-situ* particle sizing in estuaries and coastal waters. *Marine Geology*, (140) 1-2, 47-59.

Lick, W. and J. Lick. 1988. Aggregation and disaggregation of fine-grained lake-sediments. *Journal of Great Lakes Research*, (14) 4, 514-523.

Monnier, O., J.P. Klein, C. Hoff and B. Ratsimba. 1996. Particle size determination by laser reflection: Methodology and problems. *Particle & Particle Systems Characterization*, (13) 1, 10-17.

Naito, M., O. Hayakawa, K. Nakahira, H. Mori and J. Tsubaki. 1998. Effect of particle shape on the particle size distribution measured with commercial equipment. *Powder Technology*, (100) 1, 52-60.

Nelder, J.A. and R. Mead. 1965. A simplex method for function minimization. *Computer Journal*, 7, 308-313.

Neumann, L., T. Howes and E.T. White. 2004. Breakage can cause mean size to increase. *Developments in Chemical Engineering and Mineral Processing*, (12) 3/4, 393-402.

Pandya, J.D. and L.A. Spielman. 1982. Floc breakage in agitated suspensions: Theory and data processing strategy. *Journal of Colloid and Interface Science*, (90) 2, 517-531.

Postma, H. 1967. Sediment transport and sedimentation in the estuarine environment. In: *Estuaries*; Lauff, G.H. (Ed.), American Association for the Advancement of Science, Washington, 158-179.

Ruf, A., J. Worlitschek and M. Mazzotti. 2000. Modeling and experimental analysis of PSD measurements through FBRM. *Particle & Particle Systems Characterization*, (17) 4, 167-179.

Schuetz, S. and M. Piesche. 2002. A model of the coagulation process with solid particles and flocs in a turbulent flow. *Chemical Engineering Science*, (57) 20, 4357-4368.

Spicer, P.T. and S.E. Pratsinis. 1996. Coagulation and fragmentation: Universal steady-state particle-size distribution. *AIChE Journal*, (42) 6, 1612-1620.

van Leussen, W. 1994. *Estuarine Macroflocs and Their Role in Fine-Grained Sediment Transport.* PhD Thesis, Department of Earth Sciences. Utrecht, Utrecht University, 488p.

Estuarine and Coastal Fine Sediments Dynamics
J.P.-Y. Maa, L.P. Sanford and D.H. Schoellhamer (editors)

An experimental study into the evolution of the size distribution of kaolinite flocs

Maggi[a], F. and J.C. Winterwerp[a,b]

[a]Environmental Fluid Mechanics, Faculty of Civil Engineering and Geosciences, Delft University of Technology, P.O. Box 5048, 2600 GA, Delft, The Netherlands.
[b]WL|Delft Hydraulics, P.O. Box 177, 2600 MH, Delft, The Netherlands.

KEY WORDS
Population, flocs, fractal structures, organization, complexity.

This paper presents an investigation on the flocculation of a cohesive sediment suspension consisting of kaolinite minerals. The study is based on laboratory measurements with the aim to highlight the fundamental dynamical behaviour of mud flocs. In particular, a population of flocs is observed to evolve from a non-equilibrium initial state towards a steady (statistically stationary) far-from-equilibrium state. This is evinced from analysis of experimental recordings and conceptualization of the time evolution of the floc size distribution. In addition, analysis is performed of the local, floc scale. Floc geometries are characterized by fractal properties and non-homogeneous, disordered mass-density distributions. The overall conclusion from this research is that a flocculating system is marked, on the one hand, by "organization" at global scales and, on the other hand, by "complexity" at local scales.

1. INTRODUCTION

Cohesive sediment suspensions in natural water systems are subject to turbulence-induced aggregation and breakup. These processes cause the formation of large aggregates (known as flocs) from a combination of small board-shaped clay minerals and organic filaments mainly. Although the primary particles are compact, the resulting flocs show a sponge-like structure with large porosity. Observations, both in the field and

laboratory, revealed the fractal nature of sediment flocs, which has been elaborated, for instance, by Krone (1963), McCave (1993), Kranenburg (1994), Gmachowski (1996), Winterwerp (1998), Serra and Casamitjana (1998a), Manning and Dyer (1999), de Boer *et al.* (2000) and Maggi *et al.* (2003) describing a variety of properties and behaviours. For example, a high-turbulence medium produces small, spherically-shaped flocs with high capacity dimensions, while a low-turbulence medium produces chain-like flocs with low capacity dimensions (Wells and Goldberg, 1993; Manning and Dyer, 2002). The capacity dimension of flocs can be used to describe their density, settling velocity, aggregation and breakup processes (Winterwerp 1998; 2002) and shape (Maggi *et al.*, 2003). This implies that information on the sediment behaviour can be deduced from (and related to) the geometry of the structure of individual flocs, thus to the small scales of the suspension.

At these small scales, gain and loss in floc mass result from the interaction of a large set of individuals. To model these mechanisms, multiple-size interaction models have been proposed by Smoluchowsky (1917), Friedlander (1977), O'Melia (1980; 1986) and Lick and Lick (1988). However, none of them considered flocs as fractal entities. A mono-floc growth Lagrangian equation has been proposed by Winterwerp (1998) within the framework of fractal approach. Little research has been oriented to implement the dynamics and kinematics of fractal flocs in a full, generalized population balance equation. For this purpose, we focus on the time evolution of floc size distribution of a flocculating system to study fundamental physical processes on the basis of the floc geometry.

Two main aspects are treated in this paper. The first one is the development of "organization" at large (global) scales in relation to the characteristic scales of the system. The second one is the development of "complexity" at small (local) scales in relation to the growth process of individual flocs. We will elaborate these aspects on the basis of selected results of an experimental investigation on the time evolution of kaolinite flocs.

The paper is organized as follows. In Section 2 we describe the experimental facility (settling column) used to study the kaolinite sediment. Section 3 is dedicated to the time evolution of size distribution of a population of flocs formed in the settling column. Section 4 is devoted to the geometrical properties of individual flocs. In Section 5 we elaborate on the major characteristics of the equilibrium dynamics of the population of flocs. Finally, in Section 6 we summarize the main conclusions on the dynamics of a flocculating cohesive suspension.

2. EXPERIMENTAL SETUP

2.1. Facility

The experimental facility used was the settling column (Fig. 1) recently constructed in the Laboratory for Environmental Fluid Mechanics at Delft University of Technology (Maggi *et al.*, 2002).

A high-concentration suspension c_s of kaolinite was prepared and continuously mixed in a storage tank. The suspension was injected into the buffer tank mounted on top of the settling tube. Sediment injection was automatically controlled via an optical silt measuring instrument placed in the buffer tank to either start or stop the sediment pump according to the difference between the measured concentration c in the buffer tank and the desired concentration c_d. Concentration variability in the buffer tank was about ± 0.015 g/L.

The buffer tank diluted the concentration c_s down to c_d and made the particles uniform by mixing them before entering the column. The buffer tank was a symmetric container divided into three sub-sections; sediment in the two outer sub-sections was stirred by two vanes, while the mid sub-section was connected to the settling column (Fig. 1b). The re-circulating flow generated by the counter-rotating vanes can pass through two narrow openings and the sediment was released from the buffer tank into the column by natural settling. In the settling column, flocculation was induced by turbulence generated with an oscillating grid.

This grid consisted of four one-meter-long elements connected to each other, generating an isotropic, nearly homogeneous turbulence field over 4 m length. A grid element consisted of a mesh of 75 mm size, with square cross-sectional rods and deck distance of 75 mm (Fig. 1c). The grid was placed inside the settling tube, which was a 4.8 m high perspex pipe of 300 mm diameter.

Flocculated sediment passed through the turbulence field of the column and then reached the measuring section underneath the settling tube, and eventually settled at the bottom of the settling column. The measuring section was provided with a separation chamber consisting of an horizontal plate with a small opening section that allowed to collect a tiny stream of settling flocs. This stream passed through a confined chamber were the optical recordings were performed.

2.2. Measurement technique

Particle Image Velocimetry (PIV) was used in the facility to perform the measurements. The PIV optical system was placed between the measuring section and the bed section, enabling the observation of flocculated Suspended Particulate Matter (SPM). The optical system consisted of a digital camera and a laser sheet directed to the measuring

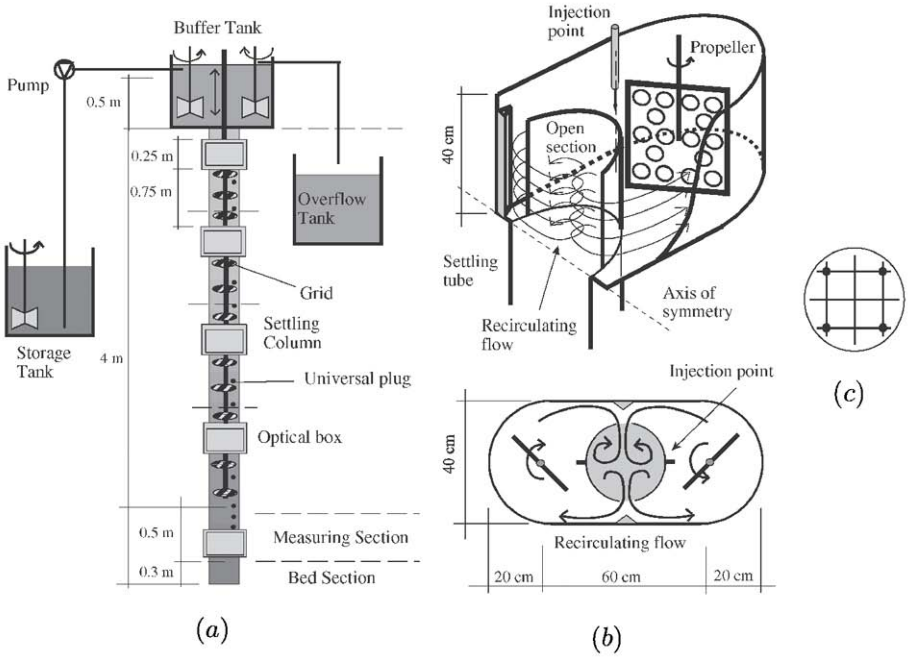

Fig. 1. Schematic representation of the facility. In particular, (a) the settling column, (b) the buffer tank and (c) the grid design are shown.

section from the side. The camera recorded 8 bit gray-scale digital images with a resolution of 720-by-512 pixel, focused on an observation window of about 3-by-2 mm size, thus obtaining about 4.16 μm/pixel resolution.

The images were recorded at 25 frames per second and stored on digital tapes. Every measurement consisted of 7 minutes recording, eight times per day, with a corresponding time interval (or experimental time resolution) of 3 hours. The experiment described in this paper lasted for 7 days, thus yielding a total of 577,500 images.

Gray-scale images recorded during the experiment were then processed with the algorithm proposed in Maggi and Winterwerp (2003), to obtain black-and-white images of individual flocs. The results presented in this paper comprise a selection of those frames.

2.3. Experimental conditions

Kaolinite was used in the experiment with primary mineral size between 3 and 5 μm, with sediment density $\rho_s \approx 2650$ kg/m^3. The suspension in the storage tank was prepared at approximately $c_s = 10$ g/L. The target desired sediment concentration in the column was set at $c_d = 0.5$ g/L, in slightly salt water at salinity $s = 5$ ppt. The environment

temperature was set at $T = 18$ °C, while the grid oscillated with an amplitude of 84 mm at a frequency of $f_g = 0.5$ Hz, corresponding to a turbulence shear rate of about $G = 18$ 1/s. The value of G was determined as $G = \sqrt{\varepsilon/\mu}$, with μ the water viscosity, where the energy dissipation ε was computed from the particle velocity spectra of several 3D laser doppler anemometry measurements collected in the column. The experiment started at time $t = 0$ with an equilibrium turbulence field without sediment.

3. TIME EVOLUTION OF FLOC SIZE DISTRIBUTION

The aim of the measurement of the time evolution of Floc Size Distribution (FSD) is twofold: (1) quantify how a non-flocculated cohesive suspension evolves into a flocculated suspension, and (2) characterize its FSD (unimodal, bimodal, statistical moments, *etc.*).

In order to characterize the flocculation processes, we present the FSD measured in the measuring section at experimental time $t = 3, 120, 162, 165$ hours after the sediment injection system was started. The probability $p(L)$ to find flocs of size L (Fig. 2) indicates that the majority of the flocs were small at initial conditions and become larger after time $t = 120$ hours. The modal floc size was about 16.6 μm, then it increased to 66.5 μm at time $t = 162$ h. FSD_{162h} and FSD_{165h} appear almost similar, without strong variability, which is an evidence that the system asymptotically approaches a steady state that appears statistically stable, see $\overline{L}$ and σ_L in Fig 2. Unlike the unimodal FSD_{3h}, FSD_{162h} and FSD_{165h}, FSD_{120h} is bimodal with a second maximum of $\widetilde{L}_{120h} \approx 120$ μm, a value which is slightly higher than the peak of FSD_{162h}. However we do not consider FSD_{120h} to be fully representative of the floc population at $t = 120$ hours because we had too little floc samples at that time to obtain a proper floc size distribution. This was due to a stable vortex caused by the asymmetric geometry of the separation chamber inside the measuring section, where the samples were collected. The vortex caused the flocs to pass through the measuring window too fast to have good quality images. Because of this, flocs could be measured properly only few times during the experiment.

Statistical moments of $p(L)$ at different times are given in Fig. 2. The time evolution of the population is marked by a shift of the modal size $\widetilde{L}$ (from about 17 μm to about 67 μm) and by a widening of $p(L)$ (from $\sigma_L = 31.4$ μm to $\sigma_L = 73.5$ μm).

Turbulence in the column replicated clearly the natural turbulence, but it was kept constant and homogeneous to isolate flocculation processes from other interfering processes, such as periodic or aperiodic fluctuations in sediment concentration, water temperature and salinity, turbulence gradient, *etc.*

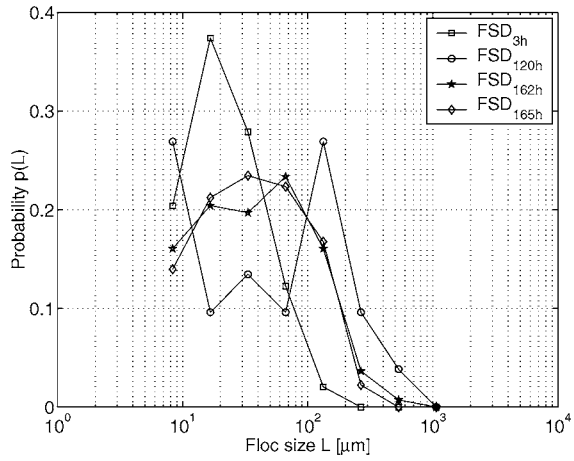

	FSD_{3h}	FSD_{120h}	FSD_{162h}	FSD_{165h}
Number of flocs	163	58	156	208
Mean $\overline{L}$ $[\mu m]$	34.0	120.3	71.8	61.4
Modal $\widetilde{L}$ $[\mu m]$	16.6	133.1	33.28	66.5
Standard deviation σ_L $[\mu m]$	31.4	150.9	86.7	73.5

Fig. 2. FSD of kaolinite flocs at experimental time $t = 3, 120, 162$, and 165 h. Statistical parameters are given in table.

4. GEOMETRICAL ORGANISATION OF INDIVIDUAL FLOCS

Our analysis of flocs is based on geometrical concepts of (multi) fractality and entropy. Most part of the interpretation tools have been recently developed in Maggi *et al.* (2003) and Maggi and Winterwerp (2004), but not yet applied to an abundant data set.

4.1. Capacity dimension

The capacity dimension d_0 of a three-dimensional (3D) fractal body $\Omega_3 \subset \mathbb{R}^3$ of size L (with $\mathbb{R}^3$ the three-dimensional embedding space) is defined as $d_0 = \log(N)/\log(\ell)$, where N is the number of boxes of size ϵ required to cover Ω_3 (ϵ-covering) and $\ell = L/\epsilon$ is the dimensionless size of Ω_3 (Vicsek, 1992). The technique to estimate d_0 from two-dimensional (2D) projections was described in Maggi and Winterwerp (2004). It is based on the idea that the information of fractality is concealed in the perimeter segmentation of projected images $\Omega_2 \subset \mathbb{R}^2$ of the flocs (with $\mathbb{R}^2$ the two-dimensional embedding space), thus related to the perimeter-based fractal dimension d_P, which is defined as $d_P =$

$2\log(P)/\log(A)$ such that $1 \leq d_P \leq 2$, with P and A the dimensionless perimeter and area of Ω_2, respectively (Meakin, 1998). d_P is related to d_0 by the following function:

$$d_0 = \sqrt{\frac{a(\ell)}{d_P - b(\ell)}}, \tag{1}$$

where $a(\ell)$ and $b(\ell)$ are known functions of ℓ (Maggi and Winterwerp, 2004).

Massive primary particles and very small aggregates have a high capacity dimension $d_0 \lesssim 3$, and d_0 decreases sharply with floc size, *i.e.*, larger flocs have lower capacity dimension (Fig. 3). In particular, d_0 seems to approach an asymptotic value of about $d_0 \approx 2$, a value observed in earlier investigations, as discussed in Winterwerp (1999) from an analysis of in-situ measurements. Further, we note a large variation in d_0 for flocs of similar size, hence implies a large variation on structure and density too.

4.2. Entropy and disorder

The fractal structure of flocs can be further characterized in $\mathbb{R}^2$ through the presence of (deterministic) recursive patterns and substructures irregularly distributed within Ω_2. To this end, we compute the entropy and disorder indexes (Maggi *et al.*, 2003).

We consider an ϵ-covering of $\Omega_2 \subset \mathbb{R}^2$ as in Section 4.1, with variable box size ϵ : $1 \leq \epsilon \leq L$ ($\epsilon = 1$ is the pixel size). If $M_i(\epsilon)$ is the number of measuring points in the i^{th} box (in practice, the number of activated pixels), then $N(M)$ is the number of boxes containing the same amount of mass M and $p_m(\epsilon) = N(M)/N$ is the probability to find

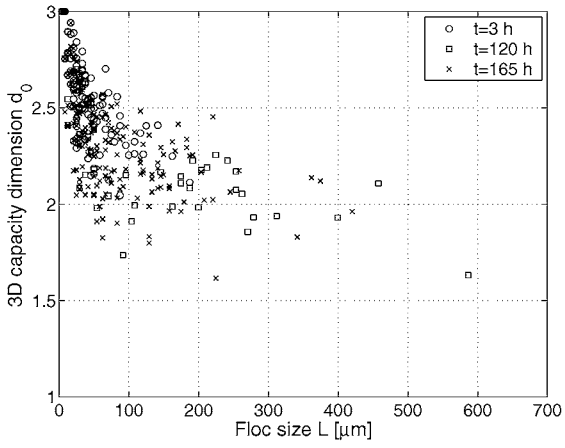

Fig. 3. Representation of the capacity dimension d_0 of individual flocs at $t = 3, 120, 165$ h.

a pattern M within Ω_2. The entropy function $S(\epsilon)$ is written as:

$$S(\epsilon) = -\sum_{m=1}^{N_p(\epsilon)} p_m(\epsilon) \ln[p_m(\epsilon)], \tag{2}$$

with $N_p(\epsilon) \leq N$ the number of different patterns found in the ϵ-covering. $S(\epsilon) = 0$ for both $\epsilon = 1$ and $\epsilon = L$ pixel, while $S(\epsilon) \geq 0$ for $1 < \epsilon < L$, with a maximum S' at a given $\epsilon = \epsilon'$. We call $S' = S(\epsilon')$ the *specific entropy* of Ω_2, since the value of S' is associated to a unique value of ϵ. In analogy with S' we compute the maximum entropy $S'_{max} = 2\ln[\epsilon']$ corresponding to the equiprobability to find *any* possible pattern (white-noise) in the ϵ'-covering, *i.e.*, $p_m(\epsilon') = 1/N_p(\epsilon') = 1/\epsilon'^2$. Since the number of observed patterns is less then or equal to the possible number of patterns ($S' \leq S'_{max}$), we can write the following disorder index[1]:

$$\Upsilon' = \frac{S'}{S'_{max}}, \qquad \text{such that} \qquad 0 \leq \Upsilon' \leq 1. \tag{3}$$

Υ' measures the level of disorder of Ω_2. $\Upsilon' = 1$ corresponds to maximum disorder (or complexity), while $\Upsilon' = 0$ means that Ω_2 possesses a fully redundant mass organization (without pattern variability).

Small flocs have a highly homogeneous mass distribution, corresponding to small values of Υ' (Fig. 4a). For larger flocs, higher values of Υ' are found, *i.e.*, flocs become less and less homogeneous. The data in Fig. 4a suggest an asymptotic trend towards a value of $\Upsilon' \approx 0.5$. In addition, high-dimensional aggregates show a low level of disorder, while mid-dimensional aggregates possess higher level of disorder (Fig. 4b). This correlation can be expressed by means of the following linear function:

$$\Upsilon' = -\frac{1}{2}d_0 + \frac{3}{2}. \tag{4}$$

In this way, flocs with $d_0 = 1$ have a white noise-like, fully disordered structures (disjointed nevertheless) for which $\Upsilon' = 1$. However, this is an extreme case that is not realistic or measurable in the real world.

4.3. Generalized dimensionality and multifractality

Irregular, non-recursive patterns within Ω_2 (measured by means of Υ') are related to a non-homogeneous mass-density distribution. A fruitful tool to scale such non-homogeneity is the multifractal spectrum (Argyris *et al.*, 1994; Grassberger and Procaccia, 1983; Hentschel and Procaccia, 1983). Its application in the analysis of SPM in natural waters was proposed in Maggi *et al.* (2003), together with a detailed discussion. Conceptually we

[1] Based on the disorder function $\Upsilon(\epsilon)$ according to Shiner (2000).

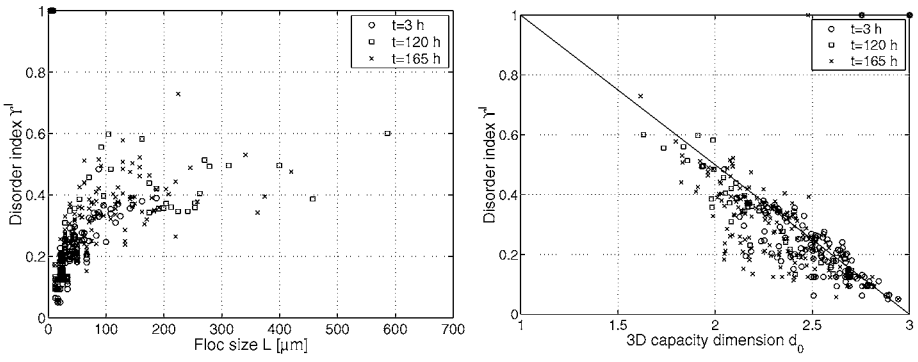

Fig. 4. Representation of the disorder index Υ' as a function of (a) floc size L and (b) of the capacity dimension d_0 at times $t = 3, 120, 165$ h.

can describe monofractality and multifractality as follows. For monofractals, a generalized probability of a measure P within any i^{th} box of an ϵ-covering scales with ϵ as $P = P_i \sim \epsilon^{d_f}$, where d_f =const $\forall\, i$ is a fractal dimension. For multifractals, in contrast, the generalized probability P within any i^{th} box scales as $P = P_i \sim \epsilon^{\alpha_i}$, with α_i the Lipschitz-Holder exponent or singularity strength. The number $N(\alpha)$ of boxes where P_i has singularity strength between α_i and $\alpha_i + d\alpha$ scales as $N(\alpha_i) \sim \epsilon^{-f(\alpha_i)}$. Here $f(\alpha)$ is called the spectrum of fractal dimensions (or multifractal spectrum) of the family of boxes with singularity α. The spectrum $f(\alpha)$ is a continuous function of α and, usually, a unimodal curve with a maximum at $\mathrm{d}f(\alpha)/\mathrm{d}\alpha = 0$.

Chhabra and Jensen (1989) proposed an efficient technique to compute $f(\alpha)$. Following this ideas, we applied an ϵ-covering to $\Omega_2 \subset \mathbb{R}^2$ with ϵ arbitrary larger then the pixel size, such that $N = (L/\epsilon)^2 = \ell^2$ is the total number of boxes. We counted the number $N_i(\epsilon)$ of pixels within each i^{th} box and derived a probability $p_i(\epsilon) = N_i(\epsilon)/N_f$. We now build a one-parameter family of normalized measures $\mu(q, \epsilon)$:

$$\mu_i(q,\epsilon) = \frac{[p_i(\epsilon)]^q}{\sum [p_i(\epsilon)]^q}, \qquad \text{such that} \qquad \sum_{i=1}^{N} \mu_i(q,\epsilon) = 1. \tag{5}$$

The exponent q, typically in the range $q = \{-20, ..., 20\}$ (Mach *et al.*, 1995), is a weighting moment (or family order) which strengthens high concentration regions if $q > 1$. It strengthens the low concentration regions if $q < 1$, and it replicates the original measure

if $q = 1$. The multifractal spectrum $f(q)$ and the average singularity strength are:

$$f(q) = \lim_{\epsilon \to 0} \frac{\sum_{i=1}^{N_b} \mu_i(q,\epsilon) \cdot \ln[\mu_i(q,\epsilon)]}{\ln \epsilon}, \tag{6}$$

where $N_b \leq \ell^2$ is the number of occupied boxes (where $p_i \neq 0$). The average value of the singularity strength α_i is computed as follows:

$$\alpha(q) = \lim_{\epsilon \to 0} \frac{\sum_{i=1}^{N_b} \mu_i(q,\epsilon) \cdot \ln[p_i(\epsilon)]}{\ln \epsilon}. \tag{7}$$

The function $f(q)$ corresponds to the generalized dimensionality d_q. The measure $p_i(\epsilon)^q$ scales as:

$$\sum_{i=1}^{N} p_i(\epsilon)^q \sim \epsilon^{\tau(q)} \qquad \text{with} \qquad \tau(q) = (q-1)d_q, \tag{8}$$

where $\tau(q)$ is the mass correlation exponent of the q^{th} order defined by Halsey *et al.* (1986b). $\tau(q)$ and $f(\alpha)$ are related to each other by Legendre transformation (Meakin, 1998):

$$f(\alpha(q)) = q\alpha(q) - \tau(q), \qquad \alpha(q) = \frac{\mathrm{d}\tau(q)}{\mathrm{d}q}. \tag{9}$$

As observed in the numerical analyses in Maggi (2002), Euclidian structures fully filling the embedding space (*i.e.*, $d_0 = n$ with n the embedding dimension $\epsilon \mathbb{N}$) are characterized by $\alpha(q) = 0$ and $\tau(q) = 0 \; \forall \; q$. The corresponding multifractal spectrum f is a straight, horizontal line in the (f,q) representation, which collapses into a unique point at $\alpha = 0$ with dimensionality $f(\alpha) = n$ in a (f,α) representation. In this case, $\tau(q) = 0 \; \forall \; q$. Euclidian and fully self-similar structures with $d_0 < n$ are characterized by $\mathrm{d}\tau(q)/\mathrm{d}q = \alpha(q) = \text{const} \neq 0 \; \forall \; q$ and $f(\alpha) = \text{const} = d_0 \; \forall \; \alpha(q)$. In particular, the correlation exponent τ is not a constant with q, but a monotonic increasing function with constant slope $\alpha(q) \neq 0$. Furthermore, multiscaling geometries (statistical self-similarity) are characterized by $\mathrm{d}\tau(q)/\mathrm{d}q = \alpha(q) \neq \text{const}$ and by a unimodal multifractal spectrum f in both the (f,q) representation and (f,α) representation. In this case the mass-correlation exponent τ is a monotonic function of q with various slopes. From a combined analysis of f, α and τ we can therefore establish the dominant scaling behaviour of the geometry of flocs.

We note from Fig. 6 that α ranges in the interval $\alpha \in (0,3)$ for negative values of q and for the major part of floc sizes L. Only few small flocs show invariant values of α in the chosen interval $q \in [-20,20]$. The function α is related to the spectrum f shown in

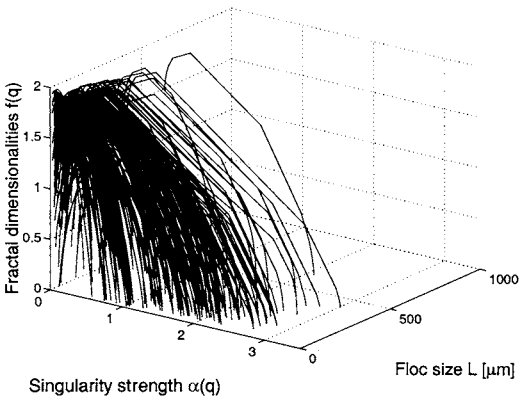

Fig. 5. Representation of multifractal spectra $f(q)$ as a function of singularity strength $\alpha(q)$ and floc size L at time $t = 165$ h.

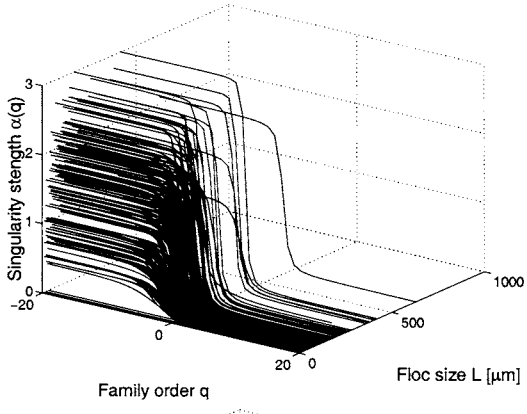

Fig. 6. Representation of singularity strengths $\alpha(q)$ as a function of family order q and floc size L at time $t = 165$ h.

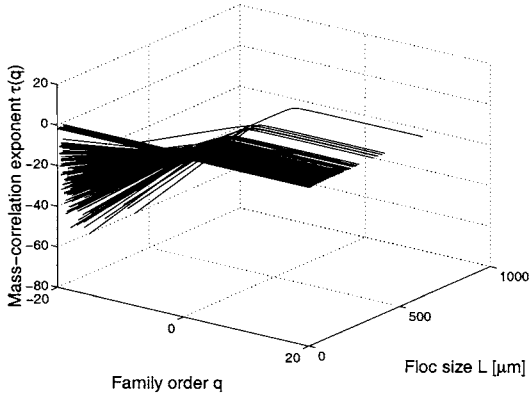

Fig. 7. Representation of mass-correlation exponents $\tau(q)$ as a function of family order q and floc size L at time $t = 165$ h.

Fig. 5, as a function of floc size L. In particular, we note two main characteristics: (1) small flocs have a constant singularity strength α ($\mathrm{d}\alpha(q)/\mathrm{d}q = 0$) and mass-correlation exponent τ while (2) large flocs show a variation in α ($\mathrm{d}\alpha(q)/\mathrm{d}q \neq 0$). So, small flocs do not present multifractality while the largest part of the flocs posses multifractal scaling represented by the functions f in Fig. 5, which do not collapse into unique points at given values of α, but yield a typical unimodal curve spread over α. Flocs with sizes $L \lesssim 15\mu$m can be considered as either fully self-similar fractals (when $\tau = \text{const} \neq 0$) or Euclidian (when $\tau = \text{const} = 0$). The mass-density distribution of small, fully self-similar flocs is therefore described by a unique scaling exponent. This exponent is related to the slope of the mass-correlation exponent τ represented in Fig. 7. Unlike small flocs, large flocs ($L \gtrsim 15\mu$m) are statistically self-similar, with multiscaling geometries. These flocs require more than one scaling exponent to describe their mass-density distribution. These exponents are related to the two dominant slopes of the mass-correlation exponent τ, for $q < 0$ and $q > 0$.

Fractal growth of flocs is governed by the kinetics of approaching particles. Numerical investigations by Halsey *et al.* (1986b), Amitrano and Coniglio (1986), Vicsek (1992) and Meakin (1998) revealed that the growth probability in diffusion limited aggregation and cluster-cluster aggregation processes can be established from the left side of the $f(q)$ curve (Fig. 5), corresponding to small values of α. Those values of α are related to high values of q (Fig. 6), and to $\tau(q)$ for $q > 0$ (Fig. 7). The slope of $\tau(q > 0)$ is therefore an indication of the growth rate of an aggregate and a measure of its mass organization. We consequently expect highly segmented, branch-like flocs to posses low values of α related to steep slopes of $\tau(q)$ for $q > 0$ (Eq. 9). Although this was shown for some large flocs in Maggi *et al.* (2003), it appears that the organization of large flocs is marked by wider ranges of α (Fig. 6). In view of this, high values of α are related to low values of q and, consequently, to $\tau(q)$ for $q < 0$. As a consequence, larger and more complex (or disordered) flocs are associated, in general, to steep slopes also in the negative range of the mass-correlation exponent $\tau(q < 0)$ (Fig. 7). The quantities f and τ are not universal but vary with floc size. This means that, in general, floc properties are not fully self-similar; non-homogeneity implies multifractal scaling and, therefore, monoscaling is valid only over small ranges of length scales and for small flocs.

5. EQUILIVRIUM DYNAMICS OF THE POPULATION

The flocculation processes govern the large scale FSD ($p(L)$) and the small scale structural parameters of individual flocs (Υ', d_0, f and τ). In this section we discuss how

these scales are related.

The FSD is subject to a shift of the modal floc size $\widetilde{L}$, and a change in shape. This reshaping is a consequence of the transformation of a large set of primary particles into a smaller set of larger aggregates. We first attempt to conceptualize and visualize the evolution of a flocculating system, in an abstract way, to analyze what flocculation implies from the point of view of the system length scales. Next, we elaborate further with the aid of the results presented in Section 3 and 4.

Let us consider a set of $N \gg 1$ particles in a given domain, in which they can move freely. Let us characterize the state of the system by means of the total particle distance H:

$$H(t) = \sum_{i=1}^{N-1} \sum_{j=i+1}^{N} d(\mathbf{p}_i, \mathbf{p}_j, t), \tag{10}$$

where $d(\mathbf{p}_i, \mathbf{p}_j, t)$ is the distance between any two particles i and j at positions $\mathbf{p}_i$ and $\mathbf{p}_j$ at time t. Then we can define four levels of organization.

Class C1 (disperse system): Let us first consider particles colliding elastically, thus preserving their kinetic energy (fully conservative system). Since there is no aggregation, the system does not change its character in time, therefore $H_{C1}(t_\infty) = H(t_0) = \text{const} \; \forall \, t$ (Fig. 8*a*).

Class C2 (fractal system): Now, let us introduce cohesiveness properties. Assuming that each collision results in particle aggregation and that aggregates larger than a critical size L_c breakup into the original primary particles. In a short time the (dissipative) system will attain a steady state size distribution with $N_a < N$ fractal aggregates. $H_{C2}(t)$ has an asymptotic limit at $H_{C2}(t_\infty) \leq H_{C1}(t_\infty) = H(t_0)$, when aggregation and breakup occur simultaneously in the system (Fig. 8*b*).

Class C3 (fractal system): Penultimately, consider that aggregates cannot break up, that is a unique, large fractal aggregate will grow it contains all the primary particles. The system will reach a stable equilibrium after some time, showing a unique fractal individual. This implies $H_{C3}(t_\infty) \leq H_{C2}(t_\infty)$, because now $N_a = 1 \ll N$ (Fig. 8*c*).

Class C4 (crystal system): Finally, consider the primary particles to result in the nucleation of a unique crystal. The system will manifest a fully-dense, Euclidian structure at stable equilibrium. The quantity $H_{C4}(t)$ is now $H_{C4}(t_\infty) \leq H_{C3}(t_\infty)$, because all the particles are collected in the most dense structure (Fig. 8*d*).

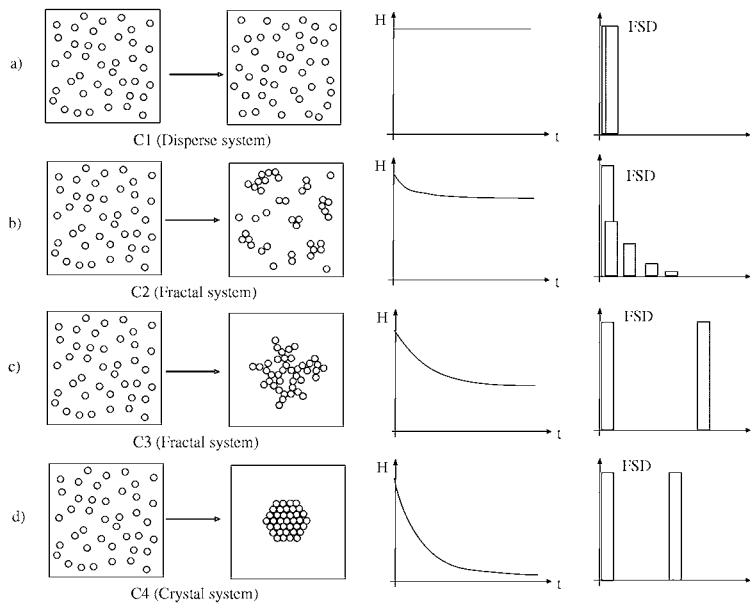

Fig. 8. Various organization levels in an evolving particle system. The evolution is here described by means of the total particle distance H and by the floc size distribution FSD. Dark gray refers to initial conditions while light gray refers to final conditions.

The H function is a measure of the space-distribution of the particles, therefore it is a measure of the large scale organization of the system. For the scheme in Fig. 8 we write $H(t_0) \geq H_{C1}(t_\infty) \geq H_{C2}(t_\infty) \geq H_{C3}(t_\infty) \geq H_{C4}(t_\infty)$, that means that the disorder of the system decreases when subject to processes of aggregation and breakup, thus moving towards a more organized state. Under certain conditions the system may show Euclidian organization (crystal) that is the highest level of order (C4). In most of the cases the organization is less regular (C2 and C3), as typically studied in DLA and CCA processes in Pietronero (1983), Vicsek (1992) and Meakin (1998). From a physical point of view, systems like C2 and C3 produces fractal-organised structures during their non-equilibrium transition. The difference between C2 and C3 is that the final state of C3 is a stable equilibrium while C2 does not reach a stable equilibrium, but a state at which the FSD is steady. The steady state of C2-class systems is a statistically stationary state, because the FSD does not show appreciable time variations, see FSD_{162} and FSD_{165} in Fig. 2. This dynamical state is called a far-from-equilibrium state (Nicolis and Prigogine, 1974; Meakin, 1998). It is associated to non-linearities in the kinematics of aggregation

and breakup, occurring continuously in time due to energy supply and dissipation. The distance from the equilibrium can be quantified by the quantity H (proportional to the exergy content of the system and related to the entropy, therefore also to the difference between supplied and dissipated energy). In other words, flocculating process can be represented physically by C2-class systems as flocs grow to a critical size (normally the Kolmogorov length scale) beyond which they breakup, developing a size distribution, Fig. 8. From this, it can be concluded that flocculating is evolving from a non-equilibrium initial state towards a far-from-equilibrium statistically stationary steady state.

C2-class systems show "fractal organisation" in the resulting aggregates, and this kind of systems evolves from a low-order geometrical organization (C1-class system) into a higher-order geometrical organization. Thus, a flocculating system has the following characteristics: (1) self-organizing property that is detectable from the observation of the evolution of the floc size distribution. (2) the fractal geometry of individual flocs, not present in the elementary particles constituting the system at initial state, show a significant complexity. To summarize, the far-from-equilibrium dynamical state of the system may be a key point for understanding the relation between the characteristics at small and large length scale of a flocculating C2-class system. At large scale we observe organization while at small scales we observe complexity.

6. CONCLUSION

Experiments to observe the floc size distribution and individual floc geometry with kaolinite suspensions in a settling column were carried out. The time evolution of the floc size distribution from both an experimental and a conceptual point of view were analyzed. Next we focused our analysis on the floc's local scales, quantifying fractal properties and non-homogeneity of mass organization.

A cohesive sediment suspension can be regarded as a set of a large number of individual particles interacting in time. At system scales, a population of interacting flocs stabilizes at a far-from-equilibrium steady state, which is statistically stationary at constant environmental forcing. At system scales, a flocculating suspension manifests a tendency to self-organization. An antithetic tendency is observed at floc scales, as flocs develop geometries characterized by multifractality and disorder. The far-from-equilibrium state of the system may be caused by the development of disordered structures from regular (ordered) primary particles. However, the extent to which far-from-equilibrium behaviour can be explained by means of the kinematics of gain and loss in floc mass must still be understood. The knowledge acquired here will be used to formulate a population balance

equation to model the time evolution of the floc size distribution of a cohesive sediment suspension.

ACKNOWLEDGMENTS

The authors like to thank prof. Jurjen Battjes for his critical suggestions addressed during the development of the content exposed in this paper, Remi Jouan and Dalia dal Corso for their skills and motivation in the experimental activities. This study is financed from Delft University Research funds through the BEO-Program.

LIST OF THE SYMBOLS

A		Dimensionless floc area
c	$[g/L]$	Sediment concentration measured in the buffer tank
c_d	$[g/L]$	Desired sediment concentration in the column
c_s	$[g/L]$	Sediment concentration in the storage tank
d_0		3D capacity dimension
d_p		Perimeter-based fractal dimension
f		Multifractal spectrum
f_g	$[Hz]$	Grid frequency
G	$[1/s]$	Turbulence shear rate
H	$[\mu m]$	Total interparticle distance
ℓ		Dimensionless floc size
L	$[\mu m]$	Floc size
P		Dimensionless floc perimeter
q		Family order in the multifractal formalism
s	$[ppt]$	Water salinity
S		Entropy function
S'		Specific entropy
S'_{max}		Maximum entropy
t	$[h]$	Time
α		Singularity strength
μ	$[kg/ms]$	Water viscosity
ε	$[m^2/s^3]$	Energy dissipation rate
ϵ	$[pixel]$	Box size in the ϵ-covering
ρ_s	$[kg/m^3]$	Sediment density

τ	Mass-correlation exponent
Υ	Disorder function
Υ'	Disorder index
$\Omega_{2,3}$	2D and 3D sets

REFERENCES

Argyris, J.G., G. Faust and M. Haase. 1994. *An exploration of chaos*, North-Holland, Amsterdam, 751p.

Amitrano, C. and A. Coniglio. 1986. Growth probability distribution in kinetic processes. *Physical Review Letters*, 57(8), 1016-1019.

Chhabra, A. and R.V. Jensen. 1989. Direct determination of the $f(\alpha)$ singularity spectrum. *Physical Review Letters*, 62(12), 1327-1330.

de Boer, D.H., M. Stone and L.M.J Lévesque. 2000. Fractal dimensions of individual flocs and floc population in streams. *Hydrological Processes*, 14, 653-667.

Dyer, K.R. 1989. Sediment processes in estuaries: future research requirements. *Journal of Geophysical Research*, 94(c10), 14,327-14,339.

Friedlander, S.K. 1977. *Smoke, Dust and Haze, fundamentals of earosol behavior*, Wiler, New York, 317p.

Gmachowski, L. 1996. Hydrodynamics of Aggregated Media. *Journal of Colloid and Interface Science* 178, 80-86.

Grassberger, P. and I. Procaccia. 1983. Characterization of strange attractors. *Physical Review Letters*, 50(5), 346-349.

Halsey, T.C., M.H. Jensen, L.P. Kadanoff, I. Procaccia and B.I. Shraiman. 1986a. Fractal measures and their singularities: The characterization of strange sets. *Physical Review Letters*, 33(2), 1141-1151.

Halsey, T.C., P. Meakin and I. Procaccia. 1986b. Scaling structure of the surface layer of Diffusion-Limited Aggregates. *Physical Review Letters*, 56(8), 854-857.

Hentschel, H.G.E. and I. Procaccia. 1983. The infinite number of generalized dimensions of fractals and strange attractors. *Physica*, 8D, 435-444.

Kranenburg, C. 1994. On the fractal structure of cohesive sediment aggregates, *Continental and Shelf Science*, 39, 451-460.

Krone, R.B. 1963. *A study of rheologic properties of estuarial sediments*, Tech. Bull. 7, USAE, Committee of Tidal Hydraulics, Vicksburg, MS.

Lick, W. and J. Lick. 1988. On the aggregation and disaggregation of fine-grained sediments. *Journal of Great Lakes Research*, 14(4), 514-523.

Mach, J., F. Mas and F. Sagues. 1995. Two representations in multifractal analysis. *Journal of Physics*, 28, 5607-5622.

Maggi, F. *Survey of the numerical characterisation of 2-D complex clusters*. 2002. Report No. 4-02, Delft University of Technology, 30p.

Maggi, F., J.C. Winterwerp, H.L. Fontijn, W.G.M. van Kesteren and J.M. Cornelisse. 2002. A settling column for turbulence-induced flocculation of cohesive sediments. *Proceedings of HMEM2002 Conference*. Wahl, T.L. (ed.), Estes Park CO, USA. CD-ROM.

Maggi, F. J.C. Winterwerp. In review. Mud flocs - Part 1 - Efficient thresholding method for image analysis. Submitted to *Journal of Hydrology*.

Maggi, F., A.J. Manning and J.C. Winterwerp. In review. Mud flocs - Part 2 - On the characterisation of floc geometry and floc dynamics. Submitted to *Journal of Hydrology*.

Maggi, F. and J.C. Winterwerp. 2004. Method for computing the three-dimensional capacity dimension from two-dimensional projections of fractal aggregates. *Physical Review E*, 69, 011405.1-011405.8.

Manning, A.J. and K.R. Dyer. 1999. Observation of the size, settling velocity and effective density of flocs and their fractal dimension. *Journal of Sea Research.*, 41, 87-95.

Manning, A.J. and K.R. Dyer. 2002. The use of optics for the *in situ* determination of flocculated mud characteristics. *Journal of Optics A*, 4, S71-S81.

Maturana, H.R. and F.J. Varela. 1972. *Autopoiesis and cognition: the realization of the living*. Cohen, R.S. and M.W. Wartofsky (eds.), Reidel, Dordrecht, Holland, 141p.

Meakin, P. 1998. *Fractals, Scaling and Growth Far From Equilibrium*, Cambridge University Press, Cambridge, UK, 674p.

McCave, I.N. 1993. Size spectra and aggregation of suspended particles in the deep ocean. *Deep-Sea Research*, 31(4), 329-352.

Nicolis, G. and I. Prigogine. 1974. *Self-organisation in non equilibrium systems*, Wiley, New York, 491p.

O'Melia, C. 1980. Aquasols: the behaviour of small particles in acquatic systems. *Environmental Science and Technology*, 14(9), 1052-1060.

O'Melia, C. 1986. The influence of coagulation and sedimentazion on the fate of particles, associated pollutants, and nutrients in lakes. *Chemical Processes in Lakes*. Stum, W. (ed.), Wiley, New York, 207-224.

Pietronero, L. 1990. Theory of fractal growth. *Physica A*, 163, 316-324.

Serra, T. and X. Casamitjana. 1998a. Effect of the Shear and Volume Fraction on the Aggregation and Break-up of particle. *AIChE Journal*, 44(8), 1724-1730.

Serra, T. and X. Casamitjana. 1998b. Structure of the Aggregates During the Process of Aggregation and Break-up Under a Shear Flow. *Journal of Colloid and Interface Science*, 206, 505-511.

Smoluchowsky, M. 1917. Versuch einer Mathematischen Theorie der Koagulationskinetik Kolloid Losungen. *Zeitschrift fur Physikalische Chemie*, Leipzig, 92, 129-168 (in German).

Shannon, C. 1948a. A methematical theory of communication. *Bell Labs Technical Journal*, 27, 379-423.

Shannon, C. 1948b. A methematical theory of communication. *Bell Labs Technical Journal*, 27, 623-656.

Shiner, J.S. 2000. Self-organized criticality: self-organized complexity? The disorder and "simple complexities" of power law distributions. *Open Systems and Information Dynamics*, 7, 131-137.

Van Leussen, W. 1994. *Estuarine Macroflocs*, Ph.D. Thesis, University of Utrecht.

Vicsek, T. 1992. *Fractal growth phenomena*, World Scientific, Singapore, 355p.

Wells, M.L. and E.D. Goldberg. 1993. Colloid aggregation in seawater. *Marine Chemical*, 41, 353-358.

Winterwerp, J.C. 1998. A simple model for turbulence induced flocculation of cohesive sediment. *Journal of Hydraulic Research*, 36(3), 309-326.

Winterwerp, J.C. 1999. *On the dynamics of high-concentrated mud suspensions*, Ph.D. Thesis, Delft University of Technology.

Winterwerp, J.C. 2002. On the flocculation and settling velocity of estuarine mud. *Continental Shelf Research*, 22(9), 1339-1360.

Estuarine and Coastal Fine Sediments Dynamics
J.P.-Y. Maa, L.P. Sanford and D.H. Schoellhamer (editors)
Published by Elsevier B.V.

Constancy of the relation between floc size and density in San Francisco Bay

Ganju, N.K.[a], D.H. Schoellhamer[a], M.C. Murrell[b], J.W. Gartner[c] and S.A. Wright[a]

[a]U.S. Geological Survey, 6000 J Street, Sacramento, CA 95819
[b]U.S. Environmental Protection Agency, NHEERL, Gulf Ecology Division, 1 Sabine Island Drive, Gulf Breeze, FL 32561
[c]U.S. Geological Survey, 345 Middlefield Road, Menlo Park, CA 94025

KEY WORDS
Cohesive sediment, flocs, floc size, floc density, laser diffraction, San Francisco Bay

The size and density of fine-sediment aggregates, or flocs, govern their transport and depositional properties. While the mass and volume concentrations of flocs can be measured directly or by optical methods, they must be determined simultaneously to gain an accurate density measurement. Results are presented from a tidal cycle study in San Francisco Bay, where mass concentration was determined directly, and volume concentration was measured in 32 logarithmically spaced size bins by laser-diffraction methods. The relation between floc size and density is investigated assuming a constant primary particle size and fractal floc dimension. This relation is validated with measurements from several sites throughout San Francisco Bay. The constancy of this relation implies a uniform primary particle size throughout the Bay, as well as uniform aggregation/disaggregation mechanisms (which modify fractal dimension). The exception to the relation is identified during near-bed measurements, when advected flocs mix with recently resuspended flocs from the bed, which typically have a higher fractal dimension than suspended flocs. The constant relation for suspended flocs simplifies monitoring and numerical modeling of suspended sediment in San Francisco Bay.

1. INTRODUCTION

Measurement of in situ particle size is critical to understanding the dynamics of fine-sediment flocculation and settling. The methods used to evaluate size distribution range from video camera-based (Manning and Dyer, 2002) to laser-diffraction, *e.g.*, Laser In-Situ Scattering Transmissometer-100[1] (LISST-100; Agrawal and Pottsmith, 1994). The LISST-100 system is an autonomous unit that measures laser diffraction from suspended particles, and assigns each particle to 1 of 32 logarithmically spaced size classes (1–250 μm). The output of the LISST-100 is total volume concentration in each size class. While these results are helpful in analyzing particle-size evolution, the evolution of mass distribution can be estimated only with knowledge of the average mass density of each size class. Mass distribution is necessary to estimate mass concentration and settling flux for each size class, both of which have ramifications for numerical modeling and contaminant transport.

Converting a volume distribution to a mass distribution requires knowledge of the floc density for a given size class. Kranenburg (1994) suggests that sediment flocs aggregate in a fractal manner, requiring that a given fractal dimension and primary particle size will yield a specific density for a corresponding floc size. Varying fractal dimension and primary particle size will alter the floc density, though actual floc size may remain unchanged. If one assumes that fractal dimension and primary particle size remain unchanged over space and time for a given system, then Kranenburg's floc size–density relation also will hold. This relation then can be applied to volume-distribution data to yield the mass distribution.

This study tests the hypothesis that the floc size–density relation is constant in San Francisco Bay, California. Tidal cycle, synoptic, and continuous measurements of floc size and Suspended Sediment Concentration (SSC) will provide the means to investigate the floc size–density relation. If the relation is constant, the underlying implication is that primary particle size and fractal dimension also are constant throughout the Bay.

San Francisco Bay (Fig. 1) drains a 154,000 km^2 watershed through the confluence (Delta) of the Sacramento and San Joaquin Rivers. Downstream of the Delta are four subembayments: Suisun Bay, San Pablo Bay, Central Bay, and South Bay. The first three subembayments are affected primarily by freshwater flow from the Delta and tidal forcing from the Golden Gate, while exchange in South Bay is governed mainly by

[1]Any use of trade, product, or firm names is for descriptive purposes only and does not imply endorsement by the U.S. Government.

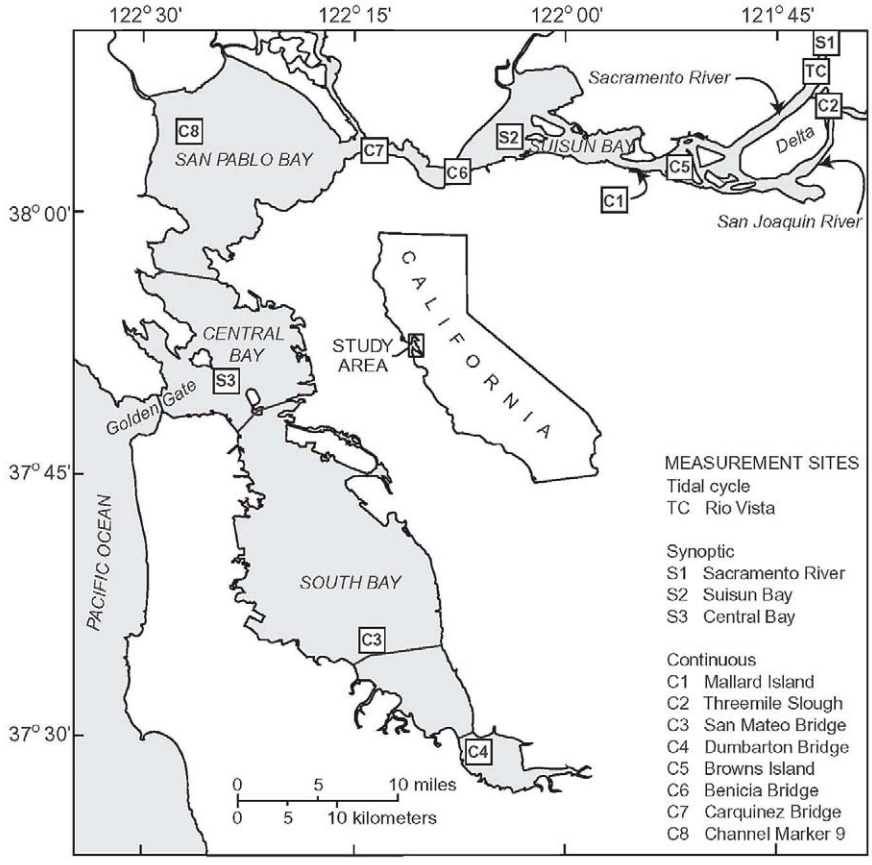

Fig. 1. Area map, showing measurement sites for tidal cycle, synoptic, and continuous studies.

tidal forcing, as freshwater flow is relatively minimal. Freshwater flow generally is low from late spring to late fall, while flow increases during winter and spring due to rainfall, snowmelt, and reservoir releases.

2. METHODS

2.1. Tidal-cycle measurement

A preliminary study of floc size (Sacramento River to Central Bay) suggested that vertical variability may be greater than longitudinal variability. Therefore, on

November 5, 2002, a fixed, vertical-profiling deployment was initiated near the freshwater-saltwater interface, at Rio Vista (Sta. TC, Fig. 1). The date was chosen to coincide with a spring tide and low freshwater input. Prior to deployment, it was confirmed that freshwater and saltwater were present during ebb and flood tides, respectively, at the site. The specific site was at the edge of the main channel in 10 m of water. Measurements were performed from an anchored vessel.

Floc identification was performed with the LISST-100, which can measure particles ranging in size from 1–250 μm, in 32 bins (logarithmically spaced). Details of the instrument can be found in Agrawal and Pottsmith (1994). Output consists of particle volume concentration in microliters per liter [μL/L] for each size class. The volume concentration for a given aggregate includes sediment particles, interstitial water, and any other material bound into the floc (*e.g.*, extracellular polymeric substances).

Suspended-sediment concentration was determined with a nephelometric turbidity sensor, which was part of a multi-probe unit (Datasonde 4, Hydrolab Corp.). Other sensors on the unit were conductivity, temperature, and depth. The turbidity output of the sensor (nephelometric turbidity units or NTU) was calibrated to SSC using water samples collected using a peristaltic pump. Water samples were analyzed gravimetrically for SSC.

The profiling package consisted of the multi-probe and LISST-100; a 10-m tube was secured to the package and delivered water samples to the peristaltic pump. The tube opening, LISST-100 optics, and multi-probe sensors were positioned as closely together as possible without interference from one another. The package was raised and lowered through the water column at 1-m intervals every 2 min. Vertical profiles ranged from 1–8-m depths, and measurements were taken every minute during a flood tide, to yield replicate measurements at every vertical location. The duration of each vertical profile was approximately 15 min, and 20 vertical profiles were collected during a flood tide from slack after ebb to slack after flood. A boat-mounted acoustic Doppler current profiler (ADCP) collected profiles of velocity continuously during the deployment. Water samples were collected at various depths and stages of the tide.

2.2. Synoptic measurement

Surface-water samples were collected monthly from April to October 1996 at three stations in northern San Francisco Bay (Stas. S1, S2, and S3; Fig. 1) as part of a study of bacterioplankton dynamics (Murrell *et al.*, 1999); these samples were analyzed to determine mass concentration and volume concentration. Part of the sample was used to determine SSC by the traditional filtering and weighing procedures while part of the sample was used to determine floc size by filtering onto 0.45-μm filters.

Photomicrographs were taken of the filters and the effective size distribution that could be observed was 2–25 μm. The photographic slides were digitized. Particle areas were converted to equivalent circular diameters and accumulated into 1-μm-diameter bins. Particle volumes were calculated assuming that the particles were spherical.

2.3. Continuous measurement

Primary particles: Mallard Island

In December 1996 and January 1997, water samples were collected at Mallard Island (Sta. C1; Fig. 1) and analyzed to determine primary particle size. The site is located on the edge of a wide channel, in 8 m of water. Sampling was done during a relatively large freshwater flow pulse as part of a study of sediment-associated pesticide transport. Two-hundred and four samples were collected with a peristaltic pump at a depth of 1 m below the surface. The particles were disaggregated and particle size was determined with a Coulter Counter.

LISST-100: Threemile Slough

During July 2002, the LISST-100 was deployed at Threemile Slough (Sta. C2; Fig. 1), within the Delta. Flow is bi-directional at the site, with salinity present during flood tides. Total depth at the site is 4 m, while the LISST-100 was located 2 m above bottom. The unit was situated at an existing fixed site on the levee at the edge of the channel. A peristaltic pump was deployed on the levee, with the sampling tube near the optics of the LISST-100. During a 24-hour period (July 25–26, 2002), a water sample was collected each hour, while the LISST-100 was sampling. Water samples were analyzed gravimetrically for SSC.

LISST-100: South Bay

Two locations in South Bay, near the San Mateo and Dumbarton Bridges (Stas. C3 and C4; Fig. 1), were occupied in October 1998. These experiments focused on near-bed processes; therefore, a package consisting of a LISST-100, optical backscatterance sensor, and ADCP was deployed 2 m above the bed at each site. Total depth at the San Mateo site was 16 m and 7 m at the Dumbarton site. Optical sensors were calibrated to SSC by immersing the sensor in a bucket of well-mixed surficial sediment, and withdrawing water for SSC analysis (Gartner *et al.*, 2001). The LISST-100 and optical sensors collected measurements in 15-min intervals for 4 days at the San Mateo site and 6 days at the Dumbarton site.

Turbidity and SSC: Bay-wide

The relation between turbidity and SSC will be used to postulate the constancy of the floc size–density relation. Data from turbidity sensors at four sites in San Francisco Bay will be used: Carquinez Bridge, Benicia Bridge, San Pablo Bay channel marker 9 (1998–2002; Buchanan and Ganju, 2003), and Browns Island (1-month deployments in May and November 2002 and April and November 2003; Ganju *et al.*, 2003) (Fig. 1). The first two sites have two sensors each, one at mid-depth and one at near-bottom. Water samples are collected periodically during the entire duration of each sensor's operation. These samples are analyzed for SSC and used to convert the turbidity output to SSC.

3. RESULTS

3.1. Tidal-cycle measurement

Tidal variability

Floc-size distribution at the site was controlled by mean velocity (max. 0.67 m/s) and SSC (6–83 mg/L). At slack after ebb, quiescent conditions led to a median volumetric floc diameter (D_{50}) range of 20–80 μm (increasing with depth). At maximum flood, D_{50} became more uniform with a range between 45–65 μm in the water column. Once currents subsided, higher SSC during slack after flood (as compared to slack after ebb) led to a wider D_{50} range of 40–110 μm (also increasing with depth). Salinity varied between 0 and 1.6 psu. Any possible effect of salinity on flocculation is difficult to infer, because the source of salinity and suspended sediment are the same (Suisun Bay), and increasing SSC may have a greater influence on particle size.

Floc size versus density

Volume concentration distributions from the LISST-100 were converted into mass concentration distributions, using a size-dependent floc density function given by Kranenburg (1994):

$$\rho_f = \rho_w + (\rho_p - \rho_w)[(D_p/D_f)^{3-n}] \quad (1)$$

where ρ is density, D is diameter, n is fractal dimension, and subscripts f, p, and w indicate floc, primary particle, and water, respectively. Fractal dimension is a measure of the packing of individual particles – larger fractal dimension indicates tighter packing.

Water samples collected at different elevations in the water column and different tidal stages during the study were analyzed for SSC. The simultaneous LISST-100 volume concentration distribution was multiplied by the above density distribution, yielding a mass concentration distribution by size class. The sum of mass concentration for all classes provided a LISST-100-derived SSC. The best agreement between actual SSC and LISST-100-derived SSC was achieved with a primary particle diameter of 2.5 μm and fractal dimension of 2 (Fig. 2).

3.2. Synoptic Measurement

The median diameter, by volume, of the material on the filters was 14.0 ± 0.8 μm, 13.4 ± 1.5 μm, and 12.6 ± 0.6 μm at Stas. S3, S2, and S1, respectively. These diameters are greater than the primary particle diameter and less than the diameter of flocs. Thus, filtration appears to have broken flocs apart and into lower-order aggregates that comprise the larger floc.

The ratio of SSC to aggregate volume (Fig. 3) equals the dry density of the lower-order aggregates. Fitting a line to the data in Fig. 3, the dry density of the lower-order aggregates is 0.117 grams per cubic centimeter (g/cm^3), which equals a wet density of 1.07 g/cm^3. The constant slope indicates constant aggregate dry density for an SSC

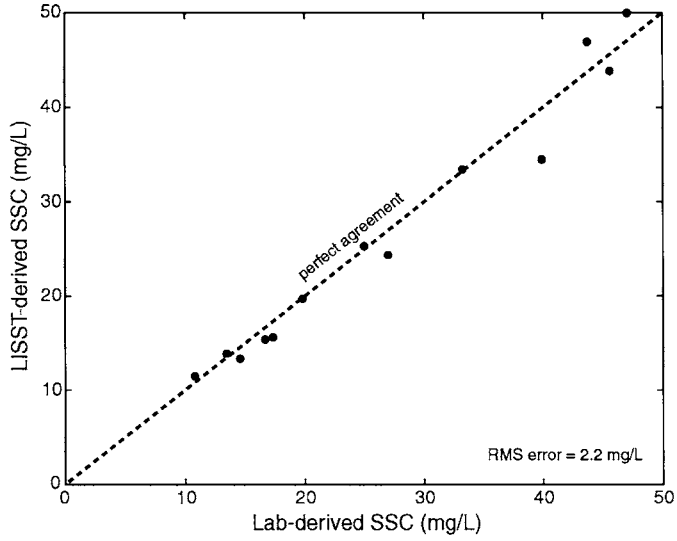

Fig. 2. Validation of floc size–density relation, from LISST-100 data and lab-analyzed water samples. Volume concentration data (LISST-100) was converted to mass concentration data via Eq. 1, with D_p = 2.5 μm and n = 2. Primary particle diameter (D_p) was varied to yield best fit between LISST-derived SSC and lab-derived SSC.

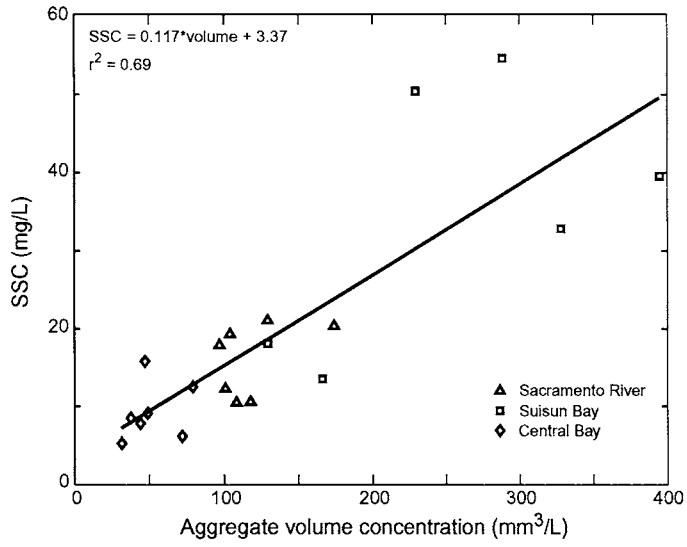

Fig. 3. Relation between SSC and aggregate volume, from synoptic measurements. Slope of the fitted equation indicates a constant aggregate dry density.

range of 35 – 400 mg/L. Thus, the size and the density of the lower-order aggregates on the filters are fairly constant, longitudinally and temporally. The density is less than expected from Eq. 1 (1.29–1.33 g/cm^3) because filtration somewhat flattened the material on the filters, but the material was assumed to be spherical to estimate particle volume, and therefore, the volume may be overestimated.

3.3. Continuous measurements

Primary particles: Mallard Island

Median primary particle size at the landward boundary of the Bay usually was 4–6 μm and increased to 12 μm for only a few hours during a large flood (Fig. 4).

The observed primary particle size was greater than the primary particle size calculated from the Rio Vista data and found by Krone (1962) in laboratory experiments (2.5 μm). Incomplete disaggregation of flocs in the samples probably contributes to the discrepancy.

LISST-100: Threemile Slough

LISST-100-derived SSC corresponds well with actual SSC at Threemile Slough (Fig. 5). The density relation determined by the tidal cycle study was applied to the

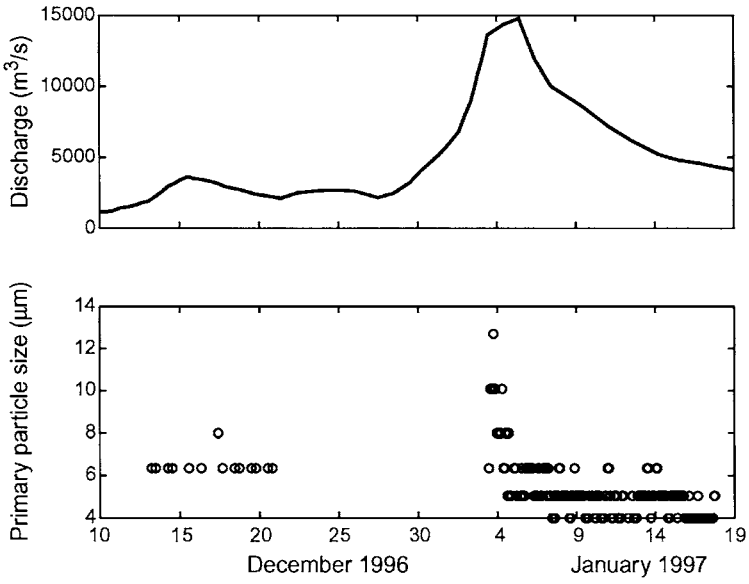

Fig. 4. Median primary particle size at Mallard Island, during freshwater flood period, December 1996 to January 1997.

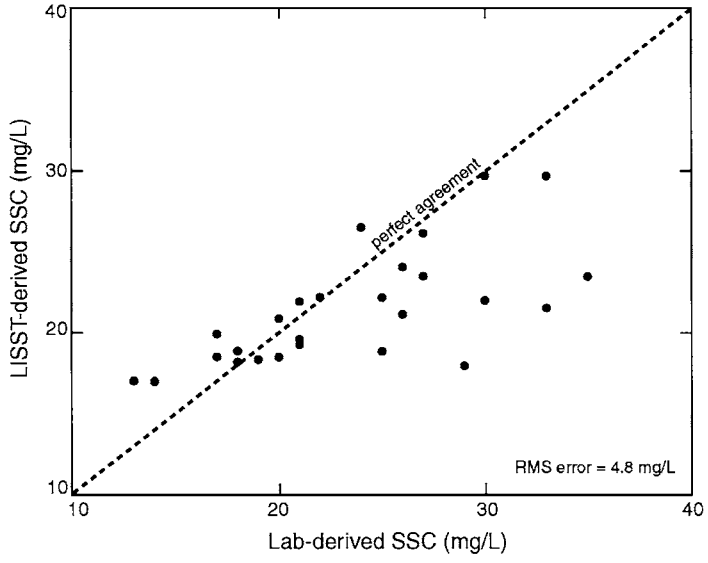

Fig. 5. Comparison of lab-derived SSC with LISST-100-derived SSC at Threemile Slough. LISST-100-derived SSC was calculated using density relation determined from data obtained at Rio Vista.

volume concentration distributions measured at Threemile Slough. The agreement between LISST-100-derived SSC and actual SSC (as determined by 24 concurrent water samples) suggests that the density relation at Rio Vista is suitable for Threemile Slough. The mean error of the LISST-100-derived SSC is 14 percent, with an RMS error of 4.8 mg/L.

LISST-100: South Bay

LISST-100-derived SSC corresponds with OBS-derived SSC at South Bay sites C3 and C4, though LISST-100-derived SSC is consistently lower than the OBS value (Figs. 6, 7). Again, the density relation from the Rio Vista study was applied to the volume concentration distributions. The best relation between OBS and LISST-100-derived SSC was achieved with larger fractal dimensions than 2 (2.3 and 2.1 for San Mateo and Dumbarton Bridges, respectively). Winterwerp (1999) noted that average fractal dimension of suspended particles is about 2, while greater fractal dimensions (> 2.6) are found within the bed. The intermediate values at the South Bay sites suggest a mixing of suspended particles and bed-derived flocs, which is plausible due to the near-bed deployment of instruments. The mean error of the LISST-100-derived SSC (with

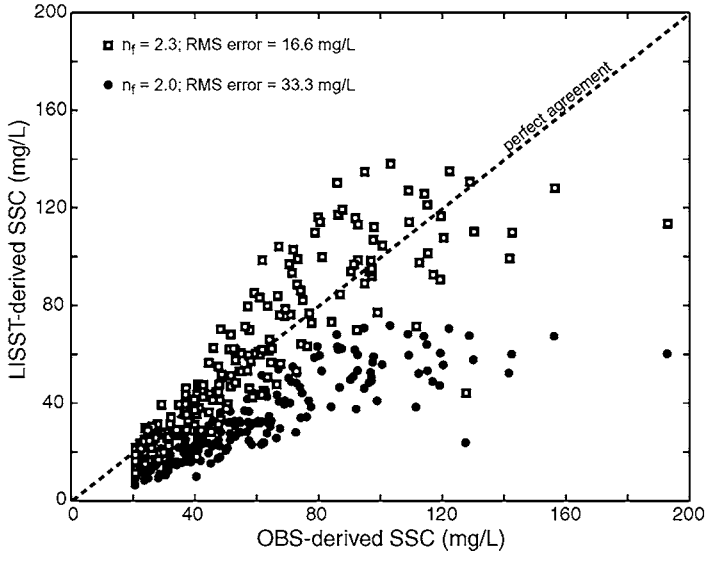

Fig. 6. Comparison of OBS-derived SSC with LISST-100-derived SSC at San Mateo Bridge. LISST-100-derived SSC was calculated using density relation determined from data obtained at Rio Vista, with fractal dimension 2. Best fit was obtained with fractal dimension 2.3.

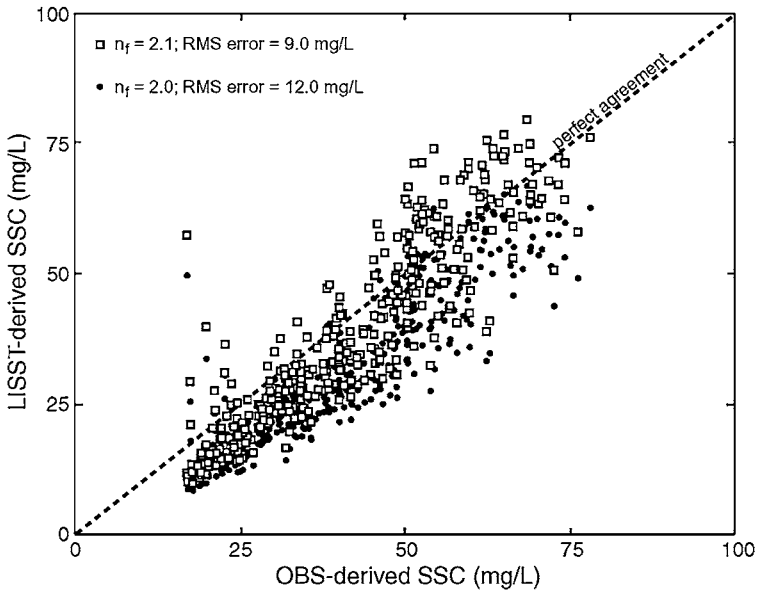

Fig. 7. Comparison of OBS-derived SSC with LISST-100-derived SSC at Dumbarton Bridge. LISST-100-derived SSC was calculated using density relation determined from data obtained at Rio Vista, with fractal dimension 2. Best fit was obtained with fractal dimension 2.1.

fractal dimension 2) is 27 percent at the Dumbarton site (RMS error of 12.0 mg/L) and 46 percent at the San Mateo site (RMS error of 33.3 mg/L). Usage of the higher fractal dimension yielded lower RMS errors of 9.0 and 16.6 mg/L for Dumbarton and San Mateo Bridge, respectively.

Turbidity and SSC: Bay-wide

Correlation between turbidity and SSC at four sites throughout the Bay is high, with an r^2 value of 0.92 (Fig. 8). One hundred and fifty-seven samples were collected at the four sites during 4 years. Individual sites have similarly good correlations by themselves (Buchanan and Ganju, 2003).

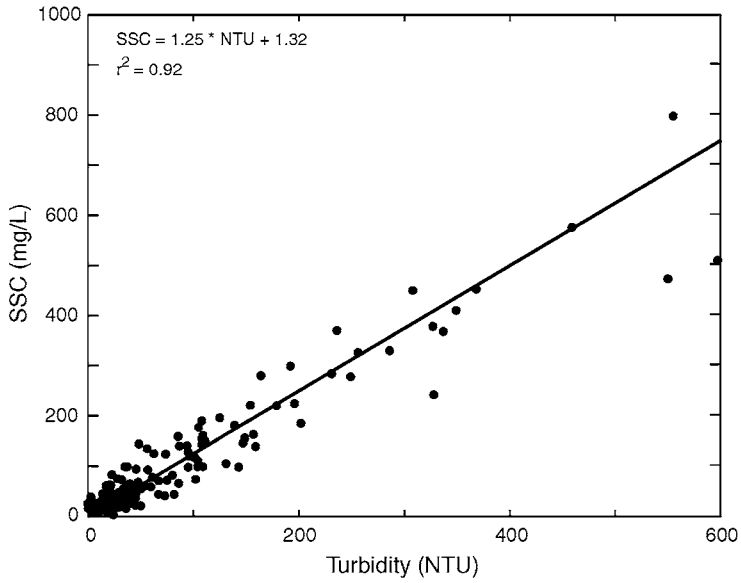

Fig. 8. Comparison of turbidity and SSC measurements, from four locations in San Francisco Bay.

4. DISCUSSION

4.1. Homogeneity of turbidity/suspended-sediment concentration and floc size/density

The homogeneous relation between turbidity and SSC can be shown to verify the floc size–density relation (Eq. 1) and its homogeneity. Turbidity is an optical measure of light scattering and is proportional to the surface area of flocs, as follows:

$$\text{Turbidity} \propto N D_f^2 \tag{2}$$

where N is the number of flocs per unit volume of water. SSC is proportional to dry density of the floc (ρ_{fd}) multiplied by the floc volume:

$$\text{SSC} \propto N \rho_{fd} D_f^3 \tag{3}$$

in which

$$\rho_{fd} = \rho_p (\rho_f - \rho_w)/(\rho_p - \rho_w) \quad (4)$$

By setting turbidity and SSC proportional and combining Eqs. 2–4, for turbidity and SSC to be proportional, the following condition must hold:

$$(\rho_f - \rho_w) D_f = \text{constant} \quad (5)$$

Rearranging the floc size–density relation, and setting n=2 (Eq. 1) gives

$$(\rho_f - \rho_w) D_f = (\rho_p - \rho_w) D_p \quad (6)$$

The left sides of Eqs. 5 and 6 are equal and the right side of Eq. 6 is constant if D_p is constant (and for n=2), so the floc size–density relation satisfies the condition required for turbidity to be proportional to SSC (Eq. 5). If primary particle size varied or if fractal dimension varied (or was not equal to 2), then turbidity and SSC would not be proportional throughout the Bay. Thus, the homogeneity of the turbidity and SSC relationship throughout San Francisco Bay indicates that the floc size–density relation must be constant.

4.2. Constancy of floc size–density relation

The floc size–density relation (Eq. 1) is remarkably constant in San Francisco Bay. This relation was developed from tidal cycle measurements at a fixed point. It then was used to convert volume concentration and size distribution to total mass concentration at three sites. The comparison between calculated and measured mass concentration is good (Figs. 5, 6, 7), indicating the validity of the relation for different sites and different times.

The homogeneity of lower-order aggregates confirms that the floc size–density relation is homogeneous. Photomicrographs of filtered water samples collected during low inflow showed that the median size (12.6–14.0 μm) and density (1.07 g/cm^3) of lower-order aggregates did not vary longitudinally (Fig. 3). This is an independent measure of one point on the floc size–density relation, and that relation is constant in space (sites S1, S2, S3) and time (April – October 1996). In Krone's (1986) model of aggregation, (homogeneous) lower-order aggregates combine to form larger flocs, which, in turn, have a homogeneous relation between size and density.

We hypothesize that constant primary particles and constant turbulence and flocculation mechanisms are responsible for the constancy of the floc size–density relation. Median primary particle size appears to be constant, even during large floods

where it would be expected to be most variable (Fig. 4). This eliminates one source of variability that could vary the floc size–density relation (Eq. 1). In addition, constant primary particle size is required to have the observed homogeneous relation between turbidity and SSC (Fig. 8, Eq. 6).

The two primary flocculation mechanisms in San Francisco Bay, biological activity and turbulent shear, are, to some extent, spatially homogeneous. The bottom of San Francisco Bay is dominated by *Potamocorbula amurensis* (Asian clam) with densities sometimes exceeding 12,000 clams per square meter (Carlton *et al.*, 1990). Werner and Hollibaugh (1993) measured individual clam filtering rates of 45 milliliters per hour, so the water column can be filtered at rates up to 0.5 meters per hour. This grazing rate is a homogeneous bioflocculation mechanism. San Francisco Bay has an average depth of 2 m and is a partially mixed estuary with semidiurnal tides. Deeper portions of the Bay undergo repeating cycles of vertical mixing and turbulent shear followed by a brief (less than 1 hour, typically) period around slack tides when currents are small and turbulence is damped by vertical stratification (Brennan *et al.*, 2002). Thus, the general production and dissipation of turbulence is similar throughout the channels of the Bay, which leads to similar turbulent shear and flocculation mechanisms. These homogeneous flocculation mechanisms probably account for the constant fractal dimension n=2 in the floc size–density relation (Eq. 1) being homogeneous.

An exception to the homogeneous floc size–density relation is near the bed in relatively deep areas where sediment eroding from the bed may increase the fractal dimension (Figs. 6, 7). Bed sediment has a greater fractal dimension, due to consolidation processes (Winterwerp, 1999). For the near-bed measurements, a combination of recently resuspended flocs and advected flocs (subjected to turbulence and mixing) yielded a fractal dimension greater than 2, though less than the normally assumed fractal dimension of flocs in the bed (> 2.6).

4.3. Mass distribution versus volume distribution

Application of a floc size–density relation (Eq. 1) to a LISST-100 volume distribution yields a mass distribution that differs substantially in character. For example, a unimodal volumetric size distribution with high concentrations of larger flocs becomes a weakly bimodal mass-based size distribution (Fig. 9). This is due to the high density of small flocs (despite low volumetric contribution) and the low density of large flocs (despite high volumetric contribution). As a consequence, the median particle diameter by mass typically will be smaller than the median particle diameter by volume. When evaluating particle distribution data, the differences between mass and volume distributions should be considered.

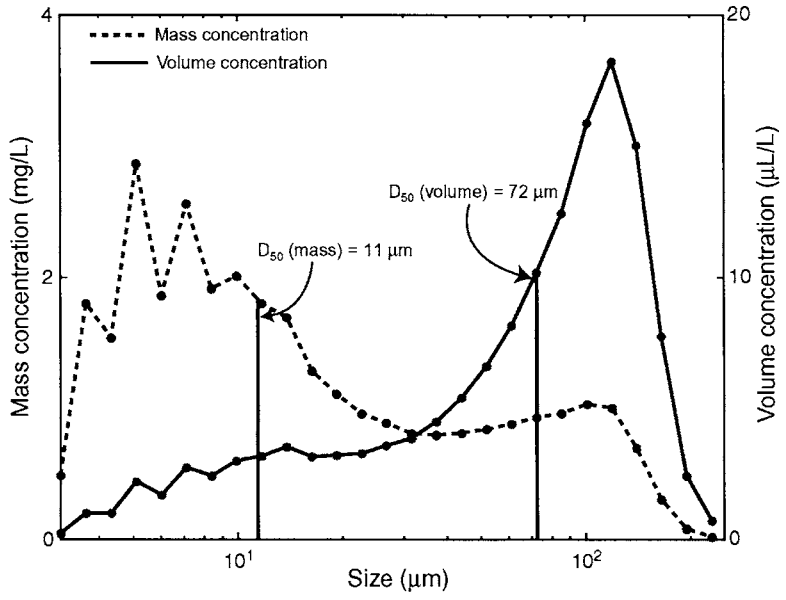

Fig. 9. Mass and volume concentration distributions for an individual 1-minute sample. Note unimodal volume concentration distribution becomes weakly bimodal mass distribution after floc size–density relation is applied to volume data.

4.4. Implications for monitoring and numerical modeling

The homogeneity of the floc size–density relation in San Francisco Bay simplifies monitoring and numerical modeling. One consequence is that turbidity and SSC are proportional throughout the Bay (Fig. 8). Thus, for monitoring SSC, optical sensors can be calibrated to turbidity and the output of the sensors can be converted to SSC without the need for detailed site-specific calibration. Samples still should be collected to verify sensor operation and the validity of the conversion to SSC. Numerical modeling of SSC in San Francisco Bay also is simplified by the existence of a homogeneous relation between floc size and density. This removes some of the potential variability that can confound model development, such as variability of settling velocity.

5. CONCLUSIONS

The floc size–density relation proposed by Kranenburg (1994) is validated, determined through tidal cycle measurements at a single site. This relation holds for other sites in San Francisco Bay. Homogeneity between turbidity and suspended-sediment concentration and homogeneity of lower-order aggregates supports the constancy of this relation. The two variables that control the relation are primary particle diameter and fractal dimension. Median primary particle size appears to be constant, even during large floods where it would be expected to be most variable and fractal dimension is constant because the mechanisms of flocculation and breakup are spatially homogenous throughout the Bay. An exception to the homogeneous floc size–density relation is near the bed in relatively deep areas where sediment eroding from the bed increases the fractal dimension. Otherwise, the floc size–density relation is constant in San Francisco Bay.

ACKNOWLEDGMENTS

Support for this study was provided by the CALFED Bay/Delta Program, U.S. Army Corps of Engineers as part of the Regional Monitoring Program for Trace Substances, Interagency Ecological Program, U.S. Geological Survey Priority Ecosystem Science, Toxic Substances Hydrology, and Federal/State Cooperative Programs. Michael Murrell's participation in this study was supported by California Department of Water Resources contract B-80883 to James T. Hollibaugh and California Water Resources Center grant W-875 to Mary W. Silver. We thank Kathryn Kuivila, James T. Hollibaugh, Greg Brewster, Paul Buchanan, and Brad Sullivan for their assistance.

REFERENCES

Agrawal, Y.C. and H.C. Pottsmith. 1994. Laser diffraction particle sizing in STRESS. *Continental Shelf Research*, 14 (10/11), 1101-1121.

Brennan, M.L., D.H. Schoellhamer, J.R. Burau and S.G. Monismith. 2002. Tidal asymmetry and variability of bed shear stress and sediment bed flux at a site in San Francisco Bay, USA. In: *Fine Sediment Dynamics in the Marine Environment.* Winterwerp, J.C. and C. Kranenburg (eds.), Elsevier Science B.V., 93-108.

Buchanan, P.A. and N.K. Ganju. 2003. *Summary of suspended-sediment concentration data, San Francisco Bay, California, water year 2001.* U.S. Geological Survey Open-File Report 03-312, 54p.

Carlton, J.T., J.K. Thompson, L.E. Schemel, and F.H. Nichols. 1990. The remarkable invasion of San Francisco Bay, California (USA) by the Asian clam *Potamocorbula amurensis*. 1. Introduction and dispersal. *Marine Ecology Progress Series*, 66, 81-94.

Ganju, N.K., B. Bergamaschi, and D.H. Schoellhamer. 2003. Tidal wetland fluxes of dissolved organic carbon and sediment at Browns Island, California: Initial evaluation, *Proceedings of the 2003 CALFED Science Conference,* Sacramento, California, January 14-16, 2003, 208. http://ca.water.usgs.gov/abstract/sfbay/abstractwetlandflux2003.html

Gartner, J.W., R.T. Cheng, P. Wang and K. Richter. 2001. Laboratory and field evaluations of the LISST-100 instrument for suspended particle size determinations. *Marine Geology*, 175, 199-219.

Kranenburg, C. 1994. On the fractal structure of cohesive sediment aggregates. *Estuarine, Coastal and Shelf Science*, 39, 451-460.

Krone, R.B. 1962. *Flume studies of the transport of sediment in estuarial shoaling processes.* Final report, University of California, Berkeley, Hydraulic and Sanitary Engineering Research Laboratory, 110p.

Krone, R.B. 1986. The significance of aggregate properties to transport processes. In: *Estuarine Cohesive Sediment Dynamics.* Lecture notes on Coastal and Estuarine Studies. Mehta, A.J. (ed.), Springer-Verlag, New York, 14, 66-84.

Manning, A.J., and K.R. Dyer. 2002. The use of optics for the *in-situ* determination of flocculated mud characteristics. *Journal of Optics A:* Pure and Applied Optics, 4, 571-581.

Murrell, M.C., J.T. Hollibaugh, M.W. Silver and P.S. Wong. 1999. Bacterioplankton dynamics in northern San Francisco Bay: Role of particle association and seasonal freshwater flow. *Limnology and Oceanography*, 44 (2), 295-308.

Werner, I. and J.T. Hollibaugh. 1993. *Potamocorbula amurensis:* Comparison of clearance rates and assimilation efficiencies for phytoplankton and bacterioplankton. *Limnology and Oceanography*, 38, 949-964.

Winterwerp, J.C. 1999. *On the dynamics of high-concentration mud suspensions.* PhD thesis, Delft University of Technology, The Netherlands, also Delft University of Technology, Faculty of Civil Engineering and Geosciences, Communications on Hydraulics and Geotechnical Engineering, Report 99-3, 172p.

Estuarine and Coastal Fine Sediments Dynamics
J.P.-Y. Maa, L.P. Sanford and D.H. Schoellhamer (editors)

Effects of different erosion techniques on sediment beds in the laboratory

Sills, G.[a], G. Lintern[b] and J. Leung[c]

[a]Oxford University Engineering Department, Oxford, UK
[b]previously Oxford University, UK, now Fisheries and Oceans Canada, Vancouver, Canada
[c]previously Oxford University

KEY WORDS
Sedimentation, erosion, density, consolidation

In clean sand, erosion occurs by the loss of particles from the surface, with little apparent effect on the material lower in the bed. In contrast, in beds of clays and silty clays, an increase in turbulent energy in the overlying water leads first to movement within the whole surface layer, followed by mass erosion as clumps of particles are torn from the bed. This paper reports the results of laboratory experiments in which erosion of silty clays was produced by various means, and the process was monitored by comparing measured densities throughout the beds before and after erosion. It is shown that density changes occur in the bed to depths that are significantly greater than those corresponding to the level of erosion, and that these changes can be either an increase or a decrease.

1. INTRODUCTION

Cohesive sediment has a dynamic impact on the environment. It is transported as suspended material and in density flows, it accumulates through settlement and consolidation, and it becomes resuspended through erosion. The latter process is a complex one, with the susceptibility to erosion depending upon the physical characteristics of the

sediment, on the stress history, including deposition rate and period of consolidation, on the biology and on the energy and turbulence available in the overlying water. Sediment erosion is assumed to occur once a critical value of erosion shear stress is exceeded by the action of the eroding fluid. However, this shear stress cannot be measured directly but must be inferred from other measurements, typically velocity in the overlying fluid at a time when it is known that the sediment is eroding. Given that it is impossible in the natural environment to distinguish between material that has been carried into a control volume from outside and material that has been eroded within it, measurements are normally made in a closed system. This allows the eroded mud to be quantified, and the eroding shear force to be calibrated. This can be achieved on a comparatively large scale in a flume and on a smaller scale both in the laboratory and in the field by devices that are placed on a sediment bed. Different systems impose different conditions on the sediment: linear water flow in straight or race track flumes; components of flow in two directions, radially and tangentially, in a circular flume or carousel; radial water flow; a rotating propeller in EROMES; jet pressure in the Cohesive Strength Meter (CSM) and small scale turbulence with rotating grids. Comparisons have been made between the results of different devices (*e.g.,* Tolhurst *et al.* 2000), with the unsurprising conclusions, amongst others, that the size and duration of the shear stress increments is extremely important, as is the choice of criterion used to calculate the erosion threshold.

Typically, the focus in measurement programmes has been on the initiation of movement in the surface layers. However, in contrast to the behaviour of sand beds, the erosion of cohesive beds visibly occurs over a finite depth of the surface layer, as water is entrained and the mud dilates before lifting into the overlying water. It would therefore not be surprising if the erosion process had also affected the bed that remains. The purpose of this paper is to examine the condition of the bed after erosion has occurred, and to explore the role of consolidation history and erosion mechanism.

2. EXPERIMENTAL CONDITIONS

2.1. Density measurement

An X-ray system has been developed at Oxford University to measure density in acrylic settling columns. Highly collimated X-rays are passed through the column, and, after absorption that is related to the density, they reach a sodium iodide crystal and photomultiplier assembly, which provide a count rate which can be correlated with soil density through appropriate calibration. The X-ray system is traversed vertically up and

down the settling column and typically produces count rate profiles which are almost indistinguishable for the two directions. The results are presented as continuous profiles of density with height at different times during each experiment, with an accuracy and a spatial resolution respectively of the order of 0.002 g/cc and 1 mm. Details of the system as originally developed may be found in Been (1980) and Been (1981), while the current facility is described in Sills (1998).

2.2. Erosion methods

For the erosion experiments, three different devices were used inside the 100mm diameter settling columns. The first was ISIS, developed at HR Wallingford for *in-situ* erosion measurements by Williamson & Ockenden (1996), in which water circulates down the outer walls of the settling column, radially across the sediment surface and back up a central tube. The instrument was designed to give a uniform shear stress across the surface of the mud. Fig. 1 combines a schematic and a photograph. The

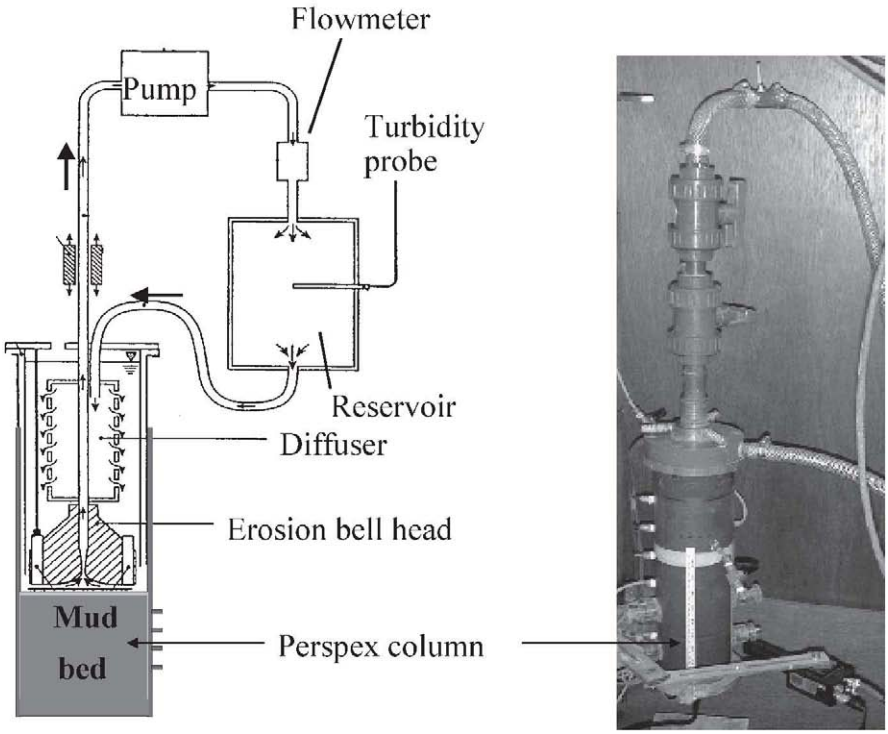

Fig. 1. ISIS erosion device, after Williamson & Ockenden (1996).

system was used as described in Lintern *et al.* (2000), with the erosion bell head placed 6mm above the mud bed. The pump speed was increased incrementally from a slow value to one high enough to cause erosion.

The second device was a 95mm diameter vane, 70mm in height, located above the sediment surface at a distance of 10mm operated at a range of rotation speeds from 0.5 to 2.5 rps. The vane had two blades, so the associated pressure wave would have had a frequency in the range 1 to 5Hz. A photograph of this device is shown in Fig. 2. A typical test consisted of a series of stages in which the speed of rotation was increased from its previous value and held constant for 10 minutes, before being increased again in the next stage. In the interval between stages, the vane was removed so that density and pore water pressures could be recorded.

The third was a perforated disc, with a diameter of 98mm and a thickness of 5mm, made to oscillate vertically in the overlying water. Eighteen holes of diameter 14mm were spaced in two rings, the radius of the inner ring being 17mm to the centre of the holes and the outer having a radius of 36mm. The grid was moved vertically between positions 10mm and 60mm above the bed, as shown schematically and as a photograph in Fig. 3. The grid oscillation frequency could be varied in the range 0.43 to 2.5Hz, corresponding to speeds of the disc at mid-stroke in the range 0.07m/s to 0.4m/s.

Fig. 2. Rotating vane

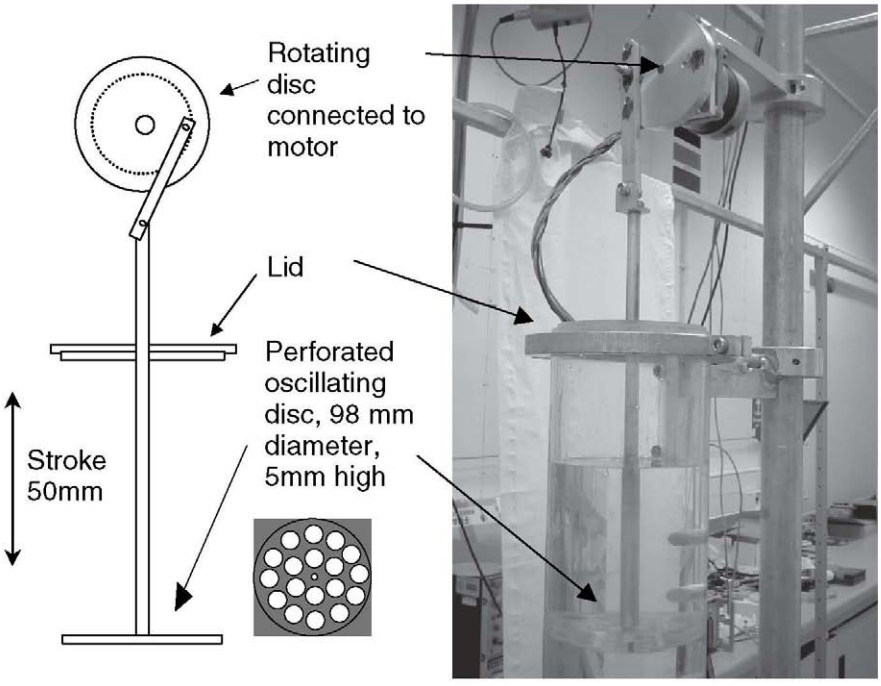

Fig. 3. Oscillating grid.

2.3. Soil

Experiments were carried out on two soils, characterised in Table 1. Measurement of the particle size of Dibden Bay mud gave a range of results, probably according to the amount of break down of the flocs. The dominant clay mineral in both soils was illite, with randomly inter-stratified illite/smectite in Dibden, but not Tamar.

The soil was prepared by mixing it to a uniform density, and placing it in 100mm diameter acrylic settling columns. The slurry was either eroded soon after being placed or was allowed to settle and consolidate under its own weight for periods up to a few weeks before being eroded.

Table 1. Soil classification.

Sediment	Description	% clay	LL, %	PL, %	PI, %	s.g.	% org
Dibden Bay	Clayey silt	35-45	65	35	30	2.47	7
Tamar Estuary	Clayey silt	23	88	64	24	2.67	20

2.4. Experimental programme

More than twenty experiments have been undertaken as the basis for the present paper, but detailed results will be reported for only a subset of this number, representing typical behaviour. The conditions of these experiments are listed in Table 2 (for Dibden Bay mud) and Table 3 (for Tamar sediment).

3. RESULTS

The variables to be considered are consolidation history, erosion device and soils. The results are presented first for Dibden Bay mud, divided into two sections, one for beds in which some consolidation has occurred and the other for newly-deposited sediment. Results for Tamar sediment are then presented in the reverse order: unconsolidated, followed by consolidating beds.

3.1. Consolidated beds of Dibden Bay mud

A typical evolution of density is shown in Fig. 4, for experiment JL_3, with an initial uniform slurry density of 1.151Mg/m^3, indicated by the profile marked 0. Consolid-

Table 2. Experiments using Dibden Bay mud.

Expt. name	Initial density, Mg/m^3	Initial height, m	Consolidation time, days	Erosion device
JL_2	1.139	0.222	12	Vane
JL_3	1.151	0.202	43	Grid, then vane
JL_5	1.234	0.102	0	Vane
JL_15	1.224	0.101	0	Grid

Table 3. Experiments using Tamar sediment.

Expt. name	Initial density, Mg/m^3	Initial height, m	Consolidation time, days	Erosion device
DGL_isis2	1.164	0.188	13	ISIS
JL_T4	1.164	0.165	31	Grid, then vane
JL_T3	1.170	0.101	0	Oscillating grid

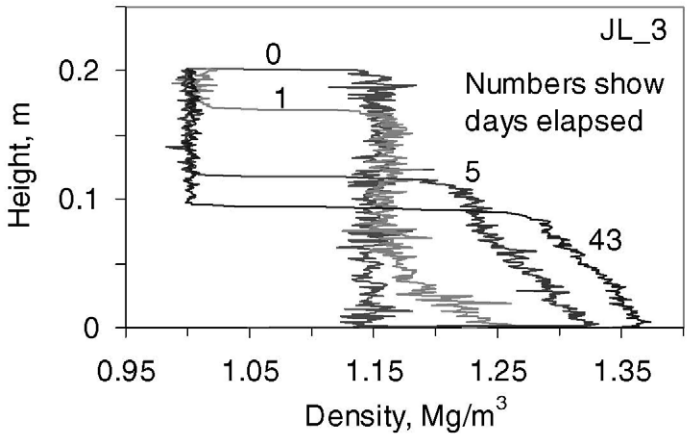

Fig. 4. Density profiles for self-weight consolidation of Dibden Bay mud.

adation took place first at the bottom of the settling column, since the pore water flow was upward, and this can be seen in the day 1 profile which has a triangular shape at the bottom and a uniform value over the top part. Pore pressures were measured at various levels in the column and the results showed that in the upper part, they were equal to the total vertical stress at the level of measurement, while in the lower part, they were less. This demonstrates that effective stresses (defined as total stress minus pore water pressure) began to develop as the soil consolidated. In the top section, although there was no effective stress (since total stress and pore water pressure were equal), it can be seen that a small increase in the density by comparison with the original value has occurred, due to creep processes. After 5 days, the triangular section had reached the top of the bed and consolidation was occurring throughout, and by 43 days, consolidation was virtually complete and the density profile has acquired the rounded shape that is typical of this stage. Further discussion of these processes may be found in Sills (1998).

Experiment JL_2 had an initial bed depth that was 10% greater than that of JL_3, and the longer drainage path length meant that consolidation occurred relatively more slowly. After 12 days consolidation, the density profile had a similar triangular shape to the five-day profile of JL_3, as shown in Fig. 5. This bed was then eroded using the vane, and the densities were measured immediately after each erosion stage. Figure 5a shows density profiles immediately after two such stages, with rotation speeds of 1.3

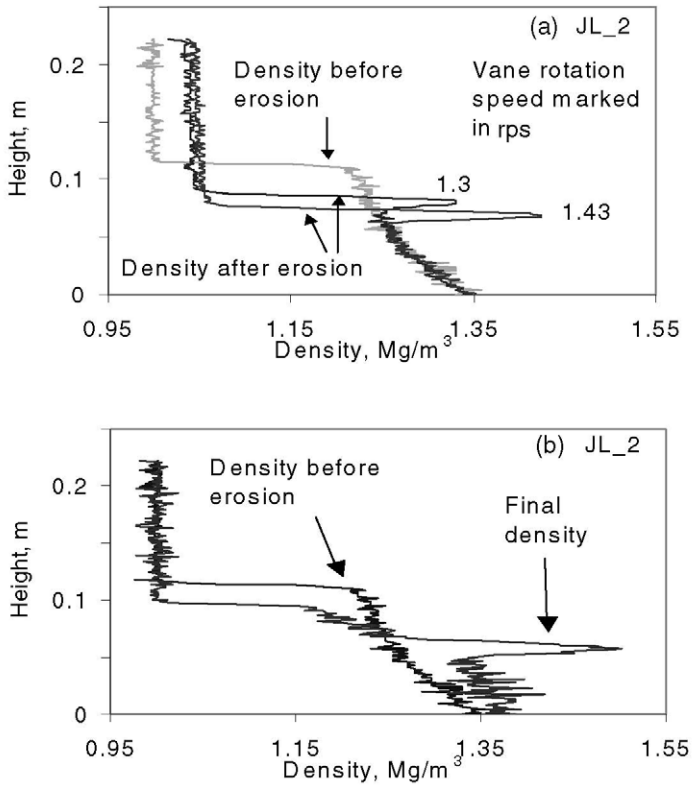

Fig. 5. Density profiles in erosion test using rotating vane for consolidated Dibden Bay mud. (a) initial stage and two stages immediately after erosion, (b) final stage.

and 1.43 rps. It can be seen that the surface of the bed has been lowered by the two stages of erosion, that the density of the fluid overlying the bed has been increased as sediment is held in suspension and that there has been a significant increase in the density of the surface layer over a depth of about 20 mm.

Figure 5b shows the final state of experiment JL_2, after the eroded sediment has been allowed to settle back onto the bed. This sediment has formed a loose low density top layer, while just below it, the high density layer has reached an even greater density than it had immediately after erosion at 1.43 rps. Also, the density of the underlying sediment bed has increased.

After consolidation of experiment JL_3, the oscillating grid was used in an attempt to cause erosion. However, even at the maximum vertical oscillation rate that could be achieved (2.5 Hz, corresponding to a maximum grid speed of 0.4 m/s) there was little

effect on the state of the consolidated bed. The vane was then used on the same bed, and a density increase was produced in the surface of the bed similar to that reported for JL_2 in Fig. 5a.

3.2. Unconsolidated beds of Dibden Bay mud

Figure 4 has shown the density increase that occurs throughout a slurry bed as a result of consolidation and creep. Since it is the surface density that may be expected to influence the resistance to erosion, a series of experiments was undertaken in which the initial slurry density was similar to the density reached at the surface during consolidation. That is, the density for these experiments was around the structural density for the soil, or the density that marks the transition from a fluid-supported suspension to a soil in which effective stresses exist (Sills 1998). In the chemical engineering literature, this is often referred to as the gel point. After placing the slurry, a piece of filter paper was laid on top of the soil (to protect it) and water added to bring the total height up to around 0.2 m. The filter paper was then removed and the erosion device inserted into the column.

Figure 6 shows the result of two erosion stages using the vane for experiment JL_5, with rotation speeds of 1.17 and 1.30 rps. The density of the overlying fluid was increased as a result of the material eroded into suspension and again a layer of higher density was produced at the surface. After rotation at 1.17 rps, the increased density extended down approximately 0.03 m from the surface, while the bed density beneath

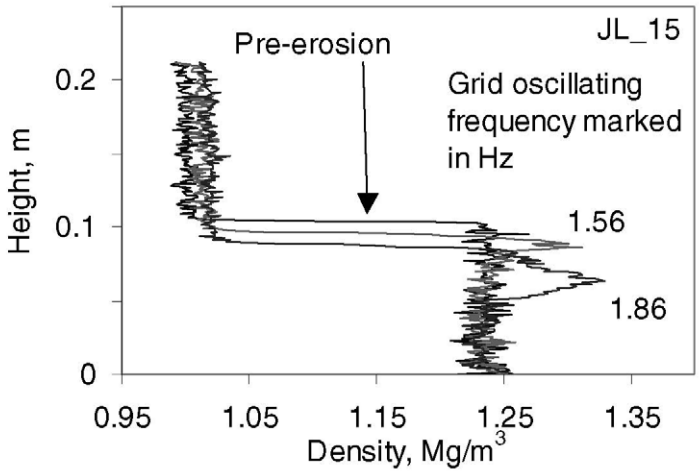

Fig. 6. Density profiles before and after erosion with rotating vane for unconsolidated Dibden Bay mud.

that was unchanged. After the second stage of rotation, most of the bed remaining after erosion had achieved a higher density.

Figure 7 shows the results of an experiment using the oscillating grid to produce erosion. Frequencies of oscillation of 1.56 and 1.86 Hz have been used, corresponding to maximum grid speeds of 0.25 and 0.3 m/s. As with the vane, there is a clear increase of density of the surface layer that exists after erosion. A similar pattern was seen in other experiments in this series.

3.3. Unconsolidated beds of Tamar sediment

The structural density of Tamar sediment is a little lower than that of Dibden Bay mud, so the initial slurry densities of the unconsolidated experiments were also chosen to be lower, with values from 1.170 Mg/m^3 for JL_T3 to 1.208 Mg/m^3 in experiments not presented here, but which showed very similar results. Figure 8 shows a typical result in which the oscillating grid left a higher density layer above a bed of overall increased density.

3.4. Consolidated beds of Tamar sediment

In experiment JL_T4, a slurry of Tamar sediment of initial density 1.164 Mg/m^3 was allowed to consolidate under its own weight for 31 days, by which time excess pore pressures had practically dissipated and consolidation was complete. Figure 9 shows the

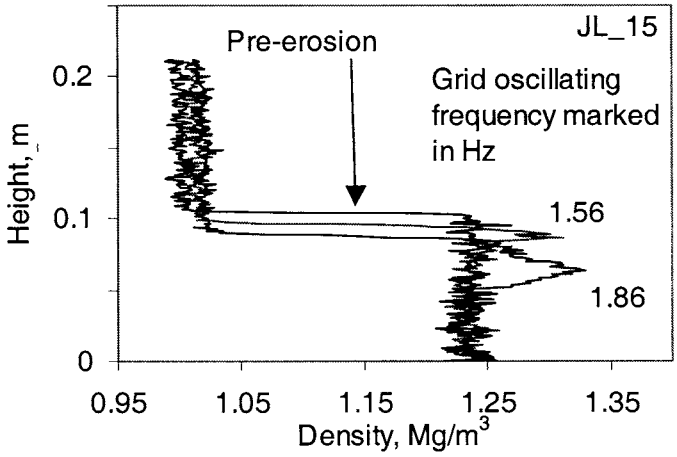

Fig. 7. Density profiles before and after erosion with oscillating grid for unconsolidated Dibden Bay mud.

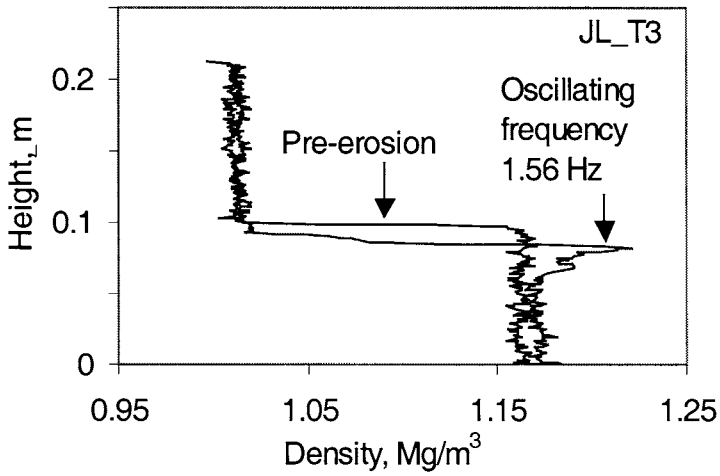

Fig. 8. Density profiles before and after erosion with oscillating grid for unconsolidated Tamar sediment.

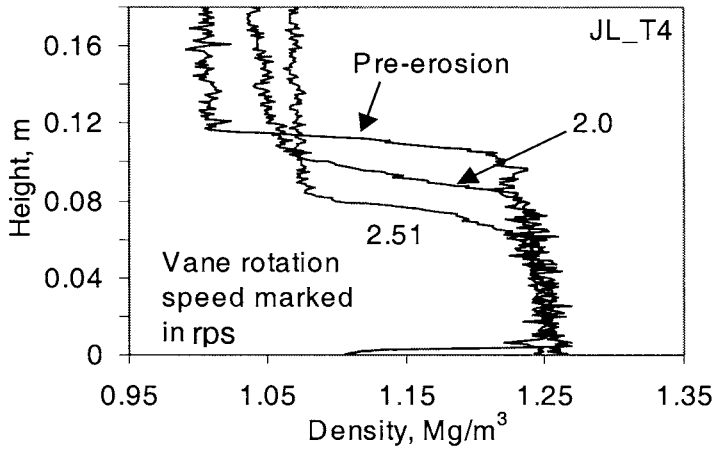

Fig. 9. Density profiles before and after erosion with rotating vane for consolidated Tamar sediment.

the final density profile at the end of consolidation (labelled "pre-erosion"), along with two profiles following erosion with the rotating vane. The eroded sediment is in suspension in the overlying fluid, but there is no sign of the increased density that had been seen at the surface of the Dibden Bay beds that had been deposited in a similar manner. In fact, the density of the bed that has resisted erosion appears to have remained constant during the process.

An earlier series of erosion experiments was undertaken on consolidated Tamar sediment using the ISIS device and has been reported in Lintern *et al.* (2000). One of the results is reproduced here, in Fig. 10. The experiment differed from those with the rotating vane and oscillating grid, in that the eroded sediment was removed from the settling column, so no sediment existed in suspension above the remaining bed. It can be seen that the erosion again affected the bed that remained, although in this case, there was a reduction of density in the surface layers, to a depth of around 60 mm, corresponding to nearly 80mm below the original bed surface before erosion. A video of the erosion process using ISIS in a similar experiment indicated that the upper part of the bed liquefied to a similar depth before a shallower section broke off into the overlying water. This is described in more detail, accompanied by still images of the process, in Lintern *et al.* (2000).

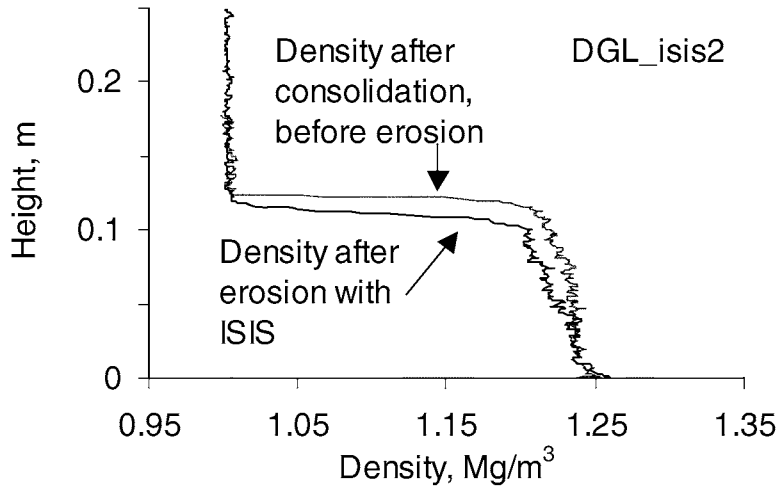

Fig. 10. Density profiles before and after erosion using ISIS on consolidated Tamar sediment.

4. DISCUSSION

The most consistent behaviour occurred when the sediments were in an unconsolidated state, eroded with either the rotating vane or the vertically oscillating grid, and this will therefore be discussed first. A layer of increased density always occurred at the surface of the bed remaining after erosion, with a depth which was generally of the same order of magnitude as the depth that had been eroded. The time scale was comparatively short, in that this high-density surface layer was visible within a few minutes of halting the erosion process (the time it took to record the X-ray profile for the density calculation). Later profiles show a longer term consolidation effect, causing a general increase of density throughout the bed, below the surface layer, as can be seen in Fig. 5b for Dibden Bay sediment and Fig. 8 for Tamar mud.

The results demonstrate that the vane was more effective than the oscillating grid, both in producing erosion and the increased density at the surface. Not surprisingly, the fully or partly consolidated beds were more resistant to erosion than the unconsolidated ones, and attempts at producing erosion with the grid were unsuccessful for both soils.

The main differences between the soils occurred in the consolidated beds, where the vane applied to Dibden Bay mud produced a high density surface layer in the same way as for the unconsolidated sediments, but did not produce any change in density when applied to consolidated Tamar sediment. There were a number of differences in the soils and in the conditions of the experiments that may provide an explanation for this behaviour. Both soils were placed in the settling columns at water contents significantly higher than their Liquid Limits, but, since the Liquid and Plastic Limits of Dibden Bay sediment are lower than those of Tamar, so Dibden Bay, at the same density as Tamar, was closer to a fluid state. The effect of this may be seen in comparing the consolidated profiles of Dibden and Tamar in Figs. 4 and 5a for Dibden and Figs. 9 and 10 for Tamar. In the former, the density profile has a more sloping character. The Tamar sediment has a higher initial density, both in actual value and in its proximity to its Liquid Limit, so that it can be expected to have a higher surface strength. Indeed, it required a higher rotation rate to produce erosion, with a correspondingly increased rate of cyclic application of the associated pressure wave, and this would have shortened the time in which water flow could occur to produce a density change before the hydraulic gradient changed. It is clear that the soil, its condition and the precise nature of the stresses provided by the erosion device have all influenced the results.

The density profile measured after the use of the ISIS instrument demonstrates that water was entrained into the bed during erosion, causing a reduction in density for a significant depth below the level of erosion. The density profile before erosion was

similar in shape to that shown in Fig. 9, although consolidation had not been allowed for quite so long, so the densities achieved are not quite so high. The ISIS instrument is one in which water is pumped down close to the bed, so that it is perhaps not surprising that it has become entrained into the bed below the level of sediment that has broken away. This result demonstrates that there is a clear difference in the stress states produced by the vane and ISIS.

5. CONCLUSION

There are obvious differences between the physical conditions of the field and the settling columns in the laboratory. In the former, the length scales of water flow are on the scale of metres or tens of metres, and there may be significant lateral flows as well as vertical and lateral pressure gradients generated due to turbulence. In the latter, the length scales are much smaller and the time period of variations is typically shorter than in the field. Experiments such as the ones described therefore only have a value if some of the same mechanisms exist as in the field, so that they provide insight into the important processes, or if some of the same physical constraints exist in field instruments. Erosion is typically modelled on the assumption that it occurs once the bed shear stress reaches a critical value, and such an approach has the value of simplicity. However, there is considerable evidence from observation of erosion events in cohesive sediments in the field and in flumes to suggest that there can be significant movement over a finite depth of bed before it begins to break up, and that the eventual failure is not just a surface phenomenon. For example, Mehta (1991) describes erosion where the bed is first fluidized and then destabilized, causing the fluid mud to be entrained and mixed into the overlying water. Thus, erosion in a cohesive sediment involves a finite depth of the bed, and, if the stresses need to reach a critical value for failure, the bed beneath the failure plane will certainly have been subjected also to increased stresses. In theories of soil behaviour, the shear stresses that can be supported by a soil are related to the normal stresses and pore pressures, and it is possible that behaviour in the sediment bed in the laboratory has significant similarities with that which occurs in the field, even though the overlying water conditions are very different. At the very least, the current experiments demonstrate how processes in the overlying water can have a significant effect in a recently deposited or a consolidated sediment well below the level to which erosion occurs. They also show how different soils, or the same soil with a different

consolidation history, may respond differently to the same input of energy, and particular soil characteristics have been identified that might influence these responses.

The experimental results have also demonstrated the importance of the erosion device in determining the state of the sediment bed remaining after erosion. It has already been noted that none of the three erosion devices is likely to produce conditions in the settling column that match very well those that exist in the sea, and each produces its own unique situation. The rotating vane, with a much higher velocity at the outside of the column than at the centre, produces a large and unrealistic variability of shear stress across the sediment surface. It will also produce a complex pattern of pressures in the water as significant volumes are kept in motion at comparatively high speeds. The oscillating grid doesn't move such large quantities of water, and there is more lateral uniformity producing a sequence of increased and reduced pressures at the sediment surface, albeit at a higher rate than is likely to occur in the field. However, the lateral uniformity is also unrealistic, since there will undoubtedly be some horizontal flow in the natural bed. The ISIS device has the advantage that a steady state can be achieved with the eroding forces of the fluid flow and there is no high frequency oscillation of force, but it is still a constrained device. Thus, it is not possible to obtain quantitative information about the erosion process from these experiments, but, since they affect the pore water pressure in the sediment, they illustrate the possible consequences.

It has already been noted that the value of these experiments is in the way they highlight possible mechanisms of behaviour of a cohesive sediment bed. They have demonstrated clearly that changes in pressure in the overlying water can have a significant effect well into the bed, and they have also shown the importance of time scale of events in relation to the time scales of water flow in the soil.

The research described in this paper also has important consequences for the measurement of critical erosion stress. As noted earlier in this paper, existing devices have the common factor of a closed system, but differ widely in the mechanisms used to initiate erosion. It is therefore likely that the effect of each device on the bed is also different and in some cases, this will affect the relevance and reliability of the measurement being made. There is therefore an urgent need for further research into the processes occurring in the bed to complement the work that has already been carried out for the overlying water. Examples of measurements that should be made include pore water pressures and density in the seabed, both in natural conditions and during the use of erosion devices.

ACKNOWLEDGEMENTS

The loan of the ISIS erosion equipment from HR Wallingford is gratefully acknowledged. The main experimental programme described in this paper was undertaken as a fourth year undergraduate project in Engineering Science, and valuable assistance was provided by Mr C Waddup, Dr G Bartholomeeusen and Mr R Morton, as well as by other staff in the Department of Engineering Science.

REFERENCES

Been, K. 1980. *Stress-strain behaviour of a cohesive soil deposited under water.* Ph.D. thesis, Oxford University.

Been, K. 1981. Non-destructive soil bulk density measurement using X-ray attenuation. *Geotechnical Testing Journal,* December, 69-176.

Lintern, D.G., G.C. Sills, N. Feates and W. Roberts. 2000. Erosion properties of mud beds deposited in laboratory settling columns. In: *Fine sediment dynamics in the marine environment.* Winterwerp J.C. and C. Kranenburg (eds.), Elsevier, Amsterdam, 343-358.

Mehta, A. J. 1991. Review notes on cohesive sediment erosion. *Coastal Sediments* 91(1), 40-53.

Sills, G.C. 1998. Development of structure in sedimenting soils. *Philosophical Transactions of the Royal Society of London Series A, Mechanics of Granular Materials in Engineering and Earth Sciences.* Muir Wood, D. , G.S. Boulton and J.M. Rotter (eds.), 356 (1747), 2515-2534.

Tolhurst, T.J, K.S. Black, S.A. Shayler, S. Mather, I. Black, K. Baker and D.M. Paterson. 2000. Measuring the *in situ* erosion shear stress of intertidal sediments with the Cohesive Strength Meter (CSM). *Estuarine, Coastal and Shelf Science*, 49, 281-294.

Williamson, H. J. and M. C. Ockenden. 1996. ISIS: An instrument for measuring erosion shear stress *in situ. Estuarine, Coastal and Shelf Science*, 42, 1-18.

Estuarine and Coastal Fine Sediments Dynamics
J.P.-Y. Maa, L.P. Sanford and D.H. Schoellhamer (editors)

Approximate equations for sediment erosion rates

Lick, W.[a], J. Lick[a], L. Jin[a] and J. Gailani[b]

[a]Department of Mechanical and Environmental Engineering, University of California, Santa Barbara CA 93106
[b]USACE, Engineer Research and Development Center, 3909 Halls Ferry Road, Vicksburg, MS 39180

KEY WORDS
Erosion rates, cohesive, non-cohesive, approximate equations

In the present article, approximate equations for sediment erosion rates are illustrated and compared with experimental data. These equations are expressed in terms of the applied shear stress and critical shear stresses; these latter stresses depend on the sediment bulk properties such as particle diameter, bulk density, and mineralogy as well as others. Equations for erosion rates of natural sediments are presented which are (a) valid for fine-grained, cohesive sediments but not for coarse-grained, non-cohesive sediments, (b) valid for coarse-grained, non-cohesive sediments but not for fine-grained, cohesive sediments, and (c) uniformly valid for both fine-grained and coarse-grained sediments. Good agreement between this latter equation, the previous equations (when they are valid), and experimental data on quartz particles is demonstrated. As a preliminary step in quantifying erosion rates for more general sediments and especially to show the effects of clay minerals, the uniformly valid equation is also applied to sediments consisting of (a) quartz particles of different sizes with and without 2% bentonite, and (b) quartz particles of a single size (48 μm) but with the addition of varying amounts of four different types of clays. The clays reduce erosion rates with the greatest reduction for bentonite and illite, a lesser reduction for kaolinite, and the least for mica. Good agreement with experimental data is found in all cases.

1. INTRODUCTION

For purposes of understanding and quantifying sediment transport in nature as well as the transport of hydrophobic contaminants associated with the sediments, it is especially important to understand and quantify sediment erosion rates and the parameters on which these rates depend. These parameters are the shear stress due to wave action and currents and the shear erosion resistance due to bulk properties of the sediments, primarily the particle size, bulk density (especially for cohesive sediments), and mineralogy. To a lesser extent, the rates depend on the salinity of the pore waters, volume of gas in the sediments, oxidation and other chemical reactions at the sediment-water interface, organic carbon content, and time after deposition (gellation).

For convenience, cohesive sediments and non-cohesive sediments have generally been treated experimentally and theoretically as two separate entities. Of course, natural sediments have a continuous range of properties from very cohesive, consolidated muds to cohesive, but unconsolidated muds to mixtures of sands, silts, and clays to coarse-grained, non-cohesive, sandy materials. Considerable work has been done on the erosion properties of non-cohesive sediments, but less on cohesive sediments; the behavior of sediments in the transition region between non-cohesive and cohesive sediments is especially poorly understood. This is particularly true for natural sediments where particles are often coated with other substances.

In order to better understand the cohesive behavior of sediments and especially the transition from non-cohesive to cohesive behavior, experimental studies were recently done which determined erosion rates of sediments consisting of different-size quartz particles (Roberts *et al.*, 1998); median particle diameters varied from fine (5 μm) to coarse (1350 μm). The results showed cohesive behavior for the fine-grained sediments and non-cohesive behavior for the coarse-grained sediments with a smooth transition between the two limits as the median particle diameter changed. These experiments were unique in that the sediments tested consisted of particles of different sizes but otherwise had almost identical mineralogies and other particle properties such as surface coatings and cohesive forces; bulk densities of the sediments only varied because of consolidation of the sediments with depth and time. In contrast, previous investigators have done experiments with sediments consisting of particles of different sizes but with different mineralogies and other particle properties. This is discussed more extensively and references are given by Lick *et al.* (2004). In order to demonstrate the effects of clay minerals on erosion rates, the Roberts *et al.* experiments were later supplemented to include sediments consisting of (a) quartz particles of different sizes with and without

2% bentonite (Jin *et al.*, 2002) and (b) quartz particles of a single size (48 μm) with the addition of varying amounts of four different types of clay minerals (Lick *et al.*, 2002).

Based on these as well as other experimental data, approximate equations for sediment erosion rates have been investigated and are here illustrated and compared with experimental data. These equations are expressed in terms of the applied shear stress and critical shear stresses; these latter stresses are functions of the sediment bulk properties. In the following section, relevant results of the above as well as other experiments and recent work on critical shear stresses is briefly summarized. In the third section, experimental data and known physical relations are used to develop equations for erosion rates of quartz particles which are (a) valid for fine-grained, cohesive sediments but not for coarse-grained, non-cohesive sediments, (b) valid for coarse-grained, non-cohesive sediments, but not for fine-grained, cohesive sediments, and (c) uniformly valid for both fine-grained and coarse-grained sediments. In the fourth section, the uniformly valid equation is then applied to sediments consisting of (a) quartz particles of different sizes with and without 2% added bentonite and (b) quartz particles of a single size (48 μm) but with the addition of varying amounts of four different clays. The functional forms of the derived equations are a first step for developing erosion rate equations which are uniformly valid for natural sediments. A summary and concluding remarks are given in the final section.

2. PREVIOUS WORK

Considerable work has been done recently on the effects of sediment bulk properties on erosion rates, *e.g.*, see summary by Lick and McNeil (2001). Recent investigations particularly relevant to the present work are summarized here. The emphasis is on the effects of the most generally significant parameters which are bulk density, particle size, and mineralogy.

In order to determine the effects of bulk density on erosion rates, experiments have been done on reconstructed (well-mixed), but otherwise natural sediments from three locations: the Fox River, the Detroit River, and the Santa Barbara Slough (Jepsen *et al.*, 1997). These were generally fine-grained, cohesive sediments with mean particle diameters of 12, 20, and 35 μm respectively. For each of these sediments and for consolidation times varying from 1 to 60 days, the erosion rate as a function of shear stress and with depth below the sediment bed surface was measured and related to the spatially and temporally varying local sediment bulk density. It was shown that, for each type of sediment, the erosion rate was well approximated by

$$E = A\,\tau^n\,\rho^m \qquad (1)$$

where E is the erosion rate (in cm/s); τ is the shear stress (in N/m^2); ρ is the bulk density (in g/cm^3); and A, n, and m are constants that depend on the type of sediment.

In a later experimental study by Roberts *et al.* (1998), the effects of particle size and bulk density on the erosion of different-size quartz particles were investigated. Average particle sizes ranged from 5 to 1350 μm, while bulk densities ranged from approximately 1.65 to 1.95 g/cm^3. As representative examples of this data, erosion rates are shown in Fig. 1 as a function of bulk density with shear stress as a parameter for particles with diameters of (a) 14.8 μm and (b) 1350 μm. For the sediment with diameter of 14.8 μm, erosion rates are a strongly decreasing function of density. For the other sediment, erosion rates are essentially independent of density. In general, it was shown that the slope of $E(\rho)$ is greatest for the smallest particles, decreases as the particle size increases, and is essentially zero for particle diameters greater than 220 μm, *i.e.*, erosion rates were independent of the density for the larger particles. Ap-

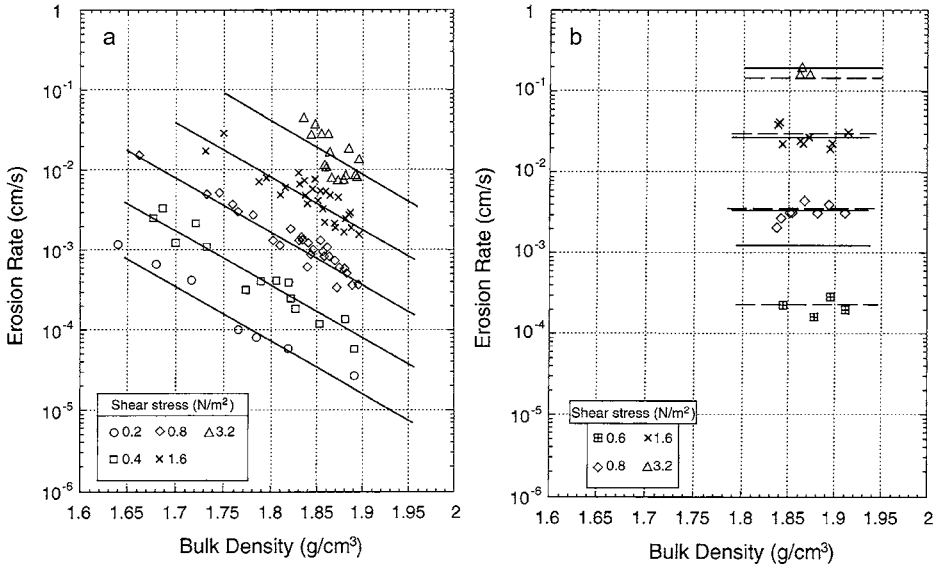

Fig. 1. Erosion rates as a function of bulk density with shear stress as a parameter. Modified from Roberts *et al.* (1998). (a) Data are for quartz particles with an average diameter of 14.8 μm. The solid lines are approximations by means of Eq. 1, or Eqs. 9 and 10. (b) Data are for quartz particles with an average diameter of 1350 μm. The solid lines are approximations by means of Eq. 1; the dashed lines are from Eqs. 12 or 13.

proximations to the data by means of Eq. 1 are shown as the solid lines in Figs. 1a and b. It can be seen that the data in Fig. 1a (14.8 μm) are well approximated by Eq. 1; however, the data in Fig. 1b (1350 μm) are not. For the entire range of particle diameters, Eq. 1 represented the data well for the smaller and intermediate particles but did not do as well for the largest particles. This will be discussed further in the following section.

For fine-grained, cohesive sediments with a wide range of bulk properties, Eq. 1 has been shown to be a valid approximation for erosion rates (*e.g.*, see Lick and McNeil, 2001). The equation is significant in that it shows the effects of hydrodynamics (dependence on τ) and consolidation (dependence on ρ where $\rho = \rho(t)$ and t is time after deposition). However, the parameters A, n, and m are dependent on sediment bulk properties (but not ρ) and must be determined independently for each type of sediment.

Besides erosion rates, critical shear stresses for erosion, τ_c, were also determined in the Roberts *et al.* study. Because of the difficulty in precisely defining and measuring a critical stress, this quantity was defined as the shear stress at which a small, but accurately measurable, rate of erosion (10^{-4} cm/s) occurs (McNeil *et al.*, 1996). Experimental results of this investigation for the critical stress as a function of particle diameter with bulk density as a parameter are shown as the dashed lines in Fig. 2. It is evident that (a) as the particle size decreases from its largest value, τ_c first decreases rapidly and then more slowly, reaches a minimum, and then increases rapidly for the smallest particles; and (b) τ_c is independent of bulk density for the larger particles but is strongly dependent on bulk density for the smaller particles.

As a preliminary step in quantifying erosion rates for more general sediments and especially to show the effects of clay minerals, these experiments were later supplemented to include sediments consisting of (a) different-size quartz particles with and without 2% bentonite (Jin *et al.*, 2002) and (b) quartz particles of a single size (48 μm) but with the addition of varying amounts of four different types of clays (Lick *et al.*, 2002).

In the first set of supplemental tests, the sediments were quartz particles similar, but not identical, to the particles used by Roberts *et al.* Average particle diameters tested were 15, 48, 140, 170, 280, 390, and 1350 μm. Each of the sediments had a narrow size distribution. Erosion rates of each size sediment, with and without 2% bentonite, were measured as a function of shear stress. The addition of 2% bentonite caused a significant reduction in erosion rates. This reduction was dependent on the size of the quartz particles; it was greatest for the 140 and 170 μm particles (almost an order of magnitude reduction in erosion rate), but was relatively small for the largest and smallest particles.

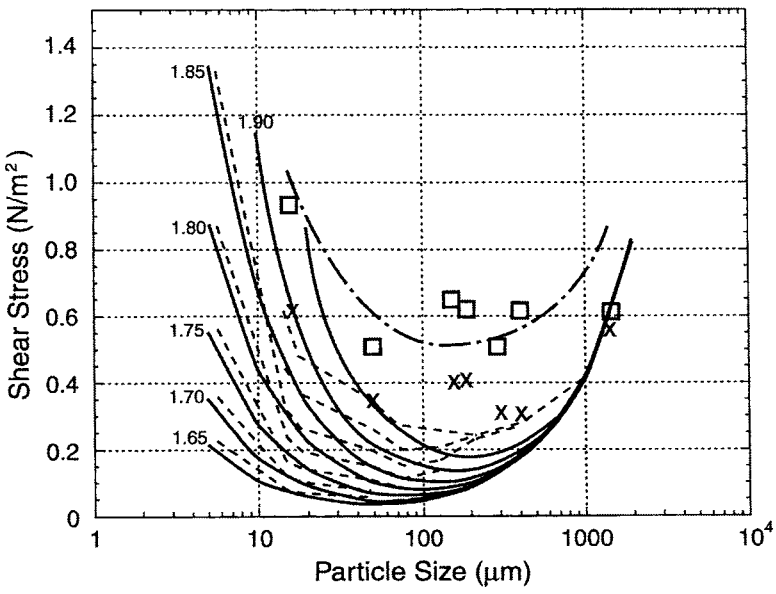

Fig. 2. Critical shear stresses as a function of particle size with bulk density as a parameter. The dashed lines represent experimental data by Roberts *et al.* (1998) for quartz particles. The solid lines represent theoretical values calculated from Eq. 11. Experimental data by Jin *et al.* (2002) is denoted by the symbol **x** for zero bentonite and □ for 2% bentonite. The theoretical values for τ_c for 2% bentonite as calculated from Eq. 2 are shown as the dot-dash line.

In the second set of supplemental experiments, differing amounts of a clay (bentonite, kaolinite, plainsman clay, or mica) were added to a sediment of quartz particles with an average diameter of 48 μm. Erosion rates of each of the sediments were then determined as a function of shear stress and percent clay. As the percentage of each clay increased, erosion rates generally decreased. The greatest reductions were for bentonite; smaller but still significant reductions occurred for kaolinite and plainsman clay; a small effect was observed for mica. Plainsman clay is a commercially available clay whose largest component is illite, but the clay also contains kaolinite, smectite, and non-clay minerals. By assuming that the reductions in erosion rates due to the different clay minerals were additive, it was shown that bentonite and illite had the greatest (and comparable) effect, kaolinite had less, while mica had the least.

Based on the data from the above experiments, a theoretical description of the initiation of movement of sediments consisting of uniform-size, quartz particles with and without small amounts of clay minerals was developed (Lick *et al.*, 2004). For sediments consisting of quartz particles alone, the analysis included gravitational, lift, drag, and cohesive forces and was uniformly valid for the complete range of particles investigated, from fine-grained, cohesive particles to coarse-grained, non-cohesive particles. Effects of sediment bulk density were significant and were included in the analysis. Good agreement between the theory and experiments by Roberts *et al.* (1998) was obtained. As shown by the data in Jin *et al.*, (2002) and Lick *et al.* (2002), the addition of varying amounts of bentonite and other clays to the quartz particles made the sediment significantly more cohesive. Because of this effect, an additional binding force due to clay minerals had to be included in the analysis.

Many different forces act on particles in a sediment bed. However, from the experimental data and subsequent analyses (Lick *et al.*, 2004), it was determined that the critical shear stress for erosion for the above sediments could be expressed as

$$\tau_c = \left(\frac{F_g + F_c + F_b}{F_g} \right) \tau_{cn} \tag{2}$$

where F_g is the gravitational force on a particle, F_c is the cohesive force between individual quartz particles, F_b is the binding force due to the presence of clay minerals, and τ_{cn} (in N/m^2) is the critical shear stress for the erosion of non-cohesive particles.

The gravitational force is given by

$$F_g = c_3 d^3 \tag{3}$$

where d (in m) is the particle diameter, $c_3 = \pi(\rho_s - \rho_w)g/6$, and g is the gravitational constant; c_3 is equal to 8.21×10^3 N/m^3 when it is assumed that $\rho_s = 2.6$ g/cm^3 (particle density) and $\rho_w = 1.0$ g/cm^3 (water density). The cohesive force between particles is given by (Ducker *et al.*, 1991; Israelachvili, 1992; Lick *et al.*, 2004)

$$F_c = c_4 d \tag{4}$$

where c_4 is a function of the particle properties and the bulk density. As a first approximation for quartz particles, c_4 can be written as

$$c_4 = a^* e^{b\rho} \tag{5}$$

where $a^* = 7 \times 10^{-12}$ N/m and b = 9.07 cm^3/g. The binding force is given by

$$F_b = c_5 d^2 \tag{6}$$

where c_5 is a function of the clay mineralogy and bulk density of the sediments. This binding force can be derived by assuming a coating of clay on the quartz particles or by assuming the clay almost fills the pores between the quartz particles. It follows that this binding force is the force required to fracture the clay layer; it is the force per quartz particle and is proportional to d^2 (Lick *et al.*, 2004). For 2% bentonite and ρ approximately 1.95 g/cm^3 corresponding to the Jin *et al.* (2002) data, a first approximation to c_5 is 7 N/m^2. More accurate (but non-constant) values for c_4 and c_5 will be presented and discussed below. The parameter τ_{cn} is given (Chepil, 1959; also see compilation of data by Miller *et al.*, 1977) approximately by

$$\tau_{cn} = 0.414 \times 10^3 d \tag{7}$$

For comparative purposes, F_g, F_c, and F_b as given by the above formulas are shown in Fig. 3 as functions of the particle diameter. It can be seen that F_c is dominant for small particles, F_g is dominant for large particles, while F_b is the largest of these forces for intermediate size particles. All three forces will be active for any natural sediment. However, the diameters at which any of these forces is dominant will vary with sediment bed properties such as grain shape and size distribution, particle coatings, mineralogy, water chemistry, and possibly other parameters.

Comparison of Eq. 2 with experimental data is shown in Fig. 2. For quartz particles alone (F_b is negligible), the solid lines are theory, while the experimental results of Roberts *et al.* (1998) are shown as the dashed lines. Reasonably good agreement

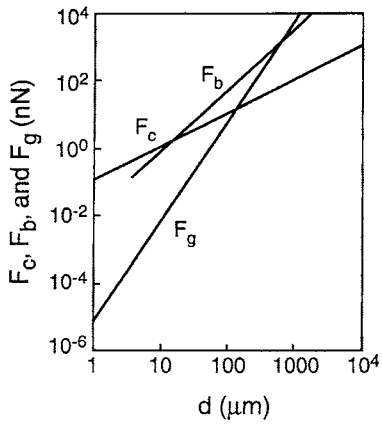

Fig. 3. Gravitational (F_g), cohesive (F_c), and binding (F_b) forces as functions of particle diameter.

between theory and experiments is evident. For zero percent bentonite, the bulk densities were generally between 1.9 and 2.0 g/cm^3. For these densities, the results are in reasonable agreement with those by Roberts *et al.* for ρ = 1.95 g/cm^3. The theoretical results for τ_c for 2% bentonite from Eq. 2 are shown as the dot-dash line and show a considerable increase in τ_c over that for zero bentonite. The effect is greatest for particle diameters of 140 and 170 μm and decreases as the diameter increases or decreases from these values. The agreement between theory and experiment is good for small and intermediate size particles; the theory is not valid for the coarsest particles where it was observed that the bentonite did not bind with the quartz particles.

3. EROSION RATES OF QUARTZ PARTICLES

3.1 Fine-grained, cohesive sediment

Fine-grained, quartz particles behave in a cohesive manner, *i.e.*, they consolidate relatively slowly and the erosion rates are a strong, decreasing function of density as well as particle diameter. For these fine-grained sediments, the data can be well approximated by Eq. 1 as is shown in Fig. 1a and has been demonstrated more generally by previous investigations. In general, A, n, and m are parameters that depend on particle diameter as well as other sediment properties (but not density) so that Eq. 1 only shows the explicit dependence of E on τ and ρ with all other sediment properties fixed.

The data in Fig. 1 can equally well be approximated by straight lines given by

$$E = C\tau^n \, e^{-k\rho} \tag{8}$$

where C, n, and k are positive constants that again depend on particle diameter as well as other sediment properties. Because the density range is small, Eqs. 1 and 8 give essentially the same results. Most data has been reported in the form of Eq. 1 because it is somewhat simpler. Equation 8 is more useful for present purposes.

In the article by Roberts *et al.*, the critical shear stress is defined as the shear stress at which an erosion rate of 10^{-4} cm/s occurs. With this definition, Eqs. 1 and 8 can be written as

$$E = 10^{-4}\left(\frac{\tau}{\tau_c}\right)^n \tag{9}$$

Comparison of the above equation with Eq. 8 then gives

$$\tau_c = \left(\frac{10^{-4}\, e^{k\rho}}{C} \right)^{1/n} \tag{10}$$

Equation 9 is useful because it explicitly shows the dependence of E on τ_c, a quantity which can be measured independently and does not need to be determined from Eq. 10, *i.e.*, the validity of Eq. 9 is not dependent on the validity of Eq. 10.

Equation 10 is only valid for small d and only takes into account the cohesive forces between particles. With the inclusion of gravitational forces (but no binding forces), it has been demonstrated (Lick *et al.*, 2004) that a reasonable approximation for τ_c for the quartz particles used by Roberts *et al.* which is uniformly valid for all d is

$$\tau_c = \left(1 + \frac{a e^{b\rho}}{d^2} \right) \tau_{cn} \tag{11}$$

where $a = 8.5 \times 10^{-16}$ m^2 and $b = 9.07$ cm^3/g. For small d, this equation is consistent with Eq. 10; for large d, $\tau_c = \tau_{cn}$.

Equation 9 has been applied to approximate the erosion data on the quartz particles used by Roberts *et al.* With the above approximation for τ_c, the values of n in Eq. 9 can be determined by nonlinear regression (*e.g.*, see Chapra and Canale, 1988). The results for n as a function of d are shown in Table 1. For small and intermediate d, n is ap-

Table 1. Quartz Particles. The values of n in Eq. 9 as a function of particle diameter. The parameters a and b in Eq. 11 are assumed constant. Also shown is R^2, a goodness of fit parameter.

d(mm)	n	R^2
0.0057	1.61	0.934
0.0148	2.48	0.896
0.0183	2.57	0.883
0.048	1.86	0.947
0.075	1.83	0.966
0.125	2.04	0.834
0.222	2.31	0.878
0.432	3.12	0.916
1.02	4.61	0.813
1.35	5.17	0.778

proximately two but increases rapidly for large d as d increases. Also shown is R^2, termed "coefficient of determination," a quantity that measures the proportion of variance explained by the proposed equation. If $R^2 = 1.0$, Eq. 9 perfectly predicts the observed data; if $R^2 = 0$, Eq. 9 does no better than using the mean value of E. The table demonstrates that Eq. 9 with Eq. 11 is a valid approximation to the data for all particle diameters equal to or less than 432 μm but is not a good approximation for non-cohesive particles, *i.e.*, for $d \geq 1020\ \mu m$.

In the above analysis, Eq. 11 with both a and b constant was used to approximate τ_c. As noted by Lick *et al.* (2002), Eq. 11 is a uniformly valid expression for τ_c but, for specific values of d, this equation may not be the best approximation. The reason is as follows. "The experiments were done with natural quartz particles obtained from one location; they were separated into different particle size groups by sieving. Because they all came from the same source, the coatings on their surfaces should be similar. These coatings are responsible for most of the cohesive forces between these particles. However, even for particles of the same size, erosion rates and critical stresses varied from one batch to another indicating that coatings and cohesive forces varied between batches." This is probably the main cause of the differences between $\tau_c(d)$ as determined (a) directly from the experimental data and (b) from Eq. 11; *i.e.*, the theory assumes a and b in Eq. 11 are constants while they actually vary somewhat from one batch of particles to another.

Better values for τ_c can be determined by allowing a and b to be variable parameters to be determined as part of the analysis by nonlinear regression. If this is done, then the agreement between Eq. 9 and the experimental data is now significantly better, *i.e.*, R^2 is greater; however, the results show (in a similar manner to Table 1) that Eq. 9 is a good approximation for small d but is not as good an approximation for large d, *i.e.*, for non-cohesive sediments.

This can also be seen in Fig. 1b which shows erosion rates as a function of bulk density with shear stress as a parameter for $d = 1350\ \mu m$. For coarse-grained sediments, because of the absence of cohesive forces, E is not a function of ρ. The approximation by Eq. 9 is shown as a solid line and does not compare well with the data at the lowest stress.

3.2 Non-cohesive sediments

For coarse-grained non-cohesive sediments, a generally accepted equation for $E(\tau)$ is (*e.g.*, see van Rijn, 1993)

$$E = A\,(\tau - \tau_c)^n \tag{12}$$

where A, τ_c, and n are functions of particle diameter but not a function of density. For non-cohesive sediments, the parameter $\tau_c = \tau_{cn} = 0.414 \times 10^3$ d, while the parameters A and n can be found by nonlinear regression. For the data on quartz particles from Roberts *et al.* with d = 1350 μm, it is found that A = 0.0296 and n = 1.49. With these values, E as given by Eq. 12 is shown in Fig. 1b as the dashed line; it is obviously a better approximation than Eq. 9, the solid line, and fits the data quite well for all shear stresses.

By nonlinear regression, A and n can be found for other particle diameters as well. Although the results are quite good for large particle diameters, the results are not good as d decreases. One reason is that, by this formulation, E is not a function of density; this of course is required by the experimental results. A variation of this approach is to assume that τ_c is given by Eq. 11 (with a and b constant) so that τ_c and hence E are now functions of density. The method of nonlinear regression then gives the results for A, n, and R^2 shown in Table 2 for different particle diameters. The results are somewhat better than before, but again the accuracy of the approximation is best for large d (non-cohesive sediments) but decreases as d decreases (cohesive sediments). In general, it can be demonstrated that Eq. 12 is a valid approximation for non-cohesive sediments but is not a good approximation for cohesive sediments.

3.3 A uniformly valid equation

In order to approximate the data for all size ranges, the following equation is proposed:

Table 2. Quartz Particles. The values of A and n in Eq. 12 as functions of particle diameter. Also shown is R^2, a goodness of fit parameter.

D (mm)	A	n	R^2
0.0057	1.13×10^{-3}	1.31	0.846
0.0148	3.64×10^{-3}	1.35	0.778
0.0183	4.67×10^{-3}	1.34	0.801
0.048	6.02×10^{-3}	1.53	0.902
0.075	4.52×10^{-3}	1.29	0.907
0.125	9.42×10^{-3}	2.14	0.896
0.222	0.0116	2.06	0.937
0.432	0.0314	2.60	0.947
1.02	0.0328	1.82	0.984
1.35	0.0296	1.49	0.983

$$E = 10^{-4}\left(\frac{\tau-\tau_{cn}}{\tau_c-\tau_{cn}}\right)^n \tag{13}$$

where τ_c, τ_{cn}, and n are functions of particle diameter. From Eqs. 7 and 11, it follows that

$$\tau_c - \tau_{cn} = \frac{0.414\times10^3\, ae^{b\rho}}{d} \tag{14}$$

As $d \rightarrow 0$, $\tau_{cn}\rightarrow 0$ and is much smaller than τ_c or τ. Equation 13 then reduces to Eq. 9 which is valid for fine-grained, cohesive sediments. For large d, $b \rightarrow 0$, and $\tau_c - \tau_{cn}$ is therefore not a function of ρ. Equation 13 can then be written as

$$E = A\,(\tau - \tau_{cn})^n \tag{15}$$

where A is proportional to d^n but is not a function of ρ. The above equation has the same form as Eq. 12, which is valid for coarse-grained, non-cohesive particles.

Good agreement between Eq. 13 and the experimental data on quartz particles can also be demonstrated. With a and b as parameters to be determined, the method of nonlinear regression gives the results for n, a, b, and R^2 as functions of d shown in Table 3. Here it has been assumed that $b = 0$ for $d \geq 222$ μm, consistent with the experimental data that shows E is not a function of ρ. By comparison with Tables 1 and 2, Table 3

Table 3. Quartz Particles. The values of n in Eq. 13 with a and b from Eq. 11 as functions of particle diameter. Also shown is R^2, a goodness of fit parameter.

d (mm)	a (N/mm^2)	b (cm^3/g)	n	R^2
0.0057	2.89×10^{-9}	8.43	1.87	0.956
0.0148	1.63×10^{-8}	7.23	2.17	0.944
0.0183	1.72×10^{-7}	5.97	2.25	0.974
0.048	7.62×10^{-7}	5.52	2.14	0.987
0.075	2.86×10^{-7}	6.08	1.94	0.981
0.125	7.48×10^{-6}	4.61	2.37	0.946
0.222	0.0854	0	2.46	0.939
0.432	0.0711	0	2.03	0.899
1.02	0.106	0	1.84	0.983
1.35	0.0819	0	1.54	0.985

demonstrates that Eq. 13 is uniformly valid for all d and gives results which are as good as or better than Eq. 9 (valid for fine-grained, cohesive sediments) and as good as or better than Eq. 12 (valid for coarse-grained, non-cohesive sediments).

4. EFFECTS OF CLAY MINERALOGY

4.1 Quartz particles with and without 2% bentonite

Erosion rates have been measured as a function of shear stress for sediments consisting of quartz particles of different sizes, with and without 2% added bentonite. Average particle sizes of the quartz particles used in the tests were 15, 48, 140, 170, 280, 390, and 1350 μm. Equation 13 was used to approximate this data. With zero bentonite, Eq. 11 was used to evaluate τ_c; a, b, and n were coefficients to be determined by nonlinear regression. The results are similar to those shown in Table 3 for similar, but not identical, sediments consisting of quartz particles. The values of R^2 (greater than 0.900) indicate that there is good agreement between Eq. 13 and the experimental data.

For sediments with 2% bentonite, the experimental results were also approximated by Eq. 13. In this case, for an approximation for τ_c which is uniformly valid for all d, gravitational, cohesive, and binding forces are all significant and must be considered. With the inclusion of the binding force from Eq. 6 and as a generalization of Eq. 11, Eq. 2 can now be written as

$$\tau_c = \left(1 + \frac{ae^{bp}}{d^2} + \frac{c_5}{c_3 d}\right)\tau_{cn} \tag{16}$$

The coefficients a and b were assumed to be the same as those for sediments with no bentonite, while c_5 and n were coefficients to be determined by nonlinear regression. The results for c_5 and n as a function of particle diameter are shown in Table 4. Generally good agreement between Eq. 13 and the experimental data is demonstrated. The coefficient c_5 is reasonably constant, (except for d = 1350 μm, for which value the theory is not valid). In general, c_5 should depend on the density; however, the experimental data is not sufficient to warrant this refinement.

Table 4. Quartz Particles with 2% Bentonite. The values of n in Eq. 13 with c_5 as in Eq. 6 as functions of particle size for Jin *et al.* data, 2% bentonite. Also shown is R^2, a goodness of fit parameter. The parameters a and b are assumed to be the same as those for sediments with no bentonite.

d (mm)	a (N/mm^2)	b (cm^3/g)	c_5 (N/m^2)	n	R^2
0.015	1.01×10^{-6}	3.77	8.37	2.72	0.948
0.048	2.20×10^{-5}	2.46	6.69	2.10	0.877
0.140	9.51×10^{-4}	1.33	6.19	3.28	0.918
0.170	.0159	0	6.93	3.74	0.906
0.280	.0157	0	3.36	3.60	0.939
0.390	.0191	0	4.22	3.54	0.904
1.35	.123	0	0.82	3.94	0.986

4.2 Single-size quartz particles with additions of clay minerals

In order to obtain preliminary information on the effects of different clay minerals on erosion rates, a series of measurements of erosion rates as a function of shear stress were made for sediments consisting primarily of single-size (48 μm) quartz particles but with each sediment differing due to the addition of one of four clays, each at several different percentages. The clays and the percentages of each that were added to the quartz particles were as follows: bentonite (0.5, 2, 4, 8); kaolinite (5, 10, 20); plainsman clay (10, 20); and mica (10, 20, 40).

As in the above analysis, the experimental results were approximated by Eq. 13. Equations 2, 11 and 6 were used to evaluate τ_c. The coefficients a and b were assumed to be the same as those for 48 μm quartz particles with no clay additives. The method of nonlinear regression then gave the coefficients c_5 and n. For the different minerals, these quantities are shown in Table 5 along with R^2. Reasonably high values of R^2 demonstrate generally good agreement between the calculations and experimental results and demonstrate that Eq. 13 is a valid approximation for these sediments.

Two phenomena which affect erosion rates and are unique to clay minerals are swelling and gelling (Mitchell, 1993). Swelling, or a decrease in density of the bulk sediments in the absence of changes in other bulk properties, occurs when a clay mineral is added to quartz particles. The amount of the density decrease is dependent on the type of clay and on the amount of added clay; this decrease may not be evident for some clays and for small percentages. For the present clays, this swelling was most obvious for bentonite. For 0.5 and 2% added bentonite, there was little change in density; however for 4 and 8%, the densities decreased by about 0.20 g/cm^3 (from 1.95

Table 5. Parameters for Sediments Consisting of Quartz Particles with Different Percentages of Clay Minerals. The coefficients, c_5 and n, as well as R^2 were determined by nonlinear regression.

Clay	Percent	c_5 (N/m^2)	n	R^2
Bentonite	0.5	1.76	1.96	.750
	2	6.65	2.10	.877
	4	15.11	3.19	.968
	8	11.82	2.47	.618
(no 2-day data)	8	20.61	2.96	.703
Kaolinite	5	-1.92	1.37	.744
	10	5.32	2.37	.940
	20	20.44	2.34	.918
Plainsman Clay	10	15.43	2.60	.914
	20	33.74	3.59	.933
Mica	10	.188	1.92	.747
	20	3.92	2.33	.883
	40	6.84	2.04	.976

to 1.75 g/cm^3). This swelling occurs relatively rapidly (generally in less than two days) so that the swelling effect, when present, was the same for all tests at the same bentonite percentage.

For other clays, the effects of swelling were less. For kaolinite, the densities were unchanged (1.95 g/cm^3) for 5%, but decreased to approximately 1.85 g/cm^3 for 10 and 20%. For plainsman clay, reductions to 1.85 g/cm^3 for 10% and to 1.80 g/cm^3 for 20% were measured. For mica, densities decreased to 1.90 g/cm^3 for 10%, 1.82 g/cm^3 for 20%, and 1.75 g/cm^3 for 40%.

As is known from previous experiments with fine-grained sediments, a decrease in density increases the erosion rate (see Eq. 1), *i.e.*, the effects of swelling alone should therefore increase erosion rates. This effect is approximately accounted for by the dependence of τ_c on density as shown in Eq. 1 and related equations.

In the present suite of experiments, gelling is also present and is evident as a decrease in erosion rates with time in the absence of any changes in sediment bulk properties (including density). Gelling occurs in approximately two days or less for bentonite, and less than that for the other clays.

Because of this gelling and reduction in erosion rates with time while all other sediment properties are constant, the parameters c_5 and n in Eq. 16 should also be functions of time. However, once gelling has occurred, these parameters should be

constant. This behavior is indicated by the experimental data as follows (see Table 5). For 8% bentonite and including data for all consolidation times, R^2 is 0.618, a relatively low value. When the two-days data are excluded, R^2 increases to 0.703, a somewhat better approximation.

The coefficient c_5 is a measure of the binding force (see Eq. 6) and should increase as the binding force increases. From Table 5, it can be seen that (a) for each clay, c_5 increases as the percent of clay added increases, and (b) for the same percent of added clay, c_5 is greatest for bentonite and decreases in the order: bentonite > plainsman clay > kaolinite > mica. Plainsman clay is a commercially available clay with a mineralogy of 37% illite, 25% kaolinite, 3% smectite, and 35% non-clay minerals, primarily quartz. From this and by assuming that the reductions in erosion rates due to different clay minerals are additive, it can be shown that the effect of illite is comparable to that of bentonite, the effect of kaolinite is less, while the effect of mica is least, a sequence that is generally followed in quantifying the effects of clay minerals on soil properties (*e.g.*, see Mitchell, 1993).

5. SUMMARY AND CONCLUDING REMARKS

Approximate equations to describe the dependence of sediment erosion rates on the applied shear stress, the critical shear stress for erosion, and the critical shear stress for erosion of non-cohesive sediments have been given and discussed. As shown in Eq. 2, the critical shear stress for erosion is dependent on the gravitational force (F_g), the cohesive force (F_c), and the binding force (F_b) of the particles, and hence is dependent on the bulk properties of the sediment.

Equation 1 has been shown previously to be valid for a wide range of fine-grained, cohesive sediments. Equation 9 is more general, includes Eq. 1 as a subset, and also is generally valid for fine-grained, cohesive sediments. Equation 12 is generally accepted as valid for non-cohesive sediments. Equation 13 is proposed as an equation uniformly valid for both fine-grained (cohesive) sediments and coarse-grained (non-cohesive) sediments. It reduces to Eqs. 9 and 12 in the limits as $d \rightarrow 0$ and $d \rightarrow \infty$, respectively.

In order to demonstrate the general usefulness of Eq. 13 and also to show the effects of clay minerals, erosion rates as determined by this equation were compared with data from sediments consisting of (a) different-size quartz particles, (b) different-size quartz particles with and without 2% bentonite, and (c) quartz particles of a single size (48 μm) but with differing added amounts of bentonite, kaolinite, plainsman clay, and mica. In all cases, good agreement between Eq. 13 and the experimental data was

obtained. In addition, preliminary and approximate values for the parameters a, b, c_5, and n and their dependence on the sediment bulk properties of density, particle size, and mineralogy were determined.

Equations 9, 12 and 13 are written in terms of the general parameters τ_c and τ_{cn}. As such, they are of general applicability and do not depend on specific forms for τ_c and τ_{cn} such as Eqs. 10 and 11. In particular, τ_c may be determined directly from experiments.

This work is a first step in the quantitative prediction of erosion rates for a wide range of sediments from a knowledge of the sediment bulk properties. The emphasis has been on the most significant sediment parameters which affect erosion rates, *i.e.*, bulk density, particle size, and mineralogy. Much more extensive experiments need to be done to generalize the present results and to include the interactive effects between changes in density, particle size, and different mineralogies. Additional parameters whose effects need to be quantified are particle size distribution, organic content, oxidation and other chemical reactions, volume of gas in the sediment, salinity of pore waters, and time after deposition (gellation). Nevertheless, it is hoped that the present results and approach will serve as guidance in the approximate prediction and quantification of erosion rates.

ACKNOWLEDGEMENT

This research was supported by the U.S. Army Corps of Engineers.

REFERENCES

Chapra, S. and R. Canale. 1988. *Numerical Methods for Engineers*. McGraw-Hill, New York, N.Y.

Chepil, W. S. 1959. Equilibrium of soil grains at the threshold of movement by wind. *Soil Science Society of America Proceedings*, 23, 422-428.

Ducker, W.A., T.J. Senden and R.M. Pashley. 1991. Direct measurement of colloidal forces using an atomic force microscope. *Nature*, 353, 239-241.

Israelachvili, I. 1992. *Intermolecular and Surface Forces*. Atomic Press Inc., San Diego, CA.

Jepsen, R., J. Roberts and W. Lick. 1997. Effects of bulk density on sediment erosion rates. *Water, Air and Soil Pollution*, 99, 21-31.

Jin, L., J. McNeil and W. Lick. 2002. *Effects of bentonite on sediment erosion rates.* Report, Dept. of Mechanical and Environmental Engineering, University of California, Santa Barbara, CA

Lick, W., L. Jin and J. Gailani. 2004. Initiation of Movement of Quartz Particles. *Journal of Hydraulic Engineering*, ASCE, 130(9), 755-761.

Lick, W. and J. McNeil. 2001. Effects of sediment bulk properties on erosion rates. *The Science of the Total Environment* 266, 41-48.

Lick, W., J. Lick, L. Jin, J. McNeil and J. Gailani. 2002. *Effects of Clay Mineralogy on Sediment Erosion Rates.* Report, Dept. of Mechanical and Environmental Engineering, University of California, Santa Barbara.

McNeil, J., C. Taylor and W. Lick. 1996. Measurements of erosion of undisturbed bottom sediments with depth, J. Hydraulic Engineering, ASCE, 122, 316-324.

Miller, M., I.N. McCave and P.D. Komar. 1997. Threshold of sediment motion under unidirectional currents. *Sedimentology*, 24, 507-528.

Mitchell, J.K. 1993. *Fundamentals of Soil Behavior.* John Wiley & Sons, New York, N.Y.

Roberts, J., R. Jepsen, D. Gotthard and W. Lick. 1998. Effects of particle size and bulk density on erosion of quartz particles. *Journal of Hydraulic Engineering, ASCE*, 124(12), 1261-1267.

van Rijn, L.C. 1993. Principles of Sediment Transport in Rivers, Estuaries, and Coastal Seas. Aqua Publication, Amsterdam, The Netherlands.

Estuarine and Coastal Fine Sediments Dynamics
J.P.-Y. Maa, L.P. Sanford and D.H. Schoellhamer (editors)

Estimation of annual average propeller erosion rate in San Diego Bay, California

Maa, J. P.-Y.[a] and B. Chadwick[b]

[a]Virginia Institute of Marine Science, The College of William and Mary, Gloucester Point, VA 23062, USA
[b]Marine Environmental Quality Branch, SPAWAR System Center San Diego, Code D362, 53475 Strothe Road, San Diego, CA 92152

KEY WORDS
Propeller erosion, harbor environments, pollutants transport, *in-situ* measurements, critical bed shear stress for erosion, erosion rate, effective erosion rate

In-situ measurements of the critical bed shear stresses at the water-sediment interface (τ_{cr} at z = 0) in the San Diego Bay reveal that the sediment has a relatively high erosion resistance (0.17 Pa). Tidal current-induced bed shear stress in this well-protected harbor environment is less than the measured τ_{cr}, and thus, has no contribution to the possible re-entrainment of any buried contaminant back to the water column. Propeller wash is the major possible physical forces that will cause erosion and release the buried contaminants. Because of the highly non-uniform distribution of propeller wash both in temporal and spatial domain, a suggestion to estimate the yearly average erosion rate caused by propeller wash was proposed, and an example was given to estimate this effective erosion rate.

1. INTRODUCTION

Pollutants absorbed to deposited marine sediment may have many ways to re-enter the water column. Consequently, an originally inactive source of pollutants may become active again and cause concerns. The possible mechanisms that can carry pollutants away from their buried locations may include advection from ground water flow,

pure diffusion from sediment, redistribution caused by bioturbation, and sediment erosion caused by physical forces. To evaluate the importance of each possible pathway, an index equation that includes all the possible processes to compare the importance among each other has been proposed by Reible and Thibodeaux (1999) as follows.

$$\sum \text{flux} = F_{dc} + F_{bc} + W(C_o - C_H) + R_d H + \varepsilon_{eff} \quad (1)$$

where F_{dc} is the chemical diffusion term, F_{bc} is the bioturbation term, $W(C_o - C_H)$ is the ground water advection term, $R_d H$ is the chemical degradation term, and ε_{eff} represents the effective erosion rate (OSWER Directive 9285.6-08, 2002). Considering the complexity of the marine environment, it is not a simple task to obtain a reliable estimation on each process mentioned above. *In-situ* measurements would be the only reliable approach for acquiring the needed information because only *in-situ* approaches can minimize the possible error caused by changing experimental environments. For this reason, the following *in-situ* experiments were carried out in the San Diego Bay: (1) The Benthic Flux Sampling Device (BFSD, Chadwick *et al.*, 1992; Leather *et al.*, 1995) to measure the diffusion rate, (2) the Tidal Seepage Meter (TSM, Paulsen *et al.*, 2000) to measure the ground water flow rate across the water-sediment interface, (3) a Sediment Profile Imaging (SPI) camera system (Germano, 1995) to measure the depth of bioturbation, and (4) the VIMS Sea Carousel (Maa *et al.*, 1993) to measure the erosion rate. Other basic information, *e.g.*, tidal level, current, sediment cores, sediment traps, *etc.* were also measured or collected to support the study. Although there are many processes involved in the possible release of contaminants back to the water column, only the erosion process is presented in detail and an approach to estimate the effective erosion rate is proposed.

The sediment erosion process itself is not well-understood yet because of the significant variation among sediment composition, consolidation history, ambient water conditions, and benthic bioactivities (Wright *et al.*, 1997). In other words, each system may have a different response because of the varying natural environments. For this reason, we conducted the field experiments using the VIMS Sea Carousel (Maa *et al.*, 1993) to address sediment erosion behavior in the San Diego Bay. The typical *in-situ* approach for finding the erosion rate was addressed first, and then, an approach to address the effective erosion rate was suggested with an example applied at the San Diego Bay.

2. STUDY SITES

Two sites (P04 and P17) were selected for *in-situ* erosion experiments (Fig. 1). Site P04 (32° 40.287" N and 117° 7.2984" W) has a water depth of 10.4 m and is close to the channel. Site P17 (32°40.417" N and 117° 06.967" W) has a water depth of 7.6 m and close to the end of Seventh St. Channel. Sediment samples collected from these two sites reveal that sediment at Site P17 has more coarse material (39% clay, 30%silt, and 31% sand) than that at Site P04 (51% clay, 31% silt, and 18% sand). Clay mineral contents are similar (about 62% Illite and Mica, 23% random mixed-layer Illute/Smectite, 8.3% Kaolinite, 1.3% Plagioclase, and others) at these two sites about 500 m apart. Because the clay content at both sites are more than 30%, the erosion process is controlled by the electric static force between clay particles/flocs rather than the gravity force.

At the study sites, tidal range varies from about 2 m for spring tides to about 1 m for neap tides. The measured maximum near-bed tidal current is about 8 cm/s, which gives an estimated maximum bed shear stress around 0.15 Pa (Carlson, personal communication).

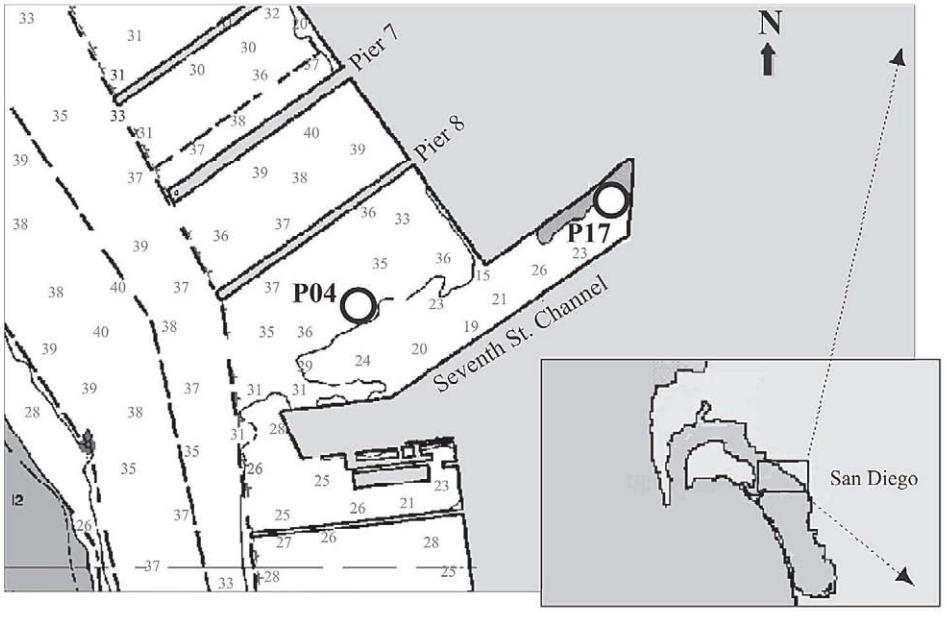

Fig. 1. VIMS Sea Carousel experimental sites (P04 and P17) in the San Diego Bay. Numbers are water depth in feet.

3. INSTRUMENTS

The VIMS Sea Carousel (Fig. 2) was used for the experiments. Details of the VIMS Sea Carousel can be found elsewhere (Maa, 1993; Maa *et al.*, 1993; Maa and Lee, 1997; Maa *et al.*, 1998). The Carousel is an annular flume with an inside diameter of 2.0 m and an outside diameter of 2.3 m. The cross section (width x height) is 0.15 m x 0.1 m. The driving shear force is coming from a rotation ring on top of the flume. Responses from the seabed (*i.e.*, erosion), and consequently the change in Total Suspended Sediment (TSS) concentration within the flume, is measured by using an Optical Backscatter Sensor (OBS, Downing, 1983) mounted at the middle elevation of the inner wall. The OBS was calibrated using an *in-situ* calibration procedure (Maa *et al.*, 1993) because the response of OBS is sensitive to the grain size distribution in suspension.

The deployment of the VIMS Sea Carousel requires a vessel with lifting capability of 1000 kg or more because of the flume weight about 800 kg in air. After deployment, the control and monitoring system can be transferred to a smaller vessel, if needed. The carousel was lowered into the water slowly and used its own weight (about 200 kg in water) to pierce into the sea floor and build up an annular flume. A bearing plate prevented it from sinking into soft mud beds. Deployment of the carousel was usually carried out during a slack tide with care not to seriously disturb the bottom fluffy sediment.

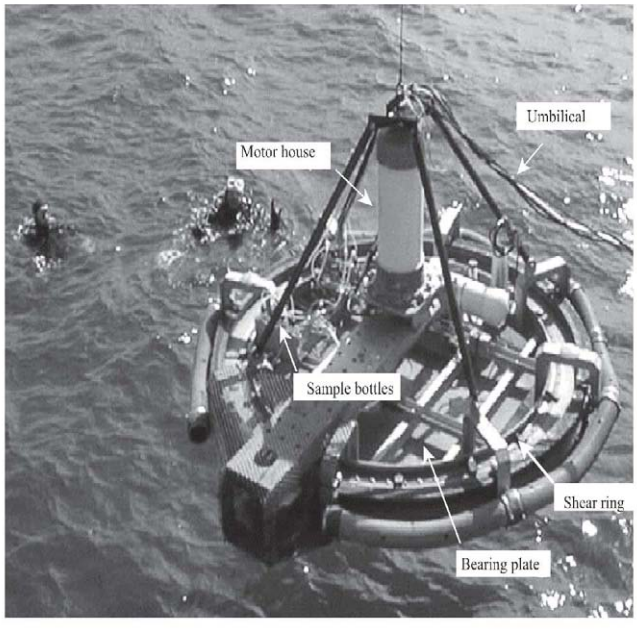

Fig. 2. VIMS Sea Carousel during a deployment in the San Diego Bay.

The spatial-averaged bed shear stresses, τ_b, caused by the rotating ring can be calculated as $\tau_b = 0.0114\ \Omega^{1.693}$, where τ_b is in Pascal (N/m^2) and the ring speed (Ω) is in rpm (Maa, 1993; Maa *et al.,* 1995). The actual ring speed was calibrated with the speed signals from the motor controller. The maximum spatial variation of τ_b is about 15% of the average value at a large bed shear stress, 0.8 Pa.

There were two types of tests at each site: an incipient test and an erosion rate test. The difference in operation procedures will be given in next two sections. All the operation parameters (ring speeds and durations) were pre-programmed and only a minor modification was possible during the experiment. Details of the criterion for selecting the critical bed shear stress and the method for finding the erosion rates are not duplicated here, but can be found in Maa and Lee (1997) and Maa *et al.* (1998).

4. CRITICAL BED SHEAR STRESS AT SEDIMENT SURFACE

An incipient test starts with a small τ_b and uses a small increment of τ_b (*e.g.*, τ_{b1} = 0.02 Pa and $\Delta\tau_b$ < 0.02 Pa) to identify the critical bed shear stress (τ_{cr}) at the water-sediment interface, z = 0. The TSS concentration inside the carousel changes only when the applied bed shear stress is large enough to stir up sediment from the bed. However, it is impossible to notice the change of TSS unless the change is significant. Because of the high background TSS concentration (about 70 mg/L) during the field experiments, the noticeable change of TSS was selected as 5 mg/L. When the change of TSS is more than this critical level (5 mg/L) and continue to increase for the next few higher bed shear stresses, we then define the average of the two successive bed shear stresses that cause the noticeable change on TSS is the τ_{cr} at the sediment-water interface. This critical value is rather subjective, but it well serves the purpose.

The first experiment was conducted at Site P17. After deployment (by the *R/V Acoustic Explorer*), the carousel control and monitoring system was transferred to a smaller *R/V Ecos*. The first bed shear stress, 0.03 Pa, although small (Fig. 3a), stirred up surficial fluff and caused a temporary raise of the TSS reading (Fig. 3b). The TSS readings, however, decreased slowly until the end of the seventh bed shear stress, 0.085 Pa. The next six higher bed shear stresses, from 0.1 to 0.155 Pa, could not further increase the TSS significantly. When the bed shear stress increased to about 0.19 Pa, we notice a clear increase of TSS more than 5 mg/L. Thus, we selected the average bed shear stress, 0.17 Pa, as the τ_{cr} for incipient motion at water-sediment interface.

The significant resuspension at the first τ_b (0.03 Pa) was caused by the dispersion of freshly deposited sediment stirred up by the *R/V Acoustic Explorer* during the flume

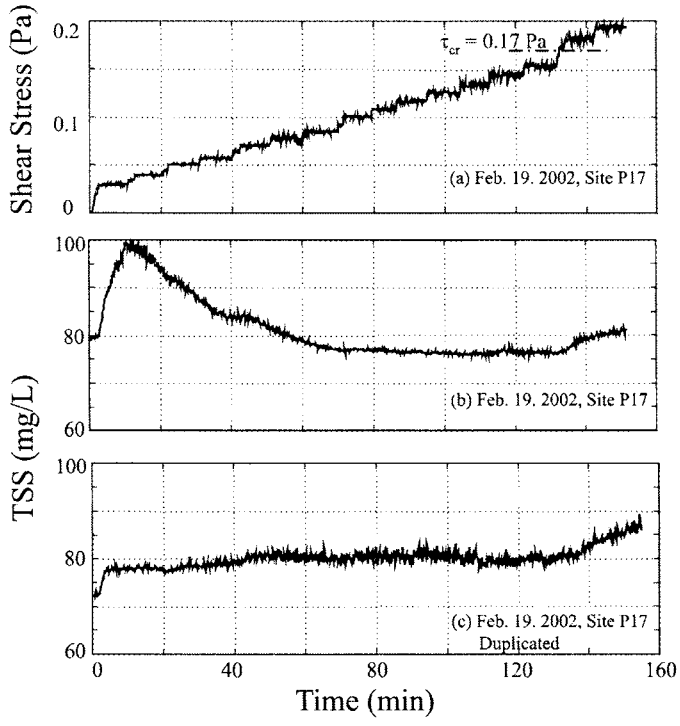

Fig. 3. Experiments to measure the critical bed shear stress at the water-sediment interface at Site P17. (a) Applied bed shear stresses, (b) TSS concentration time series, and (c) TSS concentration time series for the duplicated experiment.

deployment. A noticeable plume was visually observed on the water surface at that time. A fluffy sediment layer was commonly observed during most of the flume deployments, and this dispersion event should not be treated as the erosion of the seabed.

After the experiment for measuring τ_{cr} at the sediment surface, we immediately began the experiment for measuring the erosion rate. However, we will show the details of the erosion rate experiment later. Here we will proceed to report the results of a duplicate incipient test that was performed next day.

After the erosion rate experiment, we lifted the Sea Carousel and moved the *R/V Ecos* about five meters. The Carousel was then redeployed for a repeated test. The results are given in Fig. 3c. This time, however, we did not see the initial big plume generated during the first few bed shear stresses. The TSS concentration inside the carousel increased a little, but then maintained at a near-the-same level until $\tau_b = 0.19$ again. Thus, the same conclusion of $\tau_{cr} = 0.17$ Pa was obtained. This duplication is a demonstration of the repeatability of the experiment.

The incipient erosion experiment carried out at Site P04 also found that $\tau_{cr} = 0.17$ Pa (Fig. 4). For the first experiment, a rise of TSS reading at the elapsed time = 20 minutes indicated that there was a partially consolidated thin layer (of a patch) with an

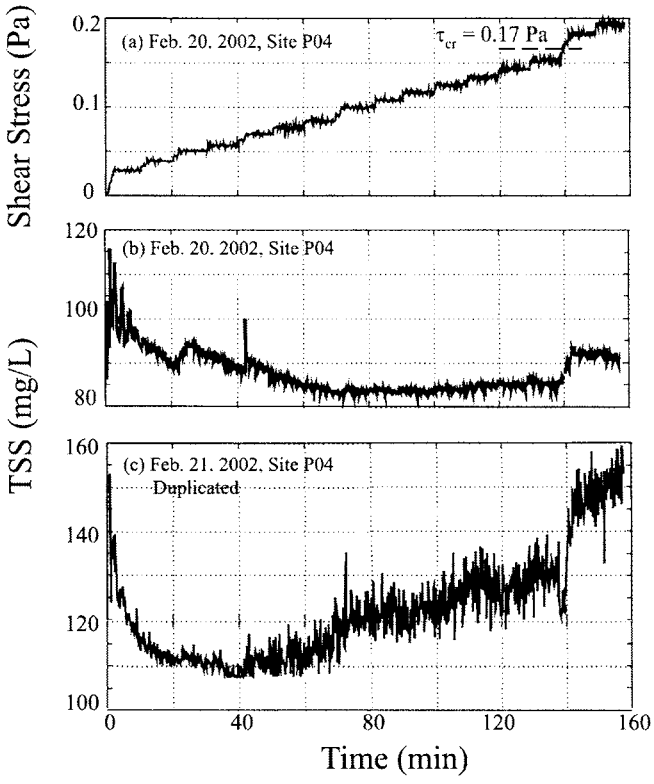

Fig. 4. Experiments to measure the critical bed shear stress at the water-sediment interface at Site P04. (a) Applied bed shear stresses, (b) TSS concentration time series, and (c) TSS concentration time series for the duplicated experiment.

erosion resistance about 0.04 Pa. Another sharp rise at the elapse time = 42 minutes might indicate another thin layer (or patch) because it was a rather isolated event. Because of the decreasing TSS after these two events, these two small τ_b's were not selected as the τ_{cr} and a resuspension event happened after τ_b = 0.15 Pa was selected, and thus, τ_{cr} = 0.17 Pa was identified. The response of seabed was slightly different for the duplicate experiment at this site. For the elapsed time between 40 and 80 minutes, it seemed there was a partially consolidated sediment layer with an erosion resistance less than 0.1 Pa. After 80 minutes, this layer was probably nearly depleted, and thus, the TSS concentration only increased slightly even the τ_b increased from 0.1 to 0.15 Pa. Notice that there were significantly more fine sediment fluffs at this site that contributes to the generation of a rather large plume spike at the beginning.

5. EROSION RATE EXPERIMENTS

The erosion rate test starts with a relatively large τ_b and uses a large and unequal $\Delta\tau_b$ (*e.g.*, τ_{b1} = 0.2 Pa and 0.05 < $\Delta\tau_b$ < 0.2 Pa) to observe the sediment bed responses for finding erosion rates (Fig. 5).

As mentioned in the previous section, we did a duplicate experiment for the incipient experiment. We also carried out a duplicated erosion rate experiment. Because of time limitation, however, the duplication only had three bed shear stresses (Fig. 6) and the 3rd bed shear stress was much larger than that for the first experiment (*i.e.*, 0.59 Pa instead of 0.443 Pa). Thus the bed response is significantly different because of a much large $\Delta\tau_b$.

Experimental results for Site P04 (Figs. 7 and 8) show that the OBS sensor saturated when τ_b = 0.927 Pa. Because an OBS is much sensitive to fine material, OBS readings will be high for fine material if the sediment mass concentrations are the same. This phenomenon implies that the suspended material is much finer at this site compared with that at Site P17. A comparison of the *in-situ* OBS calibration curves between these two sites (Fig. 9) shows the difference more clearly.

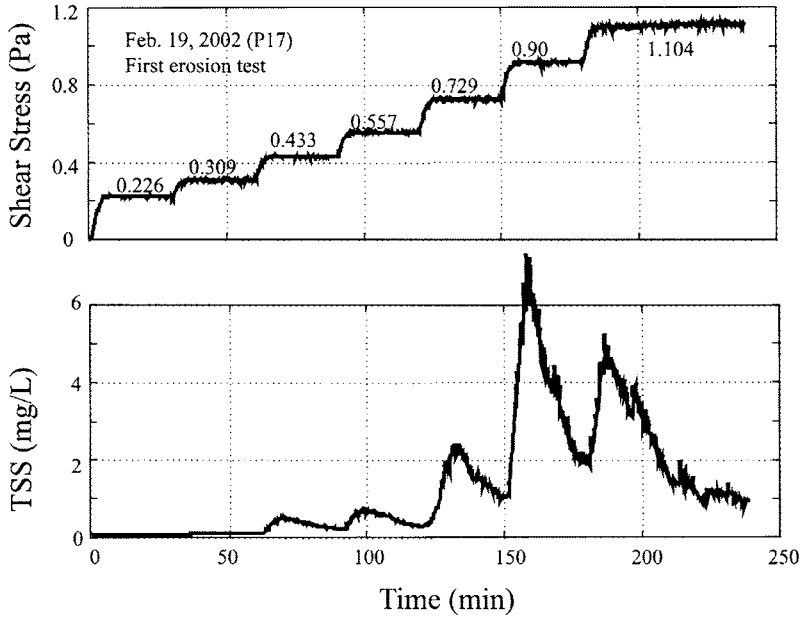

Fig. 5. Applied bed shear stresses and bed responses during the erosion test at Site P17. Numbers in the shear stress diagram are the average bed shear stresses.

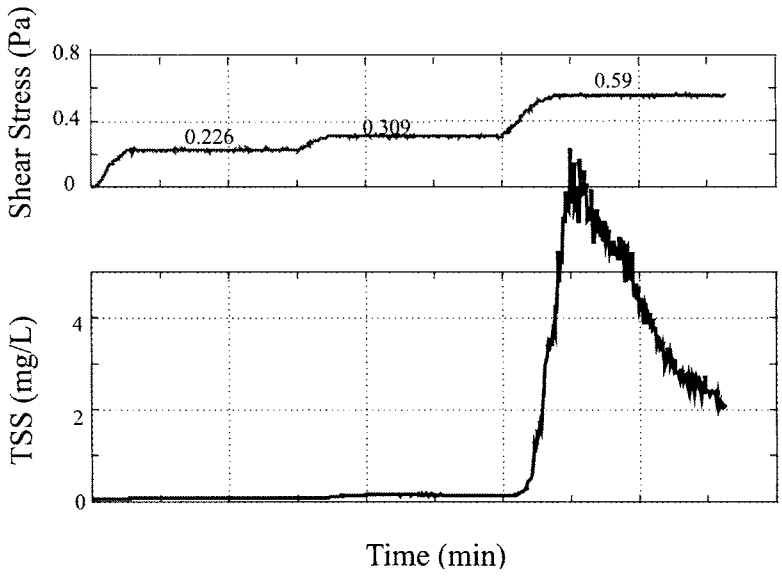

Fig. 6. Results of the second erosion test at Site P17. Numbers in the shear stress diagram are the average bed shear stresses.

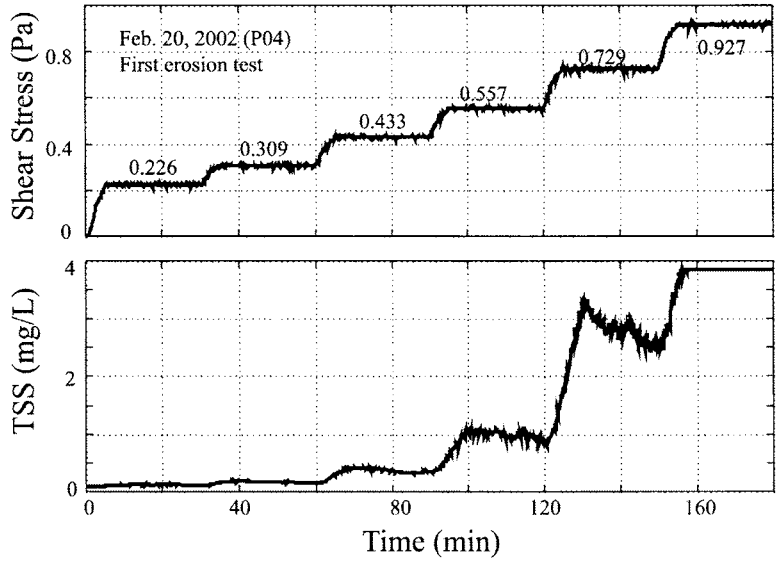

Fig. 7. Bed shear stresses and bed responses during the erosion test at Site P04. The saturation of OBS at a relative low TSS value indicates that more fine material were eroded at this site.

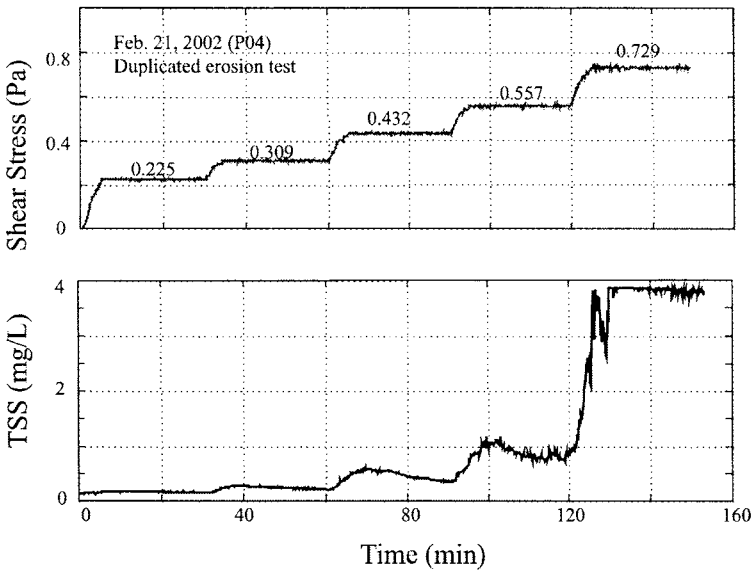

Fig. 8. A second erosion test conducted at Site P04. The OBS was saturated after 130 minutes.

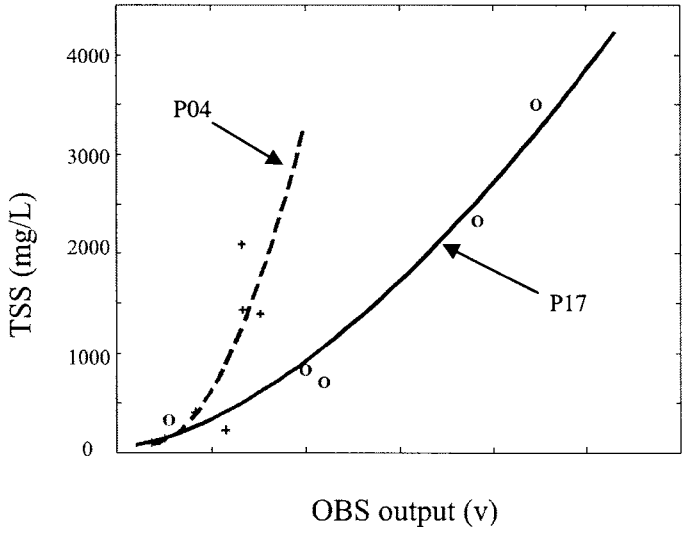

Fig. 9. OBS calibration curves for Sites P04 and P17. The different responses imply that suspended sediment in the flume is finer at P04 compared with that at P17.

6. EROSION RATES

A general pattern observed from the erosion rate experiments was that within a constant τ_b, the TSS concentration increased for the first several minutes and then decreased. This phenomenon was also observed in other tests carried out in the Chesapeake Bay (Maa *et al.*, 1993; Maa and Lee 1997, Maa *et al.*, 1998) and in the York River (Maa and Kim, 2002). This phenomenon can be described using Eq. 2, which shows the change of TSS concentration as the result of a decreasing resuspension rate with time (Yeh, 1979; Fukuda and Lick, 1980) and a constant leakage of water from the rotating ring (Lee, 1995).

$$Ah \frac{dc}{dt} = AE_o e^{-\lambda t} - c(t) Q_L \tag{2}$$

where A (10132 cm^2) is the area covered by the VIMS Carousel, h = 10 cm is the channel depth, c is the TSS concentration in g/cm^3, t is time in seconds, Q_L is the leakage rate of water in cm^3/s, E_o is a erosion rate constant (in $g/cm^2/s$), and λ is a time rate constant (in s^{-1}).

Equation 2 can be solved analytically with the three parameters (*i.e.*, E_o, λ, and Q_L) in the solution, and then using a least square technique to find the three parameters that are best fitted the measured TSS time series. Details of the data analysis can be found elsewhere (Maa and Lee, 1997; Maa *et al.*, 1998). Results of the data analysis (Fig. 10) show that λ varies between 0.002 and 0.008 with an average of 0.005 s^{-1} (Fig. 10b). This is an indication that erosion is a fast process because $e^{-\lambda t}$ approaches zero with λ = 0.005 s^{-1} and t > 1200 s (20 min). Thus, the erosion process can be considered ceased at the ends of all the applied bed shear stresses given in our experiments. For this reason, the difference between any two successive bed shear stresses given in Figs. 5 to 8 are the excess bed shear stress, τ_{ex}, and thus, the experiments results are the erosion rate, ε, versus τ_{ex} (Fig. 10a).

The fast erosion process also implies that τ_{cr} vary significantly in the vertical direction near the water-sediment interface. For example, Fig. 5 indicates that τ_{cr} = 0.17 Pa at the initial water-sediment interface, and τ_{cr} could reach 1 Pa within 1 cm below the original water-sediment interface.

Notice that the erosion rate given above cannot be applied to Eq. 1 directly because tidal force alone is too small to cause erosion. Only the propeller wash and the possible high velocity under hull of a large vessel can cause erosion. But these are isolated episodic erosion events in a deposition dominant environment. For this reason, a concept of the effective erosion rate, ε_{eff}, is introduced next.

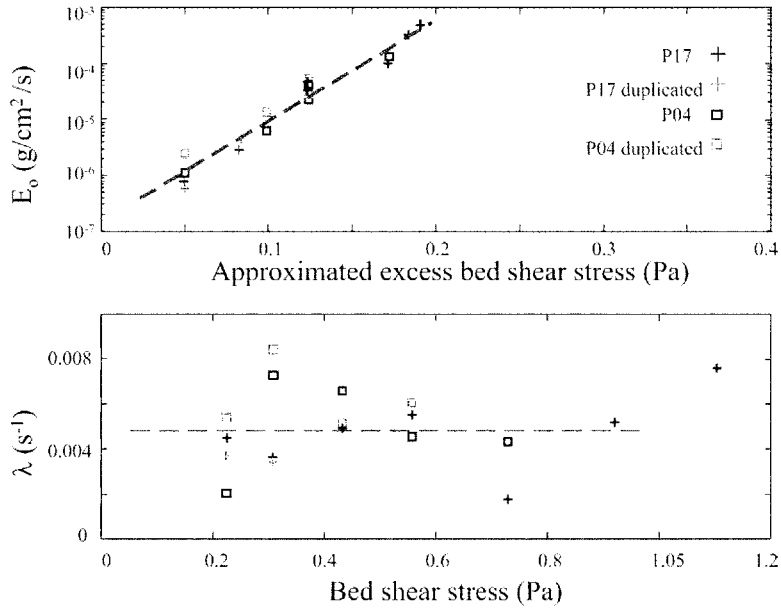

Fig. 10. Summary of measured erosion rates and time rate at San Diego Bay sites.

7. MODIFICATIONS FOR NON-UNIFORM DISTRIBUTION IN TIME AND SPATIAL DOMAIN

For a deposition-dominant environment, *e.g.*, a semi-enclosed basin like the San Diego Bay, tidal current is usually too weak to cause erosion. As a matter of fact, the measured maximum tidal current at 1 m above bed between Pier #8 and Seventh Street Channel (Fig. 1) during a month-long survey in 2002 was around 8 cm/s, weak as expected. This implies that only surficial fluffy sediment is possible for resuspension (technically, this is re-dispersion). Once there is a sufficient time for consolidation, the erosion rate caused by tidal force alone would be negligible small, if not at all. At any particular location, the propeller wash and possible large current under hull when there is a large, fully loaded vessel passing over are the only erosion forces (if dredging activities are excluded). Since the current under hull is usually smaller compared with the jet speed of propeller wash (a possible maximum up to 8 m/s, Hamill *et al.*, 1998) and it usually happened when the propeller washing occurs, the former erosion mechanism might be ignored at this stage. Inclusion of the erosion caused by the possible

under-hull high current is possible at a later time. To estimate possible re-entrainment of buried pollutants, the episodic erosion by propeller wash is the most important erosion force for finding the effective erosion rate. Because a propeller erosion event does not happen uniformly either spatially or temporally, assumptions are needed in order to estimate a spatially and temporally averaged erosion rate to compare with other processes mentioned in Eq. 1.

There are several assumptions required to estimate the spatial correction coefficient, C_s, caused by propeller erosions in a basin or a harbor (Fig. 11). These assumptions are (1) the area affected by a propeller wash is W_v^2, where W_v is the width of the vessel that causes the erosion, (2) the average ratio between a vessel width and a vessel length is 1/6, (3) the average ratio between a vessel length and a quay length, L_q, is 0.8, and (4) the number of quays in the selected basin is N. An accurate number for the above-mentioned ratios can be obtained from the harbor authority to further improve the estimation of C_s. The physical meaning of C_s is that it represents the ratio of area for N propeller erosion events and the area of entire basin, A_b at a time. For the rectangular basin (width = W_b and length = L_b) given in Fig. 11, C_s can be calculated as $N W_v^2 / A_b$ which can also be expressed as $0.018 N (L_q)^2/W_bL_b$.

Another coefficient, C_t, for correcting the non-uniformity in temporal domain can also be estimated with the following five assumptions: (1) The average vessel moving speed in a basin/harbor is 5 knots, (2) the percentage of quay uses is p_s, (3) it takes M days for one loading and unloading, (4) each docking only has one move-in and move-out, and (5) all propeller erosions are independent events.

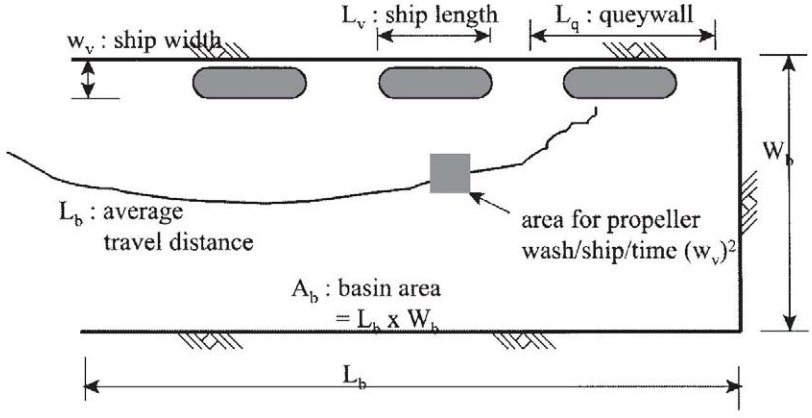

Fig. 11. A conceptual diagram to estimate the correction coefficients, C_s and C_t, for spatially and temporally non-homogeneous propeller erosion in a basin.

The physical meaning of C_t is the percentage of total time within one year that the propeller-erosion events may happen. Since there are two times for propeller erosion to occur for each docking (*i.e.*, when a vessel approaches and leaves the pier), there will be 2N*365 days * P_s/M times that erosion may occur at a location within the basin. Assuming the averaged vessel moved distance for one docking is the same as the basin length, L_b, and with the average vessel moving speed of 5 knots (2.5 m/s), the total time for propeller erosion to happen is (L_b /2.5 m/s)* (2N*365* P_s/M). When normalize this value by the duration of one year, *i.e.*, 86400 s/day * 365 days, the percentage of time in one year that erosion may occur can be estimated.

Here an example is given by using the small basin located between Pier 8 and Seventh Street Channel in the San Diego Bay. This small basin can be represented by a 300 m x 100 m rectangular basin, 5 quays were assigned for this particular basin with an average quay length of 70 m. The spatial correction coefficient C_s can be calculated as $0.018*5*(70)^2 / (300 \times 100) \approx 0.015$. The temporal correction coefficient with a 5 knot vessel speed, 50% usage rate for quays (*i.e.*, $p_s = 0.5$), and M = 4 days would give $C_t \approx 0.0035$.

For propeller erosion events, a rather large excess bed shear stress, τ_{ex}, should be used. Unfortunately there is no information on how large this excess bed shear stress should be. It is understood that within the selected area (*i.e.*, W_v^2), the excess bed shear stress distribution would be highly non-uniform. To select a representative value for τ_{ex} for propeller erosion is a big challenge, and more studies are necessary to properly address this question. At this time, it is assumed that the average τ_{ex} over the selected area for propeller erosion is the possible maximum τ_{ex} that can be confidently extrapolated from the *in-situ* measurements. The maximum range of τ_{ex} is about 0.2 to 0.25 Pa. For this reason, the maximum τ_{ex} of 0.3 Pa was selected, and therefore, an extrapolated erosion rate of 0.015 g/cm^2/s at the San Diego Bay sites was established. The selection of above specified τ_{ex} may be subjective, but it is probably the best that can be done at this time. Thus the effective erosion rate at the San Diego sites would be 0.015 * 0.0035* 0.015 g/cm^2/s = 0.788 x10^{-6} g/cm^2/s (about 250 kg/m^2/year).

8. DISCUSSION AND CONCLUSIONS

The measured critical bed shear stresses at the water-sediment interface are quite high, 0.17 Pa, at the San Diego Bay. It is actually the highest value that the VIMS Sea Carousel has ever identified. For example, at the Baltimore Harbor on the east coast

with a similar hydrodynamic environment, τ_{cr} is only about 0.1 Pa (Maa *et al.*, 1998). The reason of this high τ_{cr} is not clear yet, and it may be because of the special combination of clay minerals, among other factors, at the San Diego Bay.

In a deposition dominant environment, propeller wash would be a major possible erosion mechanism, except dredging. Because of the high irregularity in space and time domain, an average technique is necessary to obtain an effective propeller erosion rate in order to compare with other possible mechanisms that transfer pollutants back to the water column.

Currently, the time required to dock a vessel with help from tugboats are not included. A tugboat may also cause significant propeller erosion, especially during the period of performing its duty. A better selection on the currently used 5 knots for vessel speed is also possible. As a matter of fact, only the percentage of quay use and the docking time of each vessel can be obtained from the port authority with high accuracy, all other parameters may have large ranges. For example, the different vessel drafts will have a quite different propeller wash. Because of the random nature of vessel operation, it is impossible to use a deterministic approach for estimating the spatial and temporal correction coefficients. The presented approach, although rather rough, can be used relatively easy for obtaining the required information.

In this study, we selected a well-defined basin to estimate the correction coefficients. In reality, however, more efforts are needed to deal with an irregular and complex harbor geometry, and other affecting parameters.

The conclusions are summarized as follows:

1. The measured critical bed shear stresses for sediment erosion at the water-sediment interface is about 0.17 Pa, which is the highest value that has been identified so far using the VIMS Sea Carousel. The high $\tau_{cr}(z = 0)$ may be attributed by the particular combination of clay minerals and others. Further study is necessary to clarify this issue.
2. For a well-protected harbor environment, tidal force is usually too weak to cause erosion. If the critical bed shear stress at the water-sediment surface is high (true for the San Diego Bay), then tidal force itself does not play any role in the re-entrainment of pollutants back to the water column.
3. Because of the high $\tau_{cr}(z = 0)$, the only possible major erosion mechanisms are propeller wash and the associate erosion under a hall. However, the occurrence of a propeller wash is highly non-uniform both in spatial and temporal domain, and thus, corrections are needed.
4. A rather simple approach that is based on harbor geometry and several assumptions was suggested to get the correction coefficients for converting the spatial

and temporal non-uniform propeller erosion events to a basin-averaged erosion rate.

5. The suggested approach for getting the correction coefficients is rather preliminary and refinements on the correction coefficients are possible.

ACKNOWLEDGMENTS

We sincerely appreciate J. Grave, R. Gammisch, W. Reisner, and T. Nelson for their dedication to the field works. Support for the development of the VIMS Sea Carousel was provided by the Environmental Protection Agency (Grant #: R-817182-01-0). Support for the field deployments at the San Diego Bay was provided by the Marine Environmental Quality Branch, SPAWAR System Center San Diego via Computer Scientific Corporation (Contract #: N66001-99-D-5010). Clay minerals identification was conducted by K/T GeoServices, Inc. This paper is a contribution (No. 2469) of the Virginia Institute of Marine Science.

REFERENCES

Chadwick, D.B., S. Stanley, S.H. Lieberman and C.E. Reimers. 1992. A benthic flux chamber for monitoring pollution exchange rates at the sediment-water interface. *Proceedings of MTS '93*, Long Beach, CA, 1, 196-206.

Downing, J. P. 1983. An optical instrument for monitoring suspended particles in ocean and laboratory. *Proceedings of Oceans '83* (San Francisco), IEEE & MTS, 199-202.

Fukuda, M.K. and W. Lick. 1980. The entrainment of cohesive sediments in freshwater. *Journal of Geophysical Research*, 85(5), 2813-2824.

Germano, J.D. 1995. Sediment profile imaging: a rapid seafloor impact assessment tool for oil spills. *Arctic and Marine Oil spill Program Technical Seminar 1995*, 18, 1271 – 1279.

Hamill, G.A., J.A. McGarvey and P.A. Mackinnon. 1998. A method for estimating the bed velocities produced by a ship's propeller wash influenced by a rudder. *Coastal Engineering 1998*, ASCE, Reston, VA, 3, 3624-3633.

Leather, J.M., D.B. Chadwick and G. Koon. 1995. Contaminant flux measurements across the sediment-water interface in San Diego Bay, *Proceedings of Oceans '95*. 3, 1700-1713.

Lee, C.H. 1995. *Erosion behavior of natural sediments*. Ph.D. dissertation, School of Marine Science, College of William and Mary, Williamsburg, VA.

Maa, J. P.-Y. 1993. VIMS Sea Carousel: Its hydrodynamic characteristics. In: *Near-shore and Estuarine Cohesive Sediment Transport*, A.J. Mehta (ed.), Coastal and Estuarine Studies, 42, American Geophysical Union, Washington, DC, 265-280.

Maa, J.P.-Y., L.D. Wright, C.H. Lee and T.W. Shannon. 1993. VIMS Sea Carousal: A field instrument for studying sediment transport, *Marine Geology*, 115, 271-287.

Maa, J. P.-Y., C.H. Lee and F.J. Chen. 1995. VIMS Sea Carousel: Bed shear stress measurements, *Marine Geology,* 129 (1/2), 129-136.

Maa, J. P.-Y. and C.H. Lee. 1997. Variation of the resuspension coefficients in the lower Chesapeake Bay, *Journal of Coastal Research,* Special Issue No. 25, 63-74.

Maa, J. P.-Y., L.P. Sanford and J.P. Halka. 1998. Sediment resuspension characteristics in the Baltimore Harbor, *Marine Geology*, 146, 137-145.

Maa, J. P.-Y. and S.-C. Kim. 2002. A constant erosion rate model for fine sediment in the York River, Virginia, *Environmental Fluid Mechanics*, 1, 345-360

OSWER Directive 9285.6-08. 2002. Principles for Managing Contaminated Sediment Risks at Hazardous Waste Sites, Environmental Protection Agency memorandum, February 12, 2002

Paulsen, R.J., C.F. Smith, D.E. O'Rourke and T.F. Wong. 2000. Development and evaluation of an ultrasonic groundwater seepage meter. *Ground Water*, 2001 Nov-Dec, 39(6): 904-911.

Reible, D.D. and L.J. Thibodeaux. 1999. Using natural processes to define exposure from sediments. In: *Sediment Management Work Group; Contaminated Sediment Management Technical Papers*, http://www.smwg.org/

Wright, L.D., L.D. Schaffner and J. P.-Y. Maa. 1997. Biological mediation of bottom boundary layer processes and sediment suspension in the Lower Chesapeake Bay, *Marine Geology*, 27-50.

Yeh, H.-Y. 1979. *Resuspension properties of flow deposited cohesive sediment beds*, M.S. Thesis, University of Florida, Gainesville, FL. 32611.

Estuarine and Coastal Fine Sediments Dynamics
J.P.-Y. Maa, L.P. Sanford and D.H. Schoellhamer (editors)

Organic-rich fine sediments in Florida Part 1: Sources & nature

Kirby, R.

Visiting Research Scientist, Department of Civil & Coastal Engineering, 336 Weil Hall, University of Florida, Gainesville, Florida 32611-2088, USA

KEY WORDS
Organic sediments, peat-forming environment, black organic mud, carbon sources, lake mud, estuarine mud.

The Floridean environment gives rise to prolific and highly varied organic deposits. This overview considers sources of carbon and the nature of the deposits this element forms. The environmental conditions leading to "carbonate-forming" and to "peat-forming" deposits are described. The marine coast, together with the terrestrial environment, waterways and lakes of Florida, are large scale sources of carbon production, the precise origin and fate of which is not always clear. Carbonate depositional systems occur mainly in the south of the state and at the marine coast. Peat type deposits include mangrove peats at the marine coast and the vegetation-type-dependent, fresh water Everglades Okeelanta, Gandy and Loxahatchee peats of the interior. None of these deposits give rise to major management problems. On the other hand the "peat-forming" sedimentary regime also includes the finely divided black organic muds locally called "mucks." Poorly consolidated black muds are presenting severe problems in a large number of lakes, estuaries and marine coastal zones in Florida. The rate of production of black muds has accelerated a great deal in the last century and in the last few decades the degree to which loosely bound industrial contaminants have become associated with these has created a major challenge to society.

Examples of black mud production in the various typical regimes, based on co-operative research programmes in the University of Florida over more than a decade and focused mainly in lakes and estuaries, are presented. An overview of black organic muds around the marine coast is provided. Original research on black muds in the

Cedar/Ortega estuaries, a tributary of the major St Johns River system, is described. Similarly, literature review reveals environmental conditions determining the production rate, together with external and internal forcing factors determining black mud distribution in small lakes. The distributions in these vary, and include broad even distribution, focusing in bathymetric depressions or, alternatively, deposition around the littoral margin. Further original research on the issue of black mud distribution in large lakes, this time Lake Okeechobee, indicates an additional source of carbon production, namely the repeated wind-induced nutrient cycling leading to plankton blooms. None of the known forcing functions, alone or in combination, seem wholly to explain the distribution of black mud in the lake. Options for remediation and some trends for the future are suggested. Not only is black mud management a challenge, but a reminder is given that aqueous microbial systems are still imperfectly understood in terms of carbon sources.

1. INTRODUCTION

The State of Florida, USA, is low-lying with large areas occupied by limestone bedrock. The low elevation, coupled with the soluble nature of limestone, implies low gradient, generally lazy streams and rivers carrying little detrital sediment. For example, the northward flowing St Johns River has a length of 500 km in the course of which it falls about 10m - an overall gradient of 1.6 cm/km. Much of the southern part of the state is occupied by the Everglades forest and wetlands, which are fed in part from the state's largest lake, Okeechobee. Flows are maintained from daily summer thunder storms and seasonal cyclones. Very occasional hurricanes with damaging winds and extremely high rainfall lead to episodic and high peak flows. The sub-tropical climate and absence of detrital erosion products lead to the modern sediments in water courses, rivers, lakes, estuaries and the marine coastal zone being predominantly authigenic. Anthropogenic changes in the last 100 years or so, especially large scale rises in nutrient input and introduction of a number of exotic plant species, are the most recent and potentially most intractable of a range of alterations to the natural environment arising from development. These combined factors have contributed to the variety of organic sediment being formed. Floating and rooted vegetation tends to choke slow flowing waterways, whereas large rises in production rates of black organic muds threaten to block and infill lakes and drainage channels.

This summary arises from a number of research contracts and is intended to draw these together and set the scene for more specific studies reported elsewhere in this volume (Gowland *et al.*). The US Army Corps of Engineers requested an overview of

the types and nature of organic deposits in Florida, with particular interest in sources of carbon and understanding how these deposits are manifest, with a view to wise management of the black organic mud. South Florida Water Management District requested a research programme into nutrient re-entrainment, black mud erodibility and plankton production in Lake Okeechobee. St Johns River Water Management District have required specific studies of Newnans Lake near Gainesville and a proper quantification in anticipation of remediation of a PCB contaminated black organic mud patch in the Cedar/Ortega Rivers, a tidal tributary of the St Johns River south of Jacksonville.

2. TYPES & NATURE OF ORGANIC SEDIMENT IN FLORIDA

Carbon is manifest in the Floridean environment in two principle regimes, either as "carbonate-forming" or, alternatively, as a "peat-forming" depositional system. Carbonate sediments formed by solitary or colonial reef-building organisms, or by precipitation or secretion from plants and animals, occur widely in Florida, especially at the marine coast, Cohen *et al.* (1994), Brown and Cohen (1995). Inland, especially in the south of the state, carbon is incorporated into carbonate sediments in shallow water aerobic environments subject to a pronounced wet and dry season. Carbonate-forming regimes are not considered further here. Peat-forming depositional systems, similarly, have a maritime coastal and a fresh water inland manifestation. In fresh deeper water, permanently-inundated anaerobic environments, for example within stands of vegetation, carbon is incorporated into a wide variety of peat-forming depositional systems.

At the marine coast Florida has mangrove swamps, subtidal sea grass beds and salt marshes. *Rhizophora mangle* dominates the mangrove species. Mangroves are extensive in some coastal areas around the Florida coast, as shown for the southern tip of the peninsula (Fig. 1). Where abundant and prolific, mangroves are especially productive, which leads to the export of carbon and to the formation of mangrove peat - a very pure form of organic sediment. *Thalassia testudinum* dominates the sea grasses. Fleming *et al.* (1990) specify mangroves and sea grasses as the major carbon producers in fringe coastal communities and the basis of trophic food chains in coastal ecosystems in southern Florida. Whittaker and Likens (1973) examined ecosystem characteristics for 20 different environments, finding wetlands the most prolific (average annual production 1,125g $C/m^2/yr$). In the coastal zone the energy balance of salt marshes has been one of the most hotly debated issues amongst ecologists over the last three decades. In the 1960s, Odum (1969) concluded that 45% of production is removed by tides before marsh consumers have a chance to use it, and in so doing this permits estuaries to

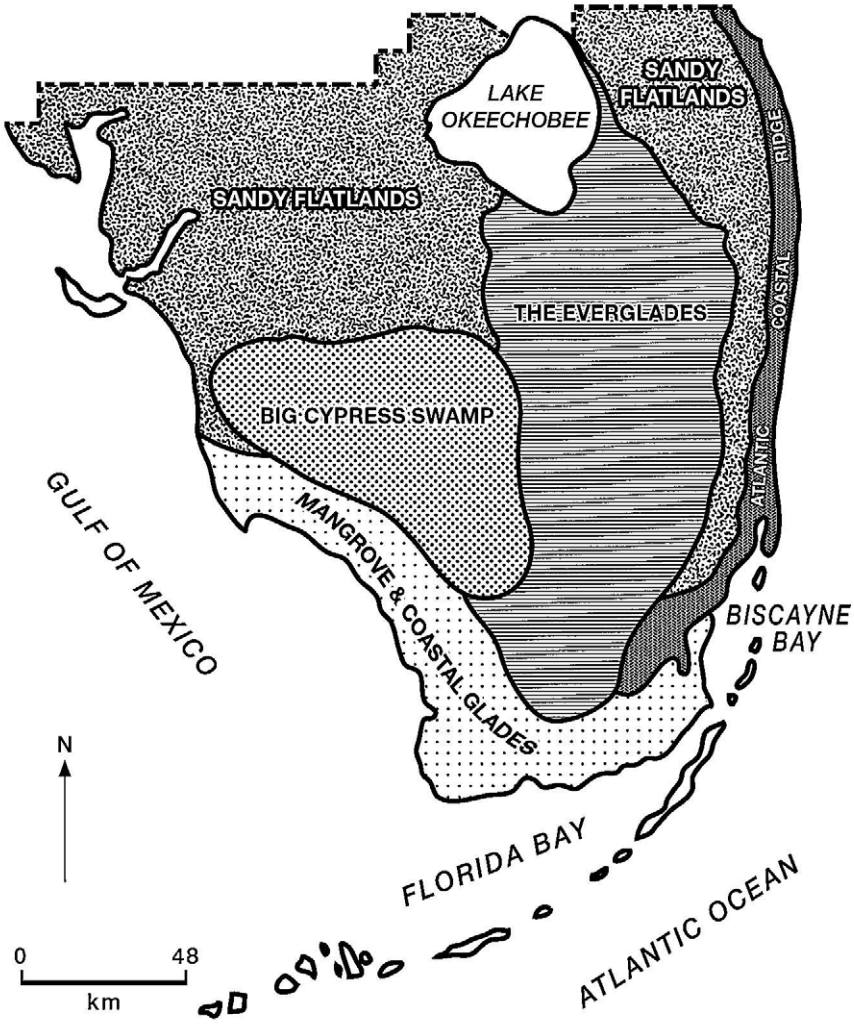

Fig. 1. Physiographic divisions in southern Florida including the coastal mangrove belt (adapted from Kohout and Kolpinski, 1967)

support a wealth of animals. This new concept was supported by particulate organic detritus studies and was the origin of the "outwelling hypothesis," which proposes that salt marshes produce more material than can be degraded or stored within the system, and that the excess is exported to coastal waters, where it supports ocean productivity.

However, when whole systems from land to sea were later considered, it became clear that *Spartina* marshes can be sinks for nutrients. This and other work led to many studies in a wide variety of systems and to conflicting evidence about whether salt marshes were exporters or importers of carbon. This matter has subsequently been resolved.

Childers (1994) carried out a large scale study of this topic at eight sites around the southeastern US (three in Louisiana, one on the Georgia/Florida border, but none actually in Florida itself). This study showed that where tidal ranges are low, less than 1m, as is typical in Florida, marsh/open water exchanges of nutrient and organic matter are primarily intertidal and fluxes measured on these marshes are export-dominated. At higher tidal ranges horizontal sub-surface flow and subtidal benthic advection become important, as marshes tend to take up nutrients and organic matter from the inundating water column, while exporting these constituents to adjacent tidal creeks. These latter tend to be importers of nutrients and organic matter.

"Peat-forming" deposits also occur widely in the fresh water environment of streams, rivers, wetlands, lakes and estuaries. They are especially broadly distributed in the southern part of the state. The distribution of surface sediments of south Florida is shown in Fig. 2.

The total system embraces the headwaters and drainage basin of the Kissimmee River and several smaller streams and rivers, the largest lake (Okeechobee), the southerly and part- westerly directed outflow from this lake forming the Everglades Wetland and its broad outlet to the sea in the extreme south, the Shark River Slough. The peat-forming province has its locus in the north of the mapped region. A number of the extensive peat provinces have been given names. These are the Everglades peat, the Okeelanta peat and two separate large expanses of Loxahatchee peat (Table 1). The justification for giving and maintaining these names is that the peats derive from different plant groups and consequently show contrasting features. A further aspect is the application of the word "muck" to certain organic deposits.

Carbon in the peat-forming provinces has at least three broad sources and includes that generated in situ from the great variety of plant species:

1. Terrestrial inputs via rivers, aquatic plants in rivers
2. Small lakes or the margins of bigger lakes, *i.e.,* the fresh littoral zone
3. Open water systems in larger lakes with little or no link to terrestrial inputs or the indigenous littoral zone.

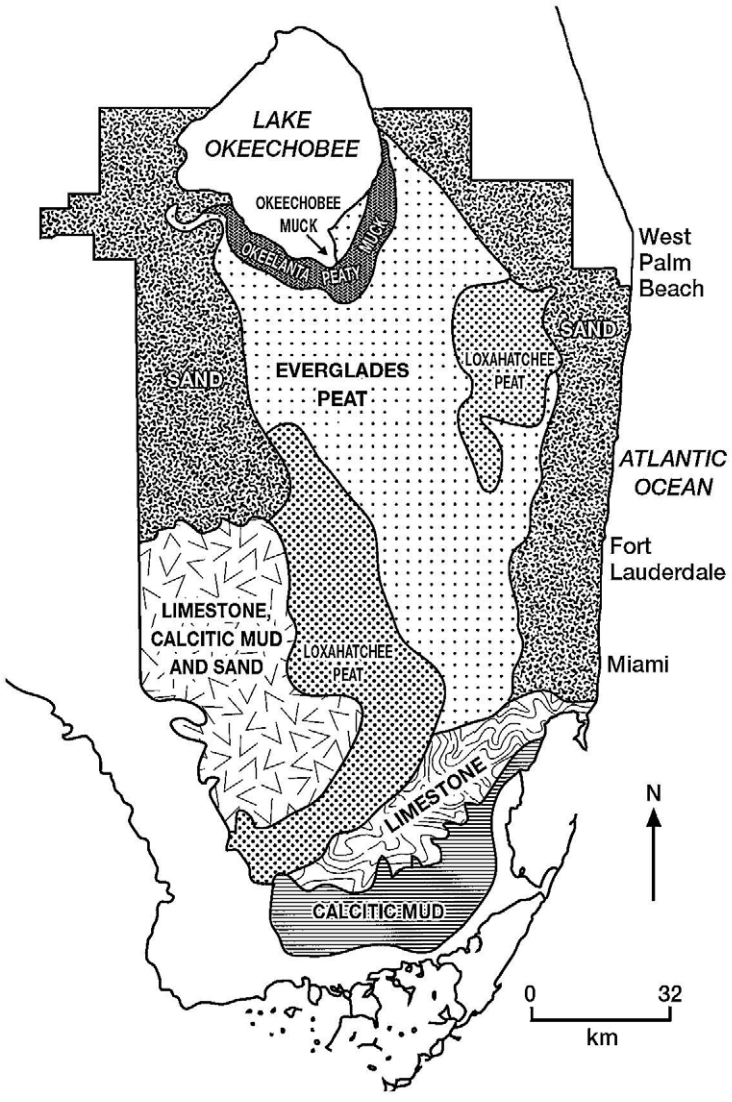

Fig. 2. Surface sediments covering southern Florida (adapted from Gleason and Stone, 1994).

For more detailed discussion and quantification of relative abundance of these carbon sources, see Mehta *et al.* (1997).

Marine and fresh water peats do not present the same types of practical problem as those arising from a further intrinsic component of the peat-forming province, the black

Table 1. Linkage between organic sediment type and plant community.

Organic Sediment Type	**Plant Community**
Everglades peat	Sawgrass marsh
Loxahatchee peat	Water lily marsh or slough
Gandy peat	Tree island
Okeelanta peaty muck	Elderberry-willow swamp[a]
Okeechobee muck	Custard apple swamp[a]
Custard apple muck	Custard apple swamp
Torry muck (modern terminology synonymous with Okeechobee muck)	Custard apple swamp

[a] Not necessarily the vegetation initially forming the organic sediment

organic muds locally known as "mucks." As mentioned above, introduction of and proliferation of exotic vegetation species, coupled with widespread burning and herbicide spraying to control this and further exacerbated by large increases in nutrient input to water bodies, all being recent anthropogenic factors, have led to an increase by two orders of magnitude in the rate of production of black organic muds in Florida. Stoermer *et al.* (1992) obtained a core from Lake Okeechobee, sampling it at 1 cm intervals and analysing the sub-samples for chemical, biological and physical characteristics. ^{210}Pb, diatom zonation and porosity were all determined on this minute scale and then linked to lithology and records of past weather. The core was dated back to an assumed date of 1610AD. The time period 1880-1946 was highlighted as that when "substantial anthropogenic modification" was becoming apparent. One change, which accelerated further after 1946, was an increase in black mud deposition rate. Brenner *et al.* (1996), using contrasted but similar measurements, showed the same pattern of increased rates of mud production during the last century. Other investigations have shown the same results for marshes, rivers, estuaries and coastal embayments. Furthermore, in some areas this increased production has been accompanied by contamination by a wide range of chemical pollutants. The black organic muds themselves are widespread, occurring in streams, rivers, lakes, estuaries and coastal embayments of the sea, and present their own set of intractable problems. These are made worse where the additional complicating factor of chemical contamination occurs. The remainder of this paper is concentrated on the various manifestations of black organic mud in maritime coastal embayments, lakes and estuaries.

2.1 Black organic mud

As explained, in recent decades, production rates of black organic mud have risen to the extent that the discharge capacity of many waterways has become impaired, lakes are silting up and major environmental changes have been induced by black organic mud incursion. A related problem is that the muds provide a host for anthropogenic contaminants. Management, in particular reducing rates of mud production in future, removal of what is already present and dealing in the most effective manner with hazardous contaminants are all fairly intractable issues. Central to many is knowing how the muds are distributed as well as a sound understanding of where carbon in these systems comes from.

2.2 Maritime coastal embayments

No specific studies by the author have been made in these environments but results of several investigations have been published. For example, Roman *et al.* (1983) studied Biscayne Bay, Gu *et al.* (1987) researched the Indian River Lagoon, McPherson *et al.* (1990) describe a comparable situation in Charlotte Harbour in SW Florida, Carr *et al.* (1996) and Johansson *et al.* (1985) have made investigations in much of Tampa Bay, as have Brooks *et al.* (1991) in Hillsborough Bay, the NE lobe of Tampa Bay. Typical of many sites, Trefrey *et al.* (1992) researched Manatee Pocket in the St Lucie Estuary on the SE coast of Florida. Here recent black muds give rise to direct and indirect problems. The natural sand substrate is blanketed by black mud, reducing and altering the benthic community. These materials are highly susceptible to resuspension, increasing turbidity and inhibiting light penetration. These various changes have smothered the formerly extensive sea grass beds removing the foodstuff of manatees. A range of anthropogenic contaminants are also adsorbed onto the fine particles.

2.3 Lakes

There are in excess of 8,000 lakes in Florida. Brenner *et al.* (1995) note that only about 10% of these have been studied limnologically and in only a small fraction of these has attention been given to sediments. For example, Whitmore *et al.* (1996) have reported sediment distribution patterns from seven Florida lakes and some distribution patterns from others are known. They studied Lakes Maggiore, Hollingsworth, Clear, Thonotosassa, Marianna, Parker and Seminole. These lakes, as with many others in Florida, are highly productive, and a superficial assumption might be that a high flux of organic breakdown products would give rise to a thick and even deposit of black muds on the beds of such lakes. Following surveys, probing and coring these lakes, and from experience with others, they discovered some hypereutrophic lakes in which organic

sediments were of minimal scale or completely lacking. This situation arose due to the shallow depth, frequent mixing, lack of stratification and warm temperatures, all of which promote rapid breakdown of organic material.

In lakes containing a significant amount of black mud, including the seven above, an unexpected discovery was that sediment distributions were highly variable. Whitmore *et al.* (1996) were able to categorise black mud distributions into three types:

1. Uniform across the lake
2. Confined to deeper zones where these were present
3. Restricted to the littoral zone and embayments

These distributions (Fig. 3) and aspects of their consequences are discussed in detail in Mehta *et al.* (1997) but not repeated here. Black organic mud distribution has obvious implications for management. In this regard the necessarily limited and laboriously conducted investigation by Whitmore *et al.* (1996) is of great value, indicating, as it does, that several factors contribute to black mud distribution in small shallow lakes: these being the strength and direction of the wind and the amount of shelter, the presence and distribution of macrophytes, basin shape, and basin bathymetry.

The largest, and in many ways statewide most important water body, is Lake Okeechobee. With respect to distribution and nature of its black mud deposits, the existence of this lake introduces a further controlling factor. In addition to the meteorologic, hydrologic, topographic and geologic factors relevant to the suite of lakes described by Whitmore *et al.* (1996), Okeechobee is of a size large enough to permit the establishment of large scale patchiness of its phytoplankton composition. This phenomenon is familiar to oceanographers and in the lake is another possible contributor to variability in black mud distribution. The nature and distribution of black mud has been investigated by several research groups. The lake occupies an area of 1,700 km^2, Phlips *et al.* (1997), or 1,810km^2, Stoermer *et al.* (1992). It is roughly circular in shape and close to 48km in diameter. It is an eutrophic lake with a maximum depth of about 4.5m. Many attributes of the lake are poorly established, not least of which relate to the distribution and origin of its black mud.

When the distribution of black mud in plan or its variation with depth are considered, much is known but many more questions are thrown into sharp focus. In plan the sediment is disposed in four major facies - 44% black mud, 28% marl and sand, 19% littoral and 9% peat (Olila and Reddy, 1993).

Maps of mud thickness contours (Fig. 4) are found in Kirby *et al.* (1994) - the bed thickness contour map being compiled from geophysical surveys, 31 vibrocore stations and combined with 131 hand pushed core samples obtained by the Soil Science

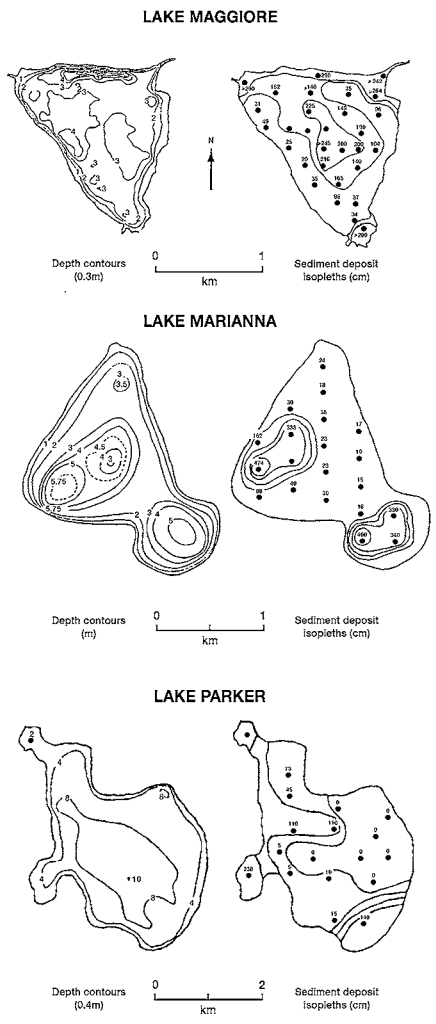

Fig. 3. Maps of organic black mud distribution in Lake Maggiore (relatively even distribution across whole lake). Lake Marianna (mud concentrated in bathymetric hollows), and Lake Parker (mud concentrated in peripheral areas and embayments) (adapted from Whitmore *et al.*, 1996)

Department of the University of Florida. The total volume of the mud patch is approximately 193 x 10^6 m^3. The black mud patch is asymmetrically disposed in the lake (Fig. 4), occupying much of the centre, with a northerly tongue reaching to Taylor Creek. The littoral zone, even on the eastern margin, is virtually devoid of black mud, as is the zone around the mouth of the Kissimmee River. The reason for the absence of black mud in the approaches to the Kissimmee River, which must be a major nutrient input point, is not altogether clear, although almost the entire black mud body is contained within the -3m bathymetric contour.

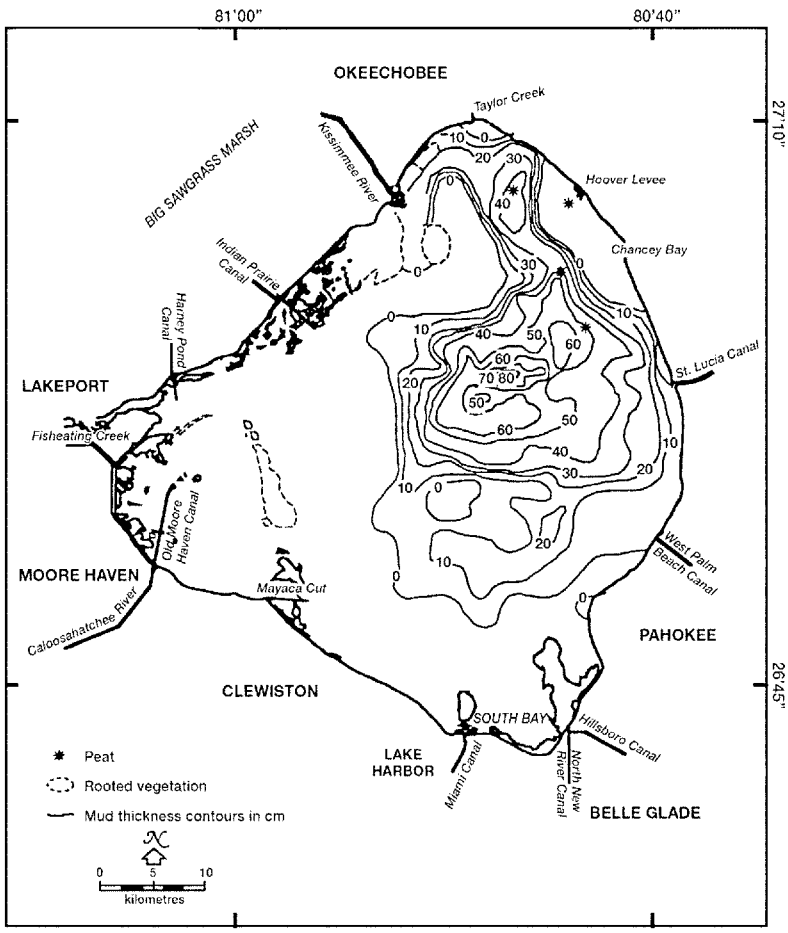

Fig. 4. Distribution and depth of unconsolidated sediment types in Lake Okeechobee. Away from the shore, organic sediment mainly occupies the northern two-thirds of the lake bed (after Kirby *et al.*, 1994)

One important clue to the distribution of black mud in Lake Okeechobee may, therefore, be its association with the bathymetry. In this respect it may be comparable to Lakes Thonotosassa, Marianna and Clear Lake in the descriptions of Whitmore *et al.* (1996). However, there are very likely other contributing factors and issues. Attempts have been made to quantify carbon sources within the lake itself, Zimba *et al.* (1995) (Table 2).

Table 2. Tonnage of carbon in submerged vegetation in littoral zone of Lake Okeechobee.

Vegetation	**Carbon (Metric Tonnes)**	
Year	*1990*	*1991*
Hydrilla	7,269	8,531
Potamogeton	5,805	6,446
Najas	13	1,221
Chara	3,967	2,469
Vallisneria	7,991	9,569
Totals	**25,044**	**28,235**

In addition to the possibly unexpected absence of black mud from the Kissimmee River approaches, the carbon production of submerged littoral vegetation is given by Zimba *et al.* (1995) as 25,000 metric tons in 1990 and 28,000 tons in 1991 (Table 2). Evidently very little, if any, of this forms black mud and accumulates close to its site of production. The proportions exported in dissolved, compared to particulate, form appear unknown and the fate, especially whether they escape the lake southwards or instead are reworked into the mud patch is unknown.

Phlips *et al.* (1997) has provided an important contribution to the issue of black mud distribution in Lake Okeechobee. These investigations have distinguished four ecologically distinct regions of the lake waters. These are:

1. The large central region of muddy bottom sediments coincident with the deepest water and frequently overlain by a turbid water column.
2. A northern region of muddy sediments in intermediate water depths subject to the major influence of nutrient-rich inflows.
3. A western perimeter region with firm bed materials and subject to frequent plankton blooms.
4. A littoral fringe region along the western and southern boundaries of the lake enclosing a significant proportion of the submerged aquatic vegetation, combined with an extensive littoral community encompassing about 20% of the lake area.

It seems that local wind-induced circulation is what determines black organic mud distribution in Okeechobee. The lake is an important drinking water source but high in nutrients from these highly varied "natural" sources, as well as from run-off of fertilizers used in agriculture. Black organic mud production rates in the lake can be reduced in

part by controlling input of these agricultural fertilizers. This in itself is a quite intractable challenge. Even more challenging, the weakly consolidated muds are also enriched in nutrients which are recycled into the water column during windy periods inducing further plankton blooming and carbon fixation.

It was established over a prolonged period, Green (1968), that the base of most aquatic food chains lay in the primary production provided by phytoplankton. We appreciate quite well how, in eutrophic systems, *i.e.*, those abundantly supplied with nutrients, the carbon base is supplied by bacteria and phytoplankton. These are grazed upon by the zooplankton species, *Daphnia*, or its equivalents, as an indicator that carbon is being cycled through the microphytoplankton. In contrast, in oligotrophic lakes, *i.e.*, those deficient in nutrients, resource limitation inhibits the phytoplankton, and zooplankton feeding strategies dependent solely upon filtering, applicable to the prolific systems, are no longer viable.

There are many implications for management. Should the nutrient status of an organic system be changed then the entire micro-floral and micro-faunal community will be altered too. Similarly, management techniques for lakes which envisage drawdown or alternatively raising lake elevation are likely to alter the extent of light penetration, especially at the bed and will, similarly, induce alterations in the community of microorganisms underpinning the ecosystem. A seemingly new and unproven suggestion (pers. comm. C. Reynolds, Freshwater Biology Association and Institute of Freshwater Ecology, UK) is that bacteria may be the primary reservoir of carbon. There has always in the past been a question in aquatic biology of whether zooplankton really feed on phytoplankton, but this new question is in respect of a possibly similar relationship between bacteria and phytoplankton. These matters, naturally, are of importance in management.

2.4 Estuaries

Black organic mud is forming in many estuaries in Florida. A specific study has been made of the muds of the Cedar/Ortega River system. These small confluent estuaries lie south of Jacksonville, the former draining the recently urbanised outskirts of this city. The muds of the Cedar River are contaminated with PCBs following a fire in a transformer recycling factory in the early 1990s. In addition to a general desire to reduce the rate of black organic mud production in the system, a more urgent issue is to find the optimal route to remediating the PCB contaminated sediments. It had been hypothesised that these might be susceptible to re-erosion and wider dispersal in the event of a hurricane-induced flash flood. These are intrinsically unpredictable such that there is some urgency in respect of finding a solution.

Chemical and sedimentological studies have been made of the sediments of the main stem of the St Johns River and its tributaries, for example, the Cedar/Ortega river system immediately above Jacksonville. Much of the beds of these systems consist of weakly consolidated black muds. Cooper and Donaghue (1999) describe these sediments as "overwhelmingly fine-grained, averaging 80% fines, unusually high in moisture content, averaging 79%, and in organic material, averaging 29% by weight," all leading to extremely low dry bulk densities, averaging 0.24 g/cm^3. Various organic geochemical analyses on this material, Mulholland and Olson (1992) and Tissot and Welte (1984), suggest for the entrance to the Cedar/Ortega Rivers a marine-derived portion of the black muds in the region 20 - 30%. C:N ratios of many core samples were found to lie in the range 10 - 14:1 and did not vary significantly with depth. This and other contributory evidence is consistent with the organic components in terrestrial soils and in the surface sediments of lakes. The values are consistent with derivation of a large proportion of the black muds from degraded higher plant (terrestrial) sources. The various contributing analyses suggest that in the reaches of the Cedar/Ortega River entrance perhaps 10 - 20% of the black muddy sediment is derived from autochthanous, planktonic algal, aquatic sources.

The sedimentary regime of the Cedar/Ortega River estuaries is known from 172 cores taken by Morgan and Eklund Inc. (1995) and 51 grab samples obtained by Battelle Ocean Sciences (Mote Marine Laboratory, 1998). The sediments of the Ortega River exhibit the highest organic content (Fig. 5) and the smallest anthropogenic alteration. The Ortega watershed remains heavily forested and perhaps the most significant change in the last 100 years has been an increase in the sedimentation rate. Deforestation and residential development is manifest in the sediments entering the Cedar/Ortega River system perhaps by an increase in black mud siltation rate, but also by multiple layers of wood chips and occasional yard grass (grass cuttings) in the sedimentary sequence. The sediments of the Cedar River reflect a more advanced stage of urbanisation and show the greatest anthropogenic effects. The upper black mud reaches here contain sand and clay deposits washed off urbanised areas. There are no wood chip zones to indicate recent deforestation but the sediments are significantly contaminated by fuel oil and a wide range of industrial pollutants - most notably PCBs at elevated levels. The hypothesised accelerated deposition rates over the last 100 years are exacerbated further along the north coast of the confluent reaches of the Cedar/Ortega Rivers by the blocking effect caused by a number of large marinas. The siltation rate reaches 20 mm/yr in this zone, but more generally lies in the region 4 – 8 mm/yr. Measured values for points in the main stem of the St Johns River range between 6 and 39 mm/yr, Ravensrodd Consultants Ltd (2002).

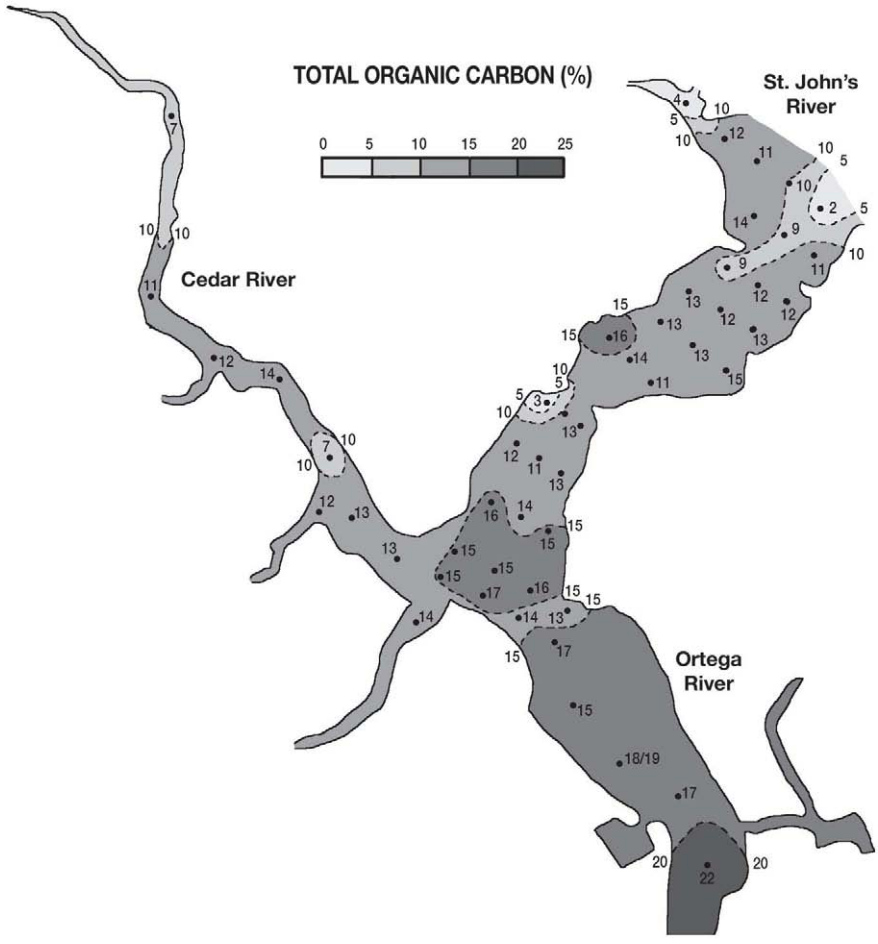

Fig. 5. Variation in percent Total Organic Carbon (TOC) in black organic mud samples in the lower reaches of the Cedar and Ortega Rivers, where high levels of PCB occur. The high TOC of Ortega River samples, spreading into the inner confluent region, together with the low TOC at the confluence with the St Johns River, is evident

It is envisaged that further PCB inputs to the Cedar River can be reduced by redirecting the flow through a sediment trap in the upper riverine reaches where the stream is still narrow. Dealing with the existing contaminated sediment patch will require thin layer dredging followed by onshore disposal or possibly a confined disposal facility in

an artificial island located close to the Cedar/Ortega confluence. Such remediation is rendered more urgent by the recognition arising from this study that in addition to large scale flushing during hurricane-induced spates, the contaminated black organic muds have long been routinely reworked by propeller wash from recreational vessels in these extremely shallow waters.

3. CONCLUSIONS

A very wide variety of sources of organic carbon have been identified by this review. At the sea coast of this subtropical state mangroves, sea grass and salt marshes all produce large amounts of carbon. Some previously contentious issues, such as whether salt marshes are sources or sinks for carbon are now resolved. Those in Florida are sources. Similarly, in the fresh water zone there are a great variety of sources of carbon and the climate ensures that productivity is naturally high. A range of vegetation-dependent types of peat are formed, especially around the drained margins of lakes and in the southern Everglades. Whilst these might give rise to a range of intrinsic problems if subjected to human development, they do not, in the main, contribute significantly to the blocking of drainage channels, siltation of lakes and are not a host for contaminants. The escalation in the production rate of black organic muds is presenting severe problems in rivers, lakes, estuaries and marine coastal embayments in Florida. The problems are rendered even more severe and urgent where the muds are combined with recent anthropogenic contaminants. In addition to natural high productivity a number of anthropogenic factors, deliberate burning or herbicide spraying of recently introduced exotic plant species, high rates of agricultural and waste water nutrient input *etc.* are all exacerbating this high productivity. Production rates have risen by two orders of magnitude.

Management of these systems points to the need in some cases for removal of the mud. This intrinsically demands a place to store or a beneficial use of the material. A further issue is that of preventing rapid formation of further black mud. This requires, amongst other items, modification of agricultural methods as well as of waste water treatment. There can be no wise management in the absence of understanding. The latter requires knowledge of the sources and cycles of carbon production. Sources can in part be distinguished from application of sophisticated geochemical methods. This has been further advanced by improved knowledge of carbon pathways and cycling in natural systems.

Further management options for lakes involve lowering or alternatively raising water level and this can have a fundamental effect on the tropic status of lakes, which must be anticipated. Nevertheless, the sources and transport paths of carbon in large lakes such as Okeechobee are complex and still incompletely understood. A further unresolved issue is that fresh water microbiologists are now speculating that perhaps plankton do not form the base of aquatic food chains, rather this might be provided by bacteria.

Wise management demands that these complex issues be resolved. Added to it, only a small number of the 8000+ lakes in the state have had their bed sediment distribution mapped. This lack of knowledge is a further constraint on progress. In estuaries, exemplified by the Cedar/Ortega rivers, it is now clear that not just unpredictable spates might contribute to flushing and spreading of contaminated black organic mud. The spreading has been continuously enhanced by recreational vessel propeller wash. In rivers, lakes, estuaries and marine coastal inlets some kind of intervention is frequently the only way forward. Proper understanding of the issues outlined here, and more, is necessary if further problems are not to be inadvertently created somewhere down the line.

REFERENCES

Brenner, M., T.J. Whitmore, J.H. Curtis and C.L. Schelske. 1995. Historical ecology of a hypereutrophic Florida lake. *Lake & Reservoir Management*, (11) 3, 255-271.

Brenner, M., T.J. Whitmore and C.L. Schelske. 1996. Paleolimnological evaluation of historical trophic state conditions in hypereutrophic Lake Thonotosassa, Florida, USA. *Hydrobiologia,* 331, 143-152.

Brooks, G.R., L.J. Doyle, R. Johansson, A. Squires, H.D. Zsoldos and R.H. Byrne. 1991. Distribution patterns and accumulation rates of fine-grained sediments in upper Tampa Bay, Florida. *Transactions of the 41st Annual Convention.* Schumacher, D. and N.C. Rosen (eds.), Gulf Coast Association of Geological Societies, New Orleans, LA, 60-71.

Brown, K.E. and A.D. Cohen. 1995. Stratigraphic and micropetrographic occurrences of pyrite in sediments at the confluence of carbonate and peat-forming systems, southern Florida, USA. In: *Collected Papers from the 10th Annual Meeting of the Society for Organic Petrology*. Cardott, B.J., C.L. Thompson-Rizer and R. Woods (eds.). *Organic Geochemistry*, (22) 1, 105-126.

Carr, R.S., E.R Long, H.L. Windom, D.C. Chapman, G. Thursby, G.M. Sloane and D.A. Wolfe. 1996. Sediment quality assessment studies of Tampa Bay, Florida. *Environmental Toxicology & Chemistry*, (15) 7, 1218-1231.

Childers, D.L. 1994. Fifteen years of marsh flumes: a review of marsh-water column interactions in south eastern USA estuaries. In: *Global Wetlands: Old world & New*. Mitsch, W.J. (ed.), Elsevier, Amsterdam, 277-293.

Cohen, A.D., T.D. Davies and W. Spackman. 1994. Sulfur contents of peats at the confluence of carbonate and peat-forming depositional systems, southeastern Florida. In: *Studies in Eastern Energy and the Environment: AAPG Eastern Section. Special Volume.* Schultz, A.P. and E.K. Rader (eds.), Publication No.132, Virginia Division of Mineral Resources.

Cooper, W.T. and J.F. Donoghue. 1999. *Investigation of historic sedimentation rates in the Lower St Johns River.* Report to SJRWMD, Florida State University, Tallahassee. Davis, S.M. and J.C. Ogden, (eds), 1994. *Everglades: The Ecosystem and its Restoration*, St Lucie Press, Delray Beach, Florida.

Fleming, M., G. Lin and L. da Silveira-Lobo-Sternberg. 1990. Influence of mangrove detritus in an estuarine ecosystem. *Bulletin of Marine Science*, (47) 3, 663-669.

Gleason P.J. and P. Stone. 1994. Age, Origin & Landscape Evolution of the Everglades Peatland. In: *Everglades: The Ecosystem & its Restoration.* Davis, S.M. and J.C. Ogden (eds.), St Lucie Press, Fort Pierce, Florida.

Gowland, J.E., A.J. Mehta, J.D. Stuck, C.V. John and T.M. Parchure, in press. Organic-rich fine sediments in Florida. Part II Effects of resuspension on a lake. In: *Estuarine and Coastal Fine Sediment Dynamics – INTERCOH 2003.* Maa, J.P.-Y., L.P. Sandford and D.H. Schoellhamer (eds.), this volume.

Green, J. 1968. *The biology of estuarine animals.* Sidgwick & Jackson, London, 401pp.

Gu, D., N. Iricanin and J.H. Trefrey. 1987. The geochemistry of interstitial water from a sediment core from the Indian River Lagoon, Florida. *Florida Scientist*, (50) 2, 99-110.

Johansson, J.O.R., K.A. Steidinger and D.C. Carpenter. 1985. Primary production, Tampa Bay, Florida, a review. In: *Proceedings of Tampa Bay Area Scientific Information Symposium.* Treat, S.F., J.L. Simon, R.R. Lewis III and R.L. Whitman (eds.), 65, 279-298.

Kirby, R., C.H. Hobbs and A.J. Mehta. 1994. Shallow stratigraphy of Lake Okeechobee, Florida: a preliminary reconnaissance. *Journal of Coastal Research,* (10) 2, 339-350.

Kohout, F.A. and M.C. Kolpinski. 1967. Biological zonation related to ground water discharge along the shore of Biscayne Bay, Miami, Florida. In: *Estuaries.* Lauff, G.H. (ed.), Publication No 83, American Association for the Advancement of Science, Washington DC, 488-499.

McPherson, B.F., R.T. Montgomery and E.E. Emmons. 1990. Phytoplankton productivity and biomass in the Charlotte Harbor estuarine system, Florida. *Water Research Bulletin*, (26) 5, 787-800.

Mehta, A.J., R. Kirby, J.D. Stuck, J. Jiang and T.M. Parchure. 1997. *Erodibility of organic-rich sediments: A Florida perspective.* Report No. MP-87/01. Coastal and Oceanographic Engineering Dept., University of Florida, Gainesville, FL.

Morgan and Eklund Inc. 1995. *Ortega River & Cedar Creek, Duval County, Florida. Investigations of Water Depth and Sediment Characteristics*, Report for St. Johns River Water Management District.

Mote Marine Laboratory. 1998. *Analysis of sediment samples for St Johns River Water Management District: Methodology and Seventh Data Report.* Mote Marine Laboratory Technical Report No. 610, submitted through Battelle Ocean Sciences.

Mulholland, P.J. and C.R. Olsen. 1992. Marine origin of Savannah River estuary sediments: Evidence from radioactive and stable isotope tracers. *Estuarine, Coastal & Shelf Science*, (34), 95-107.

Odum, E. 1969. The strategy of ecosystem development, *Science*, 164, 262-269.

Olila, O.G. and K.R. Reddy. 1993. Phosphorus sorption characteristics of sediments in shallow lakes of Florida. *Archiv Für Hydrobiologie*, (129) 1, 45-65.

Phlips, E.J., M. Cichra, K. Havens, C. Hanlon, S. Badylak, B. Rueter, M. Randall and P. Hanson. 1997. Relationships between phytoplankton dynamics and the availability of light and nutrients in a shallow sub-tropical lake. *Journal of Plankton Research*, (19) 3, 319-342.

Ravensrodd Consultants Ltd. 2002. *The Sedimentary Regime of the Lower Cedar/Ortega River System and its Environs, Florida.* Unpublished report to Civil & Coastal Engineering Department, University of Florida, Gainesville, FL, 22pp.

Roman, M.R., M.R. Reeve and J.L. Froggatt. 1983. Carbon production and export from Biscayne Bay, Florida. 1. Temporal patterns in primary production, seston and zooplankton. *Estuarine, Coastal & Shelf Science*, (17) 1, 45-59.

Stoermer, E.F., N.A. Andresen and K.E. Schols. 1992. Diatom succession in the recent sediments of Lake Okeechobee, Florida, USA. *Diatom Research*, (7) 2, 367-386.

Tissot, B.P. and D.H. Welte. 1984. *Petroleum Formation and Occurrence.* Springer-Verlag, New York, 699pp.

Trefry, J.H., N.-C. Chen, R.P. Trocine and S. Metz. 1992. Impingement of organic-rich contaminated sediments on Manatee Pocket, Florida. *Florida Scientist*, (55) 3, 160-171.

Whitmore, T.J., M. Brenner and C.L. Schelske. 1996. Highly variable sediment distribution in shallow, wind-stressed lakes: A case for sediment mapping surveys in palaeolimnological studies. *Journal of Palaeolimnology*, 15, 207-221.

Whittaker, R.H. and G.E. Likens. 1973. Carbon in the biota. In: *Carbon in the Biosphere*. Woodwell, G.M. and E.R. Pecan (eds.), US Atomic Energy Commission Symposium. Series. No. 30, Washington DC, 281-300.

Zimba, P.V., M.S. Hopson, J.P. Smith, D.E. Colle and J.V. Shireman. 1995. Chemical composition and distribution of submerged aquatic vegetation in Lake Okeechobee, Florida (1989-1991). *Archiv Für Hydrobiologie. Special Issue on Advances in Limnology*, 45, 241-246.

Estuarine and Coastal Fine Sediments Dynamics
J.P.-Y. Maa, L.P. Sanford and D.H. Schoellhamer (editors)

Organic-rich fine sediments in Florida, Part II: Resuspension in a lake

Gowland, J.E.[a], A.J. Mehta[b], J.D. Stuck[c], C.V. John[d] and T.M. Parchure[e]

[a]Erickson Consulting Engineers, Inc., 1819 Main Street, Suite 402, Sarasota, FL 34236
[b]Department of Civil and Coastal Engineering, University of Florida, Gainesville, FL 32611
[c]Everglades Research and Education Center, University of Florida, Belle Glade, FL 33430
[d]Taylor Engineering, Inc., 9000 Cypress Green Drive, Suite 200, Jacksonville, FL 32256
[e]Coastal and Hydraulics Laboratory, U.S. Army Engineer Research and Development Center, Vicksburg, MS 38180

KEY WORDS
Erosion, consolidation, Florida, organic material, sediment aggregates, water waves, wind

The dependence of fine sediment resuspension on the organic fraction in bottom sediment is examined. Based on data from studies in Florida's muck-laden waters, sediment density, erosion flux and settling velocity (hence flux) are shown to vary with organic content in a reasonably well-behaved manner. The effect of changing organic content on the potential for resuspension is considered for Newnans Lake, a shallow hypereutrophic water body subject to wind-wave action. Increasing organic content decreases the critical wind velocity for resuspension. A characteristic decrease in the organic content with depth within the lake bed implies that dredging the submerged bottom would increase the critical wind velocity due to this effect as well as the curtailed ability of waves to penetrate deeper water. Thus dredging enhances bed stability by two distinct but not entirely uncorrelated mechanisms.

1. INTRODUCTION

The role of waterborne organic matter in modulating electrochemical bonds in clayey aggregates and their resuspension was demonstrated decades ago (*e.g.*, Kandiah, 1974). In response to the need to account for this effect in calculating the rates of scour and shoaling in waters laden with organic-rich sediments, data on the erosion and settling fluxes have been collected in laboratory studies at the University of Florida using muck-like sediment derived from eight sites in peninsular Florida (Fig. 1). An effort has been made to show the utility of the resulting erosion and settling velocity functions by examining the potential for wind-wave induced resuspension in Newnans Lake in north-central Florida.

2. EROSION AND SETTLING VELOCITY FUNCTIONS

2.1 Aggregate structure

Muck aggregates in water (*e.g.*, Fig. 2) tend to be heterogeneous in composition, containing inorganic particles (*e.g.*, clay minerals) as well as organic material derived from a variety of sources such as diatoms, worm tubes, biopolymers and wood fragments (Decho, 2000). For the present purposes we will consider the organic fraction to be represented by the loss in mass upon ignition of the sample. We will further consider

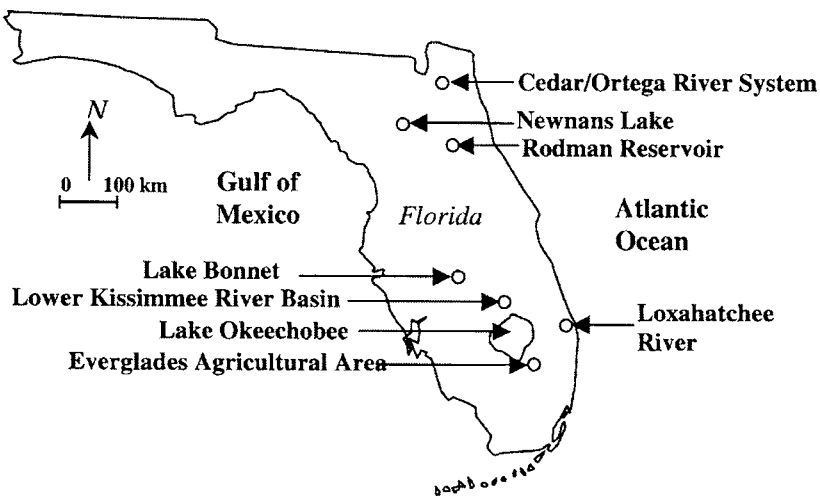

Fig. 1. Bottom muck sampling sites in peninsular Florida.

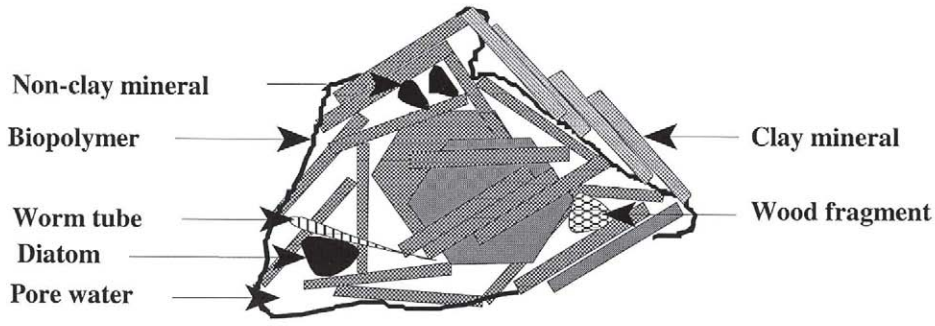

Fig. 2. Fine sediment aggregate constituents.

that all aggregates contain the same or similar inorganic and organic constituents, but that the organic fraction may vary from sample to sample. This premise, which will allow us to link the variability in the erosion and settling properties of sediment with organic content, is rationalized by the occurrence of a unique ancient source of inorganic sediment in peninsular Florida. There the clay minerals, mainly montmorillonite, kaolinite and chlorite, and non-clay calcareous, silicate and phosphatic sediments, are believed to have deposited during the Miocene (24M to 2M BP) as a result of alluvial transport from southern Georgia to then submerged shallow Florida platform (Weaver and Beck, 1977). Also, the organic matter is largely derived from fresh and brackish water wetlands within a reasonably homogeneous subtropical environment (Kirby, this volume).

Support for the above assertion concerning the uniformity of organic and inorganic mineral compositions is found in Figs. 3 and 4, in which the bottom sediment (wet) bulk density ρ and the dry (bulk) density ρ_D, respectively, from six sites are plotted as functions of organic content (OC). These relationships should be considered to be applicable to reasonably consolidated beds, corresponding to the bottom samples from which the data were derived. Site to site variability in bottom composition and aging of organic material are likely to be major contributors to data scatter. Sampling was carried out by using grab-samplers and push-corers, and the cores varied in thickness between ~0.1 m and ~1.5 m. Mean trends can be identified and approximated as follows:

$$\rho = 912.2 \exp(-0.123 OC) + 1046 \tag{1}$$

$$\rho_D = 1448 \exp(-0.0992 OC) + 92 \tag{2}$$

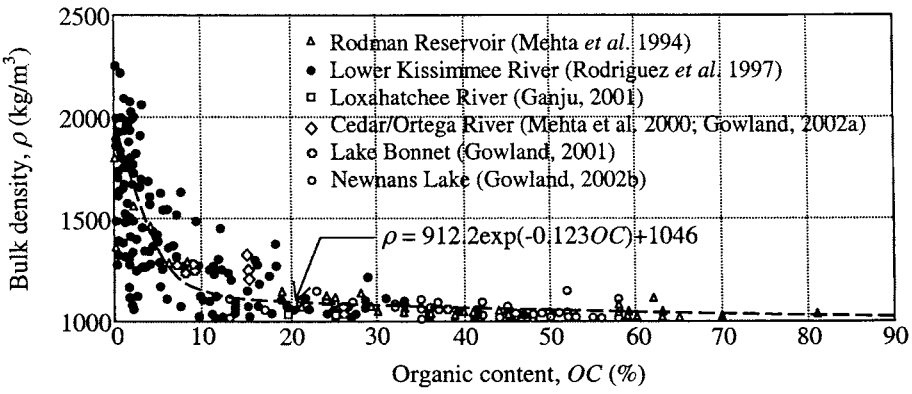

Fig. 3. Variation of wet bulk density with organic content.

The particle density ρ_s is related to ρ and ρ_D by mass balance, $\rho_s = \rho_w \rho_D / (\rho_D + \rho_w - \rho)$, where ρ_w is water density. Equations 1 and 2 are applicable in the range of OC from 1% to 82%, and indicate a rapid decline in ρ and ρ_D as OC increases from 1% to about 25%. This trend is the result of aggregates acquiring an increasingly open structure, so that for a given total mass the aggregate volume increases with increasing OC.

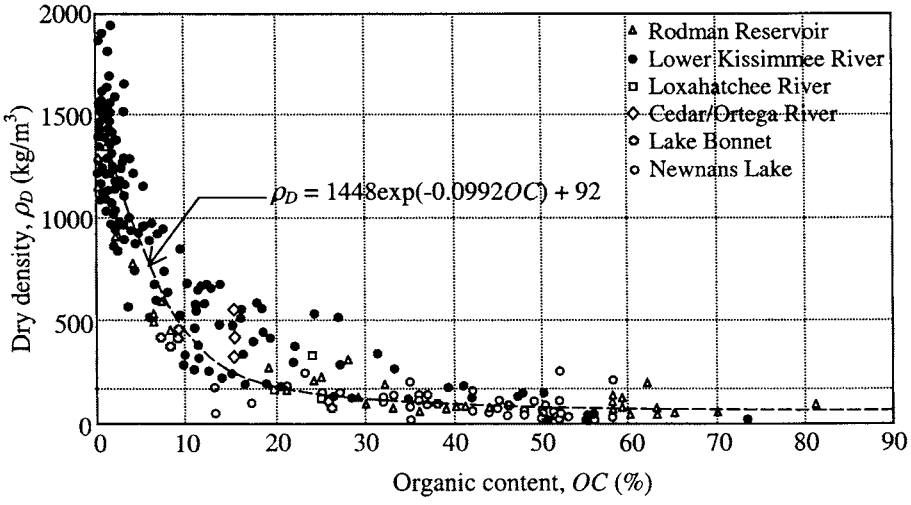

Fig. 4. Variation of dry density with organic content.

An artifact of the forms of Eqs. 1 and 2 is that at freshwater density (ρ_w = 1,000 kg/m^3) they cause ρ_s to vary non-monotonically with OC. At OC = 1%, ρ_s = 2,549 kg/m^3 and at OC = 25%, ρ_s decreases to 1,704 kg/m^3. From then on ρ_s increases and reaches 1,999 kg/m^3 at OC = 81%. We recommend that for OC equal to or greater than 25%, ρ_D may be assumed to be constant at 1,704 kg/m^3 as an approximation. In salt water (ρ_w = 1,030 kg/m^3), ρ_s decreases steadily from 2,489 kg/m^3 at OC = 1% to 1,246 kg/m^3 at OC = 81%.

2.2 Erosion function

For modeling bed erosion by waves we will select the linear equation

$$\varepsilon = \delta \frac{dc}{dt} = \varepsilon_N (\tau_b - \tau_s) \tag{3}$$

where $\varepsilon = \delta \partial c / \partial t$ is the erosion flux, δ is a characteristic bottom water layer height, c is the total suspended solids concentration within this layer, t is time, ε_N is the erosion flux constant, τ_b is the bed shear stress (the periodic maximum value in case forcing is by waves) and τ_s is the bed shear strength against erosion (Dennett *et al.* 1998). For a bed or a bed layer of given (uniform) density to which this equation is applicable, ε_N and τ_s were determined in laboratory apparatuses by applying a series of stresses τ_b of increasing magnitude over constant durations (typically ranging between 1 and 4 h) and measuring, for each τ_b, the quantity $\varepsilon \approx h \Delta c / \Delta t$, where h is the water depth in the apparatus, and Δc is the increment in c over a duration Δt. At a given τ_b the ratio $\Delta c / \Delta t$, and therefore ε, were found to remain constant. In turn, from the best-fit line plot of ε against τ_b, ε_N (line slope) and τ_s (intercept on the τ_b axis) were determined.

Erosion tests were conducted in a Counter Rotating Annular Flume (CRAF), and others in a Particle Erosion Simulator (PES). In both devices beds of 3 to 5 cm thickness were allowed to consolidate between 24 and 96 h before each test. The CRAF has been described in detail elsewhere (Stuck, 1996; Parchure and Mehta, 1985). Employing this flume, the results from a set of tests using muck from a farm drainage ditch in the Everglades Agricultural Area (EAA) of south-central Florida (Fig. 1) are shown in Fig. 5.

In the PES described by Tsai and Lick (1986), the bed was prepared inside a 15 cm diameter perspex cylinder. A porous vertical grid submerged in water over the bed was then oscillated at different angular speeds (*rpm*), which caused the sediment to erode. The grid-associated shear stress was obtained from the calibration relationship τ_b

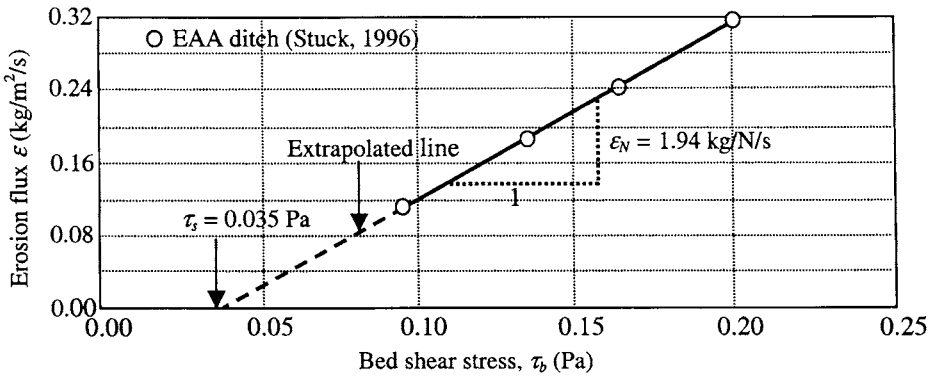

Fig. 5. Erosion flux versus bed shear stress; data from an EAA ditch.

=5.91x10^{-4} x *rpm* derived by measuring and comparing the erosion of EAA muck concurrently in the PES and the CRAF (Stuck, 1996; Mehta *et al.* 1994).

Erosion test results using sediment from the sites in Fig. 1 (with the exception of Lake Bonnet, for which such tests were not conducted) suggested that following the feasibility of representing the density measurements on a collective basis (Figs. 3 and 4; Eqs. 1 and 2), the behaviors of ε_N and τ_s may also be similarly examined. In agreement with the analysis of Mehta and Parchure (2000), these two parameters, plotted against each other in Fig. 6 using all available data, show a characteristic inverse dependence. Thus, as τ_s increases ε_N decreases rapidly at first and more slowly later as τ_s approaches

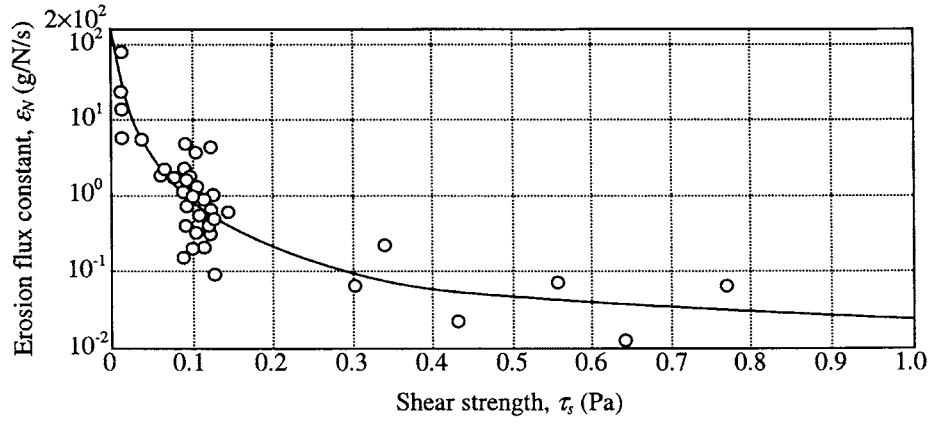

Fig. 6. Variation of erosion flux constant with shear strength.

unity. The initial value of ε_N = 200 g/N/s is taken from the work of Mehta and Parchure. Despite evident hiatuses in the data (over the range of τ_s) as well as data scatter, the plotted mean trend suggests that increasing bed stability manifests itself as increasing strength and, hence, decreasing bed scour.

The shear strength shows a consistent variation with dry density ($\tau_s = 0.025\rho_D^{0.3}$; Fig. 7). However, in comparison with what is found for inorganic clay sediments, which carry exponents of ρ_D between 1 and 2 (Mehta and Parchure, 2000), the variation of τ_s with ρ_D characterized by the exponent 0.3, is weak. In other words, due to the presence of organic matter, closer packing of particles with increasing density does not significantly increase aggregate strength.

2.3 Settling velocity function

We will use the following function to describe the dependence of the settling velocity w_s on suspended sediment concentration c (Hwang, 1989):

$$w_s = w_0, \quad c \le c_f ; \quad w_s = \frac{a c^n}{\left(b^2 + c^2\right)^m}, \quad c > c_f \tag{4}$$

in which c_f, typically ranging between 0.1 and 0.3 kg/m^3, is the concentration limit at and below which w_s is practically free of the effect of inter-particle collisions and is assumed constant (w_0). The corresponding settling flux is calculated as $w_s c$. The quantities *a, b, n,* and *m* are sediment-specific coefficients which describe: 1) flocculation settling, in which w_s increases with c above c_f due to aggregation by collisions, and 2) hindered settling, in which w_s decreases with increasing concentration at high values of c. Based on data obtained in a settling column using sediment from the Cedar/Ortega

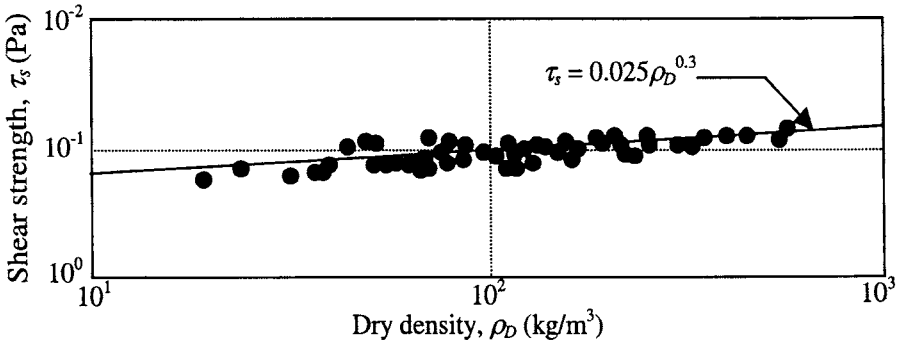

Fig. 7. Shear strength variation with bed dry density.

River system, the Loxahatchee River and Lake Okeechobee (Fig. 1), Marván (2001) and Ganju (2001) noted that the influence of organic content (OC) can be conveniently ascribed to the velocity-scaling coefficient a while holding b, n, and m constant. Accordingly, selecting b = 6.4, n = 1.8, and m = 1.8, Table 1 gives values of a, and the Stokes' diameter, d_s, calculated from the corresponding w_0. The w_0 value is conveniently chosen as the settling velocity at 0.25 kg/m^3 concentration.

The a-values in Table 1 yield the following dependence on OC (Fig. 8):

$$a = a_0 + a_1 OC + a_2 OC^2 + a_3 OC^3 + a_4 OC^4 \tag{5a}$$

where a_0 = 0.2, a_1 = 6.6x10^{-4}, a_2 = -1.7x10^{-4}, a_3 = 7.1x10^{-6} and a_4 = -1.3x10^{-7}. Equation 4 along with these coefficient values is consistent with the trend of decreasing d_s (Table 1) and w_0 with increasing OC, as the aggregates become lighter and smaller because the effect of cohesion decreases in the overall sense. An example of Eq. 4 along with data from Table 1 applied the Loxahatchee River sediment is shown in Fig. 9.

In Fig. 10 free settling velocities w_0 from the sites in Table 1 as well as Rodman Reservoir, Cedar/Ortega River system, Kissimmee River and Newnans Lake are plotted against OC. Notwithstanding considerable data scatter, the values suggest the expected mean trend of decreasing w_0 with increasing OC.

3. WIND-WAVE RESUSPENSION

3.1 Bed sediment properties

For convenience of treatment we will divide Newnans Lake (Fig. 11) into three sub-areas based on bathymetry – an inner open water zone, an outer open water zone and the exposed zone (Environmental Consulting & Technology, Inc., 2002). In 2001,

Table 1. Velocity-scaling coefficient a, free settling velocity w_0 and Stokes' diameter d_s

Source in Florida	Approximate organic content, OC (%)	Approximate particle density, ρ_s (kg/m^3)	Scaling coefficient, a	Free settling velocity, w_0 (m/s)	Stokes' diameter, d_s (μm)
Low OC mud	2	2,700	0.20	2.60x10^{-5}	6
Loxahatchee River	15	2,620	0.19	1.80x10^{-5}	5
Cedar/Ortega River	28	2,360	0.16	1.65x10^{-5}	5
Lake Okeechobee	38	2,190	0.09	0.93x10^{-5}	4
Lake Okeechobee	40	2,000	0.08	0.78x10^{-5}	4
Lake Okeechobee	43	1,710	0.03	0.31x10^{-5}	3

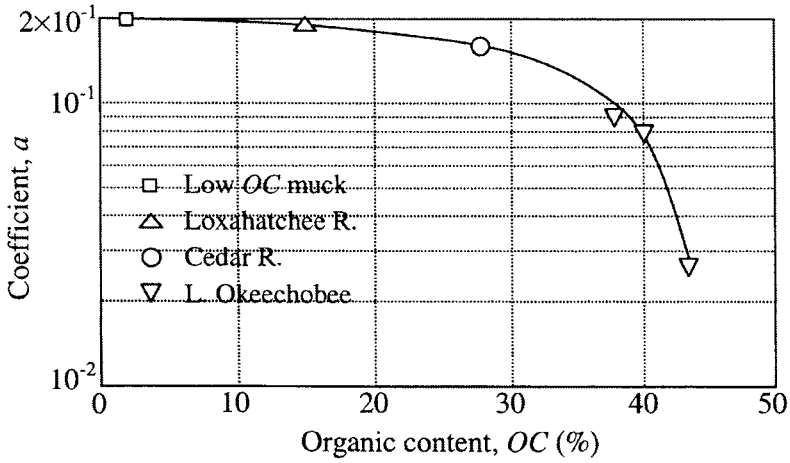

Fig. 8. Variation of velocity coefficient a with organic content.

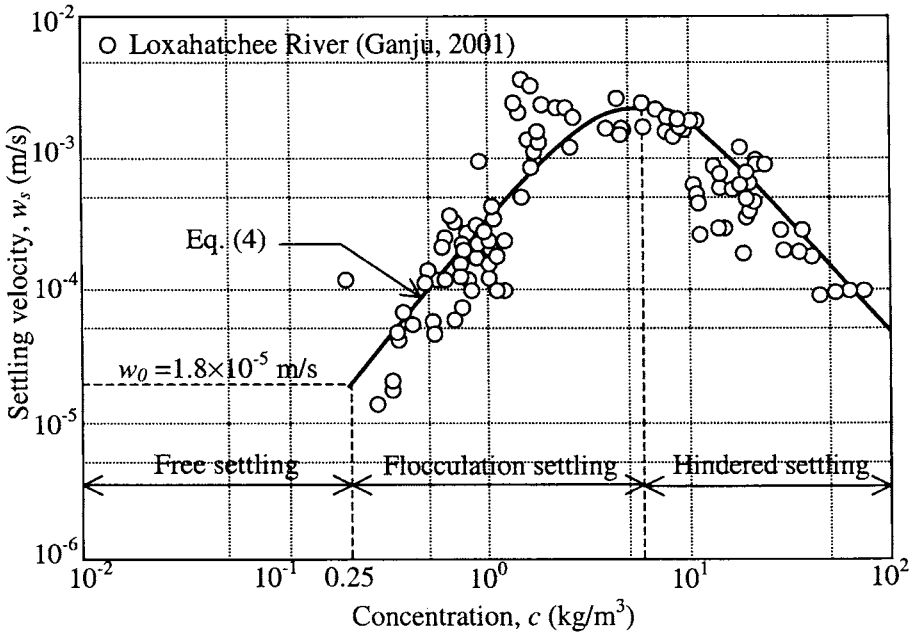

Fig. 9. Settling velocity variation with concentration for Loxahatchee River sediment.

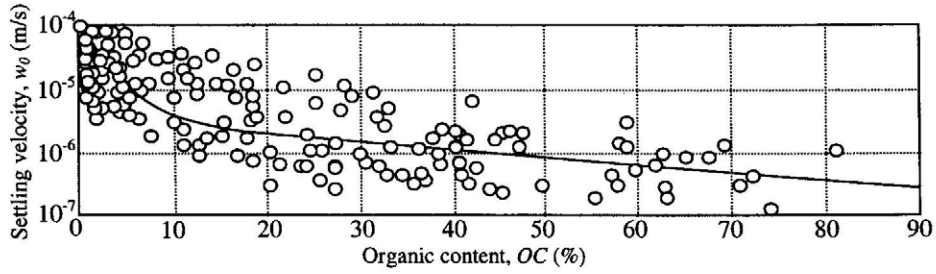

Fig. 10. Variation of free settling velocity with organic content.

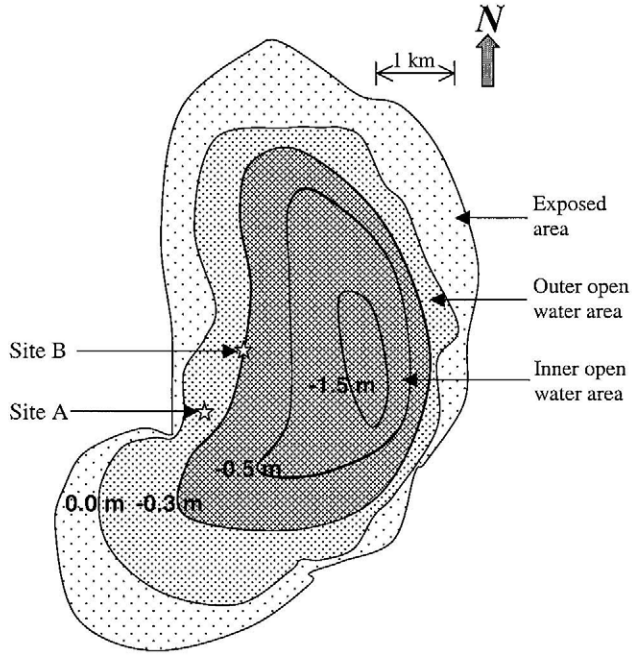

Fig. 11. Newnans Lake zones based on bathymetry. Suspended sediment concentration was measured at Sites A and B.

forty-five bottom muck samples (40 by push-cores in the open water area and 5 by a shovel in the exposed area) were obtained, and short duration (~10 min) wind-wave and suspended sediment data were collected at Sites A and B in this shallow, hypereutrophic water body. At that time the lake stage was considerably lower (by 1.1 m) compared to

~20 m (NGVD) for the 1995-1998 period, and almost 2 m below the El Niño high in February 1998 (Fig. 12), resulting in the large exposed area seen in Fig. 11.

Total core lengths ranged from 1.05 to 1.74 m with a mean of 1.50 m. The submerged bed was accordingly divided into a weakly consolidated upper layer of 0.40 m mean thickness and a lower, more consolidated layer of 1.10 m (mean) thickness. The exposed area samples were from the top ~0.30 m. In Table 2, the means and standard deviations of selected parameters (*OC*, ρ, dry bulk density ρ_D, ρ_s and median particle diameter d_{50}) for these layers in the three zones are given. The water density ρ_w is taken as 1,000 kg/m^3.

The parametric values in Table 2 indicate that, overall, sediment in the inner open water zone had the highest organic content, the lowest bulk, dry and granular densities and the smallest particle size. At the opposite end was exposed bed, with the outer open water zone in-between. These trends correlate with decreasing *OC* from inner open water to the exposed zone, the latter having been subjected to desiccation and oxidation with the lowering of stage over the previous two years. In turn, the particles were large (260 μm) in this zone because of the loss of organic matter as well as the presence of sand. Sand also contributed to the large (190 μm) size in the lower layer of the outer open water zone. Elsewhere the material was fine-grained (< 63 μm).

The dependence of the erosion flux on organic content is evident from Fig. 13, and conforms to the inverse variation of ε_N with τ_s shown in Fig. 6. Since ρ_D decreases with increasing *OC*, the data in Fig. 13 also imply an increase in τ_s with increasing ρ_D, which in turn is found to agree with the trend in Fig. 7.

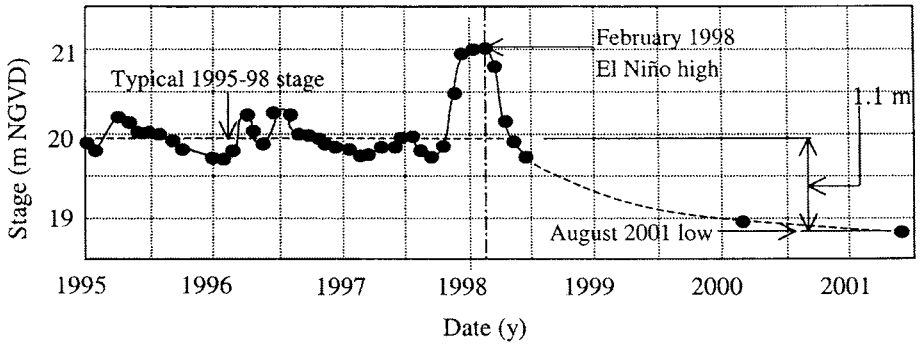

Fig. 12. Stage variation in Newnan's Lake, 1995-2001.

Table 2. Characteristic properties of upper and lower bed layers by zone

Bed layer	Zone	Organic content OC (%)		Bulk density ρ (kg/m^3)		Dry density ρ_D (kg/m^3)		Particle density ρ_s (kg/m^3)		Median Diameter [a] d_{50} (μm)	
		Mean	S.D.	Mean	S.D.	Mean	S.D.	Mean	S.D.	Mean	S.D.
Upper	Exposed	30	11	1156	63	267	105	2296	210	262	100
Upper	Outer	45	8	1050	30	98	56	2098	411	38	14
Upper	Inner	52	4	1023	11	51	27	1986	491	26	7
Lower	Outer	28	11	1090	28	161	43	2283	280	174	104
Lower	Inner	43	7	1047	29	94	36	2037	531	45	22

[a] The overall ranges of d_{25} and d_{75} sizes were 8 μm to 248 μm and 58μm to 417 μm, respectively.

In Fig. 14 settling velocity data obtained in a series of settling column tests are presented in accordance with Eq. 4. For plotting the curves it was found convenient to hold the coefficients a (= 0.7), n (= 1.4) and m (= 2.5) constant and vary b, in contrast to the use of Eq. 5 based on an analysis (Ganju, 2001), in which b, n and m were left unchanged. The experimental points are included after a careful reinterpretation of the data (Gowland, 2002b). A consequence of data scatter is that the free settling velocity values given in Table 3 show large standard deviations compared to means.

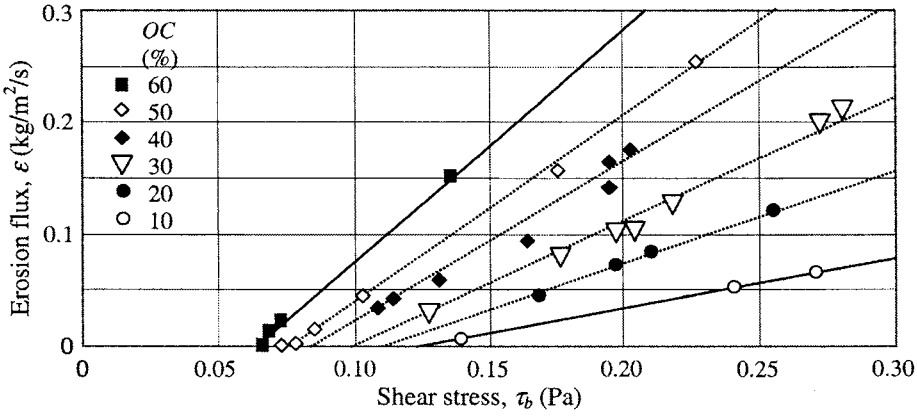

Fig. 13. Erosion flux versus bed shear stress with lines of constant OC; data from Newnans Lake.

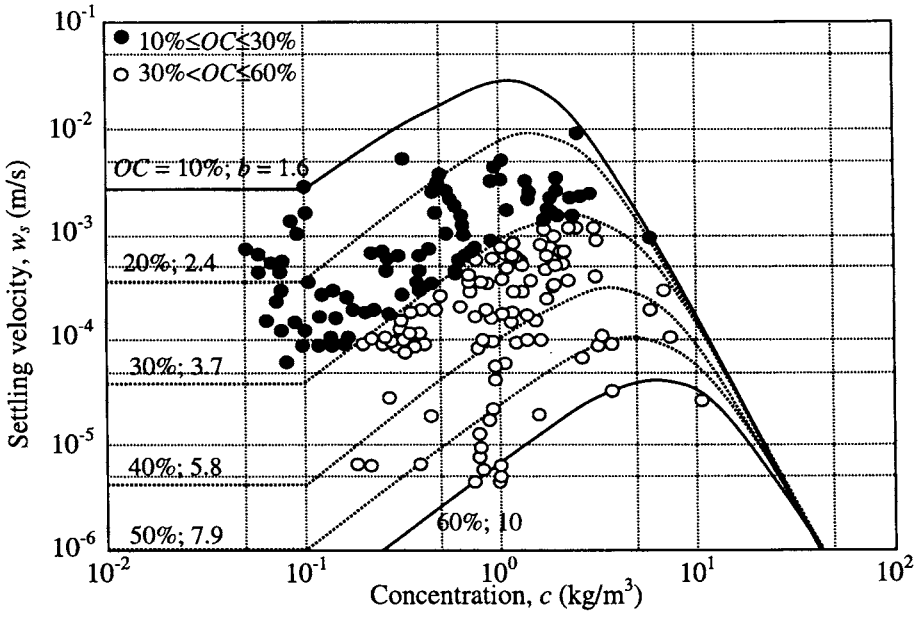

Fig. 14. Settling velocity variation with concentration for Newnans Lake sediment.

In addition to the means and standard deviations of the free settling velocity characterizing the usually low-turbidity environment of the lake, erosion parameters are also given in Table 3. In general, trends in the mean values imply that the organic-rich material in the inner open water area was potentially more erodible than in the outer open water. It must be noted however that in the deeper (than the outer area) inner bottom the potential for erosion of the weaker material would be countered by lower wave-induced bed shear stresses.

To a certain extent the settling velocities in Table 3 show an inverse correlation with *OC* due to the associated decrease in the density of the aggregates. For example, increasing *OC* from 28 to 52% decreases w_0 from 5.8×10^{-4} to 1.3×10^{-4} m/s. Since the suspended material in the settling velocity tests did not contain sand particles, w_0 did not correlate consistently with what was present in the bed. For example, in the exposed area, even though settling tests yielded a value of $w_0 = 2.7 \times 10^{-4}$ m/s suggesting a high *OC* (30%), grain size analysis of the bed sample yielded $d_{50} = 262$ μm for practically clean sand.

Table 3. Erosion parameters and settling velocity for upper and lower bed layers by zone

Bed layer	Zone	Organic content OC (%)		Erosion flux constant ε_N (g/N/s)		Bed shear strength τ_s (Pa)		Free settling velocity w_0 (m/s)	
		Mean	S.D.	Mean	S.D.	Mean	S.D.	Mean	S.D.
Upper	Exposed	30	11	0.87	0.35	0.08	0.013	$2.3\text{x}10^{-4}$	$2.5\text{x}10^{-4}$
Upper	Outer	45	8	1.61	0.25	0.08	0.009	$2.4\text{x}10^{-4}$	$1.3\text{x}10^{-4}$
Upper	Inner	52	4	1.82	0.13	0.07	0.005	$1.3\text{x}10^{-4}$	$0.7\text{x}10^{-4}$
Lower	Outer	28	11	0.99	0.38	0.10	0.014	$5.8\text{x}10^{-4}$	$2.0\text{x}10^{-4}$
Lower	Inner	43	7	1.53	0.23	0.08	0.008	$2.9\text{x}10^{-4}$	$1.2\text{x}10^{-4}$

3.2 Concentration profiles

We followed the technique of Li and Parchure (1998) to simulate the vertical profile of total suspended sediment solids concentration c due to wind-waves in the lake. For that purpose, the governing sediment mass balance is simply stated as

$$\frac{\partial c}{\partial t} - \frac{\partial}{\partial z}\left(K\frac{\partial c}{\partial z} + w_s c \right) = 0 \tag{6}$$

in which z is the vertical elevation coordinate with origin at the bed and K is the sediment mass diffusion coefficient. According to Eq. 6 the temporal rate of change of concentration, $\partial c/\partial t$, is determined by the net vertical sediment flux, which is the algebraic sum of the diffusive flux, $K\partial c/\partial z$, and the settling flux, $w_s c$. The diffusion coefficient, which in general must accounting for the effect of the buoyancy of the sediment suspension, was obtained from

$$K = \frac{K_n}{(1+\alpha \mathrm{Ri})^{\beta}} \tag{7}$$

where K_n is the (neutral) diffusion coefficient for non-stratified flows, α (= 0.5) and β (= 0.33) are sediment-specific coefficients and Ri is the gradient Richardson number defined as

$$Ri = -\left(\frac{g}{\rho_f}\right)\frac{\partial \rho_f / \partial z}{(\partial u / \partial z)^2} \tag{8}$$

In Eq. 8, u is the horizontal (flow) velocity, $\rho_f = [1-(\rho_w / \rho_s)] = \rho_w$ is the fluid density and g is gravitational acceleration. The neutral diffusivity was obtained from

$$K_n = \alpha_w H^2 \sigma \frac{\sinh^2 k(z-h)}{2\sinh^2 kh} \tag{9}$$

where α_w (=0.35) is a site-dependent coefficient, H is the wave height, $\sigma = 2\pi/T$ is the wave angular frequency, T is the wave period, $k = 2\pi/L$ is the wave number and L is the wave length. For calculating Ri the velocity u as a function of H, T and water depth h (hence L) was calculated from a wave theory incorporating the bottom boundary layer (Li and Parchure, 1998). For the erosion flux (Eq. 3) the bed shear stress was estimated from: $\tau_b = 0.5\, f_w \rho_w u_b^2$, where f_w (= 0.026; Gowland, 2002b) is the wave friction factor and u_b is the wave velocity amplitude at the bottom. The net sediment flux at the bed was calculated from Eqs. 3 and 4.

Inasmuch as Sites A and B (Fig. 11) were close to each other, with the exception of water depth identical parametric values were selected for simulation purposes (Table 4). Note that these (site-specific values) differ in some cases (*e.g.*, free settling velocity) from the means given for the upper outer open water zone in Tables 2 and 3.

For the numerical solution of Eq. 6, the water column was discretized into 30 sub-layers and the time step for simulation was 60 s. For Site A the resulting increase in concentration under constant wave action is shown in Fig. 15. The initially uniform con-

Table 4. Input parameters for concentration profile simulation.

Parameter	Value
Water depth h (m)	0.25[a], 0.30[b]
Wave height H (m)	0.05
Wave period T (s)	1.0
Background c (kg/m^3)	0.04[c]
Bed particle density ρ_s (kg/m^3)	2059
Bed dry density ρ_D (kg/m^3)	96
Free settling velocity w_0 (m/s)	0.1×10^{-5}
Velocity coefficients a, b, n, m	0.7, 7.9, 2.5, 1.4
ε_N (g/N/s)	1.82
τ_s (Pa)	0.07

[a] At Site A; [b] At Site B; [c] Present as washload, i.e., non-depositable matter.

centration of 0.04 kg/m^3 (not plotted) evolves into a bottom-weighted profile at 90 min, which seemingly agrees with measurements of concentration under a wave height of 0.05 m and a wave period of 1 s (Table 4) at this site. The profile at this time was nearing an equilibrium shape. Since the "initial time" for wave action in the lake was not measured (as a time-series), the comparison between prediction and measurement can be only on a qualitative basis. Nonetheless we note that the measured and simulated values of c were both close to 0.4 kg/m^3, which is high in comparison with some other lakes (Hwang, 1989), and is an indicator of the easily erodible material at the site.

An interesting feature of the simulated profiles, not captured by the measurements because they were not made sufficiently close to the bed, is the development of a lutocline within the first few centimeters from the bottom. Concentrations in this layer well exceed 1 kg/m^3, and lead to the formation a dense suspension (in relation to the upper water column) beneath the lutocline.

Without changing any of the constants in Table 4 used in simulating the profiles of Fig. 15, the profiles of Fig. 16 were generated merely by increasing the water depth from 0.25 m at Site A to 0.30 m at Site B. In this case it is seen that under the same wave conditions resuspension was slower due to the greater water depth. Consequently,

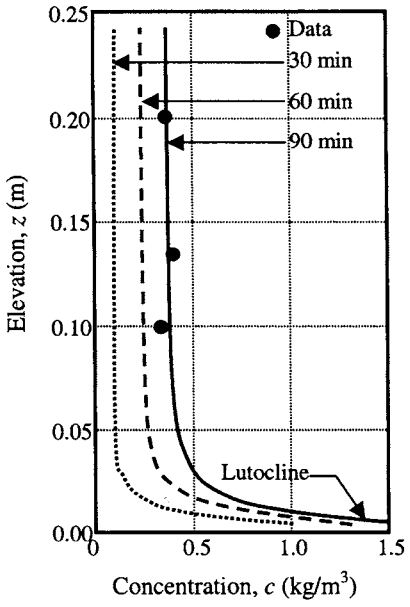

Fig. 15. Concentration profiles at Site A in Newnans Lake.

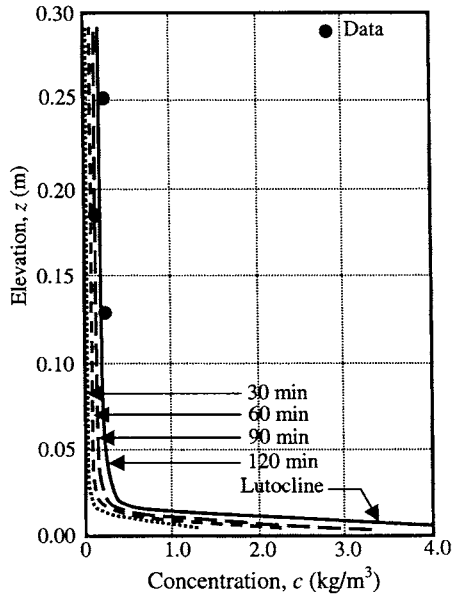

Fig. 16. Concentration profiles at Site B in Newnans Lake.

in 120 min the concentration rose to only ~0.2 kg/m^3 from the start of simulation. The measured concentrations, approaching equilibrium, are commensurate with this value.

3.3 Critical wind speed

As a corollary to the above simulation we will now examine the correlation between wind speed and resuspension. Typical hourly-mean westerly surface winds at this lake are only on the order of 3 m/s. However, 2-min maximum values range between 10 and 20 m/s over an effective fetch length of ~3,000 m during the December-August period. A cursory examination of the relationship between wind speed measured at a nearby site and wave height (measured by a graduated staff) in the lake showed that wave height prediction could be made using the empirical formulation of Young and Verhagen (1996) with only minor modifications (Gowland, 2000b).

In Fig. 17 the mid-depth concentration c_m is plotted against time for the inner open water zone (Tables 2 and 3) and assumed steady (or quasi-steady) wind speeds $U = 7$, 8 and 9 m/s. At 7 m/s no erosion took place. At 8 m/s erosion occurred and as the time neared 400 min the rate of erosion began to decrease due to a corresponding increase in the rate of deposition of the suspended matter. However, an equilibrium condition (marked by no-net increase in concentration) was not attained in this simulation for 2 additional hours (Gowland, 2002b). An inference one may draw from this observation is that inasmuch as wind almost never remains steady for durations of such lengths (~10 h) in this region, resuspension in the lake is in a continued state of disequilibrium, except when there is a prolonged period of calm.

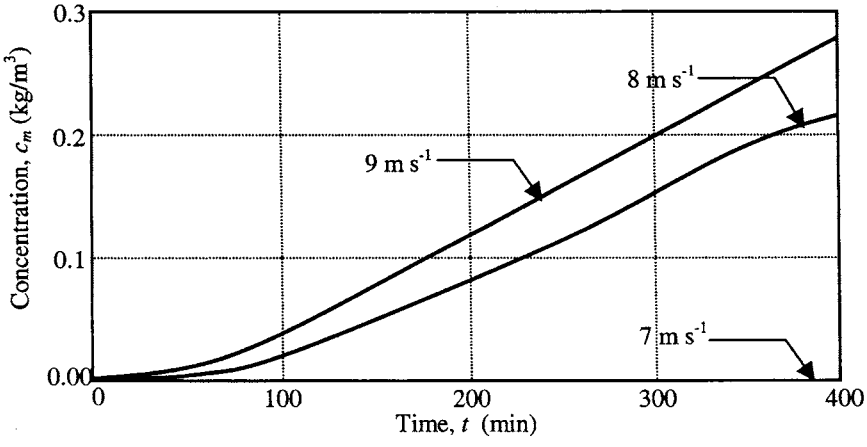

Fig. 17. Wind-induced resuspension simulation in Newnans Lake.

In the above case the critical wind speed for initiation of resuspension, U_c, was found to be 7.2 m/s in the outer zone and 7.5 m/s in the inner zone. In that regard, it is interesting to examine the effect of changing the organic content of bed sediment on U_c. Let us consider a case in which OC in the peripheral part of the outer open water zone is reduced from 45% to 30%, the same as in the exposed zone, during a severe but temporary drought. Using the same analytic approach and relationships dependent on OC we find that U_c would increase from 7.2 to 7.8 m/s, implying greater bed stability.

Next let us look at a somewhat different case in which the bottom is dredged out from the inner open water zone. As a starting point it is necessary to examine the state of consolidation of the bed. Although the lake has been slowly accumulating muck since its inception as a lake-like body about eight millennia ago (Holly, 1976), a substantial amount of additional accumulation occurred when in the 1970s a program of herbicide spraying was carried out to eliminate several species of macrophytes, and the dead material was allowed to settle out. For our purposes we will assume that this process was rapid enough (in relation to the time-scale of consolidation) for it to be treated as a case of self-weight consolidation of "instantaneously formed" deposit at the bottom.

In Fig. 18 we have shown results obtained from the self-weight consolidation equation of Been and Sills (1981) calibrated with sediment-specific parameters obtained

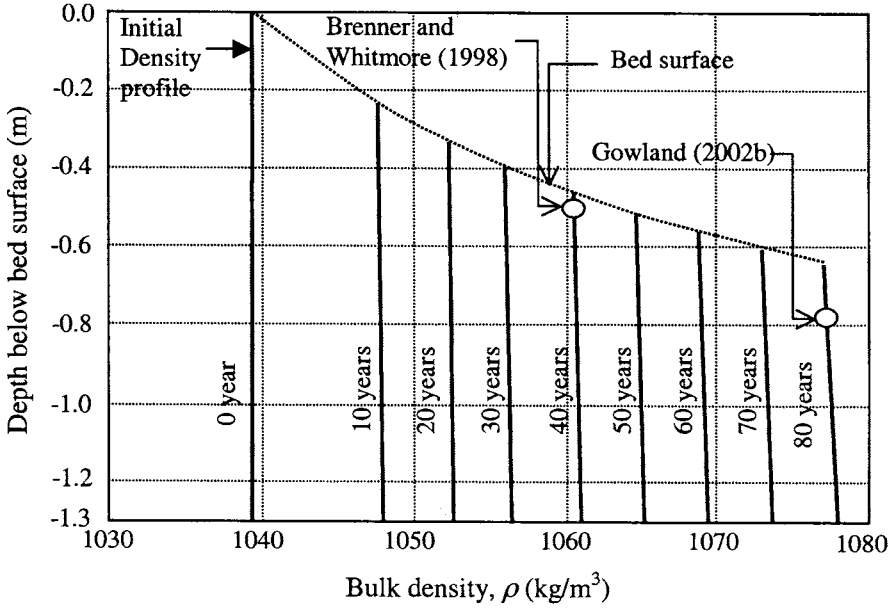

Fig. 18. Bed density variation due to consolidation.

from laboratory tests on the consolidation of muck from the lake (Gowland, 2002b). The starting uniform density of 1,039 kg/m^3 represents a fresh deposit having an assumed thickness of 1.3 m. After 40 years of simulation the bed attained a density close to what was measured (~1,061 kg/m^3) by Brenner and Whitmore (1998). This period is in acceptable agreement with the over three-decade duration between the initial accumulation of material and density measurement. The density reported by Gowland (2002b), 1,078 kg/m^3, was higher, and according to the model would take 80 years of self-weight consolidation, an unusually long duration compared with 40 years. This seeming discrepancy may be due to the limitation arising from the assumption that the bed everywhere in the inner open water area was subject to self-weight consolidation only. In reality the additional effect of overburden in further densifying the bed may not have been negligible.

Now we will consider the top 0.3 m of the bottom in the inner open water zone to be dredged out, and the properties of the newly exposed bed to be described by the denser lower layer having a lower *OC* (Tables 2 and 3). It was found that in this case the critical wind speed for resuspension would increase from 7.5 to 10 m/s (Table 5). About one-half of this increase would be due to reduced wave penetration in deeper water, and the other due to a reduction in the organic content (from 52 to 43%) and concomitant increase in bed density.

4. CONCLUDING COMMENTS

Sediment density, erosion flux and settling velocity (and therefore flux) are found to vary with organic content in a reasonably well-behaved manner. In Newnans Lake, increasing organic content decreases the critical wind velocity for resuspension. Dredging the submerged bottom would increase the critical wind velocity due to this effect as well as the curtailed ability of waves to penetrate deeper water. Thus dredging can enhance bed stability by two distinct but not entirely uncorrelated mechanisms.

Table 5. Critical wind speeds for resuspension

Condition (%)	Mean water Depth, h (m)	Critical wind speed, U_c (m/s)
Outer open water zone, OC = 45%	1.25	7.2
Inner open water zone, OC = 52%	1.50	7.5
Outer open water zone, OC = 30%	1.25	7.8
Dredged inner zone, OC = 43%	1.80	10.0

The effect of dredging has relevance to areas where water quality degradation by frequent and significant resuspension of muck is a problem. The described approach provides a simple but useful tool for analyzing the basic physics linking wind to muck resuspension.

For the dredging question we used measured values of the requisite parameters from Tables 2 and 3. In that regard we must note a constraint inherent in using the developed general relationships between bed density measures and organic content. This constraint arises because while density increase with depth is due to consolidation, reduction in organic content with depth is a biogenic process that is not uniquely correlated to densification by consolidation. We therefore recommend that the use of density-versus-organic content relationships be limited to naturally consolidated, top ~0.1-0.3 m thick muck layers that are not overly aged with respect to organic content.

REFERENCES

Been, K. and G.C. Sills. 1981. Self weight consolidation of soft soil: an experimental and theoretical study. *Geotechnique*, 31(4), 519-535.

Brenner, M., and T. J. Whitmore. 1998. *Historical sediment and nutrient accumulation rates and past water quality in Newnans Lake.* Final Report, Department of Fisheries and Aquatic Sciences, University of Florida, Gainesville.

Decho, A.W. 2000. Microbial biofilms in intertidal systems: an overview. *Continental Shelf Research*, 20, 1257-1273.

Dennett, K.E., T.W. Sturm, A. Amirtharajah and T. Mahmood. 1998. Effects of adsorbed natural organic matter on the erosion of kaolinite sediments. *Water Environment Research*, 70(3), 268-275.

Environmental Consulting & Technology, Inc. 2002. *Bathymetry and sediment thickness surveys of Newnans Lake, Project 99B250.* Report for ECT Project No. 990765-0400, submitted to the St. Johns River Water Management District, Palatka, Florida.

Ganju, N.K. 2001. *Trapping organic-rich fine sediment in an estuary.* M.S. Thesis, University of Florida, Gainesville.

Gowland, J.E. 2001. *Selective bottom sediment properties of Lake Bonnet, Florida.* Report UFL/COEL/MP-2001/01, Coastal and Oceanographic Engineering Program, Department of Civil and Coastal Engineering, University of Florida, Gainesville.

Gowland, J.E. 2002a. *Laboratory experiments on the erosional and settling properties of sediment from the Cedar/Ortega River system.* Report UFL/COEL/CR-2002/01, Coastal and Oceanographic Engineering Program, Department of Civil and Coastal Engineering, University of Florida, Gainesville.

Gowland, J.E. 2002b. *Wind induced wave resuspension and consolidation of cohesive sediment in Newnans Lake, Florida.* M.S. Thesis, University of Florida, Gainesville.

Holly, J.B. 1976. *Startigraphy and sedimentary history of Newnans Lake.* M. S. Thesis, University of Florida, Gainesville.

Hwang, K.-N. 1989. *Erodibility of fine sediment in wave-dominated environments.* M.S. Thesis, University of Florida, Gainesville.

Kandiah, A. 1974. *Fundamental aspects of surface erosion of cohesive soils.* PhD thesis, University of California, Davis.

Kirby, R. This volume. Organic-rich fine sediments in Florida part I: Sources and nature. In: *Estuarine and Coastal Fine Sediment Dynamics- INTERCOH 2003.* Maa, J.P.-Y., L.P. Sanford and D.H. Schoelhammer (eds.), Elsevier, Amsterdam.

Li, Y., and T.M. Parchure. 1998. Mudbanks of the southwest coast of India IV: Suspended sediment profiles. *Journal of Coastal Research*, 14(4), 1363-1372.

Marván, F.G. 2001. *A two-dimensional numerical transport model for organic-rich cohesive sediments in estuarine waters.* Ph.D. Thesis, Heriot-Watt University, Edinburgh, UK.

Mehta, A.J., S.-C. Lee, Y. Li, S.B. Vinzon and M.G. Abreu. 1994. *Analyses of some sedimentary properties and erodibility characteristics of bottom sediments from the Rodman Reservoir, Florida.* Report UFL/COEL/MP-94/03, Coastal and Oceanographic Engineering Program, Department of Civil and Coastal Engineering, University of Florida, Gainesville.

Mehta, A.J., R. Kirby and E.J. Hayter. 2000. *Ortega/Cedar River basin, Florida, Restoration: Work plan to assess sediment-contaminant dynamics.* Report UFL/COEL-99/019, Coastal and Oceanographic Engineering Program, Department of Civil and Coastal Engineering, University of Florida, Gainesville.

Mehta, A.J. and T.M. Parchure. 2000. Surface erosion of fine-grained sediment revisited. In: *Muddy Coast Dynamics and Resource Management*, Flemming, B.W., M. T. Delafontaine and G. Liebezeit (eds.), Elsevier, Amsterdam, 55-74.

Parchure, T.M. and A.J. Mehta. 1985. Erosion of soft cohesive sediment deposits. *Journal of Hydraulic Engineering*, 111(10), 1308-1326.

Rodriguez, H.N., J. Jiang and A.J. Mehta. 1997. *Determination of selected sedimentary properties and erodibility of bottom sediments from the lower Kissimmee River and Taylor Creek-Nubbin Slough basins, Florida.* Report UFL/COEL/MP-97/09, Coastal and Oceanographic Engineering Program, Department of Civil and Coastal Engineering, University of Florida, Gainesville.

Stuck, J.D. 1996. *Particulate phosphorus transport in the water conveyance systems of the Everglades Agricultural Area.* PhD thesis, University of Florida, Gainesville.

Tsai, C.H. and W. Lick, W. 1986. A portable device for measuring sediment resuspension. *Journal of Great Lakes Research*, 12(4), 314-321.

Weaver, C.E. and K.C. Beck. 1977. Miocene of the southeastern U.S.: A model for chemical sedimentation in a perimarine environment, *Sedimentary Geology*, 17(1/2), 1-234.

Young, I.R. and L.A. Verhagen. 1996. The growth of fetch limited waves of finite depth. Part I: Total energy and peak frequency. *Coastal Engineering*, 29, 47-77.

Estuarine and Coastal Fine Sediments Dynamics
J.P.-Y. Maa, L.P. Sanford and D.H. Schoellhamer (editors)
Published by Elsevier B.V.

A modular entrainment model for cohesive sediment

Keen, T.R. and Y. Furukawa

Naval Research Laboratory, Stennis Space Center, Mississippi 39529, USA

KEY WORDS
Cohesive sediment, entrainment, bioturbation, consolidation, models

This paper describes an entrainment model for cohesive sediments that is based on a power-law expression for the excess shear stress and a total entrainment coefficient. Total entrainment includes terms for consolidation, bioturbation, and all other processes (base entrainment coefficient). The model is used to predict entrainment rates for cohesive sediments from Lake Erie, the Tamar Estuary, Long Island Sound, and the Fox River, Wisconsin. The base entrainment coefficient, which is estimated using samples with the least post-depositional modification, is unique for each sediment suite because it includes environmentally sensitive processes like mineralogy, salinity, organic carbon content, etc. Based on available entrainment measurements, expressions are presented for the consolidation and bioturbation coefficients. The model is evaluated with entrainment data for identical sediment that has been either consolidated or bioturbated and the comparison is encouraging. A comparison of predicted and measured entrainment rates for undisturbed sediment is less favorable because of its unknown post-depositional history.

1. INTRODUCTION

Cohesive sediments are of interest because of their role in shoaling processes in estuaries and harbors, contaminant transport, and marine structural design. The primary motivation of the U.S. Navy, however, is their impact on the physical and acoustic properties of the seabed and on the optical properties of the water column. The physical

and chemical environment determines the dynamics of cohesive sediment but interactions between processes within the seafloor and the water column are poorly known. This problem is solved through a dependence on field and laboratory measurements in non-military applications, but this approach is generally unavailable for military operations. Thus, more general methods need to be developed. This paper discusses one such approach that relies less on direct observations of cohesive sediment behavior.

2. BACKGROUND

A substantial research effort has gone into understanding erosion (also called entrainment or resuspension), deposition, and consolidation (*e.g.*, Partheniades, 1993; Toorman, 1996) of cohesive sediments. The entrainment of fine grained sediment is usually parameterized using a power-law function that incorporates the bottom shear stress. For example, Ariathurai *et al.* (1983) proposed the following expression for the entrainment rate, E:

$$E = M\left(\frac{\tau_b - \tau_c}{\tau_c}\right) \quad (\mathrm{kg/m^2/s}) \tag{1}$$

where: M = the rate constant ($\mathrm{kg/m^2/s}$) at $\tau_b = 2\tau_c$; τ_b = bottom stress; and τ_c = critical shear stress for entrainment, which has been found to increase with depth for undisturbed sediment (*e.g.*, Sanford and Maa, 2001). Note that in this paper, we will use a constant value of 0.04 Pa for τ_c when it is not available. Partheniades (1965) suggested that erosion rates for mud (60% clay), while being constant for some experimental conditions, could only be described by a complex function with a large number of coefficients. Parchure and Mehta (1985) found that the erosion rate of deposited beds was not constant in part because of consolidation and dewatering. They turned to the theory of chemical rate processes to explain the dynamics of cohesive sediments, thereby implicitly making entrainment dependent on inter-particle bonds and thus the bio-geochemical environment. The parameters in their proposed formulation were determined by fitting experimental data. Lavelle *et al.* (1984) examined the data from a number of studies and proposed the following expression for the erosion rate:

$$E = \alpha|\tau_b|^{\eta} \quad (\mathrm{kg/m^2/s}) \tag{2}$$

where the parameters α and η were determined by least-squares fit to the data from each set of experiments. The parameter α varies by three orders of magnitude. More recently, Lick *et al.* (1995) proposed the following expression for the resuspension potential for cohesive sediments:

$$\varepsilon = \frac{a}{t_d^n}\left[\tau_b - \tau_c\right]^m \qquad (\mathrm{kg/m^2}) \tag{3}$$

where a, n, and m are constants, and t_d is the time after deposition in days. If the shear stress is held constant, the entrainment rate can be found from ε/T, where T is the time interval over which the entrainment remains constant (equilibrium time step). Experimental work has indicated that the mean concentration of entrained sediment in laboratory flumes reaches a steady state in approximately 1 hr (Lick, 1982). The entrainment rate can be deduced from the initial slope of the concentration time series, implying that E will go to zero when an equilibrium concentration is reached. Thus, some data are reported as a mean entrainment rate (or first-hour rate) for this equilibrium interval (see Lick, 1982). For these data, we calculate E from ε using T = 3600 s. Note that only Eq. 1 is dimensionally correct. This brief summary is intended to show that there is no unifying theory of the physical processes that control the entrainment of cohesive sediments and that most entrainment models use empirical parameters that are derived from observations of sediments from the area of interest.

The influence of biological and physical processes on the erosion of mudflats has been examined in the INTRMUD project (Black *et al.*, 1998), which demonstrated the importance of biostabilization on entrainment (de Brouwer *et al.*, 2000; Droppo *et al.*, 2001). The LISP project (Littoral Investigation of Sediment Properties) (Daborn, 1991) also examined the complex interaction of microflora and fauna in the intertidal environment. The biostabilization effect of biofilms is opposed by the destabilization caused by bioturbation (Grant and Daborn, 1994; Green *et al.*, 2002). Laboratory work with natural sediments has shown that cohesive sediment erodibility increases rapidly with the activity of infauna, presumably because of their destruction of inter-particle bonds and primary depositional fabric (Tsai and Lick, 1988; Lintern *et al.*, 2002). The complex interaction of these biological processes with physical processes like hydrodynamics and consolidation necessitates the use of more realistic entrainment models, and carefully planned measurement programs (Tolhurst *et al.*, 2000; Lick *et al.*, 1998).

3. METHODS

The purpose of this study is to evaluate sediment entrainment using a modular approach, which isolates the inherent physical properties of sediment from consolidation and bioturbation effects. The proposed model is first presented and the method of determining expressions for the coefficients for bioturbation A_B and consolidation A_C is then discussed.

3.1. The entrainment model

The entrainment expressions discussed in the literature are predominantly derived by fitting a power-law function to a series of data points on a plot of τ_b versus E. The power varies by many orders of magnitude, depending on the shear stress function. For example, powers as low as 10^{-8} were used by Lavelle *et al.* (1984) in Eq. 2, whereas a power of 1 is implied by a linear model (Eq. 1), and the resuspension potential (Eq. 3) uses a coefficient greater than 1. These expressions all have leading coefficients that are either constant or variable. This simple function fits a range of data because the sediment concentrations of interest to most problems are small, which is the appropriate application of a power-law function. This function is inappropriate for fluid mud, however, and more complex models are required (*e.g.*, Kranenburg and Winterwerp, 1997).

The model we propose to describe cohesive sediment entrainment is also based on a power-law expression, but physical and biological processes are isolated so that they can be evaluated separately. This is done conceptually by decomposing the leading constant into independent coefficients:

$$E = A_B A_C A_0 \left(\frac{\tau_b}{\tau_c} - 1 \right)^m \tag{4}$$

where A_B, A_C, and A_0 are parameters to be determined from observations. This formulation is similar to Eq. 1 but the excess shear stress power m can vary from unity. The parameter A_0 is analogous to the leading coefficients used in other expressions. It is treated as a fundamental entrainment rate for specific sediment, which has undergone no post-depositional modification (*i.e.*, no consolidation or bioturbation). The parameters A_B and A_C represent biological reworking and consolidation processes, respectively; if no consolidation or bioturbation has occurred, both A_B and A_C will equal 1, indicating no effects. We neglect biostabilization (*i.e.*, biofilms). Thus, our model incorporates a

fundamental entrainment rate that is a function of excess shear stress, and which is modified by post-depositional consolidation and bioturbation. The values of the parameters will be discussed in the results section.

This study focuses on sediment entrainment and, therefore, suspended sediment profiles will not be calculated or discussed. Equation 4 will be evaluated using entrainment rates derived from annular flumes (Fukuda and Lick, 1980; Tsai and Lick, 1988), the Instrument for measuring Shear stress In Situ (ISIS; Lintern *et al.*, 2002) and directly measured by SEDFLUME (McNeil *et al.*, 1996). The shear stress τ_b can be calculated from the hydraulic flow in all of these devices and thus the critical shear stress τ_c can be estimated. However, the definition of τ_c is partially subjective and not all workers define it the same. For example, McNeil *et al.* (1996) define τ_c as the shear stress that produces an erosion rate (measured by SEDFLUME) between 10^{-5} and 10^{-6} m/s; thus the mass erosion rate (kg/m^2/s) is dependent on the sediment bulk density. We use measured bulk densities to calculate entrainment rates for comparison to the model and other results. Lintern *et al.* (2002), however, define τ_c as the stress at which the entrainment rate increases from a previous steady value (see their Figure 3). The definition of the critical shear stress reported by different authors is dependent on measurement methods, and this variability will contribute to uncertainty in the results of this study.

3.2. Experimental procedure

The coefficients A_0, A_C and A_B in Eq. 4 must be estimated in order to isolate the impacts of bioturbation and consolidation from other processes. Ideally, this would be accomplished using entrainment data for undisturbed sediments, but this approach cannot be used because the post-depositional history of such sediments is unknown. We will use homogeneous sediment that was deposited from slurries to find functions of A_C and A_B, whereas A_0 will be independently determined for each sediment suite. The data consist of measured entrainment rates E, the resuspension potential ε, and the equilibrium concentration C_M at different shear stresses, water contents, and consolidation intervals. The sediments vary somewhat and caution is necessary in developing parameterizations for general applicability. Nevertheless, this first-order calculation of the coefficients will assist in future efforts to understand these processes. For ease of comparison, all entrainment measurements will be transformed into an entrainment rate E (kg/m^2/s), which requires approximation of unreported experimental parameters for some data.

The base entrainment parameter A_0 is strongly dependent on clay mineralogy, salinity, and seabed chemistry. These variables are not considered in this study and thus they

they are implicitly included in A_0. For this reason, A_0 is expected to have a unique value for each sediment suite discussed in this report. This coefficient should be determined from sediment that has undergone minimal post-depositional modification. For each suite of data (*e.g.*, Lake Erie sediment from Table 1), samples that are assumed to be the least modified by post-depositional processes are used to fit Eq. 4 and thus find a value of A_0. This approach assumes that $A_B = A_C = 1$, which is reasonable for newly deposited sediment. This procedure is repeated for each data set and unique values of A_0 are found.

Fukuda and Lick (1980) report entrainment results for mud (67.7% clay) from the central part of Lake Erie (Table 1). Sediment samples were allowed to consolidate from slurries for periods of 1 to 10 days. It is assumed in this study that the sediment had not consolidated significantly within one day, which is equivalent to a water content of 74% (shaded rows in Table 1). This is the shortest consolidation interval for which data are available. The solution to Eq. 4 assumes there has been no bioturbation or consolidation (*i.e.*, $A_B = A_C = 1$) and we are solving for A_0 and m only. However, we will use a constant value of 3 for the parameter m, following Lick *et al.* (1994). Fukuda and Lick (1980) do not report a value for τ_c so we use a value of 0.04 Pa, which is reasonable for recently deposited mud. Equation 4 is fit to the available high-water-content data with only A_0 as an adjustable parameter.

Table 1. Experimental conditions and entrainment rates (kg/m/s) for Lake Erie sediment (Fukuda and Lick, 1980). E_0 = measured; E_{M1} = calculated by Eq. 4 with A_C (initial) = $A_B = 1$, $A_0 = 3.61\times10^{-4}$ kg/m^2/s, $m = 3$, and $\tau_c = 0.04$ Pa.

τ_b (Pa)	Water Content (%)	Measured E_0	Predicted E_{M1}	E_0/E_{M1} (Estimated A_C)
0.0875	74.0	8.04×10^{-4}	6.04×10^{-4}	1.3300
0.0636	74.0	5.94×10^{-5}	7.41×10^{-4}	0.8012
0.0947	69.5	1.08×10^{-4}	9.23×10^{-4}	0.1170
0.0677	69.5	1.18×10^{-5}	1.12×10^{-4}	0.0984
0.1091	64.0	1.02×10^{-4}	1.86×10^{-3}	0.0548
0.0885	64.0	4.79×10^{-6}	6.43×10^{-4}	0.0074
0.1133	61.5	1.77×10^{-5}	2.22×10^{-3}	0.0079
0.0915	61.5	3.70×10^{-6}	7.70×10^{-4}	0.0048
0.0616	61.5	3.53×10^{-7}	5.68×10^{-5}	0.0062

The consolidation coefficient A_C for all sediment suites is evaluated using laboratory entrainment data for the Lake Erie sediment, which contained no organisms. The value of A_0 determined for the high-water-content data is used to calculate entrainment rates for the experiments at longer consolidation intervals, which correspond to lower water contents (Table 1). The ratio of the measured (E_0) and modeled (E_{M1}) entrainment rates is the estimated consolidation coefficient $A_C = E_0/E_{M1}$, which is plotted against the water content in Fig. 1. A function for A_C is derived from these points. Note that the selected function is strongly dependent on the larger values of A_C at high water contents. The result of this data-fitting procedure will be discussed in the results section.

An analogous procedure is used to estimate the bioturbation parameter A_B. We will use entrainment data for homogeneous slurries produced from Tamar Estuary sediments with infauna (Lintern *et al.*, 2002). These samples had consolidation intervals of 5 to 58 days (Table 2) and exhibited obvious biological effects. Although these sediments exhibited an increase in density with time, they will be treated in this study as having been dominated by bioturbation (*i.e.*, $A_C = 1$) as observed in the entrainment data, which will be discussed in the results section. To determine a baseline coefficient A_0 for these sediments, we again use samples with the shortest time since deposition, which for these sediments is 5 days (shaded rows in Table 2), and apply Eq. 4. Ideally, the value of A_0 can be determined for a specific sediment type but, since the mineralogy of the Tamar

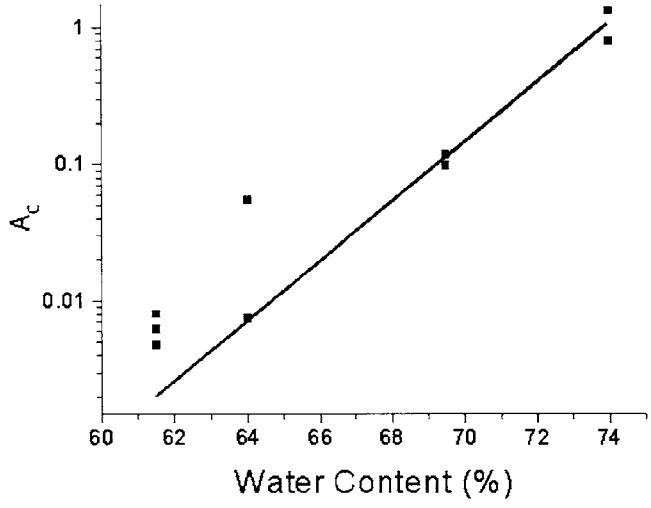

Fig. 1. Plot of the consolidation parameter A_C for the data from Table 1. The line is a plot of Eq. 5 ($r^2 = 0.4597$). Note that $A_C \equiv E_0/E_{M1}$ from Table 1.

Table 2. Experimental conditions and entrainment rates (kg/m^2/s) for ISIS experiments (Lintern *et al.*, 2002). E_0 = measured; E_{M1} = calculated by Eq. 4 with A_B (initial)= A_C = 1 , $A_0 = 1.79\times10^{-5}$ kg/m^2/s, and $m = 3$.

τ_b (Pa)	τ_c (Pa)	Consolidation Interval (days)	Measured E_0	Predicted E_{M1}	E_0/E_{M1} (Estimated A_B)
0.2	0.100	5	1.97×10^{-5}	3.92×10^{-8}	5.02×10^{2}
0.5	0.100	5	5.44×10^{-5}	1.09×10^{-4}	5.0×10^{-1}
0.1	0.010	19	2.97×10^{-5}	1.30×10^{-2}	2.28×10^{-3}
0.2	0.010	19	4.94×10^{-5}	1.23×10^{-1}	4.03×10^{-3}
0.5	0.010	19	1.43×10^{-4}	2.11	6.82×10^{-5}
0.1	0.075	30	2.11×10^{-5}	6.63×10^{-7}	3.18×10^{1}
0.2	0.075	30	5.19×10^{-5}	8.29×10^{-5}	6.27×10^{-1}
0.1	0.065	43	2.97×10^{-5}	2.79×10^{-6}	1.06×10^{1}
0.2	0.065	43	9.92×10^{-5}	1.60×10^{-4}	6.18×10^{-1}
0.1	0.073	58	5.44×10^{-5}	9.06×10^{-7}	6.01×10^{1}
0.2	0.073	58	7.55×10^{-5}	9.42×10^{-5}	8.02×10^{-1}

Estuary mud is different from that of Lake Erie mud, it is not expected that A_0 will be the same. The effect of mineralogy is beyond the scope of this work. The erosion data from Lintern *et al.* (2002) are reported as total entrainment ε, which is an equilibrium value (kg/m^2). This is transformed into the entrainment rate E_0 by dividing by an estimated time step of 3600 s, based on the results of Fukuda and Lick (1980). This permits a quantitative comparison of the solutions of Eq. 4 for the data contained in Tables 1 and 2.

The consolidation and bioturbation functions that are derived for A_C and A_B, respectively, will be evaluated using mud from Long Island Sound (Tsai and Lick, 1988) and undisturbed cores from the Fox River in Wisconsin (McNeil *et al.*, 1996). The Long Island mud was processed to be completely sterile. Some samples were subsequently seeded with *Nucula*, thus supplying an opportunity to examine the relative effects of consolidation and bioturbation on the same sediment. The Fox River data is included as a demonstration of the many problems that are encountered with cohesive sediments because of the unknown depositional history, overall coarse grain size, and high organic carbon content of this sediment.

4. RESULTS AND DISCUSSION

This section will use the laboratory entrainment data described above to determine expressions for the coefficients in Eq. 4. In all of the work discussed below, the value of m is equal to 3. Where unavailable from the source, an erosion time step of 3600 s will be assumed. The value of τ_c will be taken from the sources where given, or set to 0.04 Pa where unknown. We are unaware of experiments designed to address this specific problem so we will use available data with the understanding that they may not be well-suited for our purposes.

4.1. Base entrainment coefficient, A_0

The entrainment data with the largest water content from the Lake Erie samples (shaded rows in Table 1) are used to find a best-fit of Eq. 4 and thus the value of A_0 for this suite of data. The resultant base entrainment of 3.61×10^{-4} kg/m^2/s is used in the next section to determine the appropriate function for A_C. Similarly, Eq. 4 is fit to the Tamar mud with the shortest consolidation time and presumably least bioturbation (shaded rows in Table 2), and a value of 1.79×10^{-5} kg/m^2/s is estimated for A_0. The functional form of A_B will be found below using this value in Eq. 4 for the data in Table 2, as discussed in the previous section.

The Long Island Sound data are shown in Table 3, and the sediments with the highest water content (shaded rows) are used to calculate A_0 for this sediment. The best fit of Eq. 4 is found for A_0 equal to 1.523×10^{-7} kg/m^2/s, with τ_c = 0.04 Pa and a time step of 3600 s. The sediment cores from the Fox River (Table 4) were undisturbed. A core from a water depth of 5.9 m in Trenton Channel consists of silt and clay, with gas bubbles, and surface oligochaetes and macrophytes (McNeil *et al.*, 1996). This sediment has an unknown history of consolidation and bioturbation along with other influences that are not examined in this study. In order to determine A_0 we need to evaluate the entrainment rate for newly deposited sediment, which is unlikely for these samples. Nevertheless, this exercise is instructive in demonstrating the limitations of the model. We will neglect bioturbation in this sediment because we have no information on deposition time, whereas the water content was measured. The following variables are used: τ_c = 0.1 Pa, an erosion time step of 3600 s, and m = 3. The best-fit value of A_0 is 2.295×10^{-2} kg/m^2/s.

The base entrainment rates for the freshwater sediment from Lake Erie and the Fox River are much larger than for the estuarine sediment from the Tamar Estuary and Long Island Sound. This is a result of the salinity of seawater, which increases aggregation of clay minerals (Ariathurai *et al.*, 1983). It should be possible to identify a functional form for this process as well if appropriate experimental data are available. The large-

Table 3. Experimental conditions and entrainment rates (kg/m^2/s) for Long Island Sound sediment (Tsai and Lick, 1988). E_0 is measured; E_{M1} is calculated by Eq. 4 with $A_B = A_C = 1$, $A_0 = 1.523\times10^{-7}$ kg/m^2/s, and $m = 3$; E_{M2} is computed the same as E_{M1} but with A_C calculated from Eq. 5.

τ_b (Pa)	Water Content (%)	Measured E_0 (kg/m^2/s)	Predicted E_{M1} without consolidation	Predicted E_{M2} with consolidation
0.1	71.3	5.60×10^{-7}	4.643×10^{-7}	1.27×10^{-7}
0.2	71.3	8.06×10^{-6}	9.74×10^{-6}	2.67×10^{-7}
0.4	71.3	1.15×10^{-4}	1.11×10^{-4}	3.04×10^{-5}
0.1	71	6.14×10^{-7}	4.64×10^{-7}	1.09×10^{-7}
0.2	71	2.61×10^{-6}	1.01×10^{-5}	2.38×10^{-6}
0.4	71	9.51×10^{-6}	1.08×10^{-4}	2.55×10^{-5}
0.8	71	1.41×10^{-4}	1.04×10^{-3}	2.47×10^{-4}
0.2	69.9	1.34×10^{-6}	9.74×10^{-6}	1.32×10^{-6}
0.4	69.9	2.90×10^{-6}	1.11×10^{-4}	1.50×10^{-5}
0.8	69.9	9.83×10^{-5}	1.04×10^{-3}	1.41×10^{-4}
1.2	69.9	3.73×10^{-4}	9.56×10^{-6}	1.29×10^{-6}

Table 4. Entrainment rate for Fox River sediments (McNeil *et al.*, 1996). The model predictions (*EM*1) were calculated using $A_0 = 2.295\times10^{-2}$ kg/m^2/s, $A_B = 1$, A_C = Eq. 5, τ_c = 0.1 Pa, an equilibrium time of 3600 s, and $m = 3$.

Depth (m)	τ_b (Pa)	Water Content (%)	Measured E_0 (kg/m^2/s)	Predicted E_{M1} (kg/m^2/s)
0.017	0.25	64.8	7.74	8.13×10^{-4}
0.27	0.25	50.0	4×10^{-4}	3.07×10^{-4}
0.26	0.6	50.0	5.28×10^{-2}	1.14×10^{-2}
0.34	1.1	60.0	6.36×10^{-2}	9.11×10^{-2}
0.15	2.2	49.0	8.57×10^{-2}	8.44×10^{-1}
0.22	4.5	49.0	4.18×10^{-1}	7.76

base entrainment rate for the Fox River data further suggests that bioturbation may also be an important process at this location, as indicated by the presence of organisms at the river bed.

4.2. The consolidation coefficient, A_C

The entrainment data for the Lake Erie sediment are used to determine an expression for A_C because they have the largest range of water content (61.5 – 74%), and presumably consolidation. The values of E_0/E_{M1} from Table 1 are an estimate of the consolidation coefficient A_C, which is plotted against water content in Fig. 1. An exponential function is fit to these data:

$$A_C = C_1 e^{(W-W_0)/t} \tag{5}$$

where: C_1 = 0.00397, t = 1.99315, W = water content (%), and W_0 = 62.85 for this study. The squared correlation coefficient r^2 for Eq. 5, as plotted in Fig. 1, is 0.4597. The range of water content for which Eq. 5 is valid is limited by the data used to derive it, which in this case is 61.5 to 74%. An exponential function is reasonable because consolidation can be represented to first-order as an exponential process. However, the constants C_1, W_0, and t are dependent on the specific data used to find A_C, and their values will change as other data are examined as will the functional form of Eq. 5. Equation 5 implies that as sediment is compacted and W decreases, the entrainment rate will decrease as well. With respect to the model, this indicates that small values of A_C correct for the base entrainment rate over-predicting the entrainment, because of an increase in τ_c. This error increases with consolidation. If the data used to calculate A_0 are properly selected, A_C should always be less than unity but this is unlikely due to measurement uncertainties and the influence of processes not included in the model.

4.3. The bioturbation coefficient, A_B

The laboratory data for slurries from the Tamar Estuary are used to examine the functional form of the bioturbation coefficient A_B because they are dominated by biological processes and the results are well documented. Before determining the bioturbation function, it is useful to note the difficulty in using Eq. 4 for biologically influenced sediment. The ratio E_0/E_{M1} for the low-shear-stress data used to calculate A_0 (top row in Table 2) exceeds 500, which is significantly greater than any other value in the table. This occurs because the $(\tau/\tau_c - 1)$ term in Eq. 4 is less than unity for this experiment, resulting in a substantial decrease in the predicted entrainment. This may be due to many causes that are not included in the model. This phenomenon has been noted by

Lavelle *et al.* (1984) and it is of continuing interest in predicting cohesive sediment entrainment. We will not use the error data from this experiment in deriving A_B, however, because it skews the resulting function.

The bioturbation parameter A_B, which is estimated from the ratio of E_0/E_{M1} (Table 2), is plotted as a function of consolidation time in Fig. 2. These data are represented by the following expression:

$$A_B = C_2 + C_3 t_d + C_4 t_d^2 \tag{6}$$

where: C_2 = 5.093×10^{-3}; C_3 = 0.02186; C_4 = 6.85×10^{-4}; and t_d = consolidation time (days). The squared correlation coefficient r^2 is 0.3563, which is rather low because of the small sample size and range of reported entrainment rates. The constants C_2, C_3, and C_4 will have different values if other experimental data are used to find A_B, but we propose that Eq. 6 is a reasonable function. These data do not fit an exponential function as well as the consolidation data because of the complex impacts of biological processes. For example, Lintern *et al.* (2002) noted the presence of diatoms and other biological material within the homogenized sediment, in addition to complex structures caused by burrowing organisms. Furthermore, not all biological activity increases erodibility; for example, biofilms promote stability in sediments whereas bioturbation destabilizes the bed. Overall, these deposits were mostly bioturbated, which is the

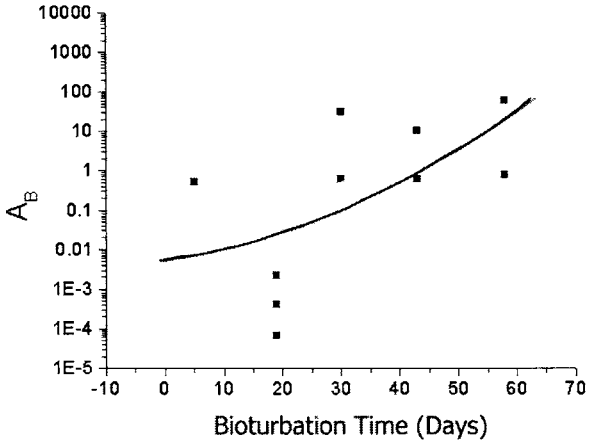

Fig. 2. Plot of the bioturbation coefficient A_B for the data from Table 2. The line is a plot of Eq. 6 (r^2 = 0.3563). The coefficient $A_B \equiv E_0/E_{M1}$ from Table 2. Note that the first data entry is not plotted. See text for explanation.

reason Fig. 2 shows a slight increase in entrainment with time. If the data used to calculate A_0 are representative of newly deposited sediment, A_B should always be greater than unity because of the increasing disruption as organisms bioturbate the bed. However, as seen in Fig. 2, A_B is less than 1 for most bioturbation times because of the experimental uncertainty (note the 3 data points at 19 days).

4.4. Comparison to other entrainment data

The sediment samples studied by Tsai and Lick (1988) were collected in a water depth of 20 m in Long Island Sound. They contained dark grey organic silt and clay with 95% finer than 74 μm. The samples were homogenized and placed in an annular flume 0.204 m deep. The water content at the time of testing varied from 70.4 to 72.2%. This is a small range and, in fact, there was some overlap in water content during the consolidation interval. The value of τ_c was not reported so we use 0.04 Pa. A comparison will be made with the first-hour resuspension rate (Fig. 4 from Tsai and Lick, 1988), so a time step of 3600 s is used. The value of A_0 (1.523×10^{-7} kg/m^2/s) was determined from samples that were measured after 1 day of consolidation as discussed above.

The entrainment data for these samples are given in Table 3. There is a significant trend of decreasing entrainment rate with time (correlated with water content) for the observations at all shear stresses (open squares in Fig. 3). This behavior is what we would expect for consolidation. Note that the consolidation interval labels (*e.g.*, 1 D) on Fig. 3 refer to the measurements only. Equation 4 is solved using the base entrainment ($A_B = A_C = 1$) and plotted on Fig. 3 as well (open circles, E_{M1} in Table 3). Note that the data points for all water contents fall upon each other, because of the lack of consolidation when $A_C = 1$. This is the reason it is necessary to adjust other parameters for Eqs. 1 – 3. The prediction is not bad because the total consolidation interval was only 7 days. The effects of consolidation are seen at all shear stresses when A_C is computed using Eq. 5, however. The results (crosses in Fig. 3) match the measurements better as well (E_{M2} in Table 3).

Some of the homogenized sediment from Long Island Sound was seeded with deposit-feeding *Nucula* clams at a density of 1150/m^2 (Tsai and Lick, 1988). This significantly increased the equilibrium concentration of sediment at all shear stresses. Tsai and Lick (1988) report the first-hour entrainment rate for the sterile data but only the mean concentration C_M at different shear stresses for the seeded samples. Nevertheless, the entrainment rate can be approximated from C_M by: $E = h[C_M(t+\Delta t) - C_M(t)]/\Delta t$, where h = the flume depth (0.204 m) and Δt = the time to reach C_M for an increase in τ_b. This calculation was performed on the data of Tsai and Lick (their Fig. 8) for comparison with the values predicted by Eq. 4 using Eq. 6 to find the bioturbation coefficient A_B.

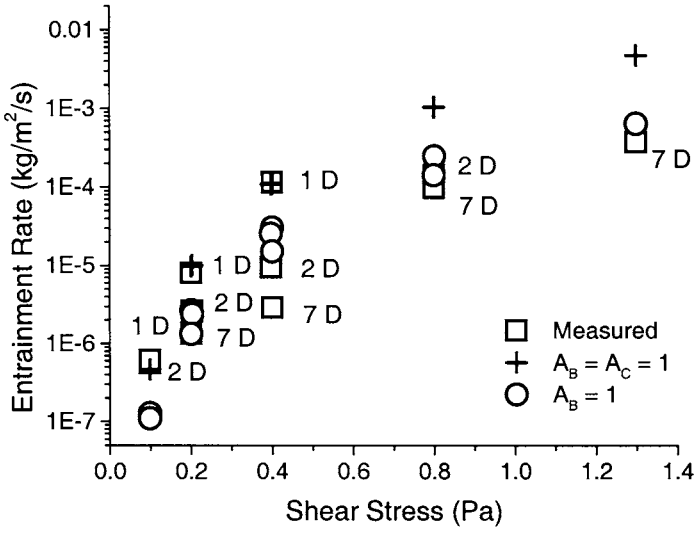

Fig. 3. Plot of the entrainment data for Long Island Sound sediment: measured (E_0) (Tsai and Lick, 1988) (squares); calculated by Eq. 4 with $A_B = A_C = 1$ (E_{M1}, pluses); and Eq. 4 with A_C calculated by Eq. 5 and $A_C = 1$ (E_{M2}, circles). The consolidation intervals in days for the measured data are indicated.

The results (Fig. 4) show that Eq. 6 is not general enough for wide application because it was derived from a limited database with somewhat unique characteristics.

The entrainment rates for the undisturbed sediment from the Fox River were measured using SEDFLUME (McNeil *et al.*, 1996). This sediment contained silt and clay (mean grain size less than 20 μm), gas bubbles, infauna, grass, and organic carbon (approximately 10%). The entrainment rate was measured at a range of depths within the core for shear stresses ranging from 0.25 – 4.5 Pa. The water content varied from 64.8% at the surface to 48.1% at depth, indicating that this sediment was not freshly deposited. A base entrainment rate (A_0) of 2.259×10^{-2} kg/m^2/s, is calculated as described in section 4.1 and A_C is computed using Eq. 5. The bulk density required to calculate E is found using bulk density data from McNeil *et al.* (1996, Fig. 8); the surface bulk density of the core was 1166 kg/m^3. The entrainment rates for the measured samples (squares in Fig. 5) vary at smaller values of τ_b and increase with shear stress. The entrainment rates predicted by Eq. 4 increase with shear stress also while being an order-of-magnitude high at large shear stresses. The predicted entrainment rates are

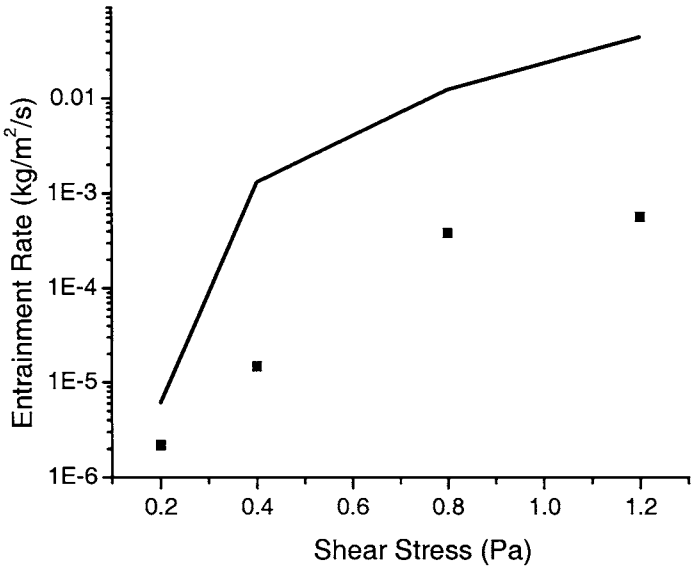

Fig. 4. Plot of the entrainment data for Long Island Sound sediment seeded with *Nucula* after 7 days (Tsai and Lick, 1988). The following conditions were used for the simulation: time step = 3600 s; τ_c = 0.04 Pa; A_B calculated from Eq. 6; A_C = 1; A_0 = 1.523×10^{-7} kg/m^2/s.

probably too high because of post-depositional modification of the sediment. The consolidation expression (Eq. 5) is based on limited data from deposited slurries. Despite the difficulties of predicting the behavior of this sediment, the fit is reasonable, especially since no curve-fitting process was used for consolidation. It should also be noted that the base entrainment coefficient for this sediment, which was estimated from a surface sample, probably does not incorporate the effects of burial as deep as 0.4 m.

5. CONCLUSIONS

Consolidation and bioturbation appear to have opposing effects on cohesive sediment entrainment for most of the sediment studied herein. For example, bioturbation by infauna reworks sediment and increases erodibility for these samples whereas consolidation and dewatering tends to decrease entrainment rates. Thus, these preliminary results

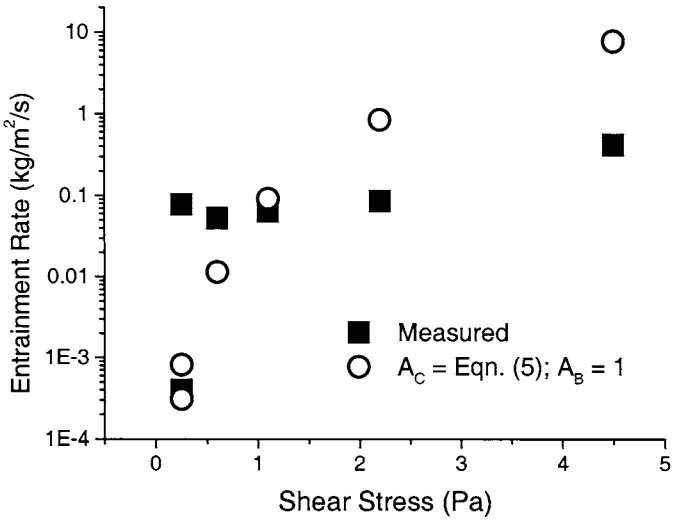

Fig. 5. Entrainment rates for Fox River sediments (McNeil *et al.*, 1996). The following conditions were used for the simulation: time step = 3600 s; τ_c = 0.1 Pa; A_C calculated from Eq. 5; $A_B = 1$; $A_0 = 2.259 \times 10^{-2}$ kg/m^2/s.

suggest that, as a first approximation, these processes can be treated as mutually exclusive. If bioturbation is significant, consolidation can probably be neglected and A_C assumed to be 1, whereas if bioturbation is negligible (*i.e.*, rapid deposition and/or a hypoxic water column), the sediment's physical properties are probably dominated by consolidation or other processes that decrease erodibility (*e.g.*, organic content). It is not suggested that this simple approach incorporates all environmental effects but it is usable until better entrainment data become available. The greatest advantage of the modular entrainment model (Eq. 4) is that it permits us to examine this complex process with a more physically realistic approach than parameter calibration based on entrainment data.

ACKNOWLEDGEMENTS

This work was funded by the Office of Naval Research (Program Element 61153N). This is NRL contribution NRL/PP/7320-03-110.

REFERENCES

Ariathurai, R., J. Golden, Jr., W.H. McAnally, Jr., G.A. Stout, and J. Neiheisel. 1983. Shoaling processes in navigable waters. *Journal of Waterway, Port, Coastal and Ocean Engineering*, 109 (2), 199-221.

Black, K.S., D.M. Paterson and A. Cramp. (eds.). 1998. *Sedimentary Processes in the Intertidal Zone.* Geological Society of London, Special Publication, 139.

Daborn, G. R. (ed.). 1991. *Littoral investigation of sediment properties*. Final Report, Acadia Centre for Estuarine Research, Publication No. 17, 239 pp.

de Brouwer, J.F.C., S. Bjelic, E.M.G.T. de Deckere and L.J. Stal. 2000. Interplay between biology and sedimentology in a mudflat (Biezelingse Ham, Westerschelde, The Netherlands). *Continental Shelf Research*, 20, 1159-1177.

Droppo, I.G., Y.L. Lau and C. Mitchell. 2001. The effect of depositional history on contaminated bed stability. *Science of the Total Environment*, 266 (1-3), 7-13.

Fukuda, M.K. and W. Lick. 1980. The entrainment of cohesive sediments in freshwater. *Journal of Geophysical Research*, (85), 2813-2824.

Grant, J. and G. Daborn. 1994. The effects of bioturbation on sediment transport on an intertidal mudflat. *Netherlands Journal of Sea Research*, 32 (1), 63-72.

Green, M.A., A.C. Aller, J.K. Cochran, C. Lee and J.Y. Aller. 2002. Bioturbation in shelf/slope sediments off Cape Hatteras, North Carolina: The use of TH-234, Ch1-a, and Br- to evaluate rates of particle and solute transport. *Deep-Sea Research Part II – Topical Studies in Oceanography*, 49 (20), 4627-4644.

Kranenburg, C. and J.C. Winterwerp. 1997. Erosion of fluid mud layers. I: Entrainment model. *Journal of Hydraulic Engineering*, 123 (6), 504-511.

Lavelle, J.W., H.O. Mofjeld and E.T. Baker. 1984. An *in situ* erosion rate for a fine-grained marine sediment. *Journal of Geophysical Research*, (89) C4, 6543-6552.

Lick, W. 1982. Entrainment, deposition, and transport of fine-grained sediments in lakes. *Hydrobiologia*, (91), 31-40.

Lick, W., Z. Chroneer, C. Jones and R. Jepsen. 1998. A predictive model of sediment transport. In: *Proceedings, Fifth International Conference, Estuarine and Coastal Modeling*, ASCE., Reston, Virginia, 389-399.

Lick, W., J. Lick and C. K. Ziegler. 1994. The resuspension and transport of fine-grained sediments from Lake Erie. *Journal of Great Lakes Research*, 20 (4), 599-612.

Lick, W., Y.-J. Xu and J. McNeil. 1995. Resuspension properties of sediments from the Fox, Saginaw, and Buffalo Rivers, *Journal of Great Lakes Research*, (21) 2, 257-274.

Lintern, D.G., G.C. Sills, N. Feates and W. Roberts. 2002. Erosion properties of mud beds deposited in laboratory settling columns. In: *Fine Sediment Dynamicss in the Marine Environment*. Winterwerp, J.C. and C. Kranenburg (eds), Elsevier, New York, 343-357.

McNeil, J., C. Taylor and W. Lick. 1996. Measurements of erosion of undisturbed bottom sediments with depth. *Journal of Hydraulic Engineering*, (122) 6, 316-324.

Parchure, T.M. and A.J. Mehta. 1985. Erosion of soft cohesive sediment deposits. *Journal of Hydraulic Engineering,* 111 (10), 1308-1326.

Partheniades, E. 1993. Turbulence, flocculation and cohesive sediment dynamics. In: *Nearshore and Estuarine Cohesive Sediment Transport*. Mehta, A.J. (ed), Coastal and Estuarine Studies, 42, 40-59.

Partheniades, E. 1965. Erosion and deposition of cohesive soils. *Journal of Hydraulics Division*, ASCE, HY 1, 105-139.

Sanford, L.P. and J. P.-Y. Maa. 2001. Toward a unified erosion formulation for fine sediments. *Marine Geology*, 179, 9-23.

Tolhurst, T.J., R. Riethmuller and D.M. Paterson. 2000. *In situ* versus laboratory analysis of sediment stability from intertidal mudflats. *Continental Shelf Research*, 20, 1317-1334.

Toorman, E.A. 1996. Sedimentation and self-weight consolidation: General unifying theory. *Geotechnique*, 46 (1), 103-113.

Tsai, C. H. and W. Lick. 1988. Resuspension of sediments from Long Island Sound (U.S.A.). *Water Science Technology*, (20) 6/7, 155-164.

APPENDIX

List of Symbols

A_0 = base entrainment ($kg/m^2/s$)

A_B = bioturbation coefficient

A_C = consolidation coefficient

C_1 = leading constant in consoledation coefficient expression

C_2, C_3, C_4 = constants in bioturbation coefficient expression

C_M = Equilibrium concentration (kg/m^3)

E = entrainment rate ($kg/m^2/s$)

E_0 = measured entrainment rate ($kg/m^2/s$)

E_{M1} = predicted entrainment rate with no consolidation or bioturbation ($kg/m^2/s$)

E_{M2} = predicted entrainment rate with consolidation ($kg/m^2/s$)

M = constant entrainment rate ($kg/m^2/s$)

W = water content (%)

W_0 = minimum water content for consolidation expression (%)

a = constant in the total entrainment expression (kg/m^2)

m = constant power for excess shear stress

n = constant power for deposition time

r^2 = square of correlation coefficient

t = constant in consolidation coefficient expression

t_d = setting interval (days)

α = constant in Eq. 2

ε = Entrainment potential (kg/m^2)

η = constant power in Eq. 2

τ_b = bottom stress (Pa)

τ_c = critical stress for entrainment (Pa)

Estuarine and Coastal Fine Sediments Dynamics
J.P.-Y. Maa, L.P. Sanford and D.H. Schoellhamer (editors)

On the sedimentation rate of cohesive sediment

Winterwerp, J.C.

Delft University of Technology, Dept. of Civil Engineering and Geosciences, PO Box 5048, 2600 GA Delft, The Netherlands; also: Delft Hydraulics, The Netherlands.

KEY WORDS
Sedimentation rate, cohesive sediment paradigm, simultaneous erosion and deposition, probability density function of bed shear stress

This paper elaborates on the current paradigm of mutually exclusive erosion and deposition for cohesive sediment in open channel flow. This is done through a discussion of data presented in literature. In particular, the deposition experiments carried out by Krone (1962) in a straight flume are re-analysed with a simple mass balance model. In this model, the water-bed exchange processes are modelled using a combination of a simple linear erosion formula and sedimentation flux. The bed shear stress is modelled with a skewed probability density function, and the threshold for erosion is assumed to increase with time as a result of consolidation and other physico-chemical effects.

The experimental results by Krone could be reproduced satisfactory, from which it is concluded that the so-called critical shear stress for deposition does not exists. In fact, this critical stress represents a threshold for resuspension, as observed by Krone in his original report. These findings also imply that common engineering practice, combining the so-called Partheniades' erosion formula with Krone's deposition formula do not describe physics properly. It is recommended to model the gross sedimentation rate D for cohesive sediment suspensions in open channel flow with its settling flux, *i.e.*, $D = W_s c$.

1. INTRODUCTION

Formulations for the deposition rate of cohesive sediment are based on two series of sedimentation experiments described in the literature. The first series consists of

experiments carried out by Krone (1962, see also Einstein and Krone, 1962) in a 33 m long straight flume, 1 m wide with a water depth of 0.33 m. A suspension of fine sediments from San Francisco Bay was mixed with fresh water, salted with sodium chloride and circulated through the flume at high flow velocity. After thorough mixing, the flow velocity was reduced to allow the sediment to settle. The floc size of the sediment was governed by the return flow system and hardly any flocculation occurred in the flume itself; its settling velocity was $W_s = 6.6 \times 10^{-6}$m/s. The decrease in suspended sediment concentration c, as measured during three experiments in the flume, is shown in Fig. 1, showing a logarithmic decay at concentrations below about 300 mg/l.

The data for $c < 300$ mg/l were fit by Eq. 1:

$$c = c_0 \exp\{-(1-p) W_s t/h\} \tag{1}$$

where c_0 is the initial concentration, t is time and h is the water depth. The coefficient p represents the overall probability of resuspension of deposited material (Krone, 1962; 1993). At present, p is often referred to as the fraction of flocs that are too weak to survive the large shear stresses near the bed, and therefore will be broken and resuspended (Partheniades *et al.*, 1968). Eq. 1 forms the basis for Krone's world-wide used deposition formula:

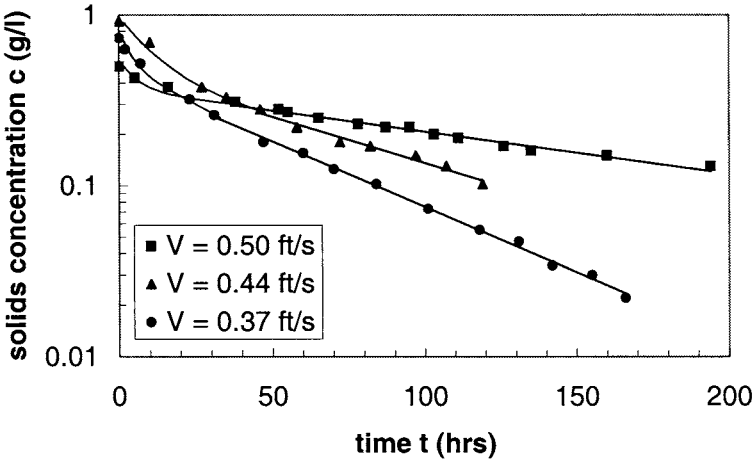

Fig. 1. Decay with time of suspended sediment concentration as measured by Krone (1962)

$$\frac{\mathrm{d}h\overline{c}}{\mathrm{d}t} = -D = -W_s c_b \left(1 - \frac{\tau_b}{\tau_d}\right) \quad \text{for} \quad \tau_b < \tau_d \tag{2}$$

where D is the deposition rate, $\overline{c}$ is the depth-averaged concentration, c_b is the near-bed concentration (often c_b is set equal to $\overline{c}$), τ_b is the bed shear stress and τ_d is the so-called critical shear stress for deposition. Note that Eq. 2 predicts that eventually all sediment will be deposited at a specific flow velocity for which $\tau_b < \tau_d$. Krone (1962; 1993) also presents a fit for the deposition rate at larger concentrations; this analysis is not presented here however. Typical values of τ_d are 0.05 - 0.1 Pa, *e.g.*, Self *et al.* (1989).

Later, similar tests in a straight flume were performed by Partheniades (1965) and Mehta *et al.* (1982). Mehta found full deposition, which was attributed to the limited length of the flume.

The second series of sedimentation experiments were carried out in rotating annular flumes, for the first time by Partheniades *et al.* (1968), later by Mehta (1973), Mehta and Partheniades (1975) and repeated by Lick and Kang (1987), amongst others. The rotating annular flume deployed by Metha and Partheniades consisted of a circular channel, 0.2 m wide and 0.45 m deep, and a mean diameter of 1.5 m. The suspension is driven by a rotating upper lid. The flume itself can rotate in opposite direction to minimise secondary currents. Sedimentation experiments by Mehta were carried out with San Francisco Bay mud, Maracaibo mud and processed kaolinite clay. A suspension was made with distilled water and salted tap water by mixing the sediment thoroughly in the flume at high flow veocity. Then the rotation of the flume was set at the required speed, and the sediment was allowed to settle. Contrary to Krone's experiments, not all sediment deposited when $\tau_b < \tau_d$, and an equilibrium concentration was found, as shown in Fig. 2.

It appeared that the equilibrium concentration c_{eq} scaled with the initial concentration C_0, and that the ratio c_{eq}/C_0 could be described with a log-normal distribution of a function of the bed shear stress (see also Partheniades, 1986). The behaviour shown in Fig. 2 is explained from a distribution in floc size, hence settling velocity and floc strength. This hypothesis is substantiated by the measured decrease in median diameter with time (Metha and Lott, 1987). Such a distribution is implicitly accounted for by the log-normal distribution mentioned above. Note that the suspension at equilibrium conditions may also contain a colloidal fraction that will not settle anyway. Moreover, the chemistry of the water (pH, salinity, etc.) starts to play a role in the behaviour of these colloidal fractions.

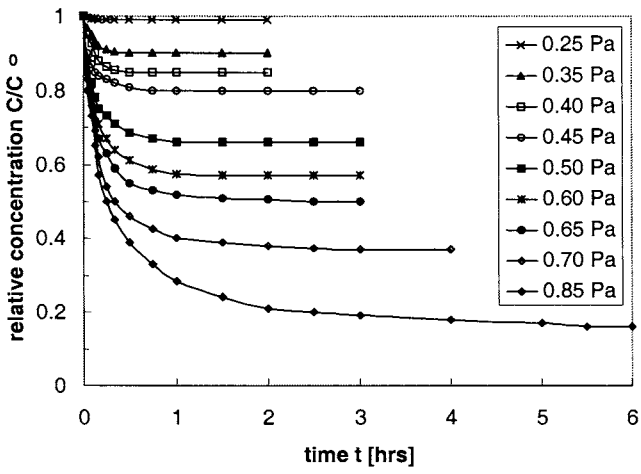

Fig. 2. Decay with time of suspended sediment concentration as measured by Metha and Partheniades (1975) for a variety of hydrodynamic conditions.

Mehta and Lott (1987) reanalysed the experiments assuming a floc size distribution in Krone's Eq. 2. This (skewed) distribution contained 14 discrete classes, each with a characteristic W_s and τ_d. Metha and Lott were indeed able to reproduce the observed concentration evolution. Also Teeter (2001) applied a multiple fraction model, distinguishing between cohesive particles (with a critical shear stress for deposition) and non-cohesive silt particles, and was able to reproduce Mehta's measurments. Later, Verbeek *et al.* (1993) were successful with a similar analysis, using a continuous distribution for W_s and τ_d however.

Self *et al.* (1989) carried out erosion and deposition experiments in a "radial flow-cell chamber" with non-cohesive silt particles of varying diameter under neutral and non-neutral chemical conditions. They observed a critical shear stress for deposition, different from a critical shear stress for the onset of movement, beyond which particles could not settle. However, the experiments were conducted under laminar flow conditions, and it is not clear how the results should be interpreted with respect to full scale field conditions with turbulent flow characteristics.

Partheniades (1965) carried out three experiments in a rotating annular flume, which form the basis of the current cohesive sediment paradigm, that sedimentation and erosion cannot occur simultaneously in cohesive sediment dynamics. The first was a deposition experiment at a specific rotational speed of the annular flume, in which a

mud suspension was allowed to settle partly. After equilibrium was obtained, the remaining suspension was carefully exchanged with clear water, maintaining the speed of the flume. It was observed that the exchanged water remained clear, from which Partheniades concluded that erosion does not occur during deposition.

Partheniades *et al.* (1968) described a second experiment, similar to the one described above. However, in this case, the suspension was only partly exchanged when equilibrium was obtained. Then, the deposited sediment was remixed over the water depth, after which the deposition experiment was repeated at the same hydrodynamic conditions, until a new equilibrium was achieved. It appeared that the new relative equilibrium concentration was lower than at the end of the first phase of this experiment, but not zero. This implies that some of the fine material, that could not settle during this second phase, was entrained into the bed during the first phase of the experiment. This behaviour was attributed to a change in flocculation properties of the sediment by removing part of the finer fraction.

In the third experiment, a mud bed was eroded at another rotational speed of the flume. Also this experiment was continued until equilibrium was achieved, and again the suspension, now containing eroded bed material, was carefully exchanged with clear water, maintaining the speed of the flume. Also in this case, the water remained clear, from which Partheniades concluded that deposition does not occur during erosion.

It is noted that the cohesive sediment paradigm does not explain an observation by Krone (1962; 1993) during another deposition experiment in his straight flume. In this experiment, sediment particles were labelled with gold, and allowed to settle fully to form a bed. Then, a suspension of the same sediment, but not labelled, was brought into the flume under such hydrodynamic conditions that the sediment could settle. It appeared that the total amount of sediment in the flume decreased exponentially with time, but that initially some gold-labelled particles were entrained from the bed. After a few hours however, the absolute amount of labelled sediment particles did not grow anymore, its fraction, with respect to the total amount of sediment that remained in suspension in the flume, kept increasing though. This implies that erosion and deposition must occur simultaneously, at least during part of the experiment.

Sanford and Halka (1993) analysed a series of field measurements under tidal conditions in Chesapeake Bay. They observed that the suspended sediment concentration started to decrease when the flow velocity started to decrease. This behaviour cannot be modelled with Krone's deposition (Eq. 2), as this formula, used in conjunction with an erosion formula, predicts that the suspended sediment concentration cannot decrease before the flow velocity (bed shear stress) drops below its critical value for deposition ($\tau_b < \tau_d$). Sandford and Halka (1993) were able to simulate the observed concentration

pattern only when they applied a continuous deposition formula, *i.e.*, $D = W_s c$, as shown in Fig. 3.

Sanford and Halka (1993) also presented an overview of (field) data with the same behaviour, *i.e.*, a decrease in concentration when the flow velocity decreases, including observations in Long Island Sound, San Francisco Bay, the Eastern Scheldt, and a number of British estuaries. From these observations and their analysis, they conclude that the paradigm of mutually exclusive erosion and deposition of mud is apparently valid under laboratory conditions, but not in the field.

This conclusion is of course rather unsatisfactory, and relies heavily on a selective set of laboratory experiments to try and understand the physics of cohesive sediment dynamics. In the next section, an alternative picture is proposed, which is elaborated and validated in the sections beyond.

2. A CONCEPTUAL PICTURE OF THE HYDRO-SEDIMENTOLOGICAL CONDITIONS DURING DEPOSITION

In this section, an alternative description of the hydro-sedimentological conditions during deposition is proposed, consisting of the following four elements:

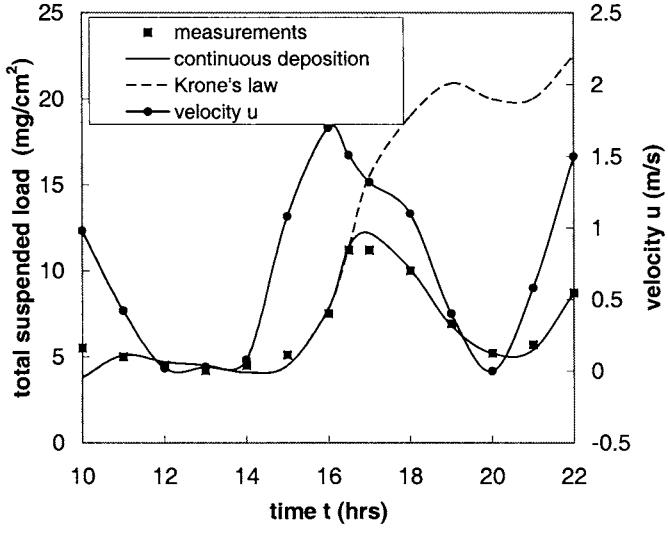

Fig. 3. Measured and predicted total sediment load, after Sandford and Halka (1993).

2.1. Simultaneous erosion and deposition

Contrary to classic cohesive sediment theory, it is assumed that erosion and deposition can occur simultaneously. The deposition rate D is given by the sediment flux at the bed, thus:

$$D = W_{s,b} c_b \tag{3}$$

where c_b and $W_{s,b}$ are the suspended sediment concentration and settling velocity of the sediment at the bed, accounting for vertical concentration gradients on c_b and possible flocculation effects on $W_{s,b}$.

2.2. Erosion rate

For the present analysis it is assumed that the erosion of sediment from the bed occurs when the bed shear stress exceeds a critical value for erosion τ_e. Because of physico-chemical effects (consolidation, gelling, restructuring), the bed strength increases with time, hence the critical shear stress for the erosion of sediment deposits increases with time. Similarly, the erosion rate coefficient will decrease in time – however, this effect will be ignored at present. The erosion rate E is assumed to scale with the erosion rate coefficient M and reads:

$$E = M\mathrm{F}\left(\frac{\tau_b - \tau_e(t)}{\tau_e(t)}\right)\mathrm{S}(\tau_b - \tau_e) \tag{4a}$$

where F is an excess shear stress function, and S(x) a step function: S = 0 for $x < 0$, and S = 1 for $x > 0$. Note that τ_e may also decrease in time because of swell, liquefaction and other processes when the sediment is subjected to turbulent shear or wave-induced stresses.

2.3. Bed shear stress

Further to Partheniades (Partheniades and Paaswell, 1970; Partheniades, 1965; 1986), it is assumed that the bed shear stress can be described by a Probability Density Function (PDF) $y(\tau)$. However, we do not use a Gaussian distribution, as it is known (*e.g.*, Christensen, 1965, amongst others) that such a density function should be skewed (*e.g.*, Section 3). If it is assumed that F in Eq. 4a is linear, then Eq. 4a becomes:

$$E = \frac{M}{\tau_e(t)} \int_{\tau_e(t)}^{\infty} y(\tau)\tau \, \mathrm{d}\tau \tag{4b}$$

This so-called stochastic erosion process is schematically depicted in Fig. 4, showing that erosion can also occur when the mean bed shear stress $\overline{\tau}_b$ is smaller than τ_e.

Note that the bed shear stress also varies in space, even for flow over a flat bed/wall. Hence, basically, the PDF should contain a spatial component as well. As no information on such spatial distributions is known at present, we confine ourselves to time effects only, and the stochastic bed shear stress should be considered as a spatial mean parameter.

The critical value for erosion τ_e may also have a probability density function. No information exists on such a function, though Partheniades (1965) reasons that this function may be quite narrow. However, the precise form of τ_e is not important for the arguments in the next sections, and it is assumed that τ_e can be represented by one value only.

2.4. Flocculation

The settling velocity W_s of cohesive sediment particles is governed by flocculation processes. It can be shown (Winterwerp, in press) that at low concentrations the flocculation time of cohesive sediment particles higher in the water column is so large that the floc size is mainly determined by the near bed turbulent flow conditions. Under tidal conditions, the high turbulent stresses around maximal flow and ebb velocities form the dominant conditions. Hence, at low-concentrations, variation in flocculation over the water depth or with time does not play an important role (see also Hill *et al.*, 2001).

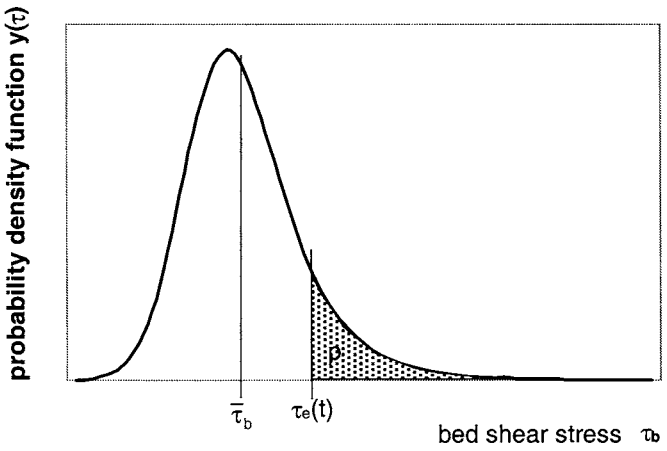

Fig. 4. Conceptual picture of stochastic erosion process.

At high-concentrated conditions, flocculation is important and results in variations in floc size over the water depth, and throughout the tide (*e.g.*, Winterwerp, 2002). However, in these cases, deposition results in the formation of fluid mud, and water-bed exchange processes are governed by other processes than treated in this paper. Here, we do not consider the effects of flocculation.

3. THE BED SHEAR STRESS DISTRIBUTION

Obi *et al.* (1996) have summarised statistical parameters of wall shear stresses measured in air, oil and water at a variety of Reynolds numbers. Mean values, based on 14 observations, are summarised in Table 1.

The following definitions are used, where $y(\tau)$ is the probability density distribution of the instantaneous bed shear stress τ:

mean: $$\overline{\tau} = \int_{-\infty}^{\infty} \tau y(\tau) \mathrm{d}\tau$$

relative standard deviation: $$\sigma = \frac{1}{\overline{\tau}} \sqrt{\int_{-\infty}^{\infty} (\tau - \overline{\tau})^2 y(\tau) \mathrm{d}\tau}$$

(coefficient of) skewness: $$m_3 = \frac{1}{\sigma^3} \int_{-\infty}^{\infty} (\tau - \overline{\tau})^3 y(\tau) \mathrm{d}\tau$$

(coefficient of) kurtosis: $$m_4 = \frac{1}{\sigma^4} \int_{-\infty}^{\infty} (\tau - \overline{\tau})^4 y(\tau) \mathrm{d}\tau$$

Miyagi *et al.* (2000) concluded from a series of experiments in air that these statistical parameters are a function of Reynolds number. However, the results of Obi *et al.* (1996) can be regarded as representative for high-Reynolds numbers. More information can be found in Gust and Müller (1997), who present PDF's of the bed shear stress for a variety of experimental devices.

Table 1. Bed shear stress statistics by Obi *et al.* (1996).

relative standard deviation	(coefficient of) skewness	(coefficient of) kurtosis
0.4	1.0	4.5

No theory exists at present to predict the actual shape of the probability density function. However, it is known that the function should be skewed towards higher shear stresses because of the occurrence of turbulent bursts. Therefore the heuristic approach by Petit (1999) is followed. He proposed the following three-parameter density function:

$$y(\tau;\mu,m,s) = \int_{-\infty}^{\infty} \frac{1}{m}\exp\left\{-\frac{\nu}{m}\right\} n(\tau+m-\mu;\nu,s)\mathrm{d}\nu = \\ = \frac{1}{2m}\left(1+\mathrm{erf}\left\{\frac{m(\tau+m-\mu)-s^2}{ms\sqrt{2}}\right\}\right)\exp\left\{-\frac{2m(\tau+m-\mu)-s^2}{2m^2}\right\} \tag{5}$$

in which

$$n(\tau+m-\mu;\nu,s) = \frac{1}{s\sqrt{2\pi}}\exp\left\{-\frac{1}{2}\left(\frac{\tau+m-\mu-\nu}{s}\right)^2\right\} \tag{5a}$$

Note that Eq. 5 allows for negative bed stresses, *i.e.*, stresses opposite the mean flow direction, which are known to occur. The nth moment M_n of the density function reads:

$$M_n = \int_{-\infty}^{\infty} \tau^n y(\tau;\mu,m,s)\mathrm{d}\tau \tag{6}$$

and the parameters of the PDF follow from:

$$\mu = M_1 \quad , \quad m = \frac{1}{2}\left(8M_1^3 - 12M_1M_2 + 4M_3\right)^{1/3} \\ \text{and} \quad s = \frac{1}{2}\sqrt{-2^{4/3}\left(2M_1^3 - 3M_1M_2 + M_3\right)^{2/3} - 4M_1^2 + 4M_2} \tag{7}$$

This density function is compared with the non-dimensionalised data by Obi *et al.* in Fig. 5, in which $\tau_w^* = (\tau-\mu)/\sigma$. A reasonable agreement is shown, bearing in mind that Eq. 5 does not contain a parameter for the flatness of the distribution.

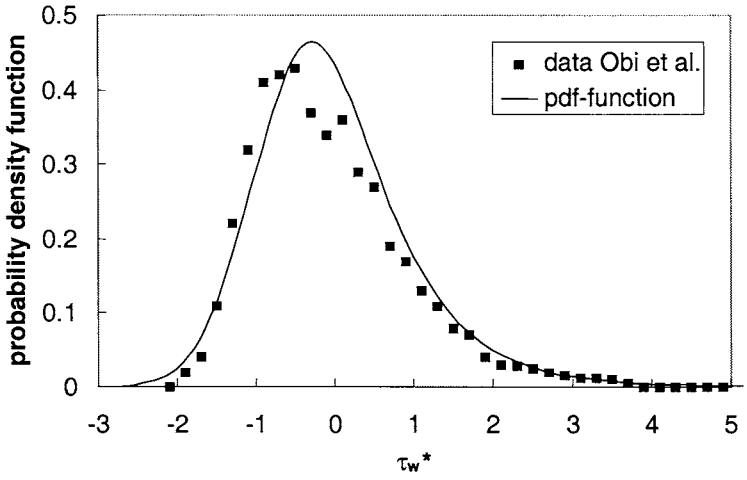

Fig. 5. Comparison of Eq. 5 with data by Obi *et al.* (1996).

4. RE-ANALYSIS OF KRONE'S (1962) EXPERIMENTS

Application of the physical picture described above to the experiments by Krone (Krone, 1962; Einstein and Krone, 1962) implies elaboration of the following mass balance equation, assuming homogeneous conditions in longitudinal direction:

$$\frac{\mathrm{d}h\overline{c}}{\mathrm{d}t} = E - D = \frac{M}{\tau_e(t)} \int_{\tau_e(t)}^{\infty} y(\tau)\tau \, \mathrm{d}\tau - W_s c_b \tag{8}$$

As the settling velocity of the sediment in the flume is very small (*e.g.*, Section 1), virtually no vertical concentration gradient is to be expected. Note that the solution of Eq. 8 does not yield an exponential decay, as observed by Krone.

Yet, this exponential decay was observed but at concentrations below about 300 mg/l (see Fig. 1). Below this concentration, the deposition flux is very small (*i.e.*, $\leq 0.3\text{x}10^{-6}$ kg/m^2/s), in fact smaller than the potential erosion flux. As also the deposited material can increase in strength significantly during the experimental time of 100 to 200 hours, the erosion flux is limited by the availability of erodible material. This explains why the settling curve is not linear in the initial phase of the deposition experiment when $c > 300$ mg/l. Therefore, the mass balance for Krone's experiments is rewritten as:

$$\frac{\mathrm{d}h\overline{c}}{\mathrm{d}t} = -D + \alpha E = -W_s c_b + \alpha \frac{M}{\tau_e(t)} \int_{\tau_e(t)}^{\infty} y(\tau)\tau \, \mathrm{d}\tau \tag{9}$$

where E is to be regarded as the *potential* erosion rate. The coefficient α is the fraction of sediment that can be eroded: $\alpha = 1$ for $D \geq E$, $\alpha = W_s c_b / M$ for $D < E$. Note that in the latter case, Eq. 9 is very similar to Krone's deposition formula, in which p represents the probability that the bed shear stress exceeds the critical shear stress for erosion of recently deposited material (*e.g.*, Fig. 4).

The probability density function, as constructed with Eq. 5 and the parameters of Table 1, for three of Krone's sedimentation experiments (V = 0.50 ft/s, τ_b = 0.0515 Pa; V = 0.44 ft/s, τ_b = 0.0415 Pa; V = 0.37 ft/s, τ_b = 0.0305 Pa) is shown in Fig. 6.

The mass balance equation (Eq. 9) still contains the two unknowns M and τ_e. These can be obtained from an analysis of one of Krone's experiments. For this, his V = 0.50 ft/sec experiment is used, yielding the values in Table 2, obtained after some trial and error. Note that in the present analysis, the variation of τ_e with time does not have to be known precisely, because of the large time scales of the processes. This is, of course, not always the case.

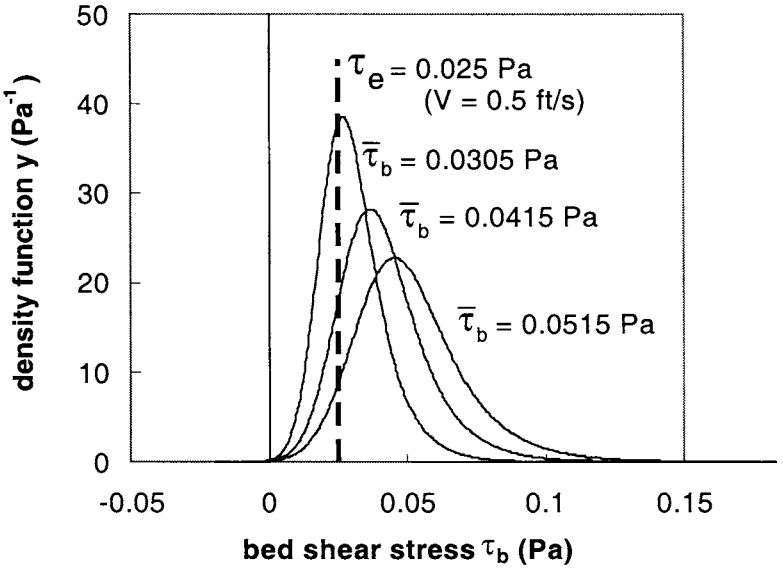

Fig. 6. Bed shear stress PDF of Krone's experiments (1962) constructed with Eq. 5.

Table 2. Erosion/deposition parameters Krone's V = 0.5 ft/s experiment (1962).

c_b	W_s	$\tau_e(t = 0)$	M
$\overline{c}$	$6.6 \cdot 10^{-6}$ m/s	0.025 Pa	$5.5 \cdot 10^{-8}$ kg/m^2/s

The resulting hind-cast with Eq. 9 of Krone's $V = 0.50$ ft/s test is shown in Fig. 7, showing a good agreement with the original data, including the observed transition from a non-linear to linear decay rate. With the parameters of Table 2 and the PDF of Fig. 6, also Krone's $V = 0.44$ ft/s and $V = 0.37$ ft/s experiments have been simulated. The results are also presented in Fig. 7, showing good agreement with the data for the $V = 0.44$ ft/s experiment, and less favourable agreement with the data for the $V = 0.37$ ft/s experiment.

It is certainly possible to tune M and τ_e further to obtain an even better overall agreement. This is not done however, as the purpose of this paper is to analyse Krone's experiments in a qualitative way, explaining the physical meaning of the "critical shear stress for deposition" and the difference in deposition rate at lower and higher concentrations. Moreover, no information is available on the accuracy of Krone's data; in particular the bed shear stress must have been difficult to measure in the smooth flume applied by Krone. A small error in τ_b will have a substantial influence on the surface below the PDF-function beyond τ_e of Fig. 6.

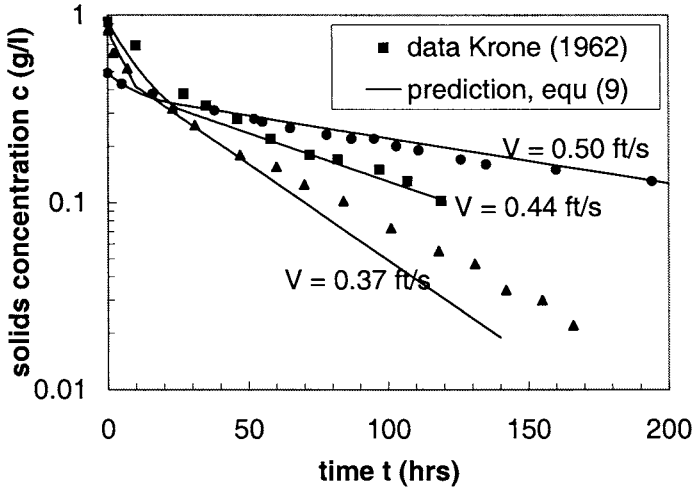

Fig. 7. Decay with time of suspended sediment concentration; comparison of measurements by Krone (1962) and prediction by Eq. 9.

4. DISCUSSION AND CONCLUSIONS

Krone's 1962 sedimentation measurements have been re-analysed in the preceding sections. Krone's observation that some of the settling particles are re-entrained into the flow shortly after their deposition, has been elaborated. It is argued that this so-called probability of resuspension is the result of two mechanisms:

1. The bed shear stress is stochastic in nature, which can be described through a skewed probability density function.
2. The erodibility of freshly deposited cohesive sediment particles decreases with time, as the critical shear stress of erosion increases with time as a result of consolidation and physico-chemical effects.

Winterwerp (in press) showed that at low suspended sediment concentration, flocculation processes are so slow, that the floc size, hence settling velocity, is fully determined by near-bed high-energetic conditions, and does not vary over the water depth. So, floc formation and floc breakup processes will only play a role in the sedimentation process at high-concentrated conditions (Winterwerp, 2002).

It is argued that the so-called critical shear stress for deposition τ_d does not exist: this stress represents a critical shear stress for erosion of freshly deposited sediment in the experiments discussed in this paper. It is remarkable that this interpretation, which was also given by Krone in his original report, was lost in the decades following these experiments.

These conclusions imply that the common engineering practice, in which the water-bed exchange processes are described with a combination of the so-called Krone's deposition formula and Partheniades' erosion formula (*e.g.*, Ariathurai and Arulanandan, 1978), does not represent physics properly.

Thus, it is proposed to model the sedimentation flux for applications at low-concentrated cohesive sediment suspensions with numerical engineering models simply by the flux itself:

$$D = W_s c_b \tag{10}$$

in which the settling velocity W_s may be a function of time, but does not vary over the water depth. It is further proposed not to use the PDF-distribution described here, or otherwise, in engineering studies as the local bed shear stress and the erosion parameters τ_e and M are poorly known in general. This approach agrees with Sanford and Halka (1993) and the data they present. The increase of τ_e with time should be modelled through a consolidation model when evolution in time is important, for

instance over a spring-neap cycle, or in case of seasonal effects. The increase of τ_e during slack water in a semi-diurnal tidal cycle is often too small to justify its modelling.

It is noted that τ_e may decrease in time as well because of swell, liquefaction, *etc.* as a result of turbulent stresses and wave-induced stresses. Ultimately, τ_e may vanish, if time scales are long enough, as argued in Winterwerp and Van Kesteren (2004).

This sedimentation concept sheds another light on the paradigm of mutual exclusion of simultaneous erosion and deposition. Such conditions indeed may occur, either in the laboratory, or in the field, but should be attributed to an increase of τ_e with time, as suggested before by Lick and Kang (1987).

The arguments above can easily be implemented in the approach by Mehta and Lott (1987) and Verbeek *et al.* (1993) to describe the sedimentation behaviour of graded sediments, as discussed in Section 1. If necessary, the effect of flocculation can be accounted for by an appropriate flocculation model.

In case that the sediment concentrations are high, sediment-turbulence interactions start to play a role, affecting the near bed shear stresses through the formation of fluid mud. Moreover, flocculation effects generally become important. However, the sedimentation flux is still described with Eq. 10, *e.g.*, Le Hir *et al.* (2001) and Winterwerp (2002).

Some decades ago, the occurrence and behaviour of wash load was attributed to non-saturation of the sediment transport capacity of a flow. Partheniades (1977) argued that this concept could not explain observations on wash load. He proposed an alternative view in which he accounted for the stochastic behaviour of the bed shear stress. He reasoned that if the entire τ_b-PDF would fall in between the critical shear stresses for deposition $\tau_{d,i}$ and erosion $\tau_{e,i}$ for a particular sediment fraction i, no exchange of that sediment fraction between water and bed would be possible:

$$\tau_{d,i} < \tau_b < \tau_{e,i} \tag{11}$$

Hence, Eq. 11 would yield the condition for the existence of wash load.

However, it is now know that τ_b can be almost zero for at least part of the time. Moreover, it was argued in this paper that the critical shear stress for deposition does not exist as such. This implies that Eq. 11 cannot yield the conditions for wash load. The arguments in this paper suggest that the behaviour of wash load is the result of a large potential erosion rate, exceeding the depositional flux greatly, or, vice versa, a small depositional flux because of small settling velocity and/or small suspended sedi-

ment concentration, smaller than the potential erosion rate. In other words, under wash load conditions, depositing particles are re-entrained immediately by the turbulent flow.

The deposition formula, proposed in this paper, allows for a continuous sedimentation flux, even for the finest sediment fractions. Hence, even some material of the finest fractions may be found in the river or sea bed if this fine wash load material is cohesive, or can be entrained into the bed by other mechanisms, such as pore water underpressure, armouring, *etc.* This is the case, for instance, in the North Sea bed, which surface sediments contain a few percent fines, even though the bed is reworked regularly by waves and fishing activities. It is to be noted though that colloidal material is not likely to be found in the bed, even under very calm conditions. Moreover, suspensions of colloidal particles are largely affected by the chemical composition of the water column.

REFERENCES

Ariathurai, C.R. and K. Arulanandan. 1978. Erosion rates of cohesive soils. *Journal of the Hydraulics Division*, ASCE, (104) 2, 279-282.

Christensen, B.A. 1965. Discussion of erosion and deposition of cohesive soils. *Journal of the Hydraulic Division*, ASCE, (91) 5, 301-308.

Einstein, H.A. and R.B. Krone. 1962. Experiments to determine modes of cohesive sediment transport in salt water. *Journal of Geophysical Research*, (67) 4, 1451-1461.

Gust, G. and V. Müller. 1997. Interfacial hydrodynamic and entrainment functions of currently used erosion devices. In: *Cohesive Sediment, 4th Nearshore and Estuarine Cohesive Sediment Transport Conference.* Burt, N., R. Parker and J. Watts (eds.), John Wiley & Sons, New York, 149-174.

Hill, P.S., G. Voulgaris and J.H. Trowbridge. 2001. Controls on floc size in a continental shelf bottom boundary layer. *Journal of Geophysical Research*, (106) C5, 9543-9549.

Krone, R.B. 1962. *Flume studies of the transport of sediment in estuarial shoaling processes.* Final Report, Hydraulic Engineering Laboratory and Sanitary Engineering Research Laboratory, University of California, Berkeley, USA.

Krone, R.B. 1993. Sedimentation revisited. In: *Nearshore and Estuarine Cohesive Sediment Transport.* Mehta, A.J. (ed.), American Geophysical Union, Coastal and Estuarine Studies, 108-125.

le Hir, P., P. Bassoulet and H. Jetsin. 2001. Application of the continuous modelling concept to simulate high-concentrated suspended sediment in a macro-tidal estuary. In: *Coastal and estuarine Fine Sediment Processes*. McAnally, W.H. and A.J. Mehta (eds.), Elsevier, Amsterdam, 229-248.

Lick, W. and S.W. Kang. 1987. Entrainment of sediments and dredged materials in shallow lake waters. *Journal of Great Lakes Research*, (13), 4, 619-627.

Mehta, A.J. 1973. *Depositional behaviour of cohesive sediments*. PhD dissertation, University of Florida, Gainesville, USA.

Metha, A.J. and E. Partheniades. 1975. An investigation of the depositional properties of flocculated fine sediments. *Journal of Hydraulic Research*, IAHR, (13) 4, 361-381.

Mehta, A.J., E. Partheniades, J.G. Dixit and W.H. McAnally. 1982. Properties of deposited kaolinite in a long flume. In: *Proceedings of the ASCE Hydraulics Division Conference on Applied Research to Hydrodynamic Practice*, 594-603.

Mehta, A.J. and J.W. Lott. 1987. Sorting of fine sediment during deposition. In: *Proceedings of the Conference on Advances in Understanding Coastal Sediment Processes*, (1) 348-362.

Miyagi, N., M. Kimura, H. Shoji, A. Saima, C.-M. Ho, S. Tung, and Y.-C. Tai. 2000. Statistical analysis on wall shear stress of turbulent boundary layer in a channel flow using micro-shear stress imager. *International Journal of Heat and Fluid Flow*, (21) 576-581.

Obi, S., K. Inoue, T. Furukawa and S. Masuda. 1996. Experimental study on the statistics of wall shear stress in turbulent channel flow. *International Journal of Heat and Fluid Flow*, (17) 187-192.

Partheniades, E. 1965. Erosion and deposition of cohesive solid. *Journal of the Hydraulics Division, ASCE,* (91) HY1, 105-139.

Partheniades, E., R.H. Cross and A. Ayora. 1968. Further research on the deposition of cohesive sediments. In: *Proceedings of the 11th Conference on Coastal Engineering*, (1) 723-72.

Partheniades, E. and R.E. Paaswell. 1970. Erodibility of channels with cohesive boundary. *Journal of the Hydraulics Division*, ASCE, (96) HY3, 755-771.

Partheniades, E. 1977. Unified view of wash load and bed material load. *Journal of the Hydraulics Division*, ASCE, (103) HY9, 1037-1057.

Partheniades, E. 1986. The present state of knowledge and needs for future research on cohesive sediment dynamics. *Proceedings of the 3rd International Symposium on River Sedimentation*, 3-25.

Petit, H.A.H. 1999. Note on the use of non-symmetrical probability density functions in Van Rijn's stochastic transport formula. In: *Stone stability - Annual Report,* Report Q2539. WL|Delft Hydraulics, Delft, The Netherlands.

Sanford, L.P. and J.P. Halka. 1993. Assessing the paradigm of mutually exclusive erosion and deposition of mud, with examples from upper Chesapeake Bay. *Marine Geology*, (114) 37-57.

Self, R.F.L., A.R.M. Nowell and P.A. Jumars. 1986. Factors controlling critical shear for deposition and erosion of individual grains. Marine Geology, 86, 181-199.

Teeter, A.M. 2001. Clay-silt sediment modelling using multiple grain classes. Part II: Application to shallow water resuspension and deposition. In: *Coastal and estuarine Fine Sediment Processes*, McAnally, W.H. and A.J. Mehta (eds.), Elsevier, Amsterdam, 173-185.

Verbeek, H., C. Kuijper, J.M. Cornelisse and J.C. Winterwerp. 1993. Deposition of graded natural muds in The Netherlands. In: *Nearshore and Estuarine Cohesive Sediment Transport*, Mehta, A.J. (ed.), American Geophysical Union, 185-204.

Winterwerp, J.C. 2002. On the flocculation and settling velocity of estuarine mud. *Continental Shelf Research*, (22) 1339-1360.

Winterwerp, J.C. In press. Equilibrium and non-equilibrium floc sizes; or: flocculation takes time. In: *Flocculation in engineered and natural systems.* Droppo, I.G., G.C. Leppard, S.N. Liss and T.G. Milligan (eds.), CRC Press, Boca Raton.

Winterwerp, J.C. and W.G.M. Van Kesteren. 2004. *Introduction to the physics of cohesive sediments in the marine environment.* Elsevier, Amsterdam.

Estuarine and Coastal Fine Sediments Dynamics
J.P.-Y. Maa, L.P. Sanford and D.H. Schoellhamer (editors)

A preliminary study on the hindered settling of kaolinite flocs

Dankers P.J.T.[a], J.C. Winterwerp[b,c], W.G.M. van Kesteren[c]

[a]Hydraulic Engineering Section, Delft University of Technology,
P.O. Box 5048, 2600 GA Delft, The Netherlands
[b]Environmental Fluid Mechanics Section, Delft University of Technology
P.O. Box 5048, 2600 GA Delft, The Netherlands
[c]WL|Delft Hydraulics, P.O. Box 117, 2600 MH Delft, The Netherlands

KEY WORDS
Hindered settling, mud flocs, settling velocity, kaolinite

This paper describes hindered settling experiments carried out with kaolinite suspensions in settling columns. In these columns, the settling velocity of the interface and the concentration in time at three or four specific heights were determined. From these measurements the gelling concentration and the settling velocity of the suspension could be determined. A mean gelling concentration of $C_{gel} = 81$ g/l was found and the settling velocities of the suspensions ranged from $w_s = 0.019$ mm/s for a suspension of 108 g/l to $w_s = 0.17$ mm/s for a suspension of 27 g/l. The settling behaviour was analysed with Kynch's theory which was found to be applicable to the measurements. In accordance with this theory, the experimental data could be divided into two groups. When the initial concentration was around a concentration of 35-46 g/l the settling behaviour changed from settling with two interfaces to settling with one interface. The experimental data was also compared with a theoretical model. The occurrence of both types of settling behaviour implied that the return flow depicts non-linear effects.

1. INTRODUCTION

High concentrations of mud flocs are present in natural environments such as estuaries, but also around dredging locations. The dispersion and the residence time of the fine

fraction in the water column is an important factor in environmental studies. Especially, as high concentrations of fine sediment may influence primary production, the growth of plants and the forage possibilities of animal species. The dispersion and residence time is determined by the settling velocity of the mud flocs. At high sediment concentrations the mud flocs interfere with each other and their settling velocity is determined by the hindered settling effect. Information, data and literature on consolidation of mud flocs is available, but data on the hindered settling of mud flocs is scarce, probably because hindered settling of mud flocs is difficult to measure.

A detailed review on hindered settling of sand was given by Scott (1984). Part of these review results were presented elsewhere (Mandersloot *et al.*, 1986). The results showed that hindered settling is often described with models which are based on the well known formula by Richardson and Zaki (1954). For hindered settling of mud flocs, Mehta (1986) suggested a modified form of the Richardson and Zaki formula:

$$w_s = w_{s,0}(1 - k\phi_p)^n \tag{1}$$

where w_s is the effective settling velocity, $w_{s,0}$ the settling velocity of a single particle in still water, k is an empirical parameter, ϕ_p is the volumetric concentration of primary particles, $\phi_p = c/\rho_s$ in which c is the mass concentration and ρ_s the density of the sediment, and n is a function of the particle Reynolds number. Although Mandersloot *et al.* (1986) and Scott (1984) focused mainly on massive, Euclidean particles (sand), Winterwerp (2002) reasoned that their rationale can be applied to cohesive sediments as well. He suggests that, as each individual floc within a suspension is considered to settle in the rest of the suspension, this would result in three hindering effects:

- Return flow and wake formation. A settling particle generates a return flow and a wake. Other neighbouring particles will be influenced by this and their effective settling velocity will be decreased by a factor (1-ϕ), where ϕ is the volumetric concentration of flocs.
- Viscosity. Each individual particle within a suspension is considered to fall in the remainder of that suspension which has an increased viscosity.
- Buoyancy or reduced gravity. For the same argument, an individual particle settles in a suspension with an increased bulk density. The effective settling velocity is decreased by a factor (1-ϕ_p).

This led to a new theoretically derived formula for the hindered settling of mud flocs:

$$w_s = w_{s,0}\frac{(1-\phi)^m(1-\phi_p)}{1+2.5\phi} \tag{2}$$

Here the factor (1-ϕ) accounts for the return-flow effect, (1-ϕ_p) accounts for the buoyancy effect and (1+2.5ϕ) accounts for augmented viscosity. The exponent m is an empirical parameter to account for possible nonlinear effects. When the return flow effect is linear, (*i.e.*, m = 1), only the volume effect of a suspension settling in a liquid is taken into account. The downward flux of sediment is thus expected to create an equal upward flux of water with sediment. When nonlinearity is taken into account, all the effects generated by a settling particle in a suspension (*e.g.*, acceleration, deceleration of flow and the curvature of streamlines) are incorporated.

The volumetric concentration is herein related to the gelling concentration ($\phi \equiv c/c_{gel}$), in which $c_{gel}$is the concentration at which flocs become space-filling and form a network structure, called a gel, and a measurable strength builds up. The volumetric concentration, ϕ can thus become larger than unity when consolidation takes place. The volumetric concentration of primary particles is also related to the gelling concentration, $\phi_p = c/\rho_s = c_{gel}\phi/\rho_s$. Winterwerp (2002) compared Eq. 2 to data by fitting the model parameters and not actually using parameter values derived from data. A reasonable fit was obtained. The objective of this study is to test this theoretical formula against data from which the necessary parameter values for the model can be obtained. Experiments were carried out in the Laboratory of Environmental Fluid Mechanics at the TU Delft, The Netherlands, to obtain a data set from which gelling concentrations and settling velocities of the different suspensions could be determined. These parameters were determined by visual observations of the interface and conductivity measurements at several heights in the suspension in the settling column. First the hindered settling theory and tools for data analysis are given, whereafter this theory is applied to the experimental data.

2. KYNCH'S THEORY

The theory of sedimentation of highly concentrated suspensions was first studied by Kynch (1952). He introduced an empirical relationship between settling velocity and local sediment concentration as he assumed that at any point in a suspension the fall velocity of particles depends only on the local concentration of particles. This implies that the settling process can be determined from a continuity equation. In this section Kynch's theory with some further elaborations by Kranenburg (1992) is described.

First the particle transport flux is introduced:

$$S = w_s\phi \tag{3}$$

in which w_s the settling velocity. The effect of hindered settling is introduced by assuming

that the settling velocity is a decreasing function of the local concentration,

$$w_s = w_{s,0} f(\phi) \tag{4}$$

where $w_{s,0}$ is the settling velocity of a single particle in still water and $f(\phi)$ is a function that describes the effect of the concentration on the fall velocity, thus $f(0)$=1 and $f(1)$=0. The one-dimensional volume balance for a settling suspension can then be written as:

$$\frac{\partial \phi}{\partial t} + \frac{\partial S}{\partial z} = 0 \tag{5}$$

where t is time and z is height, positive upwards. When Eqs. 3, 4 and 5 are combined, this leads to the following equation:

$$\frac{\partial \phi}{\partial t} + w_{s,0} F(\phi) \frac{\partial \phi}{\partial z} = 0 \tag{6}$$

where

$$F(\phi) = \frac{\mathrm{d}}{\mathrm{d}\phi}[\phi f(\phi)] \tag{7}$$

Equation 6 comprises the 1-D simple wave equation. It describes the settling process of a cohesive sediment suspension in still water. It can be solved by integrating along characteristic lines in the (z, t) plane. These characteristic lines are given by

$$\frac{\mathrm{d}z}{\mathrm{d}t} = w_{s,o} F(\phi) = C_c \tag{8}$$

they present lines of equal concentration and C_c is the celerity (wave speed). Because the characteristic lines present lines of equal concentration (ϕ), the characteristics are straight lines in the physical plane and their height in time is given by:

$$z = z_0(\phi) + w_{s,0} F(\phi) t \tag{9}$$

where $z_0(\phi)$ represents the concentration distribution at $t = 0$.

Figure 1 shows two possible characteristics and settling curves for a settling suspension. If the initial concentration is low (Fig. 1a) there will be a distinct point of contraction (A). At the point of contraction the gelling point is reached. This is the volumetric concentration at which a space filling network appears, in other words, a bed starts to form. This

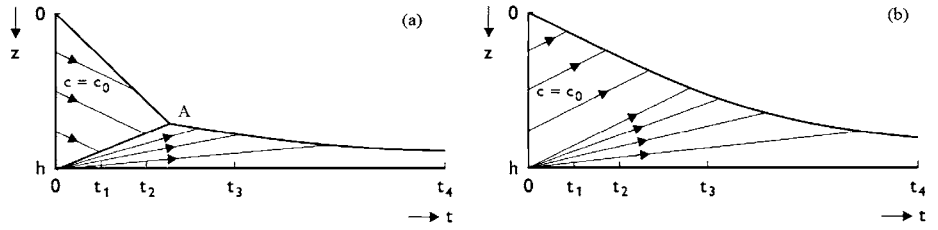

Fig. 1. Types of hindered settling: (a) low initial concentration, two interfaces develop; (b) high initial concentration, one interface develops (After Kranenburg, 1992).

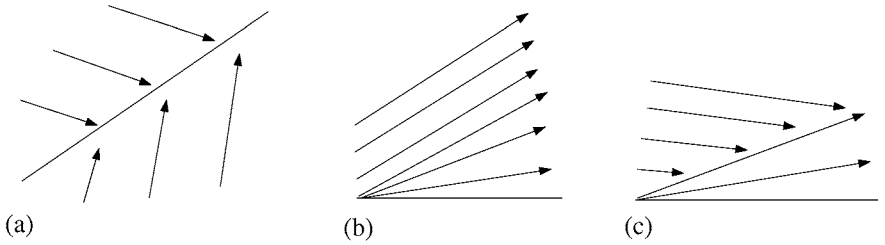

Fig. 2. Three possible types of characteristic wave paths. (a) Regular type; (b) Rarefaction type; and (c) Compound type (After Bartholomeeusen *et al.*, 2003).

point separates the hindered settling regime (steeper curve) from the consolidation regime (flat curve). In this research we only deal with the hindered settling regime; the right part of the settling curve is thus not taken into account. The second possible settling curve (Fig. 1b) is a concave, smooth line, when the initial volumetric concentration is larger than a specific concentration ($\phi > \phi_{cr}$), and indicates a different settling behaviour, or consolidation. The hindered settling phase is very short or absent in these cases.

The characteristics for both settling curves in Fig. 1 have a different appearance. When the lines converge and intersect, as in Figs. 1a, 2a and 2c, an interface develops. If such an interface develops it can be visualised by drawing a line from the origin to the gelling point. This line represents the interface of the rising bed. When the characteristic paths do not intersect, as in Figs. 1b and 2b, a rarefaction type occurs. The local wave speed in this case diverges away from the original characteristic towards the upper and lower side (Bartholomeeusen *et al.*, 2003).

The condition for convergence is that along a characteristic path the derivative of the height between two characteristics over the original height of these characteristics decreases as time elapses, $\mathrm{d}z/\mathrm{d}z_0 < 1$. In other words, the distance between two char-

acteristic lines becomes smaller with time and the concentration increases with depth $\mathrm{d}\phi/\mathrm{d}z_0 > 1$:

$$\frac{\mathrm{d}z}{\mathrm{d}z_0} = 1 + w_{s,0}\frac{\mathrm{d}F}{\mathrm{d}\phi}\frac{\mathrm{d}\phi}{\mathrm{d}z_0}t \tag{10}$$

As an interface develops when characteristic paths converge, Eq. 10 implies that an interface will therefore develop when $\frac{\mathrm{d}F}{\mathrm{d}\phi} < 0$. In settling columns this always occurs between the water above the suspension and the settling suspension (Fig. 1b). As the upper interface is always present (in a mono-dispersed suspension) it can be stated that when:

$$\frac{\mathrm{d}F}{\mathrm{d}\phi} < 0 \tag{11}$$

two interfaces develop (Fig. 1a) and when

$$\frac{\mathrm{d}F}{\mathrm{d}\phi} > 0 \tag{12}$$

one interface develops (Fig. 1b).

For both Eqs. 1 and 2, f decreases monotonically with ϕ (Fig. 3. The function F, however, behaves differently for both equations. In the case of Eq. 1, F has a minimum at a volumetric concentration ϕ_{cr}. This concentration indicates the change from Eq. 11 to Eq. 12, and thus, the change from the occurrence of two interfaces in a settling suspension to the occurrence of one interface. The function F of Eq. 2 shows different profiles depending on the choice of value for parameter m, an empirical parameter that cannot be quantified analytically. For $m = 1$, F decreases monotonically with ϕ, but for $m > 1$, F depicts a minimum. When $m = 1$ the return flow effect is linear, while when $m > 1$ there are nonlinear effects in the return flow. These nonlinear effects will lead to the occurrence of two or one interfaces, depending on the initial conditions, while a linear return flow will always give two interfaces. From the type of settling curves and the type of characteristics, one thus should be able to determine whether $m > 1$.

3. EXPERIMENTAL SET-UP AND METHODS

3.1. Experiments

The experiments were carried out in the Laboratory of Environmental Fluid Mechanics at Delft University of Technology. Small settling columns of 40 cm high with a diameter of 7 cm were used. The clay mineral kaolinite was used to make the suspensions.

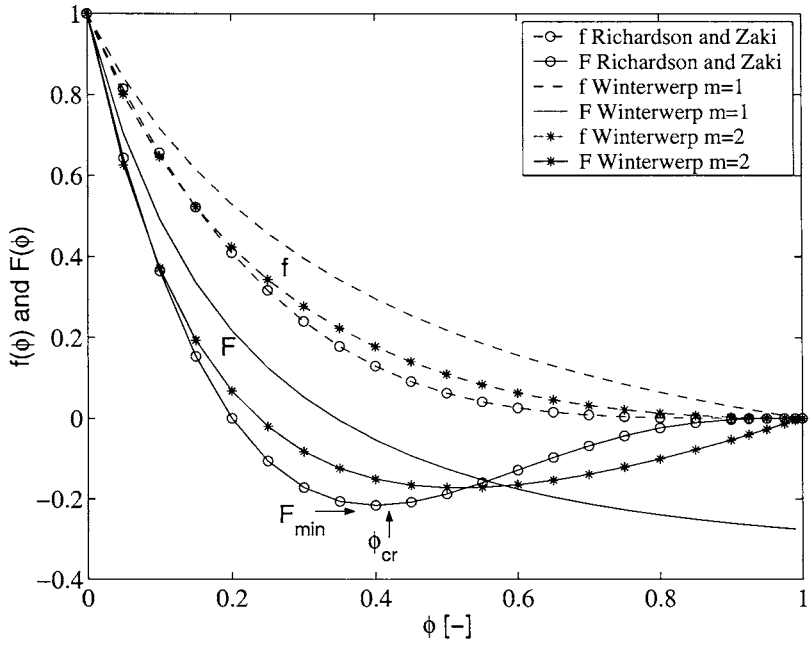

Fig. 3. Variation of hindered settling functions f and F with ϕ for Eq. 1($k = 1$, $n = 4$) and Eq. 2 ($m = 1$ and $m = 2$). Based on Kranenburg (1992) and Winterwerp (2002).

The mineral was prepared and diluted with salt water (5 promille) to a suspension of about 100-120 g/l. A 12 litre tank was filled with this mixture which was mixed thoroughly for at least 2 hours every day during at least two weeks, in order for the kaolinite suspension to reach a steady chemical state.

A total of 16 experiments was carried out in two series. The second series of experiments was performed two months later than the first series, but with the same mixture. For every experiment, a sample was taken from the tank and diluted with salt water to the desired initial concentration.

3.2. Settling of the interface

The lowering of the interface of the kaolinite suspensions was measured for various initial sediment concentrations in the settling columns. Before every experiment, the column was shaken gently, but thoroughly, in order to create a homogeneous mixture, but not disturbing the flocs. Thereafter the experiment started immediately. During the experiments the settling of the interface was observed visually. The height of the interface was recorded at an interval of one minute. When the settling slowed down strongly, *i.e.*, be-

yond the gelling point, the recording was done every 5 minutes. These measurements led to settling curves for the different suspensions. The bed interfaces could not be detected visually. Their settling curves are thus not available.

3.3. Concentration profiles

Sediment concentrations were measured using a conductivity probe developed by Delft Hydraulics. The principle of a conductivity concentration meter is based on the fact that the conductivity of a sediment mixture decreases when the concentration increases. The probe has four electrodes and is supplied with an alternating current to eliminate polarisation effects.

The aim was to measure the concentration at several heights during the settling and consolidation phase. Measuring concentrations in the vertical is a destructive process as the probe damages the structure of the bed. Therefore it was decided that every experiment should be repeated several times with the concentration measured at different heights. For the experiments in Series 1 three different levels were selected for every experiment, depending on the initial concentration and the expected level at which a bed structure would be formed. For the experiments in Series 2 four different levels were selected. In general one measurement was done in the top layer, one or two in the middle part and one 5-10 cm above the bottom of the column.

Before every measurement the probe was calibrated. To calibrate the probe the suspension had to settle first. Then, two samples were taken from the bed layer and one from the clear water layer with a pipette. The samples were placed in a small jar. The conductivity was measured and the density of the suspensions was determined with an Anton Paar density meter. Thereafter, the settled suspension in the settling column was mixed thoroughly and another sample was drawn from the suspension. From this sample, the density and conductivity were determined as well. With these four measurements calibration curves could be drawn for each experiment. Calibration before every experiment is necessary as the probe is sensitive to temperature changes and different amounts of solutes in the water. Nonetheless, during the experiments, which had a duration of approximately one hour, the temperature in the settling column always rose. This increased the conductivity which led to an under-estimation of the concentration. The maximum under-estimation of the data used in this analysis is around 5 g/l. Furthermore, due to the settings of the software of the conductivity probe, the measured concentrations has a resolution of ± 2 g/l. The data is not compensated for temperature change, because it is not known exactly when and how much the temperature changed in every experiment.

4. RESULTS

4.1. Settling curves and characteristic lines

The results of the visual observations of the settling interface are shown in Fig. 4. The height of the lines is normalised by the initial height and multiplied by 100. A majority of the lines have a similar appearance as the idealised settling curves in Fig. 1a. The curves for the lower concentrations show a kink with a clear inflection, *i.e.*, the point of contraction. The line from this point to the origin of the graph depicts the second interface of the settling suspension, the rising of the bed. For those lines with a high initial concentration in Fig. 4, this point of contraction is not clear or not present. These experiments showed a gradual transition from suspension to bed and a second interface does not exist (Fig. 1b).

The settling velocity of the suspensions and other experimentally derived parameters are given in Table 1. Only the velocities of the part above the point of contraction are elaborated as this research focuses on the hindered settling regime.

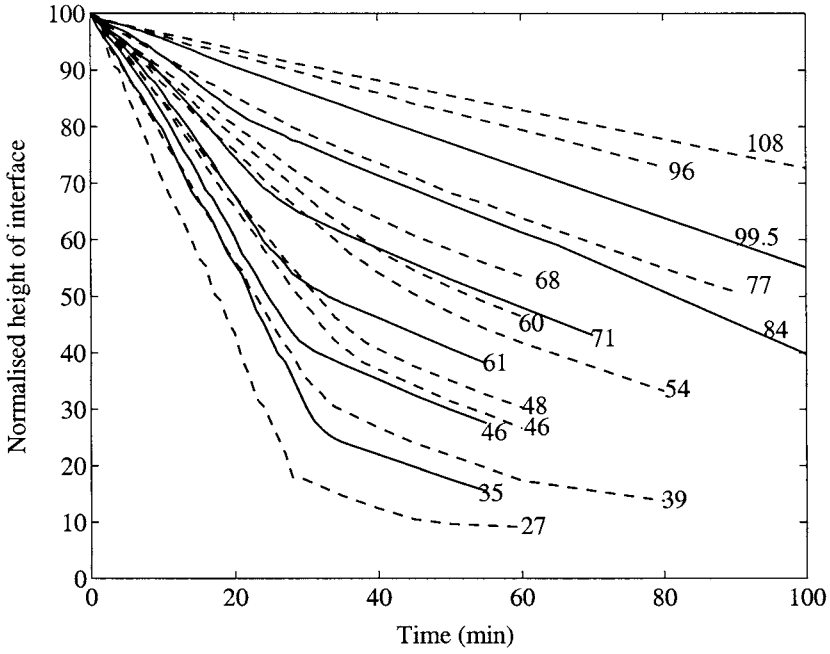

Fig. 4. The normalised settling curves of different kaolinite concentrations. Solid lines represent Series 1, dashed lines represent Series 2. Numbers indicate the initial concentration (g/l). The initial height varied between 34 and 37 cm.

Table 1. All experiments with their initial concentration, effective settling velocity and gelling concentration.

Id	Initial concentration (g/l)	w_s (mm/s)	c_{gel} (g/l)
30kol	35	0.134	66
40kol	46	0.111	83
50kol	61	0.071	87
60kol	71	0.058	90
70kol	84	0.052	-
80kol	100	0.028	-
10tt	27	0.170	-
20tt	39	0.133	80
30tt	46	0.101	67
40tt	48	0.096	77
50tt	68	0.067	88
55tt	54	0.075	85
60tt	77	0.059	-
70tt	60	0.044	83
80tt	96	0.022	-
90tt	108	0.019	-

In the settling curves lines of equal concentration, so called characteristic lines, were drawn for a further analysis of the occurrence of interfaces. Four examples of such settling curves with characteristic lines are shown in Figs. 5 and 6. Note however that many characteristic lines can be drawn only approximately, especially in the area around the second interface. Figure 5a clearly shows two interfaces. The first is the top interface, presented by the dot-dashed line, and the second interface where the characteristic lines converge. Figure 5b has a rather different appearance. It has only one interface, the top water-sediment interface, and the characteristic lines are diverging more, which implies:

- hindered settling with one interface ($\phi > \phi_{cr}$) or
- consolidation ($\phi > 1, c_0 > c_{gel}$)

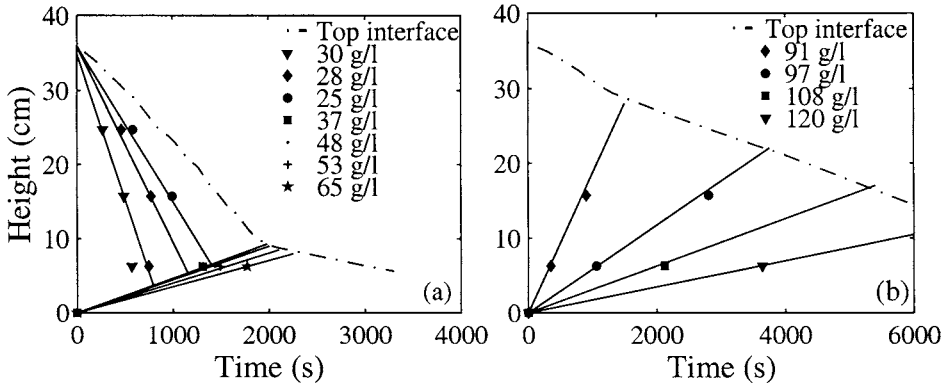

Fig. 5. Settling curves of experiment 30kol (c_0 = 35 g/l) and 70kol (c_0 = 84 g/l) with characteristic lines.

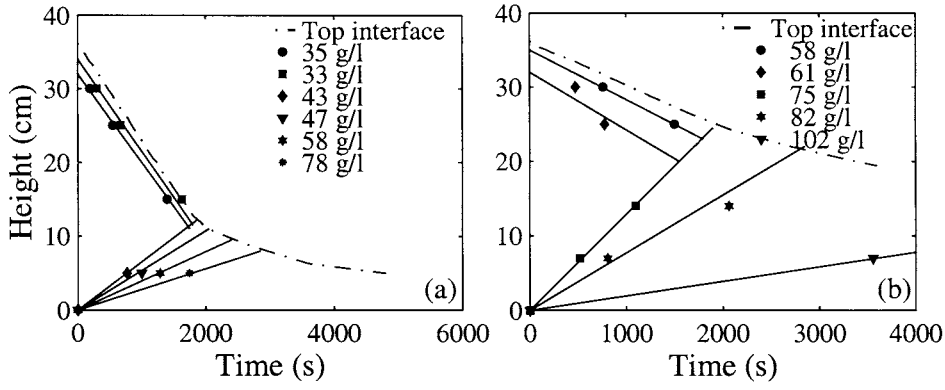

Fig. 6. Settling curves of experiment 20tt (c_0 = 39 g/l) and 5tt (c_0 = 68 g/l) with characteristic lines.

As c_0 = 84 g/l and c_{gel} = 81 g/l, the solid line drawn in this graph represents consolidation of the material. Figure 6a show a somewhat similar behaviour as that in Fig. 5a. It shows two interfaces, a point of contraction and converging characteristic lines. The point of contraction in this plot, as well as in Fig. 5a, is the gelling point or the structural density. It is however difficult to determine the point of contraction precisely. The change of slope can be abrupt, but also more gradual. Around the point of contraction, the concentration changes gradually from the initial concentration to the gelling concentration. Although this change is gradual, it still reveals the features of an interface. This in contrast to the settling type at which no interface between the suspension and the bed develops. Because of the gradual change, some of the characteristic lines may not start from the origin.

However, our data are not sufficient and accurate enough to draw such lines.

The characteristics in Fig. 6b are more ambiguous than the ones in Fig. 5b. At first sight, characteristic lines can be drawn and they reveal the occurrence of two interfaces. The occurrence of two interfaces is remarkable as at this concentration only one interface is to be expected. This will be explained in section 4.2. Note that characteristics can be drawn but their direction is not always unambiguous.

4.2. Concentration profiles

A typical result of the measurements with the conductivity probe is shown in Fig. 7. In Fig. 7a the passage of the top interface is very obvious at the three highest positions. When the interface passes, a rapid decrease in concentration occurs. The time series of the lowest position in Fig. 7 show the concentration at a position 5 cm and 6 cm above the bottom of the column respectively. This position was chosen to measure the rise of the sediment bed. This rise can be seen in the first part of the curve. After about half an hour this bed building stops and the concentration does not increase with time anymore. This implies that the suspension has attained the gelling concentration at this point. When consolidation is ignored, the flocs settling on the bed at that moment do not increase the density at that specific height anymore but cause a rise of the bed level and an increase in density in the layers above the measured layer.

The gelling concentration thus can be obtained from the bed level measurements of the conductivity meter. This has been done for most of the experiments, except for the ones in which the initial concentration was already higher than the gelling concentration, or when the conductivity probe was placed too high. Table 1 shows the gelling concentrations which are obtained with this method. From these values a mean value of $c_{gel} = 81 \pm 8$ g/l is obtained.

Another parameter that can (partly) be obtained from the concentration time series is the parameter m that accounts for nonlinearity in the return flow effect in Eq. 2. The change in concentration in the curve at the lowest position in Fig. 7a is not as abrupt as with the passage of the top interface (the lines of the three highest positions) or as the rising profile in Fig. 7b. It was explained in Section 2 that a second interface, the one of the rising bed, increases rapid and strongly in concentration. In Fig. 7a we see a more gradual change in concentration, which implies that a second interface is not present. Furthermore, Fig. 5 also indicates that at higher concentrations only a top interface exists. This would mean that for the present experiments one or two interfaces may develop, depending on the initial concentration. In Eq. 2 this implies $m > 1$, thus nonlinear return flow effects do occur. We found, from observations in the settling column and by comparing the rising bed in the concentration time series, that the settling behaviour

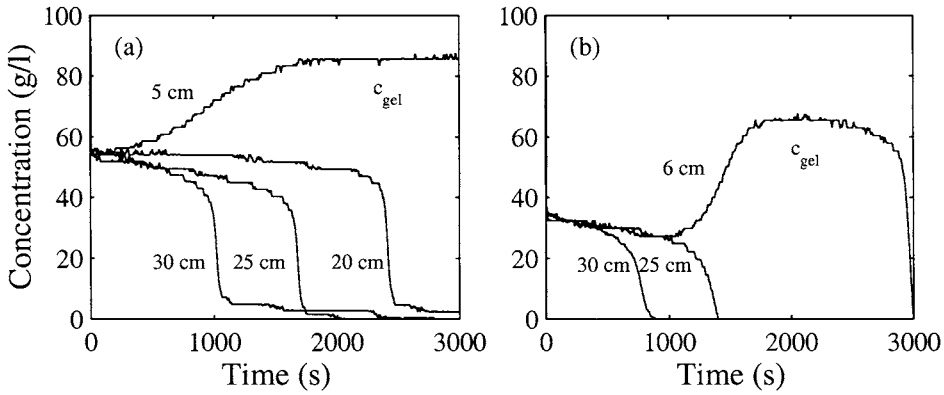

Fig. 7. Concentration time series at selected heights above the bottom. (a) For experiment 55tt with initial concentration c_0 = 54 g/l, and (b) for experiment 30kol with initial concentration c_0 = 35 g/l.

changed when $35 < c < 46$ g/l, or $0.53 < \phi_{cr} < 0.55$ for the current experiments with kaolinite. To calculate ϕ_{cr} we used the specific gelling concentration per experiment (see Table 1) and not the mean gelling concentration. Considering $\mathrm{d}F/\mathrm{d}\phi = 0$ at $\phi = \phi_{cr}$, m is obtained as follows:

$$m = \frac{1}{2}\frac{5\phi_m^2 - 2\phi_m + 4 + \sqrt{25\phi_m^4 + 60\phi_m^3 - 116\phi_m^2 + 64\phi_m + 16}}{\phi_m(2 + 5\phi_m)} \tag{13}$$

from which we find $m \approx 2.0$.

5. DISCUSSION

In this paper experiments on the hindered settling of mud flocs are described. Firstly, the settling behaviour of highly concentrated cohesive material suspensions is described and compared to Kynch's theory. Secondly, from the experiments the values of typical hindered settling parameters were determined. A method was developed to determine these values. The parameter values are used to validate the hindered settling formula (Eq. 2) for mud flocs. The relevant parameters that needed to be determined were the gelling concentration (c_{gel}), the coefficient that accounts for nonlinearity in return flow (m) and the settling velocity of single flocs in still water ($w_{s,0}$). The gelling concentration could be derived from the conductivity measurements. The conductivity time series at a height of 5-10 cm in a 40 cm settling column gave a good indication of the gelling concentration.

The measured gelling concentration differed for every settling experiment, but always was within the range of 66 and 90 g/l, with a mean of $c_{gel} = 81 \pm 8$ g/l. It was expected that the gelling concentration would decrease with increasing concentration due to the more possible collisions, the longer settling time and therefore larger flocs. This, however, did not seem to be the case for the present experiments.

The parameter m, which accounts for nonlinearity in the return flow, could be determined when ϕ_{cr} was known. The latter parameter could be derived from visual observations of the settling suspension and from the shape and especially the steepness of the conductivity time series close to the bed. This led to a value of $m = 2$. It is difficult, however, to determine the value of ϕ_{cr} and thus m accurately. The parameter m may therefore vary around 2. Most likely these parameters change in value when different clay minerals are used and when in experiments with one material the samples have a different stress history or when a different sample preparation procedure is applied.

Another method to determine the m parameter is to analyse characteristic paths from the settling suspension. When the characteristic paths converge and intersect a second interface will develop, while this will not happen with non-intersecting characteristics. From the occurrence of intersecting and non-intersecting paths in different experiments one will be able to determine the concentrations at which the settling behaviour changes. This method shall be used at a later stage of our research.

The value of $w_{s,0}$ could not be determined from the experimental data directly; it needs to be determined from model fitting.

6. CONCLUSIONS

This paper describes measurements of hindered settling velocities for highly concentrated mud suspensions. Simple techniques as visual observations of the settling interface and concentration measurements with a conductivity probe were found to perform well and produce good data. The settling behaviour was analysed with Kynch's theory. This theory was found to be applicable. The suspensions were found to develop one or two interfaces while settling, depending on the initial concentration. Beyond a critical initial volumetric concentration the settling behaviour changes from two interfaces to one interface. The fact that both settling behaviours do exist means that in the proposed formula, $m > 1$, thus that the return flow effect needs to be nonlinear.

ACKNOWLEDGMENTS

This work is funded by the DIOC-Water Project (Transient processes in Hydraulic Engineering and Geohydrology) of Delft University of Technology.

REFERENCES

Bartholomeeusen, G., H. De Sterck, and G.C. Sills. 2003. Non-convex flux functions and compound shock waves in sediment beds. *Hyperbolic problems: Theory, numerics, applications: Proceedings of the ninth international conference on hyperbolic problems*, 347–356.

Kranenburg, C. 1992. *Hindered settling and consolidation of mud–analytical results.* Tech. rept. 11-92. Delft University of Technology, Delft.

Kynch, G.J. 1952. A theory of sedimentation. *Transactions of Faraday Society*, 48, 166–176.

Mandersloot, W.G.B., K.J. Scott and C.P. Geyer. 1986. Sedimentation in the hindered settling regime. In: *Advances in solid-liquid separation.* Muralidhare, H.S. (ed). Battle press, 63-77.

Mehta, A.J. 1986. Characterisation of cohesive sediment properties and transport processes in estuaries. In: *Estuarine Cohesive Sediment Dynamics.* Mehta, A.J. (ed), Springer, Berlin, 290-325.

Richardson, J.F. and W.N. Zaki. 1954. The sedimentation of a suspension of uniform spheres under conditions of viscous flow. *Chemical Engineering Science*, 3, 65–73.

Scott, K.J. 1984. *Hindered settling of a suspension of spheres; critical evaluation of equations relating settling rate to mean particle diameter and suspension concentration.* Tech. rept. 497. Chemical engineering research group, Pretoria, South Africa.

Winterwerp, J.C. 2002. On the flocculation and settling velocity of estuarine mud. *Continental Shelf Research*, 22, 1339–1360.

Estuarine and Coastal Fine Sediments Dynamics
J.P.-Y. Maa, L.P. Sanford and D.H. Schoellhamer (editors)

A parameterised consolidation model for cohesive sediments

de Boer, G.J. [a,b], L.M. Merckelbach[c] and J.C. Winterwerp[a,b]

[a]Environmental Fluid Mechanics Section, Delft University of Technology,
P.O. Box 5048, NL-2600 GA Delft, The Netherlands
[b]WL|Delft Hydraulics, P.O. Box 117, NL-2600 MH Delft, The Netherlands
[c]Royal Netherlands Institute for Sea Research (NIOZ),
P.O. Box 59, NL-1790 AB Den Burg, Texel, the Netherlands

KEY WORDS
Cohesive sediments, mud, consolidation, parameterisation, model

In this paper a parameterisation of the Gibson equation (Gibson *et al.*, 1967; 1981) is derived using the constitutive relations of Merckelbach & Kranenburg (2004). This approximation is validated using the results of extensive laboratory experiments performed by Kuijper *et al.* (1990). The material coefficients required in this validation are determined by relatively easy methods developed by Merckelbach & Kranenburg (2004a), extended with a method to deal with inaccuracies of the data. Subsequently, the parameterisation is validated on the benchmark data set of Townsend & McVay (1990). The new model performs reasonably in both experiments: both the density profiles at different times and the settling of the interface can be predicted. A shortcoming, however, is that the new consolidation model slightly underestimates the density near the bed-water interface, and slightly overestimates the density in the deeper layers. The main advantages of the parameterisation compared to numerical models based on the Gibson equation are the speed of calculation, its robustness and the ease of implementation.

1. INTRODUCTION

In open water systems, knowledge of the transport of cohesive sediment is essential for water quality assessments and for formulating dredging strategies in navigational

channels. Sedimentation and resuspension (erosion) are key processes with respect to the transport of cohesive sediment, which are governed by the hydrodynamic forcing. During periods of mild conditions, the bed may accrete and gain strength as a result of consolidation, whereas during severe (maximum flood, storm) conditions, the bed may erode. It is thus essential to take the history of the bed into account to quantify these processes properly. At present, however, most water quality models use sediment-bed exchange models, *i.e.*, only erosion and deposition, but no consolidation. Sometimes these models include an empirical time dependent strengthening of the bed. Due to the large temporal and spatial scales involved in water quality problems, it is not feasible to include a full numerical consolidation code in water quality models, as it would be too expensive from a computational point of view. The aim of the present work is therefore to derive a sufficiently fast and accurate consolidation (strengthening) model, suitable for long-term simulations with large study domain.

Section 2 introduces the classical Gibson equation for self-weight consolidation, and, as a first step towards simplification, this equation is transformed to material coordinates. A detailed derivation is included in Appendix A. Next the material functions are introduced and substituted into the Gibson model in Section 3. The next stage (Section 4) is to simplify and solve the resulting differential equation by means of a Fourier series. In Section 5 the coefficients of the material functions are determined from experiments, and, a general procedure for determining the material constants with the method proposed by Merckelbach & Kranenburg (2004a) is applied. Following this, these values are used to compare the parameterisation both to experimental data and to the numerical benchmark data set of Townsend & McVay (1990) in Section 6. Finally, Section 7 concludes that despite some lack of accuracy near the interface, the parameterisation is capable of simulating both density profiles at different times and the evolution of the interface.

2. GIBSON CONSOLIDATION EQUATION

Consolidation of soft mud layers is described by the large strain Gibson equation (Gibson *et al.*, 1967; 1981), which is generally considered to be the state-of-the-art for applications:

$$\frac{\partial \phi}{\partial t} - \rho_s' \frac{\partial}{\partial z}\left[k\phi^2\right] - \frac{1}{\rho_w g}\frac{\partial}{\partial z}\left[k\phi\frac{\partial \sigma_v'}{\partial z}\right] = 0 \tag{1}$$

where ϕ = 1/(1+e) is the particle volume fraction with e being the void ratio, σ_v' is the effective vertical stress, k is the permeability, $\rho_s' = (\rho_s$ - $\rho_w)/\rho_w$ is the relative density of

the solids with ρ_s and ρ_w being the density of solids and water respectively, t is time and z is the vertical coordinate. For completeness a detailed derivation of this equation is also included in appendix A. The handbook of Lambe & Whitman (1979), among others, is referred to for conceptual description and definitions of the different soil properties used in this paper.

Equation 1 gives a description of the evolution of the three state parameters ϕ, σ'_v and k over the vertical coordinate and time. The most important difference compared to the notation introduced by Gibson is that Eq. 1 is written in terms of the volume fraction of mud ϕ, which ranges from 0 in clear water to 1 in solid rock, instead of the void ratio e. This use of ϕ anticipates the use of the constitutive equations used in Section 3. Equation 1 is written in an Eularian frame of reference, and thus requires the use of a moving boundary condition to solve it since the water-mud interface settles as function of time in an Eularian frame of reference. In material (or Gibson) coordinates this interface is fixed in time if no net sedimentation or erosion occurs. In order to perform a simple parameterisation, the first step is therefore to transform Eq. 1 to material coordinates (ζ, t_m) which relate to the Eulerian reference frame (z, t) as

$$\begin{cases} \zeta(z,t) = \int_0^z \phi\,(z^*,t)\,dz^* \quad \Leftrightarrow \dfrac{\partial \zeta}{\partial z} = \phi\,(z,t) \\ \\ t_m = t \end{cases} \tag{2}$$

Note that the units of both z and ζ are meters, but their meaning is completely different. An arbitrary soil layer with height dz near the water bed interface normally contains a smaller volume fraction of mud than a layer with the same thinkness much deeper in the bed. The Gibson layer thickness $d\zeta$ corresponding with equidistant dz is therefore smaller near the water bed interface than deeper down, or vice versa, an amount of material $d\zeta$ near the water bed interface occupies a larger height dz then a same amount $d\zeta$ deeper down (Fig. 1). Furthermore, Eq. 2 shows that time t does not change when transforming to Gibson coordinates. However, the partial derivative with respect to real time t is not the same as the partial derivative with respect to material time t_m. This is shown by the partial derivative transformation rules in Eq. 3 associated with Eq. 2.

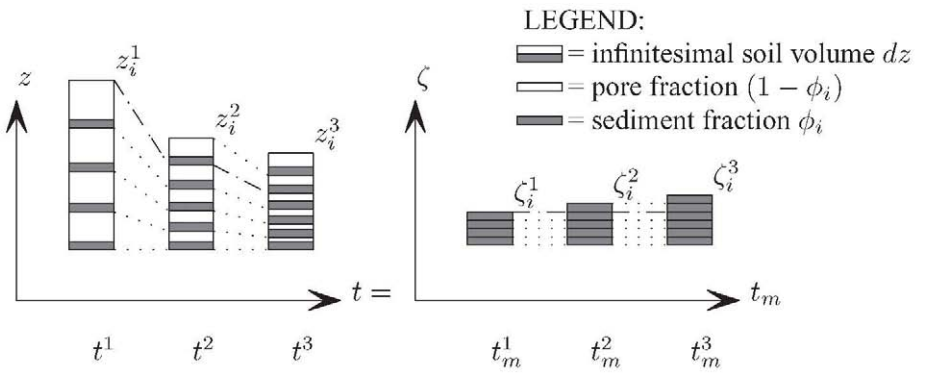

Fig. 1. Transformation of an equidistant bed discretization in material coordinates (right axes with constant $d\zeta$) to Eularian coordinates (left axes), where ζ_i and z_i denote the time-dependent water-bed interface. Note the difference in representation in Eularian and material space of two sedimentation events of equal amounts of material $d\zeta$. Also note that without these two sedimentation events the interface ζ_i in material space is fixed, whereas the interface z_i in Eularian coordinates is not.

$$\begin{cases} \dfrac{\partial}{\partial z} = \dfrac{\partial}{\partial t_m}\dfrac{\partial t_m}{\partial z} + \dfrac{\partial}{\partial \zeta}\dfrac{\partial \zeta}{\partial z} = \phi\dfrac{\partial}{\partial \zeta} \\ \dfrac{\partial}{\partial t} = \dfrac{\partial}{\partial t_m}\dfrac{\partial t_m}{\partial t} + \dfrac{\partial}{\partial \zeta}\dfrac{\partial \zeta}{\partial t} = \dfrac{\partial}{\partial t_m} - v_s\phi\dfrac{\partial}{\partial \zeta} \end{cases} \tag{3}$$

where v_s is the effective settling velocity as defined in Eq. A.6. It is therefore necessary to maintain the subscript m for material time throughout this paper.

Applying the transformation rules in Eq. 2 to Eq. 1 leads to:

$$\frac{\partial \phi}{\partial t_m} - \rho_s' \phi^2 \frac{\partial}{\partial \zeta}[k\phi] - \frac{\phi^2}{\rho_w g}\frac{\partial}{\partial \zeta}\left[k\phi\frac{\partial \sigma_v'}{\partial \zeta}\right] = 0 \tag{4}$$

The initial condition for Eq. 4 is given by an arbitrary initial density profile*. Two boundary conditions are required: (i) the mud bed is assumed to be on top of an impermeable and rigid layer at $\zeta = 0$, (ii) at the mud-water interface ($\zeta = \zeta_i$) the effective stress σ_v' is assumed zero.

*The density profile can be calculated from the effective stress σ_v' or volume fraction ϕ profile profile using Eqs. 5, 6 and $\rho = \rho_w + (\rho_s - \rho_w)\phi$

3. CONSTITUTIVE EQUATIONS

There are three dependent variables (k, σ'_v and ϕ) in Eq. 4, and thus, two constitutive equations $k = f(\phi)$ and $\sigma'_v = f(\phi)$ are needed. In this paper the relationships given by Merckelbach & Kranenburg (2004) are used:

$$\sigma'_v = K_\sigma \phi^n - K_{\sigma,0} \tag{5}$$

$$k = K_k \phi^{-n} \tag{6}$$

where K_σ and K_k are the effective stress and the effective permeability coefficient respectively, $K_{\sigma,0}$ is a coefficient accounting for creep and n is a dimensionless empirical exponent. Merckelbach & Kranenburg (2004) relate the empirical exponent n to the fractal dimension D of a consolidating mud layer as $n = 2/(3 - D)$ by assuming a scale-invariant structure of the silt-clay matrix. Within the scope of this paper, no further attention is paid to the background of Eqs. 5 and 6, nor to the meaning of D. However, whenever numerical values of the material parameters are given, values for D are preferred over values for n, since D can be interpreted in a physical manner (larger D means more dense primary mud aggregates; in the water bed values for D fall within the theoretically limited range $[2, 3]$). As creep is not dealt with at present, $K_{\sigma,0}$ can be set to zero and then only three coefficients remain to be determined. Merckelbach (2000) obtained typical values of $K_\sigma = 5 \times 10^7 - 5 \times 10^9$ Pa, $K_k = 10^{-15} - 10^{-13}$ m/s and $D = 2.6 - 2.75$ (*i.e.*, $n = 5 - 8$) for laboratory consolidation experiments with natural muds.[†] Rewriting Eq. 4 as

$$\frac{\partial \phi}{\partial t_m} - \rho'_s \phi^2 \frac{\partial}{\partial \zeta}\left[k\phi\right] - \frac{\phi^2}{\rho_w g}\left(k\phi \frac{\partial^2 \sigma'_v}{\partial \zeta^2} + \frac{\partial \sigma'_v}{\partial \zeta}\frac{\partial k\phi}{\partial \zeta}\right) = 0 \tag{7}$$

and substituting from the constitutive equations (Eqs. 5 and 6), which are rewritten as $\phi = (\sigma'_v/K_\sigma)^{1/n}$ and $k = K_\sigma K_k/\sigma'_v$ respectively, yields after laborious but straightforward algebra

$$\frac{\partial \sigma'_v}{\partial t_m} + A_1 {\sigma'_v}^{\frac{2-n}{n}}\left(\frac{\partial \sigma'_v}{\partial \zeta}\right)^2 + A_2 {\sigma'_v}^{\frac{2-n}{n}}\frac{\partial \sigma'_v}{\partial \zeta} - A_3 {\sigma'_v}^{\frac{2}{n}}\frac{\partial^2 \sigma'_v}{\partial \zeta^2} = 0 \tag{8}$$

[†]It should be noted that Eqs. 5 and 6 are only valid in the virgin loading regime. Accordingly, when alternating erosion and deposition need to be handled by the consolidation model, more complex constitutive equations need to be used. In this paper our model is not applied to conditions with swell, and Eqs. 5 and 6 can readily be used. See Lambe & Whitman (1979) for an introduction to the concept of 'virgin loading regime' and swell.

where

$$A_1 = \frac{1}{\rho_w g} K_k (n-1) K_\sigma^{\frac{n-2}{n}}, \quad A_2 = \rho'_s K_k (n-1) K_\sigma^{\frac{n-2}{n}}, \quad A_3 = \frac{1}{\rho_w g} K_k n K_\sigma^{\frac{n-2}{n}}$$

Herein the effective stress σ'_v is the only dependent variable. Equation 8 is used as the starting point for an approximate solution. Note that the two advective terms (containing $\partial\sigma'_v/\partial\zeta$) in Eq. 8 have different origins: one is the advective term in Eq. 4, while the other stems from applying the chain rule to the diffusion term in Eq. 4.

4. PARAMETERISATION

In order to find an analytical solution, Eq. 8 is rewritten in terms of the excess pore water pressure p_e as a first step towards simplification. The excess pore pressure at any time t_m is equal to the difference between the equilibrium effective stress ($\partial\sigma'_v/\partial t_m \approx 0$ at $t_m \to \infty$) and the effective stress at that time. This implies:

$$\sigma'_{v,\infty} = p_e + \sigma'_v = (\rho_s - \rho_w) g (\zeta_i - \zeta) \quad \Leftrightarrow \quad \sigma'_v = (\rho_s - \rho_w) g (\zeta_i - \zeta) - p_e \tag{9}$$

Introducing dimensionless coordinates ξ [‡] and τ as follows

$$\xi = \frac{\zeta}{\zeta_i} \tag{10}$$

$$\tau = \frac{t_m}{T} \tag{11}$$

where time scale T is introduced for convenience

$$T = \frac{\rho_w g \zeta_i^2}{K_k K_\sigma^{\left(\frac{n-2}{n}\right)} n \sigma'^{2/n}_v} \tag{12}$$

Equation 8 can finally be rewritten as

$$\frac{\partial p_e}{\partial \tau} - \frac{n-1}{n} \frac{1}{\sigma'_v} \left(\frac{\partial p_e}{\partial \xi}\right)^2 - \frac{n-1}{n} (\rho_s - \rho_w) g \frac{\zeta_i}{\sigma'_v} \frac{\partial p_e}{\partial \xi} - \frac{\partial^2 p_e}{\partial \xi^2} = 0 \tag{13}$$

[‡]The interface height ζ_i used to normalize the vertical material coordinate in Eq. 10 is assumed constant from now on. The derivations up to this point are valid for a time-dependent amount of material as in Fig. 1, whereas the subsequent derivations are valid only for a water bed without any sedimentation or erosion.

The time scale T in Eq. 12 is used to normalize the material time t_m. When the material coefficients (D, K_k, K_σ) and the material thickness of the consolidating bed ζ_i are known, T can be used to assess the consolidation time of a problem, as the forthcoming solution Eq. 14 to Eq 13 shows. In this equation the excess pore pressures dissipate $\propto \exp(-\text{constant} \times t_m/T)$, implying that the first term (the term with the smallest dissipation rate) is practically zero after just a few T.

Note that T depends on the square of the amount of material ζ_i present in the bed. Note also the presence of the (still) unknown effective stress σ'_v in T and in the coefficients of the second and third term of Eq. 13. Since the effective stress σ'_v varies with ζ, T and the second and third terms of Eq. 13 are not constant with depth. It is therefore assumed that the effective stress σ'_v in the non-dimensional time in T and in Eq. 13 is equal to a representative stress, set equal to the highest possible equilibrium stress in the bed: $\sigma'_{v,rep} \equiv (\rho_s - \rho_w)\, g\zeta_i$.

Considering thin consolidating layers (small ζ_i), so that consolidation times (proportional to $T \propto {\zeta_i}^2$) are small, we may neglect the initial phase of consolidation. This implies that the non-linear second and third advection terms of Eq. 13 are neglected, which yields a diffusion equation for the excess pore water pressure in non-dimensional material coordinates:

$$\frac{\partial p_e}{\partial \tau} - \frac{\partial^2 p_e}{\partial \xi^2} = 0 \tag{14}$$

Two boundary conditions are required to solve Eq. 14: (i) the mud bed is assumed to be on top of an impermeable and rigid layer at $\xi = 0$ (Eq. 15), (ii) at the mud-water interface ($\xi = \xi_i = 1$) the effective stress σ'_v is assumed zero (Eq. 16). The initial condition (Eq. 17) is a density or an associated effective stress profile[§]

$$\frac{\partial p_e\,(0,\tau)}{\partial \xi} = 0 \qquad \xi = 0 \qquad \tau > 0 \qquad \text{Neumann} \tag{15}$$

$$p_e\,(1,\tau) = 0 \qquad \xi = 1 \qquad \tau > 0 \qquad \text{Dirichlet} \tag{16}$$

$$p_e\,(\xi,0) = p_0\,(\xi) \qquad 0 < \xi < 1 \qquad \tau = 0 \tag{17}$$

[§] ρ, p_e and σ'_v are related to each other via Eqs. 5, 9 and $\rho = \rho_w + (\rho_s - \rho_w)\phi$.

The solution of Eq. 14 with constraints Eqs. 15 to 17 is well known from many a mathematical textbook and is written in the form of a Fourier series as follows:

$$p_e(\xi,\tau) = \sum_{k=1}^{\infty} f_k \exp\left[-\pi^2\left(k-\tfrac{1}{2}\right)^2\tau\right]\cos\left(\pi\left(k-\tfrac{1}{2}\right)\xi\right) \tag{18}$$

where

$$f_k = 2\int_0^1 p_0(\xi)\cos\left(\pi\left(k-\tfrac{1}{2}\right)\xi\right)d\xi \tag{19}$$

in which the subscript 0 refers to the initial conditions. Analytical expressions for f_k are only available for simple analytical initial profiles. For a uniform initial condition in a settling column for example, where initially the excess pore pressure $p_0 = (\rho_s - \rho_w)g\zeta_i(1-\xi)$ carries the full self-weight ($\sigma'_{v,\infty}$ in Eq. 9), Eq. 19 can be calculated as

$$f_k = 2\int_0^1 (\rho_s-\rho_w)\,g\zeta_i\,(1-\xi)\cos\left(\pi\left(k-\tfrac{1}{2}\right)\xi\right)d\xi = \frac{8\,(\rho_s-\rho_w)\,g\zeta_i}{\pi^2\,(2k-1)^2} \tag{20}$$

In all other cases f_k has to be determined numerically.[¶]

For application of the parameterisation in water quality models the density profile in real coordinates is necessary. The steps to obtain this solution are (i) to revert solution Eq. 18 back to dimensional variables, (ii) subtract this solution from the equilibrium stress according to Eq. 9 and (iii) transform it back to Eulerian coordinates according to Eq. 2. The material relations Eqs. 5 and 6 can then be used to obtain the associated density (and permeability) profile.

Lee & Sills (1981) also derived Eq. 18, although they used a completely different approach. They formulated Gibsons equation in terms of the void ratio e, and assumed the following material functions: $\sigma'_v \propto (e_0 - e)$ and $k \propto (1+e)$. These functions were chosen to immediately simplify the governing Gibson equation to Eq. 14. Subsequently, they also got the solution of Eq. 14 as Eq. 18, using f_k according to Eq. 20. Accordingly, their solution of the effective stress in the material reference system is exactly the same as ours. It should be noted that our approach of performing a full derivation and then omitting the

[¶]Fortunately, only a limited number of terms have to be used. The higher the order of the terms (large k), (i) the higher dissipation rate ($\propto exp(-\text{constant}_k \times t_m/T)$) and (ii) the finer the spatial features they describe (length $= 2/(k-\frac{1}{2})$). The required number of terms is therefore determined by the required spatial and temporal resolution.

advective terms yields the same consolidation equation as assuming $\sigma'_v \propto (e_0 - e)$ and $k \propto (1 + e)$ right away. However, the approach followed in deriving Eq. 14 in this paper does have a few advantages over that of Lee & Sills (1981).

First, simplifications have been postponed to the very end. This allows more insight into the nature and consequence of the simplifications. For instance, one could substitute Eq. 18 into the discarded terms of Eq. 8 to investigate the consequence of omitting the advective terms.

Second, for application of the parameterisation the density profile in real coordinates is needed. However, without a physically sound material function as Eq. 5, it is not possible to transform the effective stress profile to a density profile, nor is it possible to transform from material coordinates into real coordinates[‖]. Consequently, with the data available for validation and calibration in this study, *i.e.*, density profiles in an Eulerian frame given by Kuijper *et al.* (1990), it is not possible to compare the solution of Lee & Sills (1981) to our parameterisation.

5. DETERMINATION OF MATERIAL COEFFICIENTS

5.1. Experiment

Kuijper *et al.* (1990) performed two consolidation experiments in a 30 cm high settling column with natural mud from a fresh water lake in the Netherlands. During the consolidation experiments (i) the settling of the interface was measured as a function of time and (ii) density profiles were measured at several times (Table 1). Next, similar mud beds were subjected to erosion in an annular flume, rendering this data set valuable for future extensions of the model accounting for the effects of alternating schemes of sedimentation and erosion.

The material coefficients in Eqs. 5 and 6 are usually determined from measurements of density and pressure profiles. However, these data were not collected by Kuijper *et al.* (1990). So a method proposed by Merckelbach & Kranenburg (2004a) is used. In Sections 5.2 to 5.4 this method is applied and a few complications are discussed.

[‖] For instance, the equilibrium effective stress profile in Eq. 9 exhibits a linear increase with material depth. Due to the assumption $\sigma'_v \propto (e_0 - e)$, the final void ratio profile in the model of Lee & Sills (1981) will therefore show a linear decrease with material depth. Accordingly, below some material depth the void ratio e will be negative and therefore theoretically invalid. The transformation from material to real coordinates in Eq. 2 cannot deal with negative void rations (which implies $\phi > 1$). A remedy would be to limit the slope of $\sigma'_v \propto (e_0 - e)$ to the range that guarantees a positive e inside the water bed. This, however, would put a severe limit on the best linear fit of the e-profile, which is curved in reality.

Table 1. Properties of the experimental data by Kuijper *et al.* (1990)

Parameter	Experiment 1	Experiment 2	units
Duration consolidation experiment	1	7	days
Duration erosion experiment	24	12	hour
Initial dry density ρ_d in column	54	56	kg/m^3
Initial ϕ in column	0.021	0.022	m^3/m^3
Material (Gibson) height ζ_i	6.2	6.5	mm
Number of interface measurements	19	16	#
Density measurements taken at	none	4,24,50,72,151,168	hour
Density measurements resolution		5	mm

5.2. Permeability relation

Merckelbach & Kranenburg (2004a) determine the set (K_k,D) from observations of the evolution of the interface only, *i.e.*, no permeability or stress measurements have to be performed. This is based on the assumption that in the initial phase of the consolidation ($t_1 < t < t_2$ in Fig. 2a) effective stresses are so small that the consolidation process is governed by the permeability of the soil only. In this phase the interface height can be described by

$$h\left(t\right) = \left(\zeta \frac{2-n}{1-n}\right)^{\frac{1-n}{2-n}} \left[\rho_s' \left(n-2\right) K_k t\right]^{\frac{1}{2-n}} \tag{21}$$

This equation is derived from the Gibson equation (Eq. 1) after using Eq. 6 and setting $\sigma_v' = 0$. Hence Eq. 21 is valid whenever Eqs. 1 and 6 are valid. For details the reader is referred to Merckelbach (2000). With Eq. 21 the material coefficients K_k and D can be determined by plotting $h(t)$ vs. t on double logarithmic scales (Fig. 2b). Some precautions are necessary to fit Eq. 21 since only the data between t_1 and t_2 (Fig. 2a) can be used.

When the settling/consolidation experiment starts with densities below the structural density, as is the case of the data by Kuijper *et al.* (1990), two interfaces are formed initially. The upper interface is generally measured, as this one is clearly visible, while the lower one is usually practically invisible to the human eye (and can thus only be determined with density probes). Before the two interfaces have merged (point of contraction) at time t_1, the solution for h depends on the hindered settling phase only, which is not incorporated in the permeability function Eq. 6. Only after time t_1 is the solution for h independent of the initial conditions and described by Eq. 21. The data $h(t)$ collected before t_1 should therefore not be used in fitting Eq. 21. The difficulty is that t_1 is gener-

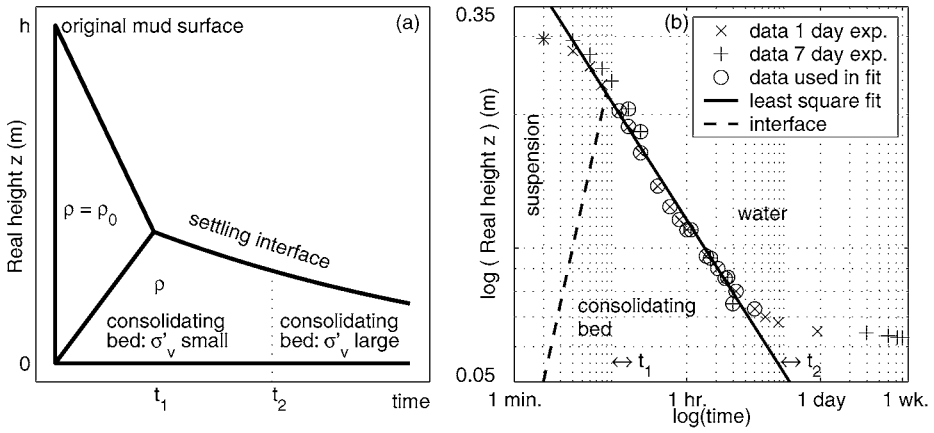

Fig. 2. An example of the fitting of Eq. 21. (a) A schematic diagram to show three different consolidation phases: hindered settling: $t < t_1$, initial consolidation dominated by permeability: $t_1 < t < t_2$ and final consolidation dominated by permeability and effective stress: $t > t_2$. (b) A representative fit of Eq. 21, where both data from the the 1-day and the 7-day consolidation experiments of Kuijper *et al.* (1990) are used. Parameters: $D = 2.59$, $K_k = 1.7 \times 10^{-12}$ m/s. Not all data points are used in the least square fit as described in section 5.4. The line indicated as "interface" refers to the interface between the consolidating bed and the mud suspension.

ally not precisely known as it requires information on the evolution of the lower interface (although sometimes, but not in our case, a point of deflection is visible in the upper interface at t_1). Consequently, it is not clear which data points should be excluded.

Further in the consolidation process, at $t = t_2$, effective stresses start to become significant so that Eq. 21 is no longer a valid approximation of the consolidation process. Note that t_2 is difficult to determine from the settlement of the interface, as this settling becomes gradual in the final consolidation phase. In general, however, we do not know t_2 either. Yet it is necessary to establish t_1 and t_2 for the estimation of K_k and D, and the fitting results can be affected by the selection of t_1 and t_2. The fit in Fig. 2a, for instance, would be steeper if a larger t_1 or a smaller t_2 were chosen (not shown). Conversely, due to the shape of the data cloud on double logarithmic paper, it would be more gentle if a smaller t_1 or a larger t_2 were chosen (not shown).

5.3. Effective stress relation

Merckelbach & Kranenburg (2004a) determine the set (K_σ, D) from basically one single density measurement at the final equilibrium stage, when only the effective stresses

in Eq. 1 govern the consolidation and the advection term is negligible. In this phase, the vertical density profile $\phi = \phi(z) = f(\rho(z))$ is implicitly described by:

$$h - z = \frac{nK_\sigma}{(n-1)(\rho_s - \rho_w)g}\phi^{n-1} \tag{22}$$

(see Merckelbach (2000) for details). The material coefficients K_σ and D can be determined by fitting Eq. 22 to volume fraction profiles measured at the final stage of consolidation on double logarithmic scales (Fig. 3b).

However, Fig. 3a shows that the accuracy of the density data is too low to distinguish between the profiles at $t > 24$ hr (for instance, the measured profile at t = 168 hr does not depict the largest densities). The differences between these profiles can be attributed to (i) inaccuracies in the density measurements and vertical position of the probe, and (ii) to the ongoing consolidation process. The difficulty is assessing for which of these profiles the latter effect is absent, *i.e.*, whether they ought to be considered to be in the final stage of consolidation. When we employ the definition of the reference time T in

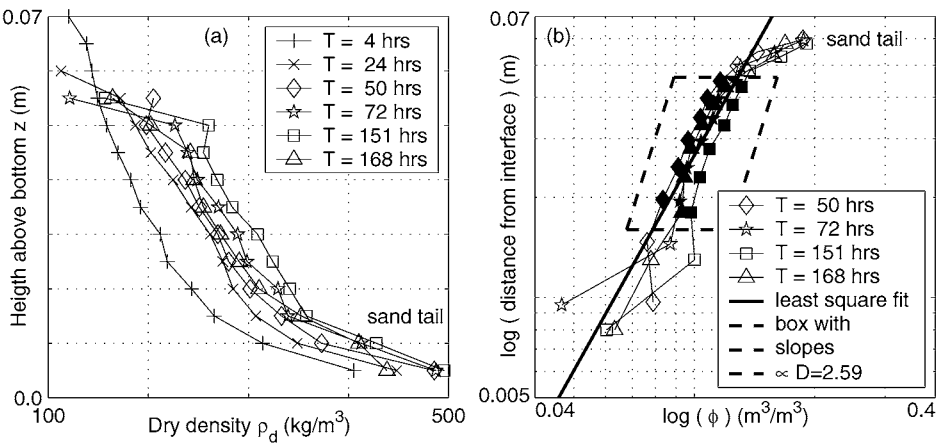

Fig. 3. An example of the fitting of Eq. 22. (a) Original data from dry density (ρ_d) meassurements by Kuijper *et al.* (1990) (with $\rho_s = 2600\ kg/m^3$). Note that ρ_d at $t = 168$ hr is lower than ρ_d at $t = 151$ hr. This gives an indication of the accuracy of the ρ_d meassurements. (b) A representative fit of Eq. 22 with the equilibrium profiles ($t > 50$ hr). Parameters: D = 2.36, K_σ = 4.04×10^4 Pa. Not all data points are used in the least square fit as described in Section 5.4: only the filled markers have been used. The box with slopes $\propto D = 2.59$ is included to show how the results would be affected by choosing the D obtained from fitting the interface in Fig. 2b.

Eq. 12 iteratively with estimated values of K_k, K_σ and D, we learn that beyond t = 50 hr the major part of the consolidation has taken place (the exponential term in Eq. 18 is practically zero after $3T$). All profiles measured after t = 50 hr are therefore treated as realisations of the same final profile. Subsequently Eq. 22 is fitted on the combined data of the profiles at 50, 72, 151 and 168 hour.

The final profiles in Fig. 3 are affected by the presence of sand in the sediment. A pure mud bed would show a gentle increase of density profile with depth, while Fig. 3 shows a sand-induced high-density tail near the bottom due to segregation in the suspension phase. According to Merckelbach & Kranenburg (2004a) this part of the vertical can be neglected in the comparison process.

5.4. A procedure for fitting material coefficients

To determine the permeability and the effective stress coefficients, an unknown number of points have to be neglected. This means that fits like those in Figs. 2b and 3b will be subjective. Therefore we propose a procedure to obtain *reproducible* results, which consists of fitting all possible combinations of leaving out data points at either end of the data sets. By determining the fit in Fig. 2b, for example, 9 data points at small t and 8 at large t have been omitted, whereas for Fig. 3b, 12 at large $(h - z)$ and 8 at small $(h - z)$ have been omitted. The only constraint is that at least three data points must remain. For the permeability coefficients, 19 (16) data points are available for the 1 (7) day experiment, giving 153 (105) possible least square fits. When combining the two data sets, there are 561 possibilities. For the effective stress coefficients, 44 observations (11 levels at 4 times) are available, resulting in 708 possibilities.

The results of all these fits are shown in Figs. 4 and 5. Panels (a) and (b) show the histograms of D and K_k in Fig. 4 and D and K_σ in Fig. 5 respectively. In panels (c) all individually fitted *sets* of (K_k, D) or (K_σ, D) are shown in a scatter plot. The line fitted through these data comprises all combinations (K_k, D) or (K_σ, D) of fits through various combinations of data in respectively Figs. 2b and 3b. Remarkably, and reassuringly, the experimental data of Merckelbach (2000) are also close to these curves.

We advocate using the median values (peak values) of the fractal dimension D in panels (a) together with the associated K_k and K_σ values according to panels (c) as the material coefficients. The fits Figs. 2b and 3b correspond to these sets. Note: this approach does not yield the same results as using the peak values of K_k and K_σ in panels (b) together with the separate peak value of D in panels (a): values of K_k and K_σ are one-to-one coupled to values of D according to panels (c).

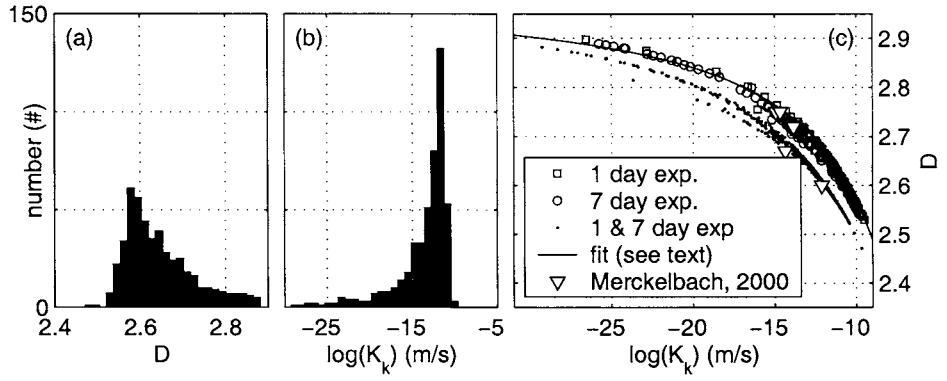

Fig. 4. Results of least square fits of $h(t)$ versus t on data by Kuijper *et al.* (1990) to determine the values of K_k and D (1 and 7 day experiment together). Modal value of fractal dimension is $D = 2.59$. The fit in panel (c) represents all the lines through point $t = 50$ min and $h = 0.1$ m in Fig. 2b.

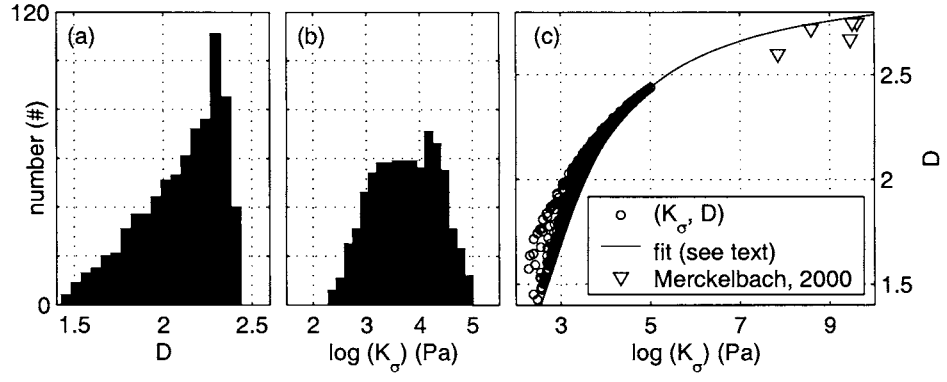

Fig. 5. Results of least square fits of the final density profile versus $(h - z)$ on data by Kuijper *et al.* (1990) to determine the values of K_σ and D. Modal value of fractal dimension is D = 2.3. Panel (c) represents all the lines through point $\phi = 0.15$ and $h = 0.048$ m in Fig. 3b.

6. VALIDATION

6.1. Parameterisation vs. experimental data

The parameterisation is compared to the experimental results of Kuijper *et al.* (1990) using the material coefficients determined in Section 5.4. The modal value of the fractal dimension D from panel (a) of Fig. 4 is used (D = 2.6) with the associated K_σ (4×10^6

Pa) and K_k (8×10^{-12} m/s). Five Fourier components are used in Eq. 18. The results do not change when more components are used because the profile is smooth.

The sediment used by Kuijper *et al.* (1990) contained sand. During the time of the measurements, the quartz fraction of the sample was determined as 30% of mass. Quartz is also found in the mud-size range, hence it does not account for the sand fraction only. As we do not have any information about the size distribution of the quartz, in this paper the whole quartz fraction is assumed to be sand. All this sand is assumed to be condensed in the bottom layer with a dry mass of 340 kg/m^3, giving a 1.46 cm layer thickness. This sand is not included in the parameterisation and a material height of 70 % of the initial mass is used.

Figure 6 shows the results of the parameterisation together with the data of Kuijper *et al.* (1990). The density in the lower layers is underestimated. When we compare these results with Fig. 3b, where K_σ was fitted, we see that this deviation is already present in the least square fit. However, the profile at 4 hours in Fig. 6 matches very well. This is promising because the 4-hour density profile was not taken into account in the fitting of the material functions, only the final profiles and the interface settling were used. It should be noted, however, that the agreement will be less if the final profile fitted better. Note also that at 4 hours ($\sim 10^4$ s) the interface starts to match well (Fig. 6b), while the fit of Eq. 21 used to determine K_k (Fig. 2a), starts to deviate there. The rest of the interface settling agrees reasonably, especially the final height of the bed. In the region before 10^4 seconds ($<$ 3 hours) the agreement is less. However, in this initial phase the material is still very fluffy and the parameterisation, which is only valid when the density is higher than the gelling density, may not be valid yet.

Besides the material coefficients applied in Fig. 6, more combinations have been selected and applied. For a number of fractal dimensions D, the best values of K_k and K_σ have been determined by means of trial and error. The best fitting sets have been selected by visual inspection (no quantitative criterion has been used). These sets (D, K_σ and K_k) lie all on (or very close to) the fitted lines in panels (c) of Figs. 4 and 5. Two examples are shown in Fig. 7. It is remarkable and reassuring that reasonable results are obtained for material coefficients ranging over several orders of magnitude (K_σ: $8 \times 10^4 - 1 \times 10^8$ Pa and K_k: $7 \times 10^{-10} - 1 \times 10^{-13}$ m/s). The reason for this is that a small change in fractal dimension D leads to large change in the exponent n in Eqs. 5 and 6, which has to be compensated by K_σ and K_k. The model can therefore be considered to be robust when the parameter setting is mutually consistent. However, the best fits for the interface height (not shown) require slightly different parameters than the best fits of the profiles in Fig. 7, because the modal (peak) values for D from the interface data and the density data in Figs. 4a and 5a are also different.

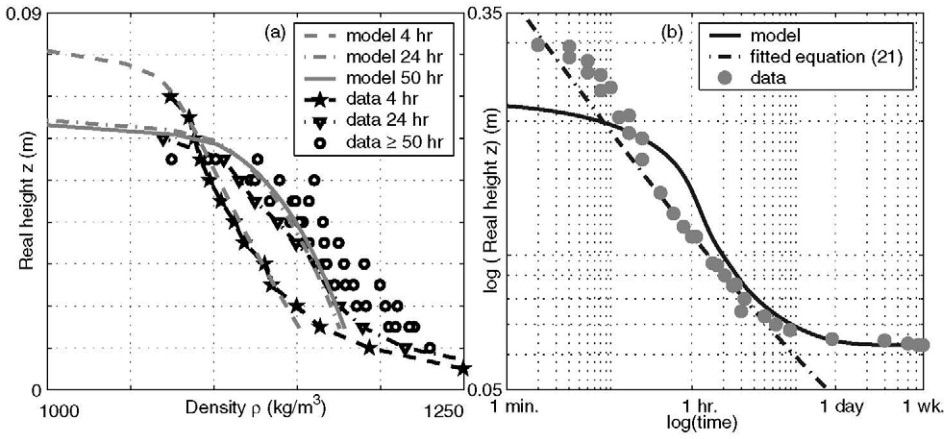

Fig. 6. Comparison of parameterisation with the data by Kuijper *et al.* (1990) with $D = 2.60$, $K_\sigma = 4 \times 10^6$ Pa and $K_k = 8 \times 10^{-12}$ m/s. (a) Density profiles. (b) Settling of the interface. Data ≥ 50 hr means all data measured at $t \geq 50$ hr, which is considered to be the final stage of consolidation.

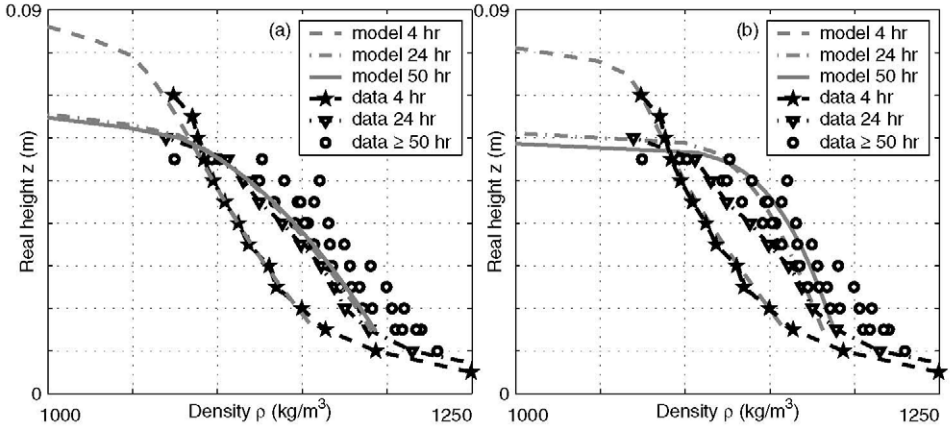

Fig. 7. Parameterisation model performance with different sets of material coefficients compared to data by Kuijper *et al.* (1990). (a) $D = 2.40$, $K_\sigma = 8 \times 10^4$ Pa and $K_k = 7 \times 10^{-10}$ m/s. (b) $D = 2.70$, $K_\sigma = 1 \times 10^8$ Pa and $K_k = 18 \times 10^{-13}$ m/s. Data ≥ 50 hr means all data measured at $t \geq 50$ hr, which is considered to be the final stage of consolidation.

6.2. Parameterisation vs. Townsend & McVay (1990)

Since the limited accuracy of the data by Kuijper *et al.* (1990) does not allow better comparison of the numerical model and the parameterisation, the parameterisation is also compared to the benchmark data set of Townsend & McVay (1990). This set has been obtained by applying several numerical models to the same standard model set-up: the consolidation of 10 m mud slurry with a uniform initial density. The material coefficients that have been determined by Merckelbach (2000) are used. Both the density profile after one year and the settlement of the interface compare favourably (Fig. 8). It is clear, however, that the parameterisation underestimates the density near the interface and overestimates the density near the rigid bottom, just as in Section 6.1. Remarkably, and unlike the results in the previous Section, the settling of the interface is predicted very well.

7. CONCLUSIONS

Consolidation of soft mud layers described by the Gibson equation (Gibson *et al.*, 1967; 1981), has successfully been solved numerically in the past (Townsend & McVay, 1990). However, for application in large scale, long term water quality models such numerical solutions are too time-consuming. The objective of this paper is therefore to

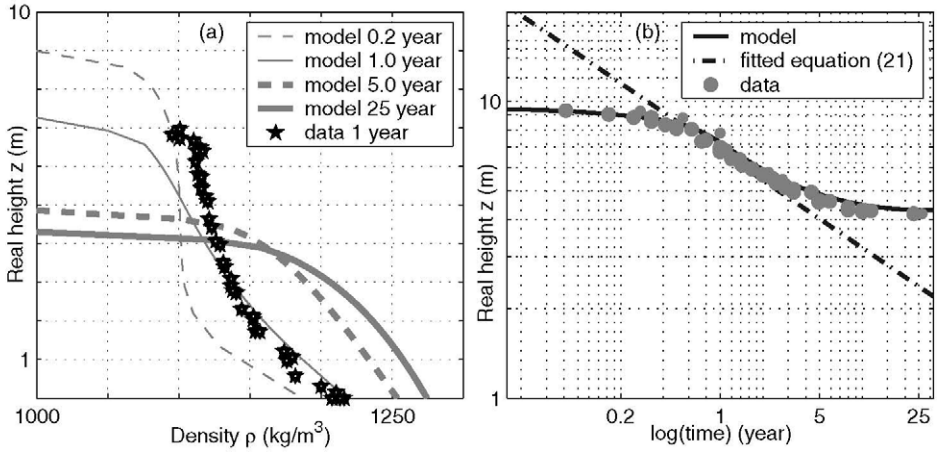

Fig. 8. Comparison of parameterisation model results ($D = 2.605$, $K_\sigma = 7.1 \times 10^7$ Pa and $K_k = 7.6 \times 10^{-13}$ m/s) and numerical data by Townsend & McVay (1990). (a) Dry density profiles. (b) Settling of the water-mud interface.

derive a sufficiently fast and sufficiently accurate approximate solution of the simplified Gibson equation for application in water quality models with large spatial and temporal scales.

The governing differential equation is derived in real coordinates with the volume fraction ϕ as the dependent variable. The material equations of Merckelbach & Kranenburg (2004) are substituted in the differential equation. The resulting model is transformed to material coordinates in order to prevent a moving interface, and rewritten in terms of the excess pore pressure. From the resulting equation the advective terms are omitted. A diffusion problem remains, which is readily solved with a Fourier series.

This parameterisation is validated on experimental data of settling column experiments performed by Kuijper *et al.* (1990). The required material coefficients for this experiment are determined with simple methods developed by Merckelbach & Kranenburg (2004a). These methods have a few complications though. A new procedure for using these methods is proposed, yielding a more objective set of material coefficient values.

The parameterisation is compared to the data by Kuijper *et al.* (1990), comprising the density profiles at several times and the settling of the interface in time. The parameterisation performs quite reasonably for both the density profiles and the interface settling, although the density near the interface is slightly underestimated and the density in the deeper layers is slightly overestimated. Especially the density profile in the initial stage of consolidation (4 hour) agrees very well. This is promising, since the material parameters governing the consolidation have been determined using only the final equilibrium density profiles and the settling of the interface. Moreover, the model results are similar for other material parameter settings, provided the effective stress and permeability coefficients are mutually consistent. The model can therefore considered to be robust.

Apart from the data by Kuijper *et al.* (1990), a 6 cm thin mud layer, the parameterisation has also been tested using the benchmark data set of Townsend & McVay (1990), describing the consolidation of a 10 m thick mud slurry. The parameterisation performs equally well in this experiment. The parameterisation can therefore be considered to be valid for a large range of consolidation problems.

It can be concluded that the overall performance of the parameterised consolidation model is reasonable. The main advantages of the parameterisation compared to (more accurate) numerical models based on the Gibson equation are the speed of calculation, its robustness and the ease of implementation. The new model is therefore concluded to be sufficiently fast and accurate to be suitable for inclusion in a long-term simulations with large study domain.

REFERENCES

Gibson, R.E., G.L. England and M.J.L. Hussey. 1967. The theory of one dimensional consolidation of saturated clays. I finite non-linear consolidation of thin homogenous layers. *Géotechnique*, 17, 261–272.

Gibson, R.E., R.L. Schiffman and K.W. Cargill. 1981. The theory of one dimensional consolidation of saturated clays. II finite non-linear consolidation of thick homogenous layers. *Canadian geotechnical journal*, 18, 280–293.

Kuijper, C., J.M. Cornelisse and J.C. Winterwerp. 1990. *Erosion and deposition characteristics of natural muds – sediment from ketelmeer.* Cohesive sediments series 30. National Institute for Coastal and Marine Management (RIKZ), Ministry of Public Works, The Hague and WL — Delft Hydraulics, Delft.

Lambe, T.W. and R.V. Whitman. 1979. *Soil mechanics, SI version.* Series in soil engineering. John Wiley & Sons, New York.

Lee, K. and G.C. Sills. 1981. The consolidation of a soil stratum, including self-weight effects and large strains. *International journal for numerical and analytical methods in geomechanics*, 5, 405–428.

Merckelbach, L.M. 2000. *Consolidation and strength evolution of soft mud layers.* PhD thesis, Delft University of Technology, Faculty of Civil Engineering and Geosciences. Also: Communications on Hydraulic and Geotechnical Engineering, Report 00-2, ISSN 0169-6548.

Merckelbach, L.M. and C. Kranenburg. 2004. Equations for effective stress and permeability of soft mud-sand mixtures. *Géotechnique*, 54, 235–243.

Merckelbach, L.M. and C. Kranenburg. 2004a. Determining effective stress and permeability equations for soft mud from simple laboratory experiments. *Géotechnique*, 54, 581–591.

Townsend, F.C. and M.C. McVay. 1990. SOA: large strain consolidation predictions. *Journal of geotechnical engineering*, 116(3), 222–243.

A. APPENDIX: Derivation Gibson equation

This appendix presents a detailed derivation of the Gibson equation, closely following Merckelbach (2000). Our derivation differs from Gibson's in two ways. First, for reasons of clarity, the derivation is performed for a Eulerian reference frame followed by a transformation to material coordinates afterwards, rather than directly using a material coordinate system in the derivation. Second, the particle volume fraction $\phi = 1/(1+e)$ is used as the dependent variable, rather than the void ratio e. Although both parameters are uniquely related, the use of ϕ anticipates the new constitutive equations introduced in

Section 3.We start with the vertical mass balance of the particle volume fraction ϕ:

$$\frac{\partial \phi}{\partial t} + \frac{\partial \phi v_s}{\partial z} = 0 \tag{A.1}$$

where t is time, z the Eulerian coordinate and v_s is the vertical velocity of the particles relative to a fixed reference plane (settling rate). The actual pore water velocity relative to the flocs is defined by $v_{eff} = v_f - v_s$, where v_f is the velocity of the water relative to a fixed reference plane. The actual pore water flow v_{eff} can be modelled with Darcys law:

$$(1-\phi)(v_f - v_s) = -k\frac{1}{\rho_w g}\frac{\partial p_e}{\partial z} \tag{A.2}$$

where k is the permeability of the soil and p_e is the excess pore water pressure, which is defined as the difference between the actual pore water pressure p and the hydrostatic pressure p_h. The vertical force balance can be written as:

$$g\left[\phi\rho_s + (1-\phi)\rho_w\right] + \frac{\partial \sigma_v}{\partial z} = 0 \tag{A.3}$$

where σ_v is the total vertical stress, g is the gravity, ρ_s is the density of the solids, and ρ_w is the density of the pore water. For reasons of continuity, the flow velocity of the fluid and v_s are related as

$$v_s\phi + v_f(1-\phi) = 0 \tag{A.4}$$

in which it is assumed that the consolidating layer is on top of an impervious base. Substituting Eqs. A.4 and A.2 into A.3, using the effective stress principle

$$\sigma_v = \sigma'_v + p = \sigma'_v + p_e + p_h \tag{A.5}$$

yields

$$v_s = -k\left[\phi\rho'_s + \frac{1}{\rho_w g}\frac{\partial \sigma'_v}{\partial z}\right] \tag{A.6}$$

where σ'_v is the effective vertical stress and $\rho'_s = (\rho_s - \rho_w)/\rho_w$ is the relative density of the solids. Substituting the settling rate Eq. A.6 into the mass balance Eq. A.1 finally gives the Gibson equation (Eq. 1).

Estuarine and Coastal Fine Sediments Dynamics
J.P.-Y. Maa, L.P. Sanford and D.H. Schoellhamer (editors)

Estimation of mud rheological parameters using genetic algorithm for a two-layer wave-mud system

Zhang, Q.-H.[a], O.W.H. Wai[b] and Z.-D. Zhao[a]

[a]School of Civil Engineering, Tianjin University, Tianjin 300072, P.R. China
[b]Department of Civil and Structural Engineering, The Hong Kong Polytechnic University, Hung Hom, Kowloon, Hong Kong

KEY WORDS
Deposited mud, mixed mud, wave attenuation, viscoelastic parameters, genetic algorithm

By assuming the mud bed is a linear viscoelastic medium, a method to estimate the rheological parameters (shear modulus and viscosity) based on the measurements of wave length and wave attenuation coefficient for a two-layer water-mud system was developed. Comparisons between the estimated and the experimental results showed that the estimated rheological parameters could represent the depth-averaged rheological parameters of the mud beds. The selected linear model, however, cannot reflect the nonlinear properties of wave-mud interactions. The results also show that the shear moduli and viscosities of mixed mud beds differ significantly from those of the deposited mud beds, even though the mud bulk densities are the same. The results suggest that when wave-mud interactions and other related issues on muddy coasts are of interest, the rheological parameters should consider the effect of mud consolidation status.

1. INTRODUCTION

The rheological properties of mud in a water-mud system are important to many observed phenomena, *e.g.*, wave attenuation, sediment resuspension, mud mass transport, and mud fluidization (Shibayama and An, 1993; Li and Mehta, 1997; Verbeek and

Cornelisse, 1997). Obtaining the rheological parameters of undisturbed mud is difficult because current available instruments (*e.g.*, dynamic rheometer) can only measure the rheological parameters after severely disturb the mud, and thus, the results are questionable. Previous studies showed that the wave damping rate differs over one order of magnitude mainly due to the differences in mud rheological parameters during various stages of consolidation (Zhang and Zhao, 2000). However, there is practically no method at the present time for obtaining the rheological parameters of a naturally deposited mud without seriously disturbing it first. In this study, a method based on the Genetic Algorithm (GA) was developed as a first step to address this issue. Laboratory experiments with two types of mud beds were also carried out to verify the method developed.

2. THEORETICAL CONSIDERATION

2.1. Rheological equation of mud

Researches on mud dynamic behaviors have indicated that mud shows complicated nonlinear viscoelastic behaviors when it is subjected to wave actions (Chou *et al.*, 1993; Jiang and Watanabe, 1995; Jacinto and Le Hir, 2001), and the mud rheological parameters are a function of shear strain, rate of shear strain, and the history of the above two parameters. To simplify the estimation of the mud rheological parameters, however, a linear viscoelastic Voigt medium is still frequently used. This assumption accurately describes mud motion for small strains, and may also adequately describe the mud motion for large strains if an equivalent linearization of constitutive equation can be found. Based on the hypothesis of linear viscoelastic medium, the constitutive equation of mud under the action of cycling loadings is given as follows (Jiang and Mehta, 1995).

$$\tau_{ij} = 2(\mu + \frac{iG}{\sigma})\dot{e}_{ij} \tag{1}$$

where τ_{ij} and $\dot{e}_{ij}$ are the shear stress tensor and rate of shear strain tensor, μ is the mud viscosity, G is the elastic shear modulus, $\sigma = 2\pi/T$ is the angular frequency of the periodic load with T = period, and $i = (-1)^{1/2}$.

To simplify the problem at this time, only one water layer on top and one mud layer at bottom were considered. Turbulence in the water layer was also ignored because this study concentrates on the estimation of mud bed properties.

2.2. Governing equations of a two-layer wave-mud system

According to Maa and Mehta (1990), the continuity equation and linearized momentum equations of the upper water layer (thickness = d_1) and lower mud layer (thickness = d_2) can be given as follows

$$\frac{\partial u_j}{\partial x}+\frac{\partial w_j}{\partial z}=0 \tag{2}$$

$$\frac{\partial u_j}{\partial t}=-\frac{1}{\rho_j}\frac{\partial p_j}{\partial x}+\nu_{ej}\left(\frac{\partial^2 u_j}{\partial x^2}+\frac{\partial^2 u_j}{\partial z^2}\right) \tag{3}$$

$$\frac{\partial w_j}{\partial t}=-\frac{1}{\rho_j}\frac{\partial p_j}{\partial z}+\nu_{ej}\left(\frac{\partial^2 w_j}{\partial x^2}+\frac{\partial^2 w_j}{\partial z^2}\right) \tag{4}$$

where the subscript j = 1, 2 denotes the upper water layer and the lower mud layer, respectively, x and z are the horizontal and vertical coordinates, t is the time, u_j and w_j are the horizontal and vertical velocities in the jth layer, respectively, ρ is the density, p is the dynamic pressure, and ν_{ej} is the apparent complex viscosity with $\nu_{e1} = \nu_w \approx 10^{-6}$ m^2/s for the water and $\nu_{e2}=\frac{\mu}{\rho_2}+i\frac{G}{\rho_2\sigma}$ for mud.

Assuming the displacements at the water surface and the water-mud interface, η_j, can be expressed as

$$\eta_j(x,t)=a_j\exp[i(kx-\sigma t)] \tag{5}$$

where a_j is the surface displacement amplitude of jth layer and $k = k_r + ik_i$ is the complex wave number to be solved. Notice that k_r denotes the wave number, and k_i denotes the wave damping rate.

If the density and viscosity of water and mud are given, Maa and Mehta (1990) used the simple secant method to solve for the k and a_j. Here a slightly different approach, Muller method (Press *et al.*, 1992) was used to solve for k and a_j, but basically the same formulation presented by Maa and Mehta (1990) was followed. After k and a_j were solved, the velocity and pressure fields can be computed.

2.3. Method for obtaining rheological parameters

If the complex wave number k and water wave amplitude a_1 are available from measurements, then the mud rheological properties can be estimated as follows.

Assuming that a total of M cases of experiments were carried out with a given mud bed density, for the mth (m = 1, ..., M) case, the complex wave number, k^e_m, can be measured from the experiment. This is because the wave length L and the wave height H along the flume are available. The theoretical complex wave number k^c_m for this mth case can also be obtained because all the factors (*i.e.*, d_1, ρ_1, μ_1, d_2, ρ_2) except v_{e2} are all given. Thus, a suitable value of v_{e2} can be found through iteration for this mth experiment. However, there are M cases to be considered for a single given water-mud system. Thus, the process is not finished yet.

Because there is no single value of v_{e2} that can satisfy all the experimental results (m = 1, ..., M), an optimum problem to find the best fitted v_{e2} is necessary. Let

$$\varphi = \sum_{m=1}^{M} \left| k^c_m - k^e_m \right|^2 \tag{6}$$

The value of v_{e2}, when φ is the minimum, can be regarded as the representative value of the assumed linear viscoelastic medium. A GA is applied to Eq. 6 to obtain this representative value of v_{e2}.

Although the linear viscoelastic Voigt properties were used for mud, it must be mentioned that the mud viscosity and shear modulus can vary with the stress due to nonlinearity (Chou *et al.*, 1993). Accuracy on the measurement of k and a_1 can also affect the estimation of the viscoelastic properties. In order to obtain the representative viscoelastic parameters for the linear viscoelastic medium, here an optimization problem was formed and solved with the experimental information.

2.4. On the solution of genetic algorithm

A GA searches the solution space of a function through the use of simulated evolution (Goldberg, 1989). This technique is particularly efficient in optimization problems, especially when the respective objective functions exhibit many local optima or discontinuous derivatives. The concept and the features of this study are briefly described as follows.

In order to solve the problem, a GA starts with a number of random and arbitrary values that are within a specified range called chromosomes, which constitute the population of the first generation. Each chromosome of the first generation undergoes evaluation by means of a pertinent function or fitness coefficient. This fitness coefficient depends entirely on the specific problem to be solved (*e.g.*, Eq. 6 in this study).

Then, the second-generation population is produced by means of certain operators, *i.e.*, selection, crossover, and mutation, which imitate biological processes and are applied to the chromosomes of the first generation. The entire process, *i.e.*, evaluation–selection–crossover–mutation, is repeated for a predetermined number of generations. At the end of each step, only part of the population (*i.e.*, these chromosomes that have a small value of Eq. 6) survives. In this way, it is anticipated that a chromosome, which represents the optimal solution to the examined problem, will prevail in the last generation (Michalewicz, 1994).

A Matlab toolbox of GA given in http://www.ie.ncsu.edu/mirage/GAToolBox/gaot (Houck *et al.*, 1995) was applied in this study to solve Eq. 6 by forming a maximum problem of $\Psi = 1 + 1/\varphi$. The float point representation of GA was used because of its efficiency over the binary representation (Michalewicz, 1994). It was found that this toolbox could provide a solution that is independent of the initial value.

3. LABORATORY EXPERIMENTS

Experiments on wave propagation over a mud bed were carried out in a wave flume of 32 m long, 0.5 m wide, and 0.75 m high at the Coastal Engineering Laboratory of Tianjin University. The mud, with a dispersed sediment medium diameter of 3.5 μm, was taken from the dredged material of Tianjin New Port and was pre-processed by filtering out coarse material using a 125 μm sieve. Two types of mud beds were prepared for the experiments: (1) mixed mud bed, and (2) deposited mud bed.

Mixed mud beds were formed by mixing mud and tap water to a specific bulk density in the flume. The wave attenuation experiment was carried out immediately after the mud bed was prepared. Thus, the mixed mud beds can be considered as mud experiencing no consolidation. The bed density, as well as the rheological parameters, can be considered as uniform in the vertical direction.

Deposited mud beds were prepared by first preparing a mixed mud bed with an initial mud density (ρ_0) of about 1120 kg/m^3, and then, the mud was consolidated for 4 - 53 days. Before an experiment, the mud layer thickness (d_2) was measured, and the water layer thickness was adjusted to 30 cm for all the experiments. At this time, the depth averaged bulk density of mud, ρ_m, was estimated as $\rho_1 + h_0 (\rho_0 - \rho_1)/d_2$ where h_0 is the original mixed mud layer thickness. Although the bulk density and rheological parameters of a deposited mud bed varies with the depth, they were assumed as a constant in this stage. Thus, the results obtained for this study represent a depth-averaged property.

The instantaneous profiles of water surface elevation along the flume were measured to provide wavelengths and wave-damping rates, and thus, the complex wave number k^e for all the experiments. With this information available, viscoelastic parameters of the mud beds were solved by using the method given in Section 2. The experimental conditions of the mixed and deposited mud beds are listed in Table 1, where H_0 is the wave height at the beginning of the mud bed. Other details of the experiments can be found in Zhang and Zhao (1999).

4. EXPERIMENTAL RESULTS

4.1. Estimated rheological parameters

When the mud density is large, the wave attenuation over any mud bed (mixed or deposited) becomes too small for having a good estimation of the mud viscoelastic parameters. Therefore, only these mixed mud beds with bulk density less than 1401 kg/m^3 and deposited mud beds with bulk density less than 1336 kg/m^3 were considered. Using the GA model given in the previous section, the model estimated shear moduli and viscosities for all the selected experiments are summarized in Figs. 1 and 2. The fitted curves between the mud density and the viscoelastic parameters given in Figs. 1 and 2 can be approximated by the following equations.

$$G_m = 8.96 \times 10^{-12} \exp(22.21\ \rho_2); \qquad G_d = 8.96 \times 10^{-12} \exp(22.21\ \rho_2)$$

$$\mu_m = 5.54 \times 10^{-8} \exp(14.97\ \rho_2); \qquad \mu_d = 4.45 \times 10^{-7} \exp(-10.55\ \rho_2)$$

where the subscripts m and d denote the mixed mud and deposited mud, respectively.

Table 1. Experimental conditions of mixed and deposited mud beds.

Parameter	Mixed mud bed						Deposited mud bed				
ρ_m (kg/m^3)	1227	1275	1341	1370	1401	1459	1218	1242	1267	1336	1378
d_2 (cm)	11.4	10.9	8.9	8.2	7.5	6.7	12.0	10.6	7.1	8.2	8.3
d_1(cm)	30						30				
T (s)	0.7~1.5						0.7~1.5				
H_0 (cm)	1.9~7.8						1.9~7.8				

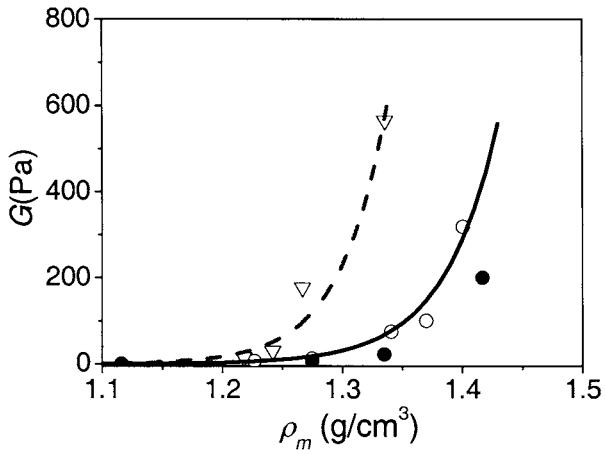

Fig. 1. GA model estimated shear moduli for mixed beds (symbol O) and deposited beds (symbol ∇). Black dots are measurements from using a rheometer. Solid and dashed lines are fitted curves.

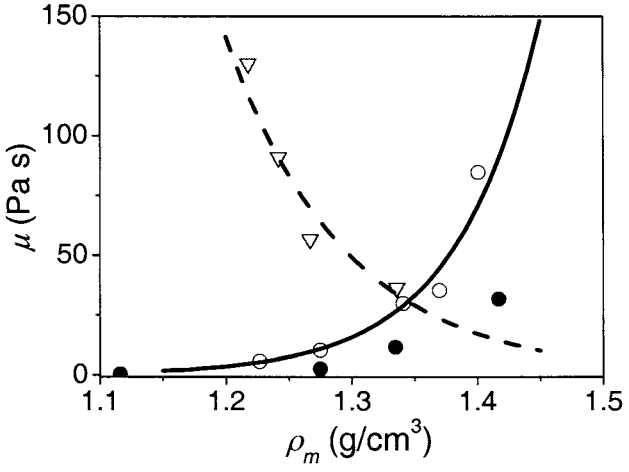

Fig. 2. GA model estimated viscosity for mixed bed (symbol O) and deposited mud (symbol ∇). Black dots are measured by a rheometer. Solid and dashed lines are fitted curves.

The results indicate that mixed- and deposited muds have significantly different viscoelastic properties, even their densities are the same. If the bulk density is large, then the shear modulus for a deposited mud can be much larger than that for the mixed mud. When the bulk density is small, the difference in shear modulus is small, but the difference in viscosity is not. Actually, the trends of changing mud viscosity for mixed mud beds and deposited mud beds are just opposite (Fig. 2). Due to the larger shear modulus, the motion of deposited mud beds would be smaller than that of the mixed mud beds with the same bulk density and under the same wave condition. This finding correlates well with the observed phenomena in the flume. The different trends on mud viscosity may be caused by the different sediment structure in the bed. A deposited mud bed is usually strongly bound together due to consolidation, *i.e.*, a large G for the deposited mud bed. The mixed mud bed with high mud density showed more viscosity because more sediment particles for providing internal friction (*i.e.*, viscosity), but has no internal structure to obtain shear strength (*i.e.*, G). The binding structure of a deposited mud bed becomes stronger and stronger with the increase of consolidation (*i.e.*, mud density), and thus, harder and harder to be broken under the action of waves. This also implies that the wave attenuation rate is low for a deposited bed because of the large shear modulus.

For the mixed mud beds, a comparison of GA model estimated shear moduli and viscosities with the measurements by using a RMS-605 dynamic rheometer (Zhao and Zhang, 1997) is possible because both muds are severely disturbed. Because the measured shear modulus depends on the mud density as well as the strain rate amplitude, the comparison given in Fig. 1 can only be treated as a reference. This is because the rheometer used a fixed shear rate amplitude of 1.0 s^{-1}, but the estimated mud shear rate amplitude is around $O(1)$ s^{-1} or less in the flume. Further information on the calculation of shear strain rate for the above two approaches is given next. Considering the differences in experimental conditions between mud beds in the wave flume and mud in the rheometer, it can be concluded that the estimated shear moduli and viscosities for mixed mud beds are reasonable. This facilitates the verification of the GA model used in Sec. 2.

Shear Strain Rate in the Rheometer: For this oscillating coaxial cylinders type instrument, the shear (strain) rate can be expressed as $\gamma_m \omega \cos(\omega t)$ where γ_m is the amplitude of the oscillating strain, ω is the oscillating angular frequency, and $\gamma_m \omega$ is the shear rate amplitude.

Shear Strain Rate in the Flume: The shear rate amplitude can be roughly calculated as the maximum of Eq. 7 (Sakakiyama and Bijker, 1989). Obviously there is a vertical

gradient of the shear strain rate amplitude because of the vertical velocity gradient. In this study, the depth-averaged values were used.

$$\left|2\left(\frac{\partial u}{\partial x}\right)^2 + 2\left(\frac{\partial w}{\partial z}\right)^2 + \left(\frac{\partial u}{\partial z} + \frac{\partial w}{\partial x}\right)^2\right|^{1/2} \tag{7}$$

4.2. Influences of rheological parameters on wave propagation

The experimental results also indicate that the wave damping rates were different for waves propagating over a mixed or deposited mud bed (Fig. 3). The different points at the same abscissa denote the cases of different wave heights. It can be seen that the wave damping rate over mixed mud beds reaches its maximum when the mud density is about 1340 kg/m^3, while the wave damping rate over deposited mud beds attains its maximum at a much lower mean bulk density, 1240 kg/m^3. The different critical densities with maximum damping rate can be attributed to the differences in the rheological parameters of mixed and deposited mud beds.

4.3. Limitations of linear viscoelastic model

It should be noted that the properties of mud may be nonlinear (*e.g.*, depends on the shear strain), but the model presented here assumed a linear Voigt element, and thus, the best this model could be was to estimate the mud properties as a linear material that

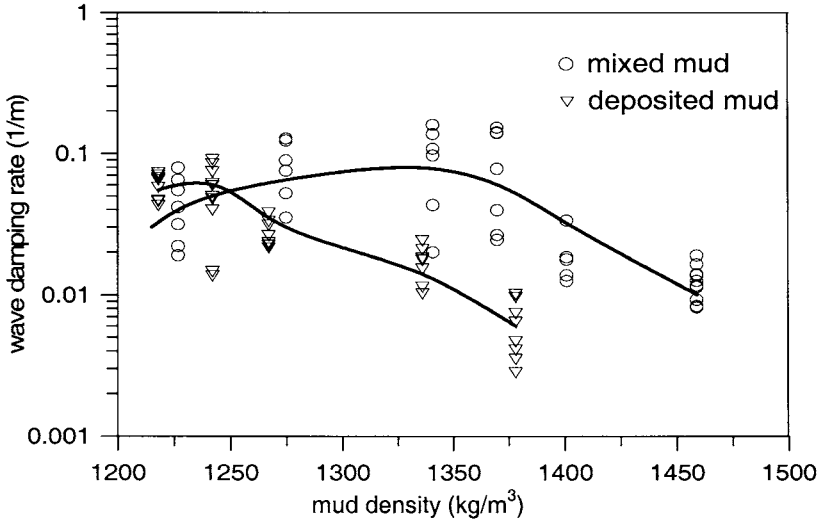

Fig. 3. Measured wave damping rates. Lines are added to show a clear trend.

approximate the mud beds used in the experiments. Similarly, because the model assumed a two-layer water-mud system, the best it could be was to reflect the average properties of the mud bed. As shown in Figs. 3 and 4, the wave damping rate for a mud bed with a given mud density changes with the wave period and wave height. The linear Viogt model of mud can explain the change of wave damping rate due to different wave periods (Fig. 4) but cannot explain the change due to different wave heights. For short period waves, and if the wave motion can be transmitted to the mud bed, the mud will oscillate fast, and thus consume more energy. For this reason, the damping rate should be high. But there is another factor should be considered too. If the wave period is too short, the wave motion will not be transmitted to the mud efficiently (see the left side of Fig. 4). Actually if the wave period is sufficiently short, wave energy will not be transmitted to the mud bed below, and under this condition, the mud bed actually would not be seen by the waves. The whole effects of wave period are reflected in the computed curves of Fig. 4. The different k_i for the same period in Fig. 4 reveal the nonlinear influences of wave height. It is clearly seen that the estimations by using the linear viscoelastic model predicted the average wave-damping rate well but cannot explain the nonlinear responses due to large wave height. Therefore, further study is needed to simulate the nonlinear rheological properties.

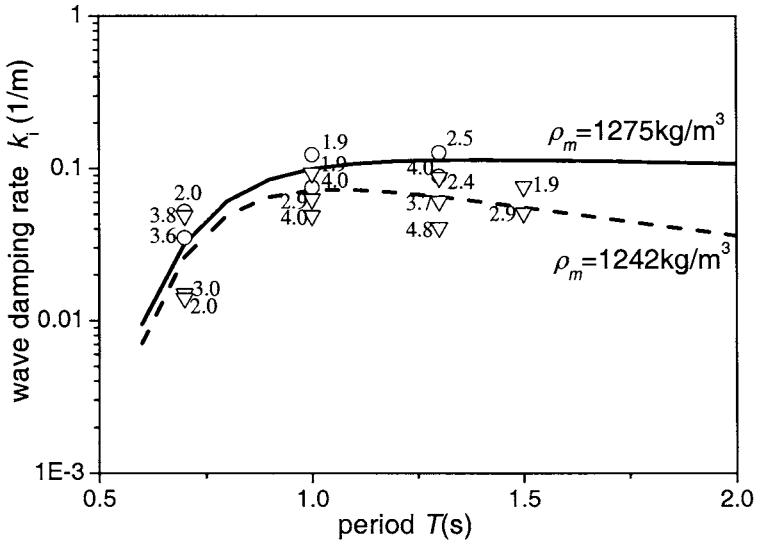

Fig. 4. Comparisons of measured and calculated wave damping rates. Solid and dashed lines are calculated for a mixed and a deposited bed, respectively, with their bulk density marked in the figure. O and ∇ are measurements from a mixed and a deposited bed, respectively. Numbers in the diagram represent wave height (cm).

5. DISCUSSION AND CONCLUSIONS

On the assumption of mud being a linear viscoelastic medium, an optimization problem has been constructed to solve the averaged rheological parameters of the mud using the measured wave data on a two-layered water-mud system. This method used a public available GA toolbox. The estimated rheological parameters represent the vertically averaged properties of mud, but cannot describe the nonlinear phenomena of wave-mud interaction because of the linear model limitation. Additional work is needed to determine the nonlinear rheological properties.

It was found that the relationship between the mud density and the rheological parameters of a mixed mud differs markedly from that of a deposited mud. This is mainly caused by the different consolidation state of mud. Therefore, in dealing with wave-mud interactions, special attention should be paid to the history of mud bed formation.

Comparisons between the rheological parameters measured by using a RMS-605 rheometer and those estimated by using the GA model for mixed mud beds in laboratory experiments indicate that the GA model presented in this paper is accurate. Although there is no way to verify the GA model estimations for the deposited mud beds (because of the inevitable severe disturbance of mud structure), the model results are reasonable. This may lead to a conclusion that the average rheological parameters of deposited mud beds can also be estimated using the proposed GA model. This is important considering that there is no practical method to obtain the parameters yet.

Inasmuch as the mud bulk density and mud layer thickness can be accurately estimated under the laboratory experiment conditions, the proposed GA model can be useful for estimating mud rheological properties. When using this technique at fields, however, there is still one difficulty that requires further studies. Although the wave conditions can be observed by using a remote sensing technique in a timely manner, the water depth information can also be estimated with reasonable accuracy, it would be hard to estimate the mud layer thickness nor the mud bulk density, and thus, at this time, the use of this technique at fields is still pending for the outcomes of more studies.

ACKNOWLEDGMENTS

The project was supported by The National Natural Science Foundation of China (No. 50279029), the Central funding of Hong Kong Polytechnic University (GT219), and Hong Kong RGC/NSFC funding (NSFC/HKU 26). The use of Matlab toolbox of

genetic algorithm from C. R. Houck, J.A. Joines and M.G. Kay is sincerely acknowledged.

REFERENCES

Chou, H.T., M.A. Foda and J.R. Hunt. 1993. Rheological response of cohesive sediments to oscillating forcing. In: *Nearshore and Estuarine Cohesive Sediment Transport*. A.J. Mehta (ed.), AGU, Washington DC, 42, 126-147.

Goldberg, D.E. 1989. *Genetic Algorithms in Search, Optimization and Machine Learning*, Addison-Wesley, Reading, MA.

Houck, R.C., J.A. Joines and M.G.. Kay. 1995. *A Genetic Algorithm for Function Optimization: A Matlab Implementation*, NCSU-IE Technical Report 95-09 (http://www.ie.ncsu.edu/ mirage/GAToolBox/gaot/).

Jacinto, R.S. and P. Le Hir. 2001. Response of stratified muddy beds to water waves. In: *Coastal and Estuarine Fine Sediment Process*. W.H. McAnally and A.J. Mehta (eds.), Elsevier, Oxford,UK, 95-108.

Jiang, F. and A.J. Mehta. 1995. Mudbanks of the southwest coast of India IV: Mud viscoelastic properties. *Journal of Coastal Research*, 11(3), 918-926.

Jiang, Q. and A. Watanabe. 1995. Rheological properties of soft mud and a numerical model for its motion under water waves. *Coastal Engineering in Japan*, JSCE, 38(2), 195-214.

Li, Y. and A.J. Mehta. 1997. Mud fluidization by water waves. In: *Cohesive Sediment*. N. Burt, R. Parker, and J. Watts (eds.), John Wiley, Chichester, UK, 341-351.

Maa, P.-Y. and A.J. Mehta. 1990. Soft mud response to water waves, *Journal of Waterway, Port, Coastal and Ocean Engineering*, ASCE, 116(5), 634-650.

Michalewicz, Z. 1994. *Genetic Algorithms + Data Structures = Evolution Programs. AI Series*. Springer-Verlag, New York.

Press, W.H., B.P. Flannery, S.A. Teukolsky and W.T. Vetterling. 1992. *Numerical Recipes in FORTRAN: The Art of Scientific Computing, 2nd ed.* Cambridge University Press, Cambridge, England.

Sakakiyama, T. and E.W. Bijker. 1989. Mass Transport Velocity in Mud Layer due to Progressive Waves. *Journal of Waterway, Port, Coastal and Ocean Engineering*, ASCE, 115(5), 614-633.

Shibayama, T. and N.N. An. 1993. A visco-elastic-plastic model for wave mud interaction. *Coastal Engineering in Japan*, JSCE, 36(1), 67-89.

Verbeek H. and J.M. Cornelisse. 1997. Erosion and liquefaction of natural mud under surface waves. In: *Cohesive Sediment*. N. Burt, R. Parker, and J. Watts (eds.), John Wiley, Chichester, UK, 353-363.

Zhang Q.H and Z.D. Zhao. 1999. Wave-mud interaction: Wave attenuation and mud mass transport. *Proceedings, Coastal Sediments*. N.C. Kraus and W.G. McDougal (eds.), *ASCE*, Reston, 1867-1880.

Zhang Q.H. and Z.D. Zhao. 2000. Damping of water waves over different kinds of beds. *Ocean Engineering,* 18(4), 36-42 (in Chinese).

Zhao Z.D. and Q.H. Zhang. 1997. Interaction between regular waves and muddy sea bed – wave attenuation. *Hydraulic Engineering*, 4, 26-34 (in Chinese).

Estuarine and Coastal Fine Sediments Dynamics
J.P.-Y. Maa, L.P. Sanford and D.H. Schoellhamer (editors)

The critical diameter for distinguishing bed material load and wash load of sediment in the Yangtze Estuary, China

Wang, Y.Y. and Q. He

State Key Laboratory of Estuarine and Coastal Research, East China Normal University, Shanghai 200062, China

KEY WORDS
Yangtze Estuary, sediment, bed material load, wash load, critical diameter

Two field surveys were conducted in the Yangtze Estuary for studying the critical grain size for distinguishing the Bed Material Load (BML) and Wash Load (WL) in the summer of 2001 and in the winter of 2003, respectively. During these periods, the suspended sediment in the Yangtze Estuary was mainly composed of clay and silt. The averaged median diameter of near-surface sediment samples was 6.2 μm. This value increased to 10.7 μm for near-bottom sediment samples. Bed sediments, mainly consisting of silt, had an averaged median diameter of 57.6 μm.

The critical diameters for distinguishing BML and WL were identified using three methods: (1) the inflexion method, (2) the most-curvature method, and (3) the definition method. Ideally, the third method would be the best approach, if properly planned and sufficiently supported. This study indicates that the most-curvature method can provide a reasonable good estimation without the need of a huge resource.

1. INTRODUCTION

Sediment particle size information plays an important role in the understanding and modeling of sediment and sediment-associated contaminants (*e.g.*, heavy metals, nutrients, phosphorus, micro-organics and radionuclide) transport in rivers and estuaries (Walling, 1996; Walling *et al.*, 2000). Sediment transported in rivers always experi-

enced a different level of sorting effect. Large and heavy particles will be suspended during high discharge events that have a large transport capability, but they will be deposited first when that capability diminishes. Small and light particles will remain in suspension for a relatively long time, even after the high discharge event. Particle size composition in suspended material also reflects the source of sediment. Therefore, it may be viewed as a key feature of the sediment delivery dynamics and sediment budget of a river basin (Stone and Walling, 1997). Characteristics of sediment movement and the properties of the flow are influenced dramatically by runoff and tides as well as the sediment grain-size distribution and mineral composition. In estuaries, waves and salt intrusion further complicate the grain size distribution by introducing strong mixing and aggregation/flocculation.

There are two types of sediment loads according to the size of particles and their origins: Bed Material Load (BML) and Wash Load (WL). The BML is composed of particles found in appreciate quantities in the channel bed, and the entrainment, transport, and deposition of BML are the primary processes involved in channel stability and morphology. The WL is composed of particles finer than those found in the bed material, and comes only from watershed (Biedenharn *et al.*, 2000). In fact, WL is washed through the channel without deposition, and thus, cannot be found in any significant amount in the bed. The amount of WL in a reach depends solely on the availability at the watershed and not on the ability of the flow to transport it (Einstein and Chien, 1953). It is important to delineate the BML and WL not only in the necessity of calculating sediment transport rate, but also in sedimentation and bed evolution (Chien, 1990).

There is a subtle difference between the above mentioned terminologies (*i.e.*, BML and WL) with the other two related and also widely used terminologies in sediment transport, Bed Load (BL) and Suspended Load (SL) which are defined according to the patterns and laws of motion (Chien and Wan, 1999). The difference is that some of the sediment particles in SL also belong to BML because of temporarily suspensions of bed material. Sediment particles that have a diameter larger than the grain size for WL will have chances to move back-and-forth between the water and the bed because of the nature of turbulent flows. On the other hand, for those sediment particles belong to WL will not have chance to deposit at all. For this reason, the measured mean grain size from water samples is larger than that of the grain size for WL.

Partheniads (1977) suggested using a fixed particle size, 60 μm, as the critical diameter for distinguishing BML and WL. That suggestion is not appropriate as pointed out by Chien and Wan (1999). In general, the following three approaches have been practiced in rivers for this purpose: (1) The inflexion method, (2) the most-curvature

method, and (3) the definition method (Chien and Wan, 1999). Although the above three methods have been used mainly in rivers, Guo *et al.* (1999) also used these methods in reservoirs and navigation channels. In estuary environments, *e.g.*, the Yangtze estuary, where fine sediment particles may aggregate easily and the flocculation process may change the grain size distribution, both for suspended and bed sediments. Are the above three methods still valid? This question has never been addressed, and thus, it is the objective of this study to check the applicability and accuracy of the three selected methods at the Yangtze estuary.

2. FIELD SITES AND METHODS

Two field surveys were conducted in the partial mixing Yangtze estuary (Fig. 1). This is a challenging site for studying the sediment characteristics because of the large study domain, highly complicated hydrodynamics, and a possible significant change of hydrodynamic environments caused by the construction of the Three Gorges Dam.

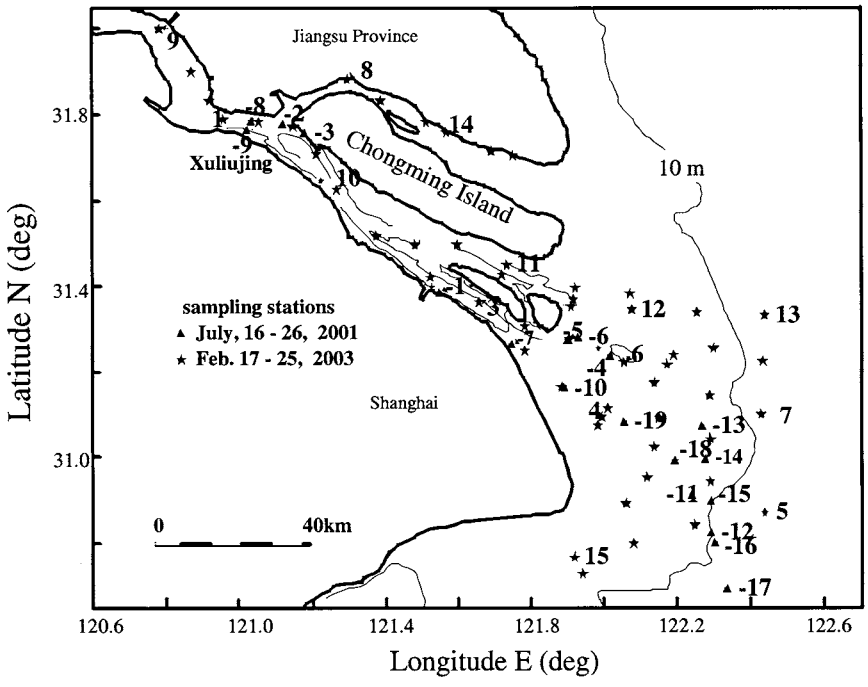

Fig. 1. Survey stations along the Yangtze Estuary. Triangles with a negative number are stations in the 2001 survey. Stars are stations in the 2003 survey.

The first survey was carried out during the neap tide on July 16 and the spring tide on July 26, 2001 with a total of 29 stations. The second survey was conducted during the spring tide on Feb. 17 and the neap tide on Feb. 25, 2003 with a total of 58 stations. Both surveys used multiple vessels (four and eight vessels for the first and second survey, respectively) and spanned a domain of more than 200 km. Measurements on water temperature, salinity, and Suspended Sediment Concentration (SSC) were carried out using a YSI 6600 Sonde profiler (YSI Co.), or an OBS 3A profiler (D&A instrument Co.), and/or water samples. Sufficient water samples were collected for changing the turbidity reading to SSC and for laboratory analysis of grain size distribution. Sediment bed samples were also collected at selected stations using a grab sampler for the grain size analysis.

The monthly averaged freshwater discharge rates during the two survey periods were available from the Xuliujing station (Fig. 1). They were quite different (40016 m^3/s in July 2001 and 17896 m^3/s in Feb. 2003). This implies that the results would also be different for these two periods.

In the first survey, only 19 stations (triangles with a negative number marked in Fig. 1, *e.g.*, -3 means Sta. 3 from the first survey) collected enough water samples for grain size distribution, and 15 stations collected bed sediment samples. In the second survey, only 14 stations (see the stars with a number marked in Fig. 1) collected enough water samples for grain size analysis, and 53 stations collected bed sediment samples.

The measurements at these sampling stations were carried out for 27 consecutive hours (more than a full tidal cycle) for observing the possible differences caused by the change of tidal conditions. Data were collected every hour at six different water depths uniformly distributed from 0.5 m below the water surface (near-surface) to 0.5 m above the bottom (near-bed).

Particle size distributions of suspended sediment samples and bed samples were measured by using a LS100Q Coulter counter (Loizeau *et al.*, 1994). Samples were fully dispersed by using 4% sodium metaphosphate.

Although there are many data collected during these two surveys, only the particle size distribution was used in this study to find the best approach for identifying the critical particle size for BML and WL.

3. RESULTS

Grain size analysis shows that the suspended Sediment Samples (SS) was composed mainly of clay and silt in the Yangtze estuary (Fig. 2). In average, near-surface

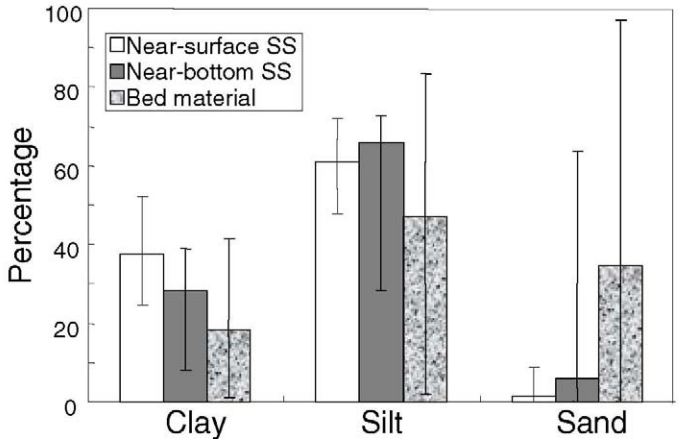

Fig. 2. Sediment composition for all sediment samples collected during the two surveys. Vertical bars show the range from a total of 75 samples for near-surface SS (33 stations), 73 samples from 34 stations for near-bottom SS, and 68 samples for bed SS.

SS had 38% of clay and 61% of silt with a median diameter of 6.2 μm (Fig. 3a). For near-bottom SS, the clay content decreased a little to 28%, but the silt content increased a little to 66% with a median diameter of 10.7 μm (Figs. 2 and 3b).

The averaged grain-size distribution of all the bed sediment samples shows a different composition with 19% of clay, 47% of silt and 34% of sand (Fig. 2). The averaged median diameter was 23 μm (Fig. 4a) for the first survey, but increased to 56 μm for the second survey (Fig. 4b).

3.1. The inflexion method

Let p is the percentage by weight of particles that are finer than a specified particle size in a sediment sample. The inflexion method chooses the particle size corresponding to p = 10% (or p = 5%, however, 10% is a popular choice, and thus, used in this study) in a particle size distribution curve from bed sample as the critical diameter to distinguish BML and WL. Because of the "steel-like bottom" at some of the bed sample stations, a brute force was necessary to acquire bed samples. Thus, the sample quality is questionable at these stations, and they were excluded in the analysis. Without these questionable data, the grain size distribution indicates that the averaged critical diameter for distinguishing BML and WL was 1.3 μm (Fig. 5a and Table 1) for the first survey. For the second survey in 2003, a similar result of 1.4 μm (Fig. 5b and Table 1) was obtained.

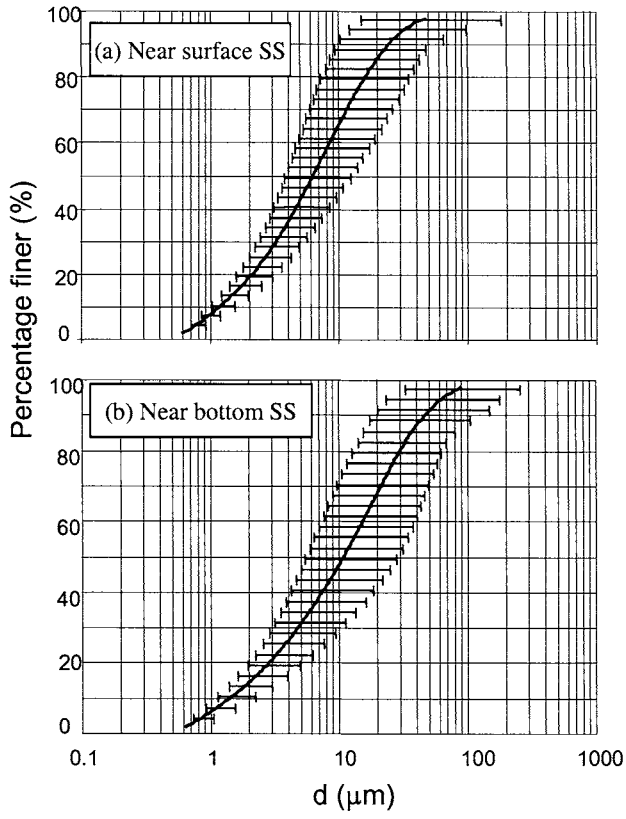

Fig. 3. Averaged grain size distribution from the suspended sediment samples. The bars show the range among samples. (a) Near-surface samples, and (b) near-bottom samples.

3.2. The Most-curvature method

In order to use this method, an analytical equation for the grain size distribution must be provided first. Past studies (Xiong, 1985; 1992) indicated that most of the grain size distributions have a normal distribution pattern, and thus, the accumulated curve can be described as Eq. 1.

$$p = 50\tanh[\varphi\log(\frac{d}{d_{50}})] + 50 \tag{1}$$

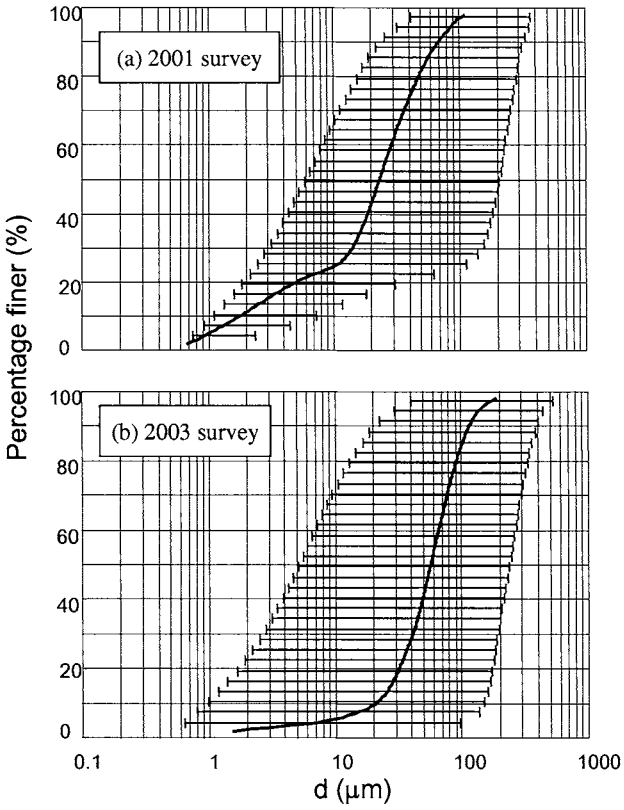

Fig. 4. Averaged grain size distribution (with range bars) for all the bed sediment samples. (a) From 15 stations in the 2001 survey period, and (b) from 53 samples in 2003.

where p is the percentage by weight of particles that is finer than a specified diameter, d, in a sediment sample, d_{50} is the median diameter, φ is a uniformity parameter (Eq. 2) of sediment grain size distribution with the following popular selection.

$$\varphi = 0.55 \log^{-1} \sqrt{\frac{d_{75}}{d_{25}}} \tag{2}$$

where d_{25} and d_{75} are the grain size with p = 25% and 75%, respectively. A large φ represents more uniformity and vice versa.

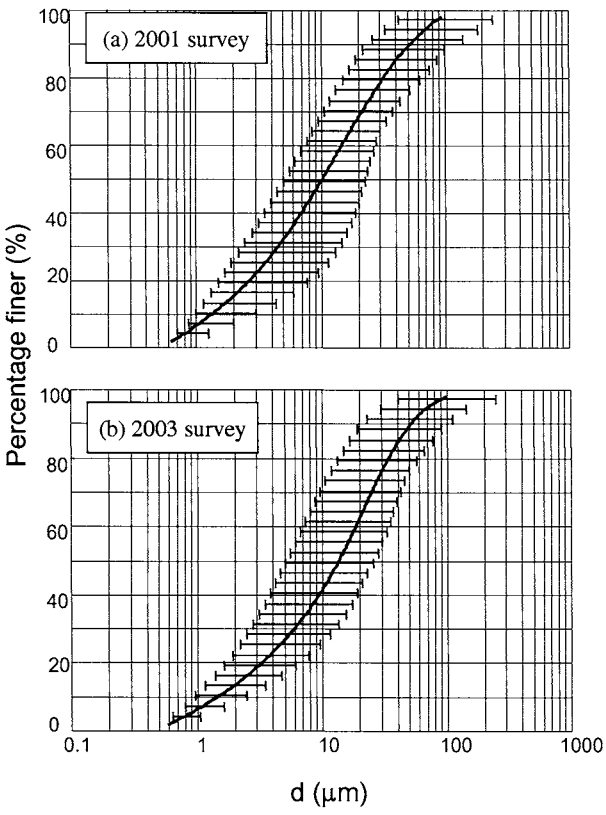

Fig. 5. Averaged grain size distribution (with range bars) for the selected bed sediment samples after removing bad-quality samples. (a) From 14 stations in 2001, and (b) from 30 stations in 2003.

Comparison between the measured particle size distribution curves and the analytical curves (*i.e.*, Eq. 1) was carried out to compare with the measurements. This was done by using field data to calculate φ (Eq. 2) and measured d_{50} in Eq. 1. The comparison is classified as "very good" if the maximum difference is less than 5% between the two curves. If the maximum difference is larger than 5% but less than 10%, then the result is classified as "good." Otherwise, the result is classified as "fair." The results of comparing 84 grain-size distribution curves for bed material and 253 grain-size distribution curves for suspended material are summarized in Table 2, which indicates that 77% of the grain-size distribution curves for bed material and more than 90% of the grain-size distribution curves for suspended material can be represented by Eq. 1 for the Yangtze estuary.

Table 1 Critical diameter calculated by the inflexion method and most-curvature method.

Methods	Survey	Sample Number	Minimum (μm)	Maximum (μm)	Average (μm)	Std. Dev.
Inflexion	1st	14	1.1	3.0	1.3	0.20
	2nd	30	0.9	2.3	1.4	0.38
Most-curvature	1st	14	1.7	4.3	2.4	0.76
	2nd	30	1.5	7.8	3.5	1.88

With Eq. 1 available, an analytical equation for the maximum curvature of the distribution curve of bed samples can be found by taking $\partial^2 p/\partial d^2$. By using the method of trial and error, one can find easily the critical grain size for wash load, d_{WL}, at the maximum curvature.

The results (Table 1) indicate that d_{WL} varies from 1.7 ~ 4.3 μm for the first survey, with an average of 2.4 μm. For the 2003 survey, a relatively large averaged d_{WL} (3.5 μm) was obtained.

3.3. The definition method

Based on the definition of WL, particles with size less than d_{WL} will not participate in bed formation. In other words, particles with size less than d_{WL} will never deposit on bed. The above statements imply that the amount of sediment with size less than d_{WL} in suspension does not change along the route of the transport, if the hydrodynamic forces along the sediment transport route (*e.g.*, the main channel) remain similar. Therefore, if

Table 2. Comparison of measured grain-size distribution and Eq. 1 in the Yangtze Estuary.

Results	Bed material		Water-bottom SS		Water-surface SS	
	Number	%	Number	%	Number	%
Very good	14	16.7	31	24.6	58	45.7
Good	51	60.7	85	67.5	68	53.5
Fair	19	22.6	10	7.9	1	0.8
Total	84	100	126	100	127	100

sufficient amount of suspended sediment samples are collected at the same time along the transport route, then the variation of SSC for selected grain size in suspended sediment samples along the route can be used to find d_{WL} directly.

This approach involves huge amount of field samples and laboratory analysis. It is also necessary to point out that simultaneous sampling over 200 km is difficult, if not impossible, and thus, some degree of relaxation on the sampling time and the route of the transport are inevitable. Nevertheless, the definition method would be the most direct approach for determining d_{WL}.

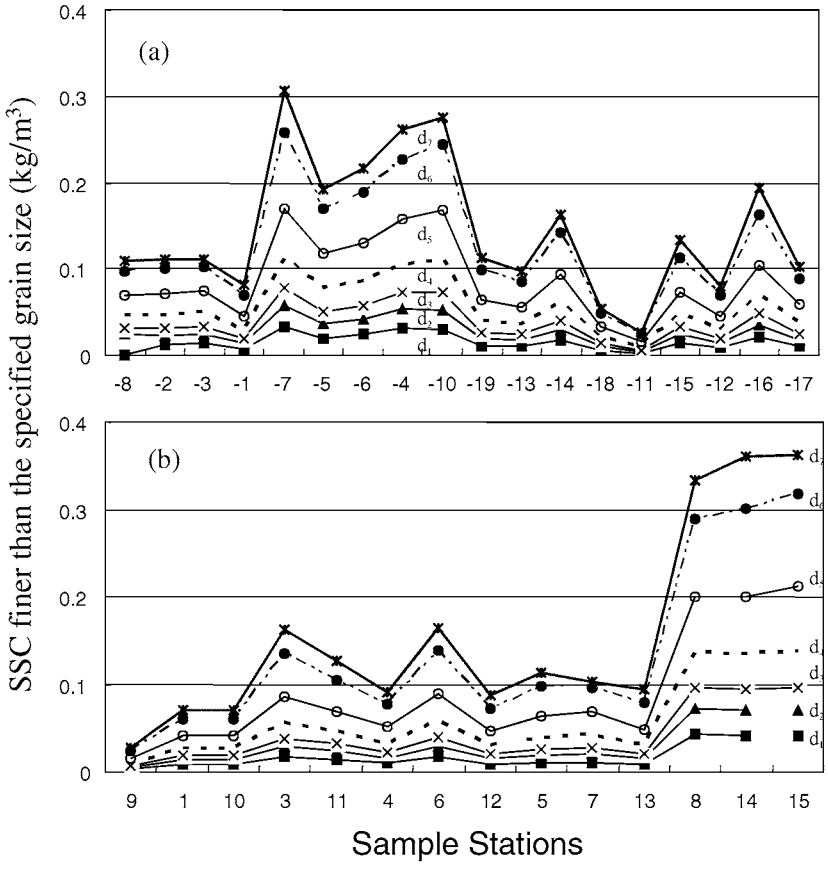

Fig. 6. Variation of suspended sediment concentration for sediment finer than the selected grain size from the accumulated grain size distribution curves along the Yangtze Estuary, where d_1 to d_7 are 1, 1.5, 2, 3, 5, 10, and 15 μm, respectively. (a) Data for the 2001 survey period, and (b) for the 2003 survey period.

The first survey result (18 stations, Fig. 6a) shows that the variation of SSC is weak for the sediment with a grain size smaller than 2.5 μm (an interpreted result by choosing the average of d_3 and d_4 in Fig. 6). For the second survey, only 11 stations were used because the other three stations (*i.e.*, Stas. 8, 14 and 15) were not in the main channel. Figure 6b shows that the variation of SSC is weak for the sediment with a grain size smaller than 5 μm. Notice that the judgment on the variation of SSC is weak or not is rather subjective at this time. A rigorous criterion is necessary to have consistent results for the following studies, but that may not be possible because of the huge resource required for this kind of operation.

4. DISCUSSION AND CONCLUSIONS

Among the three selected methods, the inflexion method is the simplest method, and thus, used frequently. The choice of p = 10%, however, is arbitrary. The most-curvature method is a little complicated because of the requirement of having an analytical equation to fit the grain size distribution data. This may cause a problem if the fitting is not good. The above two methods, however, may not have data to support their use at the Yangtze estuary, and thus, according to the definition of wash load, a direct approach (*i.e.*, the definition method) was implemented during this study.

The definition method used in this study, although not with the perfect experiment design because of the limitations imposed by reality, produced the base (d_{WL} = 2.5 and 5 μm during the first and second surveys, respectively) for comparing with other methods.

Although the exact freshwater discharges during the two survey periods are not available, the significantly different monthly averaged freshwater discharges (40016 m^3/s in July 2001 and 17896 m^3/s in Feb. 2003) imply that the d_{WL} should be different. The higher sediment transport capability associated with the high discharge does not reflect on the medium grain size of bed sediments. For example, with a high discharge in July 2001, the d_{50} measured from the bed samples (9.5 μm) is, on the contrast, smaller than that in Feb. 2003 (14 μm). Is it because of the tidal effects on the sediment carrying capacity, and thus, the grain size distribution in estuaries? More studies are necessary to address this question.

Results from the inflexion method also do not show any significant difference (d_{WL} = 1.3 and 1.4 μm, respectively), despite the significant difference in the monthly averaged freshwater discharge.

On the other hand, the other two methods all show a similar trend, the d_{WL} is relatively small for a high freshwater discharge. The most-curvature method gives a rela-

tively small d_{WL} (2.4 μm) in July 2001 and a relatively large d_{wl} (3.5 μm) in Feb. 2003. The definition method shows that d_{WL} = 2.5 μm in July 2001 versus 5 μm in Feb. 2003.

The d_{WL}'s determined by the inflexion method are low and not sensitive to the freshwater discharge. The most-curvature method gives a better result. Considering the huge resource required for the direct method, and the close result the most-curvature method can deliver, the most-curvature method is suggested for future application.

An improvement on the most-curvature method is possible. Currently, the selection of φ is fixed (Eq. 2). Since the selection of d_{75} and d_{25} is rather arbitrary, there is room for future improvement, at least to check if other options would be better. Also the raw data on grain size distribution can be best fitted by an analytical equation similar (but not necessary the same) to that given by Eq. 1. If the reason of this method is better is because of the use of the maximum curvature in the grain size distribution curve, then other numerically best fitted equation might provide a better choice, at least an alternative. It is not difficult to find a nonlinear function (*e.g.*, similar to that given by Eq. 1) to represent the measured grain size distribution through nonlinear curve fitting (*e.g.*, the Nelder-Mead simplex method, Dennis and Woods, 1987). Once the fitted equation is found, the rest of numerical process is the same as that used in this study.

Notice that the critical diameters measured in the Yangtze estuary during these two specified periods only represent the results under these hydrological conditions, and the possible effect of fine sediment flocculation and aggregation is excluded. If flocculation of clay is considered, then different approaches are necessary to identify the floc size distribution, floc density, and then, the determination of the critical diameter is possible.

ACKNOWLEDGMENTS

The authors are grateful to Mr. Yuanzhong Xue, Yue Che, and Ruiming Wu for their assistance with the intensive field and laboratory work. Acknowledgment is also given to Shuanghong Wu for her grammar check in English. Sincere appreciation goes to the reviewers for their constructive comments and suggestions. This study was co-funded by the National Key Fundamental Research Program (973 program Grant Number 2002CB412403), National Science Foundation of China (Grant Number 50379014) and National Outstanding Young Teacher Foundation of China (Grant Number 49525609).

REFERENCES

Biedenharn, D.S., C.R. Thorne and C.C. Watson. 2000. Recent morphological evolution of the Lower Mississippi River. *Geomorphology*, 34, 227-249.

Chien, N. and Z. Wan. 1986. A critical review of research on the hyperconcentrated flow in China. *Series of Publication IRT CE*, Beijing.

Chien, N. and Z. Wan. 1999. *Mechanics of Sediment Transport*. ASCE Press, Reston, VA, 913pp.

Chien, N. 1990. On the concepts of "Bed Material Load" and "Wash Load." In: *Collected papers of Chien Ning*. Lin, B.N. (editor-in-chief), Press of Tsinghua University, Beijing (in Chinese).

Dennis, J.E. Jr. and D.J. Woods. 1987. New computing environments: Microcomputers in large-scale computing. In: *Society for Industrial and Applied Mathematics*, Wouk A. (ed.), 116-122.

Einstein, H.A. and N. Chien. 1953. Can the rate of wash load be predicted from the bed-load function. Transactions, *American Geophysical Union*, 34(6), 876-882.

Guo, Q.T., Y. Yi and Z. Zhang. 1999. Division of bed material load and wash load. *Water Resources and Hydropower of Northeast*, 9, 28-30 (in Chinese).

Loizeau J.L., D. Arbouille, S. Santiago and J.P. Vernet. 1994. Evaluation of a wide range laser diffraction grain size analyser for use with sediments. *Sedimentology,* 41, 353-61.

Partheniades, E. 1977. Unified view of wash load and bed material load. *Journal of Hydraulic Division*, ASCE, 103(HY9), 1037-1058.

Stone, P.M. and D.E. Walling. 1997. Particle size selectivity considerations in suspended sediment budget investigations. *Water Air Soil Pollution*, 99, 63-70.

Walling, D.E. 1996. Suspended sediment transport by rivers: a geomorphological and hydrological perspective. *Archiv fuer Hydrobiologie*, 47, 1-27.

Walling, D.E., P.N. Owens, B.D. Waterfall, G.J.L. Leeks, P.D. Wass. 2000. The particle size characteristics of fluvial suspended sediment in the Humber and Tweed catchments, UK. *The Science of the Total Environment,* 251/252, 205-222.

Xiong, Z.P. 1985. Determination of the function expression for sediment grain size distribution curves and the critical grain diameter to demarcate bed material load and wash load. *Journal of Sediment Research*, 2, 88-94 (in Chinese).

Xiong, Z.P. 1992. Functional expression of sediment composition in river and its examination. *Journal of Sediment Research*, 2, 76-83 (in Chinese).

Estuarine and Coastal Fine Sediments Dynamics
J.P.-Y. Maa, L.P. Sanford and D.H. Schoellhamer (editors)

Seasonal variability of suspended particulate matter observed from SeaWiFS images near the Belgian coast

Van den Eynde, D., B. Nechad, M. Fettweis and F. Francken

Management Unit of the North Sea Mathematical Models (MUMM), Royal Belgian Institute of Natural Sciences, Gulledelle 100, 1200 Brussels, Belgium

KEY WORDS
Suspended particulate matter, SeaWiFS satellite images, *in situ* measurements, Belgian coastal waters

Suspended Particulate Matter (SPM) surface concentration maps in the Belgian/Dutch coastal zone are retrieved from SeaWiFS images and are corrected using *in situ* measurements to obtain depth-averaged SPM concentration maps. A spatial correlation analysis of the derived maps shows that the area could be divided into three subregions where the correlations between the SPM concentrations are higher than 70%. Examination of *in situ* SPM concentration measurements reveals that during about 1/3 of the tidal cycle the SPM concentration is significantly higher than during the rest of the cycle. Strong vertical gradients are sometimes observed during periods with increased SPM concentration. A satellite image taken during such a period would underestimate the depth-averaged SPM concentration. Images taken during other periods better represents (except for some small corrections) the averaged SPM concentration. The methodology for obtaining the depth-averaged SPM concentration maps from surface SPM distributions derived from SeaWiFS images is positive but can be further improved.

1. INTRODUCTION

Near the Belgian coast (Southern Bight of the North Sea, see Fig. 1), the harbours and navigation channels are situated in a high turbidity zone. Suspended Particulate

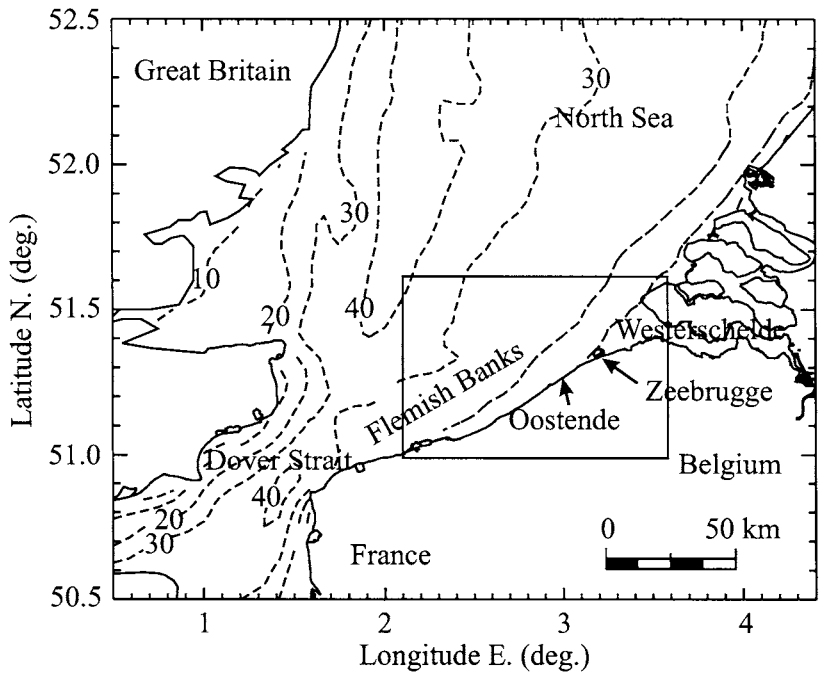

Fig 1. Map of the study area, the Southern North Sea and Belgian-Dutch coastal area. The rectangle indicates the area of interest.

Matter (SPM) concentrations of up to a few hundred mg/l are common, resulting in very high deposition of fine sediments (mainly mud). To maintain access for ships, more than 10 million tons of dry matter are dredged on average every year. In the harbour of Zeebrugge the sedimentation rate is estimated at 3.8 ton/m²/year, which corresponds to about 2.9 m/year when assuming a density of 1.3 ton/m³ (Van Lancker *et al.*, 2003). Knowledge of suspended sediment processes in the Belgian coastal zone is therefore needed to provide a sustainable management of the dredging and dumping activities.

The influence of tides and the neap-spring tidal cycle on the distribution of mud on the bottom and in suspension and the different sources of fine-grained matter in the area are discussed in Fettweis and Van den Eynde (2003) using numerical model results and field measurements. However, the development of a regional cohesive sediment transport model is— besides the difficulty of incorporating a detailed description of all processes— limited by the lack of field data. Very often the available data consist of measurements in one or several points during a limited time (a tidal cycle to a few

days). These point measurements usually show time series of SPM concentration in the vertical direction. They cannot provide horizontal information, which is especially important in high turbidity zones, where multiple sources of SPM may exist and where the SPM concentration can vary on a small spatial scale. The main source of SPM in the Belgian-Dutch coastal area is the import through the Strait of Dover. A minor source comes from the erosion of tertiary clay layers and Holocene mud deposits. The Westerschelde estuary is not an important source of mud. It may act as a sink as well as a source.

The use of optical remote sensing methods to produce SPM concentration maps benefits from the satellite capabilities to picture wide areas and provide synoptic views of SPM concentration distribution. The disadvantages are (1) they provide only data of the surface layer during cloud-free daytime, (2) the correction algorithms (section 2.1) tend to saturate at high SPM concentrations and reflectance levels, and (3) the time resolution is low (1-2 per day) (Van der Woerd *et al.*, 2000). In the current study a method is presented in which *in situ* measurements and satellite images of SPM concentrations are combined to obtain information on the total cohesive sediment distribution at a long time (season) and large horizontal scale. The incorporation of the *in situ* measured tidal variation of SPM concentration is the innovative part in this process to obtain satellite based total SPM concentration maps.

The objective of the paper is to show the results of a study on SPM concentration distribution in the Belgian-Dutch coastal zone using Sea-viewing Wide Field-of-view Sensor (SeaWiFS) satellite images and *in situ* measurements. The results can be seen as an important part in developing a sediment transport modelling system which can be used to evaluate the efficiency or the environmental impact of dumping operations.

2. SPM CONCENTRATION MAPPING FROM SEAWIFS IMAGES

2.1. Calculation of SPM concentration

In this study 370 SeaWiFS images were collected over the Belgian Coastal Zone (BCZ) from October 1997 to March 2004. Among these images, 172 scenes are entirely cloud-free over the BCZ. Most of the 370 images have been corrupted by less than 30% of clouds which were flagged during the processing of SPM concentration maps.

The SeaWiFS imagery used is the Top Of Atmosphere (TOA) radiance measured at the sensor level. Processing is needed to calculate the SPM concentration at the water surface. First the various atmospheric contributions to the TOA radiance, *i.e.*, light scattering by air molecules and aerosols, absorption by oxygen and ozone and the sky

glint, have to be removed to produce the reflectance at the sea level ρ_w. This was carried out using the SeaDAS software algorithm extended to turbid waters. The description of this algorithm is beyond the scope of the present paper, but can be found in Ruddick *et al.* (2000).

Next, a hydro-optical model (Eq. 1, given by Nechad *et al.*, 2003), designed for Belgian waters is used to convert ρ_w into SPM surface concentrations c_{surf}:

$$c_{surf} = a_1 \frac{\rho_w}{0.187 - \rho_w} + a_2 \tag{1}$$

where a_1 and a_2 are calibration parameters determined by a nonlinear regression analysis. The calibration of these parameters is carried out using 57 *in situ* reflectance spectra, measured by three Trios spectro-radiometers, and simultaneous *in situ* SPM concentration measurements. The calibration shows that the best results are obtained with the reflectance at band 670 nm ρ_w^{670} and with a_1 and a_2 set equal to 102.3 and 3.85 mg/l respectively.

The relationship between c_{surf} and ρ_w^{670} has been further validated using 1021 *in situ* SPM concentration observations in the Southern North Sea from 1997 to 2003. The data were obtained from the Belgian Marine Data Centre (http://www.mumm.ac.be/datacentre). A grid with a horizontal resolution of 1.13 x 1.13 km², *i.e.*, the resolution of the SeaWiFS image, is defined. *In situ* data are available in 38 cells of the grid. All data available in a single cell are used to compute a mean value for that cell. For the same cells, all data derived from the 370 SeaWiFS images are processed in the same way. This time-averaging is necessary since, due to the high temporal variability, the small time lag between the *in situ* data and the satellite-derived SPM concentration affects significantly the correlation. Comparison between both data sets indicates a high correlation of 81%.

Finally the Environment for Vizualizing Images (ENVI) software is used to geo-reference the ρ_w images. All satellite images were projected to the defined grid of 1.13 x 1.13 km².

2.2. SeaWiFS derived surface SPM maps

All SeaWiFS data are then used to derive SPM concentration maps (Fig. 2). The SPM average concentration map in Fig. 2a shows concentrations from 20 to 100 mg/l in the narrow 20 km band along the Belgian coast. These average concentrations do not exceed 60 mg/l except in the small area located to the south west of Zeebrugge (ZB) towards Oostende (OS). In this area, the SPM median concentration value ranges from

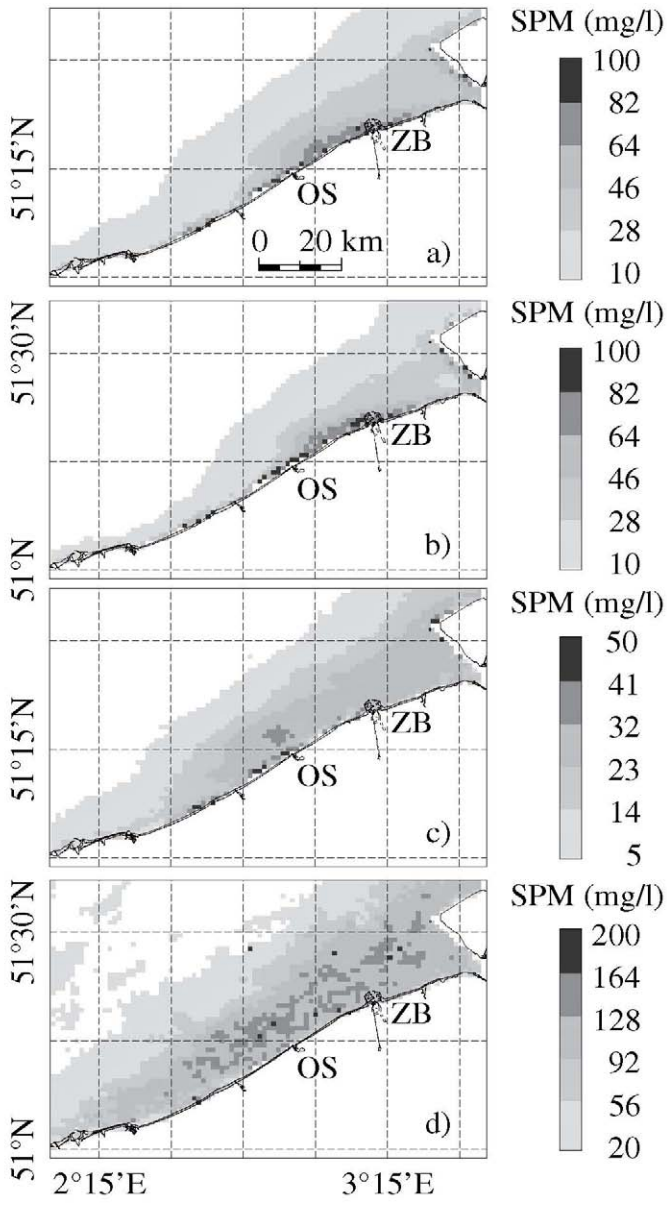

Fig 2. SeaWiFS derived surface SPM concentration maps from October 1997 to March 2004. (a) average of 370 images, (b) the median surface SPM concentrations, (c) the standard deviation of the surface SPM concentrations and (d) the maximum surface SPM concentrations.

40 to 100 mg/l (Fig. 2b) and high SPM concentration standard deviations are noted (Fig. 2c) close to the coast which indicates that this is a turbid area with high temporal variations.

The area located near the mouth of the Westerschelde estuary has average values of SPM concentrations between 20 to 60 mg/l; the median values do not exceed 40 mg/l and the standard deviation ranges from 20 to 30 mg/l. This indicates that these waters are less turbid than in the area between Zeebrugge and Oostende and that it has less temporal variation.

The most homogeneous area with the lowest spatial and time variations in SPM concentration is located offshore with an average SPM concentration less than 20 mg/l and a very low standard deviation.

The area located to the south of Oostende has a median value less than 20 mg/l, which means that this area is very often a relatively clear water area. Nevertheless very high values (from 110 to 140 mg/l) occasionally occur yielding average SPM concentrations from 20 to 40 mg/l, higher than in the offshore area. We note that high SPM concentrations occur even 20 km offshore (about 80 mg/l) as shown in the maximum SPM map (Fig. 2d).

2.3. Classification of SPM concentration maps

To further characterise the dynamics of SPM in the area of interest, the spatial correlation of the SPM concentration time-series was calculated to identify separate areas with similar SPM dynamics. The SeaWiFS images have been processed as explained below.

For each grid cell as defined above, further called a reference grid cell, the following procedure was followed:

- all valid surface SPM concentrations for the reference grid cell, not disturbed due to clouds or to atmospheric correction failure, were selected.
- for another grid cell, the valid surface SPM concentrations are selected from the SeaWiFS images as well.
- if at least 100 corresponding valid SPM concentration pairs are found, the correlation between the SPM concentrations at these two grid cells is calculated. A value of 100 pairs is taken to insure that the results are based on a large number of SeaWiFS images.
- this selection of valid surface SPM concentrations and calculation of the correlation if 100 corresponding valid SPM concentration pairs are found is repeated for all grid cells.

- when all correlations between the SPM concentrations at the reference grid cell and the SPM concentrations at the other grid cells are calculated, a map can be prepared of the area with correlations higher then 70%. This area is defined as the High Correlation Area (HCA) for that reference grid cell.

After calculating for each cell the HCA, the HCA with the largest surface is selected. This largest High Correlation Area (HCA-1) (see Fig. 3a) includes 2774 cells, which represents around 3500 km². As expected from the previous section, this HCA-1 is located offshore.

A second high correlation area was selected after masking out the HCA-1 area, by applying the same procedure as described above. For all remaining grid cells, the correlation with the other grid cells was calculated and the areas for which the correlation was higher than 70% were constructed. Amongst all the HCA's, the most extended HCA was selected again. This yields the HCA-2 area, which is located in the north east, near the mouth of the Westerschelde estuary (Fig. 3b). The area represents about 1100 km². In the west of the area, an overlap exists between the HCA-1 and HCA-2 areas. The area without the HCA-1 and HCA-2 is very narrow.

This area is actually uncorrelated with either HCA-1 or HCA-2. The standard deviation of SPM concentrations here reaches 50 mg/l (the highest throughout the BCZ). The third HCA (HCA-3) covers partly this area and was found in the 20 km band along the coast (Fig. 3c). Also for this HCA-3 area overlaps exist with the two other HCA's.

Since there are overlaps between the three HCA's and that some grid cells do not belong to any of the HCA's, an additional processing was executed to allocate each of the grid cells to one of the three defined areas. To do this for each of the grid cells, the correlation with the three reference grid cells for the HCA's are calculated. The grid cell is then appointed to that area for which it has the highest correlation with its reference grid cell. The resulting division of the BCZ in three separate areas is presented in Fig. 3d.

The SPM concentration in these three areas is characterised as follows:

- Offshore area, where SPM concentrations remain generally low (<10 mg/l).
- Zeebrugge area, which extends from about Zeebrugge to the mouth of the Westerschelde estuary. In 60% of the images, the SPM concentration is lower than 50 mg/l, while 40% of the images show a high SPM concentration in this area.
- Oostende area, which has high SPM concentrations more often than in the Zeebrugge area (70% of the images show high SPM concentrations in this area).

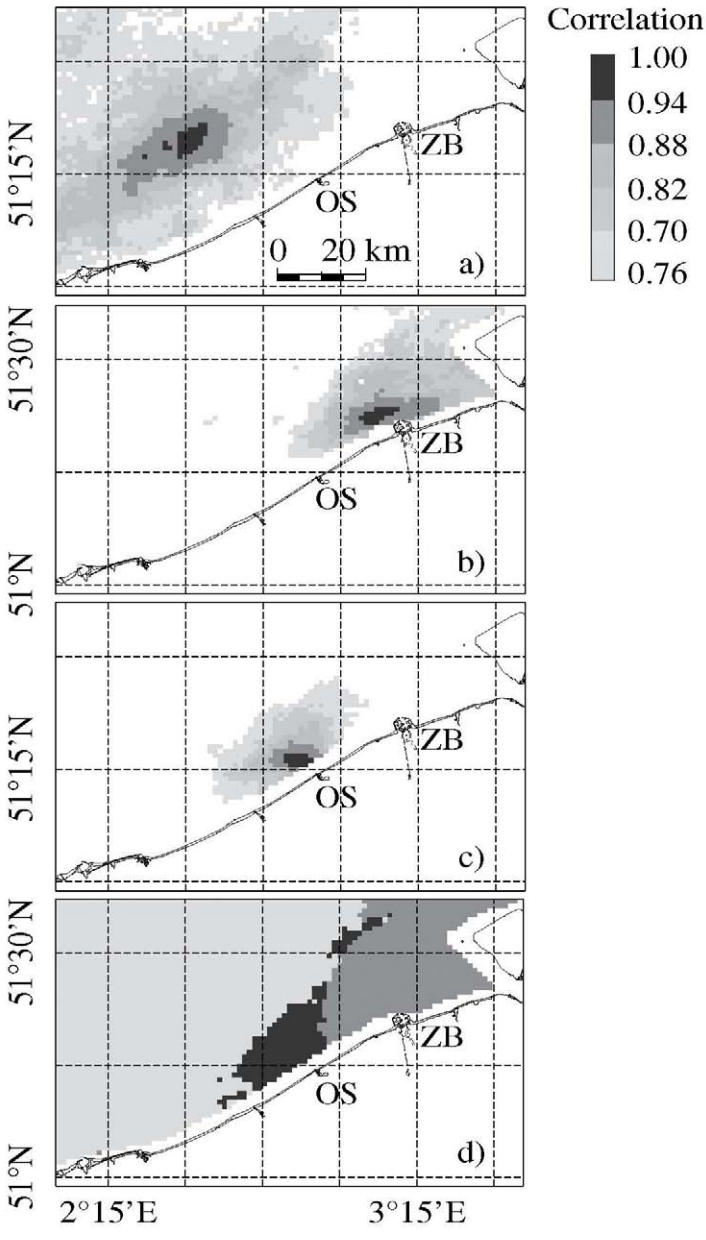

Fig. 3. (a) 1st High Correlation Area (HCA-1); (b) 2nd High Correlation area (HCA-2); (c) 3rd High Correlation Area; (d) division of the BCZ in the offshore area (light), Zeebrugge area (middle) and Oostende area (dark).

The difference between the offshore area and the coastal areas is due to the fact that (1) the transport of SPM is mainly concentrated in the coastal area and (2) the differences in bathymetry. For the apparently different SPM dynamics in the two neighbouring Zeebrugge and Oostende areas on the other hand, a convincing explanation has not yet been established. Some striking differences between both areas can however offer explanations:

- 95% of the dredging and dumping occurs in the Zeebrugge area. Comparison between the natural input of SPM and the quantities dredged and dumped at sea showed that an important part of the SPM is involved in the dredging/dumping cycle (Fettweis and Van den Eynde, 2003).
- The bottom in the Zeebrugge area consists of Holocene mud near the coast, which is difficult to erode, and shallow sand plates offshore, where the hydrodynamic conditions prevent mud from being permanently deposited (Fettweis and Van den Eynde, 2003). In the Oostende area, soft mud which has been deposited during slack water can be found (Van Lancker *et al.*, 2003). This could mean that in the Zeebrugge area the mud stays in suspension during most of the tidal cycle and that mud is only permanently deposited in the man-made environments of navigation channels and harbours. In the Oostende area on the other hand, the hydrodynamics allow SPM to be deposited and only severe storms will bring the fine material back into suspension.
- The Westerschelde estuary also has an influence, even if it is limited, on the SPM dynamics of the Zeebrugge area. Although the ratio of fluvial to marine SPM is almost constant at the mouth of the estuary (Verlaan *et al.*, 1998), the SPM concentration varies significantly as a function of river discharge.

3. SPM CONCENTRATION FROM *IN SITU* MEASUREMENTS

Knowledge of resuspension, transport and deposition of fine grained sediment is important to understand the variations in SPM concentration observed in satellite images. This knowledge is provided from *in situ* measurements. The results of ten measurements are discussed below; they have been carried out with the R/V "Belgica" from 1999 to 2002. The different measurement surveys are presented in Table 1 and Fig. 4.

Table 1. *In-situ* measurements of SPM concentration. (1) Name of campaign; (2) Starting time of the measurement; (3) Duration of the measurements; (4) Time of maximum SPM concentration related to high (HW) or low water (LW); (5) Duration of SPM concentration peak; (6) Ratio between surface and vertical averaged SPM concentration; (7) Ratio between surface and bottom SPM concentration (±3 m); (8) area in which measurement is situated.

(1)	(2)	(3)	(4)	(5)	(6)	(7)	(8)
99/07	8/03/1999 15h47	13 h	LW HW-2h	2h 3h	0.82 0.81	0.72 0.67	Oostende area
99/17	13/07/1999 06h20	13 h	No peak, background		0.92	0.83	Offshore area
00/08	21/03/2000 10h14	13 h	HW+1h LW+1h	2h 2.5h	0.77 0.67	0.62 0.58	Zeebrugge area
00/14	29/05/2000 08h53	13 h	LW-1h HW	2h 2h	0.42 0.63	0.37 0.37	Zeebrugge area
00/19	10/07/2000 09h15	13 h	No peak, background		0.91	0.74	Offshore area
00/26	23/10/2000 20h10	13 h	HW+1h LW	2h 2.5h	1.00 0.68	1.00 0.51	Zeebrugge area
00/31	07/12/2000 10h00	19 h	No peak, background		0.98	0.98	Zeebrugge area
01/01	25/01/2001 11h45	13 h	LW-2.3h HW-2.3h	1h 2h	0.88 0.39	0.87 0.26	Zeebrugge area
01/06a	07/03/2001 16h07	17 h	LW HW+1h	2h 2h	0.34 0.43	0.25 0.34	Zeebrugge area
01/06b	08/03/2001 10h41	20 h	HW+2.5 LW	1h 4h	0.45 0.45	0.30 0.14	Oostende area

3.1. Processing of the data

The turbidity in the water column was measured with an Optical Back Scatter (OBS) sensor, mounted on a Rosette water sampling - SBE09 SCTD system. Data were acquired every half second. Every hour a vertical profile was measured. Furthermore every 20 minutes, a water sample was collected at about 3 m above the bottom using the 10 litre Niskin bottles of the Rosette water sampling system. These water samples were used for gravimetrical determination of the SPM concentration.

The values of SPM concentration, determined by filtration, and the simultaneously measured OBS values are used to set up a relationship between the OBS readings and the actual SPM concentration. A linear relation between SPM concentration and OBS is assumed and calculated using a least squares method. Since the relationship depends on

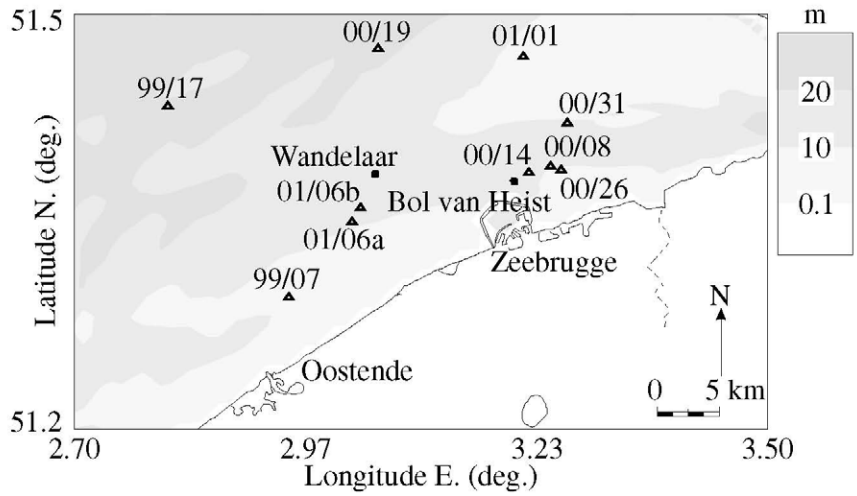

Fig. 4. Survey stations in the Belgian coastal waters. Dots are wave station Bol van Heist and wind station Wandelaar; the SPM survey stations are indicated with triangles.

the characteristics of the sediments in suspension as well as on the hydrodynamic conditions and the time of the measurements, the relationship is calculated for each survey period separately. Only for three surveys, with very low concentrations (8-25 mg/l), the correlation coefficient is less than 50%. The average correlation coefficient for the other surveys is 86%. The slope of the regression line between SPM concentration and OBS output for the other surveys varies between 1.11 FTU/mg/l and 2.08 FTU/mg/l.

Vertical profiles are measured every hour. The profiles cover the water column from about 3 m above the bottom to about 1 m below the sea surface. In order to take into account the entire profile, including the lowest layer in which the highest concentrations are expected, an extrapolation is made using a theoretical profile. This extrapolation is important to calculate an accurate depth-average SPM concentration.

The following profile was assumed (van Rijn, 1993):

$$c(z) = c_a \left(\frac{h-z}{z} \frac{a}{h-a} \right)^{\frac{w_s}{\beta \kappa u_*}} \qquad \text{for } \frac{z}{h} < 0.5$$

$$c(z) = c_a \left(\frac{a}{h-a} \right)^{\frac{w_s}{\beta \kappa u_*}} e^{-4\frac{w_s}{\beta \kappa u_*}\left(\frac{z}{h}-0.5\right)} \qquad \text{for } \frac{z}{h} \geq 0.5 \tag{2}$$

where $c(z)$ is the concentration at a height z above the bottom, h is the total water depth, c_a is a reference concentration at a reference height a above the bottom, w_s is the fall velocity, β is a factor describing the difference between the diffusion of a liquid particle and a discrete sediment particle, κ is the von Karman constant, equal to 0.4, and u_* is the shear velocity. The parameter $Z=w_s/\beta\kappa u_*$ is the Rouse parameter, which is a measure for the SPM concentration vertical gradient. van Rijn (1993) argues that this profile gives the best agreement with observations and that it has the advantage that the concentration at the surface does not have to be zero as is the case in the well-known Rouse profile. Since the reference height and the reference concentration at the bottom are only used as fitting parameters for the concentration profile, the exact value of the reference height is not important. Here a fixed value above the bottom is used (a = 0.10 m). This value is of the same order of magnitude as the minimum value for a proposed by van Rijn (1984), which was $0.01h$.

For each profile the reference concentration c_a and the Rouse parameter Z are determined using a nonlinear least squares method. The van Rijn (1993) profile gives a good fitting of the measured profiles. Assuming a standard deviation of the measuring error of 10% of the maximum concentration, the Goodness-of-Fit is better than 0.5 (0.9) in 92% (75%) of the profiles.

3.2. Tidal variations

The measurements show that the SPM concentration in the coastal zone varies with tide with minima between 20-70 mg/l and maxima between 100-600 mg/l. Low values have been measured during three surveys (8-25 mg/l). Two of these surveys were situated in the offshore area, which explains these low values. The third one (survey 00/31) is situated in the high turbidity area, *i.e.*, in the Zeebrugge area. High SPM concentrations had been measured in the vicinity six weeks before (survey 00/26) and after (survey 01/01). The low SPM concentration can be explained by a combination of differences in tidal amplitude (neap versus spring tide) together with a meteorologically induced offshore drift of the suspended matter. An almost continuous wind from S-SSW (towards offshore) (see Fig. 5c), from the beginning of November 2000 till the 7th of December 2000, the start of the 00/31 measurements, might have contributed to this drift. Thus the SPM entering through the Strait of Dover into the North Sea was blown towards the North, away from the Belgian-Dutch coastal zone.

The measurements illustrate that the peaks in SPM concentration are coupled to the peaks in current velocity and occur after the maxima in current velocity (Fettweis *et al.*, 2002). The occurrence of a time lag in suspended sediment transport is well known

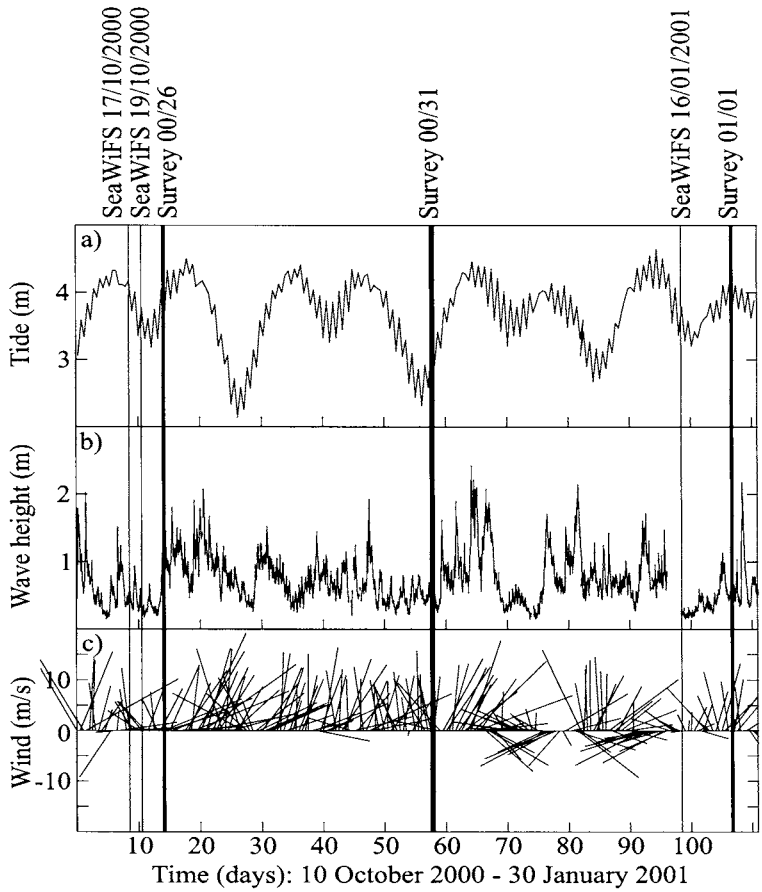

Fig. 5. Hydrodynamic and meteorological information during several of the survey periods: (a) Predicted tidal amplitude at Oostende, (b) measured wave height at 'Bol van Heist' and (c) wind speed and direction at 'Wandelaar.' The time of three SeaWiFS images (17 and 19/10/2000, 16/01/2001) and of three through tide measurements (00/26; 00/31; 01/01) are indicated.

(Bass *et al.*, 2002; Dyer, 1995; Hoitink *et al.*, 2003) and is related to the fact that the re-suspended mud needs a certain time to be distributed over the water column. Van Parys and Pieters (2001) observed this process near Zeebrugge, where the mud bed starts to be re-suspended when the tidal current increases to 0.15 m/s, but only at a later time, when the current velocity is greater than 0.5 m/s, was an increase of SPM concentration measured near the surface.

3.3. Vertical variation

The measured vertical profiles reveal that the SPM concentration is usually about 50 mg/l in the coastal area and can reach up to 600 mg/l (Fig. 6). The surface SPM concentration as well as the stratification is high only for about 2 hours during ebb and flood, *i.e.*, about 1/3 of the tidal cycle. Strong vertical gradients were observed during surveys 00/14, 01/01, 01/06a and 01/6b, when SPM concentration was high (Table 1 and Fig. 6). During the rest of the tide, which corresponds to about 2/3 of the tidal cycle, the measured SPM concentration and stratification are much lower and corre-

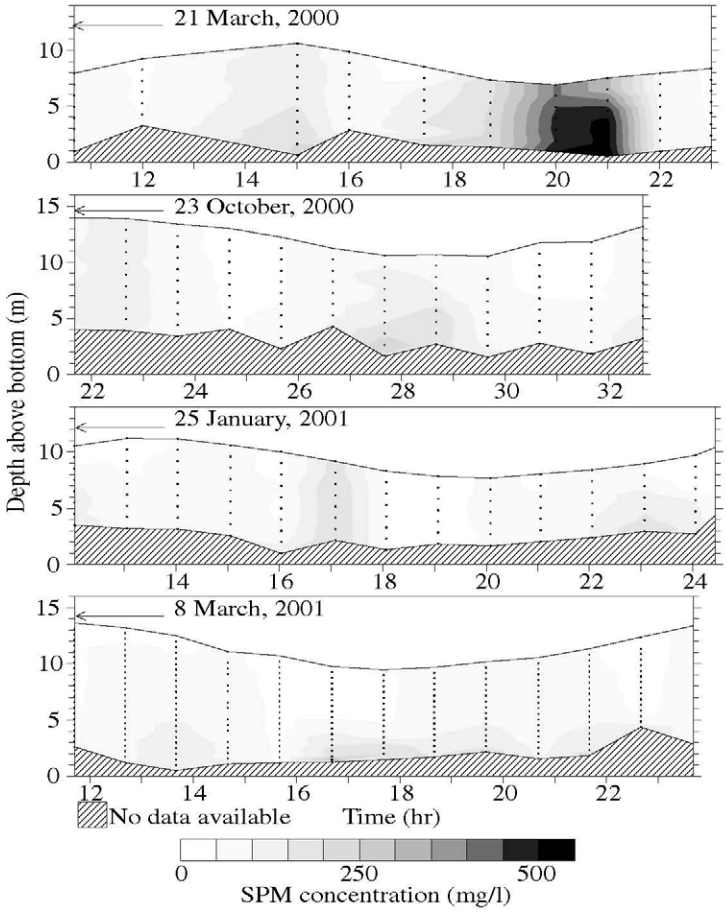

Fig. 6. Vertical distribution of SPM concentration during a tidal cycle in the Belgian coastal zone (a) at station 00/08, (b) at station 00/26, (c) at station 01/01 and (d) at station 01/06b.

spond to a background value, which is high (50 mg/l) in the high turbidity zone (Oostende and Zeebrugge area). It is still not clear what the reason is for the occurrence of strong vertical gradients during some surveys while during others only small gradients are observed, although situated in the same area.

To make an accurate estimation of the ratio between the surface and the depth-averaged SPM concentrations during the tidal cycle, for each of the profiles, Eq. 2 was used to fit the survey data for finding the best reference concentration at the bottom c_a and Rouse parameter Z. The time variation over these two parameters for survey 01/01 is given in Fig. 7 as an example, together with the total water depth. The figure shows that the vertical gradient and the reference concentration reach a maximum some hours before high and low water, *i.e.*, during periods of tidal acceleration (Maa and Kim, 2002). Furthermore it is clear that the SPM concentration gradients increase together with the reference bottom concentrations. This is observed in almost all measured profiles.

For all the profiles the depth-averaged and the surface SPM concentration were calculated, together with their ratio. For the three different areas, defined in section 2.3, the mean evolution of this ratio is calculated over the tidal cycle (Fig. 8). In the near-shore Zeebrugge and Oostende area (Fig. 3d), a clear cycle can be observed: 1 hour

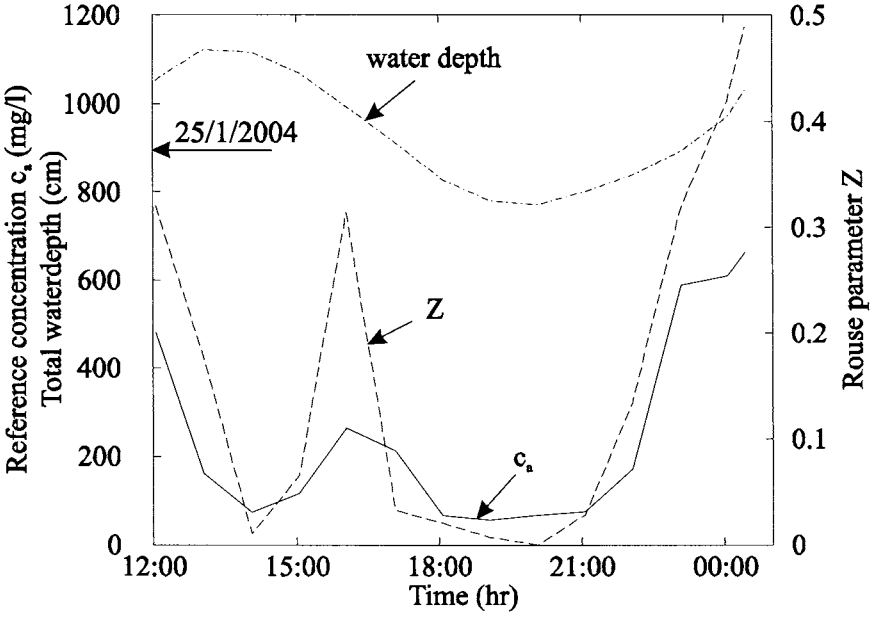

Fig. 7. Variation over time of the bottom reference concentration c_a and the Rouse parameter Z for survey 01/01.

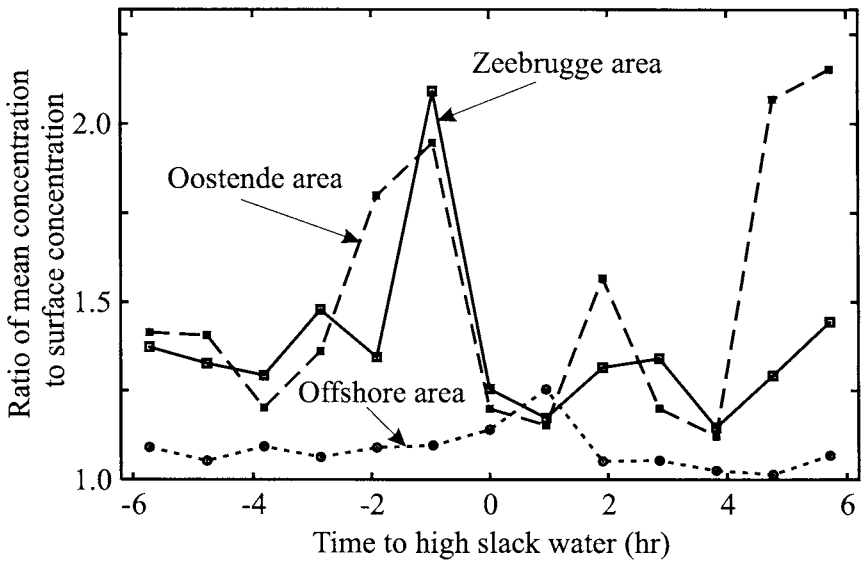

Fig. 8. Ratio of the depth averaged concentration to the surface concentration with respect to the time relative to high water for the three defined areas.

before high water and around low water, the ratio between the depth-averaged and the surface SPM concentration increases to about 2 and about 1.5 respectively. In the Oostende area the ratio around low water increases to almost 2.2. In the offshore area, on the other hand, the ratio between the depth-averaged and the surface SPM concentration stays constant over the entire tidal cycle and is limited to values below 1.1. Only one hour after high water, the ratio increases to about 1.25.

4. SEASONAL DEPTH-AVERAGED SPM CONCENTRATION MAPS

In order to obtain depth-averaged SPM concentrations from satellite measured surface SPM concentration maps, corrections have to be applied. As is shown in Fig. 8, the ratio between the surface SPM concentration and the depth-averaged SPM concentration varies during the tidal cycle. During the background period, the ratio between the surface SPM concentration and the depth-averaged SPM concentration is almost equal to one and the surface SPM concentration, derived from the satellite images, will represent well the averaged SPM concentration. During the periods with higher stratifi-

cation, however, this ratio can be higher than 2.2 and the satellite images underestimate the depth-averaged SPM concentration. Furthermore, this correction factor varies over the BCZ. Therefore different correction functions are setup for the three sub-regions identified in section 2.

The following procedure is followed:

- for each grid cell, the surface SPM concentration is calculated (section 2.1).
- the HCA-1, HCA-2 or HCA-3 (section 2.3) in which the grid cell is lying, is identified;
- the time in the tidal cycle corresponding to that of the satellite image is determined with the help of a hydrodynamic model (Luyten *et al.*, 1999);
- the correction factor from Fig. 8 is applied to calculate the depth-averaged SPM concentration.

The corrected satellite images are then used to calculate a season-averaged SPM concentration in the domain. Results are presented in Fig. 9. The influence of season is clearly visible: the SPM concentration is lower during spring and summer and higher during autumn and winter.

These seasonal maps have been used to construct boundary conditions for a cohesive sediment transport model of the area. Using a two-dimensional numerical model for hydrodynamics and sediment transport, Fettweis and Van den Eynde (2003) showed that the processes responsible for the formation of a high turbidity zone at the Belgian-Dutch coastal area (offshore of Zeebrugge) are the currents and the import of SPM through the Strait of Dover. Mainly because of the decreasing magnitude of residual transport and the shallowness of the area, the SPM is concentrated in the Belgian-Dutch coastal waters and forms a turbidity maximum near to Zeebrugge.

5. CONCLUSIONS

In the Belgian-Dutch coastal zone, SPM concentration is high. The main source of SPM in the southern North Sea is the Dover Strait. In the current study a method is presented to incorporate *in situ* measurements and satellite imagery for a better estimation of depth-averaged SPM concentration, which should help to define more realistic initial and boundary conditions for a local area cohesive sediment transport model.

A spatial analysis of the satellite derived surface SPM concentrations shows that three separate sub-regions can be identified: an offshore area with generally low SPM concentrations and two nearshore highly turbid areas.

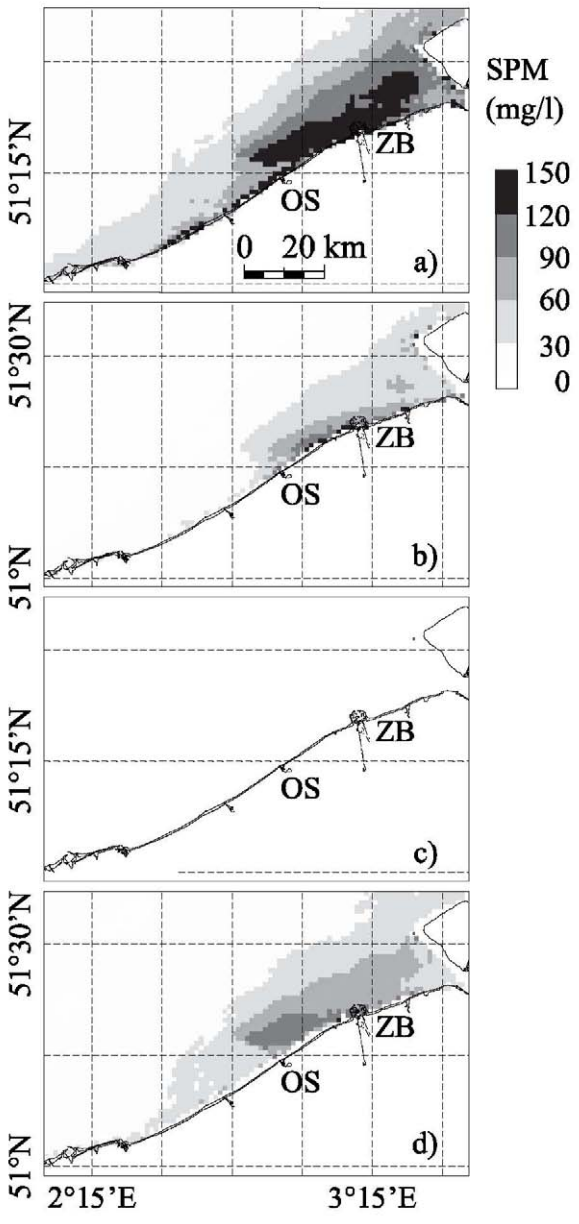

Fig. 9. Depth and seasonal averaged SPM concentration (mg/l) in the southern North Sea derived from 370 SeaWiFS maps (1997-2004) and corrected using 10 through tide measurements. (a) winter; (b) spring; (c) summer; and (d) autumn.

In situ measurements during a tidal cycle further allowed to distinguish between the SPM dynamics offshore and in the high turbidity areas. In the latter, the SPM concentration is generally high and a pronounced vertical gradient is observed during 1/3 of the tide. During such a period, the depth-averaged SPM concentration is about 50% to 100% higher than the surface SPM concentration derived from satellite images. This important variation of SPM concentration during a tidal cycle has to be taken into account when correcting satellite imagery to obtain total SPM concentration maps.

In the present paper, a procedure is proposed to derive depth-averaged SPM concentration maps from SeaWiFS satellite images. It is clear that the proposed procedure is only a first result, because all *in situ* measurements of SPM concentration profiles were used for setting up the correction factor and thus no estimation could be made on the improvement obtained.

Finally, seasonal depth-averaged SPM concentration maps were prepared and presented.

ACKNOWLEDGEMENTS

This study was funded by the Maritime Access Division of the Waterways and Marine Affairs Administration, Ministry of the Flemish Community in the framework of the SEBAB and MOMO projects. The measurements have been made with the research vessel "Belgica." The support of the measuring service of MUMM in Oostende is acknowledged as is the Belgian Marine Data Centre for providing the *in situ* data. Support was also provided by the Belgian Federal Science Policy Office within the framework of the STEREO programme BELCOLOUR project (SR/00/03). The receiving station of Dundee University, Orbimage, the SeaWiFS and SeaDAS project teams, and the Distributed Active Archive Centre at GSFC are acknowledged for providing, distributing and supporting SeaWiFS data. Finally, José Ozer (MUMM) and the anonymous reviewers are thanked for their constructive remarks.

REFERENCES

Bass, S.J., J.N. Aldridge, I.N. McCave and C.E. Vincent. 2002. Phase relationships between fine sediment suspensions and tidal currents in coastal seas. *Journal of Geophysical Research*, 107 (C10), 10,1-14.

Dyer, K.R. 1995. Sediment transport processes in estuaries. In: *Geomorphology and Sedimentology of Estuaries.* Perillo, G.M.E. (ed.) Developments in Sedimentology 53, 423-449.

Fettweis, M., B. Nechad, F. Francken and D. Van den Eynde. 2002. *Bepaling van de sedimentbalans voor de Belgische kustwateren, Dynamica van het gesuspendeerd particulair materiaal op het Belgisch Continentale Plat.* MUMM Report SEBAB/3/MF/200212/NL/AR/1, 30 pp. (in Dutch).

Fettweis, M. and D. Van den Eynde. 2003. The mud deposits and the high turbidity in the Belgian-Dutch coastal zone, Southern bight of the North Sea. *Continental Shelf Research*, 23, 669-691.

Hoitink, A.J.F., P. Hoekstra and D.S. van Maren. 2003. Flow asymmetry associated with astronomical tides: Implications for the residual transport of sediment. *Journal of Geophysical Research*, 108 (C10), 13,1-8.

Luyten, P.J., J.E. Jones, R. Proctor, A. Tabor, P. Tett and K. Wild-Allen. 1999. *COHERENS – A Coupled Hydrodynamical-Ecological Model for Regional and Shelf Seas: User Documentation.* MUMM Report, Management Unit of the Mathematical Models of the North Sea, 914 pp (available on CD-ROM at http://www.mumm.ac.be/coherens).

Maa, J.P.-Y. and S.-C. Kim. 2002. A constant erosion rate model for fine sediment in the York River, Virginia. *Environmental Fluid Mechanics*, 1, 343-360.

Nechad, B., V. De Cauwer, Y. Park and K. Ruddick. 2003. Suspended Particulate Matter (SPM) mapping from MERIS imagery. Calibration of a regional algorithm for the Belgian coastal waters. *Proceedings MERIS user workshop*, 10-13th November 2003, Frascati. Special Publication of European Space Agency SP-549, CD-ROM, ESA Publication Division, Noordwijk, The Netherlands, 6 pp.

Ruddick, K.G., F. Ovidio and M. Rijkeboer. 2000. Atmospheric correction of SeaWiFS imagery for turbid coastal and inland waters. *Applied Optics*, 39(6), 897-912.

Van der Woerd, H.J., J.H.M. Hakvoort, H.J. Hoogenboom, N. Omtzigt, R. Pasterkamp, S.W.M. Peters, K. Ruddick, C. de Valk and R.J. Vos. 2000. *Towards an operational monitoring system for turbid waters.* POWERS Final report. Institute for Environmental Studies, Vrije Universiteit Amsterdam, Amsterdam, O-00/16, 62 pp.

Van Lancker, V., S. Deleu, S. Le Bot, B. van Nieuwenhove, M. Fettweis, F. Francken, V. Pison, D. Van den Eynde, J. Monbaliu, J. Lanckneus, G. Moerkerke and S. Degraer. 2003. *Management, research and budgeting of aggregates in shelf seas related to end-users (Marebasse).* Scientific report year 1, Federal Office for Scientific, Technical and Cultural Affairs, Brussels, Belgium, 39 pp.

Van Parys, M. and M. Pieters. 2001. *Bijakte 14: Mobag 2000 - Ecologische impact. Turbiditeit op de loswal B&W Zeebrugge Oost, stationaire metingen*. Report, Tijdelijke Vereniging Noordzee en Kust, TVNK/Z/04/2001/MVP, 26 pp. (in Dutch).

van Rijn, L.C., 1984, Sediment transport: part II: suspended load transport. *Journal of the Hydraulics Division, ASCE*, 110, 1613-1641.

van Rijn, L.C., 1993, *Principles of sediment transport in rivers, estuaries and coastal seas*. Aqua Publications, Amsterdam, 686 pp.

Verlaan, P.A.J., M. Donze and P. Kuik. 1998. Marine vs. fluvial suspended matter in the Scheldt estuary. *Estuarine, Coastal and Shelf Science*, 46(6), 873-883.

Estuarine and Coastal Fine Sediments Dynamics
J.P.-Y. Maa, L.P. Sanford and D.H. Schoellhamer (editors)

A semi-analytical model for confined fluid mud flow in estuaries

Merckelbach, L.M.[a], J.C. Winterwerp[b]

[a]Royal Netherlands Institute for Sea Research (NIOZ),
P.O. Box 59, 1790 AB Den Burg, Texel, The Netherlands
[b]Delft University of Technology, Faculty of Civil Engineering and Geosciences,
P.O. Box 5048, 2600 GA, Delft, The Netherlands

KEY WORDS
Fluid mud, gravitational circulation, similarity solutions, water injection dredging

A model is presented for calculating the flow of a dredging-induced fluid mud layer. The model is aimed to give a quick and reasonable accurate estimate of the fluid mud flow as an alternative to an expensive and time consuming detailed numerical approach. A typical example for its application is estimating the production (amount of transported fluidised mud) in case of water injection dredging. The model consists of two parts: a model for the fluid mud flow and a model for the overlying water (suspension layer) to account for the shear stresses at the interface between the fluid mud and the suspension layer. The suspension layer is considered for a realistically shaped estuary with the velocity distribution affected by the horizontal salinity gradient, tidal flow and river discharge. A layer-integrated model for the fluid mud layer was set-up, including turbulent bottom friction and an interfacial shear stress derived from the velocity distribution of the suspension layer. The model is solved analytically using the technique of similarity solutions. The assumptions made in this approach limit the accuracy by which the interfacicial shear stress and bottom slope can be represented. Fortunately, on the time scale of the life time of the fluid mud layer, the errors thus introduced cancel more or less, as is shown by a comparison of the results for three scenarios elaborated with the analytical model and by the numerical code of WL | Delft Hydraulics' Delft3D-flow, adapted for fluid mud flow. It is concluded that the analytical model yields satisfactory accurate results for a quick estimate of a confined fluid mud flow in an estuary.

1. INTRODUCTION

Soft mud layers are quite common in estuaries. They may become mobile and form gravity currents under the influence of external forces. Such external forces may be induced by Water Injection Dredging (WID), a dredging technique developed by Ballast-Ham Dredging Contractors, currently Van Oord Dredging and Marine Contractors. The principle of WID is that water is injected under low pressure into the mud bed to fluidise mud and then use gravity to transport it away from the project site, for instance into the sea or ocean.

The fate of the fluidised mud depends on the forces acting on the layer. One of these is a frictional force by velocity differences between the fluid mud layer and the overlying water. Especially in estuaries, where the vertical velocity distribution is characterised by a net seaward current near the water surface and a net landward current near the bed, a net shear stress at the interface between the fluid mud and the water exists in landward direcrtion that may oppose the desired flow direction of the fluidised mud.

To study the fate of fluidised mud layers, numerical models have been applied that model both the water layer and the fluid mud layer (Winterwerp *et al.*, 2003). However, setting up and calibrating such a model for a specific situation is time consuming and therefore costly. Alternatively, if accuracy is not very important and a rough estimate of the behaviour of the fluid mud flow at low costs is sufficient, a so-called rapid assessment tool is more appropriate.

This study presents a semi-analytical model for dredging-generated fluid mud flows in estuaries, which can be used as an rapid assessment tool. The model basically consists of two parts: *i*) a semi-analytical model for the gravitational circulation in the water layer, which provides the shear stress at the water-fluid mud interface and *ii*) an analytical model for the fluid mud flow on a sloping bed (Fig. 1). Both elements are compared with the results of a numerical 2L(ayer) fluid mud model (Winterwerp *et al.*, 2003).

2. PART I: SUSPENSION LAYER

Salinity in estuaries varies gradually from salinity S_0 (constant at sea) to zero up-estuary. This salinity gradient (hence density gradient) maintains a recirculation current in the estuary, also referred to as gravitational circulation. In the 1960's and -70's many researchers studied salinity dispersion in estuaries with (simplified) mathematical models, see Fisher (1976) or Chatwin and Allen (1985) for an overview. A popular approach is to consider salinity dispersion in an estuary as a one-dimensional diffusion problem, in which the processes contributing to mixing are lumped into an overall longitudinal dispersion coefficient (Chatwin and Allen, 1985). Chatwin (1976) and Chatwin and Allen

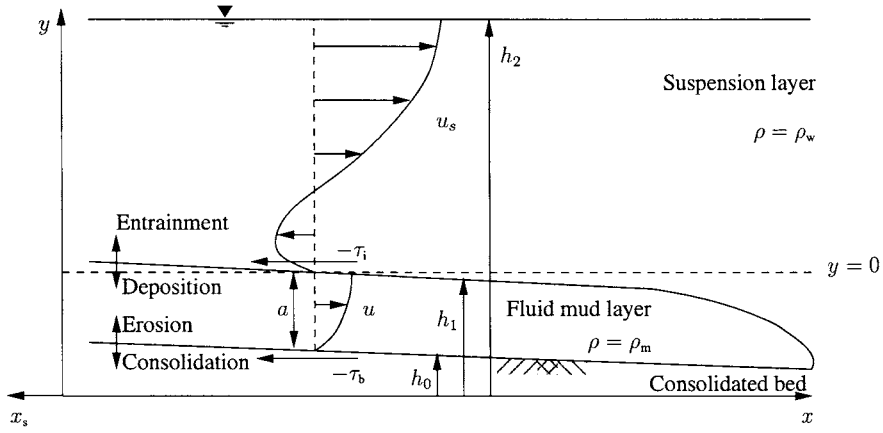

Fig. 1. Definition sketch of fluid mud layer and overlying suspension layer.

(1985) argued that the approach to describe the longitudinal salinity distribution is not entirely realistic from a physical point of view. Nevertheless, this approach has yielded good correspondence with both field and laboratory measurements (Savenije, 1992).

Hansen and Rattray (1965) started with a set of partial differential equations describing the mixing processes in the vertical plane of a prismatic estuary. Their analysis could predict observations (salinity and horizontal velocity profiles) reasonably well. However, in their analysis the longitudinal salinity gradient needs to be prescribed *a priori*.

Starting with the same set of equations, but applying a different method of analysis, Chatwin (1976) developed a model which predicts the longitudinal salinity gradient. In his analysis, Chatwin arrives at an expression for the horizontal tide-averaged velocity distribution $u_s(x_s, y)$ from the tide-averaged momentum equations and the equation of state, but without using the prismatic channel assumption. The result is

$$u_s(x_s, y) = \frac{1}{48}\frac{g\alpha}{\rho_0 \nu}\frac{\partial S}{\partial x_s}\left(15dy^2 - 6d^2y - 8y^3\right) - \frac{3}{2}\frac{U}{d^2}\left(y^2 - 2dy\right) \tag{1}$$

in which

$$U = \frac{Q}{dB} \tag{2}$$

and

$$B = B_0 \exp(-x_s/b) \tag{3}$$

Herein, x_s is the horizontal coordinate, positive in landward direction and the origin at the mouth of the estuary, y the vertical coordinate, positive in upward direction with its origin at the bed of the estuary, d the water depth, α a coefficient in the linearised equation of state: $\rho = \rho_0 + \alpha S$, ρ the density of the water, ρ_0 the density of fresh water, S the salinity, ν the depth-averaged eddy viscosity, Q the river discharge, B the width of the estuary, B_0 the width at the mouth of the estuary and b the so-called convergence length scale of the estuary. Note that the averaged velocity U is negative in downstream direction as a result of the choice of the coordinate system. In deriving Eq. 1, the assumption has been made that the longitudinal salinity gradient is approximately uniform with depth, which is probably not true at the mouth of the estuary.

Subsequently, Chatwin assumed that the vertical velocities maintain the salinity balance. In order to find a solution using the continuity equation, it was required to assume the shape of the channel to be prismatic (*i.e.*, $b = \infty$), which finally results in an expression for the salinity gradient, and thus determining Eq. 1.

For realistic estuaries an analytical expression for the horizontal salinity gradient is more difficult to find. To circumvent this problem, the horizontal salinity distribution in the present study was modelled with a dispersion model following Savenije (1992). The constraint of a prismatic estuary can be relaxed, *i.e.*, $b \ll \infty$.

The depth of the estuary is assumed constant. Savenije's analysis yields an expression for the tide-averaged salinity gradient, which he validated against many different partially and well-mixed estuaries from all over the world. Savenije's formulation for the depth-averaged salinity profile reads

$$S = S_0 \left[1 + \frac{KQb}{A_0 D_0^{\mathrm{HWS}}} \left(\exp\left(\frac{x_s + \frac{E}{2}}{b} \right) - 1 \right) \right]^{\frac{1}{K}} \tag{4}$$

where Q is the river's discharge, A_0 the area of the cross-section at the mouth of the estuary, D_0 is the dispersion coefficient at the mouth of the estuary at high-water slack, and E is the tidal excursion length. Differentiation of Eq. 4, combined with Eq. 1 gives the tide-averaged horizontal velocity profile for a negative exponential shaped estuary. Note that the result is only valid for the region where Eq. 4 is valid, *i.e.*, $S > 0$.

The lumped parameters K and D_0^{HWS} are empirical parameters. Savenije (1992) studied numerous estuaries with different characteristics and calibrated for each condition the parameters K and D_0^{HWS}. He correlated the calibrated parameters with characteristic parameters of the estuaries such as depth, tidal range, discharge, *etc.* For the parameter

K he gives the following two expressions:

$$K = 6.3 \times 10^{-6} \left(\frac{d}{b}\right)^{1.04} \left(\frac{E}{H}\right)^{2.36} \quad \text{or} \quad K = 4.38 \frac{d^{0.36}}{B_0^{0.21} b^{0.14}} \tag{5}$$

where H is the tidal range. The first expression is more accurate but requires the tidal excursion length E. If the excursion length is not known, the second, less accurate formulation can be used instead. Note that as the latter expression is not dimensionless, it is compulsory to use metres as the unit for length.

For the dispersion coefficient in the mouth of the estuary, Savenije (1992) gives the empirical relationship

$$D_0^{\text{HWS}} = 1400 d \frac{E}{b} \sqrt{-\frac{\alpha S_0}{\rho_w} \frac{gdQT}{P\hat{u}_0^2}} \tag{6}$$

where P is the tidal prism, T the tidal period and $\hat{u}_0$ the amplitude of the horizontal velocity in the mouth of the estuary. Estimations of the excursion length E and the tidal prism P are given by

$$E \approx 1.08 \frac{\hat{u}_0 T}{\pi} \tag{7}$$

and

$$P \approx A_0 E \tag{8}$$

The velocity u_s is seen to be composed of two parts, which are visualised in Fig. 2. The first term of the right-hand side of Eq. 1 represents the effect due to longitudinal salinity gradient (U_1 in Fig. 2), whereas the second term represents the river's discharge (U_2 in Fig. 2). It can be seen that if the recirculation component is relatively strong (due to a strong gradient, for example), net flow near the bed may be into the landward direction.

An estimate for the instantaneous horizontal flow velocity can be constructed by including the main, depth-averaged tidal component in the flow field. Defining the tidal velocity component as

$$U_T = u_0 \cos(\omega t) \tag{9}$$

where ω is the angular frequency of the principal tidal component and u_0 the amplitude of

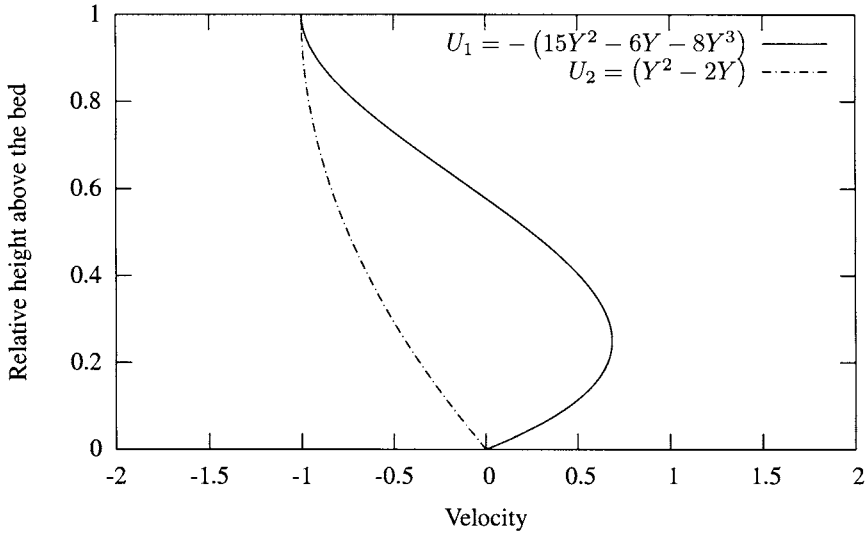

Fig. 2. Characteristics of the two components (U_1: due to salinity gradient and U_2: due to river discharge) of a tide-averaged horizontal velocity.

the depth-averaged horizontal tidal component. Including tidal action, Eq. 2 is replaced by

$$U = \frac{Q}{dB(x_s)} + u_0 \cos(\omega t) \tag{10}$$

Thus, the instantaneous profile of the horizontal velocity can be calculated using Eqs. 1 and 10. The shear stress on the bed is assumed to be proportional to the velocity gradient near the bed. An alternative approach would be to use a shear stress that is proportional to the depth averaged velocity squared, however, then the effect of estuarine circulation would vanish. To allow a future extension of the model to consider the fate of entrained material, we opt for the proportionality between the bed shear stress and the velocity gradient near the bed. From Eqs. 1 and 10 it follows that the velocity gradient reads

$$\left.\frac{\partial u_s}{\partial y}\right|_{y=0} = -\frac{1}{8}\frac{g\alpha d^2}{\rho_0 \nu}\frac{\partial \overline{S}}{\partial x_s} + \frac{3}{d}\left(\frac{Q}{dB(x_s)} + u_0 \cos(\omega t)\right) \tag{11}$$

with the longitudinal salinity gradient as

$$\frac{\partial \overline{S}}{\partial x_s} = S_0 \frac{Q}{A_0 D_0^{\mathrm{HWS}}} \exp\left(\frac{x_s + \frac{E}{2}}{b}\right) \left[1 + \frac{KQb}{A_0 D_0^{\mathrm{HWS}}} \left(\exp\left(\frac{x_s + \frac{E}{2}}{b}\right) - 1\right)\right]^{\frac{1-K}{K}} \quad (12)$$

3. PART II: FLUID MUD FLOW

Fluid mud flow generated by water injection dredging is usually turbulent, well-mixed and behaves as a turbidity current. Examples, besides the fluid mud flow as studied herein, are snow avalanches (Johannesson *et al.*, 1996) and density currents flowing down continental shelves (Lane-Serf, 1993), quoted in (Hatcher *et al.*, 2000). These phenomena have been studied both numerically and analytically. Analytical models for the rate of spreading of gravity currents have been proposed by Hoult (1972) and Grundy and Rottman (1985), for example. Most models assumed that the buoyancy force is initially balanced by inertia. In these approaches, the effect of drag was usually neglected. In Hatcher *et al.* (2000) drag force was included explicitly. They considered fluid mud flow over a horizontal bed from a continuous source as well as from an instantaneous release. They also considered the effects of a sloping bed for an instantaneous release only. For the problem of fluid mud flow as a result of water injection dredging we need an analytical solution for the fluid mud problem with a continuous release on an inclined bed. It is anticipated that the effect of drag is significant. The present approach is therefore based on the method outlined in Hatcher *et al.* (2000) and is extended to include the effect of an inclined bed in combination with a continuous production of fluid mud.

3.1. Mathematical formulation

The consequence of WID is that the fluid mud layer formed is confined to the channel. Furthermore, the WID process allows the fluid mud layer to be assumed homogeneous throughout with a constant density (Fig. 1), which is supported by a field experiment in the Haringvliet, The Netherlands (Rijkswaterstaat *et al.*, 1993). In addition, we neglect the processes of sedimentation and deposition (Fig. 1) because the time scale for these processes to have a significant effect is much longer then the life time of the WID induced fluid mud layer. This is not necessarily true for entrainment and consolidation (Fig. 1). However, the effect of entrainment and consolidation on the dynamics of the fluid mud layer are considered to be of second order. To facilitate the analysis below, it is assumed that the fluid mud layer exchanges no sediment with its surrounding.

On the scale of the fluidised mud layer the width of the estuary is assumed constant, so that we can write the layer-integrated mass balance per unit width as

$$\frac{\partial a}{\partial t} + \frac{\partial au}{\partial x} = 0 \tag{13}$$

where a is the thickness of the fluid mud layer, u the (layer averaged) horizontal velocity of the fluid mud layer, x is the horizontal coordinate and t is time. To facilitate our analysis, the reference frame of the fluid mud flow has its origin at the point where the fluid mud is generated, with positive direction down-slope. This implies that the coordinate systems of the suspension layer model given in Section 2 and the fluid mud layer do not coincide.

Neglecting the influence of the gradient of the free surface on the motion of the fluid mud layer ($\partial h_2/\partial x = 0$), the equation of motion reads

$$\frac{\partial u}{\partial t} + u\frac{\partial u}{\partial x} + \varepsilon g\frac{\partial a}{\partial x} = -\varepsilon g\frac{\partial h_0}{\partial x} + \frac{\tau_\mathrm{i}(x,t) + \tau_\mathrm{b}(x,t)}{\rho_\mathrm{m} a} \tag{14}$$

where ε is the relative density $(\rho_\mathrm{m} - \rho_\mathrm{w})/\rho_\mathrm{w}$. The solution method deployed later on requires the right-hand side of Eq. 14 to be independent of the local layer thickness. To that end, the local layer thickness a in the denominator of the second term in the right-hand side of Eq. 14 is replaced by a constant, averaged layer thickness a_0. The consequence of this simplification is that at the tip of the fluid mud layer, where the layer becomes thinner, the drag force due to bottom friction is underestimated.

The interfacial shear stresses τ_i is given by

$$\tau_\mathrm{i} = -f_\mathrm{w}\rho_\mathrm{w}\left.\frac{\partial u_\mathrm{s}}{\partial y}\right|_{y=0} \tag{15}$$

where f_w is an empirical friction coefficient between water and fluid mud layers and the velocity gradient is given by Eq. 11.

In the case of WID, the fluid mud flow is expected to be turbulent because of the way the layer is generated. Consequently, the drag force (due to the bed) is proportional to $u|u|$, where u is the horizontal velocity of the fluid mud layer. Thus, the term representing drag due to bed friction can be written as:

$$\frac{\tau_\mathrm{b}(x,t)}{\rho_\mathrm{m} a_0} = -\lambda u|u| \tag{16}$$

where, according to the classical shallow water equations,

$$\lambda = \frac{g}{a_0 C_z^2} \tag{17}$$

in which C_z is the Chézy coefficient. Furthermore, for the sake of convenience, the remaining terms in the right-hand side of Eq. 14 are grouped by

$$\mu = -\varepsilon g \frac{\mathrm{d}h_0}{\mathrm{d}x} + \frac{\tau_\mathrm{i}(x)}{\rho_\mathrm{m} a_0} \tag{18}$$

Assuming that the flow is only down-slope, so that $u|u|$ becomes u^2, the equation of motion becomes

$$\frac{\partial u}{\partial t} + u\frac{\partial u}{\partial x} + \varepsilon g \frac{\partial a}{\partial x} = -\lambda u^2 + \mu(x) \tag{19}$$

Directly after the release, the dynamics of the fluid mud layer are governed by buoyancy and inertia effects. After some time friction becomes important. The transition time in which the buoyancy-inertia regime turns into the buoyancy-friction regime can be estimated by scaling analysis of the momentum equation (Hatcher *et al.*, 2000). Introducing typical scales for velocity, layer thickness, time and space coordinate and requiring that the inertia, buoyancy and friction terms in the momentum equation become of comparable order of magnitude, leads to the scaling

$$t_\mathrm{t} = \left(\varepsilon g a_0 L_0 \lambda^3\right)^{-\frac{1}{2}} \tag{20}$$

where t_t is the transition time. A transition time $t_\mathrm{t} \approx 40$ s is obtained for $\varepsilon g = 1$ m/s^2, $a_0 = 0.6$ m, $L_0 = 1000$ m and $\lambda = 0.01$ m^{-1}. This time scale is negligible compared to the life time of a fluid mud layer, which is estimated to be of the order of roughly 1 hour.

Hence, for $t \gg t_\mathrm{t}$, Eq. 19 reduces to

$$\varepsilon g \frac{\partial a}{\partial x} = -\lambda u^2 + \mu(x) \tag{21}$$

3.2. Similarity solutions

A technique to solve Eqs. 13 and 21 is based on the assumption that the solution is self-similar. That is, the solutions of u and a are constant in time and space except from a certain scale factor. This technique has also been applied in Hatcher *et al.* (2000) on a set of similar equations, without a sloping bed, though. More information on similarity solutions can be found in (Debnath, 1997).

The basic idea is to introduce a scaling of the governing parameters in Eqs. 21 and 13, such that the scaled equivalents are composed of a function depending on time solely, and a function depending on a so-called similarity parameter η. This similarity parameter

may be considered as a scaled spatial coordinate. The transformed parameters, when substituted into the differential Eqs. 21 and 13, result in ordinary differential equations that can be treated with common techniques. It is noted that these ordinary differential equations are obtained only if the solutions of Eqs. 21 and 13 are indeed self-similar. The drawback of this technique is that the general solution can be adapted correctly to the boundary conditions (far field), but not to the initial conditions (near field) (Debnath, 1997) where the inertia forces cannot be neglected and thus the solution of the near field is not self-similar. Fortunately, the near field conditions last shortly (or, in other words, the influence of erroneously specified initial conditions dies out rapidly, as the transition time t_t was shown to be much smaller than the life time of the fluid mud layer.

The scaled parameters are given by

$$a = \frac{1}{\varepsilon g} t^{\alpha} \mathcal{F}(\eta), \tag{22a}$$

$$u = t^{\beta} \mathcal{G}(\eta) \tag{22b}$$

$$\mu = t^{\gamma} \mathcal{H}(\eta) \tag{22c}$$

$$\eta = t^{\delta} x \tag{22d}$$

where α, β, γ and δ are real constants* and η is a parameter that is scaled by x and t.

Substitution of the scaled parameters into Eqs. 21 and 13 gives

$$\frac{\partial \mathcal{F}}{\partial \eta} t^{\alpha+\delta} = -\lambda \mathcal{G}^2 t^{2\beta} + \mathcal{H} t^{\gamma} \tag{23}$$

and

$$\alpha \mathcal{F} t^{\alpha-1} + \delta \eta \frac{\partial \mathcal{F}}{\partial \eta} t^{\alpha-1} + \frac{\partial}{\partial \eta} (\mathcal{F}\mathcal{G}) t^{\alpha+\beta+\delta} = 0 \tag{24}$$

It is required that the differential equations for the scaled parameters describe the evolution of the fluid mud layer for all t, so that all factors t must vanish, and we have

$$\alpha + \delta = 2\beta \tag{25a}$$

$$\alpha + \delta = \gamma \tag{25b}$$

$$\alpha - 1 = \alpha + \beta + \delta \tag{25c}$$

*The factor $(\varepsilon g)^{-1}$ in Eq. 22a is introduced for convenience later.

Solving for α, β, γ and δ requires one additional equation, which is provided by the mass conservation (the density in the fluid mud layer is constant):

$$\int_{-\infty}^{\infty} a \mathrm{d}x = q_0 t \tag{26}$$

where q_0 is the production of fluid mud at the inflow boundary. This relationship can be rewritten as

$$t^{\alpha-\delta} \int_{-\infty}^{\infty} \mathcal{F} \mathrm{d}\eta = \varepsilon g q_0 t \tag{27}$$

in which the factor involving t must also vanish, so that

$$\alpha - \delta = 1 \tag{28}$$

Solving Eqs. 25 and 28 for α, β, γ and δ yields

$$\alpha = \frac{1}{4}, \qquad \beta = -\frac{1}{4}, \qquad \gamma = -\frac{1}{2}, \qquad \delta = -\frac{3}{4}$$

so that Eqs. 23 and 24 can be written as

$$\frac{\partial \mathcal{F}}{\partial \eta} + \lambda \mathcal{G}^2 = \mathcal{H} \tag{29a}$$

and

$$-\frac{3}{4}\eta \frac{\partial \mathcal{F}}{\partial \eta} + \frac{1}{4}\mathcal{F} + \frac{\partial}{\partial \eta}(\mathcal{F}\mathcal{G}) = 0 \tag{29b}$$

Since μ is a function of x only, we can derive the function prescription for $\mathcal{H}$. From the scaling relationship (*i.e.*, Eq. 22c) it follows that

$$\mu = t^{-\frac{1}{2}} \mathcal{H}(\eta). \tag{30}$$

Supposing that $\mathcal{H}$ takes the form

$$\mathcal{H} = \hat{h} \eta^m \tag{31}$$

and it follows after substitution of Eq. 22d that

$$\mu = \hat{h} t^{-\frac{1}{2}-\frac{3}{4}m} x^m \tag{32}$$

Again, time must vanish, so that $m = -\frac{2}{3}$ and thus

$$\mathcal{H} = \hat{h} \eta^{-\frac{2}{3}} \tag{33}$$

The function $\mathcal{H}$ represents the combined effects due to bottom slope and interfacial friction. The combined effect is proportional to $x^{-\frac{2}{3}}$, which limits the extent to which the actual bottom and interfacial friction can be represented by $\mathcal{H}$.

At this stage the partial differential equations are transformed into ordinary differential equations in which the scaled parameters depend only on the independent parameter η. Unfortunately, the transformed partial differential equations cannot be solved to yield an analytically closed form solution.† Therefore, we try to find approximate solutions of $\mathcal{F}$ and $\mathcal{G}$ by power series expansions around $\eta = \eta_\mathrm{f}$. To that end, we write

$$\mathcal{F} = c_0 + c_1(\eta_\mathrm{f} - \eta) + c_2(\eta_\mathrm{f} - \eta)^2 + c_3(\eta_\mathrm{f} - \eta)^3 + \ldots \tag{34}$$

and

$$\mathcal{G} = d_0 + d_1(\eta_\mathrm{f} - \eta) + d_2(\eta_\mathrm{f} - \eta)^2 + d_3(\eta_\mathrm{f} - \eta)^3 + \ldots \tag{35}$$

Similarly, $\mathcal{H}$ is expanded as a power series. The fourth-order series of Eq. 33 around $\eta = \eta_\mathrm{f}$ is given by

$$\mathcal{H} \approx \frac{\hat{h}}{{\eta_\mathrm{f}}^{2/3}} - 2/3\frac{\hat{h}\,(\eta - \eta_\mathrm{f})}{{\eta_\mathrm{f}}^{5/3}} + 5/9\frac{\hat{h}\,(\eta - \eta_\mathrm{f})^2}{{\eta_\mathrm{f}}^{8/3}} - \frac{40}{81}\frac{\hat{h}\,(\eta - \eta_\mathrm{f})^3}{{\eta_\mathrm{f}}^{11/3}} + \ldots \tag{36}$$

At the front of the fluid mud layer ($\eta = \eta_\mathrm{f}$) the layer thickness is equal to 0, so that $\mathcal{F}(\eta_\mathrm{f}) = 0$. From this it follows that $c_0 = 0$.

The velocity of the front v_f is given by

$$v_\mathrm{f} = \frac{\mathrm{d}x_\mathrm{f}}{\mathrm{d}t} \tag{37}$$

† An explicit analytical solution can be found though in the case of an instantaneous release on a horizontal bed, see Hatcher *et al.* (2000).

where x_f is the position of the front of the fluid mud layer. Using the scaling relations Eqs. 22d and 22b we find

$$v_f = t^{-\frac{1}{4}}\mathcal{G}(\eta_f) \tag{38}$$

and

$$\frac{dx_f}{dt} = \frac{3}{4}\eta_f t^{-\frac{1}{4}} \tag{39}$$

so that $d_0 = \frac{3}{4}\eta_f$.

The remaining coefficients c_i and d_i are found by substitution of the series approximations for $\mathcal{F}$, $\mathcal{G}$ and $\mathcal{H}$ into Eqs. 29. Both Eqs. 29 can be satisfied when the terms involving $(\eta_f - \eta)^i$ for $i = 0, 1, 2, 3, ...$ are all zero. Thus the first three dominant coefficients, *i.e.*, c_1, c_2, c_3, d_1, d_2 and d_3 are found to be

$$c_1 = \frac{1}{16}\frac{9\,{\eta_f}^3\lambda - 16\,\sqrt[3]{\eta_f}\hat{h}}{\eta_f} \tag{40a}$$

$$c_2 = -\frac{1}{48}\frac{9\,{\eta_f}^3\lambda + 16\,\sqrt[3]{\eta_f}\hat{h}}{{\eta_f}^2} \tag{40b}$$

$$c_3 = \frac{1}{432}\frac{\left(189\,{\eta_f}^{16/3}\lambda^2 - 672\,\hat{h}\,{\eta_f}^{8/3}\lambda + 1280\,\hat{h}^2\right)\left(9\,{\eta_f}^3\lambda - 16\,\sqrt[3]{\eta_f}\hat{h}\right)}{{\eta_f}^3\left(256\,\hat{h}^2 - 288\,\hat{h}\,{\eta_f}^{8/3}\lambda + 81\,{\eta_f}^{16/3}\lambda^2\right)} \tag{40c}$$

$$d_1 = -\frac{1}{4} \tag{40d}$$

$$d_2 = \frac{1}{18}\frac{16\,\hat{h} + 9\,\lambda\,{\eta_f}^{8/3}}{\eta_f\left(-16\,\hat{h} + 9\,\lambda\,{\eta_f}^{8/3}\right)} \tag{40e}$$

$$d_3 = -\frac{1}{36}\frac{256\,\hat{h}^2 - 416\,\hat{h}\,{\eta_f}^{8/3}\lambda + 9\,{\eta_f}^{16/3}\lambda^2}{{\eta_f}^2\left(256\,\hat{h}^2 - 288\,\hat{h}\,{\eta_f}^{8/3}\lambda + 81\,{\eta_f}^{16/3}\lambda^2\right)} \tag{40f}$$

Most of the parameters c_i and d_i are still not determined since η_f is unknown. To determine η_f Eq. 27, after substituting the series approximation for $\mathcal{F}$, is used. Unfortunately, no explicit solution for η_f could be found, so η_f needs to be solved numerically.

4. COMPARISON WITH NUMERICAL MODEL DELFT3D

Results from the combined semi-analytical model for the suspension layer and the fluid mud layer, derived in the previous sections, are compared with results obtained with a numerical model for two layer (2L) flow based on the code of Delft Hydraulics'

Delft3D-FLOW (Winterwerp *et al.*, 2003). A schematic estuary is considered in which at a location of 5000 m from the mouth, fluid mud is generated at a discharge of 1.0 m^2/s (per unit width) during 40 minutes. The dimensions and settings used for the analytical model and the 2L numerical model are given in Table 1. The 2L numerical model was run with the mass-exchange processes switched off for a fair comparison.

Three scenarios are considered:

Scenario *i*: $Q_r = -10$ m^3/s, during maximal ebb velocity,

Scenario *ii*: $Q_r = -10$ m^3/s, during maximal flood velocity,

Scenario *iii*: $Q_r = -200$ m^3/s, during maximal ebb velocity

The forcing term μ, which represents the combined effect of the inclined bed and the interfacial shear stress, is calculated for each of the three scenarios. The method of similarity solutions requires μ to be of the form

$$\mu = \hat{h} x^{-\frac{2}{3}} \tag{41}$$

see Eq. 32. The coefficient $\hat{h}$ is determined from a least-squares fit of Eq. 41 to the prescribed μ (see also the Table below). The prescribed forcing terms μ (lines only) and the representations by Eq. 41 (lines and symbols) are shown in Fig. 3 for each of the three scenarios. It is seen that in the similarity solutions the forcing term μ is overestimated near the discharge point and underestimated further down slope. On average, the errors up-slope are more or less cancelled by the errors down-slope. The corresponding values of $\hat{h}$, η_f, c_i and d_i are listed in Table 2.

Table 1. Specification of dimensions and settings of the test case.

Parameter	Value	Parameter	Value
Distance to mouth	5000 m	Water density	1000 kg/m^3
Depth	10 m	Mud density	1100 kg/m^3
Slope	-1.0×10^{-3}	f_w	0.005 m^2/s
Cross-sectional area mouth	2000 m^2	α	0.805 $kg/m^3/ppt$
Width at mouth, B_0	200 m	ν	1×10^{-4} m^2/s
Convergence length	27000 m	Constant assumed	
Salinity at sea	30 ppt	layer thickness a_0	1.0 m
Tidal range	1.0 m	C_z	40 $m^{1/2}/s$
Hor. velocity amplitude	0.5 m/s	λ	0.006 m^{-1}
Tidal period	12 hr		

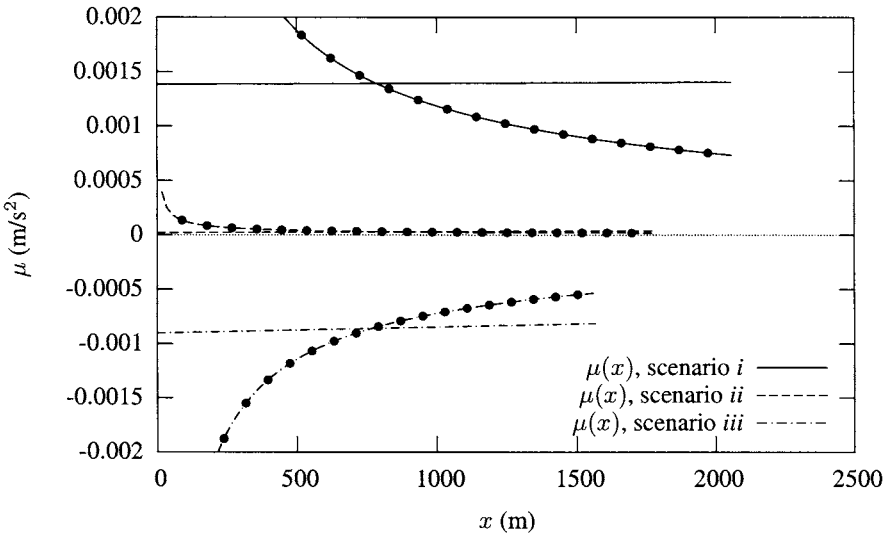

Fig. 3. The forcing term $\mu(x)$ as prescribed (lines) and according to Eq. 41 (lines and symbols).

Figure 4 shows the total amount of transported material (production) after 40 minutes as function of the distance from the source. The total amount of transported material decreases from $q_0 \times T = 1.0 \times 40 \times 60 = 2400$ m^2 at the source to zero at the front of the fluid mud layer. The fluid mud layer has advanced about 2000 m in scenario *i*) after 40 minutes. When the tidal flow direction reverses from ebb to flood (scenario *ii*) the fluid mud layer cannot travel further than about 1750 m. For a river discharge increased to 200 m^3/s (scenario *iii*), the fluid mud layer only advances 1500 m in 40 minutes. It is seen that a larger river discharge results in a shorter transport path. This can be seen as follows. A low river discharge of 10 m^3/s has little effect on the strong landward flood flow. An increase in river discharge to 200 m^3 can be shown to result in the landward flood flow to decrease from 0.5 to about 0.2 m/s near the surface, so that the combined effect of river flow and tidal flow yields a drag force that is about 2.5 times weaker. However, the total effect on the drag shear stress due to gravitational circulation, tidal flow and river discharge increases because of the stronger increase of the gravitational circulation effect, as the salinity gradient increases by a factor $\sqrt{20} \approx 4.5$ for a river discharge increase from 10 to 200 m^3/s (see also Eq. 12).

Comparing the results by the analytical model with those of the numerical 2 Layer Delft 3D model, it appears that the fluid mud layer as predicted by the analytical model,

Table 2. The values for $\hat{h}$, η_f, c_i and d_i for the scenarios *i*, *ii* and *iii*.

Scenario	$\hat{h}$	c_0	c_1	c_2	c_3
i)	0.135	0	0.159	-2.01×10^{-2}	8.23×10^{-4}
ii)	2.30×10^{-2}	0	0.163	-1.55×10^{-2}	9.23×10^{-4}
iii)	-4.80×10^{-2}	0	1.69×10^{-1}	-1.187×10^{-2}	1.12×10^{-3}
	η_f	d_0	d_1	d_2	d_3
i)	4.321	3.24	-0.250	2.11×10^{-2}	1.38×10^{-3}
ii)	3.913	2.93	-0.250	1.58×10^{-2}	8.38×10^{-5}
iii)	3.636	2.73	-0.250	1.16×10^{-2}	-8.52×10^{-4}

advances slightly further than the fluid mud layer as calculated by the numerical model. However, bearing in mind that the analtical model was aimed to provide a quick estimate of the fluid mud flow, the observed correspondence is in this view quite good.

5. DISCUSSION AND CONCLUSIONS

An analytical model for a dredging-induced fluid mud flow in an estuary was developed, which takes the effects of a longitudinal salinity gradient (if present) on the fluid mud flow into account. The approach followed considers the suspension layer and the fluid mud layer separately. The suspension layer is modelled by a combination of the approach by Chatwin (1976) and Savenije (1992). The layer-averaged one-dimensional fluid mud model, in which the interfacial shear stresses are derived from the velocity profile of the suspension layer, are solved using the technique of similarity solutions. Results were compared with results by the numerical code of WL | Delft Hydraulics' 2 Layer Delft3D-flow. Three scenarios were considered: maximum ebb and flood conditions at a low freshwater discharge, and a maximum ebb condition at a high fresh water discharge.

The method of similarity solutions, which was used to obtain an analytical solution, requires some severe assumptions. In particular, the forcing term $\mu(x)$, representing the effects due to a sloping bed and interfacial shear due to the suspension layer, is approximated only crudely by the corresponding term in the method of similarity solutions. But, in view of the aim of the present research to develop a model for a quick and easy estimate of fluid mud flow in estuaries, an analytical model such as the one presented herein, is preferable over a numerical approach, because the analytical model directly shows the importance of the required input parameters. An important output parameter is the position of the head of the fluid mud layer as function of time. This position is readily obtained from the parameter η_f.

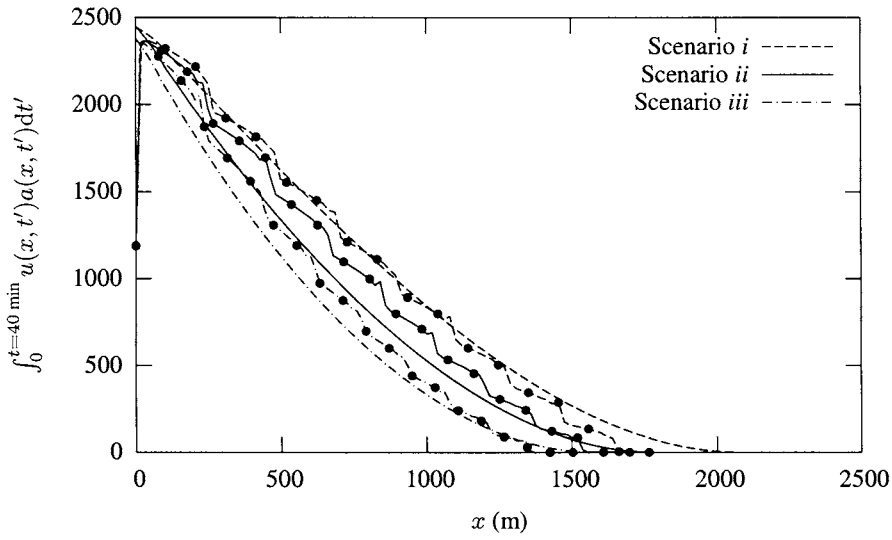

Fig. 4. Comparison of the results by the analytical model (lines) and the 2 Layer Delft 3D numerical model (lines and symbols) for the three scenarios.

In conclusion, the model presented herein provides a method to give a quick estimate of confined fluid mud flow in estuaries with an minimum amount of site specific parameters. In favour of providing more insight, an analytical approach was preferred over a numerical one, although this limits the applicability of the model. Nevertheless, a fairly good correspondence was observed between the results of the analytical model and the results of the advanced numerical code of the 2 Layer Delft3D-flow model. Mass transfer processes such as entrainment and consolidation are not accounted for. Incorporation of these processes are left for future work.

ACKNOWLEDGEMENTS

The present research was predominantly carried out as part of a project commissioned to WL | Delft Hydraulics by Ballast-HAM, Marine Dredging Contractors, currently Van Oord Dredging and Marine Contractors. The authors greatly acknowledge Van Oord Dredging and Marine Contractors for allowing the present research to be published.

REFERENCES

Chatwin, P.C. 1976. Some remarks on the maintenance of the salinity distribution in estuaries. *Estuarine and coastal marine science*, 4, 555–566.

Chatwin, P.C. and C.M. Allen. 1985. Mathematical model of dispersion in rivers and estuaries. *Ann. rev. fluid. mech.*, 17, 119–149.

Debnath, L. 1997. *Nonlinear partial differential equations for scientists and engineers.* Birkhauser Boston.

Fisher, H.B. 1976. Mixing and dispersion in estuaries. *Ann. rev. fluid. mech.*, 8, 107–133.

Grundy, R.E. and J.W. Rottman. 1985. The approach to self-similarity of the solutions of the shallow-water equations representing gravity-current releases. *Journal of fluid mechanics*, 156, 39–53.

Hansen, D.V. and M. Rattray. 1965. Gravitational circulation in straits and estuaries. *Journal of marine research*, 23(2), 104–121.

Hatcher, L., A.J. Hogg and A.W. Woods. 2000. The effects of drag on turbulent gravity currents. *Journal of fluid mechanics*, 416, 297–314.

Hoult, D.P. 1972. Oil spreading on the sea. *Ann. rev. fluid mech.*, 4, 341–368.

Johannesson, T., K. Lied, S. Margreth and F. Sanderson. 1996. *An overview of the need for avalanche protection measures in iceland.* Technical report. Report prepared for the Icelandic Ministry for the Environment and local authorities in towns threatened by avalanches, Reykjavik.

Lane-Serf, G. F. 1993. On drag-limited gravity currents. *Deep-sea res.*, 40, 1699–1702.

Rijkswaterstaat, H.A.M. and WL | Delft Hydraulics. 1993. *Evaluatierapport proef water-injectiebaggeren haringvliet.* Technical report.

Savenije, H.H.G. 1992. *Rapid assessment technique for salt intrusion in alluvial estuaries.* Ph.D. thesis, Delft University of Technology.

Winterwerp, J.C., Z.B. Wang, J.A.Th.M.van Kester and J.F. Verweij. 2003. Far-field impact of water injection dredging in the crouch river. *Water and maritime engineering*, 154(4), 285–296.

Estuarine and Coastal Fine Sediments Dynamics
J.P.-Y. Maa, L.P. Sanford and D.H. Schoellhamer (editors)

A preliminary implication of the constant erosion rate model to simulate turbidity maximums in the York River, Virginia, USA

Kwon, J.-I.[a], J.P.-Y. Maa[a] and D.-Y. Lee[b]

[a]Virginia Institute of Marine Science, College of William and Mary, Gloucester Point, VA 23062, USA
[b]Korea Ocean Research and Development Institute, P.O. Box 29, Ansan, Kyunggi, Korea

KEY WORDS
Suspended sediment transport, model simulation, turbidity maximum, erosion rate.

Numerical simulation of the formation of an Estuarine Turbidity Maximum (ETM) using a constant erosion rate with a stipulated condition that erosion only occurs at tidal accelerating phases was successfully implemented in a three-dimensional hydrodynamic model for the York River. Eight slackwater surveys were carried out during 2001 and 2002 to develop ground truths with measurements at 25 stations along the 120-km York River. Measured salinity and total suspended solid profiles were used to develop "snap shots" for calibration and comparison of results from the numerical simulations. This study indicates that the suggested simple erosion model is capable of simulating suspended sediment transport for addressing the formation of ETM(s). Both the ETM and an occasionally observed secondary turbidity maximum were simulated reasonably well.

1. INTRODUCTION

One of the major difficulties in the simulation of cohesive sediment transport, and thus, the formation of Estuarine Turbidity Maximum (ETM), is to have a simple and

reliable erosion process. Currently prevailed erosion models (Parchure and Mehta, 1985; Geyer, 1998; Hayter and Gu, 2001; Lin and Kuo, 2001), either dimensional or non-dimensional, all require at least two or three parameters (details are given in Sec. 3). Based on the conclusions from previous *in-situ* experiments (Maa and Kim, 2002), a single parameter erosion model, *i.e.*, constant erosion rate, was implemented in the three-dimensional (3-D) Hydrodynamic-Eutrophication Model (HEM-3D) to simulate ETMs in the York River (Fig. 1). This approach is a great simplification of erosion process by reducing two or three unknown parameters to a single parameter. Although the current cohesive sediment transport module does not address the flocculation and consolidation processes, it was found that this module works reasonably well for studying the formation of ETM for the two simulated periods in the York River.

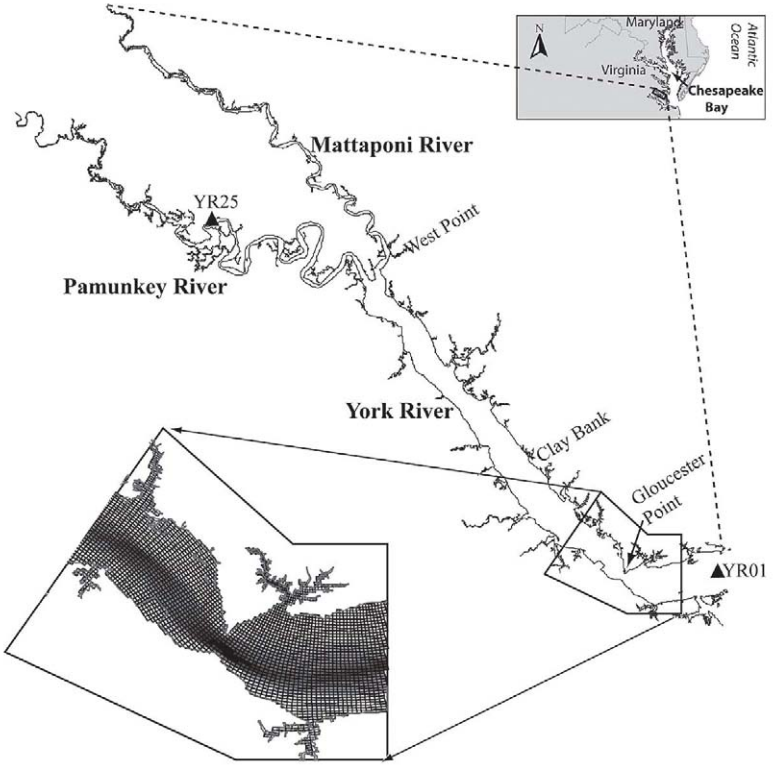

Fig. 1. The York River System, a Subestuary of the Chesapeake Bay. The lower insert shows a part of the curvilinear model grid that follows the bathymetry. Dark area in the lower insert is the channel. Only the 1st (YR01) and the last (YR25) survey stations are shown in the diagram.

The York River system was selected to implement the suspended sediment transport model because of the previous experiences in numerical modeling of hydrodynamic and salinity (Shen *et al.*, 1997), a basic understanding of the suspended sediment distribution (Lin and Kuo, 2001), *in-situ* measurements of erosion rates (Maa and Kim, 2002), and sediment accumulation rates, sediment composition, and bed shear stress measurements (Kim *et al.*, 2000) in this river. Only a small amount of additional fieldwork is required to complete the data sets, greatly facilitating the development of a 3-D suspended sediment transport model.

During 1996 and 1997, a series of slack water surveys (about once a month over one-year period) along the York River was conducted and revealed the general pictures of salinity and sediment distributions in the York River. Two possible ETMs were found. The primary ETM was found near the end of salinity intrusion at the York River, and a secondary ETM was also observed in some of the surveys in the middle of the York River. Using the HEM-3D with the traditional erosion model, Lin and Kuo (2001) revealed a potential mechanism of formation for the secondary ETM (hereafter called STM). However, the Total Suspended Solid (TSS) measurements at only three elevations at each station from that survey are not sufficient for developing a suspended sediment transport model. Thus, a short simulation period, *e.g.*, one or two months, with more TSS profiles in the simulation period would be more reasonable because the dynamics can be closely monitored and simulated.

For the above stated reason, two one-month periods of model simulation were conducted to mimic expected dry (November) and wet (March) seasons. In order to have enough data for calibrating the model, four slackwater surveys were conducted during each period to measure conductivity, temperature and vertical TSS profiles (see Sec. 2 for details).

In order to carry out a good numerical simulation of sediment transport, a basic requirement is enough resolution to address the geometry, especially the channels. Thus, a high-resolution bathymetric grid (grid size about 110 m and 170 m in the cross-channel and along channel directions) was generated. The bottom insert in Fig. 1 shows a part of the grid, near Gloucester Point. Calibration on tidal wave propagation was checked with the M_2 tide (Fig. 2). Also, salt intrusion was successfully simulated for all simulated cases (see Fig. 3 for an example). In general, salinity intrusion simulations indicated that salty water can intrude into the two upstream branches (*i.e.*, Pamunkey and Mattaponi Rivers). Although tidal propagation and salinity intrusion are not the ultimate objectives in this study, they have to be correct in order to have a valid simulation of sediment transport.

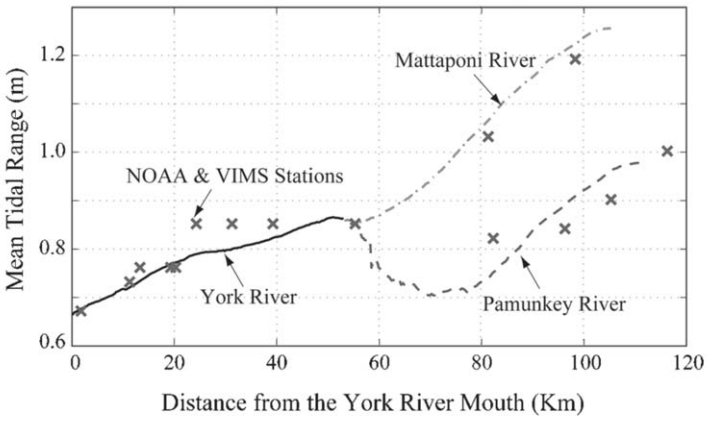

Fig. 2. Comparison of Calculated and Observed (X marks) Mean M_2 Tidal Range Using the New Curvilinear Grid for the Entire York River System.

Field survey results were presented first to show the general features of the suspended sediment distribution in the York River system during the two survey periods in 2001 and 2002. Then, the proposed constant erosion rate model for erosion was explained and implemented with details. The performance of this constant erosion rate model is discussed and suggestions for further improvements are given.

2. RESULTS OF FIELD SURVEYS

Two one-month comprehensive data sets on salinity, temperature, and TSS profiles along the York River system, including tidal freshwater, were collected along 25 stations at slack tide either after a flood or after an ebb. Because of the limited resources and the relatively small dynamic range of freshwater discharge in the Mattaponi River, the slackwater stations on the upstream side were selected along the Pamunkey River.

Freshwater discharge information was obtained from two U. S. Geological Survey (USGS) stations: near Hanover (about 170 km from the York River mouth) on the Pamunkey River and near Beulahville (about 135 km from the York River mouth) on the Mattaponi River. Even though the aim was to cover two different freshwater discharge conditions (wet and dry seasons), the two selected periods of slackwater surveys showed a similar extremely dry condition. These low freshwater discharges caused an abnormal salinity intrusion and a nearly well-mixed salinity distribution at the upstream side of the system (Fig. 3a).

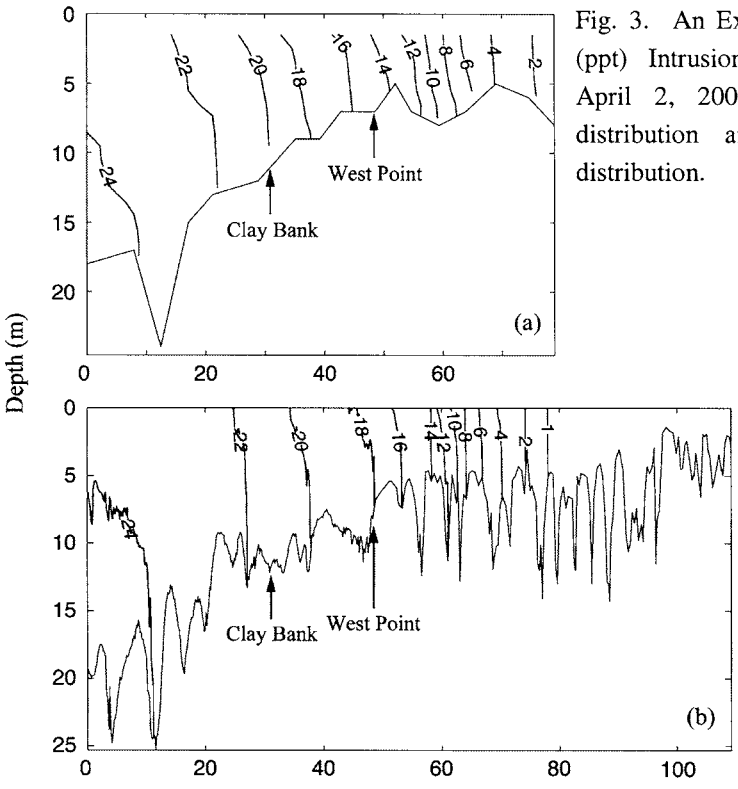

Fig. 3. An Example of Salinity (ppt) Intrusion Simulations on April 2, 2002. (a) Measured distribution and (b) modeled distribution.

The distance between each slackwater station was short (between 4 to 5 km), because the objective was to obtain a better axial resolution of salinity and TSS gradient at the place where the gradient was large. Not all stations were needed if the axial gradient was small. For this reason, not all surveys had measurements at all 25 stations. Also, some upstream stations were moved a little in each survey to find the maximum TSS profiles. All stations were located in the main channel in order to attain the maximum salinity and TSS information.

Conductivity and temperature profiles were measured using an Apply Micro CTD profiler, model 663. A Seapoint Optical Backscatter Strength (OBS) sensor was mounted with the CTD profiler to get continuous OBS readings. A water pump with inlet aligned at the same elevation as the OBS was used to take water samples whenever the OBS reading showed a significant change. As a result, water samples were taken at almost all of the surveyed stations to establish an *in-situ* calibration equation for each survey to convert the OBS readings to TSS readings.

All the salinity profiles were reasonably smooth and were used directly to construct the "snap shots" of salinity distribution. The TSS readings, however, required further processing because of many spikes in most of the profiles. Fishes, sea grasses, or any solid subject that moved around the OBS sensor may have caused the abnormal readings. For this reason, it was necessary to remove these spikes and construct smooth TSS profiles.

Not all the TSS profiles showed a high gradient near the bottom. For those stations at the downstream and upstream ends, the TSS profiles were nearly uniform. Only when local convergence was significant, or in the vicinity of ETM, the TSS profiles did have a significant gradient for the lower part of the water column.

All the eight survey results were similar because of the extremely dry year. Nevertheless, the two data sets provided an extreme case for checking the performance of HEM-3D on salinity intrusion, and for validation of TSS distribution on the module developed.

2.1. Salinity distributions

In general, the salinity at the York River mouth was approximately 24-25 ppt. The salinity was still high (*i.e.*, around 15 ppt) at West Point, which is about 50 km upstream from the York River mouth, due to the low freshwater discharge (*e.g.*, Fig. 4).

For a normal hydrological year, the salinity would be about 5 ppt at West Point, and thus, the measured salinity distributions demonstrated a severe dry condition during the two survey periods. The maximum salinity intrusion distance was found to be about 90 km from the York River mouth. The stratification caused by salinity distribution was not strong. For most of the upstream side, the salinity was almost uniform in the vertical direction (Figs. 3a and 4a).

2.2. TSS distributions

On the downstream side of the York River, the TSS profiles clearly indicated a small increase with water depth. Even at depths close to the bottom, the TSS values were small, and only increased about 10 to 20 mg/L. At stations near the upstream turbidity maximum, the TSS profiles increased quickly and had a significant gradient at the middle water depth. All available TSS profiles for one survey were used to construct a "snap shot" of the TSS distribution for that particular survey.

In general, the TSS concentrations were low and about the same near the York River mouth. The existence of the primary turbidity maximum was obvious and located in the area where the salinity varies from 2 to 10 ppt and the TSS concentration was

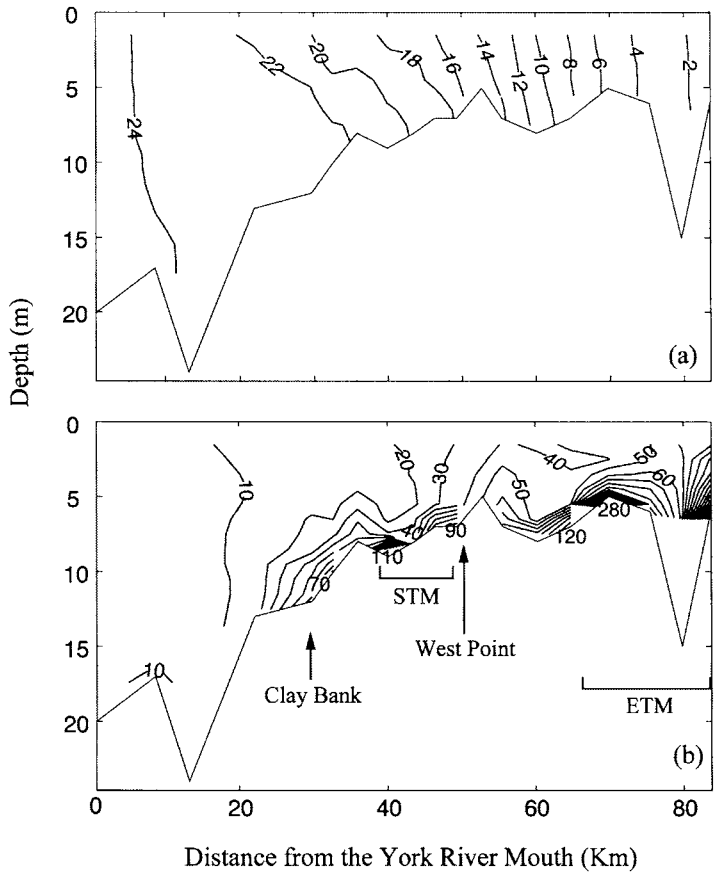

Fig. 4. An Example of Measured (a) Salinity Distribution (ppt) and (b)TSS Distribution (mg/L) on March 19, 2002.

about 100 - 300 mg/L. A STM was also identified, not always though, near Clay Bank with a much weaker signal (40 - 80 mg/L).

2.3. Downstream boundary conditions

Considering that the near-bottom TSS and salinity information in the deep channel are critical for a better simulation of salinity and TSS distributions and a better understanding of the source for TSS, we selected to extend the monitoring intensity at Station YR01 (Fig. 1) to get the required downstream side boundary conditions.

Every two or three days, salinity and TSS profiles at Station YR01 were measured during the two one-month survey periods. Thus, the TSS and salinity information was available from the channel bottom to the water surface at Station YR01. For other places within this cross section, salinity and TSS profiles were assumed to be the same as those measured at the same elevation in the channel. An example of the salinity boundary condition for the first round of slackwater surveys is summarized in Fig. 5. When using this approach for modeling the TSS and the salinity distributions, amplitudes for salinity and TSS variations should also be measured. Fortunately, these two amplitudes were small, and thus, the impact of using zero amplitude in this study is negligible.

In general, the York River mouth is not a source of TSS because of the measured small TSS values during the two observation periods. The change of salinity and TSS boundary conditions were also limited. The maximum change of salinity was only 4 ppt (*e.g.*, from 24 to 27 ppt in the first survey). Time series of the TSS profiles also indicated that TSS was low (around 10-20 mg/L) and the change of TSS was also small (10-30 mg/L).

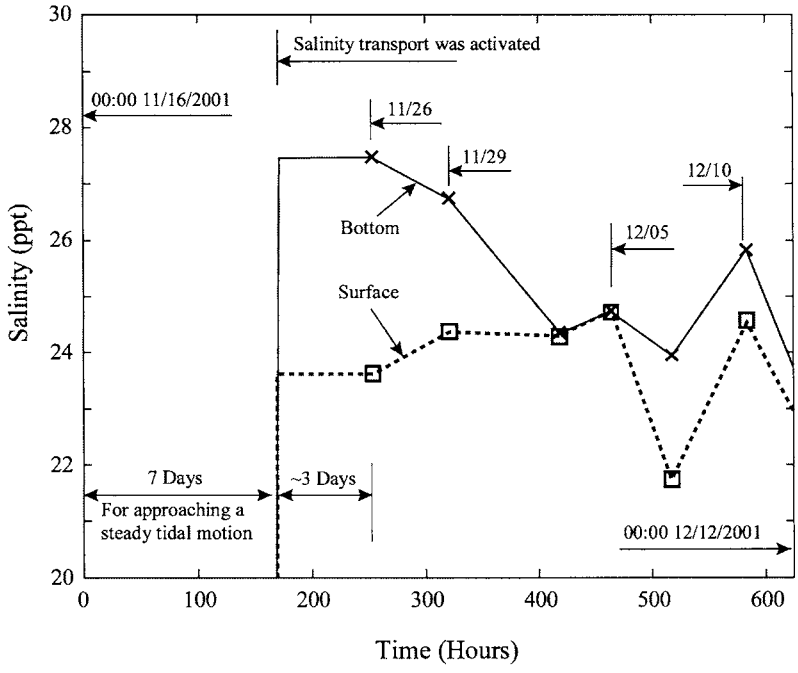

Fig. 5. Salinity Boundary Condition Specified at the York River Mouth for the First set of Slackwater Surveys.

2.4. Upstream boundary conditions

The radiation boundary condition (Chapman, 1985; Hamrick, 1996) was specified at the upstream end to allow tidal waves traveling out of the model domain. Freshwater discharge boundary condition for the modeling periods was obtained from the two USGS stations.

Based on the seven-parameter equation given by Cohn *et al.* (1992), Lin (2001) used 15 years (1979-1994) of data on suspended sediment concentration influx and freshwater discharge at the two USGS stations to work out the "best fit" coefficients for simulated TSS influx to the York River. In this study, the formulation from Lin (2001) was used to calculate TSS concentrations for the two periods of slackwater surveys. Because both periods of slackwater surveys had low freshwater discharge, this implied that the two tributaries did not provide significant sediment sources into the York River, less than 10 mg/L.

2.5. Settling velocity

Turbulence, TSS concentration, and salinity are the major three factors that affect the formation of flocs, and thus, the settling velocity. Turbulence can speed up the formation of flocs (if the turbulence is weak) or break flocs (if the turbulence is strong). TSS concentration indicates the abundance or availability of sediment to form flocs. Salinity allows sediments to form face-to-face flocs by depressing the repulsive electric force on a primary particle's surface that is much stronger than the attractive force (mainly the Van der Waal's force). Thus, the floc density in salty water is higher than that in freshwater.

The above statements suggest that the best approach for obtaining the true settling velocity would be to carry out *in-situ* measurements with the above three parameters not affected. In reality, however, a perfect approach for measuring the settling velocity for cohesive sediments does not exist yet. Even the most popular Owen tube method (Owen, 1976) is not perfect, because it blocks out the turbulence. Nevertheless, the Owen tube method was used in this study. Because the Owen tube is not a commercial product, and the limit budget prevented a full scale measurement to address the issue discussed above. Only limited information on settling velocity was obtained.

Surficial sediment collected from the York River at the Clay Bank site was used to estimate the settling velocity (Fig. 6). Because the maximum TSS concentration measured in the York River was about 300 mg/L, there was no need to find a regression equation for the settling velocity of TSS concentration higher than 300 mg/L, at least not for the current modeling effort. Thus, the measured settling velocity can be estimated using the formula

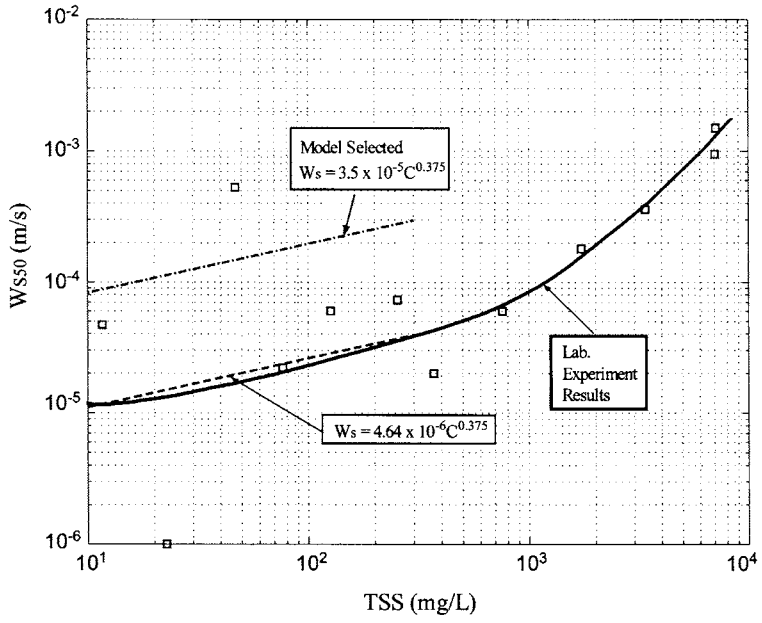

Fig. 6. Measured Settling Velocity for York River Sediments (Clay Bank).

$$w_s = aC^{0.375} \tag{1}$$

where C is the local TSS concentration in mg/L, and a is a constant coefficient equals to 4.64 x 10^{-6} m/s for freshwater. Equation 1 shows that as the settling velocity increases with the TSS concentration. Because tap water was used in the laboratory experiments, the value of a in Eq. 1 represents a possible low limit. With salinity and turbulence, the value of a should have been higher because of the face-to-face flocculation and a better chance to form flocs. For these reasons, a higher coefficient (a = 3.5 x 10^{-5} m/s) was used for model simulation.

3. A CONSTANT EROSION RATE MODEL

For sediment transport modeling, the processes that need to be addressed at the bottom boundary include: erosion, deposition, and consolidation. Maa and Kim (2002) used the VIMS Sea Carousel to measure erosion rates at the Clay Bank site in the York

River for four seasons. That is the only site in the York River that directly measurements of erosion rates were made. There is no erosion rate data for other parts of the York River, which spans more than 100 km, nor any data for deposition rate and consolidation rate for this river, therefore it is difficult, if not impossible, to accurately simulate the bottom boundary condition for the entire river.

Simplification of the bottom boundary condition is possible if the river morphology is not the objective (*i.e.*, not considering consolidation), and under this condition, an attempt (with details next) to simulate the formation of ETM was implemented.

3.1. Traditional erosion rate model

Either a dimensional or a non-dimensional excess bed shear stress (Eq. 2) was used to find the erosion rate at a particular time and location, Eq. 2 is hard to use because of the difficulty to know the vertical profile of the critical bed shear stress for erosion, τ_{cr}, at different bed level, z. In Eq. 2, M and n are two constants. Based on an analytical study, Parchure and Mehta (1985) found that n should be 1/2. For practical applications, however, n = 1 is often used for its simplicity (Geyer *et al.*, 1998; Teeter, 2001; Liu *et al.*, 2002; Ganaoui *et al.*, 2004). Even with n specified, Eq. 2 remains impractical because there is no way to know the change of $\tau_{cr}(z)$ with time, especially in the top centimeters of sediment beds because erosion and deposition occur alternatively and frequently. Therefore, an assumption of $\tau_{cr}(z)$ must be frequently made for modeling purposes. This leads to the unavoidable and an impractical tuning of M and $\tau_{cr}(z)$ in the modeling of cohesive sediment transport.

$$\varepsilon = M\left[\frac{\tau_b}{\tau_{cr}(z)} - 1\right]^n \tag{2}$$

3.2. Simplification of the erosion model

Using the VIMS Sea Carousel for *in-situ* erosion tests (Maa, 1993; Maa *et al.*, 1993; 1998), the observed erosion behavior was always the "Type 1 behavior" (see Eq. 3, Parchure and Mehta, 1985), which means that, for a given bed shear stress (τ_b) that is larger than the τ_{cr}, the eroded sediment mass decreases with time because of the increase of critical bed shear stress $\tau_{cr}(z)$ with depth.

$$\varepsilon(t) = \varepsilon_o e^{-\lambda t} \tag{3}$$

where ε_o is the erosion rate at t = 0 for the given τ_b, $\varepsilon(t)$ is the erosion rate at a given elapsed time, t, and λ is the rate constant.

In general, the rate constant, $\lambda \approx 0.005\ s^{-1}$, appears to be a universal constant if the content of sediment has more than 30% of clay. For example, in the clay-rich Baltimore Harbor, Anacostia River near Washington D.C., and San Diego Bay, λ were also around $0.005\ s^{-1}$ (Maa *et al.*, 1998; Maa and Chadwick, this volume). Figure 7a further shows the results of λ for the Clay Bank site in the York River. The physical meaning of $\lambda \approx 0.005\ s^{-1}$ is that $\varepsilon(t) \approx 0$ in 900 seconds (15 minutes). This is a condition when $\tau_b = \tau_{cr}$. Because tidal flows (*i.e.*, tidal induced τ_b's) do not change significantly within 20 minutes, tidal erosion is always nearly in equilibrium. In other words, the excess bed shear stress, or the term $[\tau_b/\tau_{cr}(z) - 1]$ is always small during a tidal accelerating phase. During a tidal decelerating phase, however, $[\tau_b/\tau_{cr}(z) - 1]$ is a negative number because $\tau_b < \tau_{cr}$. Therefore, it is reasonable to further simply Eq. 2 as follows.

ε = constant for tidal accelerating phases

$\varepsilon = 0$ for other phases

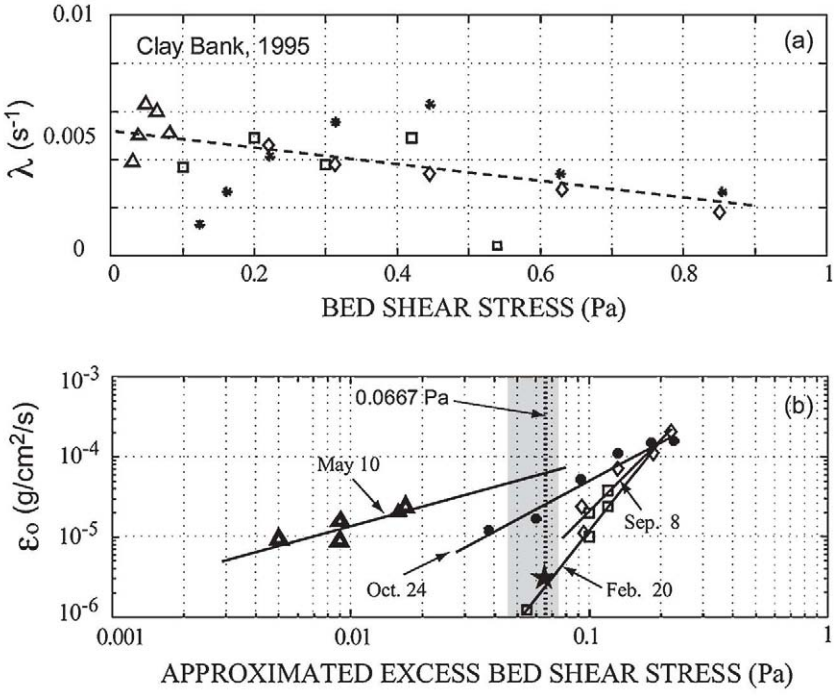

Fig. 7. VIMS Sea Carousel Measured Erosion Rate Constant: (a) λ and (b) ε_o (after Maa and Kim, 2002)

The simplified bottom boundary condition is also justified from *in-situ* tripod observations of TSS time series at the Clay Bank site (Maa and Kim, 2002). In their study, the near bed (10 cm above bed) TSS concentration always increased during tidal accelerating phases and decreased at other phases. The decrease in TSS during the decelerating phases indicated a drop, if not total stop, of upward diffusion. This implies that erosion ceased, or at least significantly reduced. These features were also observed world-wide (*e.g.*, Sanford and Halka, 1993; Nakagawa, this volume; van den Eynde *et al.*, this volume). The net downward flux would increase the TSS concentration right above the bed, which is far below the lowest sensor. When τ_b was sufficiently small, less than the critical bed shear stress for deposition, τ_{cd}, the near bed suspended sediment deposited and the consolidation process began.

Notice that the duration of erosion between the traditional with a constant τ_{cr} and current approach is different. The constant erosion rate model begins to resuspend immediately when the flow is accelerating and ceases right after the flow changes into decelerating phase. Compared to the traditional erosion model, the constant erosion rate model starts and stops erosion earlier. This is because the small shear stress at the beginning of a tidal accelerating phase can resuspend the bottom sediment that was deposited during the previous slack period. Also, because the response of sediment erosion is a quick process, the excess bed shear stress become negative when tidal flow decreases. Therefore, erosion stops. The above statements reveal that the difference between the two modules is time. This difference may not affect the formation of ETM.

3.3. Implementation of the constant erosion rate

The maximum bed shear stress induced by tidal currents may vary significantly within an estuary. For this reason, it is not good to use the same constant erosion rate for the entire estuary. Since the information of maximum bed shear stress, $\tau_{bmax}(i,j)$, at all the horizontal water cells (here i and j are cell index numbers) were saved after checking the tidal hydrodynamics and salinity intrusion, it was not difficult to categorize all cells according to their maximum bed shear stress. Thus, the first step was to categorize each cell according to its own τ_{bmax}. Assuming N categories can be established with an equal interval, the constant erosion rate for each cell can be prorated according to a cell's category. It was found that N should be selected at least more than 8 to have enough resolution (see Fig. 8). Notice that in the deep channel at Gloucester Point, between Gloucester Point and West Point, and in the Pamunkey River, the τ_{bmax} was large. On the other hand, τ_{bmax} was small at shallow areas and downstream from Gloucester Point.

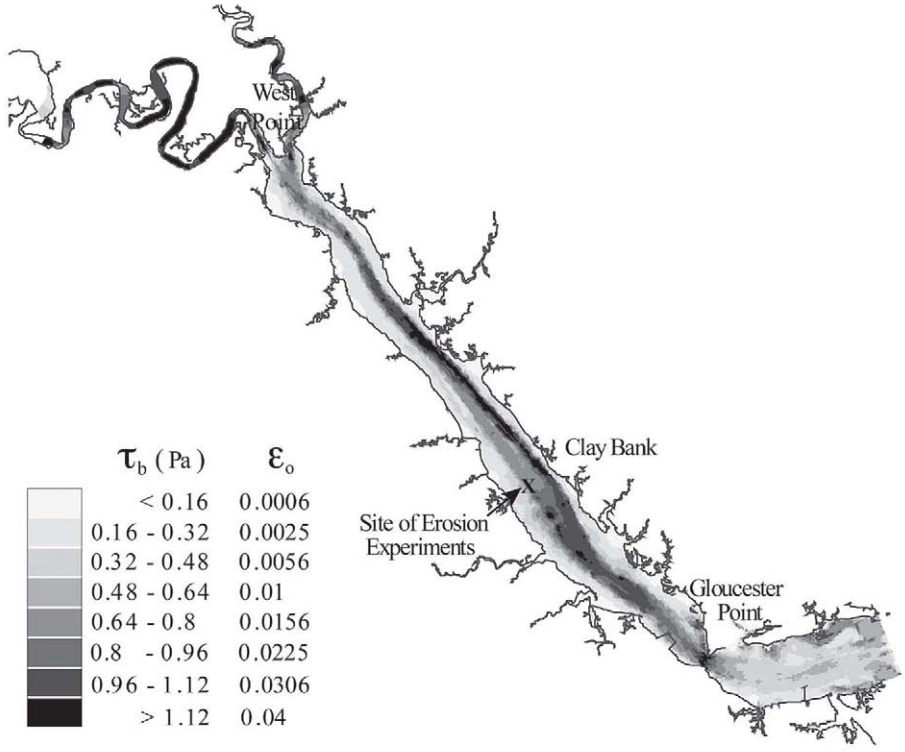

Fig. 8. Distribution of HEM-3D Calculated Maximum Bed Shear Stresses.

The next step was to determine a Reference Constant Erosion Rate (RCER) using *in-situ* measurement results and the τ_{bmax} at the measurement location. The VIMS Sea Carousel erosion experiments were carried out in the secondary channel near Clay Bank (Fig. 8) during 1995. This site had a water depth of 5 m and was located on the south side of the main channel. The maximum bed shear stress at this site was about 0.8 Pa. It was found that the duration of a tidal accelerating phase was about 4 hours at this site (Maa and Kim, 2002), and the maximum bed shear stress must be acquired across this 4 hours. Assuming it increases linearly, the excess bed shear stress can be estimated as 0.8 Pa / (240 min / 20 min) ≈ 0.0667 Pa (dotted line in Fig. 7b). Using this excess bed shear stress, the erosion rate was shown to vary between 0.02 - 0.7 $g/m^2/s$. Of course, this is an indication of a significant change with season. Nevertheless, this procedure

provided a base for selecting the RCER. The simulation results given next were based on a selected RCER of 0.0225 g/m^2/s (marked as a star in Fig. 7b). This value was chosen because of the extremely dry season that represents no new deposition from upstream discharges for a while.

It is understood that, at those places where τ_{bmax} was larger than 0.8 Pa, the erosion rate should be larger than 0.0225 g/m^2/s, and similarly, the less the τ_{bmax}, the less the erosion rate. The eight different categories of maximum bed shear stress imply eight different constant erosion rates, and each constant erosion rate is proportional to the rate of $(\tau_{bmax}/0.8)_c^2$, where c stands for a category and the power of 2 is selected to better fit a non-linear response of erosion rate versus excess bed shear stress (Fig. 7b).

4. RESULTS

One slackwater survey took about one day to finish and was usually started at the York River mouth at a slack tide. After obtaining data at a station, the survey progressed to the next upstream station. The pace of the survey usually matched the tidal propagation, so measurements were always done near slack tide at all the survey stations. Sometimes it was impossible to match with the tide, and a time lag was inevitable. The measured data were used to construct salinity contours and TSS concentration contours given in this paper, and one must know that these are not exactly "snap shots."

The model results (*i.e.*, water level, current velocity, salinity, TSS, *etc.*), however, are saved for the same time steps for the entire York River system. They are "snap shots." For this reason, a post-process of model outputs were done to obtain results with times that match with the survey times at each station for comparison. This approach is more accurate when compared with other alternatives such as averaging the results over one tidal cycle. The averaging process in the other approach actually smoothes the output and is hard to compare with the measurements, because they represent two completely different conditions.

In general, the model simulated TSS concentrations in the middle of the water column were slightly higher than observations and the locations of ETM were also off a little, on the order of 5 to 10 km (see Fig. 9 for an example). For further comparing the simulated and the measured surface and bottom TSS concentrations (Fig. 10), an average of 3 m below surface and 1.5 m above the bed were used, respectively.

For Dec. 5, 2001 (Fig. 10a), the simulated ETM was predicted quite well. The near bed TSS concentration matched at about 110 mg/L and the location also matched at about 70 km from the river mouth. But the surface TSS concentration at the ETM site

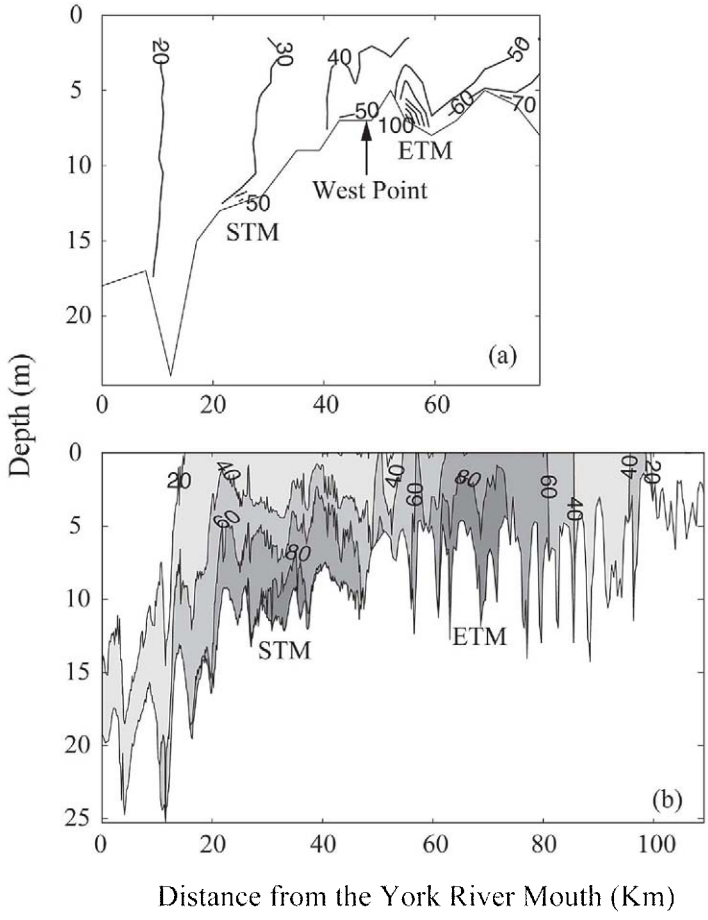

Fig. 9. Comparison of (a) Measured and (b) Modeled TSS distribution (mg/L) on April 2, 2002.

was overestimated. The other peak of measured bottom TSS concentration at 85 km from the mouth may represent a newly developed plume that moved downstream. The location of STM also matched at approximately 30 km from the river mouth, but the simulated TSS concentration was overestimated both at the surface and near the bed.

For April 11, 2002 (Fig. 10b), the center of modeled ETM was off by about 10 km upstream. However, TSS concentrations both at the surface and near the bed were predicted quite closely compared with measurements. Near Clay Bank, the model predicted a relatively weak STM that was also shown weakly during the survey.

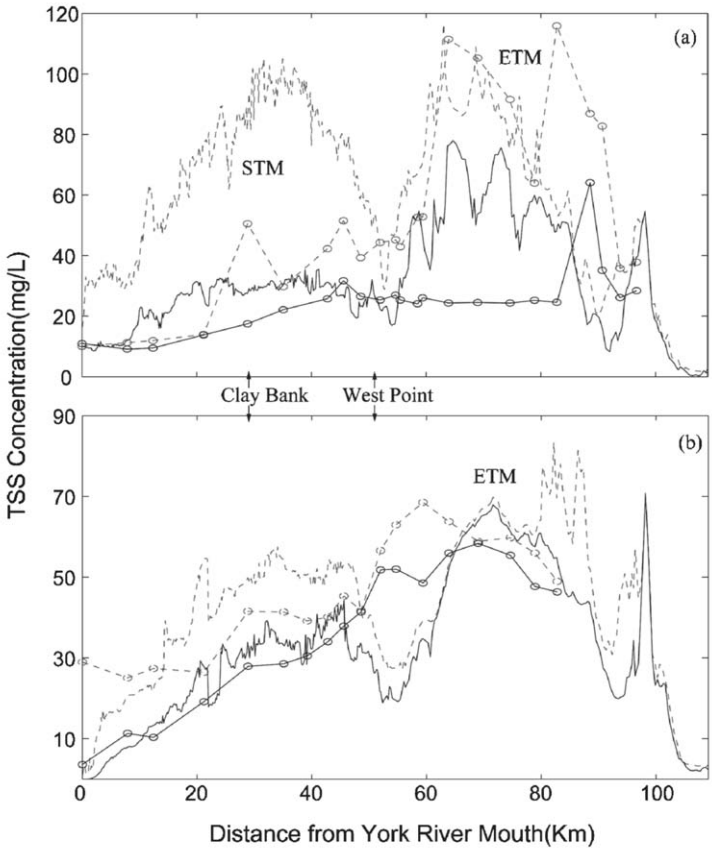

Fig. 10. Comparisons of Observed (lines with circles) and Simulated (lines without circles) TSS Concentrations at two depths. Solid and dashed lines represent surface and bottom TSS Concentrations, respectively. (a) second slackwater survey on Dec. 5, 2001 and (b) eighth slackwater survey on April 11, 2002.

Using the selected approach, a relatively high suspended TSS concentration always showed up at the Clay Bank area, and that may contribute to the existence of the secondary turbidity maximum. Nevertheless, the results presented here indicate that the proposed processes are capable of reproducing the turbidity maximum.

During the eight slackwater surveys, the ETM was always established on the downstream side of the head of salt intrusion (see Fig. 4, for example) except one case given in Fig. 11. Because all surveys were conducted in the low river discharge periods, salt

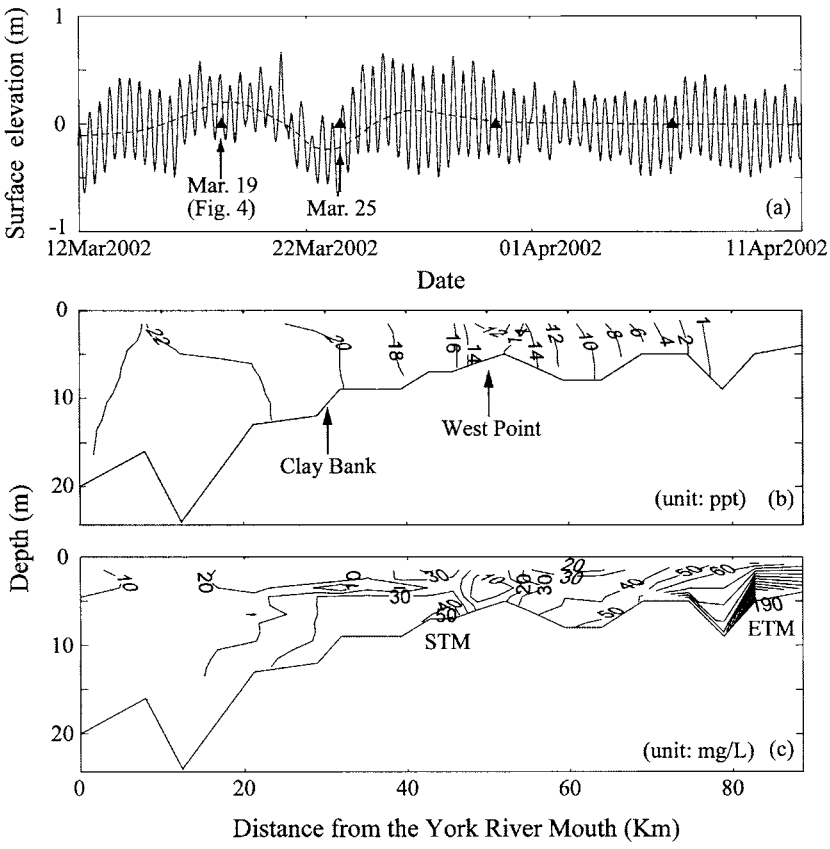

Fig. 11. Effects of a Low-frequency Disturbance on the Relative Location of ETM and Salinity Edge. (a) Time series of surface elevation at Gloucester Point during the second survey: The dashed line is the trend of Mean Water Level and the dates of slackwater surveys are marked with triangles. (b) The salinity distribution on March 25, 2002 (the second triangle on (a)) and (c) the TSS concentration distribution at the same time.

intrusion distances were quite long and the ETMs were formed at a far upstream direction, but lags behind the head of the salt intrusion. The relationship between the head of salt intrusion and ETM was discussed by many other researchers (Geyer, 1993; Uncles *et al.*, 1993; Lin, 2001). It is a complicated process interacted with several factors (*e.g.*, tide, TSS concentration, estuarine circulation, and stratification). However, in this study another possible factor was observed. Between March 19 and March 25, 2002, there was a set down of the mean water level (Fig. 11a). Due to this set down, the head

of salt intrusion (2 ppt) moved about 5 km downstream (see Fig. 4a and Fig. 11b). This is because the increase in pressure gradient produced more downstream-flux from Pamunkey River. But the ETM did not adjust immediately to the change of this hydrodynamic condition. Also, at the upstream side of West Point a relatively less saline and TSS concentration mass pocket was observed. Unfortunately there is not sufficient data to verify where this plume originated. It might have come to York River from the Mattaponi River during an ebb, and when the tide changed to flood, a part of the plume flowed into the Pamunkey River. Although in general, the freshwater discharge from the Mattaponi River is only half of the Pamunkey River, but the time to reach the York River may vary with the local rain events that there is not enough data for studying at this time. Regardless of this plume's origin, it might alter the movement of salt and sediment (see 6-14 isohalines in Fig. 11b). Notice that the freshwater discharge from the Pamunkey River also doubled from 5 to 10 m^3/s during this set down event. This increase of freshwater discharge may enhance the stratification somehow, and thus, may affect both the locations of the head of salt intrusion and the ETM. A further study is required to better understand the relationship between the head of salt intrusion and the location of the ETM in the York River system.

5. DISCUSSION

To simulate sediment transport is not a simple task, because the simulation of tidal hydrodynamics must be right (including tidal range, tidal phase, and salinity intrusion). With the new high resolution bathymetric grid, the above mentioned processes were all successfully simulated using the HEM-3D model.

One of the difficulties faced in this study was how to set a constant erosion rate for each bed cell, because there was only one *in-situ* measurement (near Clay Bank) in the York River. The method presented in this study with 8 categories of maximum bed shear stress is simple but arbitrary. It is possible to extend this approach by using the rate of the maximum bed shear stresses, $[\tau_{bmax}(i,j)*RCER\ /\tau_{Rbmax}]^k$, directly. Where τ_{Rbmax} is the maximum bed shear stress at the reference site. The use of $k = 2$ is arbitrary and may require more study to better describe the observed large range of erosion rate.

Even though the constant erosion rate gives a simple way to successfully address the erosion process, it should be noticed that both periods of simulation were under extremely dry condition. Considering various hydrodynamic and sediment bed conditions, the suggested "constant erosion rate model" must be able to reflect the change of these conditions. For example, it is shown clearly in Fig. 7b that the constant erosion

rate could vary significantly for a given excess bed shear stress, depending on the condition of the sediment bed and hydrodynamic conditions.

Inasmuch as the excess bed shear stress depends on the applied bed shear stress caused by the hydrodynamic forces and the critical bed shear stress for erosion controlled by sediments, the change of the constant erosion rate must reflect the possible change of hydrodynamics and sediment conditions in time and space. In this study the excess bed shear stress was calculated using the maximum bed shear stress from the model simulation with only M_2 tide and one bed condition. The possible changes on τ_{cr} for different beds and the change of τ_b due to flood-ebb variation and spring-neap tides variation were not included. Even with these limitations, the proposed constant erosion rate model works reasonable well because the M_2 tide is the dominant tide in the York River. It represents 89% of the total tidal energy (Sisson *et al.*, 1997). Thus, the true maximum bed shear stress and duration of accelerating phases only vary slightly for the true conditions simulated. To make a constant erosion rate more precise, the true maximum bed shear stress and the duration of accelerating phase should be found first with all the tidal components for a long enough period to cover spring-neap cycles. Thus, even for a fixed τ_{cr}, the excess bed shear stress, τ_{ex}, should have a range (see the gray area in Fig. 7b), not a single value. This will further complicate the modeling effort, and more study is necessary to fully address the need/justification of this modification.

It should be noticed that a more important factor, the bed condition, *i.e.*, τ_{cr}, should have a dominant influence on erosion. The bed conditions may also change with time, especially when there are new sediment coming with storm freshwater discharges. For example, the high erosion rate for May 10^{th} shown in Fig. 7b was caused by a significant storm event eight days before the date of the erosion test. Therefore, newly deposited materials were relatively abundant at that time at Clay Bank (Maa and Kim, 2002). With time, the consolidation process gradually changes the easily erodible sediment into ordinary sediment, and the erosion rate also decreases back to normal conditions. Since the new sediment input from the upstream side is proportional to the freshwater discharge, it is possible to assume that the change of the erosion rate is also proportional to the freshwater discharge. Thus, a constant erosion rate can be tuned with the freshwater discharge to reflect the change of bed materials. However, there should be a time delay in this process for each section of a long river. So far, the modification of the constant erosion rate at the reference site due to the change of freshwater discharge is explained. However, the freshwater discharge may also have an effect on the spatial variability. The clear spatial variability in Baltimore Harbor (Maa *et al.*, 1998) was reported, although it was not caused by the freshwater discharge. To consider the spatial variabil-

ity of the erosion rate, an additional function (varies with distance) can be used to modify the constant erosion rate model. More studies are needed to find the system response that best describes the above process. By combining the above three adjustments, it is feasible to obtain better modeling capability for suspended sediment transport.

6. CONCLUSIONS

(1) A total of eight field surveys on the salinity and total suspended sediment (TSS) profiles along the York River were conducted during two one-month periods (Nov.-Dec., 2001 and March-April, 2002). Because of the unexpected extremely dry seasons during those periods, the survey results in terms of salinity and TSS distributions were very close. There were no significant sediment inputs from both land and ocean. Therefore, sediment eroded from the bed within the York River system must be the source.

(2) The survey results showed that the estuarine turbidity maximum (ETM) was abnormally located about 30 km upstream from West Point. For a normal hydrological year, the ETM was usually located on the downstream side of West Point. A Secondary Turbidity Maximum (STM) was also identified in the York River with a much weaker signal.

(3) A new curvilinear orthogonal bathymetric grid for the York River system was developed to clearly represent all the navigation channels. Model performances on tidal propagation and salinity intrusion were excellent using this new grid.

(4) A series of experiments on the settling velocity of York River sediment indicated that the settling velocity was affected by the concentration of TSS that proved the importance of sediment availability. The influences of salinity and turbulence on the settling velocity remain unaddressed. The limited numerical experiment showed that a higher settling velocity should be used in the modeling of TSS distribution.

(5) Using a simple model for erosion, *i.e.*, erosion occurs only when the tidal flow is in accelerating phases, and during this period of time, a constant erosion rate (which was determined based on the local maximum bed shear stress and results from previous erosion tests) was successfully used to simulate suspended sediment transport for the York River system.

(6) Further improvements on the constant erosion rate model are necessary to address the temporal and spatial variation of this "constant erosion rate" approach to reflect the seasonal change on the bed condition, as well as the different hydrodynamic

conditions. Freshwater discharge is likely the most important parameter to alter the bed condition (*i.e.*, critical bed shear stress for erosion).

ACKNOWLEDGMENTS

Special thanks to Mr. S. Wilson, W. Reisner, R. Gammisch, and H.-K. Ha for their help on field work. Thanks also go to Mr. M. Sisson and Drs. S.-C. Kim and J. Shen for their support and encouragement. The support from the Chesapeake Bay Program FY2001, Environmental Protection Agency under contract number CB-983431-01-0 is also acknowledged. This is a contribution of the Virginia Institute of Marine Science (2648).

REFERENCES

Chapman, D.C. 1985. Numerical treatment of cross-shelf open boundaries in a barotropic coastal ocean model. *Journal of Physical Oceanography*, 15, 1060-1075.

Cohn, T.A., D.L. Caulder, E.J. Gilroy, L.D. Zynjuk and R.M. Summers. 1992. The validity of a simple statistical model for estimating fluvial constituent loads: An empirical study involving nutrient loads entering Chesapeake Bay. *Water Resources Research*, 28(9), 2353-2363.

Ganaoui, O.E., E. Schaaff, P. Boyer, M. Amielh, F. Anselmet and C. Grenz. 2004. The deposition and erosion of cohesive sediments determined by a multi-class model. *Estuarine, Coastal and Shelf Science*, 60, 457-475.

Geyer, W.R., 1993. The importance of suppression of turbulence by stratification on the estuarine turbidity maximum. *Estuaries,* 16(1), 113-125.

Geyer, W.R, R.P. Signell and G.C. Kineke. 1998. Lateral trapping of sediment in a partially mixed estuary. In: *Physics of Estuaries and Coastal Seas*. Dronkers, J. and M. Scheffers (eds.), A.A. Balkema, Rotterdam, 115-124.

Hamrick, J.M. 1996. *Users manual for the environmental fluid dynamics code*. Special report No. 331 in Applied Marine Science and Ocean Engineering, Virginia Institute of Marine Science, College of William and Mary, Gloucester Point, 159p.

Hayter, E.J. and R. Gu. 2001. Prediction of contaminated sediment transport in the Maurice River-Union Lake, New Jersey, USA. In: *Coastal and Estuarine Fine Sediment Processes*. McAnally, W. H. and A. J. Metha (eds.), Elsevier, Amsterdam, 439-458.

Kim, S.C., C. Friedrichs, J.P.-Y. Maa and L.D. Wright. 2000. Estimating bottom stress in a tidal boundary layer from acoustic doppler velocimeter data. *Journal of Hydraulic Engineering*, 126(6), 399-406.

Lin, J. 2001. *A study of the secondary turbidity maximum in the York River Estuary, Virginia.* Ph.D Dissertation, College of William and Mary, Williamsburg, VA.

Lin, J. and A.Y. Kuo. 2001. Secondary turbidity maximum in a partially mixed microtidal estuary. *Estuaries,* 24(5), 707-720.

Liu, W.-C., M.-H. Hsu and A.Y. Kuo. 2002. Modelling of hydrodynamics and cohesive sediment transport in Tanshui River estuarine system, Taiwan. *Marine Pollution Bulletin*, 44,1076-1088.

Maa, J.P.-Y. and B. Chadwick. This volume. Estimation of annual averaged propeller erosion rate in San Diego Bay, California. In: *Coastal and Estuarine Fine Sediment Processes*. Maa, P.-Y., L.P. Sanford and D.H. Schoellhamer (eds.), Elsevier, Amsterdam, this volume.

Maa, J.P.-Y. and S.-C. Kim. 2002. A constant erosion rate model for fine sediment in the York River, Virginia. *Environmental Fluid Mechanics*, 1, 343-360.

Maa, J.P.-Y., L.P. Sanford and J.P. Halka. 1998. Sediment resuspension characteristics in the Baltimore harbor. *Marine Geology*, 146, 137-145.

Maa, J.P.-Y. 1993. VIMS Sea Carousel: Its hydrodynamic characteristics. In: *Nearshore and Estuarine Cohesive Sediment Transport*. Mehta, A.J. (ed.), American Geophysical Union, Washington, D.C., 265-280.

Maa, J.P.-Y., L.D. Wright, C.-H. Lee and T.W. Shannon. 1993. VIMS Sea Carousel: A field instrument for studying sediment transport. *Marine Geology*, 115, 271-287.

Nakagawa, Y. This volume. Fine sediment transport in Ariake Bay, Japan. In: *Estuarine and Coastal Fine Sediment Dynamics-INTERCOH 2003.* Maa, P.-Y., L.P. Sanford, and D.H. Schoellhamer (eds.), Elsevier, Amsterdam, this volume.

Owen, M.W. 1976. *Determination of the settling velocities of cohesive muds.* Report Number IT 161, Hydraulics Research Station, Wallingford, Oxon.

Parchure, T.M. and A.J. Mehta. 1985. Erosion of soft cohesive sediment deposits. *Journal of Hydraulic Engineering,* ASCE, 111(10), 1308-1326.

Sanford, L.P. and J.P. Halka. 1993. Assessing the paradigm of mutually exclusive erosion and deposition of mud, with examples from upper Chesapeake Bay. *Marine Geology*, 114, 37-57.

Sisson, G.M., J. Shen, S.-C. Kim, J.D. Boon and A.Y. Kuo. 1997. *VIMS 3-D Hydrodynamic Eutrophication Model (HEM-3D): Application of the hydrodynamic model to the York River system.* Special report in Applied Marine Science and Ocean Engineering, No. 341, Virginia Institute of Marine Science, College of William and Mary, Gloucester Point.

Shen, J., M. Sisson, A.Y. Kuo, J.D. Boon and S. Kim. 1997. Three-dimensional numerical modeling of the tidal York River system, Virginia. *Proceedings of the 5th International Conference on Estuarine and Coastal Modeling*, ASCE, Reston, 495-510.

Teeter, A.M. 2001. Clay-silt sediment modeling using multiple grain classes. Part II: Application to shallow-water resuspension and deposition. In: *Coastal and Estuarine Fine Sediment Processes.* McAnally, W.H and A.J. Metha (eds.), Elsevier, Amsterdam, 173-187.

Van den Eynde, P., B. Nechad, M. Fettweis and F. Francken. This volume. Seasonal variability of suspended particulate matter observed form SeaWiFS images near the Belgian coast. In: *Estuarine and Coastal Fine Sediment Dynamics-INTERCOH 2003.* Maa. J.P.-Y., L.P. Sanford and D.H. Schoellhamer (eds.), Elsevier, Amsterdam, this volume.

Uncles, R.J. and J.A. Stephens. 1993. The freshwater-saltwater interface and its relationship to the turbidity maximum in the Tamar Estuary, United Kingdom. *Estuaries,* 16(1), 126-141.

Estuarine and Coastal Fine Sediments Dynamics
J.P.-Y. Maa, L.P. Sanford and D.H. Schoellhamer (editors)
Published by Elsevier B.V.

Sensitivity of estuarine turbidity maximum to settling velocity, tidal mixing, and sediment supply

Warner, J.C.[a], C.R. Sherwood[a] and W.R. Geyer[b]

[a]U.S. Geological Survey, 384 Woods Hole Rd., Woods Hole, MA, 02543 U.S.A.
[b]Woods Hole Oceanographic Institution, Mail Stop 12, Woods Hole, MA, 02543 U.S.A.

KEY WORDS
Estuarine turbidity maximum, numerical modeling, settling velocity, stratification

The spatial and temporal distribution of suspended material in an Estuarine Turbidity Maxima (ETM) is primarily controlled by particle settling velocity, tidal mixing, shear-stress thresholds for resuspension, and sediment supply. We vary these parameters in numerical experiments of an idealized two-dimensional (x-z) estuary to demonstrate their affects on the development and retention of particles in an ETM. Parameters varied are the settling velocity (0.01, 0.1, and 0.5 mm/s), tidal amplitude (0.4 m 12 hour tide and 0.3 to 0.6 m 14 day spring neap cycle), and sediment availability (spatial supply limited or unlimited; and temporal supply as a riverine pulse during spring vs. neap tide). Results identify that particles with a low settling velocity are advected out of the estuary and particles with a high settling velocity provide little material transport to an ETM. Particles with an intermediate settling velocity develop an ETM with the greatest amount of material retained. For an unlimited supply of sediment the ETM and limit of salt intrusion co-vary during the spring neap cycle. The ETM migrates landward of the salt intrusion during spring tides and seaward during neap tides. For limited sediment supply the ETM does not respond as an erodible pool of sediment that advects landward and seaward with the salt front. The ETM is maintained seaward of the salt intrusion and controlled by the locus of sediment convergence in the bed. For temporal variability

of sediment supplied from a riverine pulse, the ETM traps more sediment if the pulse encounters the salt intrusion at neap tides than during spring tides.

1. INTRODUCTION

Estuarine Turbidity Maxima (ETM) are regions of locally elevated suspended sediment concentrations often found near the landward limit of salt intrusion. The spatial and temporal distribution of suspended sediment concentrations and benthic deposits are controlled by hydrodynamic and sedimentological factors. The hydrodynamic controls for an estuary of given bathymetry are river flow and tidal amplitude. These forcings produce variations of mixing and buoyancy input that impact salinity stratification and longitudinal translation of the salt intrusion. Sediment properties of particle settling velocity and shear-stress threshold for resuspension of bottom material also exert controls on the ETM formation.

An ETM is generated and maintained by both tidal and subtidal processes and the magnitude and location are controlled by the quantity and location of available sediment. Many observational and numerical investigations have been performed to understand the dynamics of ETMs and describe their spatial and temporal behavior. Geyer (1993) discusses the significance of stratification in the downstream region of the salt intrusion compared to the unstratified fresh water zone. Stratification reduces the turbulence mixing and carrying capacity of the flow thus enhancing the focus of sediment at the limit of salt intrusion. Focusing of sediment at the ETM is shown to be dependent on particle settling velocity and optimal convergence occurs for intermediate particle sizes.

Jay and Musiak (1994) describe the process of tidal velocity asymmetry in which the convective instability during the flood tide produces a bottom intensified velocity profile and convectively stable transport during the ebb yields increased shear and reduced near-bottom currents. This results with net upstream bottom currents, and because sediment concentrations increase near the bed, a net upstream transport of suspended material is generated.

Uncles and Stephens (1993) describe the ETM dynamics of the Tamar Estuary where the ETM is upstream of the Fresh/Salt water Interface (FSI) on the order of 1-3 km. The FSI can be predicted based on a regression of river flow. Low river flow spring-tide periods produce a pronounced ETM occurring somewhat upstream of the FSI but clearly associated with the FSI. This up-estuary location is attributed to a

limited supply of sediment eroded during flood tide in the unstratified water on the landward side of the FSI. Strong vertical mixing on the flood and intense stratification on the ebb create a current phasing between the near-bed and surface currents. "Stalling" of the bottom currents enhances upstream focusing of sediment and enhanced the ETM creation. During periods of increased freshwater discharge the available supply of erodible sediment moves down-estuary to be redeposited or flushed.

Wolanski *et al.* (1995) describe field studies of the Fly River Estuary that show an ETM exists only during spring tides in the saline portion of the estuary slightly downstream from the limit of salt intrusion. ETM creation is due to influences from both tidal pumping and tidally averaged baroclinic circulation. Sanford *et al.* (2001) describe characteristics of the Chesapeake Bay ETM. Particle trapping efficiency varies on a seasonal scale attributed to variation of particle settling speeds, with increased settling velocity during the fall. The ETM roughly tracks the limit of salt intrusion but often is significantly separated from it due to increased river discharge events.

Burchard and Baumert (1998) conducted numerical experiments to compare the ETM formation processes in a flat bottom estuary. Three physical causes for the residual near-bottom upstream flow near the limit of salt intrusion are examined. Of these, the residual gravitational circulation and tidal velocity asymmetry are determined to be necessary for the development of an ETM. Tidal mixing asymmetry was deemed only to affect the ETM quantitatively, not essential for its development. These numerical experiments were conducted for one tidal frequency with limited sediment availability.

These previous experiments exhibit the complexity of ETM dynamics and demonstrate variations of multiple temporal and spatial scales. During steady river flow and neglecting geomorphic evolution, the dynamic parameters that maintain an ETM are particle settling velocity, tidal mixing, resuspension thresholds, and sediment availability. For the work in this paper we compare the significance of these factors by performing numerical experiments of an idealized estuary in a 2D (x-z) plane. This study extends the work of previous idealized studies to examine the effect of the spring/neap tidal cycle on a tidal time scale, to study the effects of sediment supply on the formation of an ETM, and to compare the trapping efficiency of an ETM during a spring tide to a neap tide for a given sediment pulse.

2. NUMERICAL EXPERIMENTS

Numerical experiments were performed to investigate processes that develop and maintain an ETM. Specifically we investigated effects of settling velocity, tidal mixing,

erosion potential, and sediment availability. Table 1 summarizes the numerical experiments and they are described as follows. Section 3.1 describes experiments to vary particle settling velocities. The settling velocity is varied with values of 0.01, 0.10, and 0.50 mm/s. These test are conducted with an unlimited supply of sediment. To determine the effects of tidal mixing and erosion potential, the tidal amplitude is varied. Increasing the tidal amplitude increases the mixing within the estuary and also enhances the potential of sediment resuspension from the bed. The tidal amplitude first is simulated with a constant 0.4 m 12 hour tide and detailed results are described in Section 3.2. Then the tidal amplitude is varied to range from 0.3 to 0.6 m over a 14 day spring neap cycle with results described in section 3.3. These simulations were also performed with an unlimited supply of sediment. To demonstrate the effects of sediment availability, first the supply of material available on the bed is limited and results are described in Section 3.4. To investigate the response of the ETM to temporal changes in sediment supply from an upstream source, we simulate two riverine pulses released during different phases of the spring neap cycle. Results are described in Section 3.5.

2.1 Description of hydrodynamic model

The three-dimensional, hydrostatic, primitive equation numerical ocean model Regional Ocean Modeling System - ROMS v2.0 (Haidvogel *et al.*, 2000; Shchepetkin and McWilliams, 2005) was selected to simulate the tidal hydrodynamics and density structure. Details of the model can be found at http://marine.rutgers.edu/po/index.php. In general, ROMS solves the Reynolds averaged form of the Navier Stokes equations on a horizontal orthogonal curvilinear Arakawa "C" grid and uses stretched terrain following coordinates in the vertical. The model allows selection of several advection schemes, pressure-gradient algorithms, turbulence closures, and boundary conditions.

Table 1. Descriptions of numerical experiments.

Experiment description	w_s (mm/s)	tidal forcing	sediment supply
3.1 – Settling velocity	0.01, 0.10, and 0.50	12 hr, 0.40 m	bed source unlimited
3.2 – Tidal time scale	0.10	12 hr, 0.40 m	bed source unlimited
3.3 – Spring/Neap	0.10	12 hr/14 day, 0.3-0.6 m	bed source unlimited
3.4 - Spring/Neap	0.10	12 hr/14 day, 0.3-0.6 m	bed source limited
3.5 – Timing of pulse	0.10	12 hr/14 day, 0.3-0.6 m	upstream source

ROMS is efficient on both single processor and shared or distributed memory computer architectures.

Parmeterization for subgrid scale mixing was characterized with the two equation Generic Length Scale (GLS) model (Umlauf and Burchard, 2003), with the implementation of this model as described by Warner *et al.* (2005b). Coefficients were set to recover the k-omega model (Wilcox, 1988) with the extension to buoyancy driven flows as suggested by Umlauf *et al.* (2003) and the buoyancy parameter as derived by Warner *et al.* (2005b). Other two-equation model parameterizations could be chosen and would not qualitatively alter the results. Stability functions were parameterized using the formulation by Kantha and Clayson (1994).

2.2 Model configuration and initial conditions

To reduce the complexity of the flow the numerical experiments are simulated in an idealized estuary configured as a rectangular channel 100 km in length (Fig. 1). Free slip on the side walls ensures no lateral variations in the flow, thus reducing the problem to a 2D x-z plane. The bottom slopes from 10 m depth at the (left) ocean end to 5 m depth at the (right) landward end. The grid consists of 400 equidistant horizontal cells spaced at 250m, and a vertical discretization of 16 terrain following levels that provide resolution on the order of 0.5 m.

All numerical experiments are initialized from a start up simulation that ran for 90 days. This spin up simulation used a semi-diurnal (12-hour) tidal forcing. After 90 days the model state lost all influence from the initial values and the baroclinic field had adjusted to produce a stable gravitational circulation pattern. Subsequent simulations restarted from this setup, introduced sediment as required, and ran until the sediment

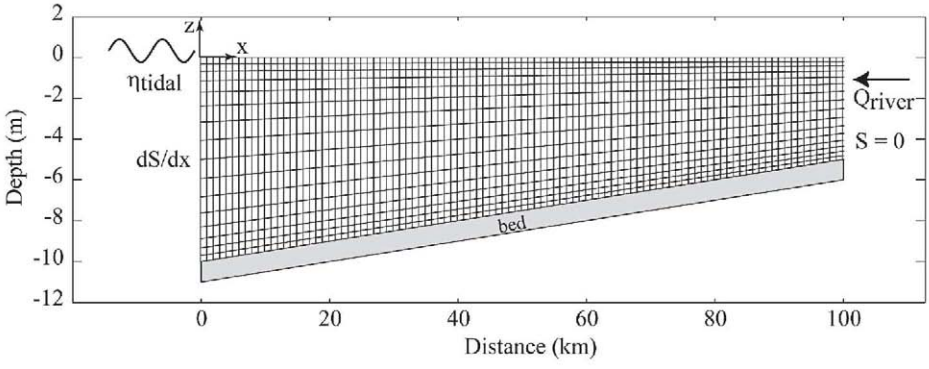

Fig. 1. Numerical grid for estuarine transport simulations (every fourth horizontal cell shown for clarity).

also reached equilibrium, on the order of 10 days for a cyclical tide or two spring neap tidal cycles for the fortnight variations.

2.3 Boundary conditions

For momentum, the water is driven at the ocean end (x=0) with an oscillatory sea level displacement of

$$\eta_{x=0} = A\,sin(\omega\, t) \tag{1}$$

where $\eta_{x=0}$ is the free surface displacement measured positive upwards from the mean water level (z =0), A is the tidal amplitude, ω is the tidal frequency, and t is time. Values for model parameters and model setup are listed in Table 2. The landward end is considered unidirectional (seaward) constant fresh water inflow and the boundary condition is imposed through the depth-averaged velocity as

$$\bar{u}_{x=L} = Q_{river} / (h+\eta)_{x=L} \tag{2}$$

Table 2. Model parameters for estuarine circulation experiments.

Model Parameter	Variable	Value
length, depth	*Xsize, h*	100000 m, linear 10-5 m
num. grid cells horiz., vert.	*Lm, Nm*	400, 16
bottom roughness	*Zob*	0.005 m
time step	*dt*	30 s
river flow @ x = 100 km	Q_{river}	0.40 m^3/s/m width
tidal free surface @ x = 0 km	$\eta_{x=0}$	$\eta_{x=0} = A\ sin\,(\omega t)$
tidal amplitude	A	0.40 m (semi-diurnal) 0.3-0.6 m (fortnightly)
tidal periods	$T = 2\,\pi/\omega$	(1) 12 hour (semi-diurnal) (2) 14 day (fortnightly)
salinity boundary at x = 0 km	dS/dx	$dS/dx = -\frac{S_0}{2\beta}\mathrm{sech}^2\left(2-\frac{X}{\beta}\right)$
maximum salinity	S_0	30
settle velocity	w_s	0.01, 0.10, 0.50 mm/s
erosion rate	E_0	$1x10^{-4}$ kg/m^2/s
critical stresses	τ_{ce}	0.05 N/m^2
porosity	φ	0.90

where $u_{x=L}$ is the depth averaged velocity at the landward boundary, Q_{river} is the (constant for all simulations) magnitude of fresh water inflow, $h_{x=L}$ is the depth (5 m) and $\eta_{x=L}$ is the free surface calculated by the model at the landward boundary. A radiation boundary condition is also imposed here to allow the tide to propagate out of the domain without reflection.

Many types of boundary conditions are available for transport of scalars. The boundary condition we used is derived from a gradient condition (Warner *et al.*, 2005a) and is briefly described here. Results are not dependent on this form of a boundary condition. For the salinity in an estuary, the longitudinal distribution is approximated with a hyperbolic tangent function as

$$S(x)=\frac{S_0}{2}\left[1+\tanh\left(2-\frac{x}{\beta}\right)\right] \tag{3}$$

where $S(x)$ is a value of salinity, S_0 is the maximum value at the oceanic end (30 psu), x is the longitudinal coordinate (km), and β is a length scale (km) for the salt intrusion and is a function of fresh water discharge. The longitudinal salinity gradient (dS/dx) can then be derived by taking the derivative of equation (3) with respect to x. Numerical simulations of a realistic estuary with similar freshwater discharge and salt intrusion length as the present idealized estuary suggest a value of $\beta = 15$ (Warner *et al.*, 2005a). The boundary value of salinity at the ocean is then obtained from

$$S_{(x=0,\,z)} = S_{(x=1,z)} - dS/dx * \Delta x \tag{4}$$

where $S_{(x=0,\,z)}$ is the magnitude of salt at the ocean boundary, $S_{(x=1,z)}$ is the magnitude of salt at the first interior cell, and Δx is the horizontal grid spacing, and dS/dx is determined by taking the derivative of equation (3) with respect to x, evaluated at x=0. Salinity at the landward end is held at zero.

2.4 Suspended sediment transport module

Sediment suspended in the water column is transported, like other conservative tracers (*e.g.*, salinity), by solving the advection-diffusion equation with two additional terms added for vertical settling and sources or sinks related to erosion or deposition as

$$\frac{\partial C}{\partial t}+\frac{\partial uC}{\partial x}+\frac{\partial wC}{\partial z}-\frac{\partial w_s C}{\partial z}=\frac{\partial}{\partial x}\left(K_x\frac{\partial C}{\partial x}\right)+\frac{\partial}{\partial z}\left(K_z\frac{\partial C}{\partial z}\right)+sources/sinks \tag{5}$$

where C is the volume concentration of suspended sediment, K_x and K_z are diffusivity in the x- and z-directions, respectively, w_s is the vertical settling velocity (positive upwards), and *sources/sinks* are parameterized interactions with the bed. The vertical advection algorithm for settling uses a Piece-wise Parabolic Method (PPM; Colella and Woodward, 1984) with parabolic splines, implemented with a Weighted Essentially Non-Oscillatory scheme (WENO; Liu *et al.*, 1994). These methods allow the integration bounds of depositional flux to use multiple grid boxes in the vertical direction and is therefore not constrained by the Courant condition. No-flux boundary conditions are imposed at the surface and bottom in the vertical diffusion equation.

The source/sink term is the net flux into the water column, calculated as the sum of depositional flux (downward advection through the bottom of the lowest grid cell by settling, equivalent to $w_s C \Delta t$) and erosional flux. Erosional flux is parameterized following Ariathurai and Arulanandan (1978) as

$$E_s = E_0(1-\varphi)\frac{\tau_b - \tau_{ce}}{\tau_{ce}} \text{ when } \tau_b > \tau_{ce} \tag{6}$$

where E_s is the surface erosion mass flux (kg/m^2/s), E_0 is a user-defined bed erodibility constant (kg/m^2/s), φ is the porosity (volume of voids/total volume) of the top bed layer, τ_{ce} is the critical shear stress for erosion, and τ_b is the bed shear stress determined by the hydrodynamic routines. The erosional flux is limited by availability in the single bottom sediment layer.

3. RESULTS AND DISCUSSIONS

3.1 Variation of settling velocity

Experiments varied the magnitude of settling velocity to determine the effect on the processes that develop and maintain an ETM. Values of w_s are 0.01, 0.10, and 0.50 mm/s, to cover a typical range of observed values (Sanford *et al.*, 2001). For these experiments, the source of sediment is not a critical issue and sediment was provided from the river as a vertically well-mixed constant supply of 100 mg/l. In general the sediment is transported towards the ocean due to the combined effects of river and tidal flow. The suspended sediment encounters the salt front and interacts with the estuarine dynamics to be trapped in the ETM or transported seaward out of the estuary. For the three settling velocities, Fig. 2 shows results of the tidally averaged suspended sediment concentrations (solid contour lines), tidally averaged isohalines (dashed contour lines),

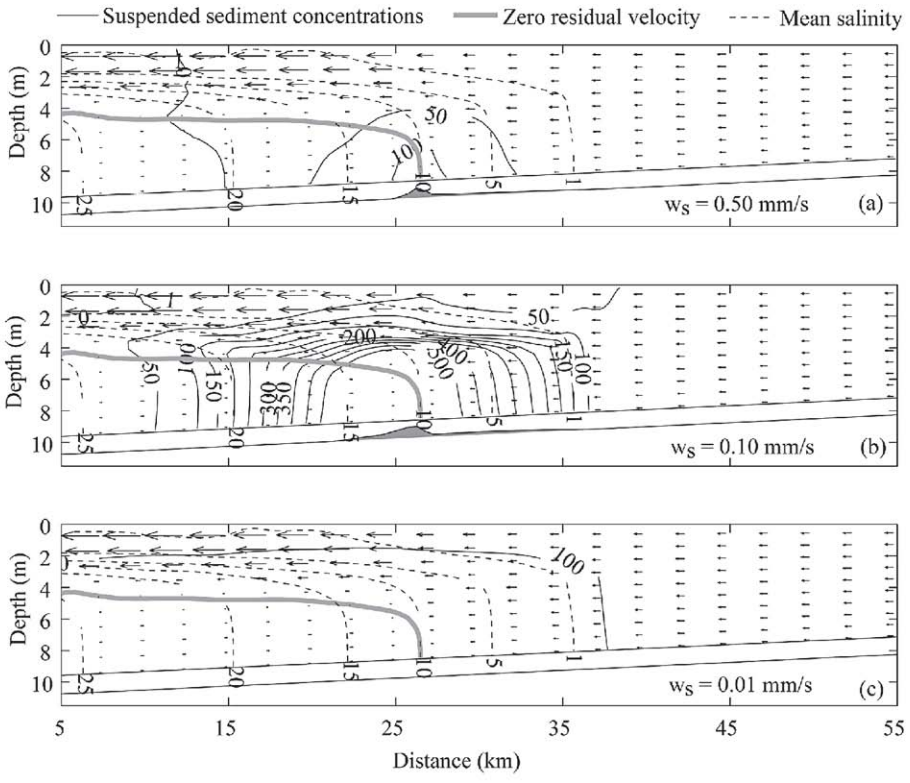

Fig. 2. Tidally averaged results of suspended sediment concentrations (solid contour lines), tidally averaged isohalines (dashed contour lines), line of zero velocity (thick solid line), and residual velocity vectors (arrows) for particle settling velocity variations of (a) w_s = 0.50 mm/s; (b) w_s = 0.10 mm/s; and (c) w_s = 0.01 mm/s.

line of zero velocity (thick solid line), and residual velocity vectors. For all three simulations, the salt front is located near x = 35 km (location of tidally averaged 1 psu isohaline). The line of zero velocity intersects the bed at x = 27 km, coincident with the greatest bed accumulation, as expected.

Results identify that the coarsests grained material with the highest settling velocity of 0.50 mm/s (Fig. 2a) tends to accumulate in the upstream landward (unstratified) section of the estuary. Limited amount of this material is transported seaward and therefore sediment concentrations remain low in the ETM. The finer grained material with a low settling velocity of 0.01mm/s (Fig. 2c) tends to stay in suspension. Most of

this material is advected seaward and with reduced amounts of deposition. The medium grained material with a settling velocity of 0.10 mm/s (Fig. 2b) provides a balance between vertical mixing, deposition, and along channel transport and produces the greatest concentrations in the ETM.

Geyer (1993) suggested a nondimensional scale, l, to compare the significance of the length of sediment trapping, u h / w_s, relative to the length of salt intrusion (L) as

$$l = \frac{u\,h}{w_s L} \tag{7}$$

where u is a representative tidal velocity (taken as the tidal average velocity in the stratified ETM), and h is the thickness of the bottom boundary layer (defined as the vertical distance from the bed to the region of strong isohalines). Using the 3 settling velocities of 0.01, 0.1, and 0.50 mm/s results with length scales of 3.20, 0.32, and 0.07, respectively. A length scale $l > 1$ implies that the sediment is transported to the seaward end of the salt intrusion with limited trapping, as occurs for the low settling velocity particles. For $l << 1$ the sediment fraction is more coarse with trapping only occurring at the nose of the salt wedge, as occurs for the high settling velocity particles. For $l \sim 1$ the sediment class will yield a stable well defined ETM, as occurred for the intermediate settling velocity particles. With this criteria, the sediment with w_s = 0.10 mm/s yields the most stable ETM and we use this value for all subsequent simulations.

A different scaling is suggested by Jay *et al.* (in press) where an advection number, A, scales the strength of horizontal advection, u/L, relative to vertical mixing, κ u*/ h, in the ETM balance as

$$A = \frac{h\,u}{L\,\kappa\,u_*} \tag{8}$$

where κ is von Kármán's constant, and u_* is the shear velocity. Equation 7 is a ratio of advective transport to gravitational settling. Equation 8 is a ratio of advective transport to vertical turbulent mixing. The importance of these scales can be related through the Rouse parameter (P) that determines the vertical distribution of sediment as

$$P = \frac{w_s}{\kappa\,u_*} \tag{9}$$

P is a ratio of the advection scale (A) to the length scale (l). Small values of P indicate low settling velocities or strong turbulence and produce a well-mixed vertical

distribution of sediment. Large values of P suggest high settling velocities or little turbulence and yield increased sediment concentrations in the near bed region. Jay *et al.* (in press) demonstrate that $P \sim 1$ (actually 0.7) is a characteristic mid ETM value. This implies that when the length scale and advection scale are near equivalent, a stable ETM can be produced. For our simulations A ~ 0.5. Suggesting a comparable value for l imposes that $w_s = 0.10$ (as was found) should produce the most stable ETM.

3.2 ETM Tidal time scale dynamics

Details of the complex ETM dynamics during a tidal cycle are revealed through observations of the salinity - velocity - sediment interactions. Figure 3 displays four sets of longitudinal profile plots from x = 20 to x = 80 km. For each set, the top panel contours the eddy diffusivity (K_z) for vertical mixing of the scalars. In general, the eddy diffusivity in the unstratified riverine section exhibits a parabolic profile in the vertical. Seaward of the salt intrusion limit, the eddy diffusivity is greatly reduced in the upper portion of the water column due to salt stratification. The second panel shows contours of Suspended-Sediment Concentration (SSC), salinity isohalines, and velocity vectors. Generally, the sediment distributions are segregated into three regimes: 1) an upstream well-mixed riverine portion; 2) a strongly stratified bottom boundary layer seaward of the salt intrusion limit that extends upwards to the isohalines; and 3) an unstratified surface mixed layer.

During flood tide (Fig. 3a) sediment is resuspended and overtaken by the advancing salt front. The highest bottom stress and greatest resuspension occurs at the toe of the salt front on the landward side. As the salt front advects landward it overtakes the suspended sediment and creates a zone of maximum concentrations on the seaward side of the salt limit. The flood tide advects saltier water over fresher water creating an unstable convective boundary layer. This instability enhances mixing in the bottom boundary layer (Fig. 3a) that reduces shear and increases the magnitude of the flooding currents (compared to the ebb tide currents).

Currents in the bottom boundary layer turn to ebb approximately 1 hour before the upper portion of the water column (not shown). During ebb, fresher water is advected over saltier water creating a convectively stable water column that decreases the amount of mixing and allows greater shear to develop, decreasing the magnitude of the near bottom currents (compared to the flood tide currents). The increase of near bottom currents on the flood and reduction during the ebb (tidal velocity asymmetry) leads to enhanced upstream residual flow in the bottom layer. Because sediment concentrations are higher near the bed, the velocity asymmetry also tends to promote landward transport of sediment. During ebb, reduced mixing within the bottom boundary layer

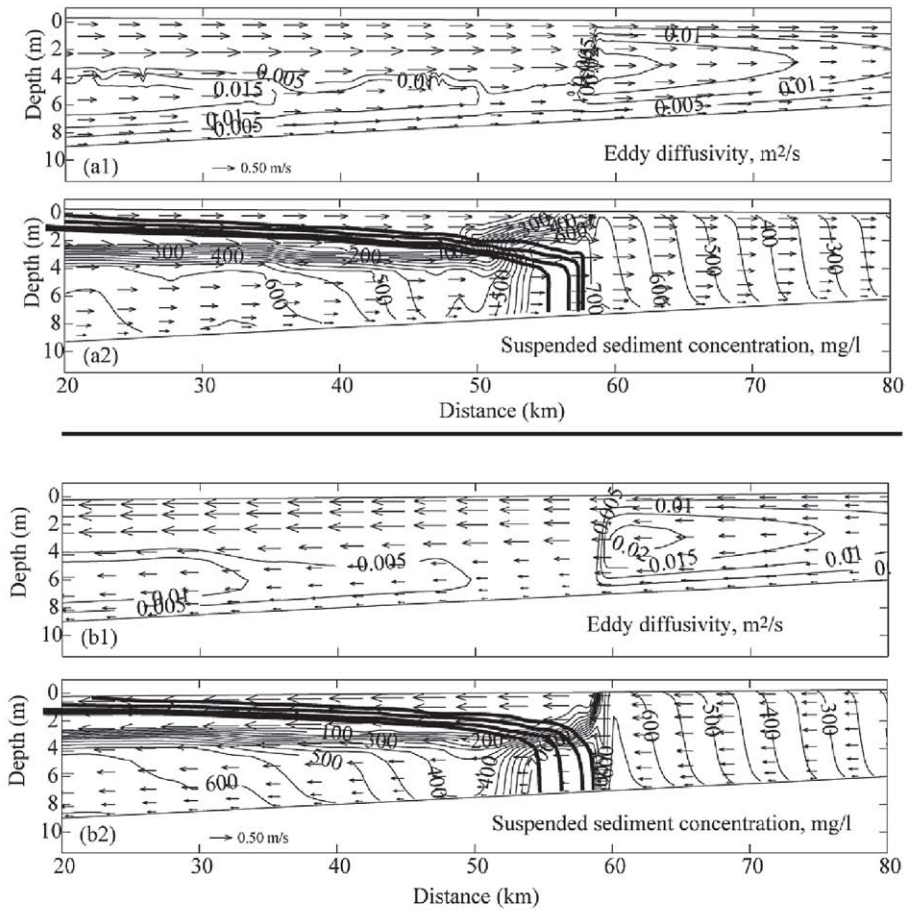

Fig. 3. Tidal time scale dynamics for ETM entrapment processes. For each set, the top panel shows contour of eddy diffusivity, and bottom panel shows contours of suspended sediment concentrations (solid lines), isohalines (1, 2, 3, and 4; thick lines), and instantaneous velocity vectors (arrows). Twelve hour tidal time scale dynamics at times of (a) 2 hours; (b) 7 hours; (c) 10 hours; and (d) 12 hours. (Figure continues on next page.)

promotes suspended sediment to settle out of the water column and deposit. The vertical eddy diffusivity is nearly an order of magnitude smaller during ebb than flood between x= 20 to 55 km (Fig. 3b). The salt front retreats over the deposited sediment and the zone of maximum bed stress resuspends this freshly deposited material. The sediment is advected upwards and over the salt front (Fig. 3c). As the currents become slack on top

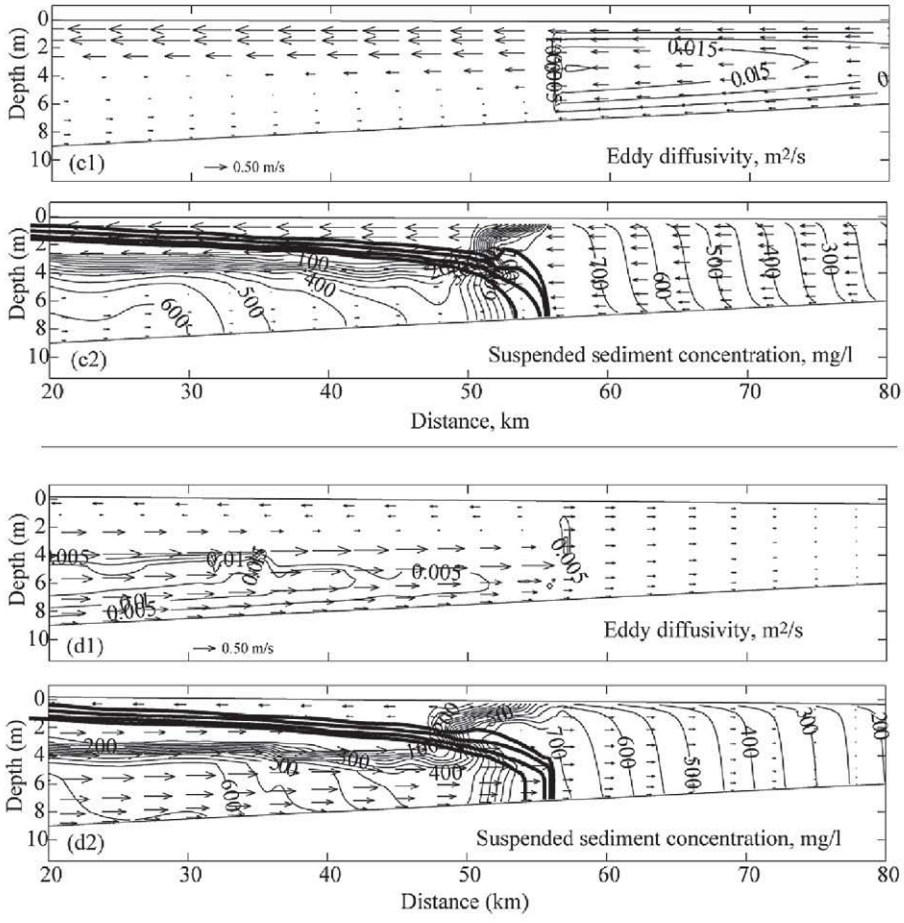

Fig. 3. continued.

of the salt front, the suspended sediment settles out through the halocline into the bottom boundary layer. But at this time the currents in the bottom boundary layer are flooding and promote landward transport of the sediment (Fig. 3d). These processes enhance trapping of the sediment at the limit of salt intrusion.

3.3 ETM Spring / Neap variations

The tidal time scale dynamics discussed in the last section are enhanced during the spring/neap cycle. During spring tides the tidal range is at maximum causing increased tidal currents and enhanced bottom stress. The increased bottom stress increases the concentrations of suspended sediment, most noticeably at the landward side of the salt intrusion (location of maximum bottom stress). Spring tides also enhance vertical mixing and the salt stratification is greatly reduced, especially at the front of the salt intrusion. The nose of the salt front is now defined by a vertically well-mixed salt limit (Fig. 4b). During ebb the vertically well mixed salt front is maintained and the

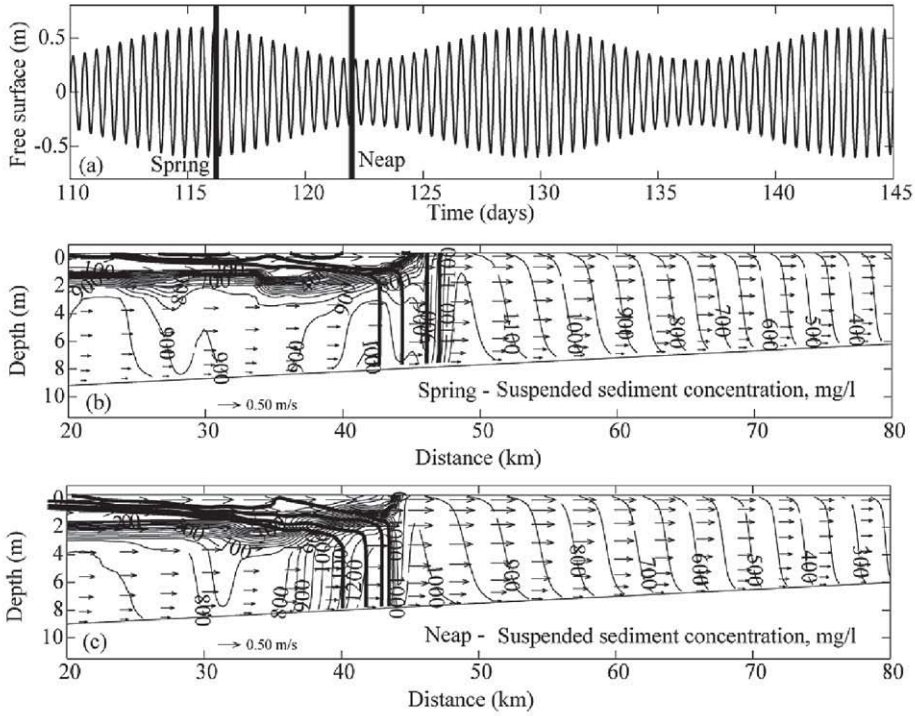

Fig. 4. ETM dynamics for spring neap tidal forcing. (a) Free surface time series. (b) Spring tide with ETM on the landward side of salt intrusion due to higher bottom stresses and well mixed vertical salt intrusion and (c) neap tide with ETM on seaward side of salt intrusion due to processes exhibited in Fig. 3. Both bottom panels show contours of suspended sediment concentrations (solid contour lines), tidally averaged isohalines (1, 2, 3, and 4; thick contour lines), and velocity vectors at max. flood (arrows).

suspended sediment is not able to be advected seaward of the salt intrusion limit. This leads to maximum concentrations on the landward side of the salt limit during spring tides (Fig. 4b). As the tidal range decreases towards neap tides, the mixing is reduced and the salt front becomes more stratified. During ebb, the suspended sediment is advected over the salt front and settles on the seaward side of salt intrusion, allowing the development of the ETM on the seaward side of the salt front (Fig. 4c).

Figure 5 demonstrates the covariability of the ETM and salt intrusion limit. The spring tides are centered on days 115.5 and 129.5, and neap tides centered on days 122.5 and 136.5 (Fig. 5a). The limit of salt front (Fig. 5b) was identified as the near-bed encounter of the 2 psu isohaline. The salt intrusion limit varies with the tide and also has a spring/neap cycle, although not in phase. On a tidal time scale, the salt front advects

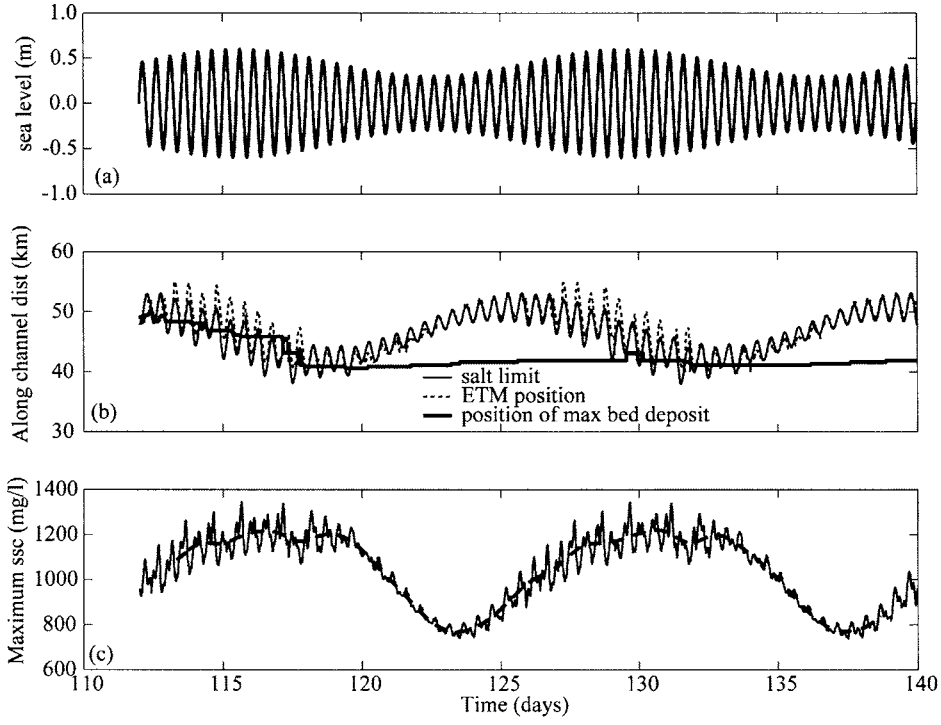

Fig. 5. Location of ETM and salt front for unlimited sediment supply. (a) Sea level at the mouth; (b) salt intrusion limit (solid line), ETM position (dashed line), and location of maximum bed deposit (thick solid line); (c) ETM tidal and tidally averaged suspended sediment concentrations.

landward and seaward with the tidal currents, on the order of 7 km during spring tides and 3 km during neap tides. On a spring/neap time scale, the salt front is displaced on the order of 10 km with a maximum landward intrusion during neap tides. The salt front intrudes further during neap tides because the reduced tidal energy allows the more dense water to migrate landward. The actual maximum landward intrusion occurs after the time of minimal tidal energy (neap tide) with a lag of nearly 3 days and is nearly in quadrature (90 degrees out of phase) with the spring neap cycle. This occurs because the salt flux and displacement of the salt front is a cumulative process as a summation of competing river flow and tidal pumping processes. Maximum landward salt flux occurs at the minimum tidal energy during a neap tide, but continues to occur into the spring transition. Therefore the maximum landward intrusion will occur after the minimum tidal energy.

The position of the ETM varies in a similar manner as salinity on tidal and spring/neap time scales. As discussed previously, during spring tides the ETM tends to occur on the landward side of the salt limit and during neap tides the ETM tends to coincide with or occur on the seaward side of the salt intrusion limit. Maximum sediment concentrations occur a few days after maximum tidal energy (spring tides) because the amount of sediment in suspension is due to the cumulative effects of resuspension and deposition. The location of maximum bed deposition occurs at the seaward limit of the salt intrusion. This is the farthest seaward that the location of maximum bottom stress reaches and this occurs at the times of greatest sediment mobilization.

3.4 ETM Spring / Neap variations (limited sediment supply)

To study the influence of limiting the available sediment supply, a simulation was performed by initializing the bed layer to a uniform layer of erodible sediment 0.10 m in thickness placed along the entire estuary. No other source of sediment was provided and any sediment advected out of the domain was unrecovered. The hydrodynamics are identical to the unlimited supply case (section 3.3), however, due to the limited sediment supply the pool of available bed sediment converged to a location near x = 38 km after several spring neap cycles (Fig. 6). Maximum suspended sediment concentrations occurred during spring tides. As tidal energy reduced towards neap tides, the maximum suspended sediment concentrations decreased by a factor of 3, but the ETM remained stationary near x = 38 km despite the salt front migrating seaward and landward during the spring neap cycle. Figure 7 shows a similar plot as to Fig. 5 displaying the position of the salt intrusion limit and ETM. However in this case the ETM clearly is not migrating with the salt front and is co-located with the bottom deposit. Thus, a pool of erodible sediment is not being translated with the salt front. The ETM location is consistent

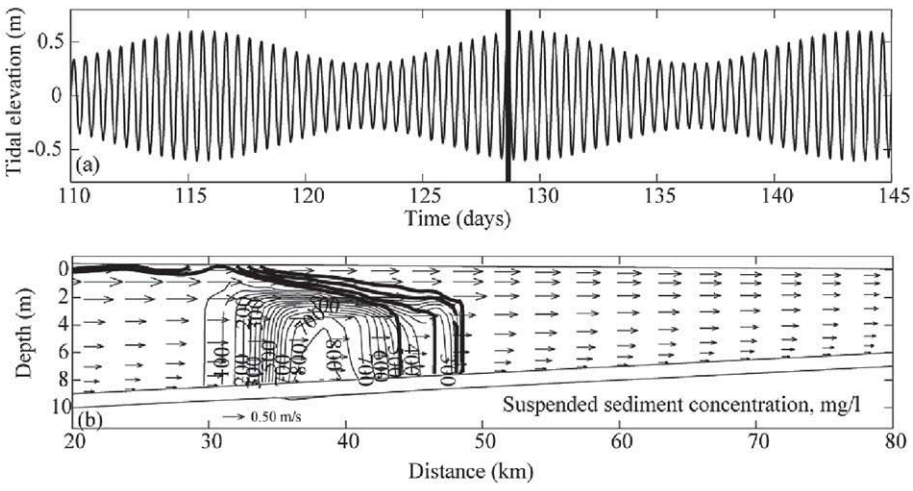

Fig. 6. Location of ETM during spring tides for limited sediment supply. (a) Free surface time series at mouth; (b) Suspended sediment concentration contours (solid lines), tidally averaged isohalines (1, 2, 3, and 4; thick lines), and velocity at maximum flood vectors (arrows). ETM is coincident with maximum bed deposition center, displaced seaward of salt intrusion.

with the region of maximum bed deposit and is controlled by sediment supply. This departs from the unlimited sediment case where the ETM was typically always coincident with the salt front.

3.5 Timing of sediment influx

For a given particle settling velocity and constant fresh water inflow, the ability of an ETM to trap sediment is primarily a function of the salt stratification. Because the stratification varies significantly over the spring neap cycle, the potential of an ETM to trap the sediment from a riverine source will depend on the spring/neap phase. To demonstrate this variability, a pulse of sediment influx with magnitude of 100 mg/l for a period of 1 day was introduced at the landward end and timed to encounter the salt front during a spring tide. A subsequent simulation releases a similar sediment pulse that encountered the salt front during a neap tide. Figure 8 presents the tidally averaged sediment concentrations 28 days after both pulses encounter the salt wedge. The sediment pulse that encountered the salt front during a neap tide retained 40% more sediment mass than the spring tide encounter. This occurs because during spring tides, there

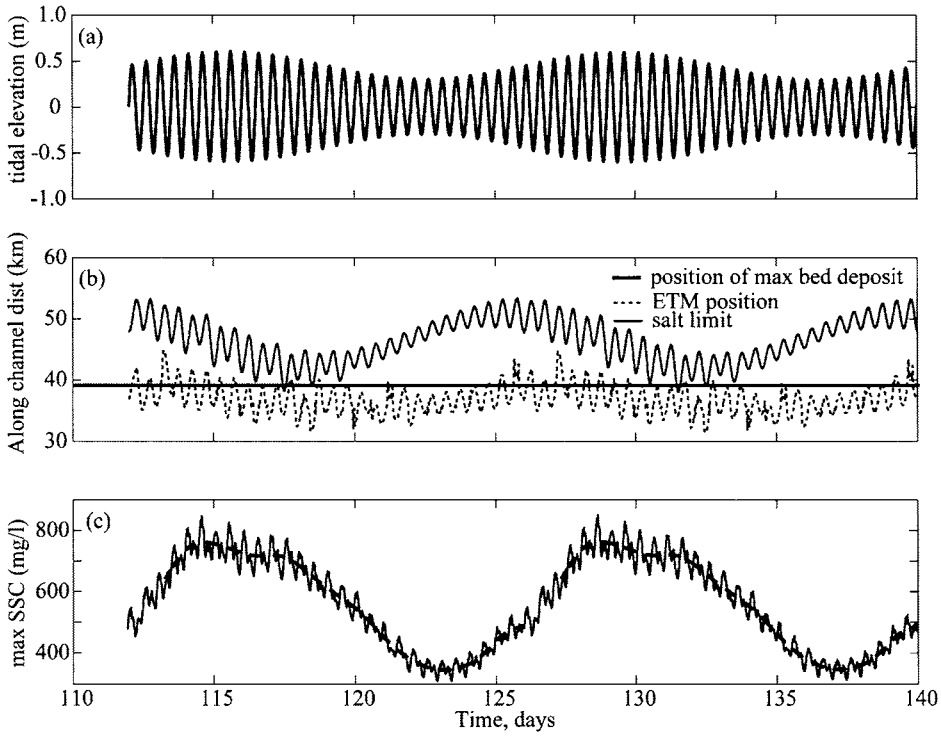

Fig. 7. Location of ETM and salt front for limited sediment supply. (a) tidal elevation at mouth; (b) salt intrusion limit (solid line), ETM position (dashed line), and location of maximum bed deposit (thick solid line); (c) ETM tidal and tidally averaged suspended sediment concentrations. ETM and salt front are not coincident as for unlimited supply (compare to Fig. 5).

is more tidal energy and more sediment was in suspension to be advected over the salt intrusion and out of the estuary.

4. SUMMARY AND CONCLUSIONS

We explored the roles of settling velocity, tidal mixing, erosion potential, and sediment supply on the processes that develop and maintain an ETM. Numerical experiments were performed in an idealized two-dimensional (x-z plane) estuary to vary

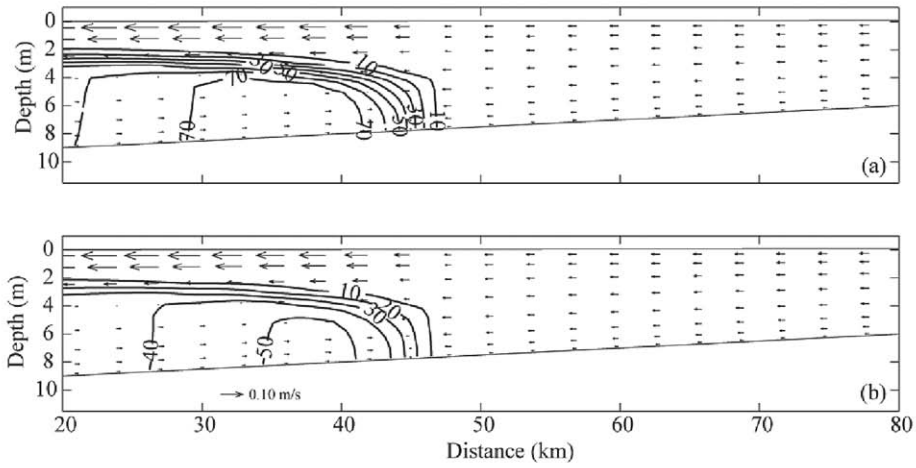

Fig. 8. ETM formation due to timing of sediment influx with spring/neap cycle. Contours are tidally averaged suspended sediment concentrations (solid lines) and residual velocity vectors (arrows) for pulse released during (a) neap tide and (b) spring tide.

the settling velocity (0.01, 0.1, and 0.5 mm/s), tidal amplitude (0.4 m 12 hour tide and 0.3 to 0.6 m 14 day spring neap cycle), sediment supply (bed unlimited or limited), and timing of the sediment pulse relative to the density field structure (well mixed spring tide vs. stratified neap tide).

Results identify that the particle settling velocity is a critical parameter for development of an ETM. Particles with a low settling velocity tend to stay in suspension and are advected seaward and not retained in the ETM. Particles with high settling velocity tend to remain in the upstream section of the river and contribute little to an ETM. Only when particles with a proper settling velocity can produce and maintain a well defined ETM. The proper settling velocity can be estimated by using an estuarine nondimensional parameter $l = (u\,h)/(w_s\,L) \sim 1$(Geyer 1993). When $l \sim 1$ a stable ETM will be formed due to a balance between longitudinal advection and vertical settling. An advection number $A = (h\,u)/(L\,\kappa\,u_*)$ defined by Jay *et al.* (in press) compares the significance of advective transport to vertical turbulent mixing. When $l \sim$ A ETMs will be well formed. For these simulations a particle settling velocity of 0.10 mm/s has the right l and A, and thus, produced the most stable ETM.

The ETM is maintained by processes of tidal velocity asymmetry that can lead to landward transport of suspended sediment. For an unlimited supply of sediment and semi-diurnal tidal forcing, the ETM forms near the limit of salt intrusion and is maintained by the process of resuspension at the toe of the salt wedge, vertical transport of sediment over the stratified bottom boundary layer, settling of sediment into the bottom layer due to suppression of turbulence by stratification, and the tendency for landward migration of sediment in the bottom layer due to tidal velocity asymmetry.

Variation of tidal amplitude to include the spring/neap cycle demonstrates that the ETM co-varies with the limit of salt intrusion if sediment supply is not limited. The ETM tends to the seaward side of the salt limit during neap tides and tends to the landward side of the salt limit during spring tides. This occurs because of the oscillation of the salt front between vertically well mixed and stratified conditions during the spring neap transition. Limiting the sediment supply during spring/neap cycles causes convergence of sediment in the bed at the seaward transgression of the salt wedge. This also identifies the location of the ETM. Under these conditions the ETM does not propagate as an erodible pool of sediment with the salt front.

Finally the timing of a pulse of sediment influx demonstrates the variability of sediment trapped in an ETM due to variations of stratification. More sediment is retained in the ETM when the sediment influx encounters the salt intrusion during a neap tide than during a spring tide. This occurs because the stronger vertical mixing during spring tides tend to bring more sediment in the water column and thus can be advected seaward over the salt intrusion.

ACKNOWLEDGEMENTS

We acknowledge the US Geological Survey's Mendenhall Postdoctoral Research Program for sponsoring Dr. John Warner and the USGS Coastal Community Sediment Transport Program.

REFERENCES

Ariathurai, C.R. and K. Arulanandan. 1978. Erosion rates of cohesive soils. *Journal of Hydraulics Division*, ASCE, 104(2), 279-282.

Burchard, H. and H. Baumert. 1998. The formation of estuarine turbidity maxima due to density effects in the salt wedge. A hydrodynamic process study, *Journal of Physical Oceanography*, 28(2), 309-321.

Colella, P. and P. Woodward. 1984. The piecewise parabolic method (PPM) for gas-dynamical simulations. *Journal of Computational Physics*, 54, 174-201.

Geyer, W. R. 1993. The importance of suppression of turbulence by stratification on the estuarine turbidity maximum. *Estuaries*, 16 (1), 113-125.

Haidvogel, D.B., H.G. Arango, K. Hedstrom, A. Beckmann, P. Malanotte-Rizzoli and A.F. Shchepetkin. 2000. Model Evaluation Experiments in the North Atlantic Basin: Simulations in Nonlinear Terrain-Following Coordinates. *Dynamics of Atmospheres and Oceans*, 32, 239-281.

Jay, D. A., and J.D. Musiak. 1994. Particle trapping in estuarine tidal flows. *Journal of Geophysical Research*, 99 (C10), 20,445 - 20,461.

Jay, D., P. Orton, T. Chisholm, D. Wilson, A. Fain and J. McGinity. In press. Particle trapping in stratified estuaries – definition of parameter space. Submitted to *Continental Shelf Research.*

Kantha, L.H. and C.A. Clayson. 1994. An improved mixed layer model for geophysical applications. *Journal of Geophysical Research*, 99, 25235-25266.

Liu, X.-D., S. Osher and T. Chan. 1994. Weighted essentially non-oscillatory schemes. *Journal of Computational Physics*, 115, 200-212.

Sanford, L.P., S.E. Suttles and J.P. Halka. 2001. Reconsidering the physics of the Chesapeake Bay estuarine turbidity maximum. *Estuaries*, 24 (5), 655-669.

Shchepetkin, A.F. and J.C. McWilliams. 2005. The Regional Ocean Modeling System: A split-explicit, free-surface, topography-following coordinates ocean model. *Ocean Modelling,* 9, 347-404.

Umlauf. L. and H. Burchard. 2003. A generic length-scale equation for geophysical turbulence models. *Journal of Marine Research*, 61, 235-265.

Umlauf, L., H. Burchard and K. Hutter. 2003. Extending the k-ω turbulence model towards oceanic applications. *Ocean Modelling*, 5, 195-218.

Uncles, R.J. and J.A. Stephens. 1993. The freshwater-saltwater interface and its relationship to the turbidity maximum in the Tamar Estuary, United Kingdom. *Estuaries*, 16 (1), 126-141.

Warner, J.C., W.R. Geyer and J.A. Lerczak. 2005a. Numerical modeling of an estuary: a comprehensive skill assessment. *Journal of Geophysical Research, Oceans,* 110, C05001, doi: 10.1029/2004JC002691.

Warner, J.C., C.R. Sherwood, H.G. Arango and R.P. Signell. 2005b. Performance of four turbulence closure models implemented using a generic length scale method. *Ocean Modeling* 8, 81-113.

Wilcox, D.C. 1988. Reassessment of the Scale Determining Equation for Advance Turbulence Models. *American Institute of Aeronautics and Astronautics Journal*, 26, 1299-1310.

Wolanski, E., B. King and D. Galloway. 1995. Dynamics of the turbidity maximum in the Fly River Estuary, Papua New Guinea. *Estuarine, Coastal and Shelf Science*, (40), 321-337.

Estuarine and Coastal Fine Sediments Dynamics
J.P.-Y. Maa, L.P. Sanford and D.H. Schoellhamer (editors)

Fine sediment transport in Ariake Bay, Japan

Nakagawa, Y.

Sedimentary Environments Division, Marine Environment and Engineering Department, Port and Airport Research Institute, 3-1-1 Nagase, Yokosuka 239-0826, Japan

KEY WORDS
Fine sediment transport, Ariake Bay, numerical model, tidal current

The transport of fine sediment, *i.e.*, silt and clay, has a key role in estuarine and coastal environments. In this study, the fine sediment transport processes in Ariake Bay are elucidated through the analysis of field data and a preliminary numerical simulation of the transport processes. The numerical model uses a multilevel hydrodynamic model to reproduce the tidal current field and an advection-diffusion model with bottom boundary conditions for erosion and deposition to estimate transport of fine sediment. Data from the field measurements indicate that the erosion and transport of fine sediments are mainly controlled by tidal current. The sediment transport model reproduces the variation of suspended sediment concentrations during neap-spring tidal cycles reasonably well, and the simulated results also reproduce the observed anti-clockwise residual transport pattern.

1. INTRODUCTION

The understanding of fine sediment transport processes has significant economical and ecological importance. The ability to predict the movement of fine sediments is necessary for port authorities to estimate the dredging cost to sustain the safety ship navigations. Furthermore, from the environmental viewpoints, the understanding of the transport process is crucial in the prediction of the distribution of contaminants in the coastal area because chemical materials are likely absorbed on to clay particles.

The present study site is the Ariake Bay, which is one of the largest estuaries in Japan. The Bay includes huge tidal mud flats along the coast and transport of cohesive sediment has a key role in the ecosystem there. The better understanding of the system is required for the restoration of the environment since the environmental features have been deteriorated including a drastic decrease in fishery resources for decades. The aim of the present study is to examine the fine sediment transport processes in the bay and develop a numerical model for simulating these processes. As a preliminary study, the driving force for simulating sediment transport is limited to tidal current only, and the simulation results are evaluated through the comparison with field measurements.

2. OVERVIEW OF ARIAKE BAY

The Ariake Bay is one of the largest estuaries in Japan on the western coast of Kyushu Island (Fig. 1), with a surface area of 1,700 km^2 and an averaged depth of 20 meters. Tidal effects are prominent all over the estuary and the range at spring tide varies from 4 m at the mouth and increases to more than 6 m towards the upper estuary.

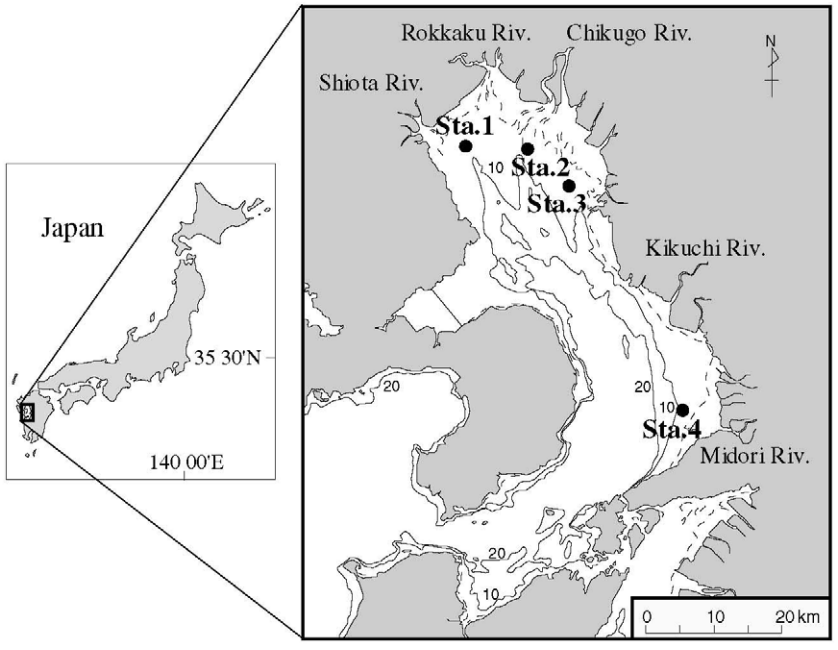

Fig. 1. The Ariake Bay, Japan, showing the locations of monitoring stations (Stas.1-4) with the contours of 10 m and 20 m depth.

Annual mean rate of freshwater supply is around 250 m^3/s flowing through main rivers including Chikugo River into the north-east and Kikuchi and Midori Rivers into east coast of the Bay, where intertidal mudflats are developed. The composition of surficial sediments varies depending on the specific location in the Bay and fine materials (less than 75 μm) are dominant off the north-west and middle-east coast of the bay (Fig. 2).

3. FIELD MEASUREMENTS OF SUSPENDED SEDIMENTS

Field observations of near-bottom Suspended Solid Concentration (SSC) and currents were carried out at four stations, indicated as Sta. 1-Sta. 4 in Fig. 1, from October through November in 2001. A frame was deployed on the bottom at each station with Optical Backscatter Sensors (OBS) for turbidity measurements at 20 cm and 50 cm above the seabed. Another OBS was moored at 100 cm under the water surface. An up-looking Acoustic Doppler Current Profiler (ADCP) was also included in the system for current measurements. The lowest elevation for ADCP measurements was approximately 70 cm above the bed. Conductivity and water temperature were also measured at the same levels as the OBSs. The recording interval of the current profiler was set at 2-

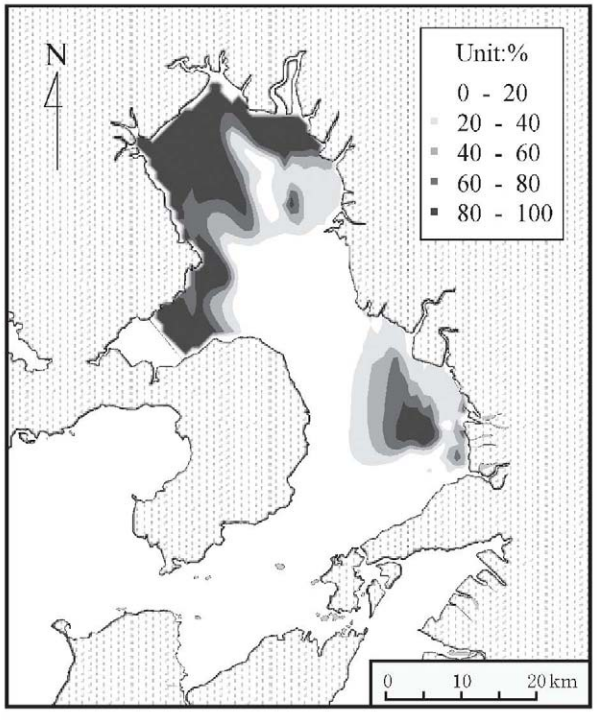

Fig. 2. Mud content distribution in the Ariake Bay.

min burst every half hour with a vertical resolution of 30 cm. All other data were measured at 10-min intervals. For removal of biofouling, all sensors were cleaned up by divers twice a week during the deployment. Turbidity measurements were converted to SSC in mg/l by applying calibrations using sediment samples taken from each site.

Measured tide elevation at Sta. 1 and SSC measurements at 20 cm above the bed at all stations during the period of the deployment are given in Fig. 3. High SSC events caused by the fresh water inflow and wind induced waves are shown temporarily on Oct. 28 and Nov. 6, and the data indicate that the variations of SSC strongly correlate with tidal motion in the neap and spring cycle as clearly shown at Stas. 1 and 2.

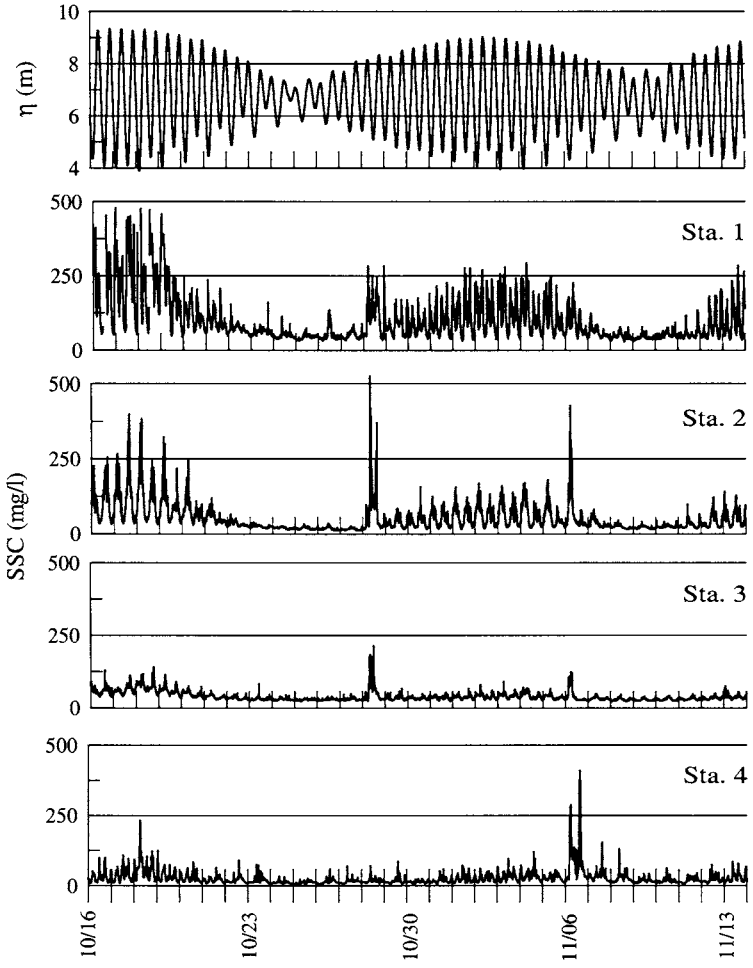

Fig. 3. Water surface level (at Sta. 1) and suspended sediment concentrations at 20 cm above the bottom during the 2001 deployment.

The detailed temporal responses of SSC at these stations, mainly caused by tide current, are different. Figure 4 shows the temporal variation of SSC, tidal level, current speed at 70cm above the bed and salinities at Sta. 1 and Sta. 2 for 48 hours during a spring tide period. The SSC variations near the bed (20 cm and 50 cm above the bed) at Sta. 1 have a strong correlation with the bottom current speed that is dominated by the northward direction component. The SSC near the water surface, however, has peaks during low tides. Local resuspension of bottom sediments by tidal current is considered to be the main source for the high concentration near the bed during the ebb and flood tides. Advection of higher turbidity and lower salinity water from the upper bay or river mouth area is the dominant source of suspended solids variability near the surface at the station. On the other hand, the increase in SSC at the low tide is prominent through the entire water column at Sta. 2. Because bottom sediment consists mainly of coarse sand at Sta. 2, resuspension of the sediment is less important for SSC variation in spite of the strong currents with the maximum speeds of around 40 cm/s at Sta. 2. The dominant factor determining the temporal SSC variation at Sta. 2 is considered to be the advection of high turbidity and low salinity water during the low tide from the mouth of Chikugo River which is the main river flowing into the Bay to the northeast of Sta. 2.

The transport rate of the suspended sediment can be evaluated by computing the sediment flux. In the present study, near bottom sediment flux is defined as the product of the suspended sediment concentration at 50 cm above the bottom and the nearest current speed measured at 70 cm above the bed. For the analysis of Sta. 3, SSC data at 20 cm above the bed is applied as a reference, though it may cause overestimation, because there were many errors in the data at 50 cm. In order to examine long-term variations in the transport rate, tidal variations are removed by low-pass filtering or taking 25 hours running mean (Fig. 5). In the upper region of the bay such as Sta. 1 and Sta. 2, the tendency of higher transport rates during the spring tide period is apparent. The result indicates the suspended solids are transported in an anti-clockwise direction in the upper Bay and it agrees with the fact that a high percentage of mud content was observed in the western part of the area. Although the effect of wind waves is not negligible during high wind conditions, the tidal effect is considered to be the fundamental force on the sediment transport processes in the Bay.

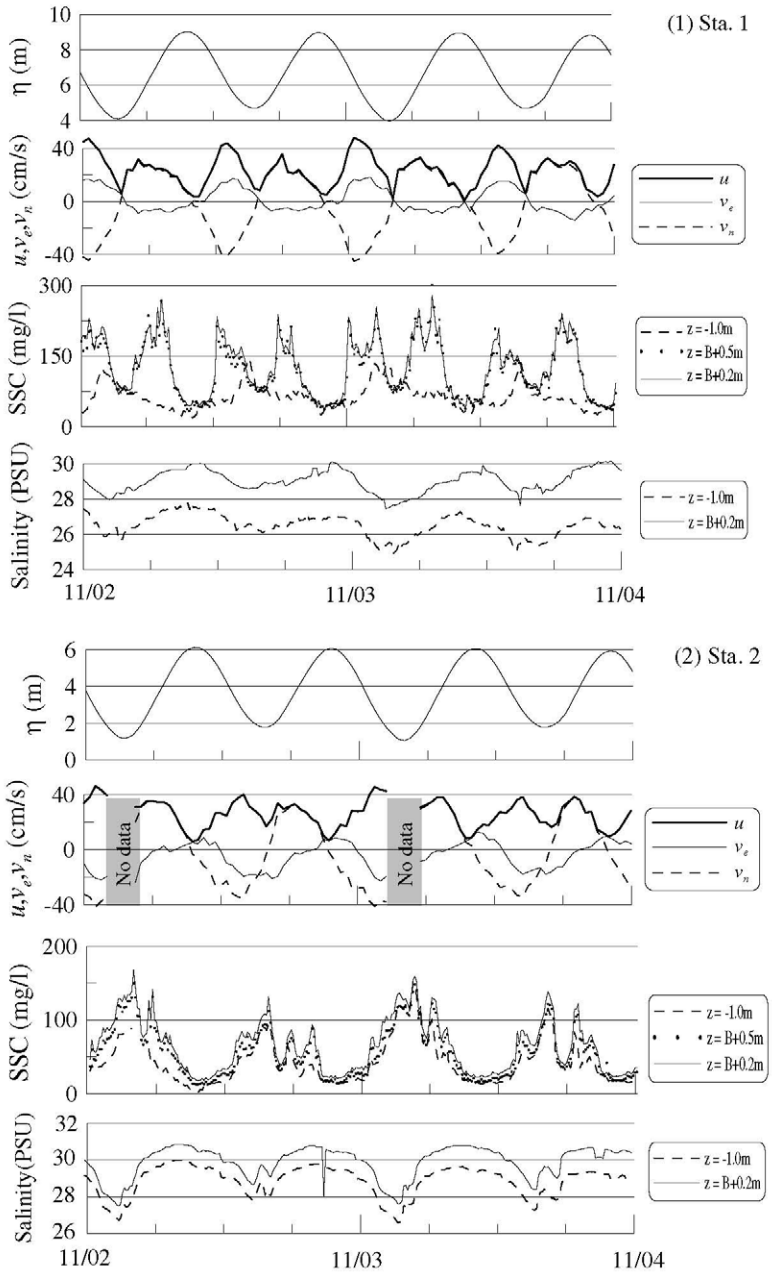

Fig. 4. Time series record of water surface level (η), horizontal current, u, with components in Eastward (v_e), and Northward (v_n) directions, suspended sediment concentration (SSC) and salinity at Sta. 1 and Sta. 2 during the spring tide period in 2001.

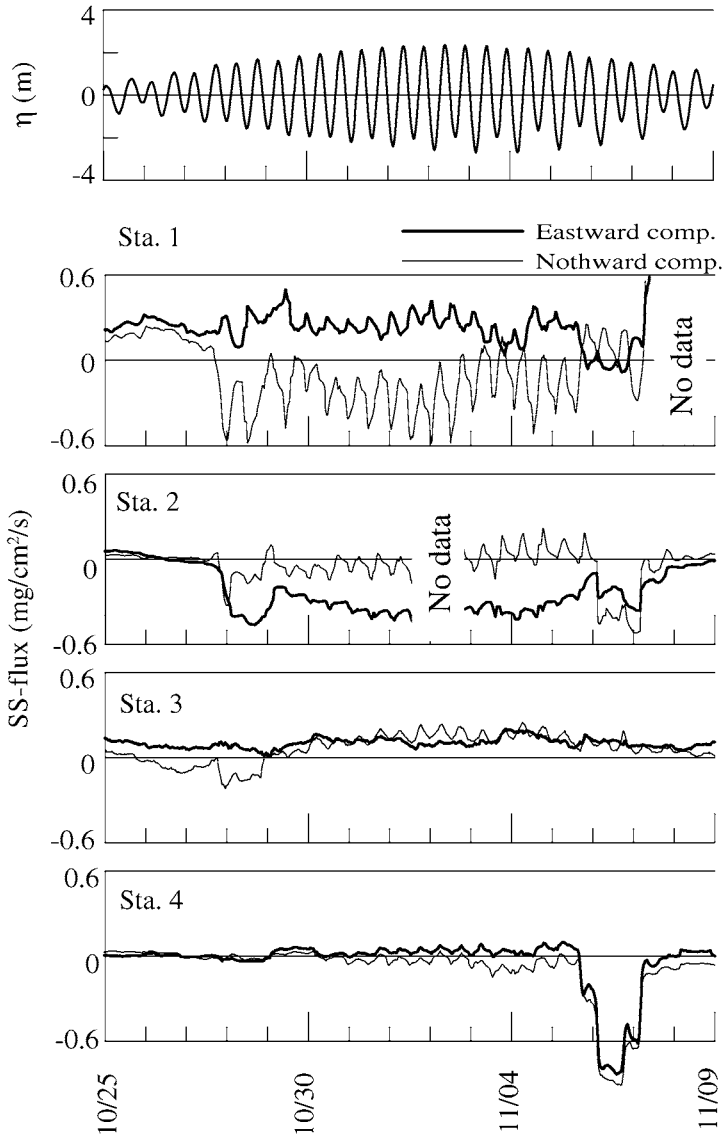

Fig. 5. Measured horizontal components of low-pass filtered (25 hours running averaged) suspended sediment transport rates near the bottom. The rates are estimated with OBS and current data measured at Stas.1-4 during the 2001 survey. Top figure is the water surface level at Sta. 1.

4. FINE SEDIMENT TRANSPORT MODEL

4.1 Model description

The fine sediment transport processes in Ariake Bay were modeled using a 3D numerical model developed originally by the Port and Harbor Research Institute of Japan (Tsuruya *et al.*, 1990; 1996). The model consists of a multilevel hydrodynamic module for tidal flow field and an advection-dispersion module for sediment transport. The governing equations (under the Bousinesq and hydrostatic approximations, Eqs. 1 to 3) are solved with the finite difference scheme in a Cartesian grid system with z-grid in the vertical direction.

$$\left.\begin{aligned} \frac{\partial \zeta}{\partial t} &= w_{3/2} - \frac{\partial M_1}{\partial x} - \frac{\partial N_1}{\partial y} \\ w_{k-1/2} &= w_{k+1/2} - \frac{\partial M_k}{\partial x} - \frac{\partial N_k}{\partial y} \quad (k=2,3,\cdots,K) \end{aligned}\right\} \tag{1}$$

$$\frac{\partial M_k}{\partial t} \cong \frac{\partial}{\partial x}\left(\frac{M_k^2}{H_k}\right) - \frac{\partial}{\partial y}\left(\frac{N_k M_k}{H_k}\right) - \left(wM\big|_{k-1/2} - wM\big|_{k+1/2}\right)/H_k + fN_k$$
$$- gH_k\left(\frac{\partial \zeta}{\partial x} + \frac{1}{\rho_k}\sum_{i=1}^{k}(H_i\frac{\partial \rho_k}{\partial x}) - \frac{1}{2}\frac{H_k}{\rho_k}\frac{\partial \rho_k}{\partial x}\right) + \left(\tau_{xz}\right)_{k-1/2} - \left(\tau_{xz}\right)_{k+1/2} + A_x\frac{\partial^2 M_k}{\partial x^2} + A_y\frac{\partial^2 M_k}{\partial y^2} \tag{2}$$

$$\frac{\partial N_k}{\partial t} \cong \frac{\partial}{\partial x}\left(\frac{M_k N_k}{H_k}\right) - \frac{\partial}{\partial y}\left(\frac{N_k^2}{H_k}\right) - \left(wN\big|_{k-1/2} - wN\big|_{k+1/2}\right)/H_k - fM_k$$
$$- gH_k\left(\frac{\partial \zeta}{\partial y} + \frac{1}{\rho_k}\sum_{i=1}^{k}(H_i\frac{\partial \rho_k}{\partial y}) - \frac{1}{2}\frac{H_k}{\rho_k}\frac{\partial \rho_k}{\partial y}\right) + \left(\tau_{yz}\right)_{k-1/2} - \left(\tau_{yz}\right)_{k+1/2} + A_x\frac{\partial^2 N_k}{\partial x^2} + A_y\frac{\partial^2 N_k}{\partial y^2} \tag{3}$$

where ζ is the water surface elevation, M_k and N_k are the horizontal flow rate in the x- and y-direction of the k-th layer, respectively, and $w_{k-1/2}$ is the vertical velocity between the k-th and (k-1)-th layers. In the momentum equations (Eqs. 2 and 3), g is the gravitational acceleration, ρ is the water density, A_x and A_y are the horizontal eddy

viscosity coefficients and τ_{xz} and τ_{yz} are the x- and y-direction components of the shear stress between the layers.

The sediment transport model is expressed as the mass conservation equation of suspended sediment concentration,

$$\frac{\partial C_k H_k}{\partial t}+\frac{\partial M_k C_k}{\partial x}+\frac{\partial N_k C_k}{\partial y}+(w-w_s)C|_{k-1/2}-(w-w_s)C|_{k+1/2} \\ -\frac{\partial}{\partial x}\left(K_x H_k \frac{\partial C_k}{\partial x}\right)-\frac{\partial}{\partial y}\left(K_y H_k \frac{\partial C_k}{\partial y}\right)-\left(K_z \frac{\partial C}{\partial z}\right)_{k-1/2}+\left(K_z \frac{\partial C}{\partial z}\right)_{k+1/2} \cong 0 \tag{4}$$

where C_k represents suspended solid concentration, w_s is the settling velocity of the suspended particles, and K_x, K_y and K_z are the eddy diffusion coefficients in the x-, y- and z-directions respectively.

For the eddy viscosity and diffusivity in the horizontal directions, the Smagorinsky model is applied as,

$$A_{x,y}=K_{x,y}=C_{dif}\Delta x\Delta y\left[\left(\frac{\partial u}{\partial x}\right)^2+\frac{1}{2}\left(\frac{\partial v}{\partial x}+\frac{\partial u}{\partial y}\right)^2+\left(\frac{\partial v}{\partial y}\right)^2\right]^{0.5} \tag{5}$$

where Δx and Δy are the horizontal grid size. Although the non-dimensional coefficient C_{dif} is 0.1 – 0.2 typically in the coastal seas (Ezer and Mellor, 2000), in the present study it is set as 0.4 for computational robustness. The vertical eddy viscosity and diffusivity depend on the Richardson number, Ri, as suggested by Munk and Anderson (1948),

$$A_z=A_{z0}(1+10Ri)^{0.5} \tag{6}$$

$$K_z=K_{z0}(1+3.33Ri)^{-1.5} \tag{7}$$

where

$$Ri=-g\,\partial\rho/\partial z/\rho(\partial U/\partial z)^2 \tag{8}$$

and the coefficients, A_{z0} and K_{z0}, in the neutral condition are set as 10 cm^2/s here.

For the erosion and deposition of cohesive sediment at the bottom boundary, the classical formulae of Partheniades and Krone (*e.g.*, van Leussen and Dronkers, 1988) are applied. The erosion bottom boundary condition reads

$$\left.\begin{aligned} E &= M\left(\frac{\tau_b}{\tau_e}-1\right) \qquad (\tau_b \geq \tau_e) \\ E &= 0 \qquad (\tau_b < \tau_e) \end{aligned}\right\} \tag{9}$$

where τ_b means the bottom shear stress. The erosion rate coefficient, M, and the critical shear stress for erosion, τ_e, in Eq. 9 are modified from constant values based on the concept of the dependency of these parameters on the relative proportions by weight of sand/mud on the bed as described in Chesher and Ockenden (1997). For the modification of the erosion rate, it is defined as,

$$M = M_0 \frac{M_c}{100} \tag{10}$$

where M_0 is the erosion rate constant for a pure mud bed, assumed to be 0.0001kg/cm^2/min. This value was determined during model calibration. The parameter, M_c, is the mud content by weight of the bed (in %) and the value is chosen considering the observed mud content distribution in Fig. 2. The distribution is assumed not to vary in time through the computation period. The critical shear stress for erosion, τ_e, is modified with the relationship between the mud content and the erosion stress as shown in Fig. 6. The value of τ_e linearly increases from the pure mud bed value, τ_{emud}, with decreasing mud content and it takes a peak value, τ_{emax}, at a mud deposition content of 20%. The values of the parameters are assumed here to be 0.1 Pa for τ_{emud}, determined from time series data of SSC and stress estimates at Sta.1, and 0.26 Pa for τ_{emax}, determined by model calibration, respectively. The erosion stress for purely sand bed without mud fraction, τ_{esand}, in Fig. 6 is defined as a function of the threshold velocity and friction factor over sand bed according to Chesher and Ockenden (1997). In the present study, however, τ_{esand} is the same value as τ_{emax} because only the transport of mud fraction is investigated here and it is considered that the contribution from the bed with the less mud content should not be an important source of suspended sediment.

The deposition process is expressed as Eq. 11, where w_s is the settling velocity of the suspended sediment, τ_d is the critical shear stress for deposition and C_0 is the sus-

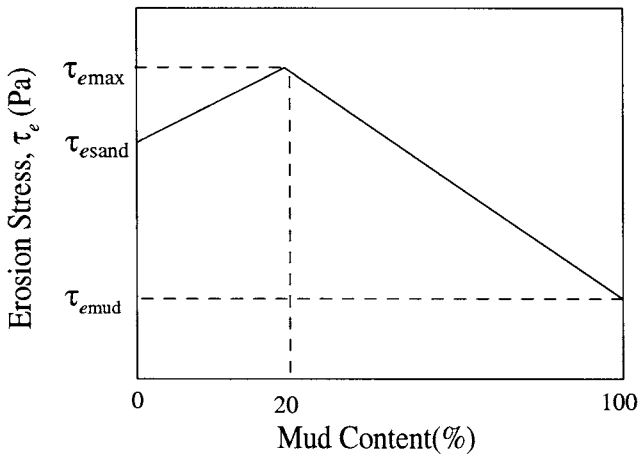

Fig. 6. Relationship between the critical shear stress for erosion and mud content (after Chesher and Ockended, 1997).

pended sediment concentration above the bottom. The settling velocity may depends on salinity and concentration (*e.g.*, Mehta, 1988) but it is, in the present study, simply assumed to be a function of the suspended sediment concentration in the following form.

$$\left.\begin{aligned} D_f &= w_s\left(1-\frac{\tau_b}{\tau_d}\right)C_0 \quad (\tau_b \le \tau_d) \\ D_f &= 0 \qquad\qquad\qquad (\tau_b > \tau_d) \end{aligned}\right\} \tag{11}$$

$$w_s = 0.0006C \tag{12}$$

where the units for w_s are in m/s and for C in g/l respectively. The constant in Eq. 12 was obtained from laboratory experiments using mud from the bay (Tsuruya *et al.*, 1990). The critical shear stress for deposition, τ_d, was set equal to the critical stress for erosion ($\tau_d = \tau_e$) in the present study. For the value of C_0, computed suspended sediment concentration of the lowest layer on the bottom boundary are applied at each time step in the numerical simulation.

4.2 Results of numerical simulations

The target area of the simulation is shown in Fig. 2 with a spatial resolution of 900 m in the horizontal direction and about 3 m in the vertical direction. The maximum number of vertical layers is 10. In order to reproduce the sediment transport pattern for a long-term simulation, the effect of floods during the rainy season on tidal currents and sediment supply should be incorporated as a boundary condition. In Ariake Bay, however, the duration of flood events is short and most of the dispersion of sediments discharged from the river is due to tidal currents as demonstrated by the field data in the previous section. For this reason, inputs of suspended sediments during flood events are not considered in this preliminary model.

The propagation of tidal waves is reproduced by specifying the water surface levels at the open boundary on the southwest border of the computational domain with six principal tidal components. Freshwater discharge from the rivers is input at a constant rate at the dry season mean value, without specifically accounting for flood events, consistent with the treatment of riverine suspended sediment inputs described above

Figure 7 shows simulation results of the water surface elevations and the near bed SSCs at the four stations compared with the field data. The tidal features of hydrodynamics at all stations agree reasonably well in terms of both semi-diurnal and spring/neap variations. Due to the accurate representations of tidal-scale hydrodynamics, the fluctuations of the SSC are also reasonably reproduced in the space and neap/spring tidal time scale by the model. Since the objective of the simulation was to focus on the effects of tidal currents on sediment transport processes, wind stress and increased bottom shear stress due to waves were excluded. Therefore the observed disturbances of the sediments by wind waves that occurred on Oct. 28 and Nov.6 do not appear in the simulation results. The figure also shows slight discrepancies between the observed concentration and those predicted by the model at Sta. 1 and Sta. 4 with better agreement at Stas. 2 and 3. The fluctuations of SSC near the bed at Sta. 1 and Sta. 4 are considered to be dominated by the local resuspension process of the bottom sediments and the dominant factor at Sta. 2 and 3 should be advection of turbid water by the tidal motion as mentioned in the previous section. One of the reasons for the deterioration of reproducibility of SSC fluctuations at Sta. 1 and Sta. 4 is likely inaccuracies in the description of the erosion process at the bottom. Equation 9 is for a fully consolidated mud (Parchure and Mehta, 1985). During the high SSC events near the bed at Stas. 1 and 4 in spring tide periods, however, the sediments on the bed surface, which could be the main source of SSC, may not be a fully consolidated bed because of frequent resuspension/deposition caused by the strong tidal current. Therefore, the modification or replacement of the

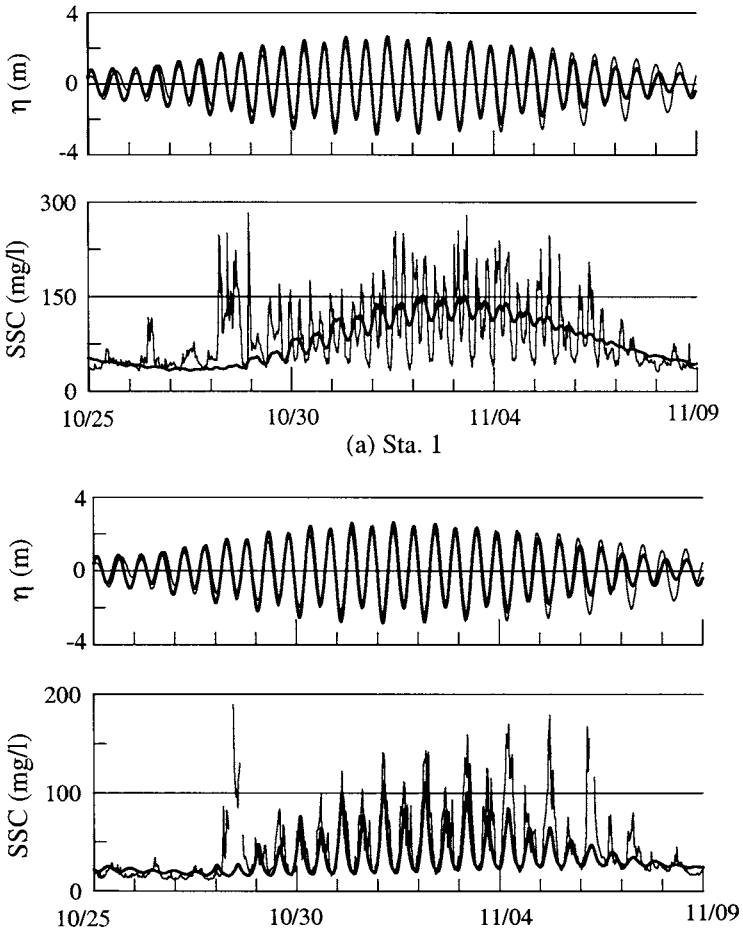

Fig. 7. Comparison of model results (thick lines) and measured data (thin lines) for the water surface level and suspended zsediment concentration near the bed. (Figure continues on next page.)

erosion model given in Eq. 9 might be required to attain the higher accuracy of the SSC variation at these sites.

The low pass filtered (25 hours running mean) sediment flux rate near the bottom was estimated with the simulated SSC and currents (Fig. 8). Although there are some

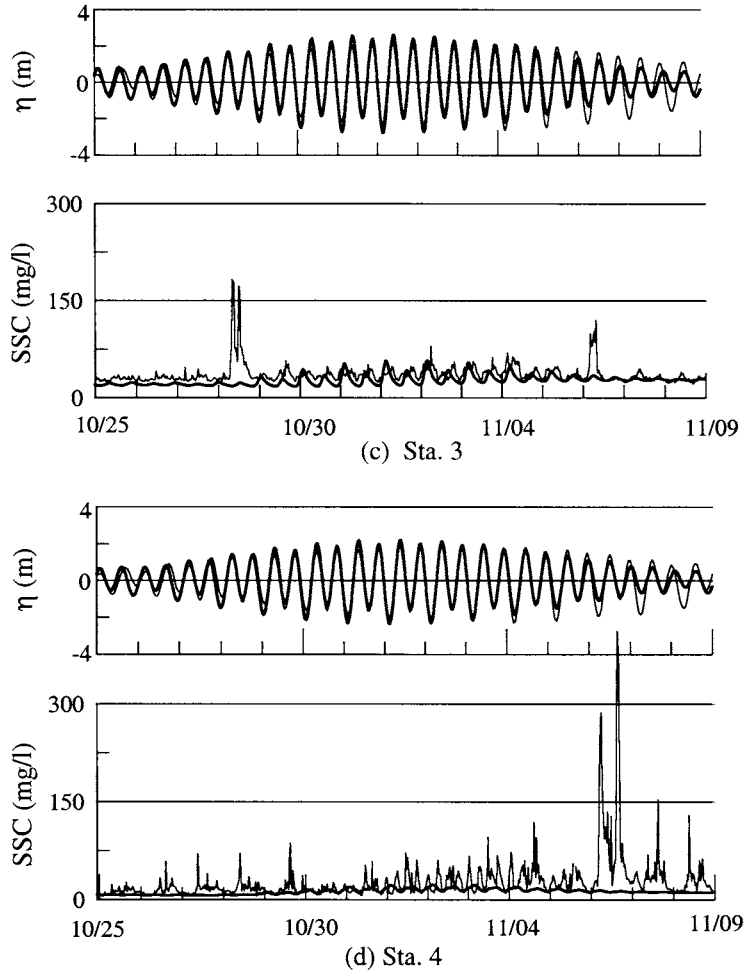

Fig. 7. (Continued)

discrepancies between the observed and simulated fluxes, the simulation result reasonably demonstrates the observed predominant pattern of residual transport (Fig. 5) during spring tides with an anti-clockwise direction in the upper bay. This model results indicate westward transport at Sta. 2 and southward transport at Sta. 1. The differences between the model and observed data may be due to inaccuracies in the predicted current field as well SSC fluctuations. The negligence of wind effect on the current field

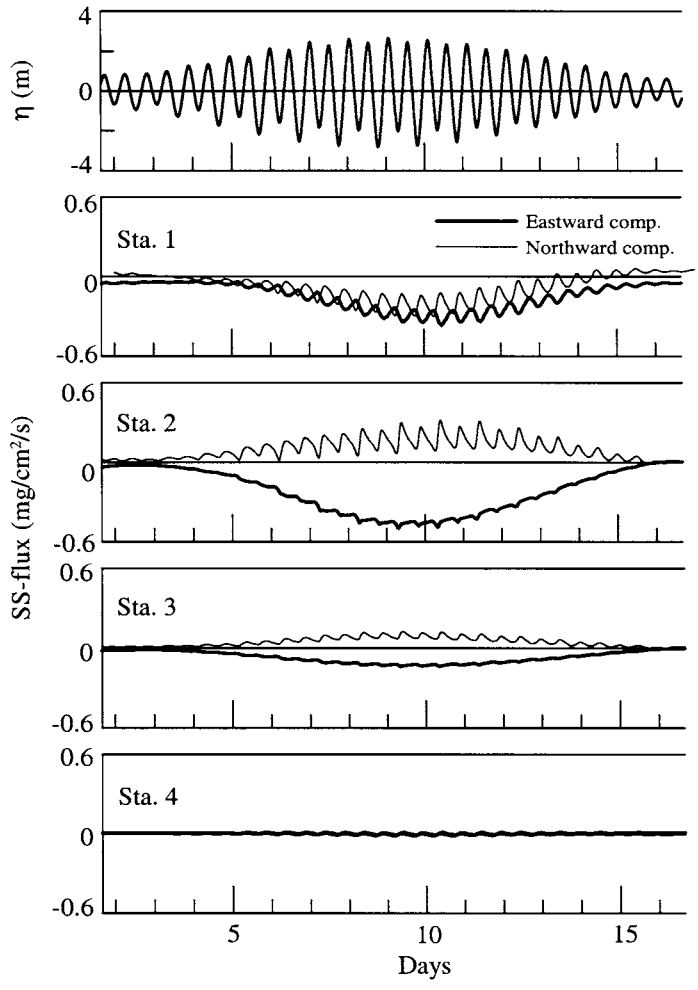

Fig. 8. Simulation results of horizontal components of low-pass filtered (25hour running averaged) sediment transport rates near the bottom with computed water level for Sta. 1.

and the relatively coarse horizontal model grid with 900 m may lead to errors in the current field simulation, especially for shallow area with complicated topography.

The model can also be used as a tool from which short-term erosion/accretion patterns (Fig. 9) are generated. Since the effects of sediment discharge through the rivers and transport of coarse or sandy materials are neglected in the present study, the result

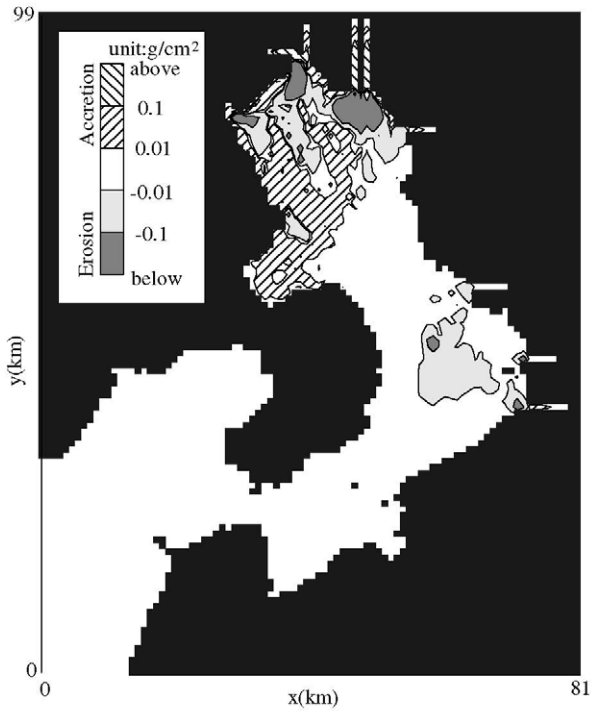

Fig. 9. Simulated erosion/ accretion pattern for one neap-spring tidal cycle (15 days).

indicates the redistribution of fine sediment in the bay by the tidal current. Figure 9 shows the tendency for higher erosion rates at the river mouth in the top of the bay and accretion on the western shore of the upper bay, which may be caused by the westward residual sediment transport process reproduced by the model as mentioned above. According to the field data of mud distribution in the bay (Fig. 2), the sediments with higher mud content dominate more in the west part in the upper bay. The westward transport, therefore, of the sediment supplied mainly through Chikugo River, which is the predominant one for freshwater and sediment discharge in the bay, is considered as one of the sources of the fine sediment in the western part, besides the discharged sediment directly from the adjacent rivers, such as Rokkaku and Shiota rivers. There is, however, not enough information on the temporal change of mud distribution in the whole bay area at the moment and such monitoring data should be collected in the future to further verify these results, including erosion in the mid-east coastal zone.

5. CONCLUSIONS

A fine sediment transport model has been developed during a preliminary study and used to simulate measured suspended sediment concentrations and residual transport rates in Ariake Bay. Temporal (in neap-spring tide scale) and spatial variations in suspended sediment concentrations are reproduced reasonably well, largely due to the accurate representation of the tidal-scale hydrodynamics and consideration of mud content spatial distribution for the estimation of erosion rate. The model demonstrates reasonable agreement also in the tidally averaged sediment transport rates in the upper bay.

Several requirements for model improvement have been identified as future work. In some locations, fluctuations of near bottom SSC due to local tidal resuspension have not been well reproduced by the present model. This probably indicates that improvements are needed in the erosion formulation at the bottom boundary. Future studies will also be concerned with the incorporation of wind wave effects in the model, which cause episodic resuspension events as demonstrated in the field data. Although the fresh water supply during the observation period in the present study is low, the effect of the input of the suspended sediment through the river should be included in the model for a long-term prediction of change in the sediment transport in the estuary.

ACKNOWLEDGMENTS

This study was supported by the Port and Harbour Bureau of the Ministry of Land, Infrastructure and Transport (MLIT) and the Kyushu Regional Development Bureau of MLIT, and carried out as a part in the Technical Committee for the Ariake Bay Restoration Project. The author would like to thank members of the committee for their valuable comments. The author would also like to express his sincere thanks to the reviewers for their constructive comments.

REFERENCES

Chesher, T.J. and M. Ockenden. 1997. Numerical modelling of mud and sand mixtures. In: *Cohesive Sediments*. Burt, N., R. Parker and J. Watts (Eds.), John Wiley & Sons, West Sussex, 395-402.

Ezer, T. and G.L. Mellor. 2000. Sensitivity studies with the North Atlantic sigma coordinate Princeton Ocean Model. *Dynamics of Atmospheres and Oceans*, 32, 185-208.

Mehta , A.J. 1988. Laboratory studies on cohesive sediment deposition and erosion. In: *Physical Processes in Estuaries*. Dronkers, J. and W. van Leussen (Eds.), Springer-Verlag, New York, 427-445.

Munk, W. and E. Anderson. 1948. A note on the theory of the thermocline. *Journal of Marine Research*, 26, 24-33.

Parchure, T. M. and A. J. Mehta. 1985. Erosion of soft cohesive sediment deposits. *Journal of Hydraulic Engineering*, 111(10), 29-47.

Tsuruya, H., K. Murakami and I. Irie. 1990. *Mathematical modeling of mud transport in ports with a multi-layered model –Application to Kumamoto Port-*, Technical report of Port and Harbour Research Institute, Port and Harbour Research Institute, Yokosuka, 29(1), 3-51.

Tsuruya, H., K.P.P. Pathirana and Y. Nakagawa. 1996. *The influence of interfacial shear stress on vertical velocity distribution in multi-level model.* Technical note of the Port and Harbour Research Institute No. 820, Port and Harbour Research Institute, Yokosuka, 32p.

van Leussen, W. and J. Dronkers. 1988. Physical processes in estuaries: An introduction. In: *Physical Processes in Estuaries*. Dronkers, J. and W. van Leussen (Eds.), Springer-Verlag, New York, 1-18.

Whitehouse, R., R. Soulsby, W. Roberts and H. Mitchener. 2000. *Dynamics of Estuarine Muds*. Thomas Telford Publishing, London, 210p.

Estuarine and Coastal Fine Sediments Dynamics
J.P.-Y. Maa, L.P. Sanford and D.H. Schoellhamer (editors)

Quadratic profile approach for profile evolutions on intertidal mudflat

Yamada, F.[a], N. Kobayashi[b], T. Kakinoki[c] and M. Nakamichi[a]

[a]Department of Civil & Environmental Engineering, Kumamoto University, 2-39-1, Kurokami, Kumamoto, 860-8555, Japan.
[b]Center for Applied Coastal Research, University of Delaware, Newark, DE, 19716, U.S.A.
[c]Department of Civil Engineering, Kobe City College of Technology, 8-3 Gakuen-nishi, Kobe, 651-2194, Japan.

KEY WORDS
Mudflat profile change, average tide level, seasonal variation, quadratic profile

A parameterized mudflat profile with no nearshore bar is proposed using a quadratic polynomial equation fitted to the measured monthly bed levels on the meso-tidal mudflats in the vicinity of a river mouth. Three profile-fitted-parameters of profile curvature, mean slope, and vertical displacement are used to examine the correlations between the profile temporal variations and time-varying driving forces. The vertical displacement and mean slope parameters are highly correlated with the seasonal tide level variation of approximately 40 cm. The profile curvature parameter varied semiannually and might be correlated with the average tide level, averaged spring-neap tidal range, and rainfall.

1. INTRODUCTION

Long-term sea level rise is likely to occur due to global warming. Eustatic (global) sea level rise has been estimated at approximately 17 cm in the last century (ASCE Task Committee, 1992). The future rate of global sea level rise will be larger than the past

rate due to the greenhouse effect. The Intergovernmental Panel on Climate Change (2001) projects that global mean sea level may rise up to 88 cm between the years 1990 and 2100. Mudflats with very gentle slopes are very sensitive to changes in sea level. Sea level rise may cause considerable land loss and flooding risk. Environmental protection and management in estuaries require the understanding of mudflat response to changing sea level, oceanography, climate, and anthropogenic pressure (*e.g.*, Dyer, 1998).

In general, mudflats are composed of a mixture of sediment with its particle diameter d in the range from 0.075 to 2 mm. As the mud content (*i.e.*, $d < 0.075$ mm) in the sediment increases, the sediment becomes more cohesive. The morphology of mudflats in estuaries depends on a number of physical processes such as tidal range, sea level (average tide level), tidal currents, wind waves, river discharge, and infrequent storm action. Hayes (1975) emphasized the importance of tidal range for the morphology of sediment deposits and classified estuaries using mean spring tidal range. However, the morphology of mud deposits is poorly understood in comparison to that of sand deposits. This arises partly from the great complexity of the behavior of cohesive sediment, being influenced by chemical and biological as well as physical processes (Kirby, 2000). Shi and Chen (1996) and Dyer (1998) discussed a number of processes that might control the erodability of the mud and the development of the profile shape. Very little work is currently available on the relationships between mudflat profiles and physical processes in the estuaries (*e.g.*, Bassoullet *et al.*, 2000; Pritchard and Hogg, 2003)

Many mudflats appear to be accreting at the same rate as sea level rise, thereby suggesting that an equilibrium condition exists between the dynamic forcing and the sedimentary response (Christie *et al.*, 2001). A concept of equilibrium beach profiles, which is proposed for sandy beach cross-shore profiles, *e.g.*, Bruun (1962), might hence be applicable in evaluating the mudflat profiles. Assuming wave action is the most predominant factor for mudflat profile changes, Friedrichs and Aubrey (1996), Lee and Mehta (1997), and Kirby (2000) extended the concept of equilibrium beach profiles to the mudshore profiles. However, the applicability of the concept of equilibrium beach profiles to the intertidal mudflat profiles is not clear in the presence of various time scales.

The mudflat profile is characterized conventionally using both its curvature and mean bed slope (*e.g.*, Kirby, 1992; 2000; Dyer *et al.*, 2000). Friedrichs and Aubrey (1996) and Kirby (1992; 2000) proposed that the curvature of the mudflat profile could be used to classify the relative contributions caused by wind waves and tidal motions to the total sediment transport. Convex-upward profiles were correlated with large tide

ranges, long-term accretion and/or low wave activity. Concave-upward profiles were correlated with small tide ranges, long-term erosion and/or high wave activity. Dyer (1998) and Dyer *et al.* (2000) proposed a statistical scheme for typology and classification of intertidal mudflats using tidal range, wave action, and mean bed slope as the most important variables. Robert and Whitehouse (2001), Pritchard *et al.* (2002), and Pritchard and Hogg (2003) predicted the profile evolution of intertidal mudflats caused by cross-shore tidal currents but did not compare their numerical models with field data. Presently, no model exists for predicting the profile evolutions of intertidal mudflats under the time-varying meteorological forces (*e.g.*, tides, waves, and river discharges).

The aim of the present work is to evaluate the dominant forces of profile evolutions on the intertidal mudflat. First step is gathering the field observation data and describing the temporal and spatial patterns of profile evolutions on the intertidal mudflat. Empirical Orthogonal eigenFunction (EOF) methods, which do not assume a specific profile form, have been used widely for the analysis of the temporal and spatial patterns of sandy beach morphology (Winant *et al.*, 1975; Dean and Dalrymple, 2002). However, eigenfunctions for the cross-shore profile are not universal among various beaches. In this study, a parameterized mudflat profile with no nearshore bar is proposed using a quadratic polynomial equation for the cross-shore mudflat profile based on the two-year field observations. This parameterization allows the separation of the temporal and spatial variations of mudflat profiles under time-varying meteorological forces. The three profile parameters for the profile curvature, mean slope, and vertical displacement of the fitted profile are used to examine the time scales and lags between the profile temporal variations and the time-varying physical processes.

2. FIELD OBSERVATIONS

2.1. Field site

The study site is located at the mouth of the Shirakawa River, which is situated on the center of the eastern coast of Ariake Bay (Fig. 1). Ariake Bay is a closed inner bay with a length of 97 km along the central axis. The average bay width is 20 km, and the total bay area is about 1,700 km^2. The average water depth is approximately 20 m, and tidal flats are common along the bay shoreline. This bay is famous for the highest tidal range in Japan with a maximum spring tidal range of almost 6 m in the northern corner.

This field site was selected partly because of the available oceanographic data such as the tide level, significant wave height and period, and wind velocity are available from the Kumamoto Port (Fig. 1). The simultaneous measurements of tides and wind

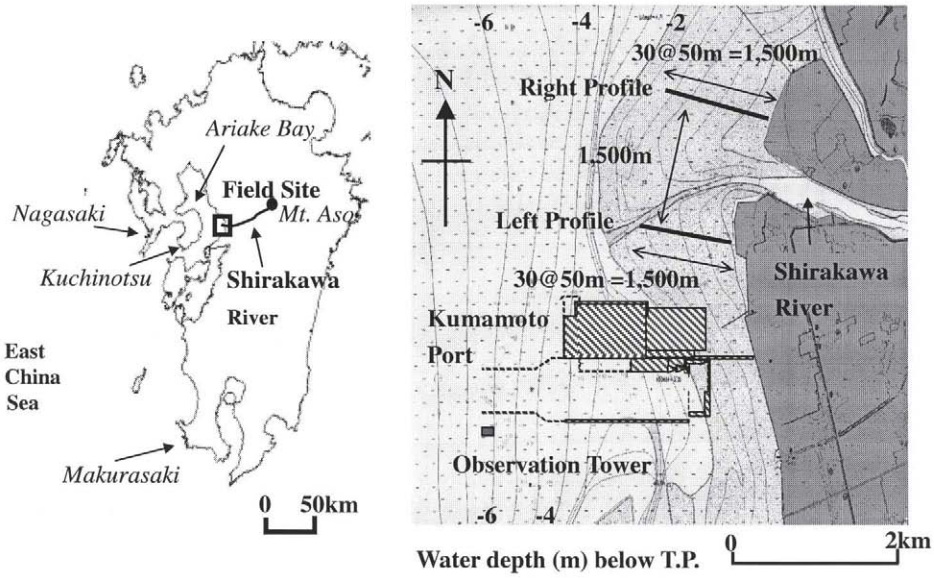

Fig. 1. Field Site at mouth of Shirakawa River.

waves in Ariake Bay are limited to this observation tower. The observation tower was built at a site with 6.45 m water depth below the Tokyo Peil (T.P.). The T.P. datum is the standard ground elevation in Japan based on the Tokyo Bay mean sea level and is used here as the datum of the water and land levels. The measured current at this site was landward during flood tides and seaward during ebb tide as may be expected from the large intertidal zone. The maximum depth-averaged tidal current velocity was in the range 30 to 40 cm/s (Yamada & Kobayashi, 2003). No dredging has been performed at this site.

Figure 1 also indicates the two cross-shore profile lines located on the left and right banks at the Shirakawa River mouth. In order to maintain fixed survey lines, ground elevations were measured using an Electric Distance Meter at fixed measuring points. A 2-m long wood stake was driven 1.7m below the mudflat surface at each point in October 2000. Each line consisted of 30 fixed measuring points spaced at an interval of 50m, and the total length was 1,500 m. Twenty profiles were measured from February 2000 to February 2003 during low water on days of spring tides. Details of bed level measuring were described in Yamada & Kobayashi (2003; 2004).

Tidal information is available from the Kumamoto Port Construction Bureau of the Ministry of Land, Infrastructure and Transport. The tide is semidiurnal, and the mean

spring tidal range is 3.86 m (Tsuruya *et al.*, 1990) and meso-tidal. The average tide level observed from 2000 to 2002 was 0.14 m above T.P. (Fig. 2). The offshore distance is measured from the vertical seawall located at the landward side. The bottom slope is approximately 1/800 above the mean monthly-lowest water level and increases to approximately 1/350 offshore. The intertidal flat is approximately 2.0 km wide. The survey was not conducted under water but extended close to the mean monthly-lowest water level.

2.2. Sediment characteristics

Six core samples were collected at the offshore distances of 100, 500, and 1200 m (Fig. 2) along the left and right cross-shore profile lines in September 2001. The core samples showed a fairly uniform characteristics vertically. The measured parameters for each 10-cm thick layer from the bed surface included the sediment water content, specific gravity, and grain size distribution. The sediments were poorly sorted and the median diameter (d50) along the left profile increased slightly downward but was in the narrow range of 0.10 to 0.15 mm. The median diameter along the right profile was in the range 0.14 to 0.18 mm. The spatial variations of d50 were similar for the two

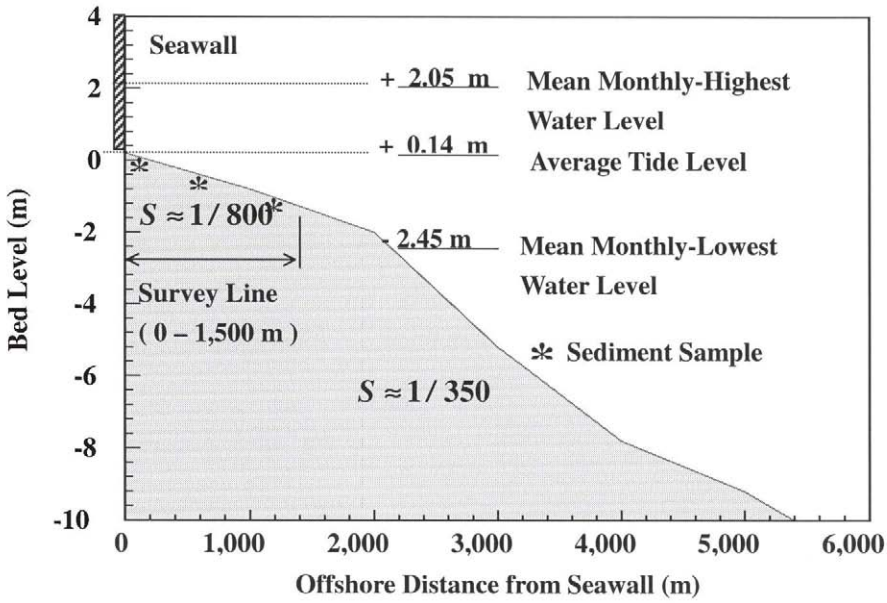

Fig. 2. Schematic cross-shore profile at the survey site together with the mean monthly-highest and lowest water levels based on the measurement at Kumamoto Port from 1975 to 1994.

profiles. Mud is defined here as the sediments with size smaller than 0.075 mm (*i.e.*, silt and clay). The averaged mud content is in the range between 13.8 to 30.1 % for the left profile but in the range between 9.4 to 17.7 % for the right profile. For both profiles, the mud content was smaller in the middle slightly below the average tide level. On the other hand, the water content and specific gravity were fairly constant except that the water content was larger near the bed surface. (Yamada & Kobayashi, 2003; 2004)

2.3. Mudflat variations

Only the bed level survey points located between 100 to 1,050 m from the seawall could be always measured (Fig. 3) because the bed surface within 100 m from the seawall and farther offshore was too soft sometimes. The fluctuations of the measured bed level increased gradually with offshore distance and then more quickly at about 800 m. The standard deviation about the average profile was in the range of 2.0 to 8.0 cm. The shape of the measured profiles was convex-upward, unlike that of sandy beaches, which usually show concave-upward. The average bottom slope for the left profiles was 1/900, slightly milder than that of the average slope of the right profiles which was 1/700. The right profiles were less convex upward than the left profiles. Both accretion and erosion along both profiles were normally larger offshore than nearshore. The profile change was not uniform along the profiles but generally positive or negative along the entire profile. (Yamada & Kobayashi, 2003; 2004)

2.4. Available oceanographic and meteorological data

The tide level (Fig. 4) was measured at the observation tower of Kumamoto Port. The measured tide level varied within -3.0 to 3.0 m. The average tide level was 0.14 m above T.P. The 56-day averaged tide level (Fig. 4b) varied annually with its peak during August to October.

The averaged tidal level is not sensitive to the duration of averaging (Fig. 4b). The difference between the maximum and minimum values of the 56-day averaged tide level at this site was approximately 40 cm. Similar seasonal variations of the tide level were observed at Kuchinotsu at the entrance of Ariake Bay, Nagasaki, and Makurasaki (Fig. 1). Approximately 40 % of the annual tide level variation of 40 cm was caused by the annual atmospheric pressure variation (Yamada and Kobayashi, 2003). However, other causes of this seasonal variation in shallow water are uncertain. The measured 2,052 tidal ranges (Fig. 4c) during this period show the spring-neap variation with different oscillation patterns. The envelopes of the spring and neap tidal ranges are used to

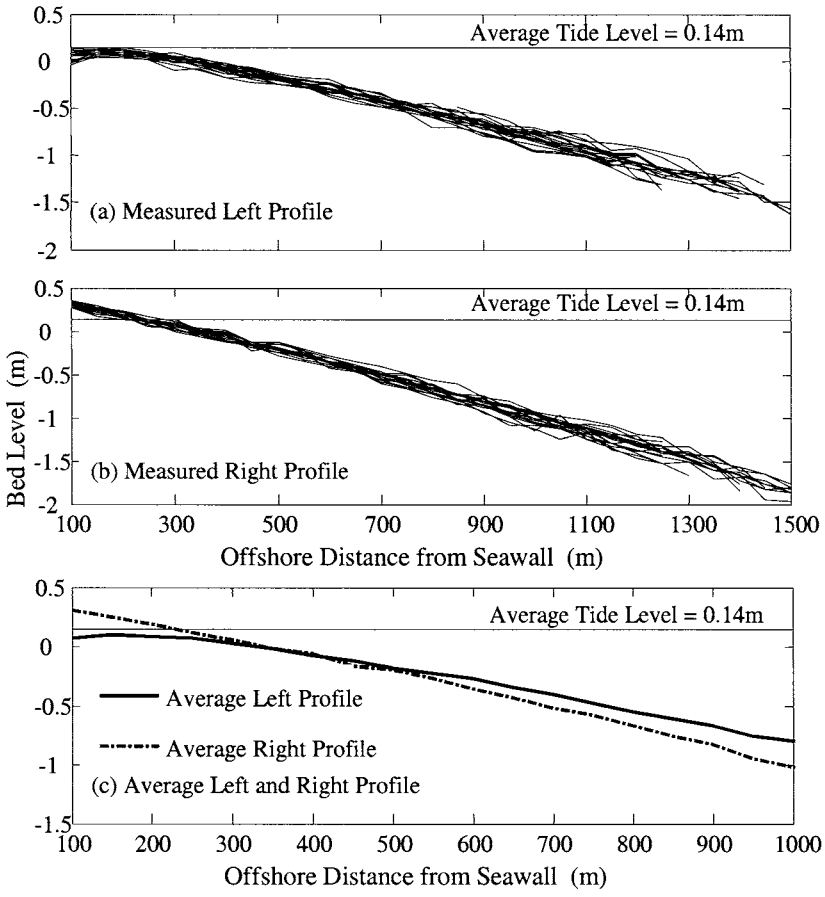

Fig. 3. Measured cross-shore mud-flat profiles from February 2001 to December 2002. (a) Left profiles, (b) right profiles, and (c) averaged profiles.

obtain the time series of the spring-neap tidal range, which varied periodically with a half-year period as may be discernible in this figure.

Wind waves were measured every two hours using an ultra-sonic wave gage (Fig. 5). Wave height during 2001 was obviously larger that that during 2002. From February to April 2001, the wave height was over 1.0 m frequently but decreased abruptly after August 2001. The average wave height during these two years was 0.2 m. The average wave period was 3.0 sec and almost constant during the two years. The wave heights in Ariake Bay are small partly because the fetch lengths are limited in this

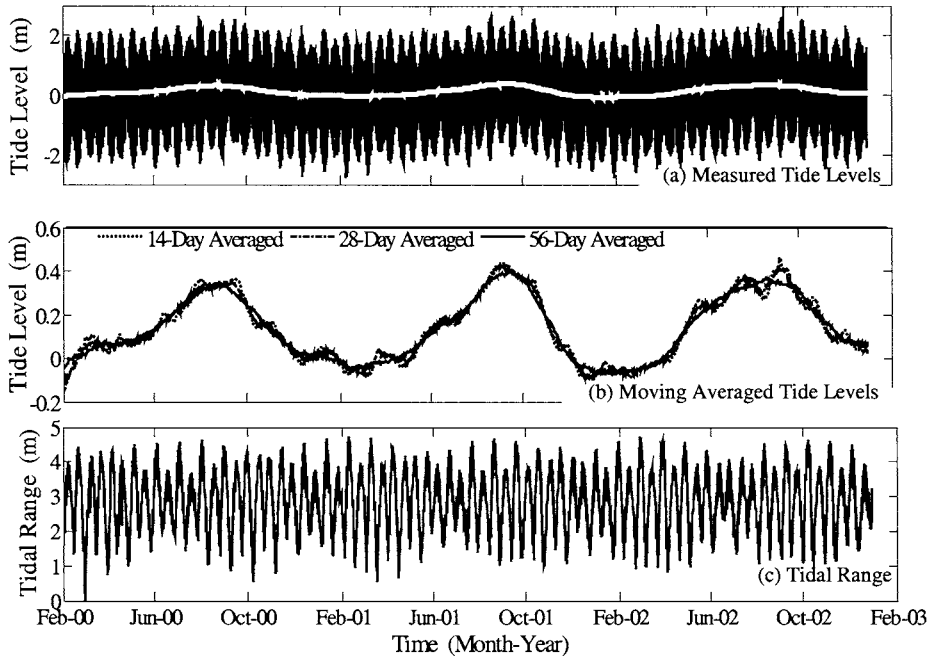

Fig. 4. Measured tidal data at Kumamoto Port (a) Hourly tide levels, (b) moving averaged tide levels, and (c) tidal range.

closed shallow bay. The north-west and south-west fetch lengths are relatively large but less than 60 km.

The measured hourly wind velocities (Fig. 6) show no distinct difference during the two years, except that the maximum wind speed was larger in 2001, about 20 m/s in March. Sixty percent of the strong (over 10 m/s) wind direction was west-northwest during February to April 2001.

Although the Shirawaka River discharge information is available at the Ministry of Land, Infrastructure and Transport, this information only released after the entire yearly data was collected and analyzed. Therefore, it is not available for this study. Since daily rainfall information in Kumamoto City (observed every hour by the Kumamoto meteorological observatory) is available, a relationship between the river discharge and rainfall in Kumamoto City is examined for their correlation (Fig. 7). This figure indicates a good correlation, and thus, the measured rainfall in Kumamoto City is used instead of the discharge of the Shirakawa River.

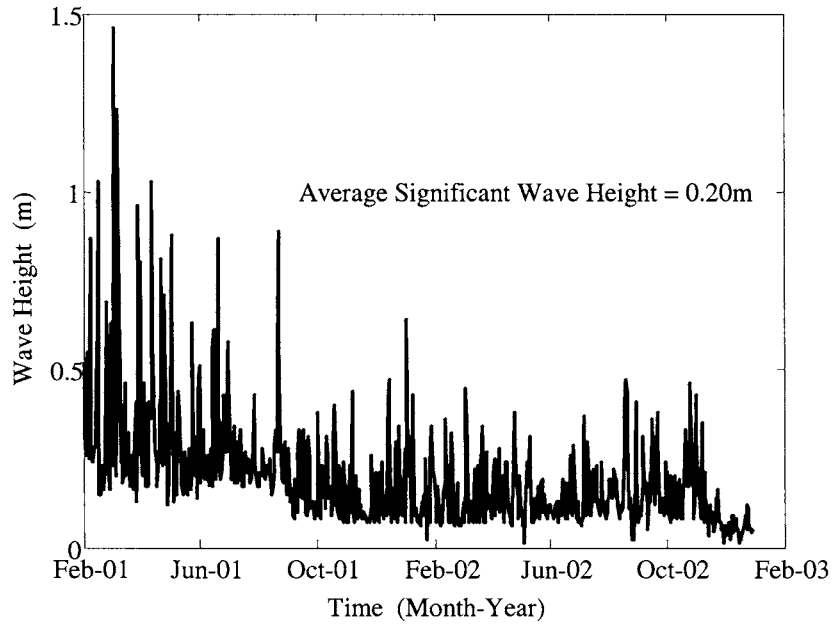

Fig. 5. Measured significant wave heights at the observation tower of Kumamoto Port.

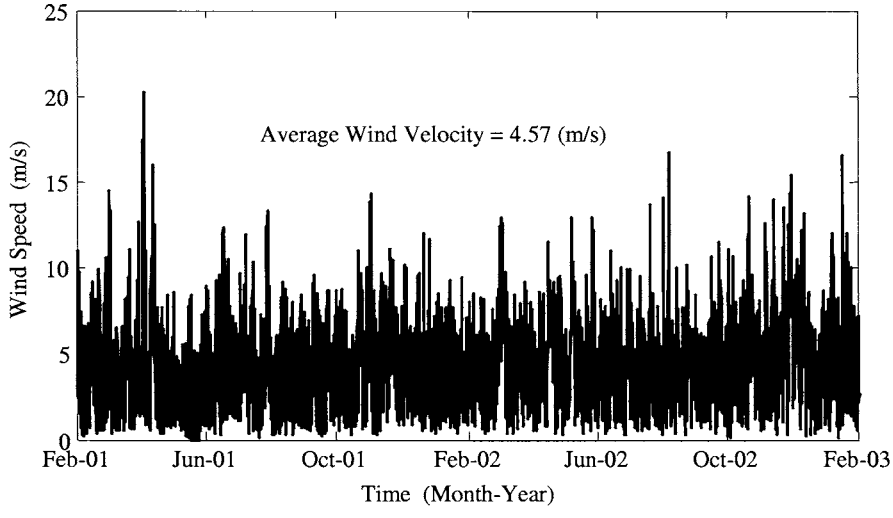

Fig. 6. Measured wind speed at the observation tower of Kumamoto Port.

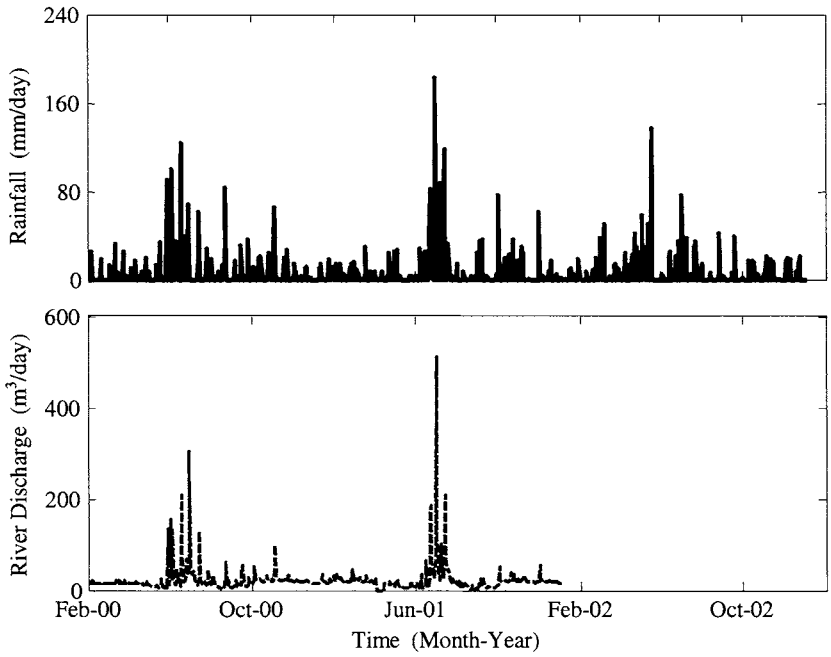

Fig. 7. Relationship between Shirawaka River discharge and rainfall at Kumamoto City.

3. EXISTING APPROACH

The EOF method allows us to separate the spatial and temporal variations of the measured bed level (*e.g.*, Winant *et al.*, 1975; Dean & Dalrymple, 2002). The primary advantage of the EOF analysis is its ability to compress the complicated variability of the observed data set into the fewest possible modes where the first three eigenfunctions are normally used for the sandy beach profile. The physical interpretations of these three modes were given by Winant *et al.* (1975).

The first eigenfunction (Fig. 8) is called a mean beach function, analogous to the arithmetic mean profile given in Fig. 3c. For a sandy beach, the second spatial eigenfunctions (Fig. 9) is named a bar-berm function that is associated with a strong seasonal variation with peaks in the nearshore and offshore. However, there is no distinct peak along the entire surveys as shown in Fig. 9 because no bar and berm existed for the present profiles. Thus, the physical interpretation of the second eigenfunction is difficult

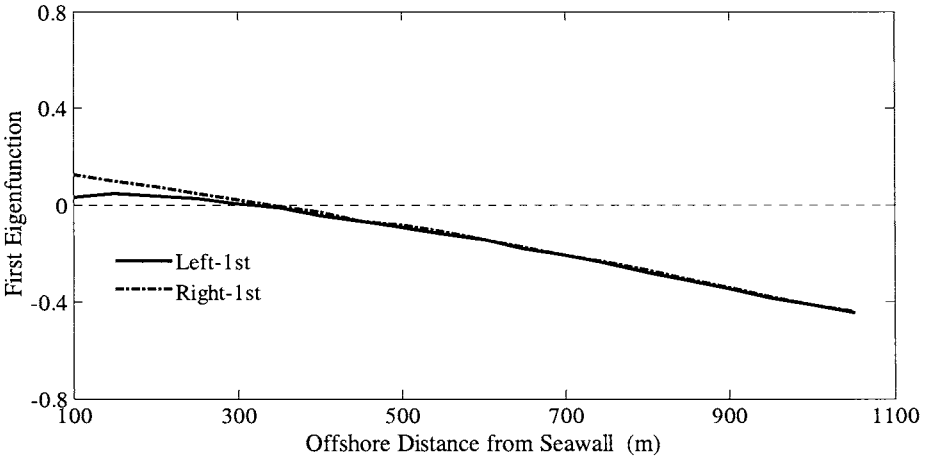

Fig. 8. First spatial eigenfunctions for left and right profiles.

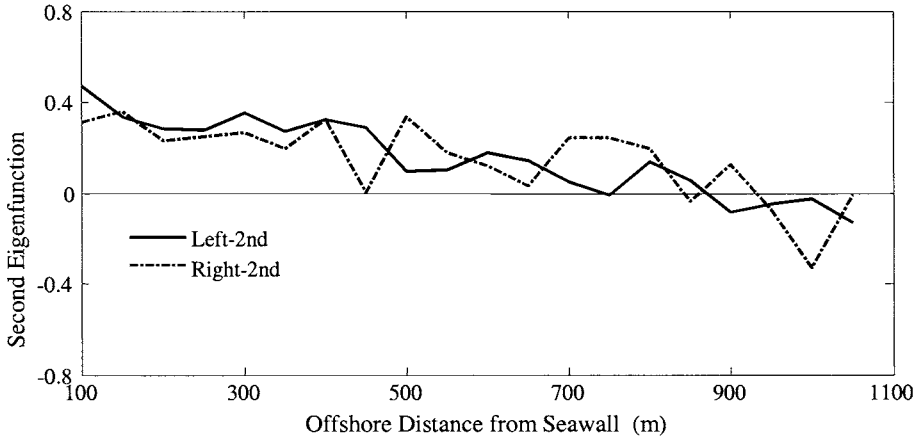

Fig. 9. Second spatial eigenfunctions for left and right profiles.

due to the similarity of the first and second eigenfunctions. For a sandy beach, the third eigenfunction called a terrace function, which has a broad maximum near the low-tide terrace. The fitted third spatial eigenfunctions of both profiles (Fig. 10) indicate a large spatial variation at a distance about 800 m on the offshore direction. This location corresponding to the mean low water neaps at –0.77 m (T.P.). Thus, the physical meanings of eigenfunctions for intertidal mudflats are somewhat different with those for sandy beaches, and more difficult to interpret.

Table 1 lists the percentage of the mean square value of the measured bed level of the left and right profiles explained by the three largest eigenfunctions where the percentage in parentheses indicates the residual mean square value explained after removing the first eigenvalue. The EOF results for the sandy beach obtained by Winant *et al.* (1975) are also listed for comparison. Like the sandy beach, the first eigenfunctions for the left and right profiles explain the most of the mean square value and the second eigenfunction describes approximately 50 % of the residual mean square value. However, the residual mean square value of the third eigenfunction and the subtotal of the mudflat profile were less by about 20 % relative to the sandy beach. As a result, additional eigenfuncions, which are more difficult to interpret physically, will be needed to explain the mudflat profile change using the EOF method. Thus, it is desirable to develop a simpler model for tidal flat profiles.

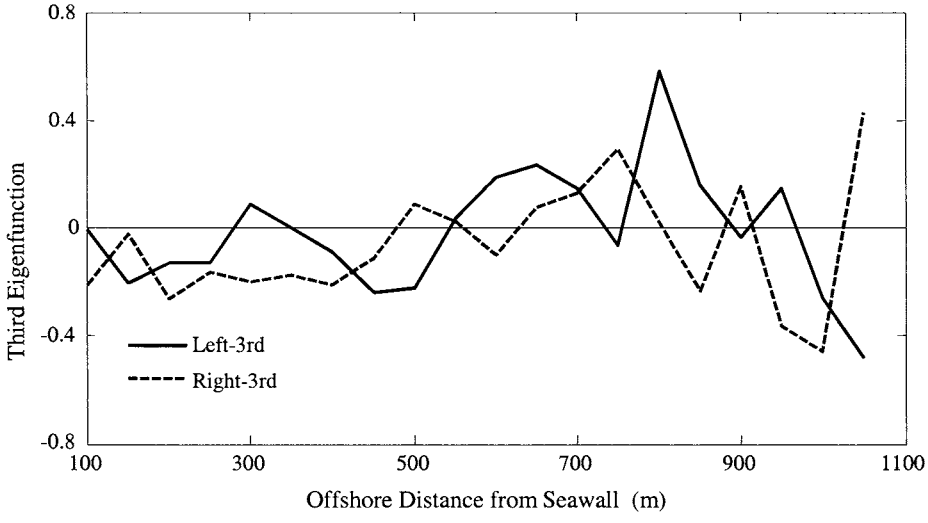

Fig. 10. Third spatial eigenfunctions for left and right profiles.

Table 1. Summary of Empirical Orthogonal Eisenfunction (EOF) analysis.

Eigenfunctions	Left Profile (%)	Right Profile (%)	Sandy Beach (Winant et al. 1975)
1st	99.52	99.67	99.70
2st	0.25 (53.2)	0.14 (43.4)	0.16 (56.5)
3rd	0.05 (10.0)	0.06 (18.2)	0.08 (28.8)
Sub Total	99.82 (63.2)	99.87 (61.6)	99.94 (85.3)

4. QUADRATIC PROFILE APPROACH

The simpler model specifically for the mudflat profile change is developed in the following manner. The measured cross-shore profiles with no nearshore bar on the meso-tidal estuary are parameterized using a quadratic polynomial equation to interpret the spatial and temporal variations of the measured profile changes. The quadratic equation fitted to the measured profiles is expressed as

$$z(t,x) = -a(t)x^2 - b(t)x + c(t) \tag{1}$$

where z = measured bed level defined to be positive upward, t = time in months, x = offshore distance, a = convexity parameter which is positive for a convex upward profile, b = local slope at x = 0 which is positive downward, and c = bed elevation at x = 0. The parameters a, b and c are assumed to depend on t only. The temporal variation of the bed level z can be interpreted using the temporal variations of a, b and c if the measured cross-shore profiles can be fitted by Eq. 1 accurately.

An example of the measured and fitted cross-shore profiles, together with the average profile, are shown in Fig. 11, which is an eroded left profile. The measured profiles are fitted by Eq. 1 using the method of least square. In order to evaluate the degree of agreement quantitatively, the average deviation between the measured and fitted profiles is calculated according to the following equation

$$\varepsilon = \frac{1}{N}\sum_{n=1}^{N}\left|z_n - (-ax_n^2 - bx_n + c)\right| \tag{2}$$

where N is the total number of data points indicated by the integer n along the survey line in the region, x = 100 - 1050 m and N = 20 for each measured profile.

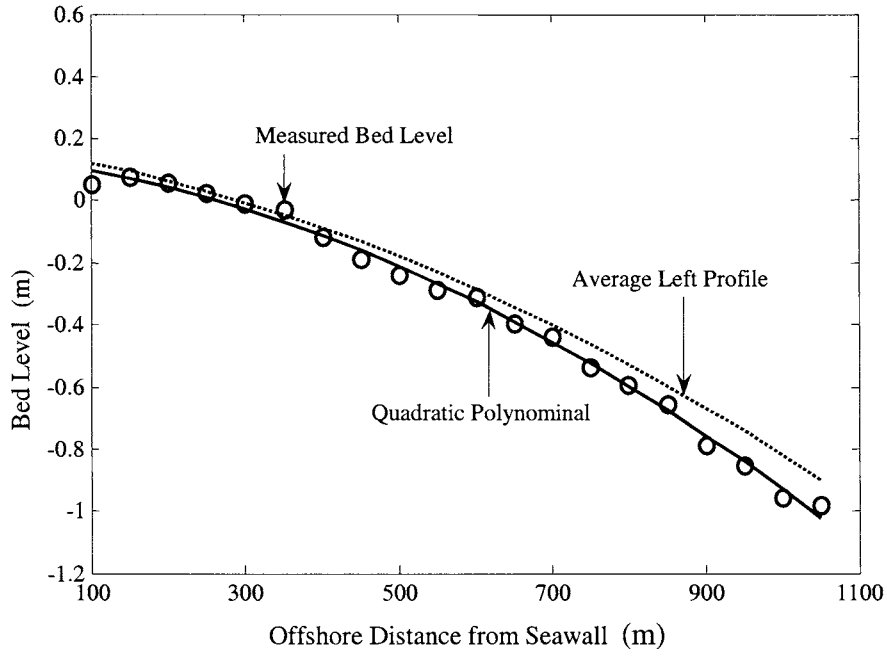

Fig. 11. Quadratic equation fitted to eroded left profile.

Table 2 lists the range of the fitted values of a, b and c and the average deviation for the entire measured left and right profiles. The fitted profile agrees with the measured profile with an error of 3 cm, where this error is slightly larger than the survey error of 2 cm. The average cross-shore profile of all the measured profiles is also expressed as

$$z_m = -a_m x^2 - b_m x + c_m \tag{3}$$

where z_m is the time-averaged bed level during the entire survey period, a_m, b_m and c_m are coefficients for this time-averaged profile. The arithmetic mean values of a, b and c are identical to a_m, b_m and c_m, respectively, because time-averaging of Eq. 1 yields Eq. 3.

Table 2. Fitted parameters and estimated errors for left and right profiles

	Left Profiles				Right Profiles			
	$a\times10^{7}$ $(m)^{-1}$	$b\times10^{3}$	$c\times10$ (m)	$\varepsilon\times10^{2}$ (m)	$a\times10^{7}$ $(m)^{-1}$	$b\times10^{3}$	$c\times10$ (m)	$\varepsilon\times10^{2}$ (m)
max	7.76	0.60	2.31	2.85	4.55	1.26	4.68	2.72
min	4.48	0.22	0.89	1.27	1.58	0.93	3.72	1.18
mean	5.82	0.40	1.69	2.16	3.14	1.11	4.17	1.89

4.1. Temporal variations of three profile parameters

The vertical displacement parameter, c, (Fig. 12a), which is the bed elevation at x = 0, is different significantly between the left and right profiles (see Fig. 8), and it also shows a clear signal on seasonal variation. It accreted during summer and fall (started July, 2001 and 2002) and eroded during winter and spring. The annual rate of accretion for the last two years was 4.2cm/year and 1.6cm/year on the left and right profiles, respectively. This may be related to sea level rise in the Ariake Bay, which was in the range of 1.7-2.8mm/year for the last 35 years.

Figure 12b indicates that the mean slope parameter, defined as the cross-shore average of the local slope (2ax + b), also varies annually in a similar manner, like the vertical displacement parameter. The mean slope became steeper during erosion and gentler during accretion.

The curvature parameter (Fig. 12c) appears to vary semiannually but their temporal patterns are not always similar. The left profile has more curvature than the right profile. This may be related to local wave conditions, flow patterns and sediment transport in the vicinity of the river mouth.

5. CORRELATIONS OF THREE PROFILE PARAMETERS AND DRIVING FORCES

The time variations of these three parameters, *i.e.*, curvature, mean slope, and vertical displacement, are compared with the available time series of the average tide level, tidal range, wave height, wind speed, and river discharge.

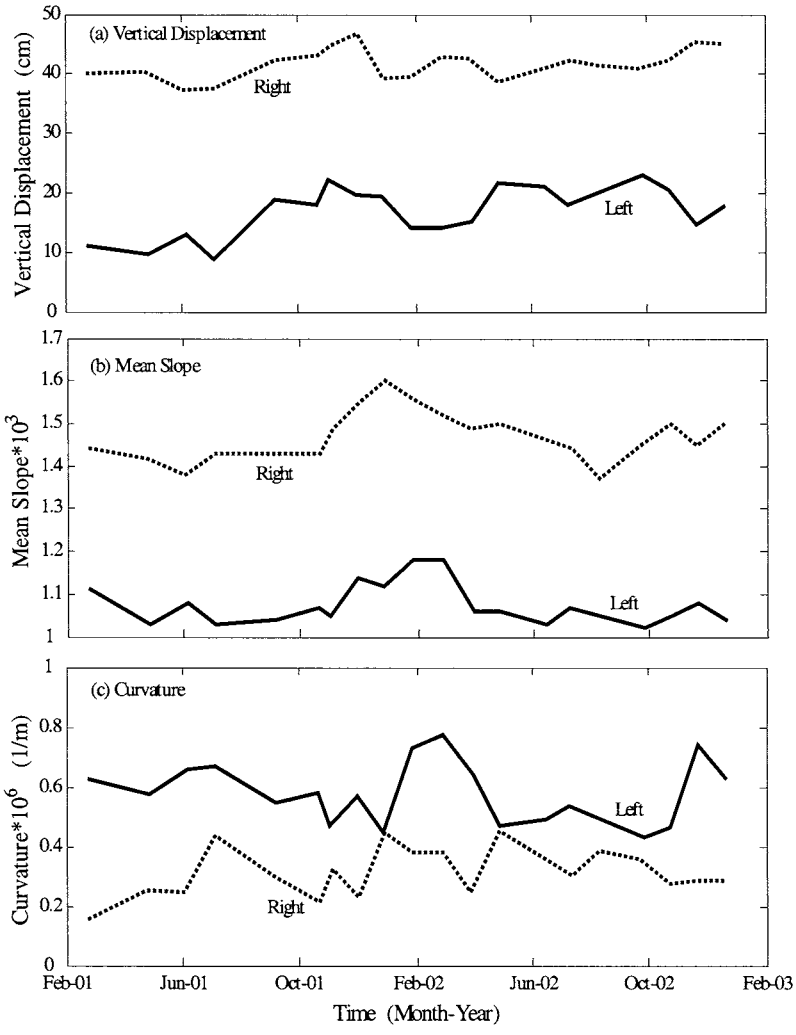

Fig. 12. Temporal variations of left and right profile parameters. (a)Vertical displacement parameter c, (b) mean slope parameter (2ax+b), and (c) curvature parameter a.

There is a good correlation (correlation coefficient of 0.7) between the vertical displacement and the 56-day averaged tidal level (Fig. 13). Both time series varied periodically with a one-year period. The mudflat accreted as the average tide level rise, and eroded as the average tide level fall.

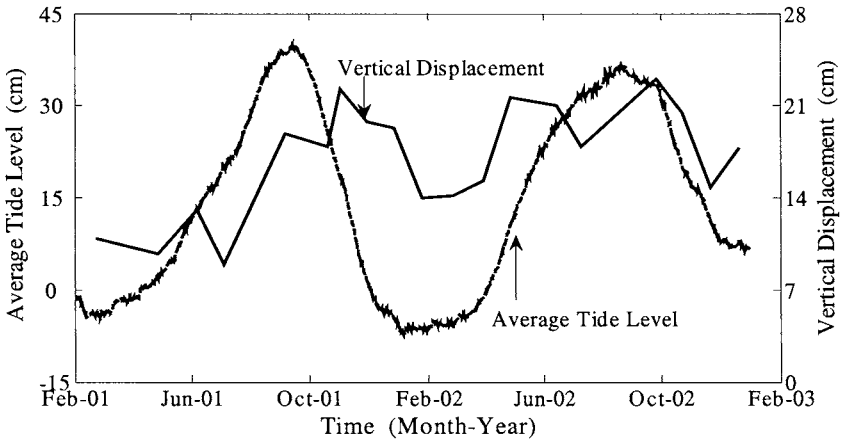

Fig. 13. Times series of the vertical displacement parameter for left profile and average tide level.

There is no obvious correlation between the vertical displacement and wind waves (Fig. 14) partly because the significant wave heights were relatively small. However, it is possible to say that the vertical displacement parameter c is small at the beginning of the observation period because of the relatively large wave heights. The effects of wind waves may be important on a time scale shorter than the monthly profile data used here.

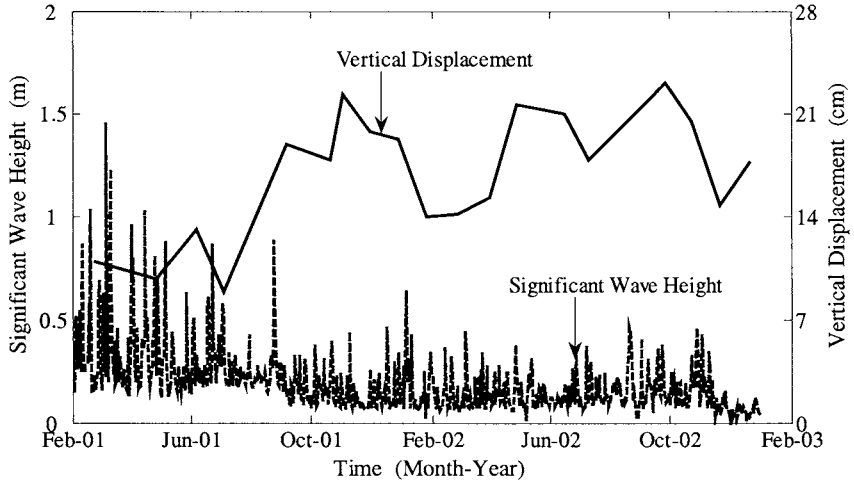

Fig. 14. Time series of left profile vertical displacement and significant wave height.

There is a negative correlation (correlation coefficient is -0.7) between the mean slope and the 56-day averaged tide level (Fig. 15). Both time series varied periodically with a one-year period. The mean slope became gentler or steeper as the average tide level rise or fall.

The correlation between the profile curvature parameter and the 56-day averaged tidal level is rather weak, if not correlated at all (Fig. 16). This might be due to the fact that the curvature varied semiannually, unlike that for the vertical displacement and mean slope parameters.

As for the wind and rainfalls, there is no obvious correlation with the time variations of these three parameters.

6. CONCLUSIONS

Knowledge of the morphological changes of mudflats due to long-term sea level rise is essential for the long-term environmental protection and management in estuaries and inner bays. However, no quantitative model exists to predict the temporal variation of the mudflat profile under time-varying driving forces. In order to facilitate the evaluation of the dominant causes of mudflat cross-shore profile changes on meso-tidal mudflats in the vicinity of the Shirakawa River mouth, a parameterized mudflat profile with no nearshore bar is proposed using a quadratic polynomial equation fitted to the measured bed levels.

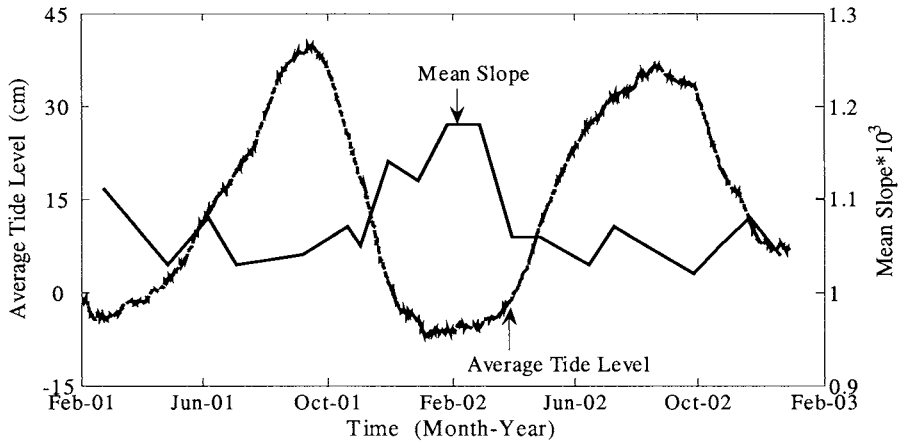

Fig. 15. Time series of left profile mean slope and average tide level.

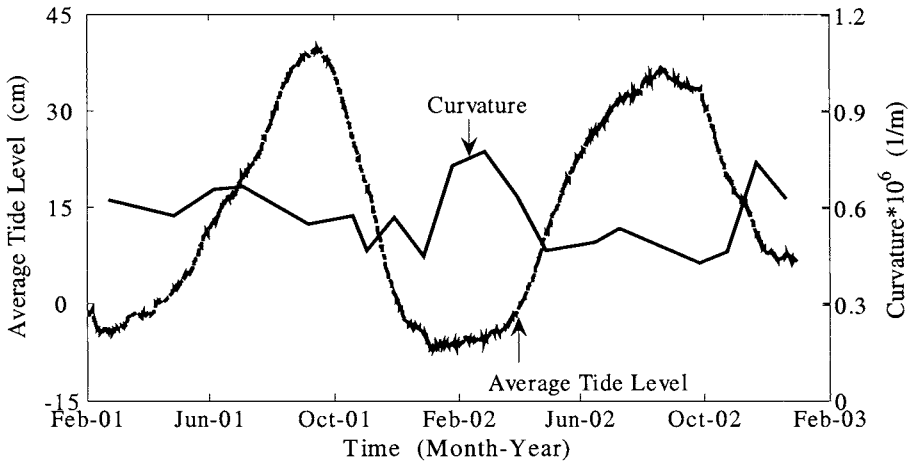

Fig. 16. Time series of left profile curvature and average tide level.

The time series of the three parameters for the vertical displacement, mean slope and profile curvature are correlated with those of the tide level, tidal range, wind waves, winds, and rainfall related to river discharge in order to identify the dominant oceanographic factors. The vertical displacement and mean slope parameters are shown to have relatively high correlations without any time lag with the seasonal tide level change of approximately 40 cm. The predominant driving forces for the profile curvature parameter are not certain but may be related with the average tide level, averaged spring-neap tidal range, and rainfall. The effect of wind waves and river discharge may be important on a time-scale shorter than the monthly profile data used here. The quadratic profile approach proposed here is simple and may be useful in assessing the mudflat profile changes in enclosed bays and estuaries. However, this approach will need additional verifications from different mudflats as well as during storms.

ACKNOWLEDGMENTS

This study was supported by the Saneyoshi Scholarship Foundation and the Japan Society for the Promotion of Science. We would like to thank the Kumamoto Port Construction Bureau of Ministry of Land, Infrastructure, and Transport in Japan.

REFERENCES

ASCE Task Committee on Sea Level Rise and Its Effects on Bays and Estuaries. 1992. Effects of sea-level rise on bays and estuaries. *Journal of Hydraulic Engineering*, ASCE, (118) 1, 1-10.

Bassoullet, P., P.L. Hir, D. Gouleau and S. Robert. 2000. Sediment transport over an intertidal mudflat: Field investigations and estimation of fluxes within the Baie de Marennes-Oleron (France). *Continental Shelf Research*, 20, 1635-1653.

Bruun, P. 1962. Sea-level rise as a cause of shore erosion. *Journal of Waterways and Harbors Division*, ASCE, 88, 117-130.

Christie, M. C., K.R. Dyer and P. Turner. 2001. Observations of long and short term variations in the bed elevation of a macro-tidal mudflat. In: *Coastal and Estuarine Fine Sediment Processes*. McAnally, W.H. and A.J. Mehta (eds.), Elsevier, Amsterdam, 323-342.

Dean, R. G. and R.A. Dalrymple. 2002. *Coastal processes with engineering applications*, Cambridge Univ. Press, Cambridge, U.K.

Dyer, K. R. 1998. The typology of intertidal mudflats. In: *Sedimentary Processes in the Intertidal Zone*. Black, K.S., D.M. Paterson, and A. Cramp (eds.), Geological Society, London, 11-24.

Dyer, K. R., M.C. Christie and E.W. Wright. 2000. The classification of intertidal mudflats. *Continental Shelf Research*, 20, 1039-1060.

Friedrichs, C. T. and D.G. Aubrey. 1996. Uniform bottom shear stress and equilibrium hyposometry of intertidal flats. In: *Coastal and Estuarine studies, 50, Mixing in Estuaries and Coastal Seas*. Pattiaratchi, C. (ed.), American Geophysical Union, Washington, D.C., 405-429.

Hayes, M. O. 1975. Morphology of sand accumulation in estuaries: An introduction to the symposium. In: *Estuarine Research*. Cronin, L.E. (ed.), Academic Press, New York, 2, 3-22.

Intergovernmental Panel on Climate Change. 2001. *Climate change 2001, Scientific Basis*. Cambridge University Press, Cambridge, 881p.

Kirby, R. 1992. Effects of sea-level rise on muddy coastal margins. In: *Dynamic and Exchanges in Estuaries and in the Coastal Zone*. Prandle, D. (ed.), American Geophysical Union, Washington, D.C., 313-334.

Kirby, R. 2000. Practical implications of tidal flat shape. *Continental Shelf Research*, 20, 1061-1077.

Lee, S.-C. and A.J. Mehta. 1997. Problems in characterizing dynamics of mud shore profiles, *Journal of Hydraulic Engineering*, ASCE, (123) 4, 351-361.

Pritchard, D., A.J. Hogg and W. Roberts. 2002. Morphological modeling of intertidal mudflats: the role of cross-shore tidal currents. *Continental Shelf Research*, 22, 1887-1895.

Pritchard, D and A.J. Hogg. 2003. Cross-shore sediment transport and the equilibrium morphology of mudflats under tidal current. *Journal of Geophysical Research*, 108 (C10), 3313.

Roberts, W. and R.J.S. Whitehouse. 2001. Predicting the profile of intertidal mudflats formed by cross-shore tidal currents. In: *Coastal and estuarine fine sediment processes*. McAnally, W.H. and A.J. Mehta (eds.), Elsevier, Amsterdam, 263-285.

Shi, Z. and J.Y. Chen. 1996. Morphodynamics and sediment dynamics on intertidal mudflats. *Continental Shelf Research*, (16) 15, 1909-1926.

Tsuruya, H., K. Murakami and I. Irie. 1990. *Mathematical modeling of mud transport in ports with a multi-layered model: Application to Kumamoto port*. Report of the Port and Harbor research Institute, (29) 1, 3-51.

Winant, C. D., D.L. Inman and C.E. Nordstorm. 1975. Description of seasonal beach changes using empirical eigenfunctions. *Journal of Geophysical Research*, (80)15, 1979-1986.

Yamada, F. and N. Kobayashi. 2003. *Parameterization of mudflat profile changes caused by seasonal tide level variations*. Research Report No. CACR-03-02, Center for Applied Coastal Research, Univ. of Delaware, Delaware 192pp.

Yamada, F. and N. Kobayashi. 2004. Annual variations of tide level and mudflat profile. *Journal of Waterway, Port, Coastal and Ocean Engineering*, ASCE, 130, 119-126.

Estuarine and Coastal Fine Sediments Dynamics
J.P.-Y. Maa, L.P. Sanford and D.H. Schoellhamer (editors)

Plume dispersion modelling using dynamic representation of trailer dredger source terms

Spearman, J.[a], R.N. Bray[b], J. Land[b], T.N. Burt[a], C.T. Mead[a] and D. Scott[c]

[a]Hydraulics Research (HR) Wallingford, Howbery Park, Wallingford, Oxon. OX10 8BA, UK.
[b]Dredging Research Ltd. (DRL), Bargate House, Catteshall Lane, Godalming, Surrey, GU7 1LG, UK.
[c]Baird, 1145 Hunt Club Road, Suite 500, Ottawa, Ontario, Canada, K1V 0Y3.

KEY WORDS
Plume dispersion, dynamic plume, dredger, numerical modelling, field experiments

The development of a dispersion model of a trailer hopper suction dredger is described that incorporates sub-models of the trailer hopper process and of the descent and collapse of the dynamic plume. This identifies the shape and magnitude of the source terms of release of fine sediment into the water column and onto the bed. The nature of these source terms is updated with time and the changing hydrodynamics. The release source terms are passed to a passive plume sub-model which is a Lagrangian random walk approach and tracks the three-dimensional movement of sediment particles over time and space. The effects of using such a process based approach are illustrated using a basic example. The need for high quality validation data requires comprehensive field measurements of the plumes arising from trailer dredging. A recent measurement campaign undertaken at Rotterdam Port is briefly described.

INTRODUCTION

This paper describes the development of a dispersion model of a trailer hopper suction dredger (henceforth referred to as trailer dredger) incorporating the processes

occurring in the dredger itself, and in the near-field and far-field zones. The trailer plume model consists of sub-models of the trailer hopper processes and of the descent and collapse of the dynamic plume, in order to identify the shape and magnitude of the source terms of release of fine sediment. The nature of these source terms is updated with time and the changing hydrodynamics. The release source terms are passed to a passive plume sub-model, which uses a Lagrangian random walk approach and tracks the three-dimensional movement of sediment particles over time and space. The dispersion model has been linked to a sophisticated user interface and three-dimensional visualisation system by Baird, Canada.

The studies described in this paper have been motivated by the TASS Project, funded by the Dutch Vereniging Van Waterbouwers in Bagger-Kust Oeverwerken (VBKO) dredging organisation, and the MMS plume model initiative in the US, both involving HR Wallingford and DRL, the latter project also involving Baird, Canada.

2. TRAILER SUCTION HOPPER DREDGERS

Trailer suction hopper dredgers consist of vessels containing a large hopper into which dredged sediment can be pumped. One or two dragheads are lowered onto (or partially into) the bed and sediment and water are sucked from the bed through the draghead via a pipe into the hopper. The sediment/water mixture is of the order of 20% solids (by volume) and so as the hopper is filled most of water. To achieve a greater load, pumping continues after the hopper is filled. This results in the hopper overflowing (either ship-side as in Fig. 1 or through a central spillway discharging through the dredger hull) into the water column. As this water overflows, it contains a proportion of sediment which is then released into the water column to form a plume in the water column.

Trailer suction hopper dredgers differ in some respects depending on their specific use. Dredgers used primarily for aggregates (common in the US and UK) can have the capacity to screen out fractions of sediment to achieve the right particle size distribution for a particular market. Such dredgers release sediment into the water column both over the shipside through a specially designed screening chute and through the overflow described above. Dredgers used for a variety of applications, maintenance, capital, aggregate, beach recharge, *etc.*, do not usually have this capacity. The variety of material from a trailer dredging for aggregate essentially means that there are two possible sources of plumes from trailer dredgers – screening and overflow.

Fig. 1. Discharge of overflow and screened.

3. SEDIMENT PLUME BEHAVIOUR

3.1 Dynamic phase

During trailer suction hopper dredging operations, bed material is disturbed and introduced into the water via spillways (centrally located or shipside spillways) as water is displaced from the hopper, or via aggregate dredger screening chutes. The introduction of this sediment, which can have significant initial momentum, into the water column results in a body of water, denser than the surrounding water, that descends towards the seabed (Fig. 2). This initial rapid descent of the plume is referred to as the "dynamic phase" of plume dispersion and the plume is referred to as the "dynamic plume."

As the dynamic plume descends, ambient water is entrained into the plume, diluting the plume and slowing its descent. If the plume is discharged sufficiently close to the bed, the majority of the released material impacts upon the bed as a density current, although a proportion of the sediment may be "de-entrained" from the plume into the surrounding water column through a variety of mechanisms (see Sections 6.5 and 7.1). Some material may be re-suspended into the water column as a result of the impact, while the rest of the material moves radially outwards across the seabed as a dense plume, slowing with time. During this radial expansion, settling of sediment occurs from the density current onto the bed. Initially, the mixing that occurs between the density current and the ambient waters is limited. If the concentration and thickness of

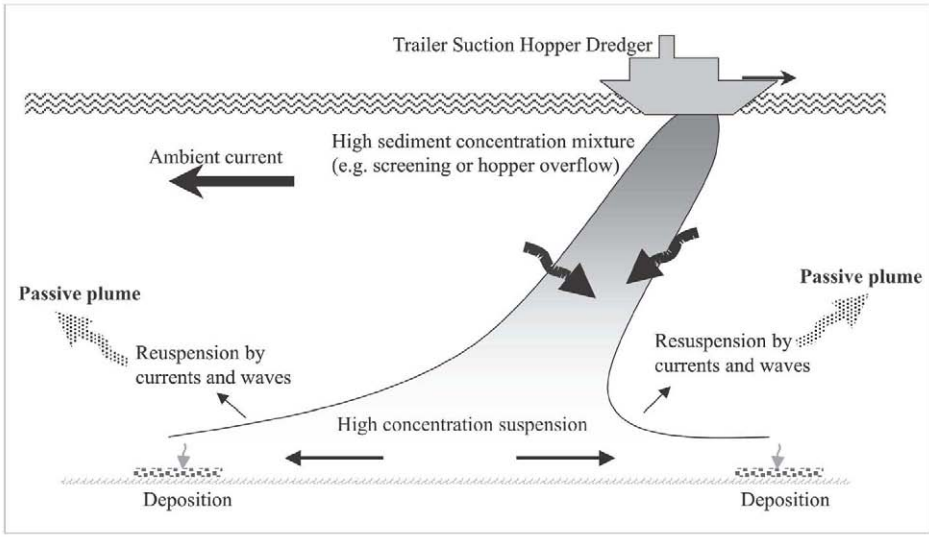

Fig. 2. Dynamic plume processes.

the density current are sufficiently low, however, and/or if the ambient currents are sufficiently high, then significant mixing occurs and sediment is released into the water column to form a "passive plume" (see Fig. 2 and Section 3.2).

If the plume is discharged sufficiently far from the bed or if the dynamic plume is of relatively low concentration the dynamic plume may never reach the bed. In this case the dynamic plume will make a gradual transition into a passive plume. In this case the dynamic plume converges on a position of neutral buoyancy and experiences internal or dynamic collapse, pancaking outward as a density current in a similar fashion to that resulting from impact on the bed.

The nature of the concentrations occurring in the different phases of the plume depends on the nature of the sediment, the size/pumping capacity of the trailer dredger and the depth of water below the point of discharge from the dredger (the dredger hull or the water surface depending on the dredging design) and the bed material. Some typical concentrations resulting from different stages of the dredging plume are presented in Table 1.

3.2 Passive phase

Material stripped from the plume into the water column during the rapid descent of material, or as a result of the impact of the dynamic plume on the bed, or subsequently

Table 1. Typical plume concentrations occurring at different stages of plumes generated by trailer dredging.

Phase	Length scale	Concentration	Comment
Immediately after discharge	A few metres from release point	10's to 100's of g/l	Depends strongly on nature of sediment
Density current on impact with bed	Several tens of metres to 200 m from release point	100mg/l to 10 g/l	In water of less than about 20 m depth
Passive plume	A few hundred metres to several kilometres	A few mg/l up to 100's mg/l	Possibly 1000's mg/l near bed in very muddy environments

during the flow of material along the bed, will form a "passive plume" of material that will slowly disperse with the mixing effects of currents and waves. This effect, together with the settling of sediment particles, will reduce the concentration of the passive plume over time. There are two main mechanisms whereby this occurs:

- "Turbulent diffusion," the small-scale temporal and spatial variations in current flow.
- "Shear dispersion," the effect of different current velocities through the water column, which results in particles at different heights travelling in different directions and at different speeds, thus spreading the plume. This effect is much larger than turbulent diffusion except in quiescent waters.

4. THE VALIDITY OF SOURCE TERMS USED IN TRAILER DISPERSION MODELS

Dispersion models applied to trailer plumes generally "assume" a distribution in space and time for the sediment released. Often the release is modelled as a uniform distribution over time. However, it is clear that both the overall rate of discharge of sediment into the water column and the particle size distribution change over time. This is more obvious at the end of the loading period when the bed level in the hopper has risen, the horizontal velocity in the hopper increases and scour of the coarser sediments in the hopper results in additional amounts of coarser material being washed over the spillways. Laboratory experiments and numerical modelling of hopper processes by

van Rhee (2002) suggest that this trend also occurs more gradually throughout the loading period and the initial conclusions of the field experiments at Rotterdam, (see Section 10), are that this gradual trend (combined with significant temporal fluctuation) is also observed in the field.

As regards the overall magnitude of the source term it is clear that this is a function of the dredger, the operation and the *in-situ* material. These considerations require the application of a hopper model or detailed *in-situ* measurements to estimate the discharge from the dredger into the water column. However, the processes occurring in the dynamic phase have also been shown to significantly reduce the initial rate of sediment release into the water column as a passive plume. The effect is well known for sediment disposal in open waters but also has been shown in the field by studies of trailer dredging activity (*e.g.*, Whiteside *et al.*, 1995; US Minerals Management Service, 1998), and on the basis of numerical modelling (*e.g.*, Dearnaley *et al.*, 1999). The use of "typical" release rates from the literature to provide source terms for any given study would appear questionable given the possible variation in all the contributing effects.

In the UK the best available trailer dredging data relate to the particle size distribution of overflow and screening discharges from small/medium sized (2500-5000 tonne capacity) aggregate dredgers (US Minerals Management Service, 1998). However, the data presented in the US Minerals Management Service report is "typical" data (albeit classified for all-in loads, over-sized screening and under-sized screening) being drawn from a number of different areas and dredgers and from different points in the loading cycle, rather than specific data for individual operations. Furthermore no data is given regarding the *in-situ* particle size distribution. These limitations rend the data set less useful.

The TGU method (Nagai, 1978) has been a popular method of providing the magnitude of dredger source terms in the US (Anderson *et al.*, 2001). The TGU method assumes that the rate of loss of fine sediment into the water column can be estimated from measurements of the increase in turbidity around a dredger. Because this method requires measurements of the turbidity increases to evaluate the source terms, it does not *a priori* estimate source terms for plume dispersion modelling. Thus this method depends on reliable measurements of losses from the literature regarding trailer dredging.

A number of measurements of releases from trailer dredgers have been made in the Netherlands (Pennekamp *et al.*, 1996). However, many of these were tailored towards the identification of S-parameter values: a measure of the release of sediment from the dredger process per unit volume of *in-situ* material dredged. The measurements defined sediment release as that contributing to total suspended sediment increases within a 50m x 50m area of the dredger. This approach at the time contributed significantly to the

understanding of the processes occurring for trailers (and other) dredger types. However, it is unlikely that the S-parameter approach can provide detailed enough information for calibrating representation of the numerous and complex processes that occur within and outside of this defined zone of release. There is a question mark, for instance, as to whether the method can be applied successfully to a moving trailer dredger owing to the practical problems of measurement. Moreover, it is unclear whether S-parameter measurements are able to discern the extent of sediment depositing on the bed within the dredger working zone which could be resuspended at a later time by larger currents and/or waves. Additionally, the number of possible combinations of operational procedures, dredger characteristics and *in-situ* sediment types encountered for dredging operations means the S-parameter values can never provide literature on the full spectrum of trailer dredging operations.

Investigating the basis of this and other methods of evaluating source terms, the data provided in the literature of losses from trailer dredgers is limited. Moreover, as regards the development of predictive models, this data is either sparse, incomplete or unreliable and as such do not encourage confidence in the validity of derivative source terms (HR Wallingford and DRL, 1999). It is concluded that source terms for trailer dredgers could be significantly improved using an approach that represents the physical processes involved, calibrated on the basis of high quality and fit-for-purpose field measurements.

5. REQUIREMENTS FOR A TRAILER PLUME DISPERSION MODEL

The complex processes involved in the generation of passive plumes arising from trailer dredging suggest that the current practice of assuming dredger source terms to be uniform in space and time is unsatisfactory. However, representing the physical processes involved in trailer plume production is by no means a trivial task. The requirements for such a trailer plume dispersion model are as follows:

- The model must be able to predict the release of sediment from the dredger *a priori* for different dredger/soil types.
- The model must be able to represent both the dynamic and passive phases and the links between them. These phases have widely different length and time scales. It should be noted that while the dynamic plume phase occurs before (and provides the input for) the passive plume phase, both plumes exist simultaneously throughout the loading period (except for the initial period before overflow commences as the hopper fills).

- It must be able to represent one (or more) moving sources.

The proposed model system addresses these requirements.

6. MODEL REPRESENTATION OF TRAILER SUCTION HOPPER DREDGER

6.1 Model overview

The proposed model system is based on five main components (Fig. 3):

- An interface which allows the specification of information regarding the dredger, the operation, the sediment, and other model parameters
- A dredger process model which models the processes occurring inside the hopper (where relevant including screening)
- A dynamic plume model
- A passive plume model
- A visualisation system enabling the results to be interrogated.

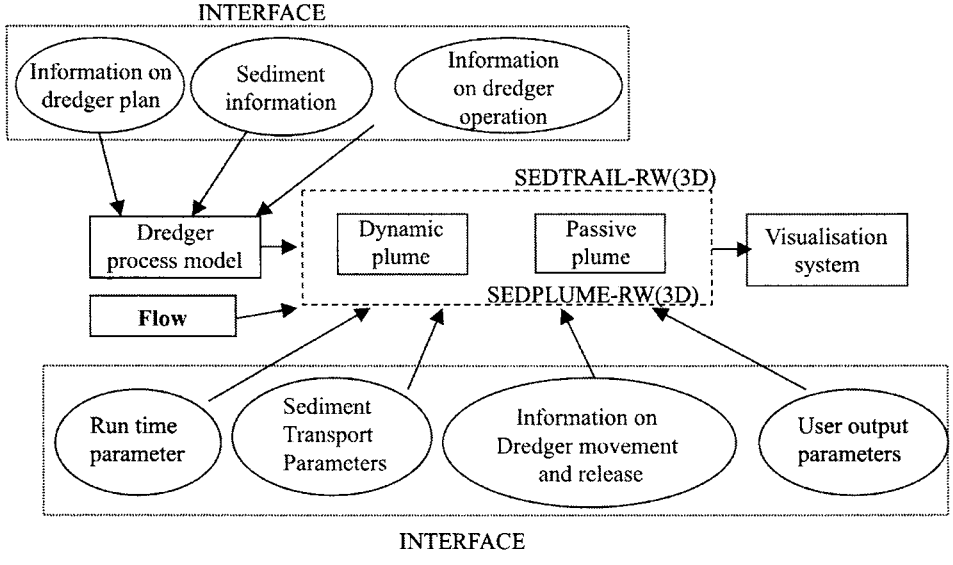

Fig. 3. Overview of model system.

Additionally the model must be able to read flow input from a detailed 3D flow model. Such a model system has been developed by HR Wallingford, DRL and Baird, Canada for the US Minerals Management Service (US Minerals Management Service, 2004). At present this model system is configured to accept 3D flow input from the unstructured finite element model TELEMAC-3D (Electricité de France, 1998) and the 2D flow model ADCIRC (Luettich and Westerink, 2004).

6.2 Dredger processes

Details of the dredger process model is described in US Minerals Management Service (2004). Here a brief description of the model is given.

The model represents the processes that occur in the hopper (and where relevant, the screening tower) and which result in a discharge of sediment of a certain particle size distribution. When overflowing commences, the hopper acts as a settling tank. The settlement process is described in Vlasblom and Miedema (1995) and relies generally on the concept of an "ideal" settling tank (Camp, 1946) with a few modifications to take account of hindered settling, scouring as the load increases and, (if required) the effects of the Constant Tonnage Loading System.

The basic concept is illustrated in Fig. 4. The ideal settling basin concept consists of an "entrance" zone where the solid/fluid mixture enters the hopper, a "settling" zone and an "overflow" zone where the water (and some sediment) leaves the basin. Each particle is assumed to enter the basin with a horizontal velocity, v_0, which depends on the water depth in the hopper, the hopper width and the discharge of water into the hopper, and a vertical velocity which is essentially a function of the particle size, adjusted for the effects of turbulence and hindered settling. Thus for a given hopper shape

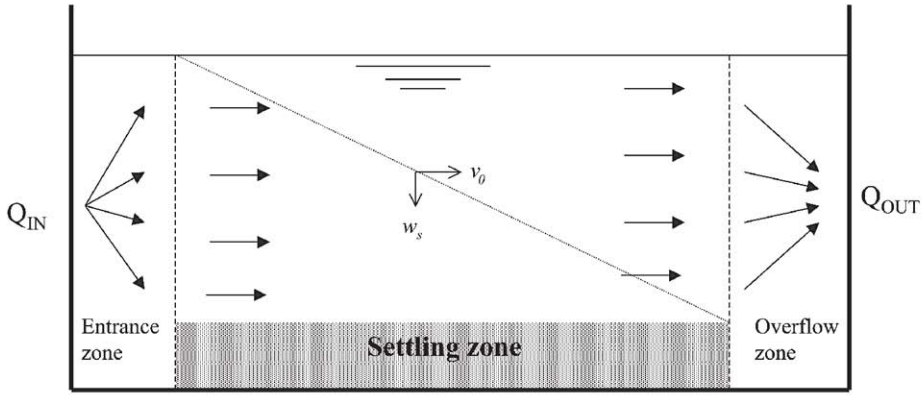

Fig. 4. The trailer hopper as an ideal settling basin (after Vlasblom and Miedema, 1995)

and discharge, a particle entering the hopper will either reach the bed or escape as overflow depending on its particle size. As the hopper fills the horizontal velocity of particles in the hopper increases and more particles will escape as overflow. As the horizontal velocity of particles in the hopper increases, it may exceed the threshold of motion for certain particle sizes and in this case all particles of that size will be discharged from the hopper.

The equations for settling velocity, and the effects of turbulence and hindered settling used in the hopper process model are the same as those presented by Camp but approximated numerically where necessary (Vlasblom and Miedema, 1995). The settling velocity for a particle, w_s, is given by Camp as follows:

$$w_s = 424(\rho_s - \rho_w)\left(\frac{d}{1000}\right)^2 \qquad \text{for d} < 100\mu\text{m} \tag{1}$$

$$w_s = 8925\left(\frac{\sqrt{1+95(\rho_s - \rho_w)(d10^{-3})^3} - 1}{d}\right) \qquad \text{for } 100\mu\text{m} < \text{d} < 2{,}000\ \mu\text{m} \tag{2}$$

$$w_s = 87\sqrt{(\rho_s - \rho_w)d10^{-3}} \qquad \text{for d} > 2{,}000\mu\text{m} \tag{3}$$

where d (microns) is the sediment particle diameter, ρ_s is the density (Tonnes/m^3) of the particle, and ρ_w is the density (Tonnes/m^3) of water. The settling velocity, w_s (m/s), is firstly adjusted by a hindered settling factor, f_h, which is given by the formula,

$$f_h = (1 - C_v)^n \tag{4}$$

where C_v is the volume concentration of sediment and n (where $2.5 < n < 5.5$) is dependent on the Reynolds number of the flow (see discussion by Winterwerp, 1999). The settling velocity, w_s , is then adjusted for the effect of turbulence by a factor, f_t, (*i.e.*, $w_s' = f_t w_s$) given by

$$f_t = \left[1 - 0.2r_h^{0.85}\left[1 - Tanh\left(\frac{0.75}{r_h^{1.5}}\left(\log\left(\frac{w_s}{v_0}\right) + 2.6 - r_h\right)\right)\right]\right], \quad \text{for } r_h = f_h w_s / v_0 < 2.94 \tag{5}$$

$$f_t = \left[0.5 - Tanh\left(\frac{0.75}{r_h^{1.5}}\left(\log\left(\frac{w_s}{v_0}\right) + 2.6 - r_h\right)\right)\right], \quad \text{for } r_h > 2.94 \tag{6}$$

where v_0 is the average horizontal velocity in the hopper given by the discharge into the hopper, Q_m, divided by the average water depth and hopper width.

The threshold bed shear stress, τ_e (N/m^2), of motion for particles on the floor of the hopper is given by (Soulsby, 1997)

$$\tau_e = \theta_{cr} g(\rho_s - \rho_w) d 10^{-3} \tag{7}$$

with

$$\theta_{cr} = \frac{0.30}{(1 + 1.2 D_*)} + 0.055[1 - Exp(-0.020 D_*)] \tag{8}$$

$$\text{and } D_* = \left[\frac{g(s-1)}{\nu^2}\right]^{0.33} d 10^{-6} \tag{9}$$

where ν is the kinematic viscosity (m^2/s), g is the acceleration due to gravity (m/s^2), and θ_{cr} is the Threshold Shield's Parameter.

The screening model is an empirical relationship based on the key parameters of screening mesh aperture size, mixture density, particle size, proportion of sediment greater than aperture mesh, water flow (and loss to the screening chute) and angle of the screening mesh. Both over-screening (removal of coarser particles) and under-screening (removal of finer particles) are represented. The discharge of fluid lost in the over-screening process, W_o, is computed from the following expression

$$W_o = Q_m - C_o r_o a_o b_o \left[\frac{a_o g}{2 V_m} + \sin(\alpha_o) V_m\right] \tag{10}$$

The percentage of incoming mixture lost, W_o%, is then given by

$$W_o\% = \frac{W_o}{Q_m} 100 \tag{11}$$

where Q_m is the mixture flow (*i.e.*, discharge of fluid), C_o is a mixture loss constant, r_o is the ratio of voids to total area, a_o is the screen length, b_o is the screen width, V_m is the mixture velocity and α_o is the screen angle with the horizontal.

The proportion of material rejected by the oversize screen, $O_o\%$, for a particle of size d is computed from the aperture size (in microns) and the suction pipe diameter, D_s, (in metres) by the following empirical relationship

$$O_o\% = W_o\% + \left(\frac{d}{S_o}\right)^{w_o} m_o{}^{x_o} \left(\frac{Q_m}{4.32D_s^2}\right)^{y_o} \left(\frac{\rho_m}{1.2}\right)^{z_o} \times 100 \tag{12}$$

where S_o is the oversize screening aperture opening in microns, m_0 is the proportion of the sediment larger than the overscreen size, ρ_m is the mixture density and x_o, w_o, y_o and z_o are empirical constants (to be defined by the user on the basis of field data).

The mixture passing through the undersize screening process, W_u, is computed from

$$W_u = C_u r_u a_u b_u \left[\frac{a_u g}{2V_{m/o}} + V_{m/o} \sin(\alpha_u)\right] \tag{13}$$

where the equation symbols have similar meaning to those of Eq. 10 except that they now pertain to undersize screening and $V_{m/o}$ is the mixture velocity after over-size screening (equal to V_m if there is no over-size screening).

The percentage of incoming mixture passing through, $W_u\%$, is then given by

$$W_u\% = \frac{W_u}{Q_o} \times 100 \tag{14}$$

The proportion of material collected (passing over) by the undersize screen, $O_u\%$, for a particle of size d is given by

$$O_u\% = 100 - W_u\% + \left(\frac{d}{S_u}\right)^{w_u} m_u{}^{x_u} \left(\frac{Q_o}{4.32D_s^2}\right)^{y_u} \left(\frac{\rho_o}{1.2}\right)^{z_u} \times 100 \tag{15}$$

where S_u is the undersize screening aperture opening in microns, Q_o is the discharge after oversize screening (or Q_m if there is no oversize screening), ρ_o is the density of the mixture after oversize screening (or ρ_m if there is no oversize screening), m_u is the proportion of material smaller than the underscreen size and x_u , w_u, y_u and z_u are empirical constants (to be defined by the user on the basis of field data).

The dredger process model also calculates the release resulting from disturbance by the draghead as the difference between the amount of material disturbed and the amount of material sucked up by the draghead.

6.3 Overflow and screening release

The overflow and screening releases are independently predicted by the dredger process model and their initial behaviour is modelled by the dynamic plume model. At any point in the simulation of dredger plume dispersion there can be two dynamic plumes: one dynamic plume resulting from screening and a second dynamic plume resulting from overflow. The dynamic plume model is used to predict how much of each sediment fraction remains in suspension (and how it is distributed spatially) and how much deposited onto the bed at the point where the dynamic phase ends and the passive phase starts. This is discussed in more detail in Section 7.

6.4 Surface release

The phenomenon of air entrainment has been noted where the overflow and screening plumes impinge on the water surface when discharged from the dredger. This causes an upward current as the air escapes and rises to the surface dragging some of the finer sediment particles with it. There is also evidence that this surface plume is enhanced by the disintegration of benthic invertebrate organic tissue matter during the dredging process (US Minerals Management Service, 1998). The mass contained in this surface plum has generally been found to be small compared to the mass of the plume involved in the downward dynamic descent. The model allows for a user-defined proportion of the mass released from the dredger to be released at the surface.

6.5 Settling of sediment particles out of the dynamic plume

As the dynamic plumes from screening and overflow entrain ambient fluid and momentum, their vertical speed decreases, in some conditions to speeds less than the settling velocity of the coarser fractions contained within the plume. In this case these coarser sediment particles will start to settle out of the plume as it continues to descend. This mechanism is usually of minor consideration because the proportion of coarser fractions in trailer dredger overflow is generally small and any coarser particles released fall rapidly to the bed and contribute little to plume dispersion. Therefore, a simple representation of this mechanism is included in the model. The total amount of sediment settling out is calculated for each particle size fraction (by comparing the settling velocity with the vertical plume velocity). This sediment is then passed to the passive plume sub-model and distributed randomly over the entire path of the dynamic plume,

in this case schematised as a linear path. It is acknowledged that this representation may be very approximate in the case of screening plumes (composed of coarser sediment) in deep water if the deposition footprint of screened sediment on the bed is the main interest.

6.6 Particle release in the passive plume model

The nature of the different sources of release of sediment represented in the model is summarised in Fig. 5. In addition, for completeness and recognising the uncertainty surrounding dynamic plume mixing, a further source of release is provided. This allows for additional detrainment from the dynamic plume (through mechanism(s) different to those above - see Section 7.1) into the ambient waters along the length of the dynamic plume path.

On each release time step the passive plume model releases a user specified number of particles (each with mass decided by the process model, the dynamic plume model and/or the user). These particles are assigned to each of the sources represented in Fig. 5, depending on the relative mass release of each, and randomly throughout the volume of space represented for each release source.

For simpler characterisations of the dredge plume, the dynamic process can be switched off so that all the sediment sources outlined above are distributed evenly throughout the water column. This can be useful as an initial test to enable plume understanding or, in situations where vessel motion or propeller thrust are considered, to distribute most of the sediment released over the water column depth.

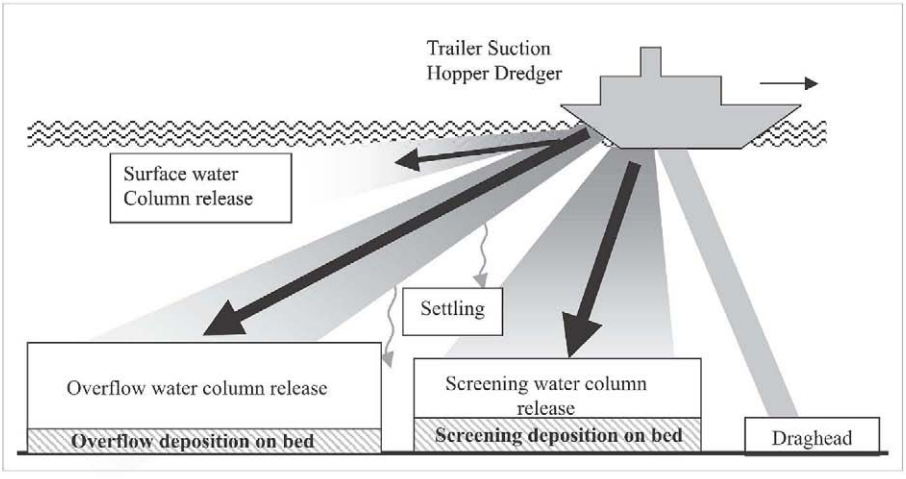

Fig. 5. Schematic summary of the different sources of sediment release represented by model system.

7. DYNAMIC PLUME MODEL

7.1 Descent of dynamic plume

The descent of the dynamic plume is reproduced using a Lagrangian technique whereby a thin disc (which can be thought of as a section of a bent cone) of the released dynamic plume is tracked as it moves downward under the forces of momentum and negative buoyancy. The technique has been used for both dredger plume and outfall plume modelling (*e.g.*, Koh and Chang, 1973; Brandsma and Divoky, 1976; and Lee and Cheung, 1990), though not for a moving source like the Trailer dredger which is the focus of this paper.

Entrainment of ambient water into the plume is modelled using the formulations of Lee and Cheung (1990) and accounts for both shear entrainment (*i.e.*, as occurs in jets and dominates the initial stages of the dynamic descent) and forced entrainment (which dominates in the latter stages of descent and is due to the flow of ambient water into the plume). The increase in mass due to shear entrainment, ΔM_s, is given by:

$$\Delta M_s = 2\pi\rho_a b_k h_k E \Delta t \left| V_k - u'_{amb} \cos\phi_k \cos\theta_k \right| \tag{16}$$

where

$$E = \sqrt{2}\,\frac{\left(0.057 + \dfrac{0.554 \sin\phi_k}{F^2}\right)}{\left(1 + 5\dfrac{u'_{amb}\cos\phi_k\cos\theta_k}{\left|V_k - u'_{amb}\cos\phi_k\cos\theta_k\right|}\right)} \quad \text{with} \quad F = \frac{\left|V_k - u'_{amb}\cos\phi_k\cos\theta_k\right|}{\left(g\dfrac{\Delta\rho}{\rho}b_k\right)^{1/2}} \tag{17}$$

and F is the local densimetric Froude number and is based on Schatzmann (1979; 1981), ϕ is the angle between the plume descent and the horizontal x-y plane, θ_k is the angle between the plume descent (as projected onto the x-y plane) and the x-axis, b_k is the radius of the dynamic plume element at time step k, h_k is the thickness of the dynamic plume element, ρ is the density of the plume, V_k is the speed of the dynamic plume element, ρ_a is the density of the ambient sea water, $\Delta\rho = \rho - \rho_a$, Δt is the time step, and u'_{amb} is the current speed (in the coordinate system moving with the dredger) of the ambient fluid. The formula suits a wide range of flows and gives the correct buoyancy for a pure jet (no buoyancy just momentum) and a pure plume (no initial momentum, just a density difference) (Lee and Cheung, 1990).

Lee and Cheung (1990) also derived an equation for forced entrainment arising in a three dimensional trajectory as follows:

$$\Delta M_k = \rho_a u'_{amb} h_k b_k \left[2\sqrt{\sin^2\phi_k + \sin^2\theta_k - (\sin\phi_k \sin\theta_k)^2} + \pi \frac{\Delta b_k}{\Delta s_k} \cos\phi_k \cos\theta_k \right. \quad (18)$$

$$\left. + \frac{\pi}{2} b_k \frac{(\cos\phi_k \cos\theta_k - \cos\phi_{k-1} \cos\theta_{k-1})}{\Delta s_k} \right] \Delta t$$

where ΔM_k is the increase in plume mass due to forced entrainment, s_k is the distance travelled by dynamic plume in timestep k, and Δb_k is the change in plume radius, $b_k - b_{k1}$.

There are three different contributions to forced entrainment. The first term represents the forced entrainment due to the projected area of the crossflow while the second and third terms represent corrections due to the growth of the plume radius and the curvature of the trajectory (Frick 1984; Lee and Cheung, 1990). The descent phase is terminated either when the plume impinges on the bed or when the vertical (downward) speed becomes less than zero (as may happen in strongly stratified conditions) or when the dynamic plume becomes sufficiently diffuse that it becomes a passive plume.

It is sometimes postulated that material is detrained (or stripped) from the plume during the descent process. A distinction will be made here between sediment settling out of the plume when the plume descent slows (see Section 6.5) and detrainment by other means. The evidence for detrainment (by other means than particles settling out of the plume) principally comes from the following sources:

- The measured loss of sediment that occurs during the descent of sediment disposed at sea (of the order of a few percent, Land and Bray, 1998) which is attributed to stripping/detrainment. However other more plausible mechanisms have been highlighted for this loss of sediment, such as air entrainment (see below), or the low momentum, low density plume (that does not descend rapidly to the bed) produced near the end of the disposal process (Johnson *et al.*, 1993).
- The visible surface plumes that can often be seen from the air above trailer dredgers. Such plumes are thought to be a function of air entrainment into the discharged overflow, a result of some of the discharged sediment being captured in the resulting detrainment of the bubble plume, because elimination of

the air before discharge through use of valves, is known to greatly reduce the surface plumes.

- More recently the results of numerical modelling have suggested a small detrainment effect (*pers. comm.* Cees van Rhee, Ballast Ham Dredging, 2004) arising from mixing between the descending plume and the ambient water.

In physical terms the basic rule is that the less turbulent fluid (the ambient water) is entrained into the more turbulent fluid (the dynamic plume) and on this basis detrainment from the plume is expected to be generally small. There remains the possibility, however, that under some circumstances - as perhaps could happen for some dredgers in relatively high currents - the turbulence in the plume and in the ambient waters could be of the same order. In this case some mixing could be expected. The process has been included in the model through means of a user-defined proportion of the overflow discharge being distributed along the length of the dynamic plume descent path.

Two experiments were chosen for the calibration of the dynamic descent – Chu and Goldberg (1974) and Chu (1975). In these experiments, the plume was simulated by injecting dyed saline solution vertically downward/upward into a flume through a hypodermic needle/injection pipe. Conditions corresponded to Reynolds numbers of 2,500-11,000. Figure 6 shows a comparison of the model predictions of the path of the plume with the results of test 2001 from Chu and Goldberg (1974). In this particular test a dense fluid ($\Delta\rho$=115kg/m^3) was injected (at the surface) with an initial velocity of 0.3 cm/s while-the current of the ambient fluid in the channel was u_{amb}' = 0.04 cm/s. The observations and model predictions of vertical height, Z, and horizontal distance X of the plume are scaled with respect to the buoyancy length scale, l_b, given by,

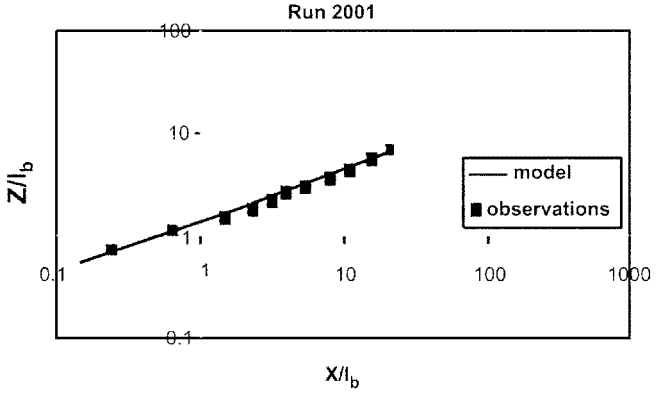

Fig. 6. Comparison of dynamic plume model with the results of Chu and Goldberg (1974).

$$l_b = \frac{4F_0}{\pi \rho_a u_{amb}^3} \tag{19}$$

where F_0 is the buoyancy flux, $F_0 = {}^1/_4\ \pi D^2 g(\rho - \rho_{amb})u_{amb}$, D is the initial diameter of the release, and u_{amb} is the current speed of the ambient fluid in the channel.

Figure 7 compares the model predictions of the path of the plume with the results from Chu (1975). The test consisted of the injection upwards near the bed of a 3% saline solution through an injection pipe of 1.0 cm diameter at 5 cm above the channel bottom. In this example (Test 5004) the initial discharge velocity of the dense fluid was 8.36 cm/s and the current speed of the ambient fluid in the channel was u_{amb} = 0.5 cm/s. The observations and model predictions of the vertical height, Z, and horizontal distance, X, are scaled by the diameter of the release (D = 1.0 cm) as given in Lee and Cheung (1990). More details regarding the validation of the model are given in Spearman *et al.* (in press) and US Minerals Management Service (2004).

7.2 Collapse on bed

7.2.1 Introduction

Collapse onto the bed is simulated using an equation attributed to von Karman. For dense thin layers, on a horizontal bed, the horizontal speed of propagation of the front of the resulting density current along the bed, is related to the thickness of the density current and the gravitational acceleration modified for buoyancy (Hallworth *et al.*, 1998).

Including friction, to first order in $\left(\frac{C_D x_f}{h_f}\right)$, yields,

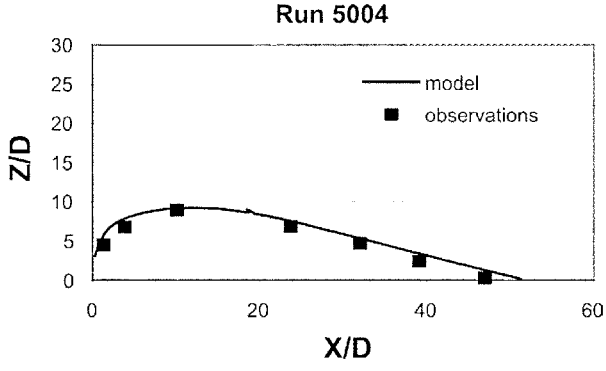

Fig. 7. Comparison of dynamic plume model with the results of Chu (1975).

$$u_f \approx F\left(\frac{g'h_f}{1+\frac{4C_D x_f}{7h_f}}\right)^{1/2} \tag{20}$$

where u_f is the horizontal speed of propagation of the front of the resulting density current along the bed, h_f is the thickness of the density current, $g' = g\Delta\rho/\rho$ is the gravitational acceleration modified for buoyancy, F is the Froude number of the flow, taking a value of approximately 1.19 (Huppert and Simpson, 1980), C_D is the drag coefficient and x_f is the half-length of the density current (from its centroid to the front of the current).

In the model the propagation of the current is achieved by repeated application of Eq. 20, assuming a flat or near flat bed level in the vicinity of the density current, keeping track of the concentrations of each sediment fraction in the plume and allowing the sediment particles to settle out continuously. A "box-model" approach has been used to describe the shape of the density current – *i.e.*, the density current height is assumed constant over the length of the density current. Box model approaches have been shown to give a good approximation to the collapse of the density current (Hallworth *et al.*, 1998). As the density current lengthens continuity of mass implies that the thickness of the density current reduces. All of the fractions are considered to be uniformly mixed, vertically and along the length of the current. Deposition onto the bed is calculated by keeping a running total of the deposition flux for each fraction from the density current. This sediment distributed over the bed following Bonnecaze *et al.* (1996), who developed the following equation for the total density of sediment deposited on the bed,

$$m_{bed}(x) = \rho_{part} A^{1/2} \sum_i \varphi_{i0} \beta_i^{2/5} W(\beta_i^{2/5} x / A^{1/2}) \tag{21}$$

where x is the distance from the point of impact, A is the initial cross-sectional area of the plume (equal to l_0h_0 where l_0 and h_0 are the initial length and depth of the density current), W is given by $W(x) = 0.820/(1 + 0.683x^2 + 0.017x^8)$, ρ_{part} is the density of the particulate plume, φ_{i0} is the initial volume of the *ith* sediment fraction expressed as a proportion of A, β_i is given by $ws_i/\left(g_0'^{1/2}A^{1/4}\right)$ and w_{si} is the settling velocity for particles of the *ith* sediment fraction.

The settling rate is calculated using Soulsby's (1997) formula for particles greater than 62 microns (fine sand and bigger) in size,

$$w_s = \frac{\upsilon}{d}\left[\left\{10.36^2 + 1.049D_*^3\right\}^{1/2} - 10.36\right] \text{ where } D_* = \left[\frac{g(s-1)}{\upsilon^2}\right]^{1/3} d \tag{22}$$

where ν is the kinematic viscosity of water, s is the specific gravity of the sediment particle, and d the particle diameter. Note that Soulsby's formula represents settling in open waters whereas Eqs. 1 to 6 relate to settling tank conditions. For particles less than 62 microns in size (silt sized and smaller) the common power law relationship depending on concentration is used (*e.g.*, Whitehouse *et al.*, 2000) which represents the process of flocculation by increasing settling velocity with concentration,

$$w_s = aC^b \tag{23}$$

where a and b are user defined empirical constants determined from field data.

The bed collapse phase ends when the turbulence within the density current has reduced sufficiently to allow mixing with ambient waters at which point the density current can be regarded as a passive plume. This criterion is based on the work of Akar and Jirka (1994) who show that for a density current at this critical point the flux Richardson Number, R_f, can be approximated as,

$$R_f = \frac{-g\dfrac{\partial \rho}{\partial z}}{\rho\sigma_s\left(\dfrac{\partial u}{\partial z}\right)^2} \approx \kappa^2 \frac{g'h_f}{u_*^2} = 0.15 \tag{24}$$

where σ_s is the turbulent Schmidt number and u_* is the friction velocity. Note that the use of this criterion means that the effect of buoyancy damping is included in the dynamic plume collapse. The additional effect of including concentration-induced turbulent (or "buoyancy") damping in the passive plume phase is investigated in Section 9.

The experiments chosen for the validation (Fig. 8) of the collapse of two-dimensional dynamic plumes resulting from impact on the bed are those undertaken by Hallworth *et al.* (1998). The figure relates to a particulate density current (*i.e.*, suspended sediment) generated by releasing water containing silicon-carbide particles of size 37μm with an initial plume excess density above the ambient water of 100kg/m^3. For details see Spearman *et al.* (in press) and in US Minerals Management Service (2004).

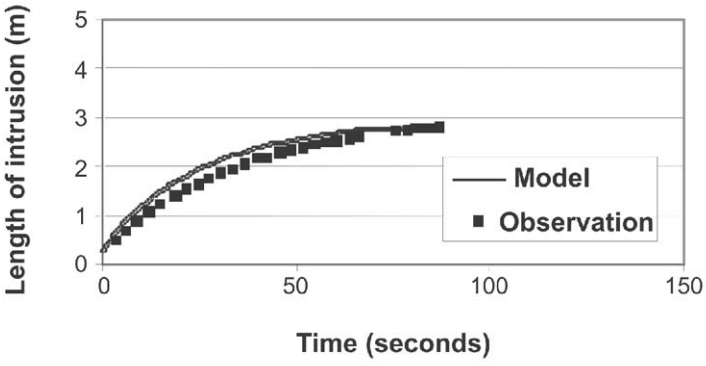

Fig. 8. Comparison of bed collapse model prediction of progress of density current front over time with the results of Hallworth *et al.* (1998) for particulate currents.

7.3 Dynamic collapse

Dynamic collapse occurs in stratified situations where the dynamic plume does not impact the bed but becomes positively buoyant as its initial momentum takes it past the level of neutral buoyancy. The plume centroid will then rise and oscillate towards the level of neutral buoyancy. Unlike the bed collapse scenario for dynamic collapse scenarios there is a marked difference in density between the top and bottom extremities of the plume.

For dynamic collapse, a "box-model" approach has been used to describe the shape of the density current. The density current height is assumed constant over the length of the density current. Entrainment and friction are neglected.

8. PASSIVE PLUME MODEL

The passive plume sub-model is the random walk dispersion model, SED-PLUME-RW(3D) developed by HR Wallingford. This model is described briefly below with details in US Minerals Management Service (2004).

The release of sediment is represented as the introduction of discrete particles which are advected by 3D flows and subject to turbulent diffusion, represented as random displacements from the advective motion. The effects of shear dispersion (which in general are much greater than turbulent diffusion) and stratification are included through the calculated depth structure in the mean current profile. The vertical diffusivity, K_z, is calculated by the model based on the 3D flow structure,

$$K_z = \kappa^2 z^2 \left(1 - \frac{z}{H}\right) \frac{\partial u}{\partial z} \left(1 + \beta R_g\right)^{\alpha} \tag{25}$$

where κ is the von Karman constant, z is the height of the particle above the bed, u is the current velocity, $\alpha = -0.5$, $\beta = 10$ and H is the water depth, and R_g is the gradient Richardson number,

$$R_g = \frac{-g \frac{\partial \rho}{\partial z}}{\rho \left(\frac{\partial u}{\partial z}\right)^2} \tag{26}$$

The settling velocity (w_s) of suspended mud is calculated using Eq. 23. Deposition occurs when particles reach the seabed and bed shear stress, τ_b, is below a user-defined threshold for deposition, τ_d. Erosion is modelled when τ_b exceeds a user-defined threshold for erosion, τ_e, using the formula,

$$\frac{\partial m_e}{\partial t} = M\left(\tau_b - \tau_e\right) \tag{27}$$

where m_e is the mass eroded, M is a constant governing the rate of erosion (Partheniades, 1965).

Note that buoyancy damping also reduces the shear stress experienced at the bed as well as the diffusion of sediment into the upper water column. The friction velocity acting on the bed, u_*, becomes $f.u_*$ where f is the eddy viscosity damping function in Eq. 25 (see Toorman, 2001, for a detailed discussion).

9. THE EFFECT OF DYNAMIC REPRESENTATION OF SOURCE TERMS: EXAMPLE CALCULATION

To illustrate the effect of representing trailer source terms dynamically on the resulting passive plume dispersion, we will compare the passive plume dispersion with a spatially uniform distributed source. To aid this illustration, we will assume steady-state source terms. Additionally we will illustrate the effect of including concentration-induced turbulent damping (henceforth referred to as "buoyancy damping") in the representation of passive plume dispersion on the resulting predicted concentration

increases and deposition. The example chosen is a dredger moving along a 3.6 km dredge path (at 0.5 m/s) in the opposite direction to a uni-directional current of 0.5 m/s (Fig. 9). Releases are simulated over a period of two hours and the simulation continues two hours after dredging ceases. The mean water depth is assumed to be 15 m. The discharge rate of sediment into the water column is arbitrarily assumed to be 100 kg/s, and for simplicity's sake all of this discharged sediment is assumed to be silt. The calculated fluid discharge is assumed to be 5 m^3/s and the overflow is assumed to be only from discharge via a central spillway mounted in the hull 7 m below the surface. The initial period during filling of the hopper where no release occurs was not included in the simulation.

The 3D flow model results represented the depth of the water column in 10 layers, resulting in nine layers of concentration output. Predictions for the uniformly distributed source term (henceforth referred to as "without the dynamic plume"), the dynamic source term (henceforth referred to as "with the dynamic plume") and the dynamic source term with the effect of concentration induced turbulent damping (henceforth referred to as "with the dynamic plume and buoyancy damping") are compared. The near bed (*i.e.*, the mean over the bottom 2 m) concentration at the end of dredging are compared in Fig. 10 and the corresponding predictions for surface concentration increases are shown in Fig. 11. A comparison of the predicted deposition (in kg/m^2) at the end of dredging is shown in Fig. 12. Note that the erosion threshold for erosion/deposition of sediment was arbitrarily set to 0.11 N/m^2 which, because of the 0.5 m/s current speed, prevented the simulation without the dynamic plume from predicting deposition. However, for simulations with the dynamic plume (with or without buoyancy), deposition occurred (Fig. 12) because the density current prevents the turbulent overlying waters from influencing the bed. Note that the deposition resulting from the dynamic plume is temporary. Eventually the density current produced by the dynamic

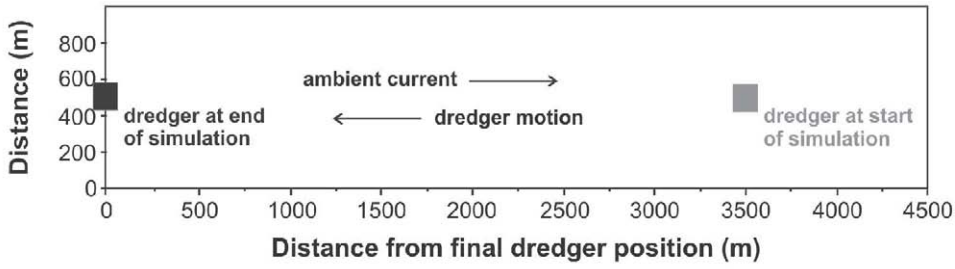

Fig. 9. Schematic layout of plume simulations.

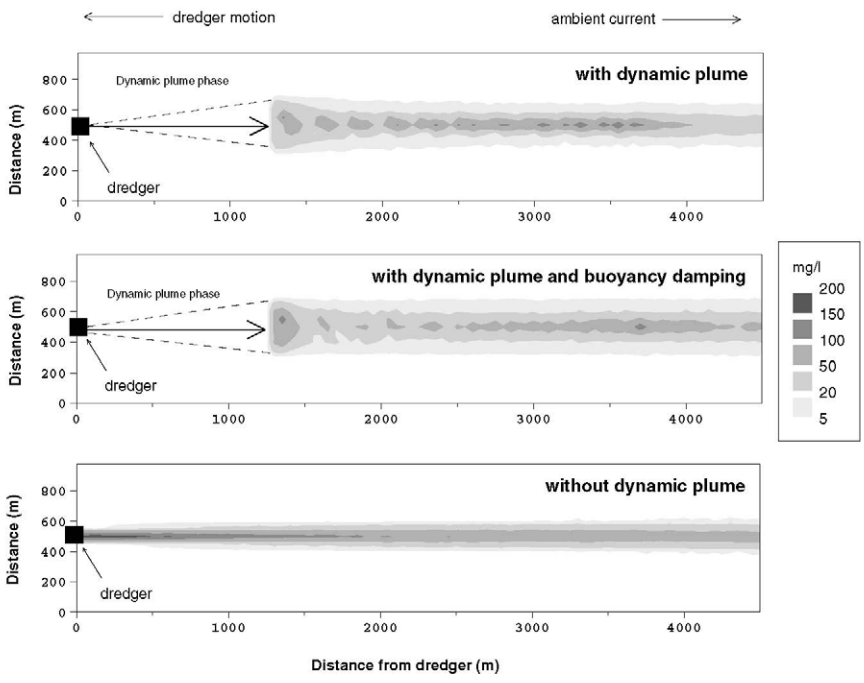

Figure 10. Comparison of predictions of near-bed concentration increases.

plume mixes with the overlying waters and the effect of the overlying turbulence is restored. Inclusion of buoyancy damping in the passive plume simulation reduces the rate at which the deposited material is re-eroded.

The simulation without the dynamic plume shows concentrations well-mixed throughout the water column (Figs. 10 and 11). Near bed concentrations reduce from around 180 mg/l in the vicinity of the dredger to around 80 mg/l at a distance of 3.5 km. The surface concentration decreases from 140 mg/l in the vicinity of the dredger to around 60 mg/l at a distance of 3.5 km. No deposition occurred during this simulation.

For the simulation with the dynamic plume but without buoyancy effects, the descent and collapse of the plume occur over the first kilometre "downstream" of the dredger (Figs. 10 and 11). Initially the width of the deposition/concentration footprint is around 120 m either side of the dredge. Along the dredge path, predicted near bed concentration increases above background from around 40-80 mg/l at about 1.3 km from the dredger to around 75-125 mg/l at a distance of 3.5 km or more. After this point concentration increases decline to 25 mg/l. The surface concentration increases rise 30

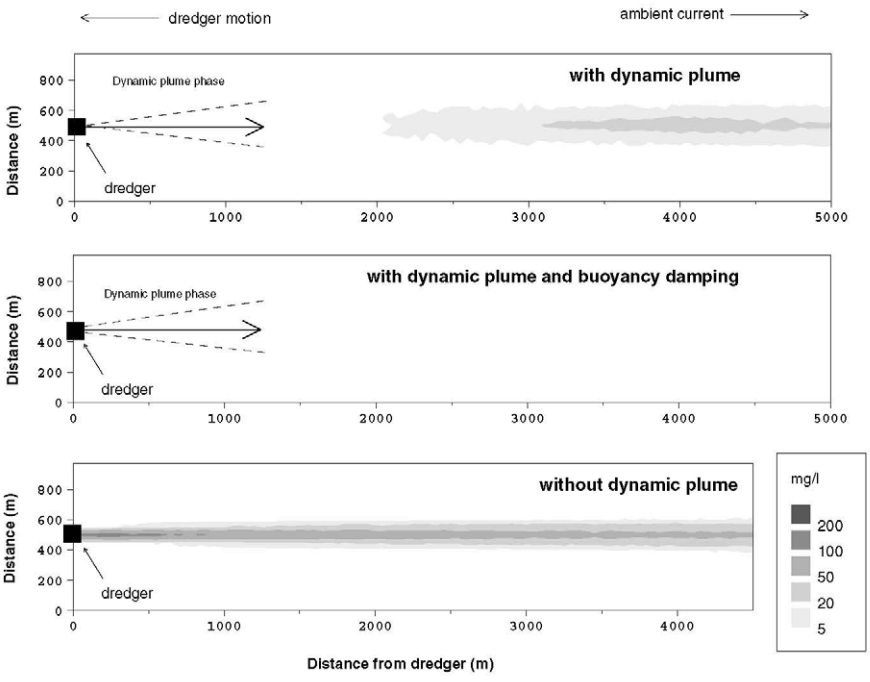

Figure 11. Comparison of predictions of surface concentration increases.

mg/l at a distance of 3.5 km declining after this point. All the sediment deposited on the bed by the dredging process is re-eroded within 2½ hours of the cessation of dredging.

For the simulation with the dynamic plume and buoyancy the dynamic plume phase again occurs over the first kilometer or so "downstream" of the dredger (Figs. 10 and 11). Near bed concentrations increase from around 60-100 mg/l at about 1.3 km from the dredger to 75-125 mg/l at a distance of 3.5 km from the dredger. Beyond this distance the predicted concentration increases decline to around 50-60 mg/l. This concentration is higher than that for the dynamic plume without buoyancy effects, reflecting the effect of turbulent damping preventing diffusion into the higher layers of the water column. Surface concentrations are less than 3 mg/l throughout the simulation. The peak mass of sediment deposited on the bed throughout the course of the simulation is around 15% more than that of the simulation without buoyancy effects and, moreover, sediment deposited on the bed by the dynamic plume process (for these current conditions) took 25% longer (over 3 hours) to re-erode.

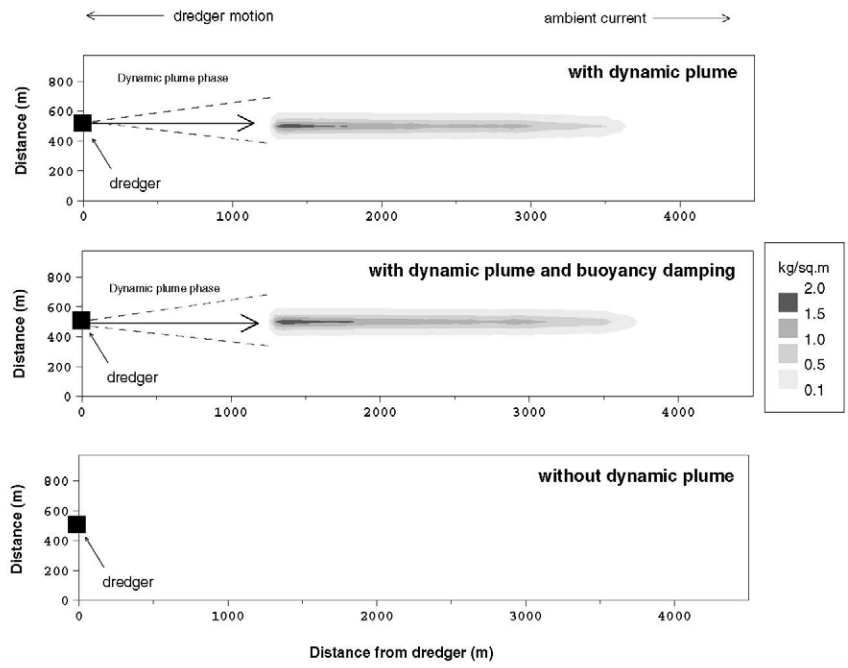

Figure 12. Comparison of predictions of bed deposition.

To illustrate the increasing effect of buoyancy damping as release rates of sediment from the trailer dredger increase, the simulation was repeated, doubling the overflow release rate (200 kg/s). The predicted near bed concentrations (Fig. 13) indicate that buoyancy damping reduces the average concentration in the 2 m above the bed by half than that predicted without buoyancy damping.

Figures 10 to 13 show that the distribution of the source term and the effect of buoyancy damping (on the passive plume) are both significant in determining the resulting behavior of the plume. In particular this example shows how the contribution of the overflow plume to increases in concentrations in the water column can be reduced considerably by the dynamic plume process but that this reduction in water column concentrations is accompanied by an increase in the footprint of deposition. Additionally it has been demonstrated that buoyancy effects further reduce water column concentrations, increase the amount of deposition on the bed and significantly increase the time taken to re-erode this sediment These examples simplify the effects of dredging by

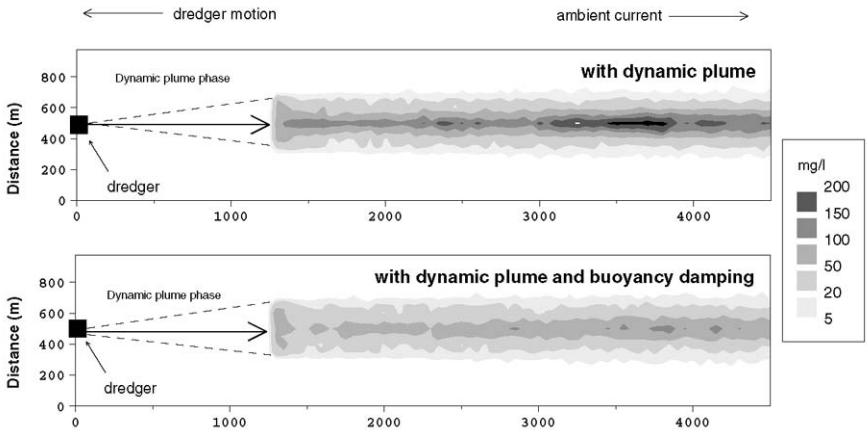

Figure 13. Effect of buoyancy damping on near bed concentrations for dredging with higher release rate.

neglecting the surface plume, draghead effect and propeller-induced resuspension, and moreover, only one sediment fraction has been modelled. However, the inclusion of these effects would not change the overall nature of the results. There would be additional sources of sediment (small in comparison to the main body of the plume) released from the dredger at the surface and the bed (which over time and distance would diffuse into the background). In this situation the behavior of a plume composed of different size fractions would be very similar because the plume would impact on the bed before coarser particles could settle out of the plume. Moreover, after deposition on the bed these coarser particles would contribute to the local sand transport regime rather than resuspend as a fine sediment plume.

Of particular relevance here is the action of turbulence generated by the dredger propeller. If the effect of the propeller is significant (as may occur in shallow waters) and if the dredging path is aligned with the flow, the propeller-induced turbulence will be sufficient to re-entrain some of the density current and/or deposited sediment. The resulting deposition and increase in concentrations in the water column will depend on the timing and dynamic plume footprint and the magnitude of the propeller turbulence. This area of study is recommended for further research.

10. FIELD EXPERIMENTS

As part of a series of studies for the VBKO dredging organisation, a recent field exercise took place at Rotterdam, Netherlands (HR Wallingford and DRL, 2004). Field measurements were undertaken while the Cornelia, a medium sized trailer dredger with a hopper capacity of around 6000 m^3, was underway dredging both sand and mud.

The analysis of the field data resulting from the Rotterdam experiment is still ongoing and a full assessment of the performance of the trailer plume dispersion model is not yet possible. However, we illustrate the usefulness of the data provided by the experiment by examining the ability of the model to reproduce the path of the dynamic plume as defined by the side scan sonar.

An example is shown in Fig. 14 corresponding to dredging in the approach channel to Rotterdam (the Maasgeul) at around 11:00am on 19 October 2002. The dredger is working in sand with a mud content of 0-30% with a under-keel clearance of about 16m. The sidescan sonar shows the leading edge of the plume (shown as a shaded area edged by black dots) and indicates that the plume hits the bed 50m away from the point of release. A prediction of the leading edge of the plume using the trailer plume model was made using the recorded concentrations for the time of release, estimates of the rate

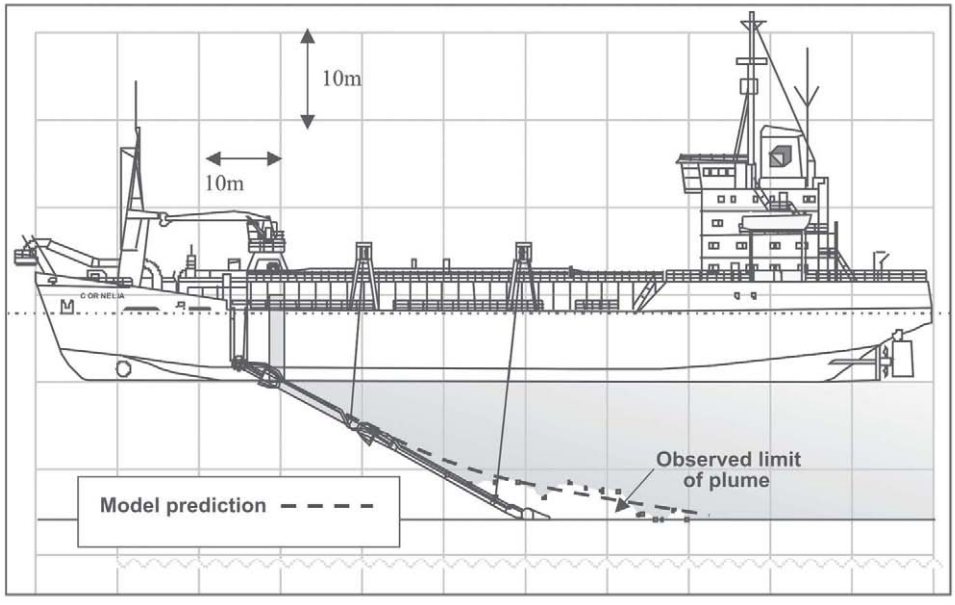

Fig. 14 Predicted and observed path of lower edge of the dynamic plume, example from the Rotterdam field experiment.

of discharge of water from the dredger and the ambient current velocity. The example shows the model successfully reproduces the descent of the dynamic plume. Although this single example does not serve to validate the model, it does suggest that the model is a reasonable framework from which to explore further validation studies.

11. CONCLUSIONS

This paper has described the development of a dispersion model of a trailer hopper suction dredger incorporating the processes occurring in the dredger itself, and in the near-field and far-field zones. The model has been developed as a result of the need for a predictive approach based on a better representation of the physical processes involved.

The model has been validated where possible using existing laboratory data. However it is clear that in order to build confidence in the model predictions comparison with field data is required. A review of the data currently available has indicated that the data is not of a sufficient standard for this task. Although the model has not yet been formally compared to the data from the recent Rotterdam field trial, initial tests indicate that the model performance is promising.

For this paper the model has been enhanced by the inclusion of buoyancy damping in the passive plume component. As well as highlighting the importance of the effect of the dynamic plume in the dredger source term, the results indicate that the effect of buoyancy damping in the passive plume is also significant, particularly for dredging operations with higher release rates of fine sediment.

REFERENCES

Akar, P.J. and G.H. Jirka. 1994. Buoyant spreading processes in pollutant transport and mixing. Part 1: Lateral spreading with ambient current advection. *Journal of Hydraulic Research*, 32(6), 815-831.

Anderson, E., B. Johnson, I. Isaji and E. Howlett. 2001. SSFATE, a model of sediment movement from dredging operations. *Proceedings of the 16th World Dredging Congress and Exhibition (WODCON XVI)*, Eastern Dredging Association, Hamilton Central, Australia, 2(6B), (9 pages).

Bonnecaze, R.T., H.E. Huppert and J.R. Lister. 1996. Patterns of sedimentation from polydispersed turbidity currents. *Proceedings of the Royal Society of London*, 452, 2247-2261.

Brandsma, M.G. and D.J. Divoky. 1976. *Development of models for prediction of short-term fate of dredged material discharged in the estuarine environment.* Contract Report D-76-5, US Army Engineer Waterways Experiment Station, Vicksburg, MS, prepared by Tetra Tech, Inc., Pasadena, CA.

Camp, T.R. 1946. *Sedimentation and the design of settling tanks.* Transactions, ASCE, 111, 895-936.

Chu, V.H. 1975. Turbulent dense plumes in a laminar cross flow. *Journal of Hydraulic Research*, 13(3), 263-279.

Chu, V.H. and M.B. Goldberg. 1974. Buoyant forced plumes in cross flow. *Journal of Hydraulic Division*, ASCE, HY9,1203-1214.

Dearnaley, M.P., J.R. Stevenson and J. Spearman. 1999. *Environmental aspects of aggregate dredging, refined source terms for plume dispersion studies.* HR Wallingford Report SR 548.

Electricité de France. 1998. *Code TELEMAC-3D-Version2.2, Manuel de Utilisateur.* Report HE-42/97/048/B, Department Laboratoire National d'Hydraulique, Electricité de France (in French).

Frick, W.E. 1984. Non-empirical closure of the plume equations. *Atmospheric Environment*, 18(4), 653-662.

Hallworth, M.A., A.J. Hogg and H.E. Huppert. 1998. Effects of external flow on compositional and particle gravity currents. *Journal Fluid Mechanics*, 359, 109-142.

HR Wallingford and DRL. 1999. *Model development for the assessment of turbidity caused by dredging.* Volume 1, Technical Report, HR Wallingford Report, EX 3998.

HR Wallingford and DRL. 2004. *Report on the TASS measurement of sediment release from the THSD Cornelia, Rotterdam, June 2002.* Report prepared by HR Wallingford and DRL for VBKO.

Huppert, H.E. and J.E. Simpson. 1980. The slumping of gravity currents. *Journal of Fluid Mechanics*, 99, 785-799.

Johnson, B.H., D.N. McComas, D.C. McVan and M.J. Trawle. 1993. *Development and verification of numerical models for predicting the initial fate of dredged material disposed in open water, Report 1: Physical model tests of dredged material disposal from a split-hull barge and a multiple bin vessel.* Dredging Research Program Technical Report DRP-93-1, Waterways Experiment Station, USACE, Vicksburg, Mississippi, USA.

Koh, R.C.Y. and Y.C. Chang. 1973. *Mathematical model for barged ocean disposal of waste*. Technical Series EPA 660/2-73-029, US Environment Protection Agency, Washington D.C.

Land, J. and R.N. Bray. 1998. Acoustic measurement of suspended solids for monitoring of dredging and dredged material disposal. *Proceedings of the 15th World Dredging Congress (WODCON XV),* Western Dredging Association, Vancouver, 1, 105-120.

Lee, J.H.W. and V. Cheung. 1990. Generalized lagrangian model for buoyant jets in current. *Journal of Environmental Engineering*, 116(6), 1085-1106.

Luettich, R.A. Jr. and J.J. Westerink. 2004. ADCIRC, A (parallel) advanced circulation model for oceanic, coastal and estuarine waters. Available at: http://www.marine.unc.edu/ _CATS/adcirc/document/ADCIRC_main_frame.html.

Nagai, O. 1978. Turbidity generated by dredging projects, Management of bottom sediments containing toxic substances. In: *Report EPA-600/3-78-084*, Peterson S.A. and K.K. Randolph (eds.), US EPA Office of Research and Development, Corvallis Environmental Research Laboratory, Corvallis, OR, 31-47.

Partheniades, E. 1965. Erosion and deposition of cohesive soils. *Journal of the Hydraulics Division*, ASCE, 91, 105-138.

Pennekamp. J.G.S., R.J.C. Epskamp, W.F. Rosenbrand, A. Mullié, G.L. Wessel, T. Arts and I.K. Deibel. 1996. Turbidity caused by dredging, viewed in perspective. *Terra et Aqua*, 64, 10-17.

Schatzmann, M. 1979. Calculation of submerged thermal plumes discharged into air and water flows. *Proceedings of the 18th International Association of Hydraulic Engineering and Research (IAHR) Congress,* IAHR, Madrid, 4, 379-385.

Schatzmann, M. 1981. Mathematical modelling of submerged discharges into coastal waters. *Proceedings of the 19th International Association of Hydraulic Engineering and Research (IAHR) Congress*, IAHR, Madrid, 3, 239-246.

Soulsby, R.L. 1997. *Dynamics of marine sands*. Thomas Telford Publications, London.

Spearman, J., R.N. Bray and T.N. Burt. In press. Dynamic representation of trailer dredger source terms in plume dispersion modelling. *Proceedings of the Central Dredging Association (CEDA) Dredging Days, 2003*, held in Amsterdam, 20-21 Nov. 2003.

Toorman, E.A. 2001. *Drag reduction in sediment-laden turbulent flow*. Report HYD/ET/00/COSINUS5, Report to Task A1 of the COSINUS project, Hydraulics Laboratory, Katholieke Universiteit, Leuven.

US Minerals Management Service, 1998. *Marine Aggregate Mining Benthic and Surface Plume Study*. Report prepared for the US Minerals Management Service, ARC Marine Ltd, South Coast Shipping Ltd., United Marine Dredging Ltd. and HR Wallingford Ltd., Published online by the US Minerals Management Service, available at http://www.mms.gov/sandandgravel/Aggregatestudies.htm

US Minerals Management Service. 2004. *Development of the MMS Dredge Plume Model*. Report prepared for the US Minerals Management Service by Bairds and Associates, Dredging Research Ltd. and HR Wallingford, available at http://www.mms.gov/sandangravel/PDF/MMS%20Plume%20 Model%20Technical % 20Report%20% 20Final.pdf

van Rhee, C. 2002. Modelling the sedimentation process in a trailer hopper dredger. *Terra et Aqua*, 86, 18-27.

Vlasblom, W.J. and S.A. Miedema.1995. A theory for determining sedimentation and overflow losses in hoppers. *Proceedings of the 14th World Dredging Congress (WODCON XIV)*, Central Dredging Association, Delft, 1, 183-202.

Whitehouse, R., R. Soulsby, W. Roberts and H. Mitchener. 2000. *Dynamics of estuarine muds*. Thomas Telford, London.

Winterwerp, J.C. 1999. On the dynamics of high-concentrated mud suspensions. Ph.D. Dissertation, Delft University of Technology, Delft, the Netherlands.

Whiteside, P.G.D., K. Ooms and G.M. Postma. 1995. Generation and decay of sediment plumes from sand dredging overflow. *Proceedings of the 14th World Dredging Congress (WODCON XIV)*, Central Dredging Association, Delft, 2, 877-892.

Estuarine and Coastal Fine Sediments Dynamics
J.P.-Y. Maa, L.P. Sanford and D.H. Schoellhamer (editors)

Modeling fine sediment resuspension due to vessel passage

Parchure, T.M., J.E. Davis and R.T. McAdory

U.S. Army Engineer Research and Development Center, Vicksburg, MS 39180

KEY WORDS
Recreational boating, inland navigation, vessel-generated waves, wave-induced erosion, environmental impact, sediment resuspension

Several types of recreational boats are in use, which generally ply at high speed in shallow near-bank areas in restricted waterways. They have a high frequency of passage in popular areas. They generate wake waves, which may cause sediment resuspension and bank erosion. Adverse biological effects of increased sediment in suspension include suppression of growth of Submerged Aquatic Vegetation (SAV) and mortality of fish. Suspension concentration caused by a series of recreational boats is examined in this paper. The study provides time-series of suspended sediment concentrations related to frequency of boat passage events. These time series estimates can be used in ecological models for evaluating the impact of suspended sediments on SAV and other light-sensitive or turbidity-sensitive biota in shallow near-shore zones.

Analytical model algorithm VESTUNS developed at the University of Florida was used to compute sediment resuspension and deposition using a schematic wave series as input. Field data on vessel type, vessel speed, vessel-induced sediment-suspension concentration, wave heights, and sediment type were used for model verification. The wave-induced bed shear stress was calculated from available equations. Outputs included the net amount of sediment in suspension. Time-series of suspended sediment concentrations are presented for 30 cm wave height for boat intervals of 1, 5, 10, 20, 30 and 60 minutes between consecutive boat passages over a total duration of 6 hours. It was noted that the equilibrium and maximum sediment concentrations decrease with lower frequency of vessels.

1. INTRODUCTION

Wave induced resuspension has been examined in the field (Sanford, 1994) and in the laboratory (Maa and Mehta, 1987). However, effect of vessel-induced waves on sediment resuspension has not been adequately examined. A variety of vessels navigate in open sea and inland areas. These include ships such as oil carriers and bulk cargo carriers, barges, naval vessels, and recreational boats. While all of these produce waves, vessels navigating in restricted inland water bodies and channels generate waves that are significant in the context of bank erosion. Several classes of recreational boats are in use, which include sailboats, fishing boats, pontoon boats, jet skis, medium powerboats, larger cruisers and houseboats. The recreational boats ply at relatively high speed mostly in shallow water near the banks and may cause significant bank erosion resulting from wake waves. Sorensen (1998) has described wake wave characteristics. These characteristics depend upon hull shape, size, weight, water-depth and boat speed. When the speed increases, bow, stern, and transverse waves develop, leaving a characteristic set of wake waves. The pattern consists of symmetrical sets of diverging bow and stern waves that move obliquely out from the sailing line, and a single set of transverse waves that move in the direction of the sailing line. The highest waves in the pattern are found along the cusp line. Study of wave-induced sediment resuspension resulting from passage of several recreational boats is described in this paper. The study was conducted for the Upper Mississippi River system. Parchure *et al.*, have given the details in a report (2001b).

2. IMPACT OF VESSEL-INDUCED SEDIMENT RESUSPENSION

The environmental aspects of boat traffic motivated the present study. Physical disturbances by boat traffic include sediment resuspension and bank erosion resulting in the loss of benthic and riparian habitat in adjacent areas. Parchure *et al.* (1996) described the effect of wave-induced resuspension of fine sediment on water quality in the near-shore zone. Fine flocculated sediment particles have a large specific surface area and the primary particle size is typically less than 4 microns. Hence a few grams of fine sediment eroded from the bed or bank may suspend millions of particles causing a greater underwater light attenuation than sand particles having the same total weight. Freshly deposited fine sediment particles are susceptible to erosion by relatively small shear forces. The free settling velocity of a 2 micron-size particle in still water is about 0.0024 mm/s. Also natural turbulence in water bodies provides a vertical uplift force

against gravity. A sand particle of 0.2 mm size has a fall velocity of about 20 mm/s. Hence, once suspended, well-dispersed individual fine particles may stay in suspension for days or weeks compared to seconds or minutes for suspended sand particles. Biological effects resulting from sediment resuspension include suppression of growth of Submerged Aquatic Vegetation (SAV) and mortality of fish by clogging of gills by fine sediments in suspension (Kemp *et al.*, 1983; Orth and Moore, 1983).

The objective of present study was to provide time-series of suspended sediment concentrations correlated to wake wave height and frequency of boat passage events. These time series estimates can be used in ecological models for evaluating the impact of suspended sediments on SAV and other light-sensitive or turbidity-sensitive biota in shallow near-shore zones.

3. RESUSPENSION ALGORITHM AND COMPUTATIONS

A PC-based sediment erosion model VESTUNS developed by Mehta and Li (1996) was used in this study. The model uses a one-dimensional (vertical) numerical solution of the convection diffusion equation to compute the vertical profile of suspended sediment. It accounts for sediment settling and deposition plus erosion from the bed and upward diffusion by short period waves and/or a superimposed current. Natural mud is a mixture of fine sediments, organic particulates of plants and animals as well as inorganic particulates of varying sizes. The model assumes the bed to be formed of mud with significant quantities of cohesive material.

The present study was conducted in the context of determining the environmental impact of vessel traffic along the Upper Mississippi River Project. Several-mile long riverbanks of this region consist of a broad range of sediments from clays to pebbles. The objective of study was to estimate resuspension of fine sediment only from the identified reaches where they existed predominantly because only fine sediments in suspension result in environmental impact on aquatic plants and animals. Hence the algorithm written with fine sediment equations was appropriate for the study.

Sediment remains in suspension when the amount of sediment eroded is greater than the amount settled out. Hence computation of suspension concentration involved determining the amount of sediment eroded from the bed due to vessel-wave-induced shear stress, its vertical diffusion within the water depth and the amount of sediment deposited under low shear stress condition.

The algorithm includes use of several mathematical equations related to diffusion under waves, fall velocity of sediment particles, gradient Richardson Number, erosion

and deposition flux, current friction factor, wave friction factor, depth-averaged current velocity, critical shear stress for erosion, wave-induced bed shear stress, and erosion rate expression for cohesive sediments. Parchure *et al.* (2001a) and Knight and Parchure (2004) have given details of all the equations used. Only the relevant erosion and settling equations are described below.

The following erosion rate equations were used. Values of coefficients used for the study are given.

$$Fn = \begin{cases} -W_s\, C_{bed}\left(1-\dfrac{\tau_b}{\tau_d}\right) & for \quad \tau_b \leq \tau_d \\ 0 & for \quad \tau_d < \tau_b < \tau_e \\ +s(\tau_b - \tau_e) & for \quad \tau_b > \tau_e \end{cases} \tag{1}$$

Fn = erosion rate (kg/m^2/s), W_s = settling velocity (m/s), τ_b = bed shear stress (Pa); τ_d = critical shear stress for deposition (Pa), determined by experiment; τ_e = critical shear stress for erosion (Pa); C = suspension concentration (kg/m^3); s = empirical aparemeter representing characteristic erosion rate constant, given by

$$s = s_{\max} e^{-a_r(\tau_e)^b} \tag{2}$$

s_{max} = empirical coefficient (0.2); a_r = empirical coefficient (8.0); b = empirical coefficient (0.5); τ_e = critical shear stress for erosion by waves, given by

$$\tau_e = \alpha_e\, (\phi - \phi_e)^{\beta_e} \tag{3}$$

α_e = wave diffusion constant (12.0); β_e = empirical coefficient (1.0); ϕ = solids weight fraction; ϕ_e = critical value below which mud behaves like fluid (0.05).

Settling velocity of fine-grained sediments significantly varies with sediment concentration in suspension. Hence a single value of settling rate cannot be used when suspension concentration is continually changing with time. The relationship between settling velocity and suspension concentration has three zones, namely free settling, flocculated settling and hindered settling. The following equation gives a combined relationship for the flocculated and hindered settling regions developed by Hwang

(1989). Values based on settling column experiments that were used for the coefficients are also given. The VESTUNS algorithm computes settling velocity as a function of time and suspension concentration.

$$W_s = \begin{cases} W_{sf} & C < C_{sf} \\ \dfrac{a\,C^{m_1}}{(C^2 + b^2)^{m_2}} & C > C_{sf} \end{cases} \tag{4}$$

W_s = sediment settling velocity; W_{sf} = Free settling velocity of sediment, determined by experiment (0.02 mm/s); a = empirical coefficient (0.16); b = empirical coefficient (7.0); C = sediment mass concentration (kg/m^3); m_1 = empirical coefficient (1.5); m_2 = empirical coefficient (1.33); C_{sf} = upper concentration limit on free settling, typically between 0.1 and 0.3 kg/m^3.

4. INPUT PARAMETERS

4.1. Wave parameters

Vessel-generated wave characteristics are the main input among various input parameters. Recreational vessels vary widely in their size, shapes of bow and keel, weight, width, configuration and so on. Knight (1999) has reported wave height predictive techniques for commercial tows. A wave height prediction model for each class vessel was beyond the needs of the study. Also, literature study and analysis of available data (Knight and Parchure, 2004) showed that there were no apparent differences in the number of waves and their periods between classes of recreational vessels. It was therefore considered sufficient to establish a generic time series representation of the wake wave train. All boat waves have a specific pattern. Wave height increases rapidly as a vessel passes by, followed by a slow decay with time and distance from the vessel. Bhowmik *et al.* (1991) observed that an individual recreational boat generated about 12 to 15 wake waves. The median duration of these events was 20 to 26 seconds. Based on observed data (example shown in Fig. 1), a schematic time series pattern for recreational boat wake waves was developed, which is shown in Fig. 2. It has 12 waves of varying heights but a constant wave period of 2 seconds. This wave series was used in computing wave-induced sediment suspension. Beginning with 2 cm waves, the peak height was attained in 3 waves, dropping to 4 cm over the next 3 waves and then con-

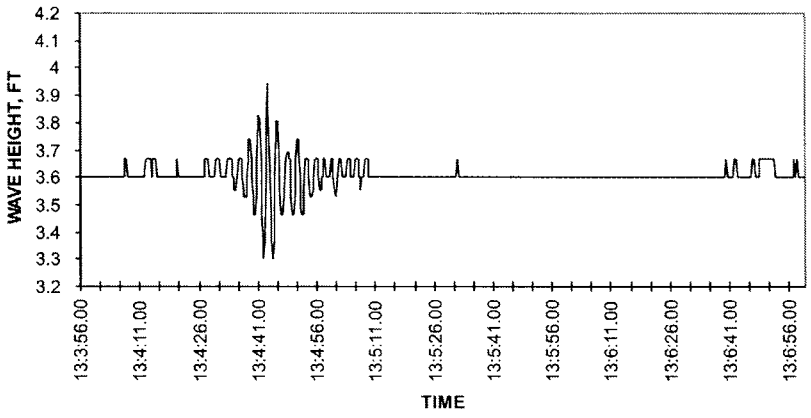

Fig. 1. Observed pattern of waves generated by recreational boat.

tinuing at 4 cm for the remainder of the 6 waves. The generic time history presented in Fig. 2 can represent the pattern for all classes of vessels by changing the maximum expected wave height.

Passing of one recreational boat near a specific site under investigation is considered one event. Each event consists of propagation of a series of waves of different heights. It was assumed that the series has only one wave with the maximum wave height with several waves of lesser height before and after the maximum height. It was also assumed that the wave train of varying heights is represented by and correlated to a single parameter, namely the maximum wave height.

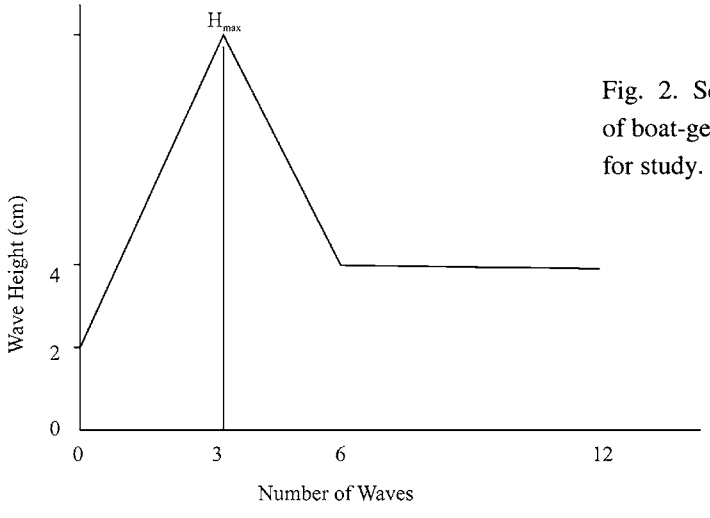

Fig. 2. Schematized pattern of boat-generated waves used for study.

4.2. Channel parameters

While the plan and profile shapes of the near-shore area contribute to the propagation, attenuation and breaking characteristics of the wave and its effects on sediment resuspension, the VESTUNS model is an approximation based on one dimension (vertical) and therefore, only requires depth as an input. While the model is capable of accepting multiple depths, all computations were performed in this study for the near-shore conditions with a water depth of one meter. The value of 1m as the Upper Mississippi River System (UMRS) system parameter was selected by the biologists at the US Army Engineer Rock Island District as the critical depth for aquatic habitat areas. The District biologists had determined that both submerged aquatic macrophytes and other benthic organisms in this zone are sensitive to light variations and thereby sediment resuspension. The depth of 1 m was given to the authors for the present study and was used along the entire UMRS in the Geographical Information System to delineate these critical ecological areas.

4.3. Sediment parameters

Parchure *et al.* (2001a) have suggested a new procedure for classifying sediment beds based on their erodibility. These were termed as soft, medium and hard in the increasing resistance to erosion. The erosional properties of bed and bank sediment must be known and provided to the numerical model as input for calculating erosion. At present there is no analytical procedure available for obtaining the exact values of the critical shear stress for erosion, vertical variation of bed shear strength and the rate of erosion as a function of bed shear stress, even if values of some of the sediment bed properties are available. These need to be determined experimentally either in the field or in a laboratory. The "soft" sediment that were considered susceptible to erosion in this study had a bulk density of 1600 kg/m^3, Critical shear stress of 0.021 Pa, and erosion rate constant of 6.27 g/m^2/min.

4.4. Traffic frequency for multiple events

Since the traffic of large vessels and towboat has a relatively low frequency of passing in a river or canal, evaluation of single events is appropriate and practical. On the other hand, in certain reaches, which are very popular for recreation, the number of recreational boats on popular summer holidays can be very high. In studies conducted by the Illinois State Water Survey, Bhowmik *et al.* (1991) observed up to 120 boats per hour during a busy holiday at a recreational boating site on the UMRS. The actual random combinations of different vessel types and inter-arrival times would result in infinite combinations of wave series inputs. The study was simplified by considering the

wave heights of constant wave period, occurring at fixed intervals instead of considering the class of vessels that generated waves of different heights and periods at random intervals. Wave inputs were prepared for sequencing boats to pass a location at intervals of 1, 5, 10, 20, 30, and 60 minutes.

The time series of waves along with inputs on channel and sediment parameters are provided to the VESTUNS model, which calculates the wave-induced bed shear stress. Erosion rate is then calculated by using values of sediment-related parameters, wave-induced bed shear stress, critical shear stress for erosion, and erosion rate constant. When the bed density is known, the thickness of eroded layer can be calculated, which is then used to calculate the volume of sediment brought in suspension per unit of time. During the initial stage of erosion, the rate of erosion is higher than the rate of sediment deposition. Later on the two rates balance each other resulting in an equilibrium suspension concentration. Parchure *et al.* (2001b) have developed and applied this methodology and model for estimating wave-induced sediment resuspension caused by towboats plying in Mississippi River.

5. MODEL VERIFICAITON

The authors conducted wave-induced sediment resuspension study for passage of towboats (also called barges) in Mississippi River (Parchure *et al.*, 2001b.) The algorithm and procedure used were the same as those used in the present study related to passage of recreational boats but the passage of one towboat generates 200 waves as against 12 waves generated by passage of recreational boats, which are much smaller than tow boats. The maximum wave height may be the same for both types of vessels. Field data collected in 1995-1996 in the UMRS (Fagerburg and Pratt 1998) were used for model verification. The data were collected for towboat traffic. Parameters measured in the field included vessel type, vessel speed, vessel-induced sediment-suspensions concentration, wave heights and sediment type. Suspension concentrations recorded at three depths after the passage of towboats were within the following ranges: Pool 8: 50-70 mg/l, Pool 26: 96-122 mg/l, La Grange: 180-400 mg/l. These data were collected at 53 locations, in different water depths and sediment compositions for a variety of vessels. The measured maximum wave height in uncontrolled tests of commercial vessels was 12 cm.

In spite of a very extensive field database, it was difficult to select field observations with conditions identical to those used in the model. A limitation was that the model wave heights extended up to 60 cm whereas the field wave heights did not

exceed 12 cm during the period when the field data were collected. Taking into account the sediment composition, which matched closer to the easily erodible sediment, the model gave maximum depth-averaged suspension concentrations 0, 13 and 241 mg/l for 10 cm wave height in water depths 1.5, 1.0 and 0.5m for the passage of towboats. These values are comparable to the field values mentioned above. Hence the model was considered satisfactorily verified for towboat traffic and the same validation was considered valid for conducting the recreational boat passage study described in this paper.

A simplified representation of natural conditions was used for the present study as was done for the earlier study. It uses generalized wave series and generalized sediment properties and gives a depth-averaged suspension concentration. The site conditions may be different from the model in terms of wave pattern, sediment properties and vertical distribution of sediment. Hence, the results obtained by the adopted procedure are most likely to be different from the actual but are expected to provide reasonably close values with better validation based on better field data.

6. RESULTS OF RESUSPENSION MODELING

The maximum values of wave height used to develop the suspended sediment concentration curves were 10, 20, 30, 40 and 50 cm. The absence of significant erosion for 10 cm waves may appear to contradict the towboat verification discussed above. However, for a single event of vessel passage, towboat passage has 200 waves as against 12 waves for recreational boat passage. Also towboats (barges) have a much larger size and a different hull shape. Hence for the same maximum wave height in a single event, towboats result in much higher sediment resuspension than that caused by recreational boats.

Initial tests indicated that the 10 cm waves did not erode even the soft sediments having relatively low shear strength, so most analysis began with the 20 cm wave height. Results of only 30 cm wave height are presented in this paper. Intervals of 1, 5, 10, 20, 30 and 60 minutes between consecutive boat passages were examined over a total duration of 6 hours. The results are presented in Figs. 3 through 8. Fluctuations of suspension concentration were observed with every wave. The suspension concentration was about 80 mg/l at the first wave in each case; however the net suspension concentration at the end of 30 minutes was lower with reduction in frequency of boat-passage. After sufficient time lapse, the suspension concentration stabilized at mean concentration with constant fluctuations around the mean value.

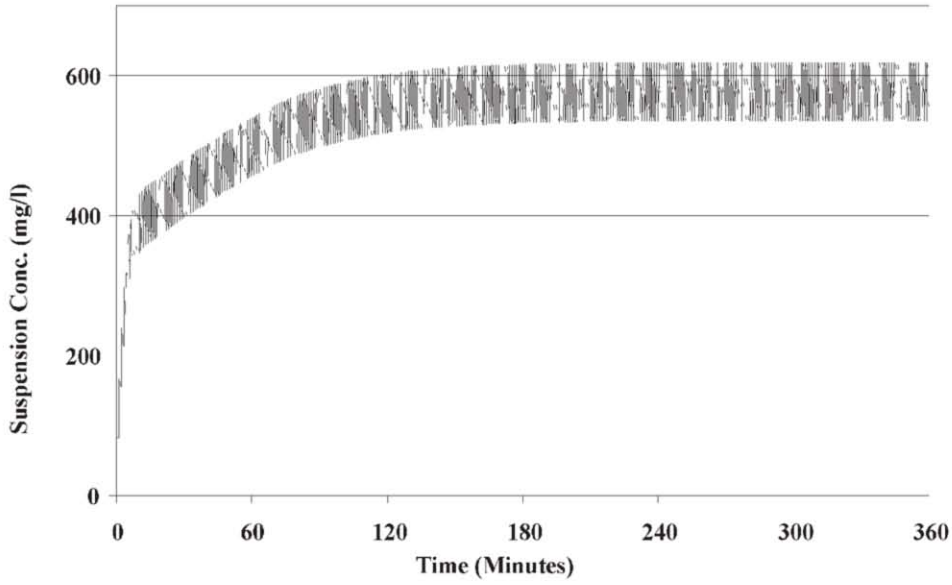

Fig. 3. Suspension concentration with 360 boats at 1-minute intervals, H_{max} = 30 cm.

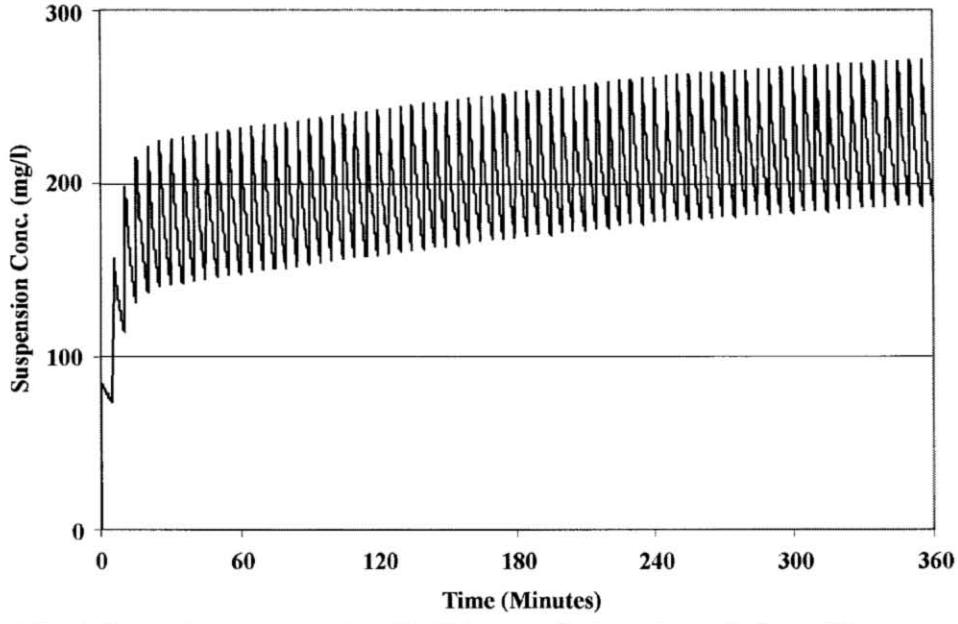

Fig. 4. Suspension concentration with 72 boats at 5 minute intervals, H_{max} = 30 cm.

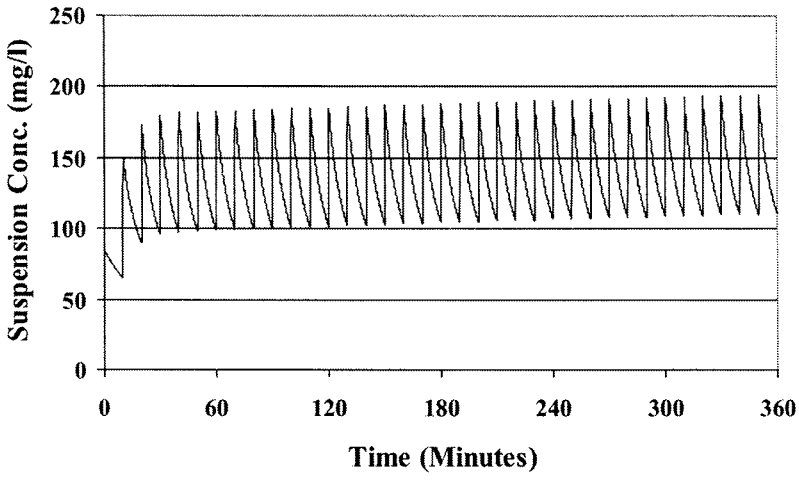

Fig. 5. Suspension concentration with 36 boats at 10 minute intervals, H_{max} = 30 cm.

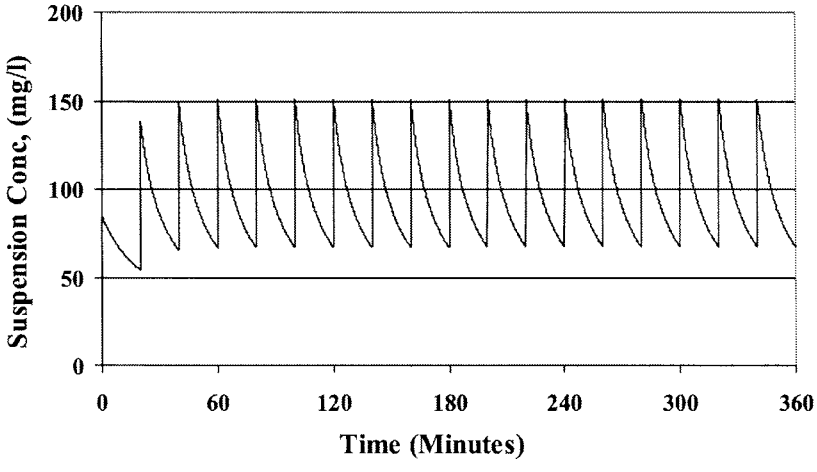

Fig. 6. Suspension concentration with 18 boats at 20 minute intervals, H_{max} = 30 cm.

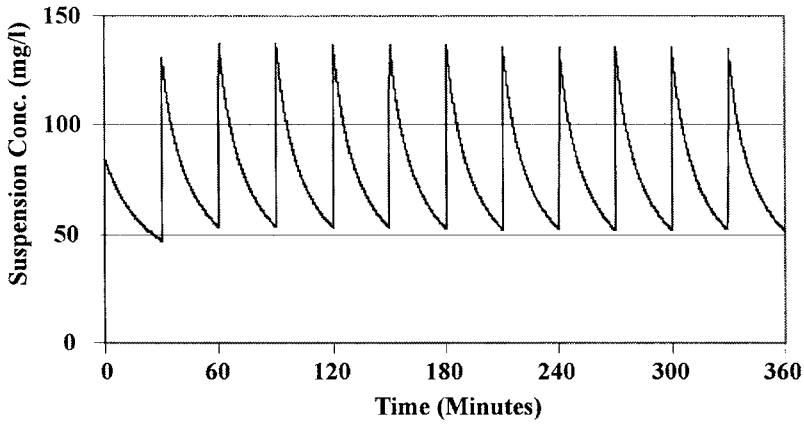

Fig. 7. Suspension concentration with 12 boats at 30 minute intervals, H_{max} = 30 cm.

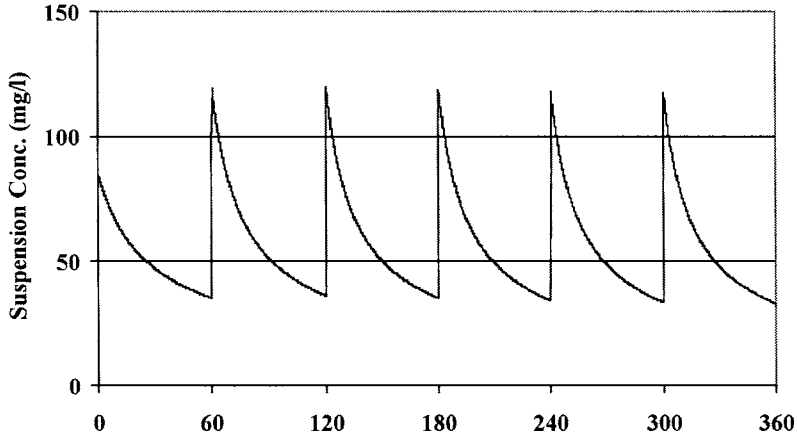

Fig. 8. Suspension concentration with 6 boats at 30 minute intervals, H_{max} = 30 cm.

Model runs were made for 10, 20, 30, 40 and 50 cm wave heights. Table 1 gives an illustration of suspension concentration as a function of recreational boat-induced waves at 1 to 60 minutes interval for a maximum wave height of 30 cm. It is noted that both the mean and peak suspension concentrations decrease with increase in boat passage interval. Higher frequency of boat passage increases and maintains the high turbulence level, thus keeping the fine sediment in suspension for a longer time.

Table 1. Mean Equilibrium Concentration as a Function of Recreational Boat-Induced Waves. Boat Interval = 1 to 60 Minutes, H_{max} = 30 cm, Water Depth = 1 m.

Boat Interval (Minutes)	Mean Equilibrium Concentration (mg/l)	Peak Suspension Concentration (mg/l)
1	565	620
5	230	280
10	160	200
20	110	150
30	95	135
60	75	120

Fine sediments remain in suspension under high turbulence (flow velocity greater than 30 cm/s) and generally settle faster under quiescent conditions. However, they may flocculate readily under a very low level of turbulence (flow velocity less than 5 cm/s), which provides increased frequency of contacts between the electrically charged particles. Hence the settling rate may be higher at low turbulence than under quiescent conditions. Secondly, at higher suspension concentration, again the particle collision frequency is higher, leading to larger flocs, which settle faster. The suspension concentration drops rapidly under low turbulence conditions and at higher concentrations. Hence the suspension concentrations are lower with longer boat intervals.

Tables 2 and 3 give peak concentration and mean concentration respectively for 10, 20, 30, 40, 50 and 60 cm maximum wave heights with a boat interval of one minute over a 6-hour duration. As would be expected, the suspension concentration increase with increasing wave heights.

Table 2: Peak Concentration as a Function of Wave Heights for 1-Minute Boat Interval

Maximum Wave Height (cm)	Peak Suspension Concentration (mg/l)
10	0.001
20	340
30	620
40	870
50	1175

Table 3: Mean Equilibrium Concentration as a Function of Wave Height for 1-Minute Boat Interval

Maximum Wave Height (cm)	Mean Equilibrium Concentration (mg/l)
10	0.001
20	325
30	580
40	800
50	1060

7. CONCLUSIONS

1. Several researchers have examined sediment resuspension under wind-induces waves. The VESTUNS model was used in the present study for estimating sediment suspension under wave action which was generated by recreational boats in the UMRS. The time series of waves used in the study applied cyclic loading on the erodible sediment beds. Quantitative predictions of wake wave-induced suspended sediment concentrations in the near shore zone were made using a verified numerical model. Extensive and precise field data having a perfect match with the conditions reported in the paper were not available for reliable model verification. In view of this limitation, field data as available had to be used for an approximate verification of the model. The absolute values of suspension concentration reported in the paper may not be accurate but the study has demonstrated application of an available algorithm for showing the influence of vessel-induced wave heights and boat frequency on suspension concentration.

2. The recreational boat wake wave sediment resuspension model approach allows determining: a) whether the sediment at any given location is susceptible to erosion or not as a result of vessel-induced waves; b) if it is erodible, what is the expected value of maximum sediment concentration in suspension, and c) how long will the sediment remain in suspension. For the model predictions to be realistic, it is essential to accurately characterize the bed sediment by conducting laboratory determination of parameters such as bulk density, critical shear stress for erosion, fall velocity and rate of erosion as a function of varying shear stress.

3. The results of the sediment resuspension and deposition study reinforce in a quantitative manner the qualitative results that might be expected as a vessel resuspends sediments in shallow near-shore zones. The maximum wave height and frequency of boats appear to be the main parameters influencing sediment suspension concentration. As vessel frequency increases, there is less opportunity for deposition of sediments after each passage, the suspended sediment concentrations accumulate to an equilibrium level and are sustained for longer periods of time. The computer-generated results show that the time-averaged equilibrium concentrations are the most significant in the context of environmental impact.

4. The model is versatile in its use. Effect of several relevant parameters such as vessel-generated wave height and wave period, time interval between passage of consecutive vessels, water depth, type of vessel, characteristics of vessel, and sediment properties can be evaluated from the use of this model. This paper provides an illustration of the type of results obtained by using the VESTUNS algorithm.

ACKNOWLEDGMENTS

The work reported herein was conducted as part of the Upper Mississippi River – Illinois Waterway (UMR-IWW) System Navigation Study. The US Army Engineer Rock Island District, St. Louis District and St. Paul District sponsored the study. Sandra Knight of ERDC provided the generic time series based on wave data analysis.

REFERENCES

Bhowmik, N.G., T.W. Soong, W.F. Reichelt and N.M. Seddik. 1991. *Waves generated by recreational traffic on the Upper Mississippi River system.* Research Report 117, Department of Energy and Natural Resources, Illinois State Water Survey, Champaign, IL.

Fagerburg, T.L. and T.C. Pratt. 1998. *Upper Mississippi River navigation and sedimentation field data collection summary report.* Interim report for the Upper Mississippi River – Illinois Waterway System Navigation Study, ENV Report 6, prepared for U.S. Army Corps of Engineers, Rock Island, St. Louis, and St. Paul Districts.

Hwang, K.-N. 1989. *Erodibility of fine sediment in wave-dominated environments.* Coastal and Oceanographic Eng. Dept., Univ. of Florida, Report UFL/COEL-89/017.

Kemp, W.M., W.R. Boyanton, J.C. Stevenson, R.W. Twilly and J.C. Means. 1983. The decline of submerged vascular plants in upper Chesapeake Bay: Summary of results concerning possible causes. *Marine Technology Society Journal*, 17, 78-89.

Knight, S.K. 1999. *Wave height predictive techniques for commercial tows on the Upper Mississippi River – Illinois Waterway System.* ENV Report 15, prepared for U.S. Army Engineer, Rock Island, St. Louis, and St. Paul Districts.

Knight, S.K. and T.M. Parchure. 2004. *Hydraulic effects of recreational boat traffic on the upper Mississippi river system.* Final report for the Upper Mississippi River – Illinois Waterway System Navigation Study, ENV Report 43, prepared for U.S. Army Engineer, Rock Island, St. Louis, and St. Paul Districts.

Maa, P.-Y. and A.J. Mehta. 1987. Mud erosion by waves: A laboratory study, *Continental Shelf Research*, 7(11/12), 1269-1284.

Mehta, A.J. and Y. Li. 1996. *A PC-based short course on fine-grained sediment transport engineering*, Coastal and Oceanographic Engineering Department, University of Florida, Gainesville, Florida.

Orth, R.J. and K.A. Moor. 1983. Chesapeake Bay: An unprecedented decline in submerged aquatic vegetation. *Science*, 222, 51-53.

Parchure, T.M., K. Kim and W.H. McAnally. 1996. *Effect of wave-induced resuspension of fine sediment on water quality in near-shore zone.* U.S. Army Corps of Engineers, 11th Seminar on Water Quality '96 held at Seattle, WA, Section 3, 94pp.

Parchure, T.M., W.H. McAnally, Jr. and A.M. Teeter. 2001a. *Desktop method for estimating vessel-induced sediment suspension. Journal of Hydraulic Engineering*, ASCE, 127(7), 577-587.

Parchure, T.M., W.H. McAnally and A.M. Teeter. 2001b. *Wave-induced sediment resuspension near the shorelines of Upper Mississippi River.* Interim report for the Upper Mississippi River–Illinois Waterway System Navigation Study, ENV Report 20, prepared for U.S. Army Engineer, Rock Island, St. Louis, and St. Paul Districts.

Sanford, L.P. 1994. Wave forced resuspension of upper Chesapeake Bay mud. *Estuaries*, (17), 18: 148-165.

Sorensen, R.M. 1998. *Prediction of vessel-generated waves with reference to vessels common to the Upper Mississippi River System.* Interim Report for the Upper Mississippi River-Illinois Waterway System Navigation Study, ENV Report 4, Prepared for U.S. Army Corps of Engineers, Rock Island, St. Louis, and St. Paul Districts.

Estuarine and Coastal Fine Sediments Dynamics
J.P.-Y. Maa, L.P. Sanford and D.H. Schoellhamer (editors)

Capping of a contaminated soft cohesive sediment bed in Stryker Bay, Minnesota

van Kesteren, W.G.M.[a], T. van Kessel[a] and M.J. Costello[b]

[a]WL | Delft Hydraulics, P.O. Box 177, 2600 MH Netherlands (also Delft University of Technology).
[b]Service Engineering Group, 675 Vandalia St., St. Paul, MN 55114

KEY WORDS
Gas, oil, pollution, consolidation, capping, remediation

Sediments in Stryker Bay, Minnesota are heavily polluted with polyaromatic hydrocarbons (PAHs) from a former coal tar production site. Pollution is transported towards the surface water through ebullition and pore water flow. The gas bubbles result from decay of organic material. This study investigates if the placement of a sand cap is sufficient to contain the pollution. It is shown that a sand cap with a thickness of 0.9 m is indeed sufficient to prevent the transport of PAHs towards the water column, through either bubble or pore water transport. Removal of contaminated sediment is therefore not required in this specific case. Bubble transport is controlled firstly by the insulating effect of the cap, thereby keeping the underlying sediment at a temperature below the threshold for biogenic gas production, and secondly by densification and strengthening of sediment via consolidation, making channel formation more difficult.

1. INTRODUCTION

At many sites around the world sediment is contaminated because of past industrial activity. Some of these sites are selected for re-development (*e.g.*, housing, recreational use) because of their favourable location. Prior to its reuse, a site has to be sanitized either by removal of the contaminated sediment or by isolating it with a layer of clean material, the former option generally being the more costly one.

One of those sites is Stryker Bay in Minnesota. Sediment is heavily polluted with polyaromatic hydrocarbons (PAHs), as coal tar production and refining units bordering this site had been in operation for tens of years. Presently, PAHs escape from the sediment via ebullition and pore water flow (Fig. 1). For remediation to be successful, the fluxes of PAH must be negligible. Both sediment capping and sediment removal are options presently under consideration. This paper focuses on the feasibility of sediment capping.

The key questions regarding capping are:

1. Do PAHs escape through gas bubble migration?
2. Do PAHs escape through advective transport of pore water?

2. METHODS

To answer the questions above, an analysis was made based on field and laboratory measurements and numerical modelling. The following procedure was followed.

Fig. 1. Oil pollution in Stryker Bay caused by ebullition of PAH from the subsoil.

To evaluate the first key question, *i.e.,* the possibility of PAH transport through gas bubble migration, it has to be assessed first how much gas bubble migration may occur. This depends on the transport capacity of the sediment on the one hand, and on the rate of gas production on the other hand.

Gas is primarily produced as a result of the biogenic decay of organic material present in the soil. Under anaerobic conditions, which prevail in cohesive sediments below the bioturbation zone at a level of 5 to 10 cm below the sediment-water interface, methane (CH_4) and carbon dioxide (CO_2) are formed in this decay process. If the CH_4 or CO_2 concentration exceeds the saturation concentration, a free gas phase is formed in the pores of the soil matrix in the shape of small bubbles, which may gradually grow in time and eventually start to rise because of pressure gradients (van Kessel and van Kesteren, 2002; van Kesteren and van Kessel, 2002).

The rate of gas production was measured by monitoring the increase in CH_4 and CO_2 concentration in the headspace volume (about one l) of pressure cells ($d \times h = 9 \times 22$ cm), which were partly filled with soil samples in an atmosphere of pure nitrogen (N_2). The temperature of the cells was controlled within 0.1 °C, as the gas production rate strongly depends on temperature. CH_4 and CO_2 concentration levels were measured with a Gas Chromatograph (GC). The detection limit is about 1 ppm. The rate of biogenic gas production was determined as a function of temperature, pressure and organic content.

To evaluate the second key question, *i.e.,* the possibility of PAH transport through the advective transport of pore water, permeability is an essential parameter. Permeability was measured with a Seepage-Induced Consolidation (SIC) test (Liu and Znidarcic, 1991), from which the compressibility of the soil is also obtained. In the SIC-test a differential pressure is applied over the sample, by means of a controlled flux of pore water through the sample, inducing consolidation. In order to investigate the capillary pressures for Non-Aqueous Phase Liquid (NAPL) and gas entering the pore system, NAPL and gas were used as boundary condition for the seepage controlled test. The pressure difference, settlement and water discharge are continuously monitored. From these parameters capillary pressures and the relationships between void ratio and effective stress on the one hand and void ratio and permeability of pore water and NAPL on the other hand are derived.

Subsequently, the transport rate of pore water, NAPL and gas in the soil was investigated as a function of external loading using DELCON (van Kesteren, 2002), a finite-strain numerical model for consolidation combined with gas production and transport. The finite strain approach is a Lagrangian description in which the vertical coordinate is

fixed to the solid phase (Gibson *et al.*, 1967, 1981). This enables computation of large strains with settlements on the order of the layer thickness.

Ebullition of gas bubbles is assumed to occur if two criteria are met:

1. the bubble diameter exceeds a critical value (4 mm) above which crack formation is possible; and
2. channel formation is possible.

The critical bubble diameter is derived from a stress analysis for the grain matrix around the bubble (van Kesteren, 1998). First of all the condition for bubble growth requires a gas-fluid interface with the grain matrix that is capable of withstanding the pressure difference between the gas phase in the bubble and the pore water pressure around the bubble. Thus the pressure difference must be less than the capillary pressure of the gas-water interface (so called gas-entry value). For the soft contaminated sediments in Stryker Bay this criterion was met.

Crack initiation around a gas bubble may only occur if the ratio between isotropic effective stress and drained cohesion of the material is less than unity. In that case the stress condition for crack initiation is satisfied. This implies that cracks are relatively easily initiated in overconsolidated material, which has a high drained cohesion.

The proper ratio between isotropic effective stress and drained cohesion is not the only prerequisite for crack formation. Crack formation also depends on the length scale of the system. Only if the diameter of a bubble is sufficient to concentrate the stress may such cracks propagate. As a result, initially no cracks are formed around a bubble, until a sufficient diameter is reached. For Stryker Bay sediment this diameter is estimated at 4 mm. This estimate is based on laboratory experiments on bubble expansion in Lake Ketel sediments, which have similar properties (van Kesteren, 1998).

Channels resulting from consolidation generally have a vertical dimension of a few tens of centimetres and therefore cannot enhance transport of gas and water from deeper layers. However, by merging of cracks created by bubbles, significantly deeper channels may be produced. A channel stability criterion is derived from a stress analysis around a cylindrical cavity. A vertical channel can remain stable until it collapses horizontally once the vertical stress is sufficiently high. The resulting channel radius r_{ch} after collapse can be found from cylindrical compression (Vesic, 1972):

$$\left(\frac{r_{ch}}{r_{ch,0}}\right)^2 = \frac{1}{1+\exp\left[-1-\ln\left(\frac{G}{2c_u}\right)+z\frac{K_0(\rho_s-\rho_w)g}{c_u(1+e)}\right]} \quad (1)$$

where z is depth , e is void ratio, K_0 is the ratio between horizontal and vertical effective stress, ρ_s is the dry density of sediment particles, ρ_w is the water density, $r_{ch,0}$ is the channel radius before collapse, G is the shear modulus, g is gravitational acceleration and c_u is undrained shear strength. When the diameter r_{ch} is reduced to the largest pore size present in the sediment skeleton, the maximum depth of the channel has been reached. Channels at a larger depth are unstable and will be closed.

For conditions typical for Stryker Bay sediment, channel formation is inhibited at a depth generally well below 0.30 m, which is the thickness of the polluted sediment layer. In the present study, gas ebullition under existing conditions is therefore not limited by channel instability.

Transport of NAPL is initiated if the excess pore water pressure minus the capillary pressure difference between water and NAPL exceeds zero. As the viscosity of NAPL is 10^5 times larger than the viscosity of water, transport of NAPL through the pores is relatively slow.

Finally, the gas and pore water flux towards the water surface was measured in situ with gas flux meters (Costello *et al.*, 2002). These data were used to validate the numerical model, which was subsequently used to assess the impact of different rehabilitative measures such as capping.

3. RESULTS

3.1. Gas production

From the gas production experiments it is concluded that at 2 °C, methane and carbon dioxide production stops (Fig. 2). This temperature effect shows that the measured gas production is mainly caused by biogenic breakdown of organic matter in the sediment. Physical processes like desorption would not be as sensitive to temperature changes. At 20 °C, the rate of CH_4 production is estimated at 4.3 ppm/day, which is equivalent with 0.09 ml gas per kg dry wt. per day. For CO_2 a similar production rate is found. The onset of gas production (threshold of bio-activity) is between 13 and 16°C (Costello *et al.*, 2002).

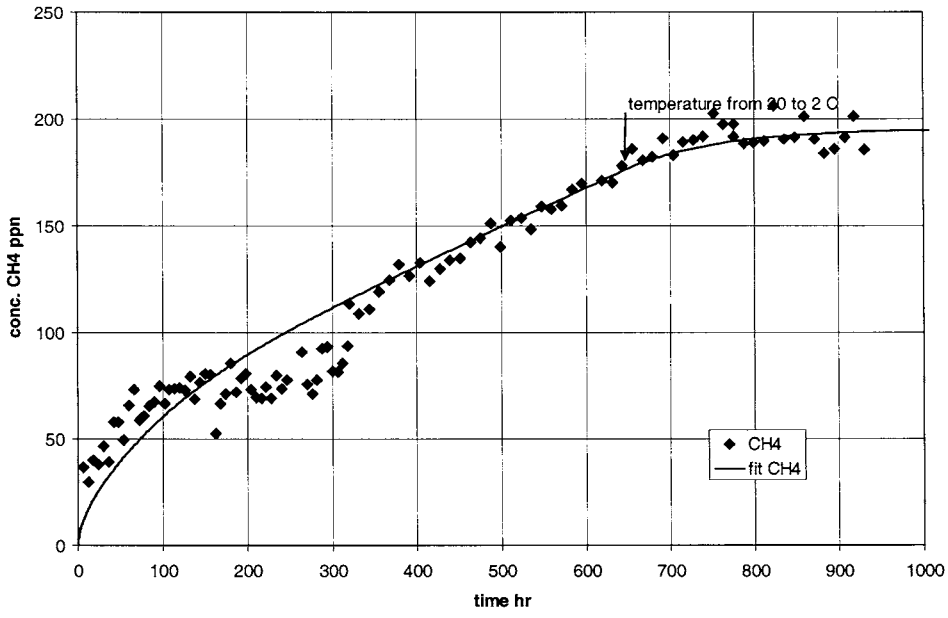

Fig. 2. Results from gas production tests (layer 102).

3.2. Consolidation parameters

Results from the SIC-test (Fig. 3) indicate that the permeability k_w is a function of the void ratio, e_w, which is a function of the effective stress, σ'. The following functions are used to fit the data points and then applied for the DELCON modelling:

$$e_w = A(\sigma' + Z)^B \; ; \; k_w = C e_w^D \tag{2}$$

where A, B, Z, C and D are coefficients following from the SIC tests. The resulting fits are shown as solid (clay content 37.6%) and dotted (clay content 25%) lines in Fig. 3.

3.3. Consonsidation calculations

First the consolidation model is calibrated. To this order, the historical soil profile of Stryker Bay is reconstructed based on known deposition events in the period 1904-2002, during which the polluted soils were placed. The calculated levels of sediment layers agreed well with the *in-situ* sediment layer levels. The calculated gas flux from the soil was tuned to the measured gas flux in the field at Station FM2, see Fig. 4. The only fit parameter used was the initial Total Organic Carbon (TOC) content of each

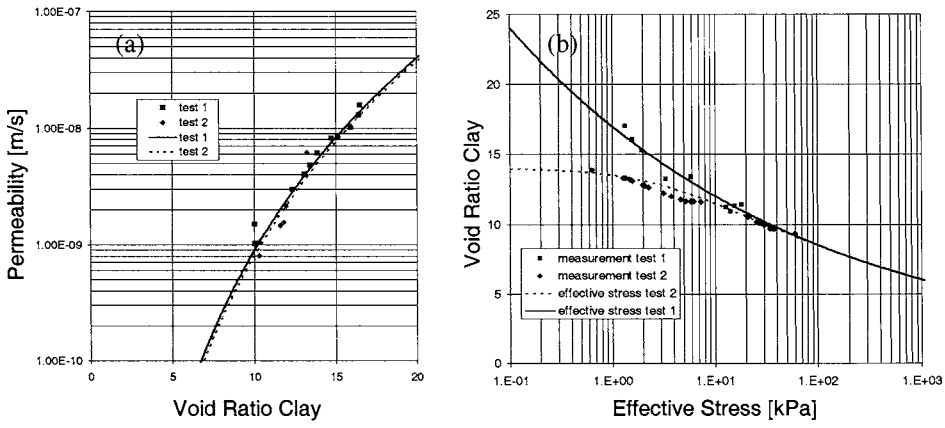

Fig. 3. Consolidation parameters obtained with SIC-test. Clay content test 1, 37.6%; test 2, 25%. (a) Permeability as a function of void ratio, and (b) void ratio clay as a function of effective stress.

sediment layer, given the measured gas production rates as function of temperature. The amount of organic matter was varied in a range of factor 3, with respect to the samples tested in the laboratory. *In situ* TOC data provided satisfactory agreement with the calibrated amount of TOC. Parameters from the SIC-tests were not altered.

Although the deeper sediment layers contain a sufficient amount of carbon to enable gas production, no gas is generated therein because of temperature limitation. Such a limitation does not currently occur for shallow layers in the summer season.

Subsequently, the consolidation model was used to investigate the impact of several capping scenarios to reduce pollution levels in Stryker Bay. If the sediment is capped, summer heat penetrates less into the contaminated sediment. A cap thickness of 0.9 m is sufficient to reduce gas production such that no bubble nucleation occurs.

Figure 5 shows the calculated gas production rate in mmol/m/s vs. time for a sand cap with a thickness of 0.6 m. Because of insulation by the cap, the amount of gas produced in the polluted layer (102) strongly decreases. However, CO_2 and CH_4 production continues at a lower level. To see if the remaining gas generation would produce bubbles, the computed gas bubble fraction (volume gas bubbles per volume soil) in the polluted layer (102) was computed from 2000 until 2030 for different cap layer thicknesses (Fig. 6). After deposition of the cap in early 2004, the gas bubble fraction increases for the 0.3 m cap and remains high. This increase is caused by the decrease of

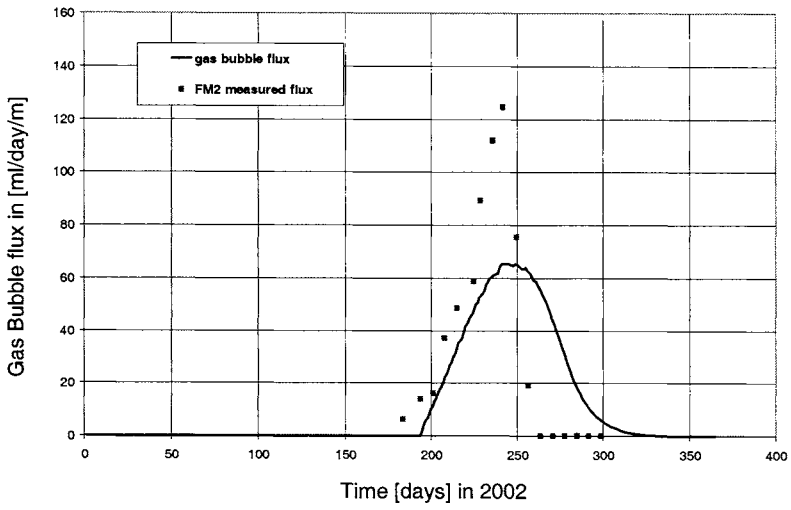

Fig. 4. Measured and computed gas flux.

the polluted layer volume by consolidation, while the volume of gas in bubbles is only slightly reduced by temperature reduction by the cap. Increasing cap layer thickness to 0.6 m results in elimination of gas bubbles in 2009. However several years later (in 2015) enough gas is accumulated in the polluted layer (102) to generate bubbles again. Only the 0.9 m cap (or larger) eliminates gas bubbles permanently.

Another effect of capping is that the strength of the underlying sediment increases because of consolidation. This reduces the formation of transport pathways for gas. Only when the sediment shear strength is increased to the point that the gas pressure necessary to expand the gas bubble is more than the air entry value of the sediment, hydraulic fracture by the bubble will occur.

Finally, the sandy nature of the cap contributes to isolation of PAH transported by bubbles. As the bubbles migrate through the sand matrix, PAH containing solids moving with the bubbles are stripped by the grain matrix.

Regarding pore water, laboratory experiments and DELCON modelling show that for caps with a thickness over 0.3 m, retardation within the cleaner organic post-industrial surficial sediment prevents PAH from migrating into the cap material and pore water dissipated from the underlying sediment remains within the cap. NAPL migration from excess pore water pressure during consolidation was insignificant due to the combination of highly viscous NAPL and the transient duration of the modest excess pore water pressure generated by a 0.9 m cap.

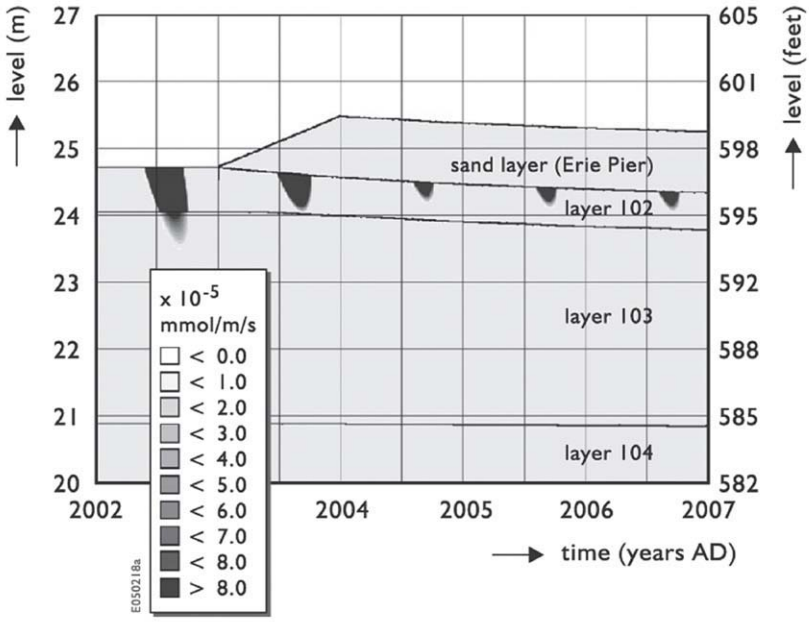

Fig. 5. Effect of 0.6 m sand cap on production rates (DELCON computations).

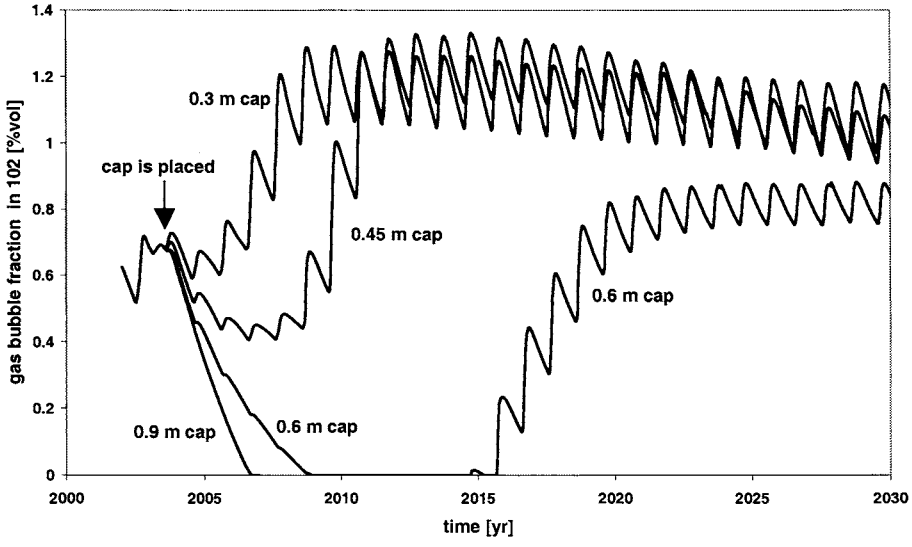

Fig. 6. Effect of cap layer thickness on gas bubble fraction in polluted layer (102)

4. CONCLUSIONS

A cap with a thickness of 0.9 m consisting of sandy material is sufficient to prevent the transport of PAH towards the water column, either through bubble or pore water transport. Removal of contaminated sediment is therefore not required in this specific case, which makes remediation of Stryker Bay, Minnesota less expensive.

Neither NAPL nor contaminants migrate into a sandy cap under the conditions tested. Placement of the sand cap eliminates bubble transport through the (cohesive) sediment bed because of:

1. insulation of the sediment to temperatures below the threshold of biogenic gas production,
2. densification and strengthening of the sediment via consolidation, making channel formation more difficult, and
3. interruption of channelization.

All three of these controls are provided by proper capping material. The second and third item result from a change in the physical properties of the (cohesive) sediment bed induced by a higher effective stress level.

REFERENCES

Costello, M., E. Hedblom and H. Huls. 2002. *Geology-Hydrogeology, Appendix GH, Data Gap Report, St. Louis River/Interlake/Duluth Tar Site Duluth, Minnesota.* Service Engineering Group, St. Paul, Minnesota USA. (ftp://ftp.visi.com/users /servenv/DataGapReport/html%20files/datagap/appendxs/prvsrpts/gh/gh.htm).

Gibson, R.E., G.L. England and J.L. Hussey. 1967. The theory of one-dimensional consolidation of saturated clays. I. Finite non-linear consolidation of thin homogeneous Layers. *Géotechnique*, 17, 261–273.

Gibson, R.E., R.L. Schiffman and K.W. Cargill. 1981. The theory of one-dimensional consolidation of saturated clays. II. Finite non-linear consolidation of thick homogeneous layers. *Canadian Geotechnical Journal*, 18, 280–293.

Liu, J.C. and D. Znidarcic. 1991. Modeling one dimensional compression characteristics of soils, *Journal of Geotechnical Engineering*, ASCE, 117 (1), 162–169.

van Kessel, T. and W.G.M. van Kesteren. 2002. Gas production and transport in artificial sludge depots. *Waste Management*, 22 (1), 53–62.

van Kesteren W.G.M. 1998. *Crack formation and gas formation in sediments.* WL | Delft Hydraulics Report no. Z2312, Netherlands.

van Kesteren, W.G.M. and T. van Kessel. 2002. Gas bubble nucleation and growth in cohesive sediments. In*: Fine Sediment Dynamics in the Marine Environment.* Winterwerp, J.C. and C. Kranenburg (Eds.), Elsevier, Amsterdam, 329–341.

van Kesteren, W.G.M. 2002. DELCON *Assessment of Gas and PAH Fluxes and PAH Flux Management Plan St. Louis River/Interlake/Duluth Tar Site, Duluth, Minnesota. Appendix GT3 of Data Gap Report St. Louis River/Interlake/Duluth Tar Site Duluth, Minnesota.* Service Engineering Group, St. Paul, Minnesota USA. (ftp://ftp.visi.com/users/servenv/DataGapReport/html%20files/datagap/appendxs /geotech/gt3/gt3.htm).

Vesic, A.S. 1972. Expansion of cavities in infinite soil mass, *Journal of Soil Mechanics and Foundations Division.* ASCE, 98 (SM 3), 265–290.

Estuarine and Coastal Fine Sediments Dynamics
J.P.-Y. Maa, L.P. Sanford and D.H. Schoellhamer (editors)

Neural networks in sedimentation modelling for the approach channel of the port area of Rotterdam

Bhattacharya, B.[a], I.K. Deibel[b], S.A.M. Karstens[c] and D.P. Solomatine[a]

[a]UNESCO-IHE Institute for Water Education, P.O. Box 3015, 2601 DA Delft, The Netherlands.
[b]Port of Rotterdam, Strategy and Communication / Maritime Development, Postbus 6622, 3002 AP Rotterdam, The Netherlands.
[c]GeoDelft, Stieltjesweg 2, 2600 AB Delft, The Netherlands.

KEYWORDS
Sedimentation, sediment transport, dredging, artificial neural networks, ANN.

The sedimentation characteristics in the Maasmond area of the approach channel of the port area of Rotterdam are studied using an Artificial Neural Network (ANN) technique. The important factors affecting the sedimentation process such as waves, wind, tides, surge, river discharge, *etc.* were studied, the corresponding time series data was analysed and the important variables behind the process were identified. An ANN model was built to predict sedimentation. The model was trained on the data collected during 1992-1998 and verified by the data of 1999-2000. The predictive accuracy of the ANN model was found to be adequate for the potential use in the operational decision making.

1. INTRODUCTION

Sedimentation in a channel is influenced by various factors such as upland discharge, sediment characteristics, meteorological causes, environmental (including biological) causes, human interventions (in the form of dredging and training measures), *etc.* Assessment of sedimentation in shipping channels leading to a port, or in general in

rivers, is carried out frequently. Such a morphological assessment is not an easy task due to the complexity of the problem. To safeguard navigation and provide a stable navigable depth, port authorities throughout the world resort to dredging. A reasonably accurate prediction of sedimentation in shipping channels and harbour basins, in addition to regular hydrographic surveys, can be utilised in developing an efficient planning of dredging activities.

The Port of Rotterdam is situated on the bank of River Rhine that discharges in the North Sea. The area near to its confluence is known as Maasmond and it is studied in the present research (Fig. 1). The port has its approach channel through Maasmond where the navigable depth is 24 m. Sedimentation in the Maasmond area depends upon several reasons mentioned above and has a high degree of variability. The sedimentation rate is governed by the availability of (suspended) sediment and the transport processes and has strongly stochastic behaviour driven by erratic meteorological effects: sediment is mobilised by wave action and carried by river floods. The transport of the

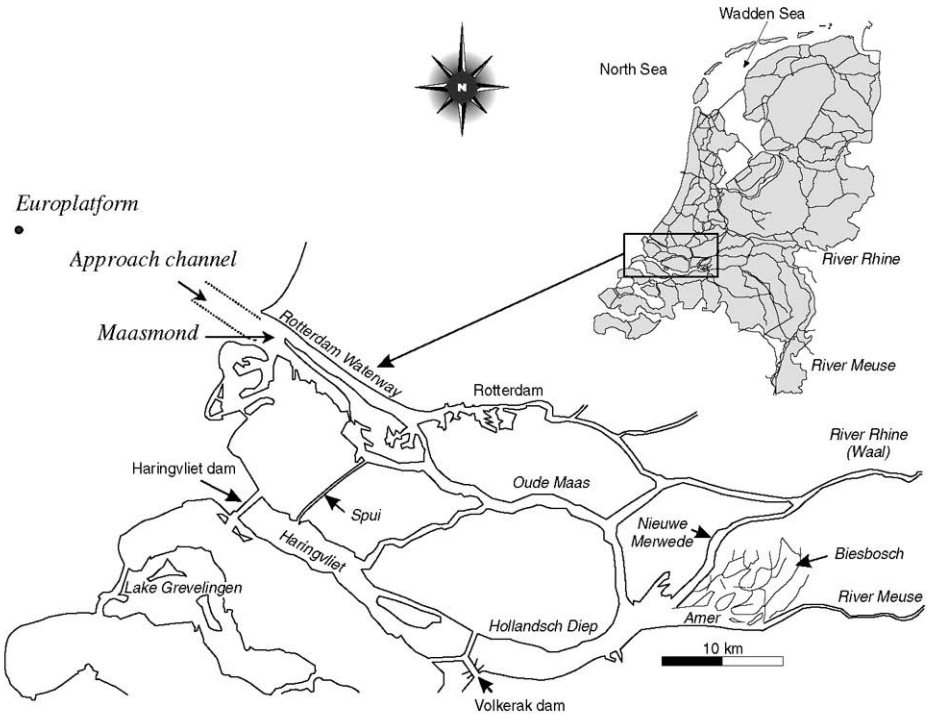

Fig. 1. Location plan showing the approach channel to the port of Rotterdam and the harbour basin at Maasmond.

suspended sediment towards the areas prone to siltation has important deterministic components (related to tide, density currents, *etc.*), but also stochastic components because of the meteorological effects. Due to the complex nature of the problem, developing a deterministic model for assessing sedimentation in the Maasmond area is an extremely difficult task.

Many water engineering problems have been successfully modelled with machine learning techniques such as Artificial Neural Networks (ANN). Examples include rainfall-runoff modelling (Minns and Hall, 1996), stage-discharge relationship (Bhattacharya and Solomatine, 2002; 2003a), water control problems (Bhattacharya *et al.*, 2003b), sediment transport (Bhattacharya and Buraimo, 2003c), etc. These successful applications prompted us to investigate the applicability of ANN in modelling the harbour sedimentation problem.

In the present paper the development of an ANN model for predicting sedimentation in the Maasmond area is presented.

2. SEDIMENTATION CHARACTERISTICS OF MAASMOND

The sedimentation characteristics in the Maasmond area largely depend upon the sedimentation and meteorological conditions of the North Sea. The major sources of sediment coming to the North Sea are Dover Strait, Atlantic Ocean, coastal erosion along the French and British cliff coasts, rivers, dredged spoil from neighbouring countries, *etc.* Around 80% of the sediment volume that accumulates in the Maasmond area has its origin in the British Channel and the French coast (WL|Delft Hydraulics, 2001; Vuurens, 2001). In this region enormous amounts of material become available every year due to coastal erosion. Along with the northerly long-shore currents, this material is transported along the French, Belgian and Dutch coastlines into the North Sea basin. On its way northward the material is deposited in several "sedimentation traps" along the Belgian and Dutch coasts. Parts of these sediments are deposited at Maasmond.

Ninety five percent of the sediments that is deposited in the Maasmond area comes via the North Sea, the contribution of sediments carried by Rhine is limited to only 5% (de Kok, personal communication; de Kok, 1994). The North Sea bed merely acts as the buffer zone for the sediments deposited in the Maasmond (Winterwerp *et al.*, 1998). Sediments carried from the downstream coastal erosion are deposited in the North Sea bed to be eroded later. The bed material in the Maasmond is mainly silty-sand with a D_{50} of 0.055 mm.

The discharge of fresh water from River Rhine creates density currents. As a result a fresh to brackish water body known as "Coastal River" is formed along the Dutch coast due to the density currents and Coriolis effects (de Kok, 1994; WL|Delft Hydraulics, 2001). Depending upon the river discharge and wind, the width of the Coastal River may vary from a few km to about 20 km. Within the Coastal River gravitational circulation perpendicular to the coast are generated, which result in an accumulation of fine-grained sediments in the coastal zone with significantly higher sediment concentrations near the coast than that further offshore. The Coastal River exhibits a strong vertical fresh-saline water induced stratification.

Tidal currents, wind-induced currents and wave-induced stirring forces govern the sediment transport in the North Sea. Transport of this sediment to the Maasmond area is additionally influenced by the Rhine discharge. Biological activity can initiate flocculation, which can increase the settling velocity and thus affects the sediment dynamics. This is particularly important for deeper water, which indeed is the case for Maasmond. During the tranquil periods of summer flora and fauna cause consolidation of the deposited sediment over the sea bed raising the impermeability substantially. This causes easier erosion of sediments during the early summer than during the early winter (de Kok, personal communication).

Winterwerp *et al.* (1998) examined the causes of rapid siltation in harbour basins. With simulation studies they argued that during the rough weather conditions the suspended sediment concentration reaches its saturation limits during slack water. A thin temporal layer of fluid mud is formed, and then it is entrained rapidly during accelerating tides. This dynamics are governed strongly by the interaction of tides, surface waves and vertical fresh-saline water induced stratification. When this sediment-fluid mixture reaches the deep approach channel where the current is slow, the suspended sediment quickly falls to the bottom layer. Sediment-driven velocities carry this collapsed mud layer to the harbour basins causing serious sedimentation.

The depth at Maasmond is deeper than its regime depth (through dredging) and acts as a silt-trap. Accumulated sediments are removed through dredging to maintain the desired navigable depth in the fairway. Sedimentation S_t at time t is defined as the material that settles at or below the 1200 kg/m^3 density level and can be computed from the mass balance principle as follows

$$S_t = Dredging_{\,t-\Delta t} + Accumulation_{\,t-\Delta t} \qquad (1)$$

The time step Δt is the time between successive surveys. The volume of the basin was computed from hydrographic surveys using GIS (for details, see Vuurens, 2001). The accumulated mass between two successive surveys ($Accumulation_{t-\Delta t}$) was found by subtracting the volumes of the basin computed from the survey charts. The Maasmond area is traditionally schematised by the port authorities as two sub-areas (*E* and *F),* and only the sedimentation in area *E* is discussed here (Fig. 2). The annual quantities of sedimentation and dredging in the Massmond area (box *E*) are shown in Fig. 3. It is evident that the annual quantity of sedimentation varies a lot giving an indication that the stochastic components play a dominant role.

3. FACTORS INFLUENCING SEDIMENTATION

Several parameters influence sedimentation in the Massmond area such as wind, waves, tides, surge, discharge through River Rhine, biological activities, *etc.* (Vuurens, 2001). The availability of sediments in the North Sea largely depends upon waves and wind, which in turn depend upon the meteorological conditions. Once the sediments are available, the local hydro-meteorological conditions govern the transport process.

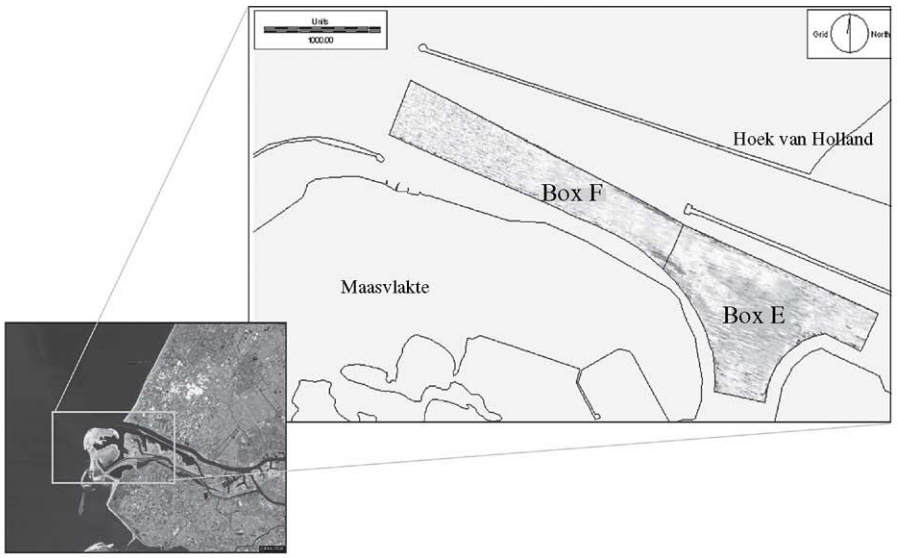

Fig. 2. The two designated areas *Box E* and *Box F* of Maasmond in the approach channel.

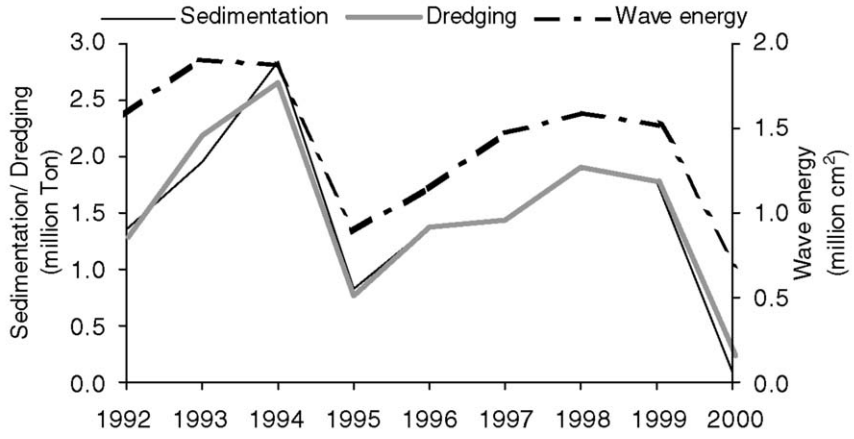

Fig. 3. Annual (October to September) sedimentation and dredging in box *E* and energy of filtered waves measured at the Europlatform.

During the data analysis too little correlation between sedimentation and most of these influencing variables were observed, possibly because their relationship is too complex to be captured by a simple linear relationship. Initial ANN modelling trials also suggested that incorporating all of these variables would not yield a model with good generalization capacity. Accordingly, we contemplated to develop a simple model by considering only the most important variables and they are listed below.

3.1. Waves

The wind generated waves are short waves with $H_{sig} < 0.1h$ and disturb the sea bed (H_{sig} stands for the significant wave height and h for the depth). As a result of these waves, in combination with currents, sediments are convected and diffused away from the bed by the action of vortices that result from flow separation over the ripples and by the turbulent fluid motions associated with the current. The sediment transport flux is related to the wave energy (*WE*), which can be expressed as

$$WE = kH_{sig}^{2} \tag{2}$$

where k is a constant.

Therefore, using *WE* as an input parameter in an ANN shall be more appropriate than using H_{sig}. Considering $k = 1$ the effect of waves is computed as

$$WE_t = \sum_{i=t-\Delta t}^{t} H_{sig_i}^2 \tag{3}$$

where WE_t provides a measure of the wave energy observed between time interval $t-\Delta t$ and t.

The wave time series showed a high variability with small waves during tranquil periods and very high waves during rough weather. As small waves do not have significant influence to sedimentation so their presence in the wave time series that would be used in ANN modelling may appear as noise, and training may be problematic (Schalkoff, 1997). One solution to this problem could be by building two models: one for small waves and the other for high waves. As an alternative, we experimented with a filter to remove the small waves and it was observed that when the filter height was chosen to be equal to the mean wave height (over the training data) the correlation between waves and sedimentation increased. Accordingly, filtering out the small waves from the wave time series was employed by adopting a filter value equal to the mean wave height.

$$If\ H_{sig} > \overline{H}_{sig} \qquad WE'_t = \sum_{i=t-\Delta t}^{t} (H_{sig_i} - \overline{H}_{sig})^2 \tag{4}$$

$$else \qquad WE'_t = 0$$

where WE'_t gives a measure of the energy of waves between time interval $t-\Delta t$ and t after filtering out the minor waves, Δt is three weeks, $\overline{H}_{sig}$ stands for the average significant wave height.

Wave data from *Europlatform* (located in the North Sea, Fig. 1) was used. In order to fill in the missing wave data, the procedure presented by Bhattacharya *et al.* (2003d) was adopted. Similar to the findings of the previous researchers (de Kok, 1994; Merckelbach, 1996; Winterwerp *et al.*, 1998; Vuurens, 2001) it was observed that waves indeed have a great influence on sedimentation in the Maasmond area (Fig. 3). Based on the data collected from 1991 to 1995, Merckelbach (1996) observed that waves with a time lag of six weeks provided the best correlation with sedimentation. In this study, however, waves with a time lag of three weeks provided a better correlation with sedimentation, and therefore, the lag of three weeks was adopted.

3.2. Rhine discharge

The fresh water discharge (Q) from River Rhine creates density currents, which ultimately bring the sediment in the estuary. The gradient of suspended sediment concentration along the lines perpendicular to the coastline depends largely on the variation of Rhine discharge. The discharge is measured daily at Lobith where Rhine enters The Netherlands. With a change in the discharge the near-shore suspended sediment concentration changes. Several experts (*e.g.*, de Kok, personal communication) opined that for computing sedimentation at Maasmond, Rhine discharge should be considered with a lag of one week, and this was employed.

3.3. Sedimentation potential

Several researchers (de Kok, 1994; Winterwerp *et al.*, 1998) have pointed out that the suspended sediment concentration in the Coastal River varies with season; this is validated with measurements (*e.g.*, Siltman, 1996). At the beginning of winters (October), usually the suspended sediment concentration is close to its minimum, and starts increasing with higher wave actions during the winter, and reaches its peak at the end of the winter. During the summer, the suspended sediment concentration decreases gradually leading to sedimentation, amount of which depends upon the hydro-meteorological conditions. Part of the sediments in suspension is brought by density currents to the Maasmond area. As a result sedimentation can occur even when there are no high waves.

In order to capture these characteristics, we introduce another variable called Sedimentation Potential (SP), which acts as a "memory" of the process. When there is a lot of suspended sediments (mobilised by waves), then because of a high SP there is a potential for deposition in the Maasmond area. As a result of particular hydro-meteorological conditions, a high value of SP may lead to high sedimentation in Maasmond. SP is a measure of the amount of sediments brought to suspension by the waves in the recent past minus the actual sedimentation that has occurred at Maasmond. It is proposed to compute SP as:

$$SP_t = \sum_{i=t_0}^{t-1} WE_i' - \sum_{i=t_0}^{t-1} S_i \tag{5}$$

where t is time, SP_t is the sedimentation potential at time t, WE_i' is the wave energy at the time i which is computed by Eq. 4, S_i is the sedimentation at time i which is computed by Eq. 1. The summation of the terms on the right hand side of Eq. 5 starts from t_0 which is a selected time in the past, typically the beginning of the season

(October). However, the two terms on the right hand side of Eq. 5 has different measurement units and therefore, we used the following normalised versions of these variables:

$$SP_t = \sum_{i=1}^{t-1} we_i - \sum_{i=1}^{t-1} s_i \tag{6}$$

where we_i and s_i are the normalised wave energy and sedimentation at time i, respectively. They are defined as:

$$we_i = WE'_i / WE'_{AV} \tag{7}$$

$$s_i = S_i / S_{AV} \tag{8}$$

where WE'_{AV} and S_{AV} are the average wave energy and sedimentation, respectively, and are computed as:

$$WE'_{AV} = \sum_{t=1}^{T} WE'_t / T \tag{9}$$

$$S_{AV} = \sum_{t=1}^{T} S_t / T \tag{10}$$

where T is the total training time.

Complying to the normalisation practice, we used Eqs. 9 and 10 for normalisation of wave energy and sedimentation respectively for computing SP during the testing.

The excessive sedimentation during the summer of 1999 can be partly explained by a high value of SP (Fig. 4). In general, it was observed that SP was close to zero at the end of most summers. It can also be explained by the fact that the suspended sediment concentration at the North Sea is usually high at the end of winters and is low at the end of summers.

4. MODELLING

4.1 Artificial neural networks

The development of ANNs was inspired by the studies of the ability of the brain to learn from experience without predefined knowledge of underlying physical relation-

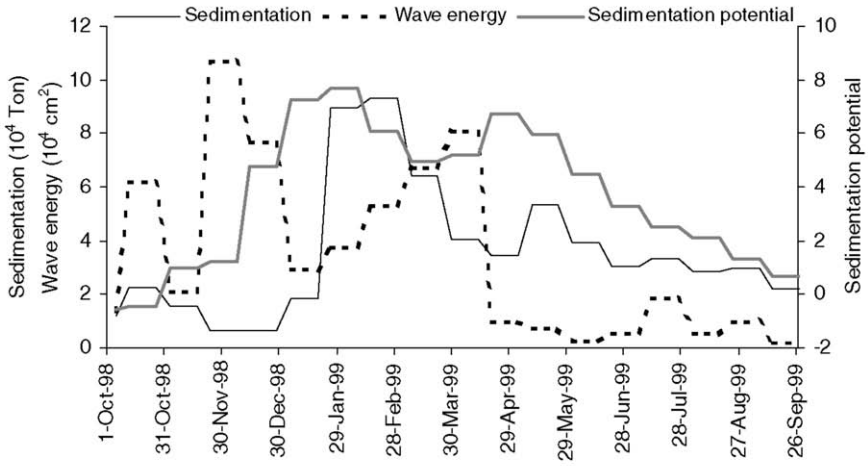

Fig. 4. The variation of sedimentation potential, sedimentation and wave energy at Maasmond.

ships. An ANN is a broad term covering a large variety of network architectures, the most common of which is a Multi Layered Perceptron (MLP). Such a network is typically trained by the so-called error-backpropagation method, which is a specialised version of a gradient-based optimisation algorithm.

Given a set of input vectors and the associated target (output) vectors, the objective of an ANN is to learn a functional relationship between the input vectors and the target vectors. Each target vector z is an unknown function f of the input vector x:

$$z = f(x) \tag{11}$$

The task of the network is to learn the function f. The network includes a set of parameters (weights vector), the values of which are varied to modify function f', which is computed by the network and should be as close to f as possible. The weight parameters are determined by training (calibrating) the ANN based on the training data set. More details about ANNs can be found in Schalkoff (1997) and Haykin (1999).

It can be noticed that quite limited amount of research has been done to explore the applicability of ANNs in predicting harbour sedimentation. A recent European project, *H-SENSE*, used ANNs, fuzzy logic and Dempster-Shafer theory of evidence in predict-

ing locations in harbour basin with high accretion rates (Rosenbaum, 2000). However, it did not consider temporal prediction of sedimentation. Bierens (2002; 1997) made an initial attempt of developing an ANN model of the sedimentation process at Maasmond, however, the accuracy of the model was poor.

Zyserman and Fredsøe (1994) used laboratory data to develop a semi-empirical equation to determine the bed concentration of sediment from Shield's parameter. Minns (2000) used ANNs, and Babovic and Abbott (1997) used genetic programming to replicate the equation of Zyserman and Fredsøe by using all available laboratory data instead of being confined to Shield's parameter and obtained promising results. Nagy *et al.* (2002) used an ANN to estimate the natural sediment discharge in rivers in terms of sediment concentration. They selected the inputs based on several trial and error experiments and reported results better than achieved by traditional models.

4.2. Training and results

Based on the previous discussion WE'_t, Q_t and SP_t were considered as the inputs to the ANN model. Sedimentation three weeks ahead (S_{t+1}) was considered as the output. The functional form of the model can be expressed as follows:

$$S_{t+1} = f(WE'_{t-1},\ Q_{t-1/3},\ SP_t) \tag{12}$$

The wave energy WE' was computed with a lag of three weeks using Eq. 4. $Q_{t\text{-}1/3}$ denotes the Rhine discharge with a lag of one week averaged over a three-week period. The sedimentation potential SP_t was computed using Eq. 6. It is evident from Eq. 6 that sedimentation potential at time t can be computed using the normalised wave energy and sedimentation data up to the time level t-1. The software NeuroSolutions (*www.nd.com*) and NeuralMachine (*www.data-machine.com*) were used for the ANN modelling. Multi-Layered Perceptron network trained by the back-propagation algorithm was used because of its simplicity and capability to learn non-linear relationship. One hidden layer was chosen. The hyperbolic tangent transfer function in the hidden layer and a linear transfer function were found to perform well. The number of nodes in the hidden layer was 4, which was found by training ANNs with the number of hidden nodes ranging from 1 to 12 and selecting the one with the minimum error. As the number of data points was not high, so instead of partitioning the total data into training, cross-validation and testing, we divided it into training (1992-1998) and testing (1999-2000) only. The maximum number of training iterations was selected as 5000, but after 300 iterations there was no further decrease in the root mean square error. As

we did not have a cross-validation dataset so it was not possible to ascertain whether there was any over-training or not.

The performance of the ANN model in training and testing are shown in Figs. 5 and 6, respectively. The correlation coefficient between the predicted and measured sedimentation was 0.90 and 0.82 for the training and testing data, respectively. The learning ability of ANN can be seen from the results of training, *i.e.,* the ANN model matched the measured data quite well (Fig. 5). However, errors in testing were not negligible (Fig. 6), particularly for high peaks. The general trend of sedimentation was predicted with the error mostly being within 10-30%. This is considered as a promising result. Improving the ANN model's predictive accuracy on the testing data, particularly for extreme events, needs further research and a research project in this regard is initiated.

5. DISCUSSIONS AND CONCLUSIONS

In order to build a sedimentation model for the approach channel of the port of Rotterdam initially two separate models for the areas *E* and *F* of Maasmond were contemplated. However, it appeared that the available number of hydrographic surveys for the area *F* was substantially less, and therefore only the model for the area *E* was built. Building a sedimentation model for the area *F* would be a challenge and can possibly be

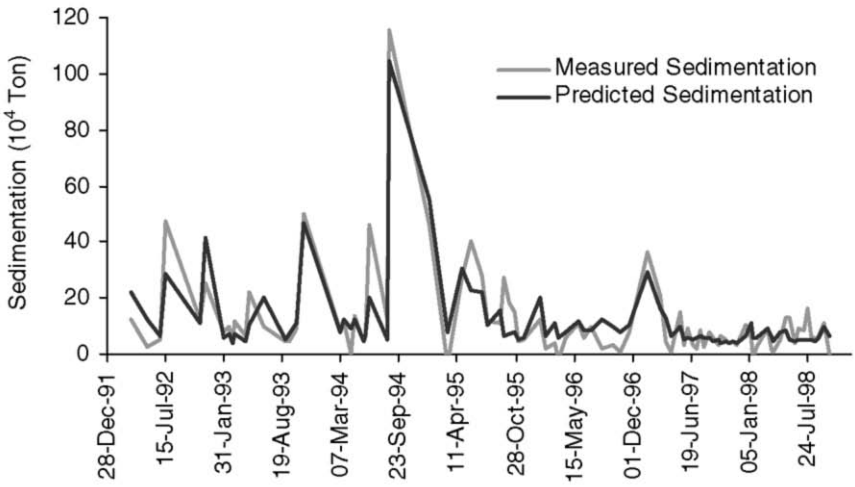

Fig. 5. Comparison of the sedimentation predicted by the ANN model (on the training dataset) with the measured sedimentation.

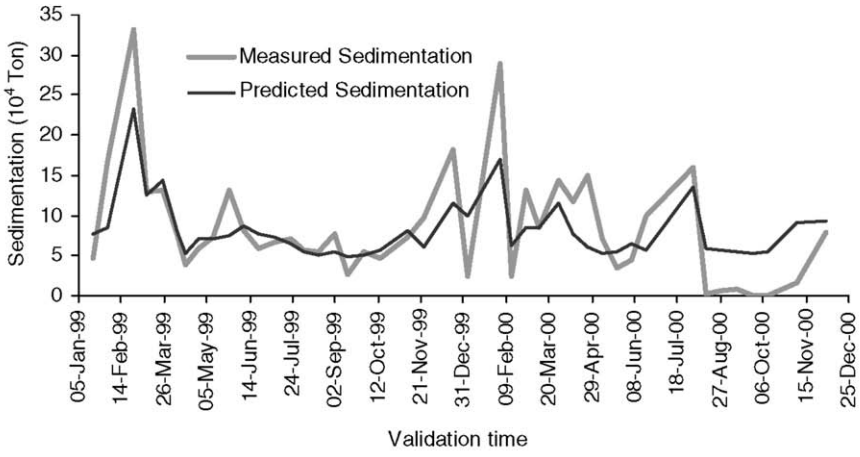

Fig. 6. Comparison of the sedimentation predicted by the ANN model (on the testing dataset) with the measured sedimentation.

carried out if the available partial surveys of the area *F* are fruitfully utilised. Similar to the findings of the previous researchers (*e.g.*, Merckelbach, 1996) it was noticed that waves cause large-scale sediment movements and eventual sedimentation at the Maasmond area. Quantifying the effects of other important variables (*e.g.,* wind) may also help in improving the modelling accuracy. It was observed that the statistical distributions of training and testing datasets were substantially different and this may cause a relatively large error on the testing dataset. One of the possible solutions to this problem could be selecting a proper partitioning of the dataset so that training and testing datasets have more or less similar statistical distributions. These issues are planned to be addressed in the future.

The main conclusions of the research are listed below:

- Data analysis corroborated the existing hypotheses about the sedimentation characteristics at Maasmond that large amounts of sediments are mobilised in the North Sea with erratic meteorological conditions. Once these sediments are available, the local hydro-meteorological conditions govern the transport process.
- The ANN model built showed reasonable performance. The data of 1992-1998 was used as the training data and the model predicted sedimentation for 1999-2000. The result was comparable to the measured sedimentation, although the error in prediction was not negligible, particularly for high peaks. Nevertheless, the general trend of sedimentation could be predicted quite well. The (ab-

solute) error in prediction mostly remained within 10-30%, which was found to be reasonable given the uncertainties associated with the assessment of sedimentation.

- Further improvements in the predictive accuracy of the model can be investigated by including additional information about the physical processes in selecting input parameters and exploring other machine learning modelling methods such as radial basis function network, M5 model trees (Solomatine and Dulal, 2003).
- The critical factor in ANN modelling is the quality and quantity of data. The number of hydrographic surveys was a limiting factor. However, it needs to be pointed out that the hydrographic surveys covering the complete area of E were only considered. In addition, a plenty of partial surveys are available; efforts are needed to incorporate these data into the model which might improve its performance. Presently, research is initiated to improve the model's predictive accuracy and to explore the possibility of using the model in a decision making framework of the port authorities.

ACKNOWLEDGEMENTS

Part of this work was performed in the framework of the projects "Sedimentation model for the port area of Rotterdam" and "Data mining, knowledge discovery and data-driven modelling" of the Delft Cluster research programme supported by the Dutch government.

REFERENCES

Babovic, V. and M.B. Abbott. 1997. The evolution of equations from hydraulic data. *Journal of Hydraulic Research*, 35(3), 397-430.

Bhattacharya, B. and D.P. Solomatine. 2003a. Neural networks and M5 model trees in modelling water level-discharge relationship for an Indian river. In: *Proceedings of the 11th European Symposium on Artificial Neural Network.* Verleysen, M. (ed.), Bruges (Belgium), d-side Pub., Evere (Belgium), 407-412.

Bhattacharya, B., A.H. Lobbrecht and D.P. Solomatine. 2003b. Neural networks and reinforcement learning in control of water systems. *Journal of Water Resources Planning and Management,* ASCE, 129 (6), 458-465.

Bhattacharya, B. and C. Buraimo. 2003c. Data-driven modelling in context to sediment transport. *Proceedings of the NCR Days-2003*, Roermond, The Netherlands, 54-55.

Bhattacharya, B., D.L. Shrestha and D.P. Solomatine. 2003d. Neural Networks in Reconstructing Missing Wave Data in Sedimentation Modelling, *Proceedings of the XXXth IAHR Congress*, Thessaloniki, Greece, vol. D, 770-778.

Bhattacharya, B. and D.P. Solomatine. 2002. Application of artificial neural networks and M5 model trees to modelling stage-discharge relationship. In: *Proceedings of the 2nd Int. Symposium on Flood Defence*. Wu, B.S., Z.Y. Wang, G.Q. Wang, G.H. Huang, H.W. Fang and J.C. Huang (eds.), Beijing, China, Science Press New York Ltd., New York, 1029-1036.

Bierens, R.W.P. 2002. *Sedimentation in the Maasmond using ANN.* Bulletin 109, PIANC, 43-53.

Biereens, R.W.P. 1997. *Sedimentation in the Maasmond using ANN.* MSc Thesis, Delft University of Technology, The Netherlands.

de Kok, J.M. 1994. *Numerical modelling of transport processes in coastal waters.* PhD Thesis, University of Utrecht, The Netherlands.

Haykin, S. 1999. *Neural networks: A comprehensive foundation.* Prentice Hall, New Jersey, USA, 161-172.

Merkelbach, L.M. 1996. *Sedimentation in the Maasmond; A correlation analysis.* Report No. NZ-96.02, Ministry of Transport, Public Works and Water Management – Directorate of North Sea, The Netherlands.

Minns, A.W. 2000. Sub-symbolic methods for data mining in hydraulic engineering. *Journal of Hydroinformatics*, 2(1), 3-13.

Minns, A.W. and M.J. Hall. 1996. Artificial neural networks as rainfall-runoff models. *Hydrological Science Journal*, 41(3), 399-417.

Nagy, H.M., B. Watanabe and M. Hirano. 2002. Prediction of sediment load concentration in rivers using artificial neural network model. *Journal of Hydraulic Engineering*, ASCE, 128(6), 588-595.

Rosenbaum, M. 2000. *Harbours-silting and environmental sedimentology (H-SENSE), Final report.* Dept. of Civil and Structural Engineering, The Nottingham Trent University, Nottingham, UK, (*http://hjs.geol.uib.no/HSense/*, 19/11/2003).

Schalkoff, R.J. 1997. *Artificial Neural Networks.* McGraw-Hill, New York, 184-197.

Siltman. 1996. *Eindrapportage* in-situ *metingen* (in Dutch), Oceanographic Company of the Netherlands, i.o.v. RIKZ, CDROM entitled "Maasmond winter 1995/1996."

Solomatine, D.P. and K.N. Dulal. 2003. Model tree as an alternative to neural network in rainfall-runoff modelling. *Hydrological Sciences Journal,* 48(3), 399-412.

Vuurens, R.S. 2001. *Data-driven Modelling of Sedimentation in the Rotterdam Port Area*. MS Thesis, Delft University of Technology, The Netherlands.

Winterwerp, J.C., R.E. Uittenbogaard and J.M. de Kok. 1998. Rapid siltation from saturated mud suspensions. In: *Coastal and Estuarine Fine Sediment Processes*, McAnally, W.H. and A.J. Mehta (eds.), Elsevier, Amsterdam, 125-146.

WL | Delft Hydraulics. 2001. *Description and model representation T_0 situation Part 1: The transport of fine-grained sediments in the southern North Sea*. Report No. WL2001003 Z3030.10, WL | Delft Hydraulics, The Netherlands.

Zyserman, J.A. and J. Fredsøe. 1994. Data Analysis of Bed Concentration of Suspended Sediment. *Journal of Hydraulic Engineering,* ASCE, 120(9), 1021-1042.

Estuarine and Coastal Fine Sediments Dynamics
J.P.-Y. Maa, L.P. Sanford and D.H. Schoellhamer (editors)

The COSINUS Database for Cohesive Sediment Transport in Estuaries and Coastal Zones

Markofsky, M. and D. Ditschke

Institute of Fluid Mechanics and Computer Applications in Civil Engineering,
Hannover University, Appelstr 9a, 30167 Hannover, Germany

The COSINUS database is an internet oriented documentation of the laboratory, field and numerical data collected during the COSINUS project. It contains information about hydrodynamics, turbulence und transport including sediment properties and concentrations as well as information on the instrumentation used, data-processing etc. The results of numerical simulations for a number of test cases are stored in the database for use as a benchmark or inter-comparison with other models.

In this paper, the structure of the database is described and its content summarized.

KEY WORDS

Data Base, Cohesive Sediment, Field and Laboratory Data, Numerical Modelling, COSINUS

1. INTRODUCTION

From 1997 - 2000 the EU funded the COSINUS Project (Prediction of **Co**hesive **S**ediment Transport and Bed Morphodynamics in Estuaries and Coastal Zones with **In**tegrated **Nu**merical **S**imulation Models) within the MAST III Program. Details of the project can be found in the papers of the INTERCOH 2000 conference.

The main objective of the COSINUS project was to establish well validated physical and mathematical descriptions of the behavior and fate of concentrated near-bed suspensions and their interaction with the water column and the sediment bed. This three year project conducted between 1997 - 2000, was funded by the EU within the MAST III Program, involved close cooperation between scientists and Engineers from 11 Institutions from 6 European countries performing numerical and laboratory studies of cohesive sediment transport as well as field investigations. This data was used for the improvement and further development of appropriate numerical models.

The following tasks were defined in the project:

- TASK A: Turbulence Modelling
- TASK B: Flocculation
- TASK C: Concentrated Benthic Suspension (CBS) Dynamics
- TASK D: Bed Dynamics
- TASK E: Applied Modelling
- TASK F: Data Management

Within this context, a large amount of data was generated. One of the project deliverables was an internet oriented data base containing the data of field surveys and laboratory experiments e.g. information about sediment properties, hydrodynamics, geometry, bathymetry,

concentrations, instrumentation, data-processing etc. Also the results of numerical simulations for a number of test cases are stored in the data base for use as a benchmark or for inter-comparison with other models.

The objective of the data base management task is to make the data collected during the project available to third parties. The reader is referred to http://www.hydromech.uni-hannover.de/cosinus/database/. The data will also be transferred to the forthcoming INTERCOH website. A CD-Version of the database at the time of publication is included in this book.

This paper reports on the data base methodology with a short description of the input tool and presents an overview of the data. Further details of the COSINUS project can be found in the COSINUS Final Scientific Report, 2000. (*Berlamont, J.E. & Toorman E.A. (ed.)* http://www.kuleuven.ac.be/bwk/cosinus/COShome.htm. and the proceedings of the INTERCOH 2000 conference (see also section 6. "LITERATURE").

2. DATABASE CONCEPT – META-DATA

Object oriented concepts need to define variables and methods. In this sense the data-base has the variable types *meta-data* (meta-data are descriptions of data), and *data* defined by their rules (see Input Tool).

A basic decision for the data management system was which data were to be stored centrally on the server of the data manager and what locally on the server of the individual partner. One must consider that with a large number of institutions working on different types of problems it is from a practical point of view difficult to impose standard data formats on a working level. One just has to consider different work sheet or word processor formats to illustrate this problem. Essentially each partner works with his data as he sees fit. Final data storage can, however, be done in ASCII format in the case of tabulated data. Results of numerical models have to be more selectively treated (see 3.5).

For meta-data this problem could be solved with the use of an Input Tool developed especially for this project thus allowing each partner to input to the data base a description of his data with a link to his computer where the data was stored.

Two possible ways of dealing with meta-data are shown in Fig. 1. In the first solution only the address of the project partner would be on the server of the data manager and all of the meta-information and the data are stored locally. The second solution has the meta-data on the central server and only the data itself are stored on the partner's server. This is the basis of the COSINUS data base and has the significant advantage that the input tool and the overall data information can be centrally managed thus avoiding redundancy and allowing the data manager to have direct access to all of the meta-data. Further, each partner can read all of the meta-data but can only change his own.

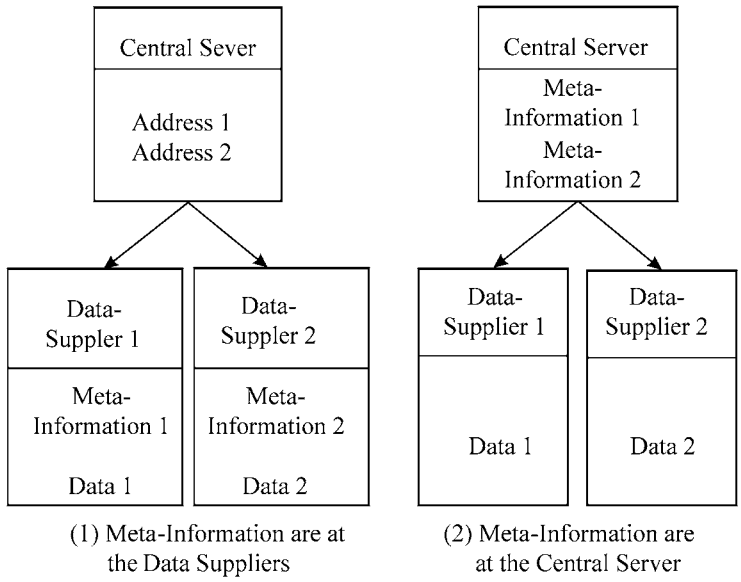

Fig. 1: Local and Centralized -Meta-Data Storage

During the project, the data itself was on the local server of the partner responsible for the collected or generated data. In this way, an overview of the data could be obtained without the necessity of physically transferring the data to the data manager. The link to the data itself was done through the internet. As such, the responsibility and the maintenance of the data itself remained at their source. Any other solution would have generated significant problems in modifying the data or the way in which it is formatted and also unnecessary data transfer.

Much of the data located on the local servers were transferred to the central server following the project. This data could then be stored on a CD such as that attached to the proceedings. This avoids the problem of maintaining the exact links to the local servers after project completion.

2.1. The Input Tool

The input tool for the meta-data was structured by institute (**Fig. 2**). Within an institute various researchers were given access with their individual passwords. The input tool enables the user to:

- create a new package with an introduction (head entry) chapter
- create a new sub-chapter
- delete a sub-chapter (with all sub-subs)
- edit text into a chapter
- connect an external data-file to a string in this chapter
- connect a reference to a string in this chapter

Welcome to COSINUS Database

Here you find results of the MAST3 COSINUS Project. Click **(download)** for a complete description.

Download the **Final Scientific Report**

CONTRIBUTING INSTITUTIONS
DH Delft Hydraulics
DHI Danish Hydraulic Institut
HR Hydraulic Research Wallingford
KUL Katholieke Universiteit Leuven
LNHE Laboratoire National d'Hydraulique et Environnement, Chatou
TUD Technische Universiteit Delft
UHA Universität Hannover
UJF Université J. Fourrier, Grenoble
UOX University of Oxford
UPL University of Plymouth
UWB University of Wales, Bangor

Participants of the COSINUS Project can use the **input tool** to complete their entries.

The data, you find in this database, were obtained from laboratory experiments, field surveys and numerical simulation in the **COSINUS** research project.

The description of the data (meta-data) and the data itself are organised in packages which are comparable to reports on paper with a data-disc attached. One package contains the description and the data of one set of experiments and was supplied by only one participant of the COSINUS project.

Fig. 2: The Input Tool

2.1.1. Meta-Data Rules

1) Each chapter and sub-chapter of the report (package) is represented by its own html file. There can not be any html file that contains both a chapter and its sub-chapter(s) (Fig. 3).

2) There have to be links to all sub-chapter files.

3) The links connecting the package internally have to be relative URL's Example: < a href = "expero_2.1.html" > Rheometer measurements < /a >.

4) The links connecting data have to be absolute URL's, pointing to a copy of your data on your internet server. Example: < a href = "http://www....." > data < /a >.

5) The html- < title > -tag contains the number of the (sub)-chapter before the headline. For example: < TITLE > 2.1 Rheometer measurements < /TITLE > With "2.1" being the number of the chapter, indicating that it is the first subchapter of "2. Mud properties" The top entry is the report (package) title., i.e. the introduction of the report, and contains no number before the headline.

6) The first link in the html file connects to the chapter above. For example: the first link in the file representing chapter 2.1 points to chapter 2. All other links point down to sub-chapters or to external references or to data.

7) repeat the headline after the first link.

2.1.2. Reasons for the Meta-Data Rules:

- Rule 1 is needed to define rules 2-6.
- Rule 2 is necessary to navigate inside a package with an internet browser.
- Without rule 3 it would be impossible to transfer the package onto another server, or onto a CD-ROM.
- Rule 4 is necessary because the data itself is on the hardware of the supplying institute.
- Without rule 5 the input-tool is not able to go up or down in the chapter hierarchy. Without rule 5 the tool that collects all chapters into a report is not able to find the right position of the chapter and is not able to build up a content list. Without it the overview tool cannot show the chapter at the right location.
- Rule 6 helps the user navigate inside the package.
- Rule 7 is recommended to improve readability.

2.1.3. Methods to Access Meta-Data and Data

The meta-data are organized in packages (reports), which are divided into chapters. The navigation within the meta-data layer includes the following steps (see **Fig. 3**):

- enter a package
- go down to a sub-chapter
- go up to chapter above
- download data connected to this chapter
- follow a reference

After accessing a package you will find the data below the description (meta-data). Once you have selected the part of the data you are interested in, you must go through the description before you access the data itself.

Each data-package is accessible via the participating institution which supplied the data (see **Fig. 2**). All data are available in a standard ASCII format. Additionally, the same data may be supplied in other formats, such as spread-sheets or images.

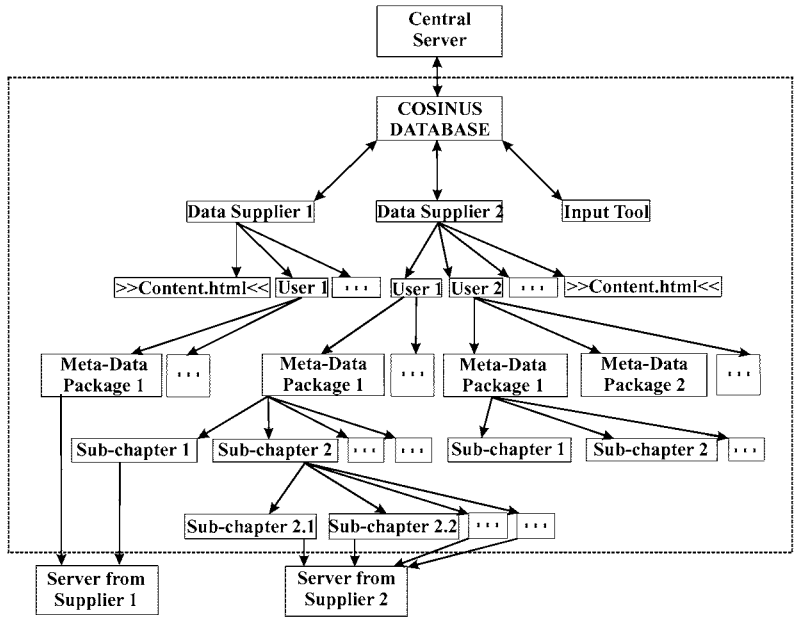

Fig. 3: Data Structure (The large box represents the meta-data located on the central server)

3. WHAT DATA IS IN IT?

Following the technical annex of the COSINUS project, the following data were collected during the project and input to the data base (The Siltman data were not collected within the COSINUS project but were made available by Rijkswaterstaat :

- Turbulence Modelling (Task A)
- Flocculation Field Test (Task B.1)
- Flocculation Laboratory Data (Task B.3)
- CBS Generation Laboratory Data (Task C.1)
- Consolidation Column Laboratory Data (Task D.1)
- Bed Erosion Laboratory Data (Task D.2)
- Numerical Data of a 1DV-Test Case for a Schematic Estuary and three 3-D case studies for Real Estuaries (Task E)

Brief descriptions of the Tasks are presented below. The reader is referred to the data base and to papers within the INTERCOH 2000 conference (see literature) for details.

3.1. TASK A: Turbulence Modelling (KUL, DH, TUD)

Task A involved the turbulence Modelling of sediment laden flow i.e. turbulence damping and turbulence production in concentrated suspensions. The major numerical data and the resulting parameterisations are summarized in section 3.5. The SILTMAN field data are described in the following section.

3.1.1. Siltman Data

The Dutch SILTMAN Data (Winterwerp, 1999) of Rijkswaterstaat (Netherlands Ministry of Transport and Public works) on turbidity concentrations close to the bed at a location offshore the entrance to the Port of Rotterdam (**Fig. 4**) is included in the data base. In this test case a lutocline is temporarily formed, resulting in complete decay of turbulence. The data include continuous measurements flow velocity (0,35 m above the bed) and turbidity (0,15 and 0,55 m above the bed) at four permanent stations and a series of "13-hour" boat-measurements. The associated wind data from the measurement location Hoek van Holland are also documented in the database. (This data was not collected within the COSINUS project but was made available by Rijkswaterstaat).

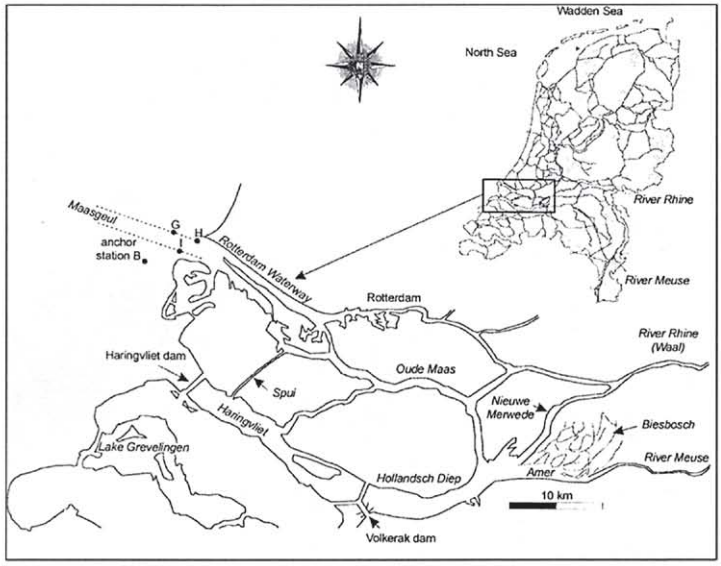

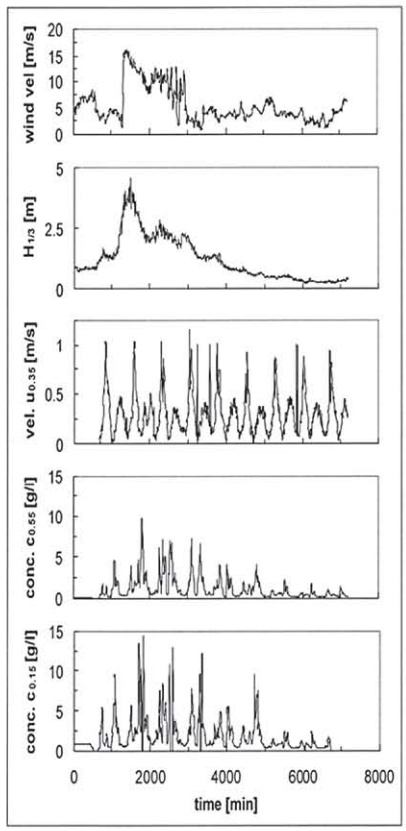

Fig. 4: Typical Data from the Siltman Study (after Winterwerp, 1999)

3.2. TASK B: Flocculation

Task B included:

- Flocculation Field Test Data (Task B.1)
- Flocculation Laboratory Data (Task B.3)

3.2.1. Flocculation Field Test Data

In TASK B.1 (UPL, HR, UWB) measurements were taken within the turbidity maximum region, at Calstock, in the Tamar Estuary in south west England at times during the tidal cycle when flow conditions were either uniform or steadily changing (Dyer *et al.*, 2002; Manning and Dyer, 2002; Winterwerp, Bale, *et al.*, 2002). Simultaneous measurements were obtained at both ends of a straight reach of the estuary to facilitate the advective gradients, and changes within the reach to be assessed. Station A was approximately 970 m below the Calstock railway bridge, and station B was situated 400 m upstream. Both stations were main channel moorings owned by the Calstock Boatyard. Both flood and ebb conditions were covered and a range of tides from low neaps through to high springs. Eight simultaneous sampling runs, each of approximately three hours duration, were completed during the experimental period.

The meta-data include:

- A summary table of the data coverage of the COSINUS experiment;
- A brief overview of each of the various data types submitted;
- Descriptions of the instruments (many of which are unique prototypes) used to measure the various parameters;
- Additional laboratory procedures employed during the data collection process, together with a systematic outline of the salient computational processes have been listed (i.e. primarily for the INSSEV floc data).

A summary report of the experiment, together with photographs of the various activities are linked to the main COSINUS website to enable potential data users a much better opportunity of being able to visualize the location and methods used during the experiment.

The data includes the following:

- Gravimetric results of sediment samples collected throughout individual runs, together with estimates of organic content;
- Profiles of temperature, salinity, and turbidity conducted at 30 minute intervals throughout individual runs (a number of summary graphs have been included);
- Time series of surface current velocity and direction;

- Time series of mean near bed current velocity profiles and direction;
- Time series of near bed suspended particulate matter concentration variations;
- Mean floc characteristics, such as: floc size, effective density, settling velocity, porosity, fractal dimension, and macrofloc / microfloc ratios.

All data have been archived in both a Microsoft Excel spreadsheet format (including some graphs) and ASCII text format. An example of the type of data input to the data base is the input of the University of Plymouth and the University of Wales from the COSINUS field experiment of September 1998 (see **Fig. 5** and the COSINUS Data Base).

The database was used successfully for inter-comparison and modelling purposes by the following COSINUS partners: UWB, PML, HR Wallingford, DHI.

Three sub-samples were taken from the Tamar mud and analyzed by Oxford University (see COSINUS Data Base, UOX). Although the mud was well mixed using both a mechanical mixer and by hand, the samples were taken from different levels (high, mid, low) in the storage container to ensure that the grain size analysis was representative of the sample. The reported measurements include organic content, grain size distribution and particle density.

3.2.2. Flocculation Laboratory Data

TASK B.3 involved:

- Grid tank experiments with oscillating grid generated turbulence (UJF);
- Settling column with compressed air generated turbulence (UOX) and
- Annular flume with shear flow generated turbulence (TUD, see 3.3.1)

Experiments on floc dynamics under controllable conditions were carried out. Natural sediments were mixed at different concentrations and added to still and turbulent water agitated using turbulent grids (UJF), compressed air (UOX) or shear flow (TUD). Concentrations and flow properties (velocities and turbulence intensities) were measured. A video camera was used to monitor the flocs. A range of sediment types and pore water pressures were used.

3.2.2.1. Grid Tank Experiments (UJF)

The Université J. Fourier's contribution to the COSINUS project deals with the generation and examination of a CBS layer. Laboratory experiments were conducted in which the production of turbulence resulted from stirring using a grid located near the bottom of a cubic tank (**Fig. 6**, Mory et al., 2002; Winterwerp, Bruens et al., 2002). This experimental procedure resulted in the formation of CBS layer with suspended sediment concentrations of up to 202 g/l. The thickness of the CBS-layer, its mean concentration and the shape of the lutocline (the interface between the CBS layer and the dilute suspension layer) were examined with respect to the production of turbulence and sediment loading. Density as well as turbulent velocity profiles were obtained and integral length scales estimated in some cases. In collaboration

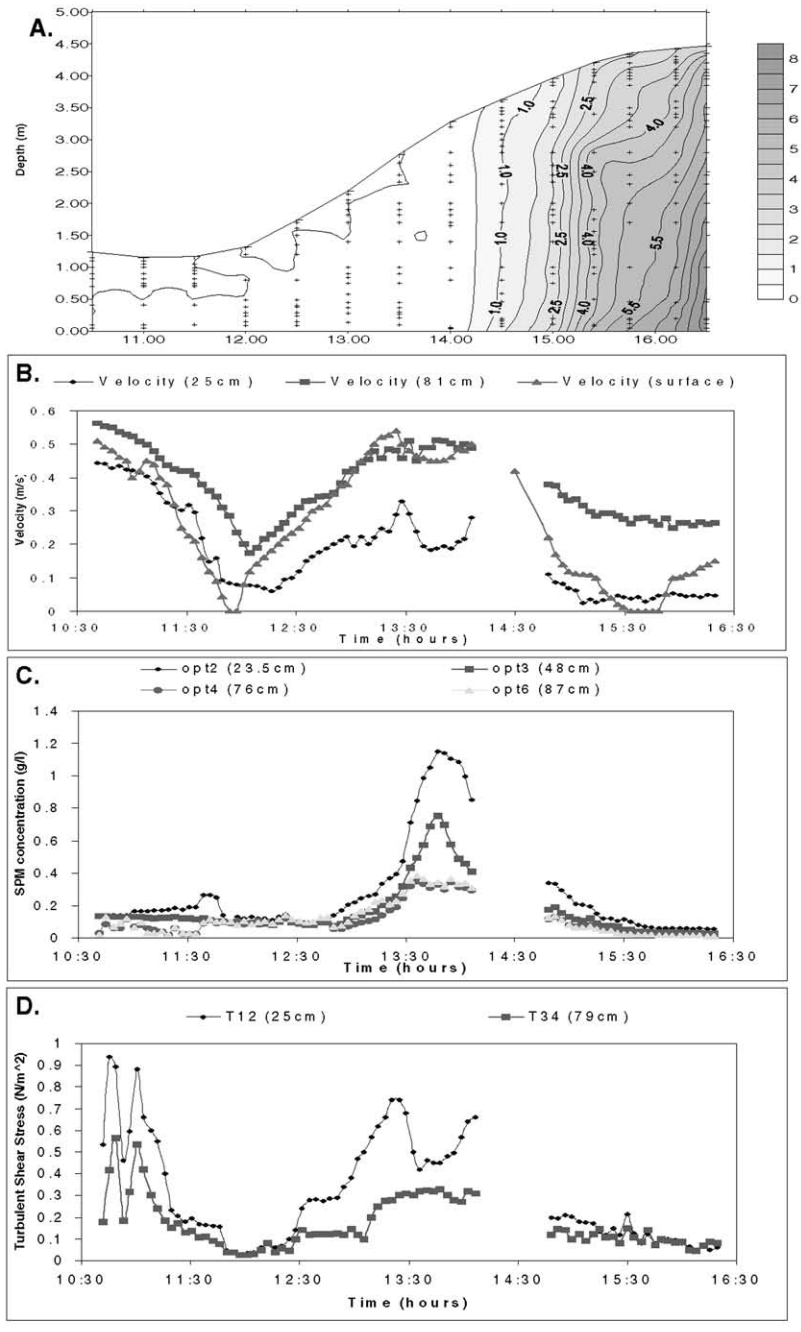

Fig. 5: Time Series of Variations in: A. Salinity, B. Velocity, C. Suspended Particulate Matter Concentration and D. Turbulent Shear Stress at Location A for the Spring Tide on the 24th June 1998 (after Manning and Dyer, 2002).

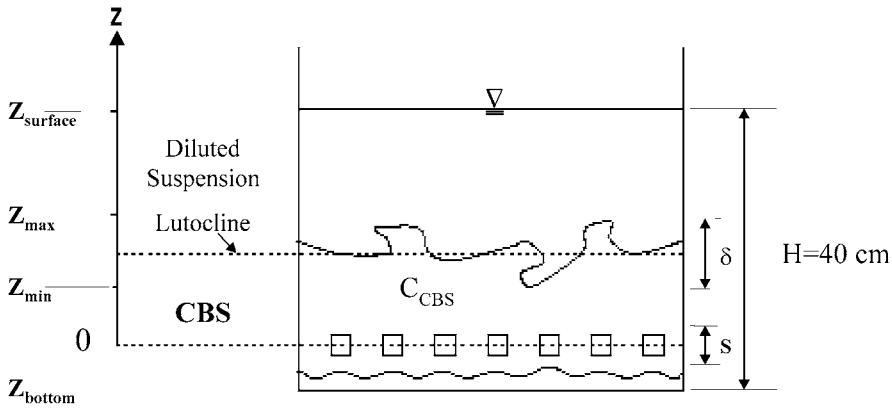

Fig. 6: Grid Tank Experiments (Mory et al., 2002)

with the Institute of Marine Studies (UPL), floc properties were measured for concentrations of up to 8 g/l in order to estimate the settling flux.

Experiments were also carried out in clear water to define a reference state for the vertical distribution of turbulence inside the tank. Comparison between experiments in clear water and experiments with sediments gives information about the influence of sediments on the damping of turbulence. The results show that the influence of the sediment on the damping of turbulent is first seen at the lutocline, where both the sediment concentration and the turbulent kinetic energy rapidly drop. The Experiments were performed with grid oscillation frequencies of 3, 4 and 6 Hz.

3.2.2.2. Settling Column Experiments (UOX)

Settling column experiments were conducted at the University of Oxford to determine the effects of flocculation and settlement on bed properties (Lintern, *et. al.*, 2002).

The studies included the measurements of floc size, shape, settling velocity, concentration, salinity and pH in a settling column 1.5 m high and 10 cm internal diameter. In the bed bulk density, pore pressures, void ratios, permeabilities, and erosion shear stress were measured.

Eight tests (COS1 to COS8) were conducted. COS1 tested the flocculation and consolidation properties of natural Tamar mud in Plymouth Harbor seawater with minimal preparation or disturbance of the natural material. COS2 and COS3 attempted to distinguish the differences between fresh and salt water conditions using brackish Tamar mud. COS4 through COS7 tested the effect that different concentrations have on both the floc properties and the subsequent bed properties. For example, in COS5 (effect of varying sedimentation rate, and added turbulence) the rate of sedimentation was altered in a single column by changing the concentration of the mud in the initial mixing basin. Turbulence was added to the column

using compressed air. It was particularly important to examine whether or not the floc properties would change under different conditions, since the subsequent research depended entirely on such changes occurring. COS7 and COS8 used the same experimental setup, except that the settling column of COS8 was filled with water of a low pH. This had the effect of making larger flocs than in the other experiments between concentrations of 200 to 500 mg/l.

UOX has produced and delivered the following data:

- Floc characteristics from over 2000 images taken throughout 6 experiments (**Fig. 7**);
- Bed data and other properties for 18 experiments.

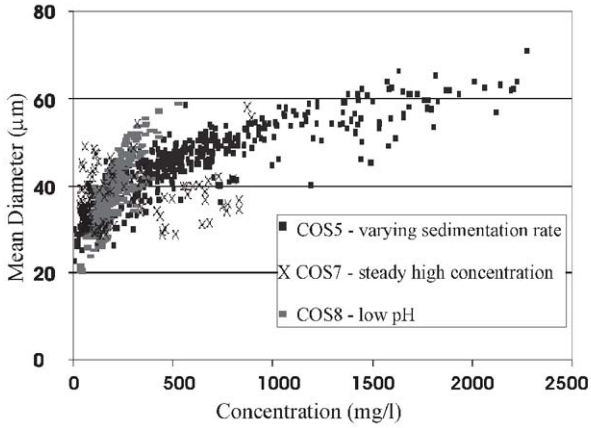

Fig. 7: Typical Data (Mean Diameter (µm) vs. Concentration (mg/l)) from the Settling Column Experiments (after Lintern and Sills, 2000)

3.3. TASK C: CBS DYNAMICS

3.3.1. Annular Flume Experiments (TUD)

At the TUD, experiments were carried in an annular flume (**Fig. 8**) to simulate the entrainment of the CBS layer into overlying turbulent water (Winterwerp *et al.*, 2002; Bruens *et al.*, 2002). The flume cross section is 0.4 m high and 0.3 m wide, and the flume has a diameter of 3.7 m. The flow in the annular flume was driven by a top lid and secondary currents were minimized by counter-rotating the flume itself. The aim of the experiments was to get insight into the process of entrainment by a turbulent CBS and to obtain data to validate numerical models of CBS dynamics.

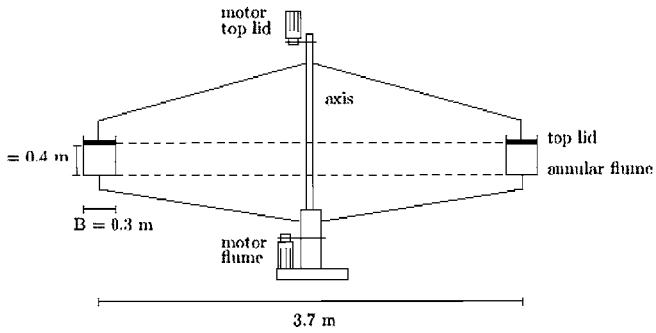

Fig. 8: Annular Flume of the TU Delft (after Bruens, Winterwerp and Kranenberg, 2002)

First, an accurate optimization of the ratio of rotational speeds of the top lid and flume had to be assessed. The balance equation of momentum was used to derive a theoretical equation for this optimal ratio. Simulations with a numerical flow model PHOENIX (Booij and Uijttewaal, 1999) and experiments with dye were carried out to validate this equation. Both the simulations and the experiments showed a minimal intensity of secondary flow and a nearly uniform distribution of bottom shear stress when the equation for the optimum ratio was applied.

The following parameters were measured during the 6 experiments with a CBS layer:

- Sediment concentration (with turbidity meters at four heights - 5, 10, 15 and 25 cm above the plate);
- Flow velocity (with electromagnetic flow meters at two heights);
- Height of the interface between the CBS and the upper water layer.

The results (**Fig. 9**) show the increase in height of the turbulent CBS layer and the decrease in concentration of this layer as a result of entrainment of the overlying water by the CBS.

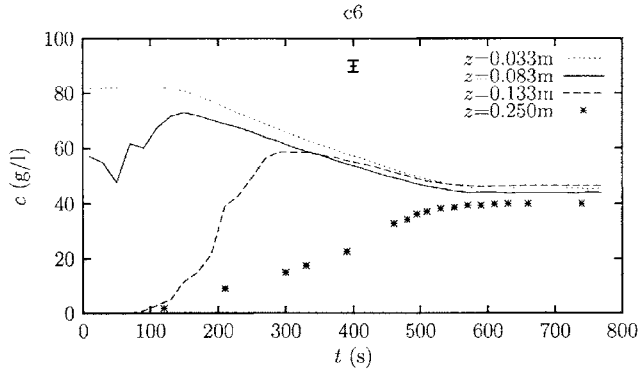

Fig. 9: Typical Temporal Concentration Data from the Annual Flume Experiments (after Bruens, Winterwerp and Kranenberg, 2002)

3.4. TASK D: Bed Dynamics

3.4.1. Laboratory Experiments on Consolidation and Strength Evolution (TUD)

The sedimentation and consolidation of Caland-Beer Channel mud and Dollard mud was simulated in segmented consolidation columns (Merckelbach et al., 2002). The use of segments made it possible to obtain well defined and undisturbed samples of the mud bed. For this reason, more accurate shear vane measurements could be taken than if conventional consolidation columns had been used.

Four segmented and one conventional consolidation columns were used (**Fig. 10**). The segmented columns were dismantled at different times to study the time evolution of the strength of the mud bed. After dismantling, shear vane tests were carried out and density measurements taken with conductivity probe. The mud layer density profiles in the conventional column were measured with a gamma-ray densimeter. Pore water pressures were measured at several times. From these measurements, effective stresses and permeabilities were calculated. Various reheological parameters were derived from four different types of shear vane measurements (i.e. **Fig. 11** and **Fig. 12**).

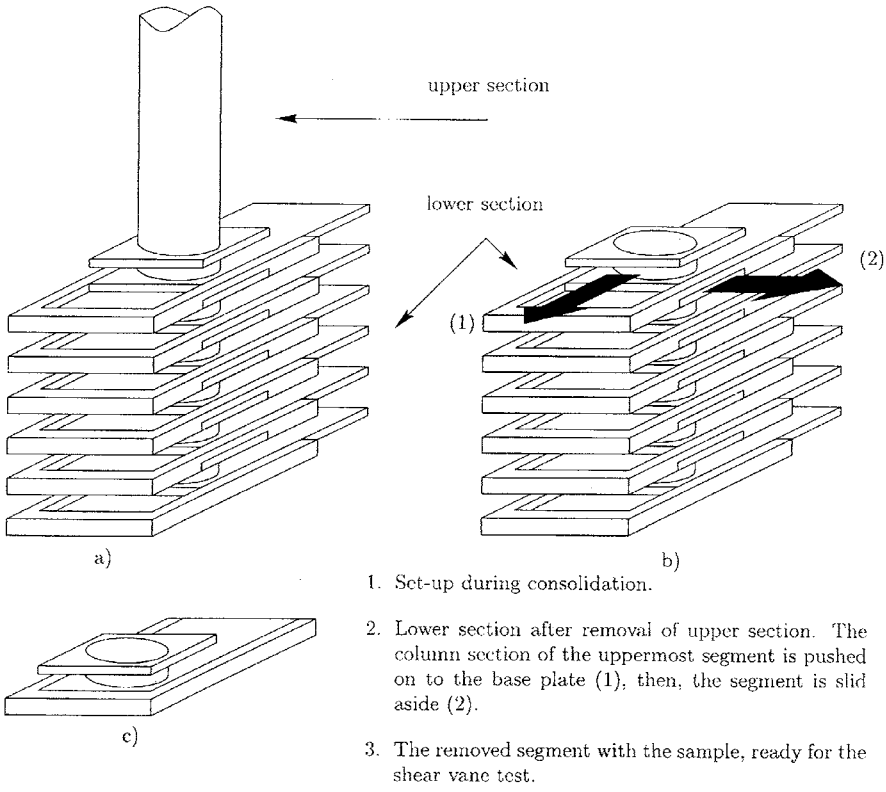

Fig. 10: Segmented Consolidation Columns (Merckelbach et al., 2002)

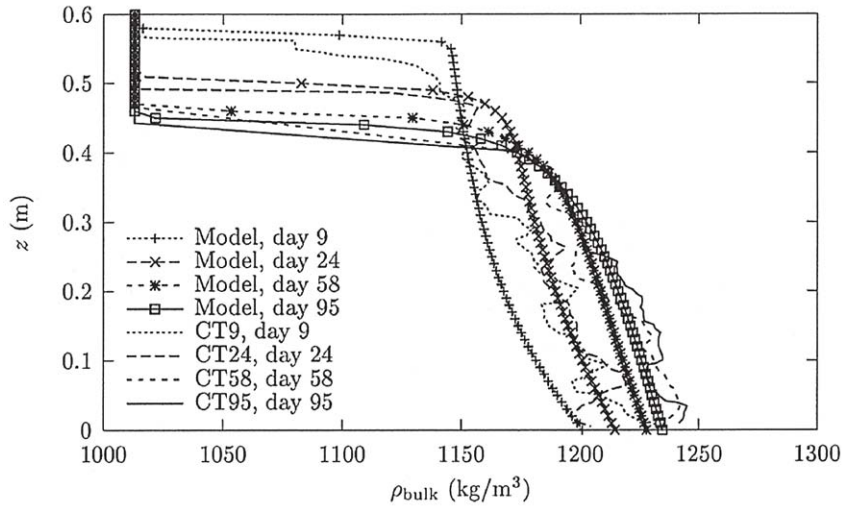

Fig. 11: Measured and Calculated Density Profiles of Experiment CT (after Dearnaley, *et al.*, 2002)

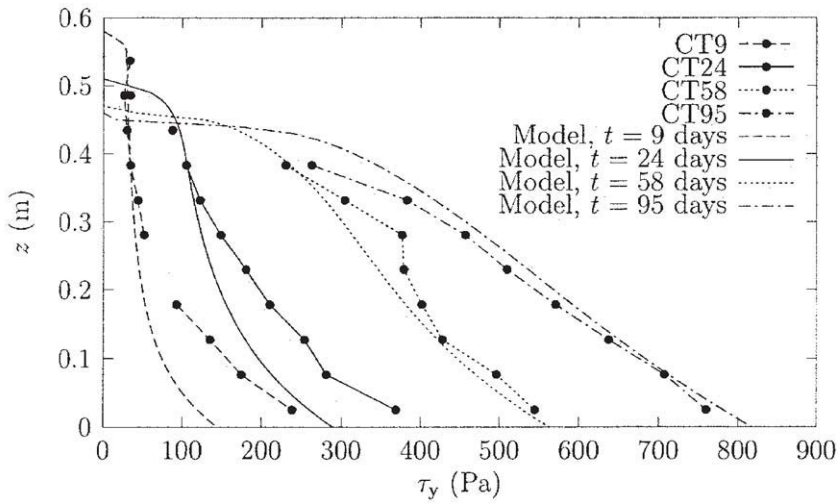

Fig. 12: Measured and Calculated Yield Strength Profiles of Experiment CT (after Merckelbach *et al.*, 2002)

3.4.2. The Effect of Consolidation Time on Bed Erodability (UOX)

Research has shown that many factors affect the erosion resistance of cohesive sediment, including hydrodynamics, sediment characteristics, chemical and biological influences. The **I**nstrument for Measuring **S**hear Stress **I**n **S**itu (ISIS) was developed by H.R. Wallingford for

measuring surface erosion shear stress and erosion shear stress profiles on mud beds. This instrument, combined with the steady sedimentation system and X-ray apparatus available at Oxford University, allows the erosion properties of various bed types to be examined (Lintern et al., 2000).

The beds were built of flocs which were sedimented under different physical and chemical conditions. Properties which were altered include organic content, pH, floc concentration and consolidation time.

The first series of tests investigated the effect of consolidation time. Five tests were conducted using mud from the Tamar estuary in Southwest England (see 3.2.1). Most of these were sedimented from an initial slurry density of 1.164 g/cc and 190 mm height, and allowed to mature for 3, 5, 15, 25 and 50 days. One column was sedimented from an initial slurry density of 1.137, an initial height of 201 mm, and allowed to settle for 7 days. During sedimentation X-ray measured density profiles showed that all columns settled at similar rates (approximately 55 mm in the first 4 days), except the column with the lower initial density which settled more quickly.

Data from the 7 ISIS erosion tests are described in terms of shear stress, the concentration of sediment eroded from the bed and rate of erosion. Shear stress is calculated mathematically using the distance between the suction head of the ISIS and the top of the bed, and by using the pump speed. Concentration is calculated from turbidity measurements made with the ISIS and indicates the amount of mud which had been eroded from the bed. The Erosion rate is calculated by measuring the turbidity over two consecutive ten second intervals, converting them to concentration and then subtracting the first from the second interval.

Plotting concentration against applied shear stress gives an indication of the rates at which the different beds erode under given increasing shear stresses. The results show that this rate is different for the different bed types. The first two results, ISIS1 and ISIS2, indicate that the upper bed strength develops with time, which is expected. Visual observation indicates that the upper bed liquefies during erosion. This was confirmed using the X-ray density profiles.

Further experiments included destroying the organic matter in the soil, altering the pH in the water, and altering the size of the flocs with which the bed is composed, in order to determine their effect on bed strength.

3.5. TASK E: Applied Modelling

This Task included the following two test cases and application to three European estuaries, i.e.:

- 1-DV case to evaluate the vertical processes such as the damping of turbulence by salinity and sediment, and a
- schematic estuary (2-DV case) to include horizontal processes (advection).
- Tamar in the UK (DHI).
- the Loire in France (LNH) and the
- the Weser in Germany (UHA).

5 Partners (HR, KUL, DHI, UHA and LNH) ran the two cases, in order to compare the sensitivity of the numerical models to the parameters.

3.5.1. Test Cases

3.5.1.1. 1-DV

The 1-DV model is a water column 16 m deep with a constant sediment concentration C_0 at the initial time step. Two values for this concentration have been considered: one below the saturation concentration (10 mg/l), and one around the saturation concentration obtained by the Delft-1D model (23 mg/l). The mean flow velocity was 0.2 m/s and the settling velocity 0.5 mm/s (Violeau et al., 2002).

Regarding turbulence, the numerical models including a Prandtl mixing length closure considered both Munk-Anderson and Kranenburg damping functions. Two equation k-ε and k-ω turbulence closure formulations were also used.

The data includes velocity and concentration profiles (**Fig. 13**) and associated parameters such as the shear velocity and the kinematic diffusivity distribution.

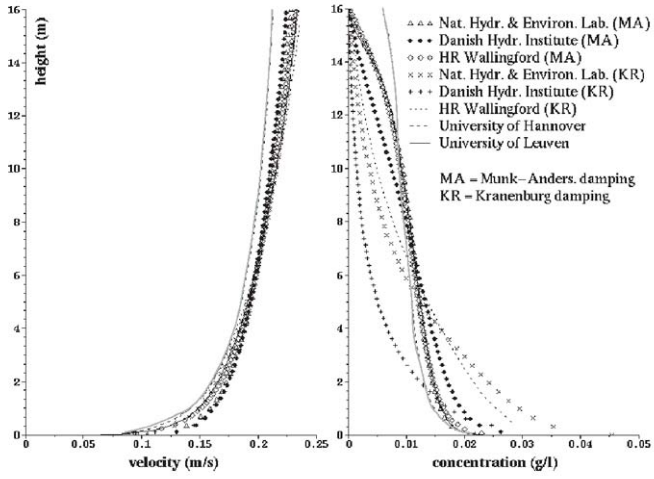

Fig. 13: Velocity and Concentration Distributions in the 1-DV Schematic Study (after Violeau et al., 2002)

3.5.1.2. 2-DV Schematic Estuary

In order to compare operational numerical cohesive transport models on a consistent basis, a schematic meso-tidal estuary with cohesive sediment transport was modeled using 3D numerical models for flow, stratification and sediment transport. The estuary is 100 km long with water depths from 15 m at the seaward side to 1 m near the head, with a strong tidal (up to 5 m range) influence (Violeau *et al.*, 2002). A comparison of suspended sediment concentrations are shown in Fig. 14 and Fig. 15.

The data files include two-dimensional current and salinity profiles at selected times during neap and spring tidal cycles.

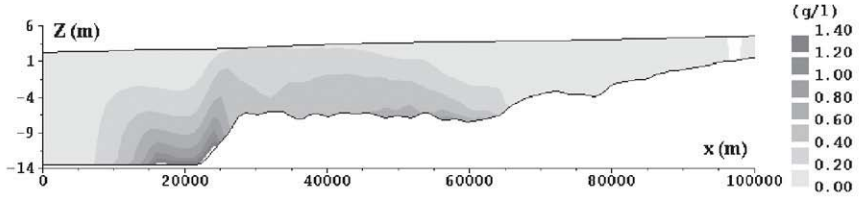

Fig. 14: 2D Schematic Estuary Case. Typical sediment distribution one hour before low tide (after Violeau et al., 2002)

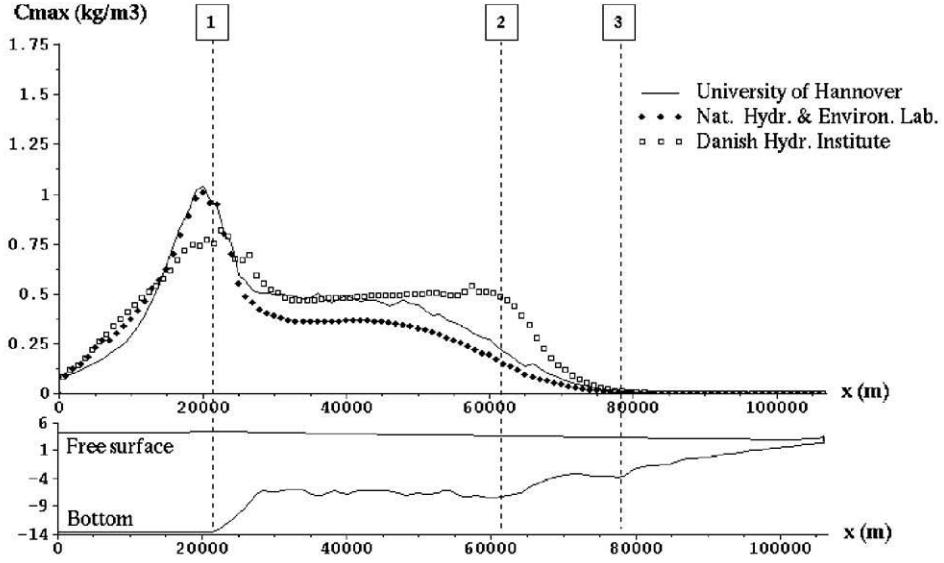

Fig. 15: Comparison of Numerical Models (after Violeau et al., 2002)

3.5.2. Case Studies

3.5.2.1. Tamar Estuary (DHI)

The upper reaches of the Tamar Estuary, a meso-tidal estuary with large quantities of cohesive sediments, has been modeled using an operational hydrostatic 3D numerical model, MIKE 3. The model solves the 3D hydrodynamic equations with a σ-coordinate transformation in the vertical and a Cartesian C-grid in the horizontal using an implicit ADI method for the coupled hydrodynamic equations and an explicit QUICK method for the transport equations. The model includes a k-ε turbulence model and buoyancy effects from salt transport and suspended sediments. The transport of suspended sediments is described using a single-phase model, which includes hindered settling, turbulence interactions and a single layer bed model without consolidation.

An idealized set up was made for the upper reach of the Tamar Estuary that enables a detailed representation of the vertical processes between two profiling stations where high-resolution measurements are available. The results show that the model does reproduce the general characteristics of the estuary, such as the asymmetric tidal flow, the intrusion of dense salt water and the stratification in the upper estuary. The simulations of suspended sediments also indicates that characteristic processes as the periodic occurrence of a turbidity maximum and the up estuary net transport of material are well represented. The results stress the importance of horizontal processes in the description of sediment processes.

The data include currents, salinities and suspended particle concentrations during spring and neap tidal cycles.

3.5.2.2. Loire (LNH)

The macro-tidal Loire estuary, located in western France experiences large river discharge fluctuations. The total mass of fluid mud in the estuary is estimated to be 1.5 million tons (Cheviet *et al.,* 2002). Suspended sediment concentrations range from 20 to 50 mg/l in the upper estuary to several g/l in the turbidity maximum. The concentration within the fluid mud layer range between 50 and 200 g/l.

The Loire was simulated using the finite element TELEMAC-3D model developed by LNH with extensions from UHA. The model uses a σ - transformation and operator splitting. For the Loire a Prandtl mixing length formulation was used for turbulence closure.

The data include water levels, velocity and suspended sediment concentrations for a spring tide with a high river discharge (Cheviet *et al.*, 2002).

3.5.2.3. Weser (UHA)

The Weser estuary is a partially mixed mesotidal estuary located at the southern coast of the North Sea. The tidal range is generally between 2.5 and 3.5 m. The estuary reach of 70-80 km is bounded at the upstream end by the Hemelingen weir (km -5), whereas the mouth of the estuary is located near Bremerhaven. A turbidity maximum exists between km 42 and km 60 and was investigated during the MASEX 85 experiment (Mud And Suspended sediment

Experiment, funded by the BMBF through the KfKI, Riethmüller et al., 1988). A five day period of this experiment was simulated, whereby in-situ measurements of velocity, salinity and turbidity (1m and 3m above bottom) at different locations indicated as Q1 (km 35,0); Q2 (km 45,3); Q3 (km 52,7) and -Q4 (km 59,5) are available. Q4 was used as the ocean boundary condition (Q4); Q1-Q3 for model validation.

The numerical model of the Weser estuary was developed by Malcherek (1995) within previous MAST projects. The computational mesh reaches from the cross-section Q4 at km 59.5 to the Hemelingen weir at km -5. It consists of 1485 nodes and 2276 elements in the horizontal plane; 12 non-equidistant layers were used for the vertical discretization. The initial conditions and the open boundary conditions used in the present study are the same as Malcherek used in his model.

The most important difference from the former work regards the turbulence modelling. In contrast to the previous used algebraic mixing length model, a two equation turbulence model, namely the k-ω model, has been implemented to determine the eddy viscosity. Application of this turbulence model has shown that the sensitivity to the shear velocity and to the relationship between both turbulent quantities is obviously less than that in the k-ε model and thus the results are more reliable. The k- ω model also seems to be more universal.

It also has two further improvements when compared with the k-ε model, namely, it is possible to integrate through the viscous sublayer and the model is known to perform better in flows with adverse pressure gradients (Fredsøe et al., 1999; Patel and Yoon, 1995; Wilcox, 1993).These advantages are, however, of minor importance for this study.

The data are measured and calculated water levels as well as velocities and concentrations 1m and 3m above ground over the study period.

4. CONCLUSIONS

Within this project extensive laboratory, field and numerical data have been collected. The data were stored as meta-data within the COSINUS data base which is available under

http://www.hydromech.uni-hannover.de/cosinus/database/.

Through the home page one can transfer to the local home page of the partner responsible for the data set. This was found to be an acceptable procedure during the project phase.

A meta-data base is an effective way of transferring and storing data during the project phase. In order to document the data base following project completion (September 30, 2000), it was necessary to transfer as much of the data as possible to the data base manager and to store the meta-data and the data on a CD. A copy of this CD is attached to the proceedings. Without this step, at least some of the data would eventually be lost since the maintenance of the links to the data requires intensive control.

5. ACKNOWLEDGEMENTS

This project was financially supported in part by the Commission of the European Community, DG XII, MAST-3 COSINUS Project (contract no. MAS3-CT97-0082). The author also thanks Jens Wyrwa for his part in the development of the data management program and Dirk Ditschke for his support in its administration.

6. LITERATURE

Booij R., and W.S. Uijttewaal. 1999. Modelling of Flow in Rotating Annular Flumes. In: *Proc. of the 4th Int. Symp. in Engineering Turbulence Modelling and Experiments*, Rodi, W. and Laurance, D. (eds.). Ajaccio, Corsica, France, 1999. 339-348.

Bruens A.W., J.C. Winterwerp and C. Kranenburg. 2002. Physical Modelling of Entrainment by a Concentrated Benthic Suspension. In: *Fine Sediment Dynamics in the Marine Environment,* Winterwerp, J.C. and C. Kranenberg (eds.), Elsevier, Amsterdam, 109-124.

Berlamont, J.E. and E.A. Toorman (eds.). 2000. *COSINUS Final Scientific Report.* Hydraulics Laboratory, K.U. Leuven.

Cheviet C., D. Violeau and M. Guesmia. 2002. Numerical Simulation of Cohesive Sediment Transport in the Loire Estuary with a Three-Dimensional Model Including New Parameterisatons. In: *Fine Sediment Dynamics in the Marine Environment,* Winterwerp, J.C. and C. Kranenberg (eds.), Elsevier, Amsterdam, 529-544.

Dearnaley, M., W. Roberts, S. Jones, K. Leurer, D.G. Lintern, L.M. Merckelbach, G.C. Sills, E.A. Toormann and J.C. Winterwerp. 2002. Measurements and Modelling of the Properties of Cohesive Sediment Deposits. In: *Fine Sediment Dynamics in the Marine Environment*, Winterwerp, J.C. and C. Kranenberg (eds.), Elsevier, Amsterdam, 57-74.

Dyer K.R., A.J. Bale, M.J. Christie, N. Feates, S. Jones and A.J. Manning. 2002. The Turbidity Maximum in a Mesotidal Estuary, the Tamar Estuary, U.K.: I and II. In: *Fine Sediment Dynamics in the Marine Environment,* Winterwerp, J.C. and C. Kranenberg (eds.), Elsevier, Amsterdam, 203-232.

Fredsøe, J., K.H. Anderson and B.M. Sumer. 1999. Wave Plus Current Over a Ripple Covered Bed. *Coastal Engineering,* 38, 177-221.

Kranenburg C. and J.C. Winterwerp. 1997. Entrainment of Fluid Mud Layers in Entrainment Model. *Journal of Hydraulic Engineering,* ASCE, 1236, 504-511.

Kranenburg C. 1998. *Saturation Concentrations of Suspended Fine Sediment. Computations with the Prandtl Mixing-Length Model.* Report No. 5-98, Faculty of Civil Engineering and Geosciences, Delft University of Technology.

Le Hir, P. 1997. Fluid and Sediment Integrated Modelling Application to Fluid Mud Flows in Estuaries. In: *Cohesive Sediments,* Burt, N., Parker, W.R. and Watts, J. (eds.). John Wiley & Sons, 417-428.

Lintern, D.G., G.C. Sills, N. Feates and W. Roberts. 2002. Erosion Properties of Mud Beds Deposited in Laboratory Settling Columns. In: *Fine Sediment Dynamics in the Marine Environment,* Winterwerp, J.C. and C. Kranenberg (eds.), Elsevier, Amsterdam, 343-358.

Lintern, D.G., and G.C. Sills. 2000. *Description and Discussion on Flocculation and Consolidation Properties of Tamar Estuary Sediment.* Report, Dept. of Engineering Science, Oxford University.

Malcherek, A. 1995. *Mathematische Modellierung von Strömungen und Stofftransport-prozessen in Ästuarien.* Ph.D. Dissertation, I.f. Strömungsmechanik und Elektronisches Rechnen im Bauwesen, Hannover University, Germany Report Nr. 44.

Manning, A.J. and K.R. Dyer. 2002. A Comparison of Floc Properties Observed During Neap and Spring Tidal Conditions. In: *Fine Sediment Dynamics in the Marine Environment,* Winterwerp, J.C. and C. Kranenberg (eds.), Elsevier, Amsterdam, 233-250.

Merckelbach, L.M., C. Kranenburg and J.C. Winterwerp. 2002. Strength Modelling of Consolidating Mud Beds. In: *Fine Sediment Dynamics in the Marine Environment*, Winterwerp, J.C. and C. Kranenberg (eds.), Elsevier, Amsterdam, 359-374.

Mory, M., N. Gratiot, N., A.J. Manning and H. Michallet. 2002. CBS Layers in a Diffusive Turbulence Grid Oscillation Experiment. In: *Fine Sediment Dynamics in the Marine Environment*, Winterwerp, J.C. and C. Kranenberg (ed.), Elsevier, Amsterdam, 139-154.

Patel, V.C. and J.Y. Yoon. 1995. Application of a Turbulence Model to Rough Surfaces. *Journal of Fluids Engineering,* 117, 234-241.

Petersen, O. and H.J. Vested. 2002. Description of Vertical Exchange Processes in Numerical Mud Transport Modelling. In: *Fine Sediment Dynamics in the Marine Environment,* Winterwerp, J.C. and C. Kranenberg (eds.), Elsevier, Amsterdam, 375-392.

Petersen, O., H.J. Vested, A.M. Manning, M. Christie and K.R. Dyer. 2002. Numerical Modelling of Mud Transport Processes in the Tamar Estuary. In: *Fine Sediment Dynamics in the Marine Environment,* Winterwerp, J.C. and C. Kranenberg (eds.), Elsevier, Amsterdam, 643-654.

Riethmüller, R., H.-U. Fanger, I. Grabemann, H.L. Krasemann, K. Ohm, J. Böning, L.J.R. Neumann, G, Lang, M. Markofsky, R. Schubert. 1988. Hydrographic Measurements in the Turbidity Zone of the Weser Estuary. In: *Physical Processes in Estuaries.* Dronkers, J. and van Leussen, W. (eds.): Hamburg: Springer Verlag. 332-344.

Spearman, J.R. and W. Roberts. 2002. Comparison of Flocculation Models for Applied Sediment Transport Modelling. Measurements and Model Parameterisation of Floc Size and Settling Velocity. In: *Fine Sediment Dynamics in the Marine Environment,* Winterwerp, J.C. and C. Kranenberg (eds.), Elsevier, Amsterdam. 277-294.

Toormann, E.A. 2002. Modelling of Turbulent Flow with Suspended Cohesive Sediment. In: *Fine Sediment Dynamics in the Marine Environment*, Winterwerp, J.C. and C. Kranenberg (eds.), Elsevier, Amsterdam, 155-170.

Toorman, E.A., A.W. Bruens, C. Kranenburg and J.C. Winterwerp. 2002. Interaction of Suspended Cohesive Sediment and Turbulence. In: *Fine Sediment Dynamics in the Marine Environment,* Winterwerp, J.C. and C. Kranenberg (eds.), Elsevier, Amsterdam, 7-24.

Violeau, D., S. Bourban, C. Cheviet, M. Markofsky, O. Petersen, W. Roberts, J. Spearman, E.A.Toorman, H.J. Vested, and H. Weilbeer. 2002. Numerical Simulation of Cohesive Sediment Transport: Intercomparison of Several Numerical Models. In: *Fine Sediment Dynamics in the Marine Environment,* Winterwerp, J.C. and C. Kranenberg (eds.), Elsevier, Amsterdam, 75-90.

Wilcox, D.C. 1993. *Turbulence Modelling for CFD.* DCW Industries Inc., La Cañada, California.

Winterwerp, J.C. 2002. Scaling parameters for high-concentrated mud suspensions in tidal flow. In: *Fine Sediment Dynamics in the Marine Environment*, Winterwerp, J.C. and C. Kranenberg (eds), Elsevier, Amsterdam, 171-186.

Winterwerp, J.C. 1999. *On the Dynamics of High-Concentrated Mud Suspensions.* Ph.D. dissertation, Technische Universiteit Delft, Faculty of Civil Engineering and Geosciences.

Winterwerp, J.C., A.J. Bale, M.C. Christie, K.R. Dyer, S. Jones, D.G. Lintern, A.J. Manning and W. Roberts. 2002. Flocculation and Settling Velocity of Fine Sediment. In: *Fine Sediment Dynamics in the Marine Environment*, Winterwerp, J.C. and C. Kranenberg (ed.), Elsevier, Amsterdam, 25-40.

Winterwerp, J.C., A.W. Bruens, N. Gratiot, C. Kranenberg, M. Mory and E.A. Toormann. 2002. Dynamics of Concentrated Benthic Suspension Layers. In: *Fine Sediment Dynamics in the Marine Environment*, Winterwerp, J.C. and C. Kranenberg (eds.), Elsevier, Amsterdam, 41-56.

List of Contributors

Agrawa, Yogesh
Sequioa Scientific, Inc.
2700 Richards Rd.
Bellevue, WA 98005, USA
yogi@sequoiasci.com

Alkhalidi, Mohamad
Civil and Coastal Engrg.
Gainesville, FL 32608, USA
khalidi@ufl.edu

Alves, Maria C. M.
School of Engineering
Federal University of Rio de Janeiro
Brasil
tina@civil.ee.ufrj.br

Andersen, Thorbjoern
Univ. of Copenhagen, Denmark
Institute of Geography
Copenhagen, Denmark
tja@geogr.ku.dk

Bass, Sarah J.
Institute of Marine Studies
University of Plymouth
Plymouth, Devon, PL4 8AA, U.K.
sbass@plymouth.ac.uk

Baugh, John V.
HR Wallingford
Estuaries and Dredging Group
Oxon, UK
jvb@hrwallingford.co.uk

Bhattacharya, B.
International Institute for Infrastructural
Hydraulic and Environmental
Engineering
P.O. Box 3015
2601 DA Delft, The Netherlands
bha@ihe.nl

Bohlen, W. Frank
University of Connecticut
Department of Marine Sciences
Avery Point, Groton, CT 06340-6048,
USA
bohlen@uconnvm.uconn.edu

Brennan, Matthew L.
Department of Civil and Environmental
Engineering
Stanford University, USA
mbrennan@alumni.princeton.edu

Bui, D. Tai
Weslake Inc.
10-120 Lancing Dr.
Hamilton, ON, Canada, L8W 3A1
bui@weslake.com

Chang, Tae S.
Senckenberg Institute
Division of Marine Research
Wilhelmshaven, Germany
taesoo.chang@sam.terramare.de

Chien, Hwa
National Cheng Kung Univ.
Coastal Ocean Monitoring Center
Tainan, 700, Taiwan, ROC
hchien@mail.ncku.edu.tw

Chisholm, Thomas
Oregon Graduate Institute
School of Science and Engineering
Oregon Health and Science University
chisholm@ese.ogi.edu

Costa, Maria Amélia
School of Engineering
University of Minho
4800-058 Guimarães, Portugal
ameliac@dem.uminho.pt

Dankers, Petra J.T.
Hydraulic Engineering Section
Faculty of Civil Engineering and Geosciences
Delft University of Technology
PO BOX 5048
2600 GA Delft, The Netherlands
p.j.t.dankers@citg.tudelft.nl

de Boer, Gerben J.
Environmental Fluid Mechanics Section
Delft University of Technology
Delft, 2600 GA, The Netherlands
g.j.deboer@cibg.tudelft.nl

Ditschke, Dirk
Hannover Univ.
Fluid Mechanics Institute/ Civil Engr.
30167 Hannover, Germany
ditschke@hydromech.uni-hannover.de

Friedrichs, Carl T.
Virginia Institute of Marine Science
School of Marine Science
College of William and Mary
Gloucester Point, VA 23062, USA
cfried@vims.edu

Gailani, Joseph
Engineer Research and Development Center
US Army Corps of Engineers
3909 Halls Ferry Rd.
Vicksburg, MS 39180-6199, USA
Joe.Z.Gailani@erdc.usace.army.mil

Ganju, Neil K.
U.S. Geological Survey
6000 J Street
Sacramento, CA 95819, USA
nganju@usgs.gov

Ha, Ho-Kyung
Virginia Institute of Marine Science
School of Marine Science
College of William and Mary
Gloucester Point, VA 23062, USA
hokyung@vims.edu

Harris, Courtney K.
Virginia Institute of Marine Science
School of Marine Science
College of William and Mary
Gloucester Point, VA 23062, USA
ckharris@vims.edu

Hayter, Earl J.
U.S. Environmental Protection Agency
National Exposure Research Laboratory
Athens, GA 30605, USA
hayter.earl@epa.gov

He, Qing
State Key Lab. of Estuarine and Coastal Research
East China Normal University
Shanghai, 200062, China
qinghe@sklec.ecnu.edu.cn

Holland, Charles W.
The Pennsylvania State University
Applied Research Laboratory
State College, PA, USA
holland-cw@psu.edu

Hollins, Suzanne E.
Environment Division
Australian Nuclear Science and Technology Organisation
New Illawarra Road
Lucas Heights, NSW, 2234, Australia
sho@ansto.gov.au

Hsu, Tai-Wen
Dept. of Hydraulic and Ocean Engineering
National Cheng Kung University
Tainan 701, Taiwan
twhsu@mail.ncku.edu.tw

Hwang, Kyu-Nam
Department of Civil and Environmental Engineering
RICT, Chonbuk National University
Chonju 561-756, Korea
khwang@moak.chonbuk.ac.kr

Jago, Colin F.
School of Ocean Sciences
University of Wales, Bangor
Marine Science Laboratories
Menai Bridge, Gwynedd L59 5AB, UK
c.f.jago@bangor.ac.uk

James, Scott
Sandia National Laboratories
Geohydrology Dept.
Albuquerque, CA 87185-0735, USA
scjames@sandia.gov

Jay, David A.
Dept. of Environmental and Biomolecular Systems
OGI School of Science and Engineering
Oregon Health and Science University
Beaverton, OR 97006-8921, USA
djay@ese.ogi.edu;

Joerdel, Olaf
Senckenberg Institute
Dept. of Marine Science
Wilhelmshaven, Germany
olaf@joerdel.de

John, Chandy
St. Johns River Water Management District
Water Resources
Palatka, FL 32178-1429, USA
cjohn@sjrwmd.com

Kao, Chia-Chuen
Dept. of Hydraulic & Ocean Engrg.
National Cheng Kung Univ.
Tainan, 700, Taiwan, ROC
kaoshih@mail.ncku.edu.tw

Keen, Timothy
Naval Research Laboratory
Ocean Dynamics & Prediction Branch
Stennis Space Ctr., MS 39529, USA
kcooper@nrlssc.navy.mil

Kim, Sung-Chan
Environmental Lab.
Engineer Research and Development Center
US Army Corps of Engineers
CEERD-EP-W, 3909 Halls Ferry Rd.
Vicksburg, MS, USA
Sung-Chan.Kim@erdc.usace.army.mil

Kirby, Robert
Ravensrodd Consultants Ltd.
6 Queen's Drive
Taunton, Somerset, TAI4XW, UK
robkirby@globalnet.co.uk

Kniskern, Tara
Virginia Institute of Marine Science
School of Marine Science
College of William and Mary
Gloucester Point, VA 23062, USA
knista@vims.edu

Koreyoshi, Yamasaki
Fukuoka Univ.
Civil Engrg.
Fukuoka, 814-0180, Japan
yama@fukuoka-u.ac.jp

Krishnappan, Bommanna
National Water Research Institute-Environment Canada
Aquatic Ecosystem Impacts Research Branch
Burlington, Ontario, L7R4A6, Canada
bommanna.krishnappan@ec.gc.ca

Kusuda, Tetsuya
Kyushu University
Urban and Environmental Engrg.
Kukuoka, 812-8581, Japan
kusuda@civil.kyushu-u.ac.jp

Kwon, Jae-Il
Virginia Institute of Marine Science
School of Marine Science
College of William and Mary
Gloucester Point, VA 23062, USA
jikwon@vims.edu

Lee, Cheegwan
Univ. of Michigan/ CILER
Ann Arbor, MI 48103, USA
cheegwan@hanmail.net

Lee, Dong-Young
Coastal and Harbour Engineering
Research Center
Korea Ocean Research and Development
Institute
Ansan P.O.Box 29
Ansan 425-600, Korea
dylee@kordi.re.kr

le Hir, Pierre
IFREMER
Centre IFREMER de Brest,
BP 70, 29280
Plouzané, France
plehir@ifremer.fr

Lick, Wilbert
Univ. of California
Mechanical & Environmental Engrg.
Santa Barabra, CA 93106, USA
willy@erode.ucsb.edu

Lin, Jing
Virginia Institute of Marine Science
School of Marine Science
College of William and Mary
Gloucester Point, VA 23062, USA

Lumborg, Ulrik
Univ. of Copenhagen
Institute of Geography
Copenhagen, DK-1350, Denmark
ul@geogr.ku.dk

Maa, Jerome P.-Y.
Virginia Institute of Marine Science
School of Marine Science
College of William and Mary
Gloucester Point, VA 23062, USA
maa@vims.edu

Maggi, Federico
Delft Univ. of Technology
Environmental Fluid Mechanics
Delft, 2600 GA, The Netherlands
f.maggi@et.tudelft.nl

Manning, Andrew
Univ. of Plymouth
School of Earth, Ocean and
Environmental Science
Plymouth, PL48AA, UK
andymanning@yahoo.com

Markofsky, Mark
Hannover Univ.
Fluid Mechanics Institute/ Civil Engr.
30167 Hannover, Germany
mark@hydromech.uni-hannover.de

McAnally, William
Mississippi State Univ.
Civil Engrg., MSU, MS 39762, USA
mcanally@engr.msstate.edu

Mehta, Ashish
Univ. of Florida
Civil and Coastal Engrg.
Gainesville, FL 32611, USA
Mehta@coastal.ufl.edu

Merckelbach, Lucas
NIOZ Netherlands Institute for Sea Research
P.O. Box 59, NL-1790 AB Den Burg
Texel, The Netherlands
merckel@nioz.nl

Mitchell, Steven
Univ. of Brighton
School of Environment
Brighton, BN2 4GJ, UK
s.b.mitchell@bton.ac.uk

Nakagawa, Yasuyuki
Port and Airport Research Institute
Sedimentary Environments Division
Yokusuka, 239-0826, Japan
y.nakagawa@ipc.pari.go.jp

Nelson, Bruce
Univ. of Virginia
PO Box 400123, Clark Hall
Charlottesville, VA 22904-4123, USA
bwn@b.mail.virginia.edu

Neumann, Luis
The Univ. of Queensland
Environmental Engrg.
Brisbane, Queensland 4072, Australia
luisn@cheque.uq.edu.au

O'Neil, Sean
HydroQual, Inc.
Mahwah, NJ 07430, USA
soneil@hydroqual.com

Ou, Shan-Hwei
National Cheng Kung Univ.
Dept. of Hydraulic & Ocean Engrg.
Tainan, 701, Taiwan, ROC
oush@mail.ncku.edu.tw

Parchure, Trimbak
U.S. Army, ERDC
Coastal and Hydraulics Laboratory
Vicksburg, MS 39180, USA
parchut@wes.army.mil

Park, Kwang-Soon
Korea Ocean Research and Development Institute
Coastal and Harbor Engrg. Laboratory
Ansan, 425-600, Korea
kspark@kordi.re.kr

Peine, Florian
Univ. of Rostock
Marine Biology
Rostock 18055, Germany
florian.peine@biologie.uni-rostock.de

Pejrup, Morten
Univ. of Copenhagen
Institute of Geography
Copenhagen, 1350, Demark
mp@geogr.ku.dk

Riethmuller, Rolf
GKSS Resarch Centre
Institute for Coastal Research
Geesthacht, D-21502, Germany
riethmueller@gkss.de

Roberts, Jesse
Sandia National Laboratory
Environmental Security
Carlsbad, New Mexico 88220, USA
jdrober@sandia.gov

Romine, Heidi
Virginia Institute of Marine Science
School of Marine Science
College of William and Mary
Gloucester Point, VA 23062, USA
heidir@vims.edu

Sanford, Lawrence P.
Horn Point Laboratory
Univ. of Maryland
Cambridge, Maryland 21613, USA
lsanford@hpl.umces.edu

Schoellhamer, David H.
U.S. Geological Survey
Water Resources Division
Sacramento, CA 95819, USA
dschoell@usgs.gov

Scully, Malcolm
Virginia Institute of Marine Science
School of Marine Science
College of William and Mary
Gloucester Point, VA 23062, USA
mscully@vims.edu

Shi, Zhong
Dept. of Harbour & Coastal Engrg.
Jiao Tong Univ.
1954 Hua Shan Road
Shanghai 200030, China
zshi@sjtu.edu.cn

Shrestha, Parmeshwar
Exponent, Inc.
Irvine, CA 92618, USA
pshrestha@exponent.com

Sills, Gilliane
Univ. of Oxford
Engrg. Science
Oxford OX1 3PJ, UK
gilliane.sills@eng.ox.ac.uk

Silva Jacinto, Ricardo
IFREMER
Centre IFREMER de Brest
BP 70, 29280 Plouzané, France
Ricardo.Silva.Jacinto@ifremer.fr

Souza, Alejandro
Proudman Oceanographic Laboratory
6 Brownlow Street
Liverpool L3 5DA, UK
ajso@pol.ac.uk

Spearman, Jeremy
HR Wallingford
Estuaries and Dredging
Oxon, OX10 8BA, UK
jez@hrwallingford.co.uk

Stoschek, Oliver
Univ. of Hannover
Franzius-Institut
Hannover 30167, Germany
oliver.stoschek@fi.uni-hannover.de

van den Eynde, Dries
Management Unit of the North Sea
Mathematical Models
Royal Belgian Institute of Natural Science
Gulledelle 100, B-1200 Brussels, Belgium
m.fettweis@mumm.ac.be

van Kessel, Thijs
WL Delft Hydraulics
Marine and Coastal Management
Delft 2600 MH, TheNetherlands
thijs.vankessel@wldelft.nl

Verney, Romaric
Geology, Univ. of Rouen
76821 Mont Saint Aignan Cedex, France
romaric.varney@univ-rouen.fr

Vinzon, Susana
Programa de Engenharia Oceanica – COPPE
Universidade Federal do Rio de Janeiro
Caixa Postal 68508
Rio de Janeiro 21945-970, RJ, Brazil
susana@peno.coppe.ufrj.br

Wai, Onyx
The Hong Kong Polytechnic Univ.
Civil and Structural Engrg.
Kowloon, Hong Kong
ceonyx@polyu.edu.hk

Wang, Harry
Virginia Institute of Marine Science
School of Marine Science
College of William and Mary
Gloucester Point, VA 23062, USA
wang@vims.edu

Wang, Yuan-ye
State Key Lab. of Estuarine and Coastal Research
East China Normal University
Shanghai, 200062, China
wyy79cn@163.com

Warner, John
U.S. Geological Survey
Coastal & Marine Geology
Woods Hole, MA 02543, USA
jcwarner@usgs.gov

Watanabe, Ryoichi
Fukuoka Univ.
Civil Engrg.
Fukuoka, 814-0180, Japan
wata@fukuoka-u.ac.jp

Winterwerp, Johan C.
Delft Hydraulics and Delft Univ. of Technology
Marine and Coastal Management
P. O. Box 177
2600 MH, Delft, The Netherlands
han.winterwerp@wldelft.nl

Wu, Jiaxue
Tongji Univ.
Key Laboratory of Marine Geology
Shanghai 200092, China
jesse-wu@mail.tongji.edu.cn

Yamada, Fumihiko
Kumamoto Univ.
Civil and Environmental Engrg.
Kumamoto, 860-8555, Japan
yamada@kumamoto-u.ac.jp

Yamanishi, Hiroyuki
Univ. of Florida
Coastal and Oceanographic Engrg.
Gainesville FL, 32611, USA
yamanishi@coastal.ufl.edu

Zhang, Qing-He
Tianjin Univ.
School of Civil Engrg.
Tianjin, 300072, China
qhzhang@tju.edu.cn

Ziervogel, Kai
Baltic Sea Research Institute Warnemunde
Biological Oceanography
Rastock, D-18113, Germany
Kai.ziervogel@io-warnemeunde.de